REPORT DOCUMENTATION PAGE

AFRL-SR-AR-TR-02-

0392

Public reporting burden for this collection of information is estimated to average 1 hour per response, including the time for reviewing instructions, data needed, and completing and reviewing this collection of information. Send comments regarding this burden estimate or any other aspect of th this burden to Department of Defense, Washington Headquarters Services, Directorate for Information Operations and Reports (0704-0188), 1215 4302. Respondents should be aware that notwithstanding any other provision of law, no person shall be subject to any penalty for failing to compl valid OMB control number. **PLEASE DO NOT RETURN YOUR FORM TO THE ABOVE ADDRESS.**

1. REPORT DATE *(DD-MM-YYYY)* 01-10-2002	2. REPORT TYPE FINAL	3. DATES COVERED *(From - To)* 01-05-1997 – 30-04-2002

4. TITLE AND SUBTITLE Plasma Ramparts Using Metastable Molecules	5a. CONTRACT NUMBER
	5b. GRANT NUMBER F49620-97-1-0312
	5c. PROGRAM ELEMENT NUMBER
6. AUTHOR(S) Rich, Joseph W. Miles, Richard B.	5d. PROJECT NUMBER
	5e. TASK NUMBER
	5f. WORK UNIT NUMBER

7. PERFORMING ORGANIZATION NAME(S) AND ADDRESS(ES) Dept. of Mechanical Eng. Dept. of Mech. & Aerospace Eng. The Ohio State University RM D-410 206 W. 18th Ave. Engineering Quadrangle Columbus, OH 43210 Princeton University Princeton, NJ 08544	8. PERFORMING ORGANIZATION REPORT NUMBER

9. SPONSORING / MONITORING AGENCY NAME(S) AND ADDRESS(ES) Director of Defense Research Air Force Office of Scientific & Engineering Research Directorate of Physics And Electronics	10. SPONSOR/MONITOR'S ACRONYM(S) DDR&E AFOSR
	11. SPONSOR/MONITOR'S REPORT NUMBER(S)

12. DISTRIBUTION / AVAILABILITY STATEMENT

20021126 067

13. SUPPLEMENTARY NOTES

14. ABSTRACT

The main goals of this experimental and theoretical project were to demonstrate the ability to create a uniform and diffuse nonequilibrium air plasma at atmospheric pressure, with an electron density of 10^{13} cm^{-3}, a temperature below 2000 K, scalable to cubic meter size, with a low power budget. The Ohio State Consortium was focusing on use of efficient ionization sources, specifically e-beams and short pulse ionization wave generators, and on mitigation of electron removal by using laser energy addition to excite the vibrational modes of the air species. By this means, the power budget to sustain a stable plasma in low temperature, atmospheric pressure air is significantly reduced. The plasma decay time has been increased by more than two orders of magnitude. In addition, there have been major efforts to investigate the relevant ionization, electron removal, and energy transfer processes in such air plasmas, to model and analyze both e-beam and short pulse ionization sources in large volume air plasmas, to develop short pulse ionization wave generators, and to develop and employ advanced diagnostic methods to characterize the air plasmas produced. There have been major positive and novel results achieved in each of these areas.

15. SUBJECT TERMS

16. SECURITY CLASSIFICATION OF:			17. LIMITATION OF ABSTRACT	18. NUMBER OF PAGES	19a. NAME OF RESPONSIBLE PERSON
a. REPORT	b. ABSTRACT	c. THIS PAGE			19b. TELEPHONE NUMBER *(include area code)*

Standard Form 298 (Rev. 8-98)
Prescribed by ANSI Std. Z39.18

DISTRIBUTION STATEMENT A
Approved for Public Release
Distribution Unlimited

FINAL REPORT

PLASMA RAMPARTS USING METASTABLE MOLECULES

Nonequilibrium Thermodynamics Laboratories
Department of Mechanical Engineering
The Ohio State University

Applied Physics Group
Department of Mechanical and Aerospace Engineering
Princeton University

J. William Rich
Principal Investigator

Phone: (614) 292-6309
Fax: (614) 292-3163
E-mail: **rich.2@osu.edu**

TABLE OF CONTENTS

PLASMA RAMPARTS USING METASTABLE MOLECULES

FINAL REPORT

THE OHIO STATE UNIVERSITY

SUMMARY

This final report incorporates the results of research conducted at the Ohio State University and Princeton University under the "Air Plasma Ramparts" MURI program. The main goals of this experimental and theoretical work are to demonstrate the ability to create a nonequilibrium air plasma at atmospheric pressure, with electron density of 10^{13} cm^{-3} at low temperatures (T<2000 K), for an extended period of time (t>10msec). Further, the method used to create this plasma must allow scalability to volumes of the order of a cubic meter, the plasma must be uniform and diffuse, and the power required must be low, ideally, < 1 W/cm^3.

It has been recognized from the inception of this program that achieving these goals requires both: 1) one of the most efficient means of volume ionization possible, and 2), a method of greatly mitigating the free electron removal processes that exist in the plasma. For this reason, work by the Ohio State Consortium focused on use of efficient ionization sources, specifically e-beams and short pulse ionization wave generators, and on mitigation of electron removal by using laser energy addition to excite the vibrational modes of the air species. A "Definitive Experiment" was set up at Ohio State to demonstrate these methods. The definitive experiment is centered around the concept of using an electron beam as an efficient volume ionization source combined with optical pumping. The optical pumping is used to vibrationally excite diatomic molecules in the plasma in order to reduce the overall electron removal rate. By this means, the power budget to sustain a stable plasma in low temperature, atmospheric pressure air is significantly reduced.

The OSU electron beam / optical pumping facility was made fully operational and time-resolved electron density measurements in e-beam excited air plasmas with vibrational excitation of the air species using optical pumping were found to reduce the effective electron removal rates by orders of magnitude. The experimental results and modeling calculations are consistent with the following hypothesis for the effect of vibrational excitation on electron attachment to oxygen and electron-ion recombination in electron beam sustained atmospheric pressure air plasmas: i) since the electron affinity of O_2^- is only about 0.4 eV, vibrational excitation of O_2^- to vibrational levels v≥2 can provide sufficient energy for the detachment of the attached electron while charge transfer from O_2^- to vibrationally excited oxygen is

sufficiently rapid to make this process very efficient and ii) superelastic collisions of the initially cold secondary electrons produced by the electron beam with highly vibrationally excited molecules increase the electron temperature significantly to $T_e \approx 5000$ K which reduces the electron-ion recombination rate. The theoretical minimum power budget to overcome attachment and recombination in our vibrationally excited air plasmas was found to be approximately 50 W/cm^3, which represents a significant reduction compared to almost 2000 W/cm^3 in cold equilibrium air.

In addition, there have been major efforts prior to and in parallel with the definitive experiment to investigate the relevant ionization, electron removal, and energy transfer processes in such air plasmas, to model and analyze both e-beam and short pulse ionization sources in large volume air plasmas, to develop short pulse ionization wave generators, and to develop and employ advanced diagnostic methods to characterize the air plasmas produced. There have been major positive and novel results achieved in each of these areas, and this work is presented in the following sections of the report.

OSU/Princeton air plasma status

- Achieved electron densities: $n_e = 4 \times 10^{12}$ cm^{-3} at 0.5 atm

  $n_e = 2 \times 10^{12}$ cm^{-3} at 1.0 atm

- Power Budget at 1 atm. and $n_e = 2 \times 10^{12}$ cm^{-3} : 2 W/cm^3

- Electron density at 1 atm and **1 W/cm^3: 1.4 $\times$ 10^{12} cm^{-3}**

- Gas temperature: $\sim$ 500 K

- The plasma is volume-scalable, uniform, diffuse and free of electrodes and electrode surface processes.

1. ANALYSIS OF THE POWER BUDGET AND STABILITY OF HIGH-PRESSURE NONEQUILIBRIUM AIR PLASMAS

Igor V. Adamovich, J. William Rich, Andrey P. Chernukho, and Serguei A. Zhdanok

This section discusses the power budget and stability of high-pressure, high electron density, nonequilibrium air plasmas. Calculations using a detailed state-specific one-dimensional kinetic model show that, if ionization in the plasma is produced by an external electric field, an electron density of $n_e=10^{13}$ cm^{-3} is sustained at the power budget of more than 30 GW/m^3. This is due to the extremely low ionization efficiency (less than 0.1%) in nonequilibrium electric discharges. Therefore, the sole use of large-volume self-sustained discharges, whether the electric field is DC, RF, or microwave, is not feasible from the energy efficiency point of view. The plasma power budget can be substantially reduced by using an efficient external ionization source, such as an e-beam (ionization efficiency up to 40-50%). This will require 60 MW/m^3 to sustain an electron density of $n_e=10^{13}$ cm^{-3}.

Calculations using a quasi-one-dimensional kinetic model suggest that the required electron density is reached under conditions where plasma collapse may be likely and glow-to-arc transition may be difficult to control over long distances. This occurs due to strong coupling between ionization and heating. However, analysis of the experiments in the high-voltage atmospheric pressure discharge in air, as well as calculations using a two-dimensional model of the discharge show that the use of the ballast resistor stabilization allows sustaining a stable constricted nonequilibrium atmospheric pressure air discharge well into the arc transition regime. The region occupied by the constricted discharge is a few cm long and a few mm in diameter. The diameter of the plasma is primarily controlled by the ambipolar diffusion of the charged species out of the high-current region. The results of calculations show that the two-dimensional kinetic model used gives an adequate description of the kinetics and the energy balance of the high-voltage atmospheric pressure discharge in air.

1. Introduction

Sustaining large-volume plasmas in atmospheric pressure air presents an extremely challenging problem. Among the most critical technical issues that have to be addressed to resolve this problem are the plasma power budget and stability. Numerous aerospace applications such as supersonic flow control, supersonic combustion control, and nonequilibrium MHD propulsion require an ability to initiate and sustain large volume (~1 m^3), relatively cold (T<2000 K) diffuse plasmas in atmospheric air, with electron density up to n_e~10^{13} cm^{-3}. For these applications, a power budget of the order of 1–10 MW/m^3 is desired. Finally, these plasma conditions are to be maintained for relatively long times, at least for 10 msec.

These goals define a highly nonequilibrium molecular plasma. The simultaneous requirement of electron densities of 10^{13} cm^{-3} and gas temperatures at 2,000 K represent an enormous departure from thermodynamic equilibrium, and rule out the use of purely thermal plasmas, such as high temperature arc discharges, to achieve this result. This can be illustrated by simple estimates using the Saha equation for a thermal equilibrium air plasma. For example, to achieve the stated electron density by merely heating the air, a gas temperature of ~ 4300 K would have to be maintained. Conversely, if atmospheric-pressure air were maintained at only the desired maximum gas temperature of 2000 K, the equilibrium electron density would be only ~ 10^6 cm^{-3}, many orders of magnitude below the desired value.

The preceding requirements have mandated examination of approaches using low-temperature nonequilibrium plasmas, of the general type characterized as glow discharges. Such systems have long been demonstrated to provide highly nonequilibrium plasmas, with relatively high free electron densities, with the requisite lower gas temperatures. However, if self-sustained discharges, lacking an external ionization source, are used, such glows are usually only struck at low pressures, well below even 0.1 atm pressure. Various methods have been used to extend the range of such self-sustained discharges to near atmospheric pressures, such as the use of individually ballasted multiple cathodes, short duration radio frequency high-voltage pulse stabilization, or aerodynamic stabilization [1-4]. Typically, however, the energy efficiency of such discharges is much lower than desired for the present goal, since only a small fraction of the input electrical power goes into ionization. As an example of operation of a nonequilibrium atmospheric pressure discharge in air, the present paper discusses earlier experimental results obtained at Chemical Physics Laboratory of A.V.Lykov Heat and Mass Transfer Institute in Minsk, Belarus [5-9]. The kinetics and energy balance in this strongly spatially nonuniform discharge are analyzed using a two-dimensional nonequilibrium flow code coupled with the key relaxation and chemical processes occurring in the air plasma, developed at Ohio State.

An alternative approach is the use of non-self-sustained glow discharges, in which some or all of the required volume ionization is provided by an external source, such as an electron beam [10,11]. Electron beams are identified as having by far the lowest power budget among all nonequilibrium ionization methods. Further, reliance on an external ionization source mitigates another principal difficulty known to exist in high-pressure discharges at large current densities. The well-known glow-to-arc-transition, with subsequent plasma thermalization, can be significantly delayed or avoided altogether. Finally, recent experiments in nonequilibrium plasmas optically pumped by a CO laser suggest a possibility of modification of electron removal rates in non-self-sustained plasmas by controlling metastable species concentrations and excited state populations [12,13]. This effect can be used to significantly reduce the power budget of electron beam sustained plasmas.

Quantitative prediction of the power budget of high-pressure air plasmas requires a model that contains not only realistic chemistry rates for the neutral and ionic species, but also processes of production and decay of excited metastable states, in particular vibrational states, and their coupling with free electrons. These latter features are essential for air plasmas, inasmuch as the free electron energies are closely coupled with the nitrogen and oxygen vibrational modes. Under these circumstances, it is impossible to transfer energy from an imposed electric discharge field to free electrons without also exciting molecular vibrational states. Accordingly, a rather detailed kinetic model of the air plasma is used for the quantitative analysis of the power budget.

2. Power budget of self-sustained and non-self-sustained air discharges

To evaluate the power budget of nonequilibrium atmospheric air plasmas, we used a nonequilibrium flow code developed at Ohio State [14,15]. The code incorporates (i) vibrational nonequilibrium of air, (ii) realistic air chemistry, including vibrationally nonequilibrium reactions, (iii) kinetics of free electrons heated by the field (vibrational and electronic excitation, ionization, recombination, and attachment), (iv) ionization by a high-energy e-beam, and (v) one-dimensional gas dynamics. The code explicitly uses a master equation to calculate the vibrational level populations of N_2, O_2, and NO, and a coupled Boltzmann equation to calculate the free electron energy distribution function. The code has been extensively validated by comparison with numerous experiments, such as electron swarm data in N_2, O_2, and air [16,17], nonequilibrium NO formation behind the shock wave [14], and alkali-seeded and unseeded air MHD accelerator performance data [15].

To explore the issues raised in Section 1, we first used the code to model an air plasma initially at equilibrium at P=1 atm, T=2000 K ($n_e \cong 3 \cdot 10^6$ cm^{-3}). A constant electric field is applied to the plasma, thereby heating free electrons, producing more ionization, and slowing down electron-ion recombination, until complete steady state is reached. Such a process models applying a transverse DC or RF bias to a pair of electrodes in the already relatively hot plasma. The 2,000 K temperature is chosen to represent the maximum temperature allowable by the research goal. For this initial modeling, this gas temperature is assumed constant, i.e. all Joule heat is removed. Results of the calculations are summarized in Fig. 1. It can be seen that electron densities in excess of $n_e = 10^{13}$ cm^{-3} can be reached at electron temperatures of $T_e \sim 17,000$ K (a typical value of T_e in glow discharges, see Fig. 1(a,b)). At these conditions, the power to sustain $n_e = 10^{13}$ cm^{-3} exceeds 30 GW/m^3 (see Fig. 1(c)). The prohibitively high power budget is entirely due to the extremely inefficient ionization. Indeed, from Fig. 1(d), one can see that less than 0.1% of the input power goes into direct ionization. This means that the remaining 99.9% goes to vibrational and electronic excitation (and ultimately to heat), i.e. is wasted. Although vibrational excitation of the gas somewhat improves ionization efficiency, this effect is not very significant (within a factor of two).

It is obvious that a dramatic power budget reduction can be potentially achieved by increasing ionization efficiency. For example, improving the ionization efficiency from 0.1% to 100% would reduce the power budget by about 3 orders of magnitude, down to ~30 MW/m^3. This level of power reduction can be approached by producing ionization by a high-power electron beam, instead of using an electric field, or by short duration high-voltage high repetition rate pulses.

In the second series of calculations, an equilibrium air plasma at P=1 atm, T=2000 K is excited by a uniform electron beam, until complete steady state is reached. Again, the gas temperature is assumed to remain constant at 2,000 K. Results are shown in Fig. 2. It can be seen that the power budget at $n_e=10^{13}$ cm^{-3} is dramatically reduced, down to 60 MW/m^3 (i.e. by a factor of 500 compared to field ionization). This power loading corresponds to an e-beam current density of $j_{beam}=20$ mA/cm^2. The ionization efficiency of the beam is 44%. Note that the use of a high-energy electron beam is equivalent to heating the electrons up to very high energies (10 keV and higher), compared to the electron heating by an electric field (1-2 eV). We emphasize that it is the use of these high electron energies that allows a dramatic increase in ionization efficiency. Figure 3 plots the power budget of the electric field sustained and e-beam sustained air plasmas as a function of the electron density. Further power budget reduction might be achieved only by reducing the electron removal rates. In particular, recent results obtained in nonequilibrium plasmas optically pumped by a CO laser [12,13] suggest that production of large amounts of metastable species in the plasma may result in a significant reduction of both dissociative recombination and the electron attachment rates.

In the next two series of calculations, the gas temperature is no longer assumed constant, and gas heating by the applied field or by the e-beam is allowed. The gas is flowing in a constant cross section area adiabatic channel 10 cm in diameter, with an initial velocity of 100 m/s, and (a) with a uniform electric field of 2500 V/cm, or (b) with a uniform e-beam with a current density of $j_{beam}=20$ mA/cm^2 applied in the channel. Results are summarized in Fig. 4. It can be seen that if ionization is produced by the field, at x≅6 cm both electron density and temperature sharply increase. This occurs because ionization is strongly coupled to gas heating by the field (so-called runaway ionization or heating instability [1,2]). It might be difficult to delay this runaway ionization since this would require extremely rapid heat removal. A nonequilibrium plasma with $n_e=10^{13}$ cm^{-3} is therefore not likely to be sustained over distances longer than ~1 mm (or ~1 cm if the initial flow velocity is 1000 m/s). This type of behavior represents a well-known effect of the glow-to-arc transition in a positive column of the glow discharge. This effect would result in a major collapse of the entire discharge, so that the nonequilibrium plasma conditions could not be sustained. On the other hand, if ionization is produced by an e-beam, no runaway ionization occurs, and the gas temperature profile becomes much more uniform (see Fig. 4).

In the final series of calculations, the approach is the same as for the conditions of Fig. 4 but the channel is no longer adiabatic. Gas temperature is prevented from rising and kept nearly constant by tailoring the wall heat flux. It is assumed that the axial temperature profile is uniform (one-dimensional flow model). The results are summarized in Fig. 5. It can be seen that if ionization is produced by the field, keeping the temperature nearly constant at T=2000 K, sustaining the electron density of $n_e=10^{13}$ cm^{-3} would require a wall heat flux of nearly 80 kW/cm^2. For a 1 m diameter channel, the calculated wall flux reaches about 800 kW/cm^2. On the other hand, if ionization is produced by an e-beam, the wall heat flux to keep the gas temperature nearly constant is about 150 W/cm^2 (or 1.5 kW/cm^2 for a 1 m diameter channel).

The one-dimensional kinetic model used in the present calculations correctly predicts the onset of the heating instability development (such as constriction of the positive column of a glow discharge, see Fig. 4). However, it cannot predict the plasma conditions within the constricted discharge. First, the model does not take into account the external circuit, in particular, the ballast resistor that limits the discharge current and prevents the runaway ionization. Also, the model does not incorporate transport processes such as electron diffusion and heat conduction that may delay the heating instability development to some extent, and which control the diameter and the temperature of the constricted discharge. To illustrate the role of these processes in sustaining thermodynamic nonequilibrium and control of stability in high-pressure air discharges, the next section discusses the experiments and the modeling of the high-voltage atmospheric pressure discharge in air.

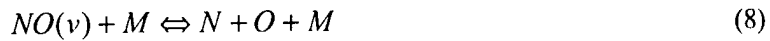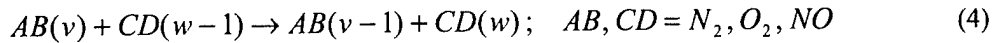## 3. Studies of a high-voltage atmospheric pressure discharges in air

3.1. Experimental

This type of electric discharge has been developed in the 1980's at Chemical Physics Laboratory of A.V.Lykov Heat and Mass Transfer Institute in Minsk, USSR [5-9]. The primary applications of the discharge have been in nonequilibrium plasma chemical synthesis, such as energy-efficient oxidation of atmospheric nitrogen [5] and dissociation of carbon dioxide [6], and in plasma material processing, such as nitriding of metal surfaces [7] and saturation of the high-temperature superconductors with oxygen [8]. This axial DC discharge is sustained between two pin or ring electrodes, typically 2 to 10 cm apart, in a quartz tube of 3-20 mm internal diameter. For large electrode separations, a separate pre-ionization circuit is used to first initiate the discharge between the cathode and the pre-ionization anode (see Fig. 6). In some cases, movable cathode has been used instead. The test gases enter the discharge tube from the cathode side and are exhausted into the atmosphere. The outer surface of the discharge tube can be cooled either by natural convection of air or by water. The discharge is powered by a 3 kW DC power supply

providing a maximum current of 200 mA. The discharge voltage and current can be varied in a range U=2-12 kV and I=30-200 mA, respectively. The mass flow rate through the discharge can be varied in a range G=100-800 g/hour. The discharge can be sustained in air, nitrogen, oxygen, and carbon dioxide at atmospheric pressure. In experiments with air, room air has been used and NO concentration has been measured in the discharge exhaust using analytical chemistry methods. The gas temperature at the discharge tube exit (a few cm downstream of the anode) has been measured using a Pt – Pt/Rh thermocouple.

3.2 Kinetic Model

Kinetic models and computer codes for modeling of high-voltage atmospheric pressure discharges in nitrogen, oxygen, and air have also been previously developed at Chemical Physics Laboratory [9,18-20], and further modified at Ohio State. In the present paper, we use a two-dimensional nonequilibrium flow code [9] coupled with the key relaxation and chemical processes occurring in the air plasma [18]. The model incorporates the following kinetic processes:

$$N_2 + e^- \rightarrow N_2(v) + e^-, \quad v = 1-8 \tag{1}$$

$$O_2 + e^- \rightarrow O_2(v) + e^-, \quad v = 1-3 \tag{2}$$

$$AB(v) + M \rightarrow AB(v-1) + M,$$
$$AB = N_2, O_2, NO; \quad M = N_2, O_2, N, O, NO \tag{3}$$

$$AB(v) + CD(w-1) \rightarrow AB(v-1) + CD(w); \quad AB, CD = N_2, O_2, NO \tag{4}$$

$$O_2 + e^- \rightarrow O + O \tag{5}$$

$$N_2(v) + M \Leftrightarrow N + N + M \tag{6}$$

$$O_2(v) + M \Leftrightarrow O + O + M \tag{7}$$

$$NO(v) + M \Leftrightarrow N + O + M \tag{8}$$

14

$$N_2(v) + O \Leftrightarrow NO + N \tag{9}$$

$$O_2(v) + N \Leftrightarrow NO(w) + O \tag{10}$$
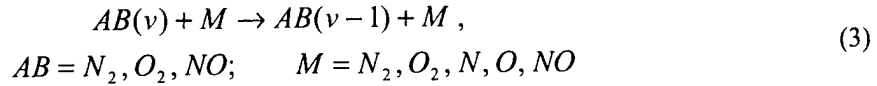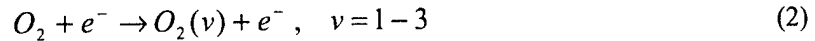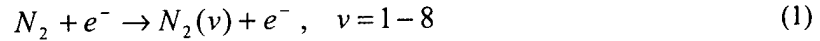
In Eqs. (1-10), v and w are the vibrational quantum numbers. This list of kinetic processes is based on the sensitivity analysis conducted using a much more detailed state-specific kinetic model discussed in Section 1 for modeling of relatively high-temperature (T>1500 K) nonequilibrium ionized reacting air flows [15]. The selected processes appear to be, by far, the most critical in such flows. At these temperatures, the vibrational mode disequilibrium of nitrogen and oxygen is not expected to be very strong. Therefore, vibrational kinetics of diatomic species is considered in the harmonic oscillator approximation.

The rates of vibrational excitation of N_2 and O_2, as well as of oxygen dissociation by electron impact are obtained from the solution of the Boltzmann equation [21]. The vibration-translation (V-T) relaxation times, as well as the rates of the vibration-vibration (V-V) energy exchange among the different diatomic species are taken to be the same as in [18]. The rates of the thermal chemical reactions are taken from [22]. The model assumes a simple dependence of the vibrationally stimulated state-specific chemical reaction rates k(v,T) on the vibrational quantum number [18],

$$k(v,T) \sim \begin{cases} A(T)\exp\left(-\dfrac{E_A - \theta v}{T}\right), & v \leq \dfrac{E_A}{\theta} \\ A(T) & , v > \dfrac{E_A}{\theta} \end{cases} \tag{11}$$

where A(T) and E_A are the pre-exponential factor and the activation energy in the Arrhenius expression for the thermal reaction rate coefficient k(T), respectively, and θ is the characteristic vibrational energy of a diatomic molecule. The state-specific rates k(v,T) are normalized on the thermal reaction rate coefficient.

The rate of electron impact ionization is determined from the following relation [23],

$$k_{ion} = A \cdot \exp\left[-\frac{B}{E/N} + \frac{Cz}{(E/N)^2}\right], \quad z = \exp\left[-\theta(N_2)\left(\frac{1}{T_v(N_2)} - \frac{1}{T}\right)\right] \tag{12}$$

where A is the electron-neutral collision frequency, E/N is the reduced electric field, $\theta_1(N_2)$=3353 K and $T_v(N_2)$ are characteristic vibrational energy of nitrogen and vibrational temperature of N_2, respectively. The coefficient B in Eq. (12) is a parameter adjusted to make the calculated discharge voltage equal to the experimentally measured voltage. This allows implicitly incorporating multiple electron impact ionization processes occurring in the discharge, including stepwise ionization from the electronically excited levels, whose rates have the same type exponential dependence on E/N. On the other hand, this approach also allows the overall power added to the discharge to be consistent with the experimental value. The last term in the exponential factor in Eq. (9) takes into account the effect of the superelastic collisions between electrons and nitrogen molecules on the impact ionization rate. The value of a coefficient C=43.5, obtained from the solution of the Boltzmann equation for the plasma electrons in air [23], turns out to be nearly the same for all high energy threshold impact excitation processes including such as excitation of electronic levels and ionization. The electron-ion recombination coefficient is taken as β_{ei}=$2 \cdot 10^{-7}(T/T_e)^{-0.5}$ cm^3/sec [1]. At the relatively high temperatures of T>1500 K, the effect of the complex ions such as N_4^+ and O_4^+, as well as the negative ions such as O_2^- and O^- is expected to be insignificant.

The model incorporates the parabolized Navier-Stokes equations in cylindrical geometry, the equations for the vibrational mode energies of N_2, O_2, and NO, the electron density equation, and the species concentration equations for N, N_2, O, O_2, and NO (see Appendix). The plasma is assumed to be quasineutral. The pressure gradient and the electric field at each axial location are found from the mass flow rate conservation and the discharge current conservation, respectively. Both the pressure gradient and the electric field are assumed to be changing only the axial direction. For these reasons, the model is not applicable for simulation of the flow field and the plasma kinetics near the discharge electrodes.

The boundary condition for the gas temperature on the wall is determined from the equality of the heat flux from the plasma into the wall and the discharge tube external cooling rate due to both natural convection by air and radiation (see Appendix).

3.3. Results and Discussion

Figure 7 shows a photograph of the discharge running in air at U=2.0 kV, I=50 mA, and G=240 g/hour. The discharge is sustained between a movable pin cathode and an annular anode 3 cm apart. The discharge tube internal diameter is 2 cm, while the apparent plasma diameter is much smaller, only about 4-8 mm. This implies that the discharge is in fact not wall-stabilized, unlike low-pressure diffuse glow discharges. In other words, the positive column of the discharge is already constricted, as discussed in Section 2.

Voltage current characteristics of the discharge in air for the tube diameter of 3.2 mm and the electrode separation of 5 cm and 7.5 cm are shown in Fig. 8. One can see that the discharge has a falling

voltage current characteristic, which indicates that it is sustained in the abnormal glow-to-arc transition regime [1,2] (region FG in Fig. 9), i.e. it is inherently unstable. The discharge stability in this case is controlled by a ballast resistor connected in series with the discharge tube, which limits the total current and prevents the discharge from converting into a high current arc. The limiting current, shown in Fig. 9, is $I_{max}=E_{max}/R$, where E_{max} is the maximum e.m.f. of the power supply, and R is the ballast resistance [1]. The voltage current characteristic of the discharge and the ballast resistor together is rising. From the data of Fig. 9, the power density in the discharge is in the range 0.5-1.0 kW/cm^3. The fraction of the total power delivered by the power supply dissipated by the ballast resistor is 40-60%.

Figure 10 plots the calculated cross-section averaged gas temperature and the experimental temperature at the exit of the 12.5 long discharge tube for the electrode separation of 5 cm (i.e. 7.5 cm downstream of the anode), showing good agreement. Figure 11 compares the experimental and the calculated mole fractions of nitric oxide at the exit of the discharge. The agreement is fair although one can see that the model underpredicts the NO concentrations by about a factor of two. We believe this to be mainly due to the use of a simplified kinetic model described in Section 3.2. However, the results displayed in Figs. 10,11 show that the model satisfactorily describes the kinetics and the overall energy balance of the discharge.

Figures 12-15 display various discharge plasma parameters for the following conditions: U=7.6 kV, I=40 mA, G=700 g/hour. Figure 12 plots the gas temperature, the vibrational temperature of N_2, and the electron temperature on the centerline of the discharge tube. Figure 13 shows the mole fractions of oxygen atoms and NO molecules, as well as the ionization fraction at the centerline. Figure 14 plots the radial distributions of the temperatures at the discharge exit (x=5 cm). Finally, Fig. 15 shows the axial distribution of the electron density at x=0.5, 1.3, and 3.0 cm. From these results, it is clear the ionization heating instability develops at 1.0<x<1.5 cm, with both the electron density and the gas temperature on the centerline rapidly rising, so that the discharge becomes constricted at x=1.3 cm (see Figs. 12,13). However, no runaway ionization (see Fig. 3) predicted by the one-dimensional model discussed in Section 2 occurs in this case. In the constricted discharge, the conditions at the centerline, where the electron density reaches $n_e \cong 10^{13}$ cm^{-3}, remain far from thermodynamic equilibrium (see Fig. 14,15). This occurs because the ballast resistor limits the total discharge current preventing it from short-circuiting and converting it into a hot equilibrium arc. In addition, the ambipolar diffusion prevents the high-current zone from shrinking below a few millimeters diameter, thereby limiting the current density and the centerline temperature. This effect makes the constricted discharge more diffuse at x>1.3 cm, reducing the electron density on the centerline (see Figs. 13,15).

Figure 16 presents the ratio of the discharge power going into ionization to the total discharge power. One can see that the ionization efficiency of the discharge is of the order of 0.1%. This result is generally

consistent with the predictions of the detailed state-specific kinetic model discussed in Section 2 (see Fig. 1(c)).

4. Summary

The calculations of the atmospheric pressure air plasma power budget (Section 2) suggest that, if ionization is produced by an electric field, an electron density of $n_e=10^{13}$ cm^{-3} is sustained at a power budget of more than 30 GW/m^3. This is due to the extremely low ionization efficiency (less than 0.1%) that prevails in nonequilibrium electric discharges (DC, AC, and RF). Therefore, the sole use of large-volume self-sustained discharges, whether the electric field is DC, RF, or microwave, is not feasible from the energy efficiency point of view.

A substantial part of the needed power budget reduction can be achieved by using an efficient external ionization source, such as an e-beam (ionization efficiency up to 40-50%). This will require 60 MW/m^3 to sustain electron density of $n_e=10^{13}$ cm^{-3}, if the electron removal process is not modified. A similar result can be potentially achieved by using short duration, high-voltage, high repetition rate pulses [3]. At the reduced electric field of $E/N=3\cdot10^{-15}$ V·cm^2, which in 2000 K air corresponds to the electric field of E~10 kV/cm, ionization efficiency of such pulses can reach approximately 10% [1]. Further power budget reduction from the 60 MW/m^3 level achieved by efficient ionization can be produced only by reducing the rate of electron removal. This may well be achieved by producing large amounts of metastable (e.g. vibrationally excited) species in the CO-seeded air using an efficient laser [12,13].

Calculations using a quasi-one-dimensional kinetic model (Section 2) suggest that the required electron density is reached under conditions where plasma collapse may be likely and glow-to-arc transition may be difficult to control over long distances. This occurs due to strong coupling between ionization and heating. However, analysis of the experiments in the high-voltage atmospheric pressure discharge in air (Section 3), as well as calculations using a two-dimensional model of the discharge, show that the use of ballast resistor stabilization allows sustaining a stable constricted nonequilibrium atmospheric pressure air discharge well into the arc transition regime. The region occupied by the constricted discharge is a few cm long and a few mm in diameter. The diameter of the plasma is primarily controlled by the ambipolar diffusion of the charged species out of the high-current region. The plasma volume can be scaled up by using multiple separately ballasted cathodes [24]. The results of calculations show that the two-dimensional kinetic model used gives an adequate description of the kinetics and the energy balance of the high-voltage atmospheric pressure discharge in air. The calculations of the discharge ionization efficiency are consistent with the predictions of the detailed state-specific kinetic model discussed in Section 2.

5. Appendix. Governing equations for the two-dimensional model of the air discharge

Motion equations for cylindrical geometry:

$$\frac{\partial(\rho u)}{\partial x} + \frac{1}{r}\frac{\partial(\rho v r)}{\partial r} = 0 \tag{13}$$

$$\rho u \frac{\partial u}{\partial x} + \rho v \frac{\partial u}{\partial r} = \frac{1}{r}\frac{\partial}{\partial r}\left(r\eta \frac{\partial u}{\partial r}\right) - \frac{dP}{dx} \tag{14}$$

Kinetic mode energy equation:

$$\rho c_P u \frac{\partial T}{\partial x} + \rho c_P v \frac{\partial T}{\partial r} = \frac{1}{r}\frac{\partial}{\partial r}\left(r\lambda \frac{\partial T}{\partial r}\right) + jE(1 - \sum_i \alpha_{vib,i}) + \rho R_0 \sum_i \frac{x_i}{\mu_i} \frac{\varepsilon_{vib,i} - \varepsilon_{vib,i}(T)}{\tau_{VT,i}}$$
$$- \rho \sum_i \left[h_i - \frac{R_0}{\mu_i}\varepsilon_{vib,i}(T)\right]\left(\frac{dx_i}{dt}\right)_{chem} - \rho \sum_i \frac{R_0}{\mu_i} x_i \left(\frac{d\varepsilon_i}{dt}\right)_{chem} \tag{15}$$

Vibrational mode energy equations (N_2, O_2, NO):

$$\rho x_i u \frac{\partial \varepsilon_{vib,i}}{\partial x} + \rho x_i v \frac{\partial \varepsilon_{vib,i}}{\partial r} = \frac{1}{r}\frac{\partial}{\partial r}\left(r\rho x_i D \frac{\partial \varepsilon_{vib,i}}{\partial r}\right) + \frac{jE\alpha_{vib,i}}{R_0/\mu_i} - \rho x_i \frac{\varepsilon_{vib,i} - \varepsilon_{vib,i}(T)}{\tau_{VT,i}}$$
$$+ \rho \sum_i x_i \left(\frac{d\varepsilon_i}{dt}\right)_{chem} \tag{16}$$

Electron density equation:

$$\frac{\rho}{\mu} u \frac{\partial y_e}{\partial x} + \frac{\rho}{\mu} v \frac{\partial y_e}{\partial r} = \frac{1}{r}\frac{\partial}{\partial r}\left(r\frac{\rho}{\mu} D_a \frac{\partial y_e}{\partial r}\right) + \left(\frac{\rho}{\mu}\right)^2 \left(k_{ion} y_e - \beta y_e^2\right); \quad y_e = \frac{n_e}{N} \tag{17}$$

Species concentration equations (N, N_2, O, O_2, NO):

19

$$\rho u \frac{\partial x_i}{\partial x} + \rho v \frac{\partial x_i}{\partial r} = \frac{1}{r} \frac{\partial}{\partial r} \left(r \rho D \frac{\partial x_i}{\partial r} \right) + \rho \left(\frac{dx_i}{dt} \right)_{chem} \; ; \quad x_i = \frac{\rho_i}{\rho} \tag{18}$$

Chemical reactions considered:

$$\sum_l a_l A_l \Leftrightarrow \sum_m b_m B_m \tag{19}$$

Rate of species i concentration change due to chemical reactions (running index j):

$$\left(\frac{dx_i}{dt} \right)_{chem} = \frac{\rho}{\mu} \sum_j \left[k_{f,j} \prod_l \left(\frac{x_l}{\mu_l} \right)^{a_l} - k_{r,j} \prod_m \left(\frac{x_m}{\mu_m} \right)^{b_m} \right] \tag{20}$$

Rate of species i vibrational energy change due to chemical reactions (running index j):

$$\left(\frac{d\varepsilon_i}{dt} \right)_{chem} = \frac{\rho}{\mu} \sum_j \left[\varepsilon_{f,j} \prod_l \left(\frac{x_l}{\mu_l} \right)^{a_l} - \varepsilon_{r,j} \prod_m \left(\frac{x_m}{\mu_m} \right)^{b_m} \right] \tag{21}$$

Mass flow rate integral and discharge current integral (used for dP(x)/dx and E(x) calculation):

$$G = \int_0^R \rho u r \, dr \; ; \quad I = \int_0^R e n_e w_{dr} (E/N) r \, dr \tag{22}$$

Boundary conditions on the discharge tube wall:

$$u = v = 0 \; ; \quad \lambda \left(\frac{\partial T}{\partial r} \right)_w = \left(\alpha_{conv} + \alpha_{rad} \right) \left(T_{wo} - T_\infty \right) \; ; \quad T_{v,i} = T \tag{23}$$

$$\left(x_i\right)_w = 0 \ (atomic\ species)\ ; \quad \left(\frac{\partial x_i}{\partial r}\right)_w = 0 \ (molecular\ species)\ ; \quad \left(y_e\right)_w = 0 \qquad (24)$$

Species vibrational temperatures and equilibrium vibrational energies:

$$T_{v,i} = \frac{\theta_i}{\ln\!\left(1 + \theta_i / \varepsilon_{vib,i}\right)}\ ; \quad \varepsilon_{vib,i}(T) = \frac{\theta_i}{\exp\!\left(\theta_i / T\right) - 1} \qquad (25)$$

7. References

1. Raizer, Y.P., "Gas Discharge Physics", Springer-Verlag, Berlin, 1991

2. E.P. Velikhov, A.S. Kovalev, and A.T. Rakhimov, "Physical Phenomena in Gas Discharge Plasmas", Moscow, Nauka, 1987

3. Generalov, N.A., V.P. Zimakov, V.D. Kosynkin, Yu.P. Raizer, and D.I. Roitenburg, Technical Physics Letters, vol. 1, p. 431, 1975

4. W. Rich, R.C. Bergman, and J.A. Lordi, AIAA J., vol. 13, p. 95, 1975

5. Zhdanok, S.A., Konysheva, N.B., Sergeeva, L.A., Soloukhin, R.I., and Yaremenko, A.I., "Experimental Study of Nonequilibrium Reaction of Nitrogen Oxidation in the High Voltage Atmospheric Pressure Discharge", Soviet Journal Doklady AN BSSR, Vol. 31, No. 2, p. 124-126, 1987

6. Zhdanok, S.A., Vasilieva, E.M., and Sergeeva, L.A., "Optimization of Parameters of the Nonequilibrium CO_2 Dissociation Process", Soviet Journal Vesti AN BSSR, Series Phys. Energ. Sc., No. 3, pp. 79-82, 1988

7. Zhdanok, S.A., Vasilieva, E.M., and Sergeeva, L.A., "Study of the High Voltage Atmospheric Pressure Discharge and its Application for Surface Treatment", Soviet J. of Engineering Physics, Vol. 58, No.1, pp.101-104, 1990

8. Zhdanok, S.A., Borodin, V.I., and Bumai, Yu .A., "The use of Oxygen Plasma of the High Voltage Atmospheric Pressure Discharge for Processing of High-Temperature Superconducting Ceramics", in "Heat and Mass Transfer with Phase and Chemical Transmissions", Heat and Mass Transfer Institute of Academy of Sciences of BSSR, pp. 3-11, Minsk, 1990

9. I.V. Adamovich, P.A. Apanasevich, V.I. Borodin, S.A. Zhdanok et al., "CARS Diagnostics of High-Voltage Atmospheric Pressure Discharge in Nitrogen", Springer Proceedings in Physics, vol. 63, "Coherent Raman Spectroscopy", Eds. G. Marowsky and V.V. Smirnov, Springer, Berlin, 1992, pp. 215-223

10. Basov, N.G., Babaev, I.K., Danilychev, V.A., et al., Sov. Journal of Quantum Electronics, vol. 6, 1979, p. 772

11. A.S. Kovalev, E.A. Muratov, A.A. Ozerenko, A.T. Rakhimov, and N.V. Suetin, Sov. J. Plasma Physics, Vol. 11, 1985, p. 515

12. Ploenjes, E., Palm, P., Adamovich, I.V., and Rich, J.W., "Control of Stability and Electron Removal Rate in Optically Pumped RF Discharges" Paper 99-3665, presented at AIAA 30th Plasmadynamics and Lasers Conference, Norfolk, VA, June 28 – July 1, 1999

13. E. Plönjes, P. Palm, I.V. Adamovich, and J. W. Rich, "Ionization Measurements in Optically Pumped Discharges", accepted for publication in Journal of Physics D: Applied Physics, 2000

14. C.E. Treanor, I.V. Adamovich, M.J. Williams, and J.W. Rich, "Kinetics of NO Formation Behind Strong Shock Waves", Journal of Thermophysics and Heat Transfer, vol. 10, No. 2, 1996, pp. 193

15. I.V. Adamovich, J.W. Rich, and G.L. Nelson, "Feasibility Study of Magneto-hydrodynamics Acceleration of Unseeded and Seeded Air Flows", AIAA Journal, vol. 36, No. 4, 1998, pp. 590-597

16. L.G.H. Huxley and R.W. Crompton, "The Diffusion and Drift of Electrons in Gases", Wiley, New York, 1974

17. J.W. Gallagher, E.C. Beaty, J. Dutton, and L.C. Pitchford, J. Phys. Chem. Ref. Data, vol.12, 1983, p. 109

18. Zhdanok, S.A., Borodin, V.I., and Chernukho, A.P.," Numerical Modeling of the Nitrogen Oxidation Process in the High Voltage Atmospheric Pressure Discharge", Proceedings of International School-Seminar "Modern Problems of Heat and Mass Transfer in Chemical Technology", Heat and Mass Transfer Inst. AN BSSR, pp.87-89, Minsk,1987

19. I.V. Adamovich, V.I. Borodin, S.A. Zhdanok, and A.P. Chernukho, "Numerical Modeling of Oxygen Plasma of the High Voltage Atmospheric Pressure Discharge. One-Dimensional Approach", in "Heat and Mass Transfer at Phase and Chemical Transformations", ITMO Press, Minsk, USSR, 1990, pp. 86-90

20. P.I. Porshnev, "Energy Balance in the Positive Column of the Axial Gas Discharge at Atmospheric Pressure", Soviet Engineering Physics Journal, Vol. 58, No. 5, 1990, p. 814

21. N.L. Aleksandrov, F.I. Vysikailo, R.Sh. Islamov, I.V. Kochetov, A.P. Napartovich, and V.G. Pevgov, "Electron Distribution Function in a N_2:O_2=4:1 Mixture", High Temperature, Vol. 19, 1981, p. 22

22. O.E. Krivonosova, S.A. Losev, V.P. Nalivaiko, Yu.K. Mukoseev, and O.P. Shatalov, "Recommended Data on the Rates of Chemical Reactions between Molecules Consisting of N and O atoms", in "Khimiya Plasmy" (Plasma Chemistry), ed. by B.M. Smirnov, vol. 14, 1987, pp. 3-31

23. N.L. Aleksandrov, A.M. Konchakov, and E.E. Son, Sov. J. Plasma Phys., Vol. 4, 1978, p. 169

24. Yu.S. Akishev, A.A. Deryugin, V.B. Karal'nik, I.V. Kochetov, A.P. Napartovich, and N.I. Trushkin, Plasma Physics Reports, Vol. 20, 1994, p. 511
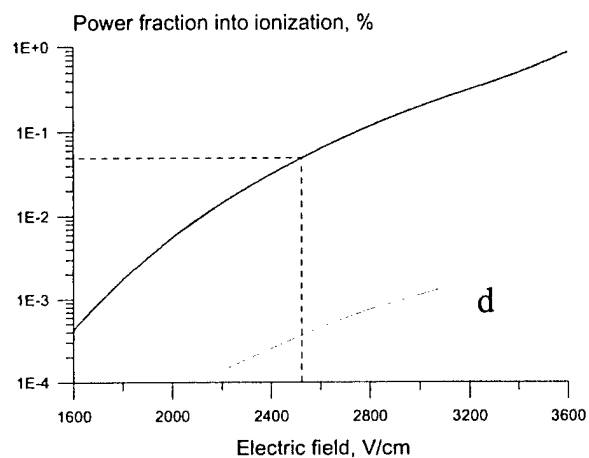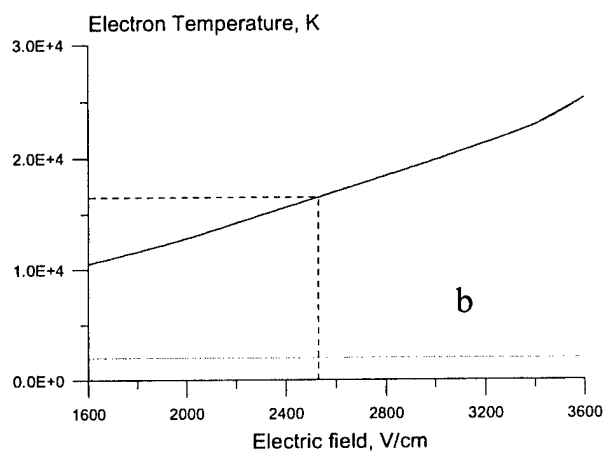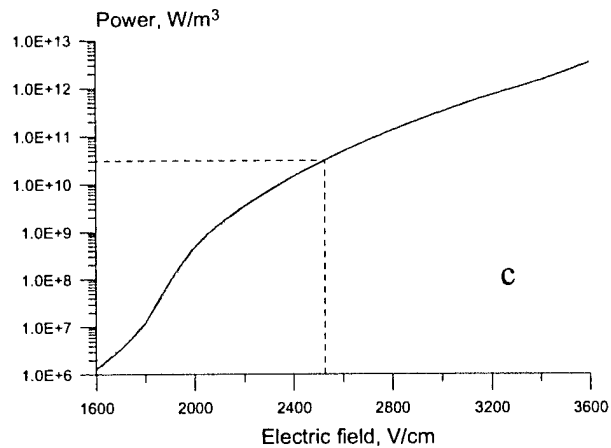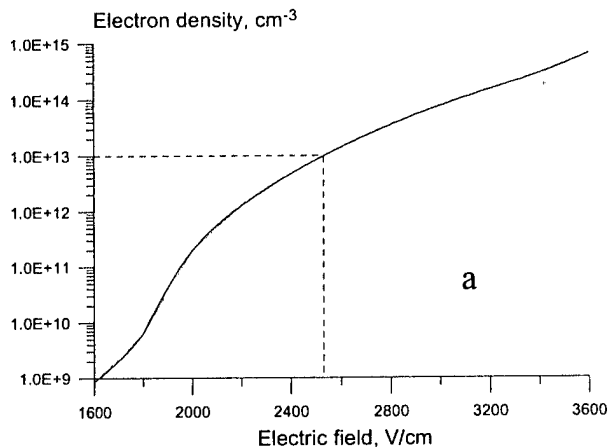
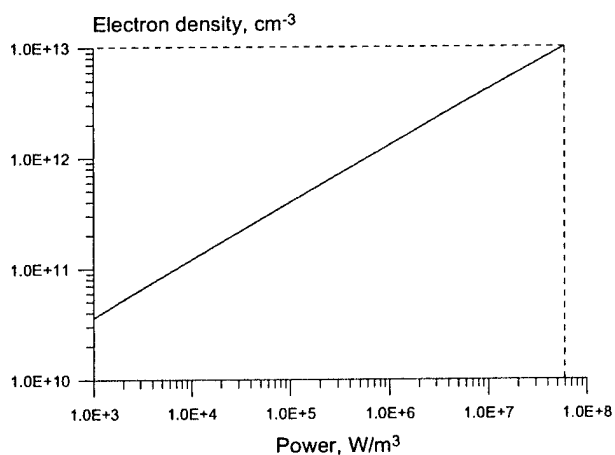Figure 1. Summary of the steady-state plasma parameters as functions of electric field.

Figure 2. Electron concentration in air as a function of electron beam power absorbed. The power loading of 58 MW/m^3 corresponds to the beam current density of j_{beam}=20 mA/cm^2

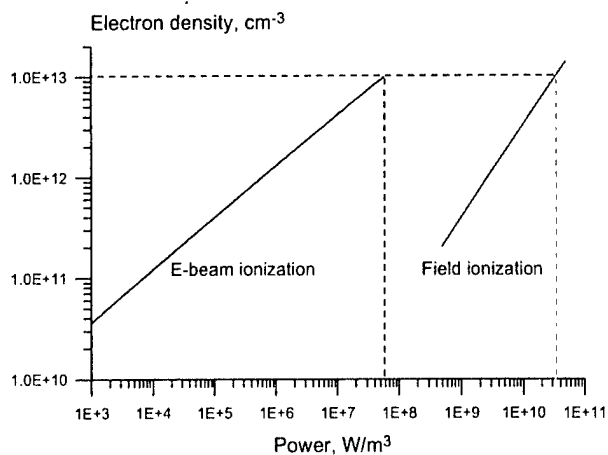Figure 3. Comparison on the power budget of the electric field sustained and e-beam sustained air plasmas

Temperature, K

Electron density, cm^{-3}
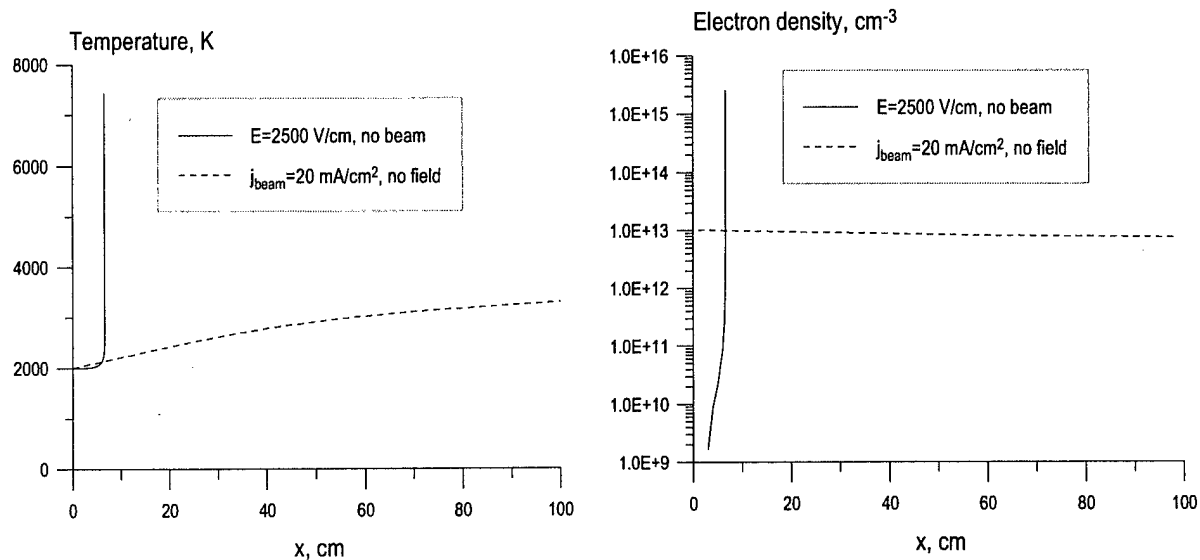

Figure 4. Heating and ionization in air plasma flow in an adiabatic channel 10 cm in diameter. Initial conditions: air at P=1 atm, T=2000 K, u=100 m/s

Electron density, cm^{-3}

Wall Heat flux, W/cm^2

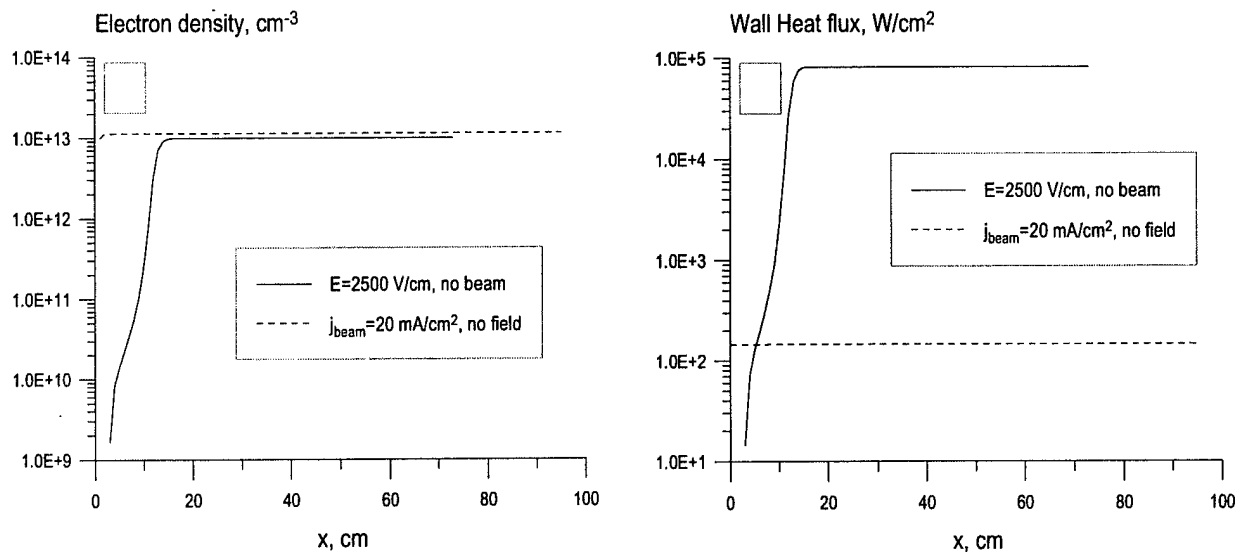Figure 5. Ionization and wall heat fluxes in air plasma flow in a constant temperature channel 10 cm in diameter. Initial conditions: air at P=1 atm, T=2000 K, u=100 m/s

25
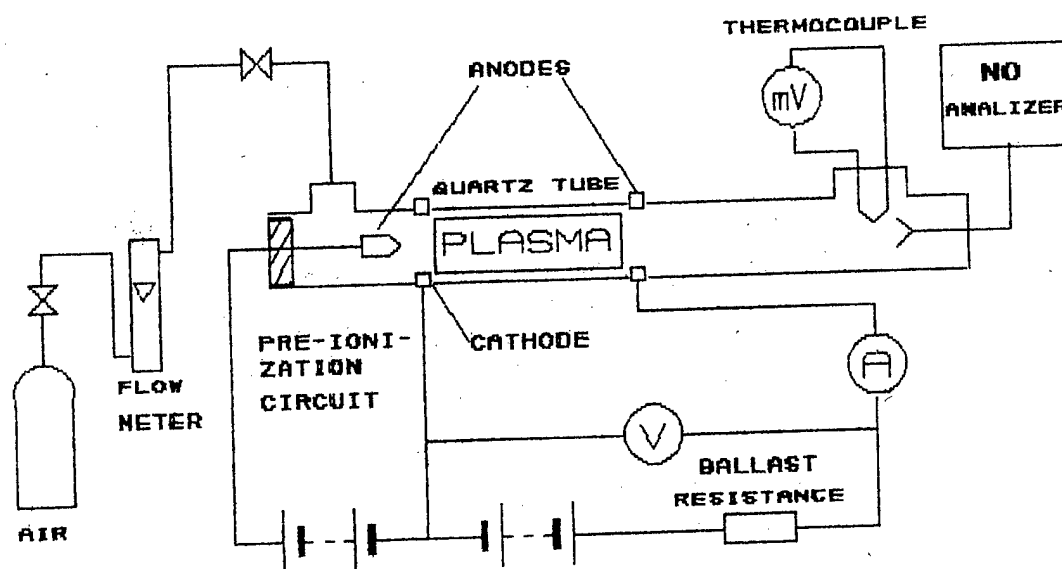
Figure 6. Schematic of the experimental setup

Figure 7. Photograph of a typical high-voltage atmospheric pressure discharge in air. U=2.0 kV, I=50 mA, G=240 g/hour, discharge tube diameter is 2 cm, distance between the electrodes is 3 cm.

26
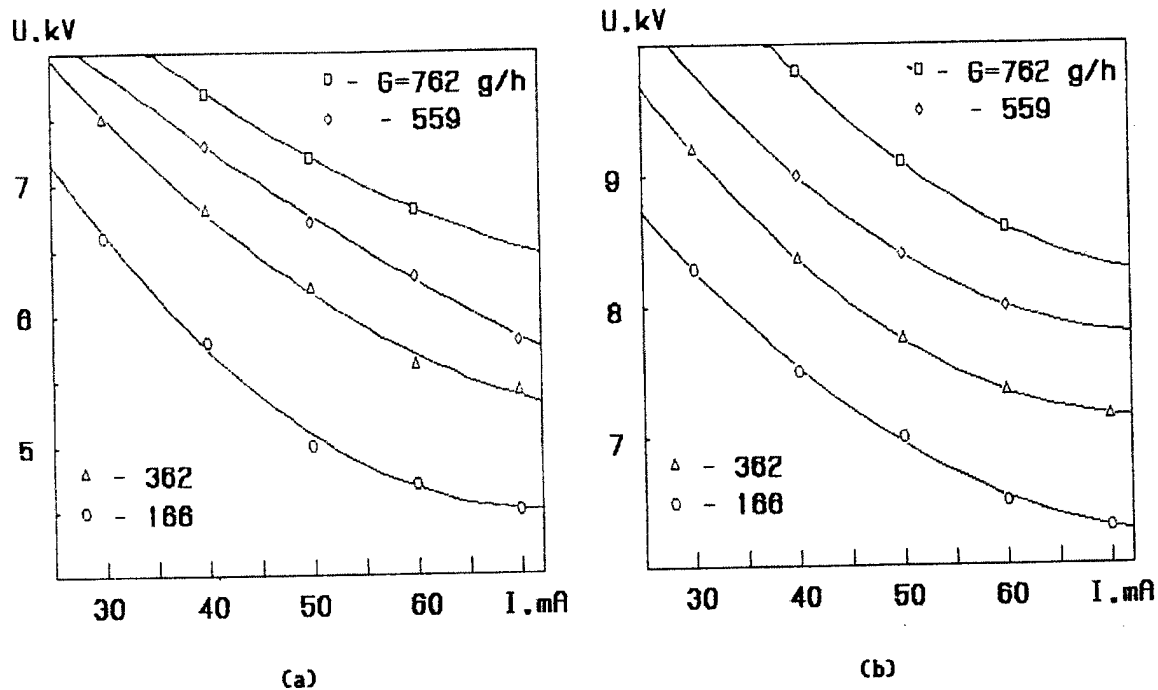
Figure 8. Voltage current characteristics of the air discharge in a 3.2 mm diameter tube at different mass flow rates for two distances between the electrodes. (a) L=5.0 cm; (b) L=7.5 cm
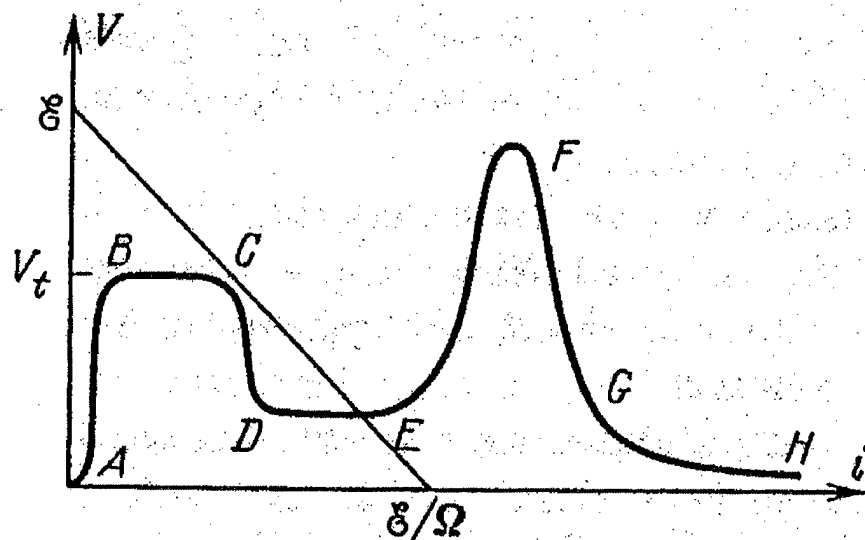
Figure 9. Qualitative voltage current characteristic of a DC discharge in a wide range of currents shown together with the loading line [1]. A, non-self-sustained Thomson discharge; BC, Townsend dark discharge; CD, transition to glow discharge DE, normal glow discharge; EF, abnormal glow discharge; FG, transition into an arc regime; GH, arc

27
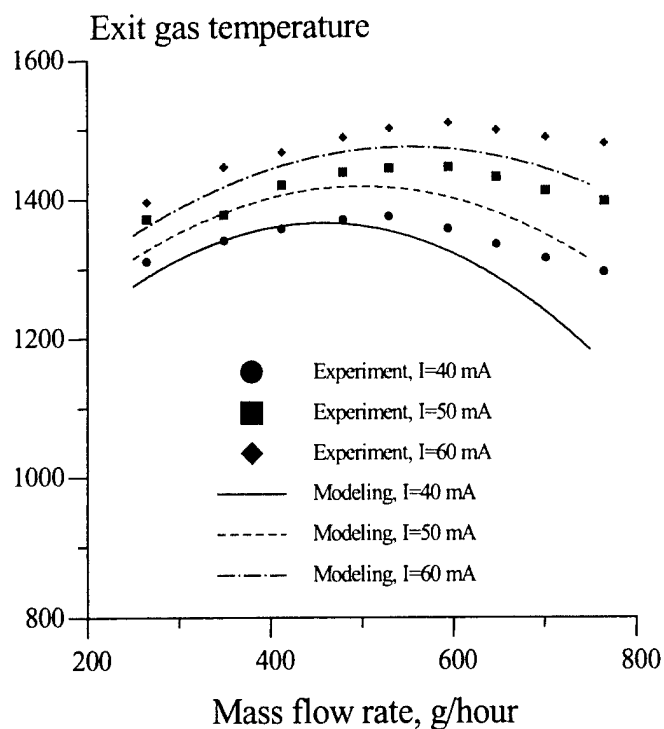
Figure 10. Comparison of the experimental and calculated gas temperatures at the exit of the discharge tube. Electrode separation is 5 cm, discharge tube length is 12.5 cm
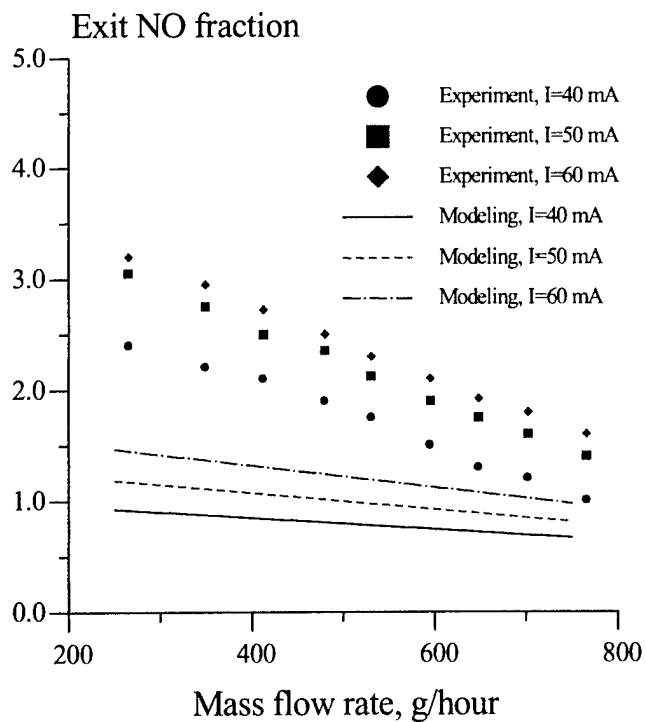
Figure 11. Comparison of the experimental and calculated NO mole fractions at the exit of the discharge tube. Electrode separation is 5 cm, discharge tube length is 12.5 cm
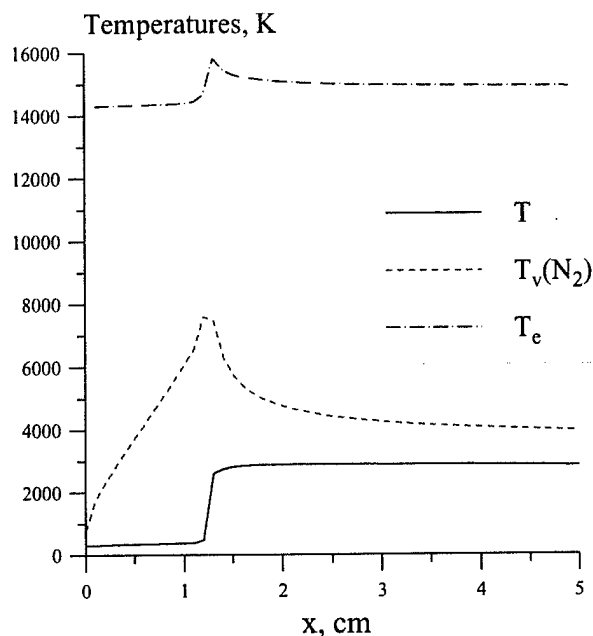
Figure 12. Axial distributions of gas temperature, vibrational temperature of N_2, and electron temperature on the discharge centerline
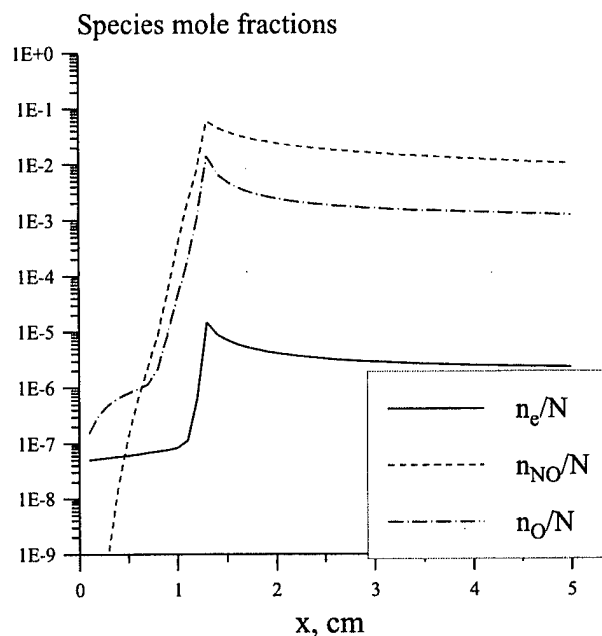
Figure 13. Axial distributions of ionization fraction, NO mole fraction, and O atom mole fraction on the discharge centerline
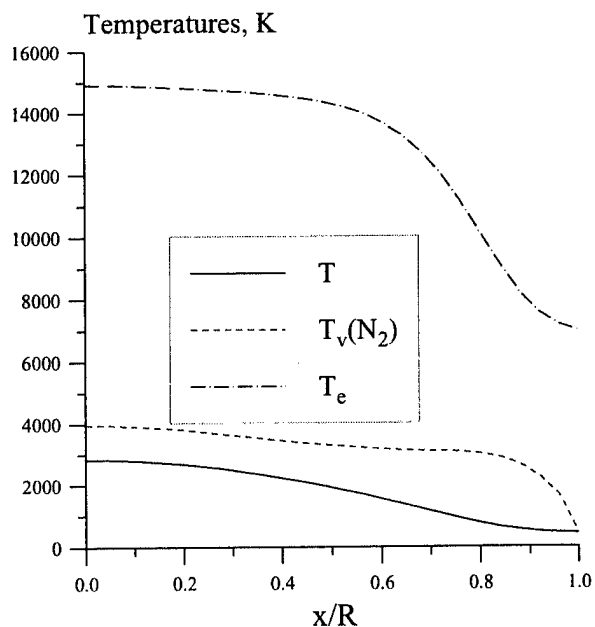
Figure 14. Radial distributions of gas temperature, vibrational temperature of N_2, and electron temperature at the discharge exit (x=5 cm)
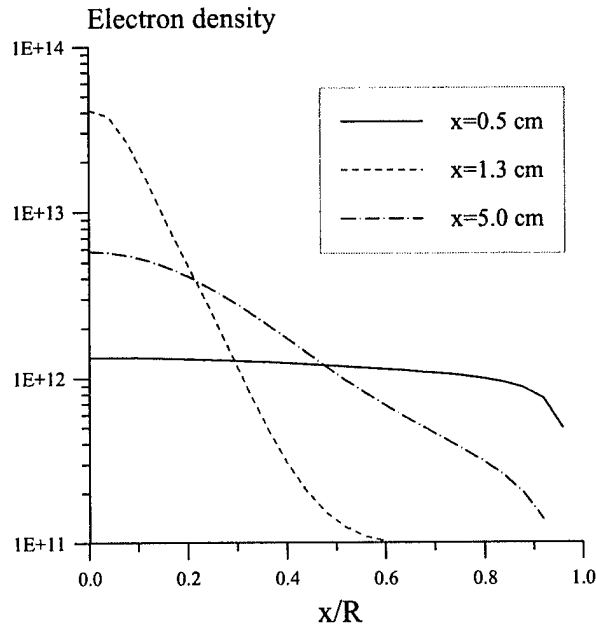
Figure 15. Radial distributions of electron density at different axial locations

Power fraction into ionization, %

Figure 16. Calculated discharge power fraction going into ionization by electron impact for the conditions of Figs. 10,11

2. IONIZATION MEASUREMENTS IN OPTICALLY PUMPED DISCHARGES

Elke Plönjes, Peter Palm, Igor V. Adamovich, and J. William Rich

Kinetics of ionization and electron removal in optically pumped nonequilibrium plasmas sustained by a CO laser is studied using non-self-sustained DC and RF electric discharges. Experiments in optically pumped CO/Ar/N_2 mixtures doped with O_2 and NO demonstrated that associative ionization of CO produce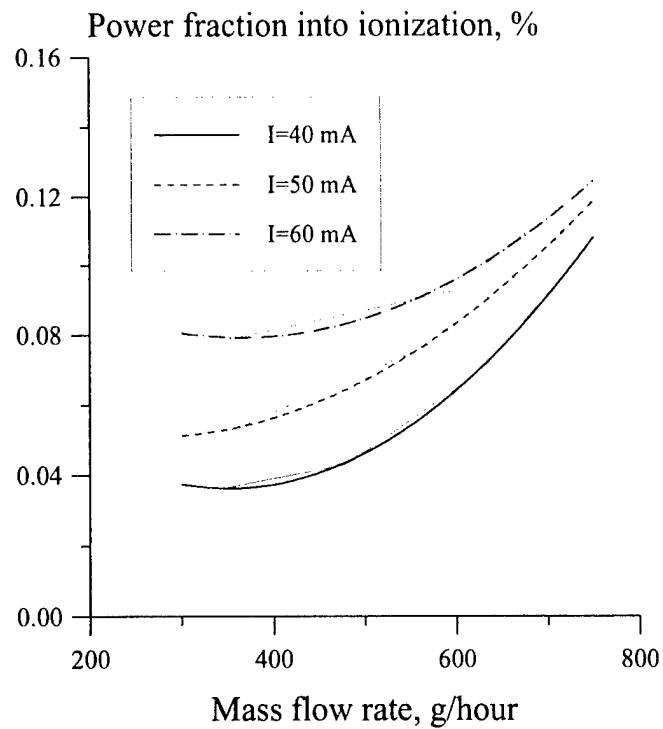s free electrons at a rate up to $S=10^{15}$ 1/cm^3/s. The ionization rate coefficient, inferred from the CO vibrational population measurements, is $k_{ion}=(1.1-1.8)\cdot10^{-13}$ cm^3/s. It is shown that excited NO and possibly O_2 molecules also contribute to the vibrationally stimulated ionization process. In a CO/Ar plasma, applying a DC bias to the cell electrodes resulted in rapid accumulation of a deposit on the negative electrode due to a large cluster ion current. The average mass of an ion in this plasma, estimated by measuring the mass of the deposit, is $m \cong 250$ a.m.u., which is consistent with the mass-spectrometer analysis of the deposit. The deposit did not accumulate when small amounts of O_2 and NO were added to the CO/Ar plasma, which presumably indicates destruction of the cluster ions.

It is demonstrated that adding small amounts of O_2 to the optically pumped CO/Ar plasmas significantly increases the electron density, from $n_e=(4-7)\cdot10^9$ cm^{-3} to $n_e=(1-2)\cdot10^{11}$ cm^{-3}. This effect occurs at a nearly constant (within 50%) electron production rate, indicating substantial reduction in the overall electron removal rate. This reduction can be qualitatively interpreted as destruction of rapidly recombining cluster ions in the presence of the O_2 additive, and their replacement by monomer ions with a slower recombination rate. Further studies of ion composition in optically pumped plasmas are suggested.

1. Introduction

Nonequilibrium optically pumped environments can be produced by resonance absorption of infrared laser radiation by molecules in the low vibrational quantum states, with subsequent vibration-to-vibration (V-V) pumping up to high vibrational levels [1],

$$AB(v) + AB(w) \rightarrow AB(v-1) + AB(w+1) \qquad (1)$$
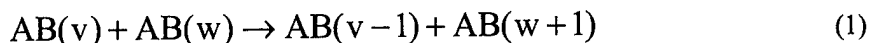
In Eq. (1), AB stands for a diatomic molecule, and v and w are vibrational quantum numbers. This approach allows sustaining strong vibrational disequilibrium at high densities and a low power budget. Optical pumping by a CO laser has been previously achieved in gas phase carbon monoxide [2-7] at pressures of up to 20 atm [2], gas phase nitric oxide [8-9], liquid phase CO [10,11], and solid CO and NO

matrices [12,13]. Recently, optical pumping has also been demonstrated in infrared inactive gases, such as nitrogen and air, at atmospheric pressure [14]. In this case, N_2 and O_2 molecules become vibrationally excited by near-resonance V-V energy transfer from CO,

$$CO(v) + N_2(w) \rightarrow CO(v-1) + N_2(w+1) \qquad (2)$$

$$CO(v) + O_2(w) \rightarrow CO(v-1) + O_2(w+1) \qquad (3)$$
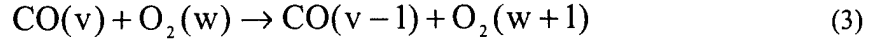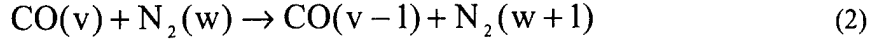
In the experiments of Refs. [2-14], the CO laser power was fairly low, ranging from a few Watts to 200 W c.w.

Ionization in optically pumped gases is produced by an associative ionization mechanism, in collisions of two highly vibrationally excited molecules when the sum of their vibrational energies exceeds the ionization potential [15,6,16],

$$AB(v) + AB(w) \rightarrow (AB)_2^+ + e^- ,$$
$$E_v + E_w > E_{ion} \qquad (4)$$
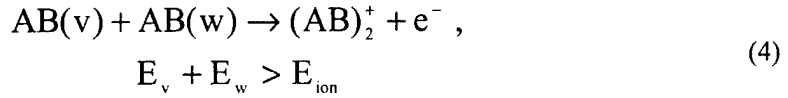
Ionization of carbon monoxide by this mechanism has been previously observed in CO-Ar gas mixtures optically pumped by resonance absorption of CO laser radiation [6,16]. The estimated steady-state electron density sustained by a 10 W CO laser in optically pumped CO/Ar/He plasmas with the high vibrational level populations of $n_{CO}(v\sim30)\sim10^{15}$ cm^{-3} is $n_e\sim10^{10}$-10^{11} cm^{-3} [16].

It is remarkable that ionization mechanism of Eq. (4) appears to be unconditionally stable with respect to the heating instability [17]. Indeed, in optically pumped plasmas both the upper level populations and the electron production rate sharply drop with temperature because of the exponential rise of the vibration-translation (V-T) relaxation rates [18]. This creates a negative feedback between the gas heating and the ionization rate, which precludes the instability development. This effect shows a possibility of sustaining unconditionally stable, strongly nonequilibrium optically pumped plasmas in high-pressure environments. Such plasmas would have a decisive advantage over electric discharge sustained plasmas, which are difficult to control at high pressures. These plasmas would find numerous applications in high-yield mode-selective chemical synthesis and high-speed aerodynamics. In particular, recent results on anomalous shock wave propagation in nonequilibrium gas discharges (see [19,20] and references therein) suggest the possibility of wave drag reduction and supersonic flow control by plasmas. This provides a strong motivation for exploring the approaches to sustain stable optically pumped plasmas in atmospheric-pressure air.

The present paper represents a first effort to study the effect of adding air species to optically pumped CO/Ar plasmas on the electron production and removal kinetics. The main objective is to investigate the role of additives, such as N_2, O_2, and NO, in the associative ionization process of Eq. (4) and to explore the effect of such additives on the electron removal rate in the plasma.

2. Experimental

To address the issues discussed in Section 1, ionization measurements using non-self-sustained DC and RF discharges have been conducted in optically pumped plasmas sustained by a CO laser. The use of the non-self-sustained discharges precludes electron impact ionization and thereby allows identification of the associative ionization mechanism of Eq. (4) [6,16].

The schematic of the experimental setup is shown in Fig. 1. A carbon monoxide laser is used to irradiate a gas mixture of CO and Ar, with additives such as N_2, NO, O_2, or air, which is slowly flowing through the pyrex glass optical absorption cell shown. The residence time of the gas mixture in the cell is about 1 sec. The liquid nitrogen cooled CO laser was designed in collaboration with the University of Bonn and fabricated at Ohio State. It produces a substantial fraction of its power output on the $v = 1 \rightarrow 0$ fundamental band component in the infrared. The laser can operate at more than 100 W continuous wave (c.w.) power. However, in the present experiment, the laser is typically operated at 20 W c.w. broadband power on the lowest ten vibrational bands, with up to ~0.3 W on the $v = 1 \rightarrow 0$ component. The output on the lowest bands ($1 \rightarrow 0$ and $2 \rightarrow 1$) is necessary to begin the absorption process in cold CO (initially at 300 K) in the cell. The Gaussian laser beam of ~6 mm diameter can be focused to a focal area of ~1 mm diameter to increase the power loading per CO molecule, providing an excitation region in the cell of ~2 mm diameter. The absorbed laser power is typically 5-6 W over the absorption length of 12.5 cm, which gives an absorbed power density of 10 W/cm^3 for the focused laser beam.

The lower vibrational states of CO, $v \leq 10$, are populated by direct resonance absorption of the pump radiation in combination with rapid redistribution of population by the V-V exchange processes. The V-V processes then continue to populate the higher vibrational levels above $v=10$, which are not directly coupled to the laser radiation (see Eq. (1)). The large heat capacity of the Ar diluent, as well as conductive and convective cooling of the gas flow, allow us to control the translational/rotational mode temperature in the cell. In steady-state conditions, when the average vibrational mode energy of the CO would correspond to a few thousand degrees Kelvin, the temperature never rises above a few hundred degrees. Thus a strong disequipartition of energy can be maintained in the cell, characterized by very high vibrational mode energy and a low translational/rotational mode temperature. As shown in Fig. 1, the population of the vibrational states of the CO in the cell is monitored by infrared emission spectroscopy. For this purpose, a Bruker Fourier transform IFS 66 spectrometer is used to record the spontaneous

emission from the CO fundamental, first and second overtone bands through a window on the side of the cell.

Two 3 cm diameter brass plate electrodes are placed in the cell as shown in Fig. 2, so that the laser beam creates a cylindrical excited region between the electrodes. The probe electrodes, which are typically 8 to 12 mm apart, can be connected to a DC or to an RF power supply. A reversible polarity DC power supply (Thorn EMI GENCOM Inc., Model 3000R) produced voltage that could be varied between 0-3000 V. The current was measured with a Keithley 2001 multimeter, with a 1 MΩ resistor connected in series with the cell to protect the multimeter in case of breakdown. The RF voltage at a frequency of $v=10$ MHz was produced by an HP function generator used as power supply without further amplification. Ionization of CO molecules in the cell occurs by an associative ionization mechanism (4). In both DC and RF experiments, the reduced electric field E/N was deliberately kept low to preclude electron impact ionization.

The electron production rate per unit volume of the plasma is determined from the saturation current of the DC Thomson discharge between the electrodes [6,16],

$$S \cong \frac{I_s}{e\pi d^2 D / 4},$$ (5)

where $d\cong1.0$ and 0.2 cm are the diameters of the excited regions created by the unfocused and the focused beams, respectively, D=3 cm is the electrode diameter, and $\pi d^2 D/4$ is the volume of the excited region. The excited region diameter was estimated from the diameter of the visible blue glow of the C_2 Swan band radiation, strongly coupled with high vibrational levels of CO [6].

The electron density was inferred from the RF conduction current between the electrodes, I_C, and the applied RF voltage, U [21],

$$n_e \cong \frac{I_C}{e\mu_e U d},$$ (6)

The conduction current was evaluated by measuring the voltage drops on a resistor R=50 Ohm connected in series with the discharge gap with the laser turned on and off, $U_{R,on}$ and $U_{R,off}$, using a 100 MHz HP54600B oscilloscope, $I_C=(U_{R,on}-U_{R,off})/R$. Note that Eqs. (5,6) are approximate since they do not account for the electrode edge effects, as well as the voltage drops across the sheaths in the RF discharge. Therefore they somewhat underestimate both the electron production rate and the electron density.

34

3. Results and Discussion

3.1. DC Thomson discharge measurements

Figure 3 shows vibrational population distribution functions (VDF) of carbon monoxide inferred from high-resolution (0.25 cm^{-1}) CO infrared emission spectra recorded by the FT spectrometer. Vibrational level populations are inferred from the spectra using a standard technique [22]. These measurements are made in a CO/Ar mixture at a total pressure of P=100 Torr, at different CO partial pressures in the cell. The translational/rotational temperatures at these conditions, inferred from the rotationally resolved R-branch of the $1 \rightarrow 0$ CO fundamental band with an accuracy of ±10 K, are also shown in Fig. 3. The distributions shown in these figures are the well-known "V-V pumped" distributions [23,24], maintained by the rapid redistribution of vibrational energy by the V-V processes, which pump energy into the higher vibrational levels. They are obviously extremely non-Boltzmann, and characterized by high population of the upper vibrational levels. Note that as the CO partial pressure increases, the high vibrational level populations v~35-40 drop, both because of the lower energy loading per CO molecule and because of the translational temperature rise.

Typical current voltage characteristics of the DC discharge, sustained by the unfocused and focused 10 W CO laser beams in a CO/Ar=3/100 mixture at P=100 Torr, are shown in Fig. 4. One can see that the discharge current reaches saturation at $U_s \cong 300$ V, $I_s \cong 2.5$ µA, when the laser is unfocused, and $U_s \cong 600$ V, $I_s \cong 7.0$ µA, when the laser is focused. In the saturation regime, the current continues to rise with the applied voltage because of the finite size of the electrodes that draw current from an increasingly larger region. As can also be seen from Fig. 4, at $U \cong 1400$-1600 V, electron impact ionization starts contributing to the discharge current, which increases by about an order of magnitude, up to $I \cong 100$ µA. In this region, the discharge is still non-self-sustained and extinguishes after the laser is turned off. Finally, at $U \cong 2500$-2700 V, breakdown occurs and the discharge collapses into an arc with a current of up to I~100-1000 µA. When the laser is off, breakdown and arcing also occur at $U \cong 2500$ V. Using I_s=2.5 µA and 7.0 µA for the two cases shown in Fig. 4, determined at the beginning of the saturation region, we obtain S=8.0·10^{12} 1/cm^3/s and 5.6·10^{14} 1/cm^3/s for the unfocused and the focused laser beam, respectively.

Figure 5 shows current-voltage characteristics of the Thomson discharge measured in CO/Ar, CO/Ar/O$_2$, and CO/N$_2$ mixtures at P=100 torr and with a higher laser power of 20 W. One can see that both adding oxygen and replacing Ar with N$_2$ reduces the electron production rate, from S=9.7·10^{14} 1/cm^3/s (I_s=12 µA) in CO/Ar, to S=5.2·10^{14} and 2.0·10^{14} 1/cm^3/s (I_s=6.5 and 2.5 µA) in CO/Ar/O$_2$, and S=1.6·10^{14} 1/cm^3/s (I_s=2.0 µA) in CO/N$_2$. The reduction of the ionization rate correlates with depletion of high vibrational level populations of CO by V-V energy transfer to N$_2$ and O$_2$ (see Fig. 6, 7), similar to

what has been previously observed in CO/Ar/He mixtures [6]. Note that the inferred electron production rates S in CO/Ar/O_2=2/100/0.5 and in CO/N_2=2/100 are about the same, while the CO level populations in the presence of oxygen are much more strongly depleted (see Figs. 6, 7). This suggests that O_2 molecules, vibrationally excited by V-V energy transfer between CO and O_2 (3) may also contribute to associative ionization of Eq. (4). This is consistent with recent Raman spectroscopy measurements of the N_2 and O_2 vibrational populations in optically pumped CO/N_2/O_2 mixtures [14]. They show that although all three diatomic species (CO, N_2, and O_2) are at strong vibrational disequilibrium, the vibrational temperatures of CO and O_2 substantially exceed that of N_2.

Figure 8, which shows DC discharge saturation currents in CO/Ar/air and in CO/Ar/O_2 mixtures at P=100 torr, demonstrates that the current is primarily controlled by the oxygen content in the plasma. A similar plot for CO/Ar/NO mixtures at P=50 torr (see Fig. 9) actually shows an increase of the saturation current (i.e. increase of the electron production rate) at low NO concentrations, from I_s=23 μA (S=1.8·10^{15} 1/cm^3/s) without NO to a maximum I_s=44 μA (S=3.4·10^{15} 1/cm^3/s) at P_{NO}=0.2 torr. This occurs even though the high vibrational levels of CO are strongly depleted by nitric oxide (see Fig. 10). This unambiguously shows that NO molecules, which may also become vibrationally excited by V-V energy transfer between CO and NO,

$$CO(v) + NO(w) \rightarrow CO(v-1) + NO(w+1), \tag{7}$$
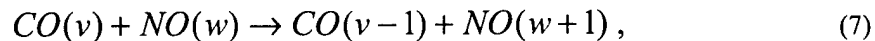
play an important role in associative ionization kinetics.

Finally, from Figs. 8, 9 it is seen that small admixtures of O_2 and NO (less than 0.1 torr) result in a fairly weak change of the net electron production rate, within 50% from the baseline value measured without additives. The measured rate of electron production in CO/Ar at P=20-100 torr, S=9.7·10^{14} - 1.8·10^{15} 1/cm^3/s is consistent with the ionization rate coefficient k_{ion}=(1.1-1.8)·10^{-13} cm^3/s, where k_{ion} is defined as

$$k_{ion} = \frac{S}{n_{CO}^2 \sum\limits_{E_v + E_w > E_{ion}} f_v f_v} \tag{8}$$

In Eq. (8), f_v and f_w are relative populations of the CO vibrational levels, inferred from the infrared spectra and plotted in Figs. 6,7,10. This value of k_{ion} exceeds the result of our previous study, k_{ion}=2.5·10^{-14} cm^3/s [16], by almost an order of magnitude. However, the present measurements of the CO vibrational

levels populations from the high-resolution CO FT spectra are far more accurate than the previous results [6] obtained using a low-resolution monochromator, and we recommend the new value of k_{ion} as more reliable.

In these experiments, it has been observed that when a DC voltage is applied to the electrodes, a dark deposit rapidly (within a few minutes) accumulates on the negative electrode in CO/Ar plasmas. The deposit quickly disappears when O_2 or NO are added to the cell gases. The deposit has the shape of a shadow image of the vibrationally excited region between the plates (see Fig. 11). No corresponding deposit is formed on the positive electrode, and there is only a small deposition anywhere in the cell except on the negatively biased electrode, even after several hours of operation. We conclude that the deposit is formed by positive ions moving toward the negative electrode in the electric field. The average positive ion mass was determined from the difference in the electrode weight before and after the experiment, $m=\Delta M/t/(I/e)\cong250$ amu [25]. These results indicate the presence of large ion clusters in the CO/Ar plasma, which are apparently destroyed by adding small amounts of O_2 and NO. Such clusters, having the general form $(CO)_2C_n$, $n=1-15$, have been previously observed in glow discharges in CO/Ar and CO/He mixtures [26]. In addition, a mass spectrum of the electrode deposit shows a number of peaks above 100 amu [25] (see Fig. 12). Odd peak numbers are most likely due to hydrogen (water vapor) impurities in the cell.

3.2. RF discharge measurements

In this series of measurements, a weak RF field with an RMS voltage $\langle U \rangle=3.5$ V at a frequency of $\nu=10$ MHz, produced by a function generator, was applied to the cell electrodes. The RF discharge RMS conduction current did not exceed $\langle I_C \rangle=500$ μA. Therefore, the maximum power coupled to the plasma by the RF field, $\langle U \rangle\langle I_C \rangle<2$ mW, was much smaller then the absorbed laser power, ~5W. This makes additional vibrational excitation by the RF field, with subsequent ionization by associative mechanism of Eq. (4), negligible. Figures 13, 14 show the RF discharge conduction current, $\langle I_C \rangle$, measured in the optically pumped CO/Ar/O_2 plasmas excited by a focused CO laser at the total pressure in the cell of P=100 torr and 20 torr, respectively.

At P=100 torr, no conduction current in CO/Ar plasma with no oxygen additive has been detected within the accuracy of the present experiment (see Fig. 13). The same result was obtained in a CO/N_2 plasma without oxygen added. We estimate a minimum detectable conduction current, $\langle I_C \rangle \sim \langle U_{R,on}-U_{R,off} \rangle/R$, to be about 1% of the displacement current $\langle I_D \rangle=\langle U_{R,off} \rangle/R=190$ μA, or $\langle I_C \rangle \sim 2$ μA. From this, using Eq. (6), one obtains an upper bound of electron density at these conditions, $n_e<4\cdot10^9$ cm^{-3}. Adding small amounts of dry or room air to the CO/Ar mixture resulted in a dramatic conduction current rise up

to $\langle I_C \rangle$=110 μA with 0.2 torr of dry air in the cell (see Fig. 13). This indicates the electron density increase by at least a factor of 50 compared with both CO/N$_2$ and CO/Ar plasmas without oxygen additive, up to n_e=2·10^{11} cm^{-3}. The results at P=20 torr are quite similar (see Fig. 14). The conduction current in CO/Ar and CO/N$_2$ mixtures is $\langle I_C \rangle$=12-17 μA, which gives an electron density of n_e=(5-7)·10^9 cm^{-3}. However, with 0.2-0.5 torr of air or 0.1 torr of O$_2$ added to the CO/Ar mixture the conduction current increases by about a factor of 15, up to $\langle I_C \rangle$=215 μA, which gives an electron density of n_e=0.9·10^{11} cm^{-3}. We emphasize that the observed sharp electron density increase occurs despite the fact that the electron production rate S in CO/Ar/O$_2$ mixtures actually somewhat drops with the O$_2$ partial pressure (see Fig. 8). Since small admixtures of oxygen are unlikely to produce a noticeable change in electron mobility, this can only mean that the electron removal rate significantly decreases in the presence of small amounts of oxygen.

This result suggests a possible qualitative scenario of the apparent electron removal rate reduction in optically pumped CO/Ar/O$_2$ and CO/Ar/N$_2$ plasmas. Indeed, the deposit formation on the negative electrode due to the heavy ion current in the CO/Ar plasma without additives, and its absence in the plasmas doped with O$_2$ (see Section 3.1) indicate that the dominant positive ions in these two cases are quite different. Dimer ions, such as (CO)$_2^+$, are known to have a very high dissociative recombination rate, β~10^{-6} cm^3/s [21]. Presumably, the recombination rate for the heavy cluster ions, such as (CO)$_2$C$_n^+$, which are likely to be the dominant ions in the CO/Ar plasma without additives [26], might well be even higher. On the other hand, adding small amounts (tens of microtorr) of O$_2$ to a glow discharge CO/Ar plasma results in destruction of cluster ions and their replacement by monomer ions such as O$_2^+$ and CO$^+$ [26], which have a much slower recombination rates, β~10^{-6} cm^3/s [17]. However, this interpretation leaves open the question what role electron attachment to oxygen plays in these strongly nonequilibrium plasmas. Indeed, one would expect the electron density to be reduced in the presence of a strongly electronegative gas such as oxygen, while the present experiments demonstrate exactly the opposite behavior. Further studies of ion composition of optically pumped plasmas using ion mass-spectrometry, such as has been previously done in CO/Ar and CO/He glow discharges [26] are expected to provide new insight into this problem.

4. Summary

Kinetics of ionization and electron removal in optically pumped nonequilibrium plasmas sustained by a CO laser is studied using non-self-sustained DC and RF electric discharges. Experiments in optically pumped CO/Ar/N$_2$ mixtures doped with O$_2$ and NO demonstrated that associative ionization of CO by mechanism (4) generates free electrons at a rate up to S=10^{15} 1/cm^3/s. The ionization rate coefficient, inferred from the CO vibrational populations measurements, is k_{ion}=(1.1-1.8)·10^{-13} cm^3/s. It is

shown that excited NO and possibly O_2 molecules also contribute to the vibrationally stimulated ionization process. In CO/Ar plasmas, applying a DC bias to the cell electrodes resulted in rapid accumulation of a deposit on the negative electrode due to a large cluster ion current. The average mass of an ion in this plasma, estimated by measuring the mass of the deposit, is $m \cong 250$ a.m.u., which is consistent with the mass-spectrometer analysis of the deposit. The deposit did not accumulate when small amounts of O_2 and NO were added to the CO/Ar plasma, which presumably indicates destruction of the cluster ions.

It is demonstrated that adding small amounts of O_2 to the optically pumped CO/Ar plasmas significantly increases the electron density, from $n_e=(4\text{-}7)\cdot 10^9$ cm^{-3} to $n_e=(1\text{-}2)\cdot 10^{11}$ cm^{-3}. This effect occurs at a nearly constant (within 50%) electron production rate, indicating substantial reduction in the overall electron removal rate. This reduction can be qualitatively interpreted as destruction of rapidly recombining cluster ions in the presence of the O_2 additive, and their replacement by monomer ions with a slower recombination rate. Further studies of ion composition in optically pumped plasmas are suggested.

References

25. C.E. Treanor, J.W. Rich, and R.G. Rehm, J. Chem. Phys., Vol. 48, 1968, p. 1798

26. J.W. Rich, R.C. Bergman, and M.J. Williams, Measurement of Kinetic Rates for Carbon Monoxide Laser Systems, Final Contract report AFOSR F49620-77-C-0020 (November 1979)

27. J.W. Rich and R.C. Bergman, Chem. Phys., Vol. 44, 1979, p. 53

28. R.L. DeLeon and J.W. Rich, Chem. Phys., vol. 107, 1986, p. 283

29. C. Flament, T. George, K.A. Meister, J.C. Tufts, J.W. Rich, V.V. Subramaniam, J.-P. Martin, B. Piar, and M.-Y. Perrin, Chem. Phys., vol. 163, 1992, p. 241

30. I. Adamovich, S. Saupe, M.J. Grassi, O. Shulz, S. Macheret, and J.W. Rich, Chem. Phys., vol. 173, 1993, p. 491

31. H.L. Wallaart, B. Piar, M.Y. Perrin, and J.P. Martin, Chem. Phys., Vol. 196, 1995, p. 149

32. H. Dunnwald, E. Siegel, W. Urban, J.W. Rich, G.F. Homicz, and M.J. Williams, Chem. Phys., Vol. 94, 1985, p. 195

33. S. Saupe, I. Adamovich, M.J. Grassi, and J.W. Rich, Chem. Phys., vol. 174, 1993, p. 219

34. D.S. Anex and G.E. Ewing, J. Phys. Chem., Vol. 90, p. 1604, 1986

35. R.S. Disselkamp and G.E. Ewing, J. Phys. Chem., Vol. 93, p. 6334, 1989

36. J.P. Galaup, J.Y. Harbec, R. Charneau, and H. Dubost, Chem. Phys. Lett., Vol. 120, 1985, p. 188

37. I. Hadj Bachir, R. Charneau, and H. Dubost, Chem. Phys., Vol. 177, 1993, p. 675

38. W. Lee, M. Chidley, R. Lieweke, I. Adamovich, and W.R. Lempert, "Determination of O_2 and N_2 Vibrational State Distributions in CO Laser-Sustained Plasmas", AIAA Paper 99-3723, AIAA 30th Plasmadynamics and Lasers Conference, Norfolk, VA, June 28 – July 1, 1999

39. L.S. Polak, P.A. Sergeev, and D.I. Slovetskii, Sov. High Temperature Physics, Vol. 15, 1977, p. 15

40. I.V. Adamovich and J.W. Rich, J. Physics D: Applied Physics, vol. 30, 1997, p. 1741

41. Raizer, Y.P., "Gas Discharge Physics", Springer-Verlag, Berlin, 1991

42. Billing, G.D., "Vibration-Vibration and Vibration-Translation Energy Transfer, Including Multiquantum Transitions in Atom-Diatom and Diatom-Diatom Collisions", Nonequilibrium Vibrational Kinetics, Springer-Verlag, Berlin, 1986, Chap. 4, pp. 85-111

43. Ganguly, B. N. , Bletzinger, P. and Garscadden, A., Physics Letters, Vol. 230, p. 218, 1997

44. H. Lowry, J. Blanks, C. Stepanek, M. Smith, L. Crosswy, P. Sherrouse, J. Felderman, and B. Wood, "Shock Structure of a Spherical Projectile in Weakly Ionized Air", AIAA Paper 99-0600

45. R. Johnsen, "Recombination of Cluster Ions", in B.R. Rowe et al. (eds.), "Dissociative Recombination", Plenum, New York, 1993

46. K.P. Horn and P.E. Oettinger, J. Chem. Phys., vol. 54, 1971, p. 304

47. J. W. Rich, "Relaxation of Molecules Exchanging Vibrational Energy", in "Applied Atomic Collision Physics", vol. 3, "Gas Lasers", ed. E.W. McDaniel and W.L. Nighan, Academic Press, New York, 1982, pp. 99-140

48. B.F. Gordiets, V.A. Osipov, and L.A. Shelepin, "Kinetic Processes in Gases and Molecular Lasers", Gordon and Breach, London, 1988

49. E. Plönjes, I.V. Adamovich, V.V. Subramaniam, and J.W. Rich, "Isotope Separation in Optically Pumped Thomson Discharges", AIAA Paper 98-0993, 36th Aerospace Sciences Meeting & Exhibit, Reno, NV, January 12-15, 1998

50. Y. Kaufman, P. Avivi, F.Dothan, H. Keren, J. Malinowitz, J. Chem. Phys., Vol. 72, 1980, p. 2606
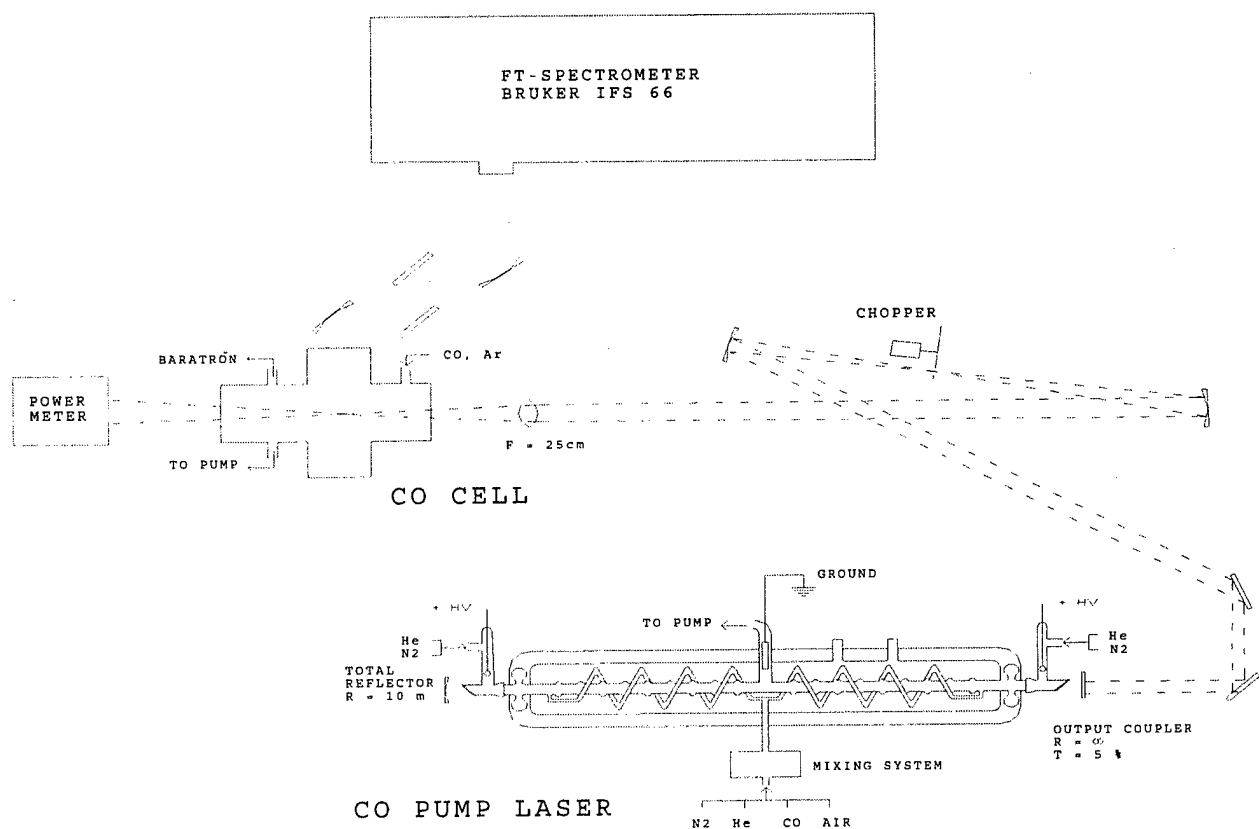
Figure 1. Schematic of the experimental setup
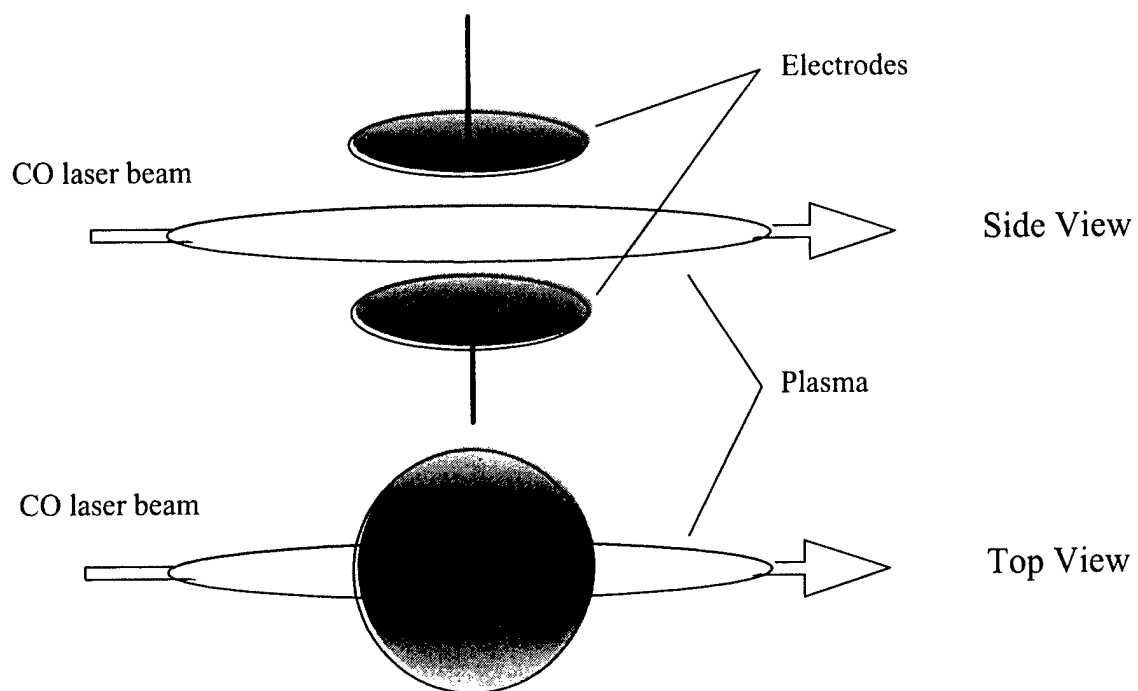
Figure 2. Schematic of electrodes in the cell
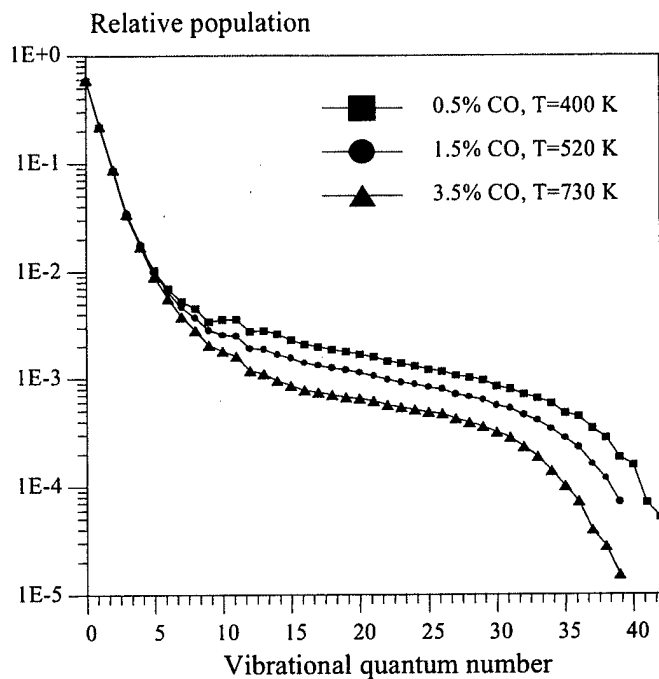
Figure 3. Vibrational distribution functions of CO in different CO/Ar mixtures. P=100 Torr, CO laser power is 10 W.
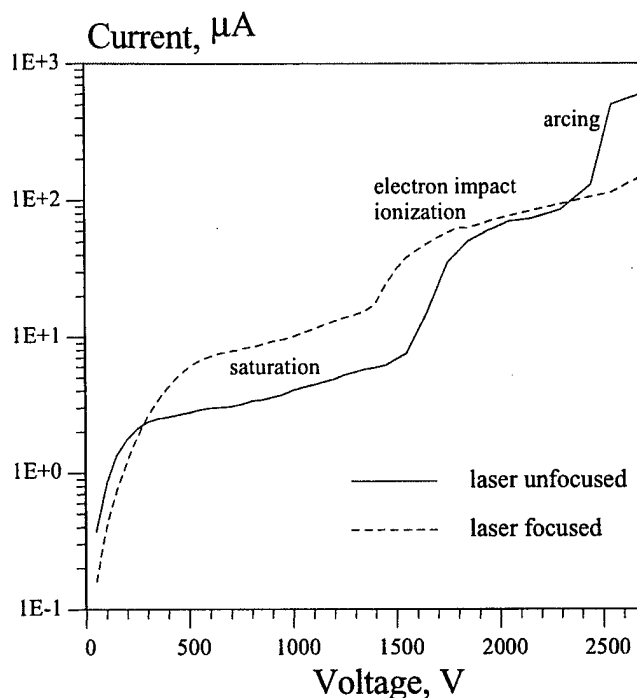
Figure 4. Current-voltage characteristics of the laser-sustained DC discharge. CO/Ar=3/100, P=100 Torr, CO laser power is 10 W.
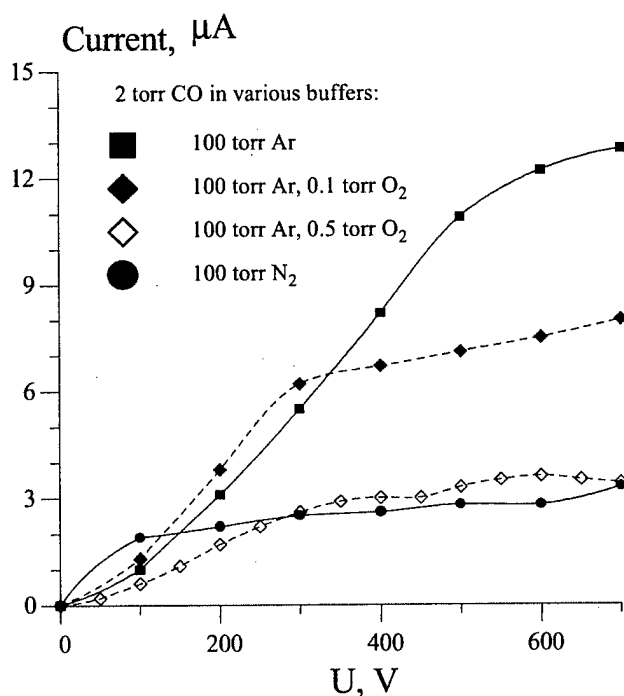
Figure 5. Current-voltage characteristics of the laser-sustained DC discharges. P_{CO}=2 torr, P=100 Torr, CO laser power is 20 W.
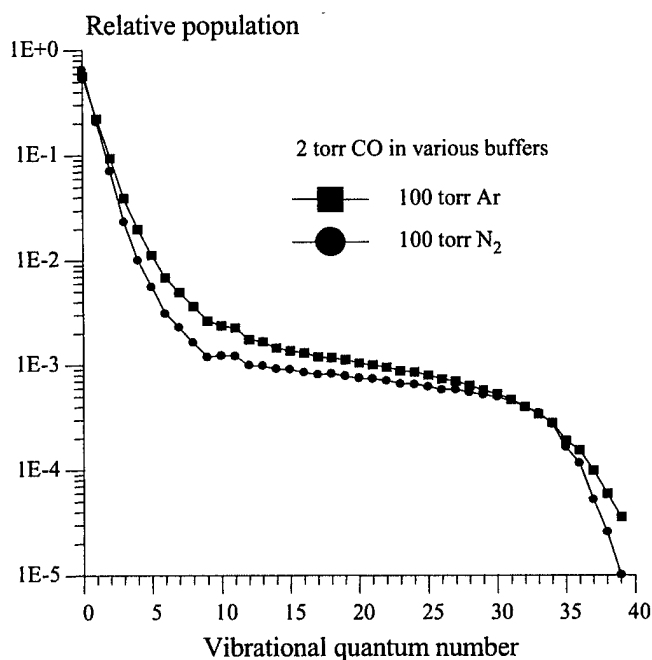
Figure 6. CO vibrational distribution function in CO/Ar (T=600 K) and CO/N$_2$ (T=450 K) mixtures

Relative population
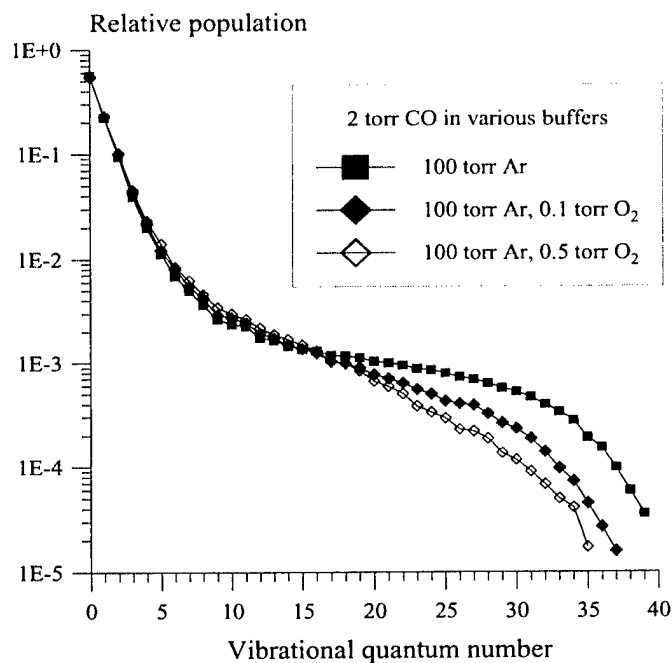
Figure 7. CO vibrational distribution function in CO/Ar/O$_2$ mixtures (T=600, 680, and 700 K, respectively)
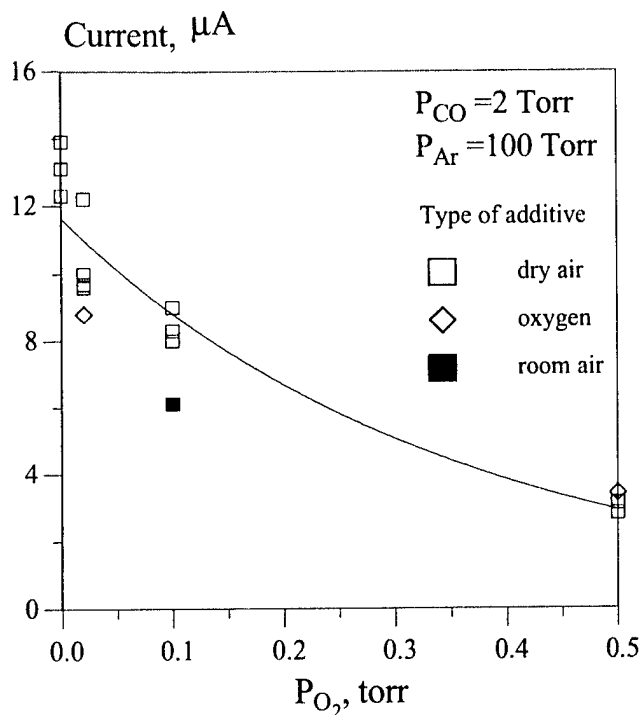
Current, μA

Figure 8. Thomson discharge saturation current in CO/Ar/air and CO/Ar/O$_2$ mixtures
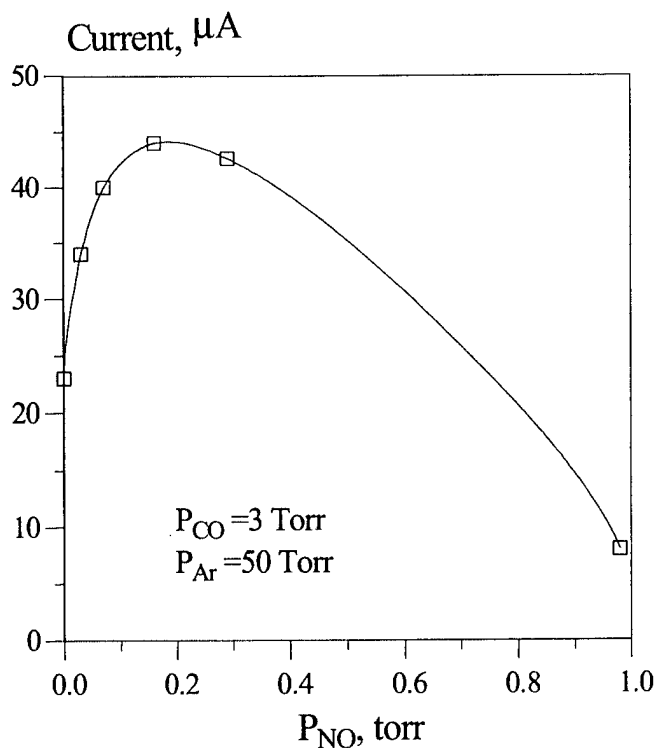
Current, μA

Figure 9. Thomson discharge saturation current in CO/Ar/NO mixtures

Relative population
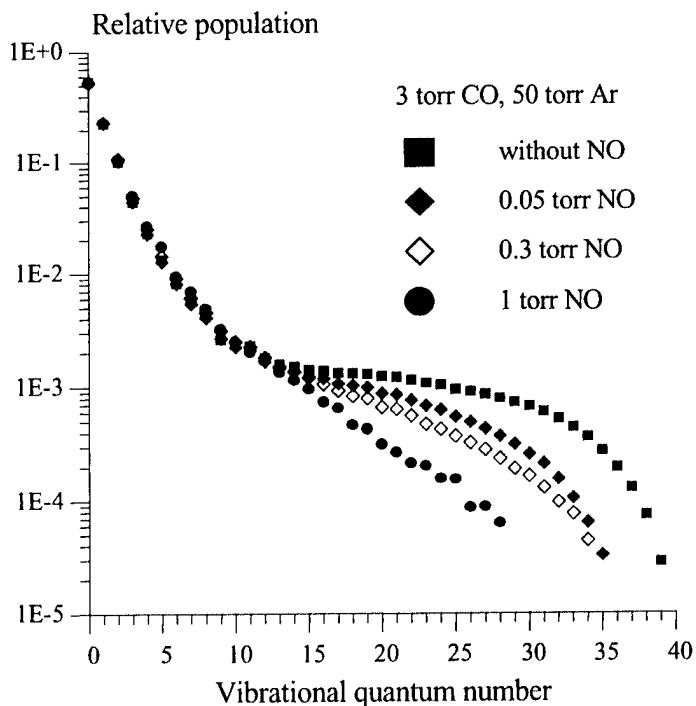
Figure 10. CO vibrational distribution function in CO/Ar/NO mixtures (T=710, 800, 780, and 770 K, respectively)
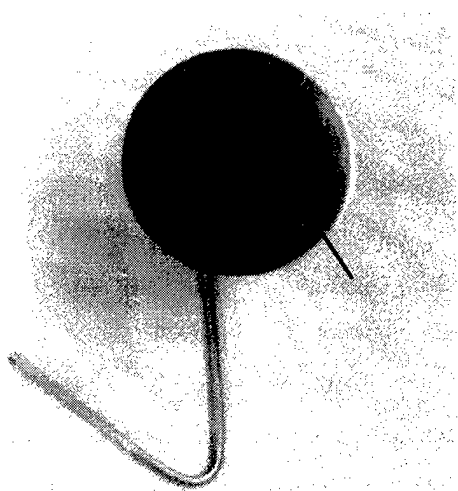
Figure 11. Photograph of a negative electrode with the deposit (shown with an arrow) accumulated during a 10 min run.
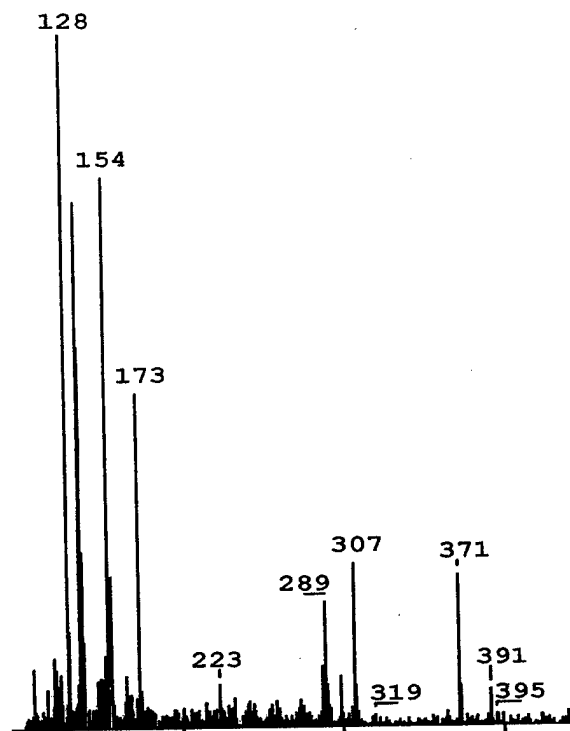
Figure 12. Mass-spectrum of the deposit shown in Fig. 11
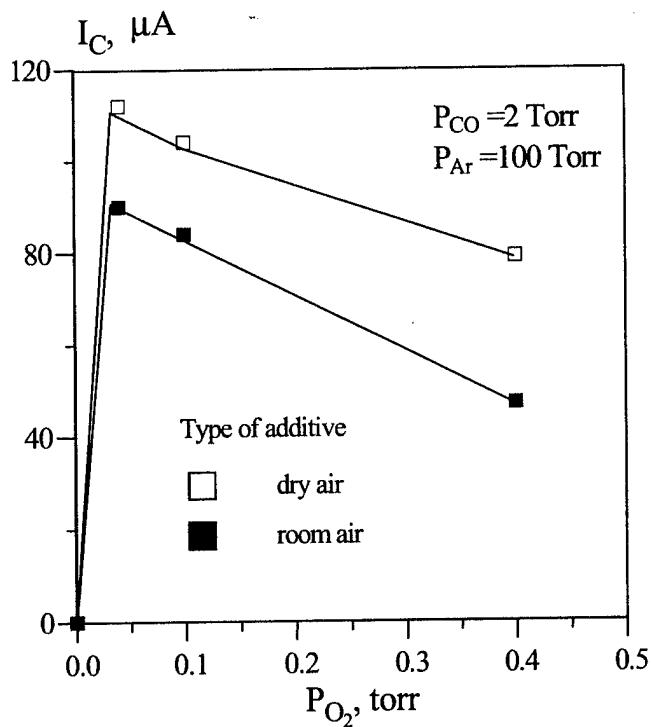
3. CONTROL OF ELECTRON RECOMBINATION RATE AND ELECTRON DENSITY IN OPTICALLY PUMPED NONEQUILIBRIUM PLASMAS

Igor V. Adamovich

A two-dimensional time-dependent model of non-self-sustained DC and RF discharges is used for analysis of recent experiments in optically pumped nonequilibrium plasmas. The analysis shows that non-self-sustained DC and RF discharges can be successfully used for measurements of electron production rate, electron recombination rate, and electron density in these plasmas. The inferred rate of electron production per unit volume by the associative ionization mechanism is $S_0=1.0 \cdot 10^{15}$ 1/cm^3/s and $S_0=2.2 \cdot 10^{14}$ 1/cm^3/s in CO/Ar=2/100 and in CO/N$_2$=2/100 plasmas, respectively. The inferred electron-ion recombination rate coefficients are $\beta > 6.0 \cdot 10^{-6}$ cm^3/s and $\beta = (7.5 \pm 1.5) \cdot 10^{-6}$ cm^3/s in CO/Ar=2/100 mixtures at P=100 torr and 20 torr, respectively. In CO/Ar=2/100 mixtures with a 0.05-0.1 torr admixture of O$_2$ at P=100 torr and 20 torr, the inferred recombination rate coefficients are $\beta = (1.5 \pm 0.3) \cdot 10^{-8}$ cm^3/s and $\beta = (5.1 \pm 2.9) \cdot 10^{-8}$ cm^3/s, respectively. Finally, the inferred electron density in optically pumped CO/Ar/O$_2$ plasmas at the laser beam axis is $n_e = (1.7 \pm 0.2) \cdot 10^{11}$ cm^{-3} at P=100 torr and $n_e = (6.2 \pm 0.8) \cdot 10^{10}$ cm^{-3} at P=20 torr. These results demonstrate that electron density in the optically pumped CO/Ar plasmas can be controlled and significantly increased by adding small amounts (up to ~0.1%) of species such as O$_2$ and NO, which result in reduction of the electron-ion recombination rate.

1. Introduction

The paper addresses analysis of a recent ionization measurement in optically pumped CO/Ar/O$_2$ and CO/N$_2$/O$_2$ plasmas using non-self-sustained DC and RF discharges [1]. Briefly, the experiments have been conducted in a flowing gas optical absorption cell, where the gas mixture was vibrationally excited by resonance absorption of 20 W continuous wave broadband CO laser radiation. The Gaussian laser beam was focused to increase the power loading per CO molecule, providing an excitation region in the cell of approximately 2 mm in diameter. The absorbed laser power was typically 5-6 W over the absorption length of 12.5 cm, which gives an absorbed power density of 10 W/cm^3. The lower vibrational states of carbon monoxide in the cell, v≤10, are populated by direct resonance absorption of the laser radiation. The higher vibrational levels, v~10-40, which are not directly coupled to the laser radiation, are populated by the rapid redistribution of vibrational energy by the vibration-vibration (V-V) exchange processes,

$$CO(v) + CO(w) \rightarrow CO(v-1) + CO(w+1) \qquad (1)$$
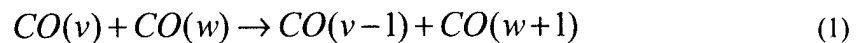
The large heat capacity of the Ar or N_2 diluents, as well as conductive and convective cooling of the gas flow, controls the steady-state translational/rotational mode temperature in the cell, T=400-700 K, while the average vibrational mode energy of CO corresponds to 2000-4000 K degrees K. Thus a strong disequipartition of energy can be maintained in the cell, characterized by very high vibrational mode energy and electron temperature, and a low translational/rotational mode temperature.

Under these conditions, ionization in the optically pumped CO is produced by an associative ionization mechanism, in collisions of two highly vibrationally excited CO molecules when the sum of their vibrational energies exceeds the ionization potential [1-3],

$$CO(v) + CO(w) \rightarrow (CO)_2^+ + e^- ,$$
$$E_v + E_w > E_{ion}$$

(2)
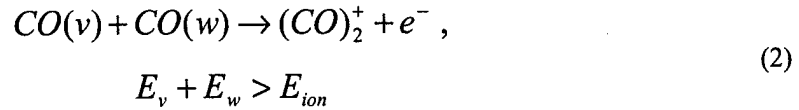
The parameters of the optically pumped plasma created in the cell have been analyzed using two 3 cm diameter brass plate electrodes, placed in the cell as shown in Fig. 1, so that the laser beam created a nearly cylindrical excited region between the electrodes. The electrodes, which were typically 8 to 12 mm apart, were powered either by a DC or by an RF power supply. In both DC and RF experiments, the applied voltage was deliberately kept sufficiently low to completely preclude electron impact ionization [1-3]. Thus, a non-self-sustained DC discharge (sometimes called a Thomson discharge [2,4]) or a non-self-sustained RF discharge can be initiated between the electrodes.

In these experiments, the rate of electron production per unit volume by the associative ionization mechanism of Eq. (2) was estimated from the DC discharge current in the saturation regime, I_S. Saturation occurs when the applied electric field removes as many electrons per second as are produced in the entire discharge volume. This rate is accordingly estimated as

$$S \cong \frac{I_s}{eD\pi a^2 / 4} \cong 10^{14} - 10^{15} \ cm^{-3} \ sec^{-1}$$

(3)

In Eq. (3), obtained in Ref. [3], a is the ionized region diameter and D is the electrode diameter. Note that in the saturation regime the electrons are removed from the discharge much faster than they recombine or attach. Indeed, simple estimates [2] show that the electron residence time in the discharge is much shorter than the time for electron-ion recombination or electron attachment. Therefore measuring the DC saturation current density directly yields the electron production rate per unit volume S, regardless of the

47

ionization mechanism and independently of the electron removal rates. The electron density in the plasma, on the other hand, was estimated from the conduction current of the RF discharge, measured as a difference between the RMS RF discharge currents with the laser turned on and off,

$$n_e \cong \frac{I_C}{e\mu_e U a} \cong 10^{10} - 10^{11} \, cm^{-3} \tag{4}$$

In Eq. (4), U is the applied RMS RF voltage and μ_e is the electron mobility. Note that Eqs. (3,4) are approximate since they do not account for the electrode edge effects and the spatial nonuniformity of the plasma (in particular, voltage drops across the sheaths in the RF discharge). Therefore they are expected to provide only rather crude estimates of both the electron production rate and the electron density.

The objective of the present paper is to use two-dimensional kinetic modeling of both the DC and the RF discharges for more accurate quantitative inference of the electron production and removal rates, as well as the electron density in the optically pumped plasma.

2. Kinetic Model

The two-dimensional time-dependent model of the non-self-sustained DC and RF discharges used in the optical pumping experiments [1] discussed in Section 1 includes the equations for electron and positive ion concentrations, and the Poisson equation for the electric field [5]:

$$\frac{\partial n_k(x, y, t)}{\partial t} + \nabla \vec{\Gamma}_k = Q_k \, ,$$

$$\vec{\Gamma}_k = D_k \nabla n_k(x, y, t) - \frac{q_k}{|e|} \mu_k \nabla \phi(x, y, t) n_k(x, y, t)$$

$$n_k(x, 0, t) = n_k(x, d, t) = 0 \tag{5}$$

$$\frac{\partial n_k(0, y, t)}{\partial x} = \frac{\partial n_k(\pm W, y, t)}{\partial x} = 0$$

$$n_k(x, y, 0) = 0$$

$$\nabla^2 \phi(x, y, t) = \frac{1}{\varepsilon_0} \sum_k q_k n_k(x, y, t) \, ,$$

$$\phi(x, 0, t) = 0 \, , \quad \phi(x, d, t) = U_0 \cos(2\pi v t) \, ,$$

$$\frac{\partial \phi(0, y, t)}{\partial x} = \frac{\partial \phi(\pm W, y, t)}{\partial x} = 0$$

$$\phi(x, y, 0) = U_0 y / d$$

(6)

$$Q_e = S(x, y) - \beta n_e n_+$$

$$Q_+ = S(x, y) - \beta n_e n_+$$

(7)

$$S(x, y) = S_0 \exp\left[-\left(\frac{y - d/2}{a/2} \right)^2 - \left(\frac{x}{a/2} \right)^2 \right]$$

(8)

In Eqs. (5-7), the index k stands for electrons and positive ions, e is the electron charge, n_k and $q_k = \pm e$ are the species concentrations and charges, D_k, μ_k, and $\vec{\Gamma}_k$ are the species diffusion coefficients, mobilities, and fluxes (conduction current density vectors), respectively, ϕ and $\vec{E} = -\nabla \phi$ are the electric potential and electric field, d is the separation between the electrodes, W is the electrode half-width, U_0 and v are the applied voltage amplitude and frequency, S(x,y) is the rate of electron production by the associative ionization mechanism of Eq. (2), and β is the electron-ion recombination coefficient. In Eq. (8), S_0 and a are the rate of electron production at the laser beam axis and the ionized region diameter. The Gaussian distribution of ionization rate S(x,y) in Eq. (8) is chosen due to the Gaussian power density distribution across the laser beam [6]. At zero frequency, $v=0$, this system of equations describes a non-self-sustained DC discharge.

The electron and ion mobilities and diffusion coefficients in argon and in nitrogen plasmas as functions of the reduced electric field E/N, where N=P/kT is the number density, are taken from [7,8]. The gas pressure and temperature in the optically pumped cell have been previously measured in a wide range of experimental conditions [1-3,6]. Thus, the only unknown parameters remaining in Eqs. (5-7) are the electron production rate, S, and the electron-ion recombination rate, β.

Eqs. (5-7) are solved numerically until either a steady-state (for a DC discharge) or a periodic (for an RF discharge) solution for $n_k(x,y,t)$ and $\phi(x,y,t)$ is reached. In the latter case this usually takes from a

few hundred to a few thousand cycles. The electrode currents in the DC and in the RF discharges are determined as follows,

$$I_{cathode} = L \int_{-W}^{W} dx \sum_{k} \Gamma_{ky}(x,0) \tag{9}$$

$$I_{RMS,cathode} = \left\{ \frac{1}{T} \int_{o}^{T} dt \left[L \int_{-W}^{W} dx \left(\varepsilon_{o} \frac{\partial E_{y}(x,0,t)}{\partial t} + \sum_{k} \Gamma_{ky}(x,0,t) \right) \right]^{2} \right\}^{1/2} \tag{10}$$

In Eqs. (9,10), Γ_{ky} is the y-component (i.e. perpendicular to the electrode) of the flux of the charged species k, E_{y} is the y-component of the electric field, L is the length of the electrode along the laser beam, and $T=2\pi/v$ is the RF field oscillation period. The anode current, which is expected to be equal to the cathode current, is calculated in a similar way.

In the calculations discussed in the following section, the 3 cm diameter circular electrodes (see Fig. 1) are modeled as square electrodes of the same surface area. The electrode separation is d=10 mm (for DC discharge) and d=7.5 mm (for RF discharge), the electrode full width and the electrode length are 2W=L=2.66 cm. The ionized region diameter, a=2 mm, is estimated from the apparent diameter of the C_2 Swan band glow, which is strongly coupled to the high vibrational level populations of CO [1]. The applied DC voltage is varied in the range U=0-1000 V. The RF voltage amplitude and frequency are U_0=5 V and v=10 MHz, respectively [1]. Calculations are made at two different pressures, P=100 torr and 20 torr. The gas temperature is taken to be T=500 K, which is in between the temperatures of T=600 K and in T=450 K measured in the optically pumped CO/Ar=2/100 and CO/N_2=2/100 mixtures at P=100 torr [1]. The system of equations (5-7) is solved using standard stiff PDE solver PDECOL [9].

3. Results and Discussion

The first series of modeling calculations have been made for a DC discharge. In these calculations, the electron production rate at the laser beam axis, S_0, was adjusted to match the experimentally measured values of the discharge saturation current, I_S, while the electron recombination rate was assumed to be equal to the rate of dissociative recombination of $(CO)_2^+$ dimer ions, $\beta=2 \cdot 10^{-6}$ [10]. Figure 2 shows experimental and calculated voltage-current characteristics for two optically pumped gas mixtures, 2 torr CO / 100 torr Ar and 2 torr CO / 100 torr N_2. One can see that the results of calculations reproduce well not only the values of the saturation current, which are controlled exclusively by the electron production rate (I_s=13.4 μA in CO/Ar and I_s=3.1 μA in CO/N_2) [2,4], but also the entire

shape of the voltage-current characteristics. The values of S_0 for the two cases shown in Fig. 2 are $S_0=1.0\cdot10^{15}$ 1/cm^3/s and $S_0=2.2\cdot10^{14}$ 1/cm^3/s, respectively. Varying the other crucial parameter, the recombination rate, in the range $\beta=10^{-7}$-10^{-5} cm^3/sec showed that although it does affect the shape of the current-voltage curves below the saturation limit, the effect is too weak for the accurate inference of the recombination rate coefficient. The best agreement with the experimental data in the entire range of applied voltage (U=0-1000 V) is achieved at $\beta>10^{-6}$ cm^3/sec. Unfortunately, above this value the calculated voltage-current curves become nearly insensitive to the recombination rate variation. Also, variation of the ion mobility μ_+ (within a factor of two) had almost no effect on the calculated voltage-current characteristics.

Figures 3 and 4 show contour plots of electron and ion concentrations, n_e and n_+, as well as electric potential, ϕ, in the optically pumped CO/Ar mixture at U=200 V. In these calculations, $S_0=1.0\cdot10^{15}$ 1/cm^3/s and $\beta=2\cdot10^{-6}$ cm^3/sec. One can see that the applied voltage displaces the highly mobile electrons toward the anode (top electrode in Figs. 3,4), which creates a region of positive space charge with stronger electric field near the center of the cathode (bottom electrode). Figure 5 displays the electron concentration in the DC discharge in the CO/Ar mixture along the axis of symmetry of the discharge (i.e. at x=0) at several values of the applied voltage. It shows that as the applied voltage increases, the electrons are indeed removed from the interelectrode space until the electron concentration is significantly reduced (by more than an order of magnitude) near the saturation point at U=800 V. At these conditions, the rate of electron removal by the field approaches the overall electron production rate, so that

$$I_S \approx eL\int\limits_{0}^{d} dy \int\limits_{-W}^{W} dx\, S(x,y) \tag{11}$$

Figure 5 and Eq. (11) also illustrate the rationale for the inference of the electron production rate per unit volume from the DC discharge saturation current.

In our previous work [1], small amounts of oxygen or air have been added to the baseline CO/Ar gas mixtures to determine the sensitivity of the measured electron production rate S to the level of O_2 impurity in the cell. It was found that addition of O_2 in small concentrations (less than 0.1 torr) only weakly affects the DC discharge saturation current (and therefore the electron production rate). In particular, the electron production rate is reduced by only about 30% if the oxygen partial pressure does not exceed 0.1 torr [1]. As discussed in our previous publication, this effect is most likely due to the reduction of the high CO vibrational level populations in the presence of oxygen, measured by infrared

emission spectroscopy [1]. In other words, the rate of electron production by the associative ionization mechanism remains nearly constant (within about 30%) in the presence of trace amounts of O_2.

The results of calculations discussed above show that the non-self-sustained DC discharge measurements indeed allow direct inference of the electron production rate by the associative ionization mechanism. Unfortunately, this method does not allow accurate inference of the electron density in the optically pumped plasma or the recombination rate coefficient since the voltage-current characteristic of the DC discharge is only weakly sensitive to the variation of these parameters. To infer the values of these parameters, we use the results of non-self-sustained RF discharge experiments in optically pumped CO/Ar mixtures containing small amounts of O_2 [1]. In these measurements, the conduction current through the non-self-sustained RF discharge, I_C, has been determined as a difference between the RF currents measured with the CO laser turned on and off. In the latter case, the RF current measured, 190 μA, is the displacement current. The most important result of these measurements is a sudden increase of the conduction current when small amounts of O_2 (0.05-0.1 torr) are added to the baseline CO/Ar gas mixture (without oxygen), from $I_C<2$ μA to $I_C=90\text{-}110$ μA at P=100 torr and from $I_C=15\text{-}20$ μA to $I_C=160\text{-}220$ μA at P=20 torr [1]. Again, we emphasize that this effect occurs at a nearly constant (within about 30%) electron production rate measured using the DC discharge [1]. A preliminary suggestion made in our previous publication [1] was that adding O_2 to the baseline gas mixture resulted in a significant reduction of the electron removal rate. In the present paper we use the RF discharge modeling to verify this suggestion and to infer the electron removal rate.

A second series of modeling calculations have been made for the RF discharge. Although the kinetic model discussed in Section 2 can be easily modified to incorporate the transport equation for the negative ions, as well as kinetic processes involving formation and decay of negative ions (including the dominant process of O_2^- ions formation by the three-body electron attachment process $O_2+e+M\rightarrow O_2^-+M$), in the present work these processes are neglected. The arguments in favor of this assumption are as follows: (i) adding O_2 to the cell gases results in an apparent increase of the electron density in the discharge, which suggests that rapid three-body elecron attachment to oxygen is mitigated to a large extent, (ii) similar results were obtained when comparable amounts of NO, which is not an efficient electron attacher, were added to the cell gases [1], and (iii) Raman spectroscopy measurements of the O_2 vibrational level populations (v=0-12) in the optically pumped CO/N$_2$/O$_2$ plasmas [11] show that O_2 in these mixtures becomes strongly vibrationally excited ($T_v(O_2)=2200\text{-}3600$ K). In particular, the latter result suggests that strong vibrational excitation of O_2 might well stimulate detachment of electrons from the weakly bound O_2^- ions (with electron affininity of ~0.43 eV). The electron production rate in these calculations was taken to be equal to the baseline value of $S_0=1.0\cdot10^{15}$ 1/cm^3/s inferred from the DC

discharge measurements in the CO/Ar mixtures. The electron-ion recombination rate in the calculations was varied in the range $\beta=10^{-9}-10^{-5}$ cm^3/s.

Figures 6,7 show contour plots of the period-averaged electron and ion concentrations, as well as the period-averaged electric potential in the RF discharge. In these calculations, the recombination rate coefficient is taken to be $\beta=2.0\cdot10^{-8}$ cm^3/s. One can see that the applied weak RF field displaces the electrons away from the electrodes, thereby creating the positive space charge areas (sheath) near the electrodes. The electric field in the sheath areas significantly exceeds its value in the quasi-neutral central region, and increases with electron density (i.e. as the recombination rate coefficient is reduced at the constant electron production rate, see Fig. 8). The electric field increase near the electrodes produces the current rise in the external circuit over the level of the displacement current, measured with the laser turned off. The kinetic model used in the present work predicts the RF discharge conduction current as a function of the recombination rate coefficient β (see Fig. 9). Therefore, with the electron production rate $S_0=1.0\cdot10^{15}$ 1/cm^3/s known, one can infer the values of the recombination rate in the baseline CO/Ar mixture (without oxygen) and in the mixture with 0.05-1.0 torr of O_2 added by comparing the RF conduction current measurements [1] discussed above and Fig. 9. Using this procedure, for CO/Ar mixtures at 100 torr and 20 torr we obtain $\beta>6.0\cdot10^{-6}$ cm^3/s and $\beta=(7.5\pm1.5)\cdot10^{-6}$ cm^3/s, respectively. For CO/Ar/O_2 mixtures at 100 torr and 20 torr, we infer $\beta=(1.5\pm0.3)\cdot10^{-8}$ cm^3/s and $\beta=(5.1\pm2.9)\cdot10^{-8}$ cm^3/s, respectively. In other words, adding oxygen to the CO/Ar mixture reduces the recombination rate coefficient by more than two orders of magnitude. A similar result is obtained in the CO/N_2 mixtures with small amounts of O_2 added [1]. Figure 10 also shows the RF conduction current as a function of the electron density at the laser beam axis. One can see that the measured values of the RF discharge conduction current correspond to an electron density of $n_e=(1.7\pm0.2)\cdot10^{11}$ cm^{-3} at P=100 torr and $n_e=(6.2\pm0.8)\cdot10^{10}$ cm^{-3} at P=20 torr. The lower electron density at the low pressure (at the same electron production rate) is due both to somewhat faster electron recombination rate and to a more significant contribution of the charged species diffusion out of the ionized region. Variation of the ion mobility within a factor of two had almost no effect on the shape of the curves shown in Figs. 9,10, and therefore on the inferred values of the recombination rate coefficient and electron density.

The inferred electron-ion recombination rates in the absence of oxygen and with O_2 added to the cell are fairly close to the measured rates of recombination of the dimer $(CO)_2^+$ ions, $\beta=2\cdot10^{-6}$ cm^3/s [10] and of the monomer O_2^+ ions, $\beta=(3-5)\cdot10^{-8}$ cm^3/s at the electron temperature of $T_e\sim0.3-0.5$ eV [5]. Also, the results of our previous coupled master equation / Boltzmann equation modeling calculations [3] suggest that the electron temperature in the optically pumped plasma, $T_e=5200$ K, is closely coupled with the CO vibrational temperature, $T_v(CO)=4100$ K. Therefore, although the detailed kinetic mechanism of the

apparent recombination rate reduction remains uncertain, one might speculate that adding oxygen to the cell gases might result in the replacement of the dominant rapidly recombining dimer $(CO)_2^+$ ions by the more slowly recombining O_2^+ ions, which also have lower ionization potential (12.2 eV vs. 14.0 eV), e.g. in an ion-molecule reaction

$$(CO)_2^+ + O_2 \rightarrow CO + CO + O_2^+ \tag{12}$$
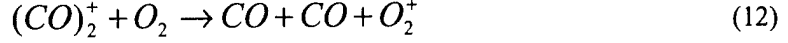
There exist some experimental evidence which is consistent with this qualitative scenario. Kaufman et al. [12] measured the ion composition in glow discharges in $CO/Ar/O_2$ and in $CO/He/O_2$ gas mixtures at P=18 torr using in situ ion mass spectrometry. The resultant mass spectra taken in CO/Ar and in CO/He mixtures without oxygen show that the dominant ions in the discharge are cluster ions of the general form $C_n(CO)_2^+$, n=1-15. However, adding a few tens of millitorr of O_2 to these gas mixtures resulted in nearly complete disappearance of these ions and their replacement by the O_2^+ ions. Additional non-intrusive electron density measurements (such as using microwave attenuation) and ion mass spectrometry measurements in the optically pumped plasmas are desirable to yield more information on the kinetic mechanism of the observed effect.

4. Summary

The analysis of the experiments reported in our previous paper [1] using modeling calculations discussed in the present work show that non-self-sustained DC and RF discharges can be successfully used for measurements of electron production rate, electron recombination rate, and electron density in the optically pumped plasmas. The inferred rate of electron production per unit volume by the associative ionization mechanism is $S_0=1.0 \cdot 10^{15}$ $1/cm^3/s$ and $S_0=2.2 \cdot 10^{14}$ $1/cm^3/s$ in CO/Ar=2/100 and in CO/N_2=2/100 plasmas, respectively. The inferred electron-ion recombination rate coefficients are $\beta > 6.0 \cdot 10^{-6}$ cm^3/s and $\beta = (7.5 \pm 1.5) \cdot 10^{-6}$ cm^3/s in CO/Ar=2/100 mixtures at P=100 torr and 20 torr, respectively. In CO/Ar=2/100 mixtures with a 0.05-0.1 torr admixture of O_2 at P=100 torr and 20 torr, the inferred recombination rate coefficients are $\beta = (1.5 \pm 0.3) \cdot 10^{-8}$ cm^3/s and $\beta = (5.1 \pm 2.9) \cdot 10^{-8}$ cm^3/s. Finally, the inferred electron density in the optically pumped $CO/Ar/O_2$ plasmas at the laser beam axis is $n_e = (1.7 \pm 0.2) \cdot 10^{11}$ cm^{-3} at P=100 torr and $n_e = (6.2 \pm 0.8) \cdot 10^{10}$ cm^{-3} at P=20 torr. These results demonstrate that electron density in the optically pumped CO/Ar plasmas can be controlled and significantly increased by adding small amounts (up to ~0.1%) of species such as O_2 and NO, which result in reduction of the electron-ion recombination rate.

References

1. E. Ploenjes, P. Palm, I.V. Adamovich, and J.W. Rich, "Ionization Measurements in Optically Pumped Discharges", Journal of Physics D: Applied Physics, vol. 33, No. 16, 2000, pp. 2049-2056

2. I. Adamovich, S. Saupe, M.J. Grassi, O. Shulz, S. Macheret and J.W. Rich, "Vibrationally Stimulated Ionization of Carbon Monoxide in Optical Pumping Experiments", Chemical Physics, vol. 173, 1993, pp. 491-504

3. I.V. Adamovich and J.W. Rich, "The Effect of Superelastic Electron-Molecule Collisions on the Vibrational Energy Distribution Function", Journal of Physics D: Applied Physics, vol. 30, No. 12, 1997, pp. 1741-1745

4. E.P. Velikhov, A.S. Kovalev, and A.T. Rakhimov, "Physical Phenomena in Gas Discharge Plasmas", Moscow, Nauka, 1987

5. Raizer, Y.P., "Gas Discharge Physics", Springer-Verlag, Berlin, 1991

6. E. Ploenjes, P. Palm, A.P. Chernukho, I.V. Adamovich, and J.W. Rich, "Time-Resolved Fourier Transform Infrared Spectroscopy of Optically Pumped Carbon Monoxide", Chemical Physics, vol. 256, pp. 315-331, 2000

7. L.G.H Huxley and R.W. Crompton, "The Diffusion and Drift of Electrons in Gases", Wiley, New York, 1974

8. E.W. McDaniel, "Collision Phenomena in Ionized Gases", Wiley, New York, 1964

9. N.K. Madsen and R.F. Sincovec, ACM Trans. Math. Software, vol. 5, 1979, p. 326

10. R. Johnsen, "Recombination of Cluster Ions", in B.R. Rowe et al. (eds.), "Dissociative Recombination", Plenum, New York, 1993

11. W. Lee, I.V. Adamovich, and W.R. Lempert, "Optical Pumping Studies of Vibrational Energy Transfer in High-Pressure Distomic Gases", submitted to Journal of Chemical Physics, May 2000

12. Y. Kaufman, P. Avivi, F.Dothan, H. Keren, J. Malinowitz, J. Chem. Phys., Vol. 72, 1980, p. 2606
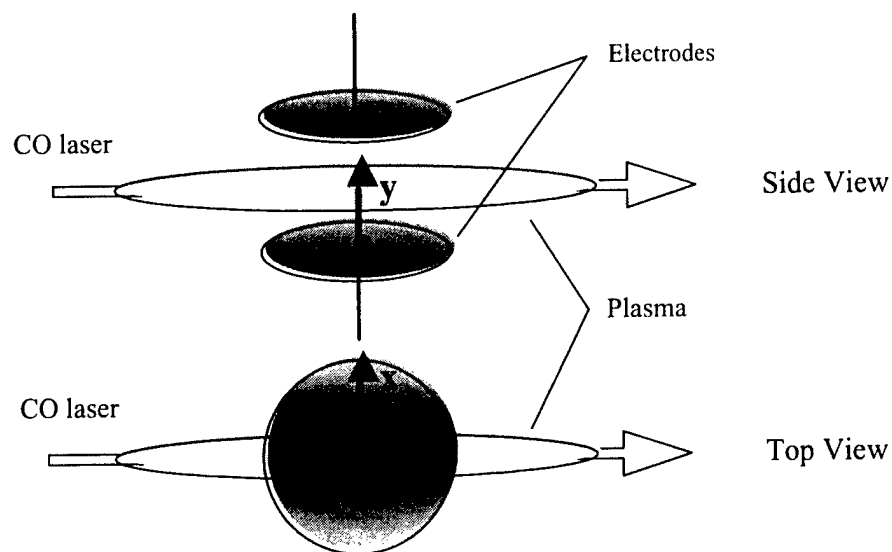
Figure 1. Schematic of electrodes in the cell and of the discharge geometry
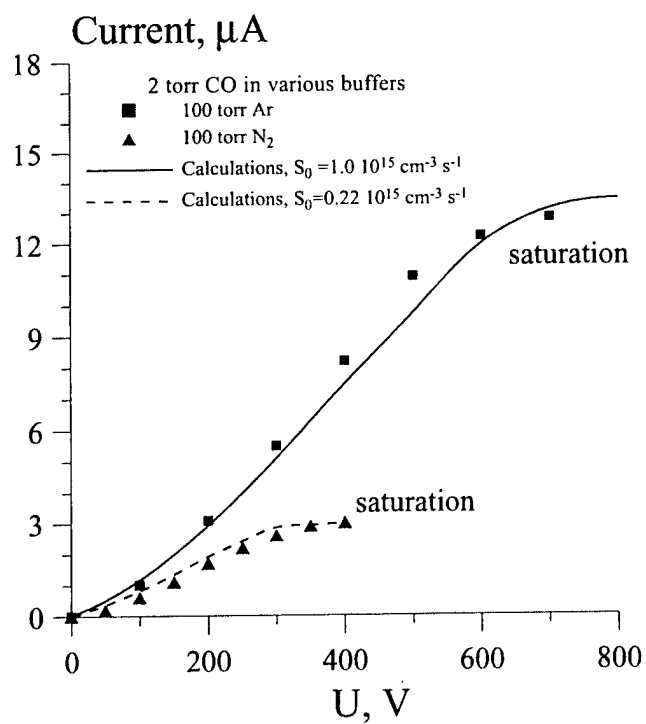
Figure 2. Experimental and calculated voltage-current characteristics of the DC discharge in the optically pumped plasmas. $\beta=2\cdot10^{-6}$ cm^3/sec

Ion Concentration   **Electron Concentration**
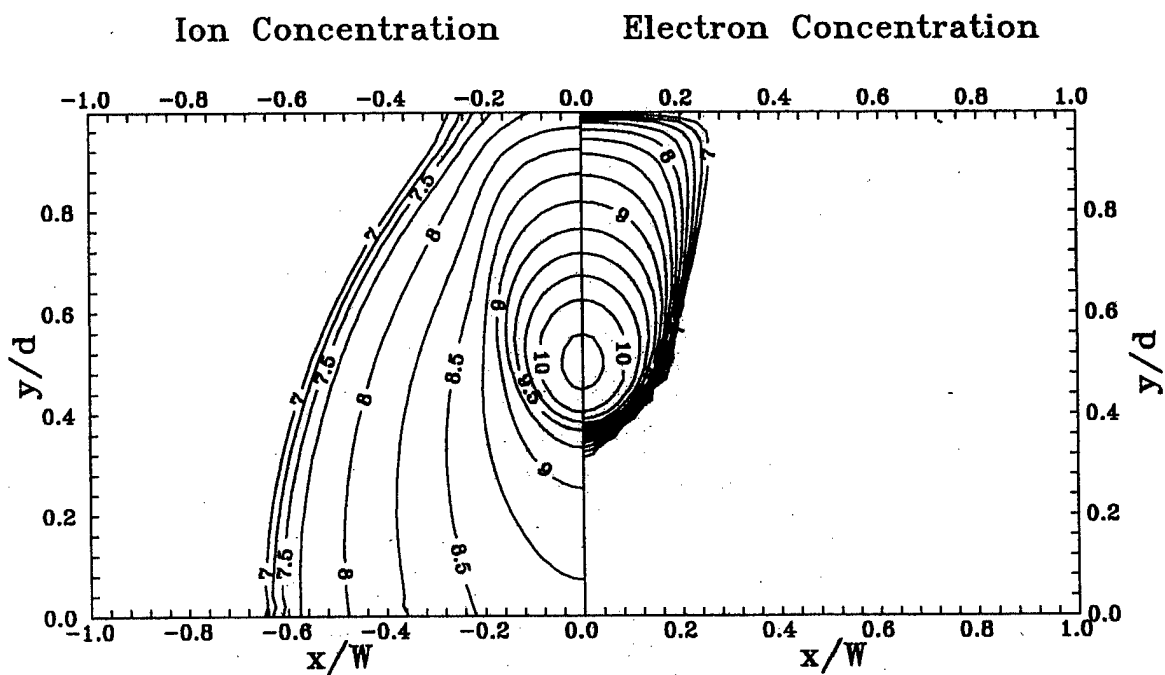
Figure 3. Calculated electron and ion concentration distributions (log scale, in cm^{-3}) in the DC discharge in the optically pumped CO/Ar plasma. $S_0 = 1.0 \cdot 10^{15}$ $cm^{-3}sec^{-1}$, $\beta = 2 \cdot 10^{-6}$ cm^3/sec, U=200 V

Electric Potential
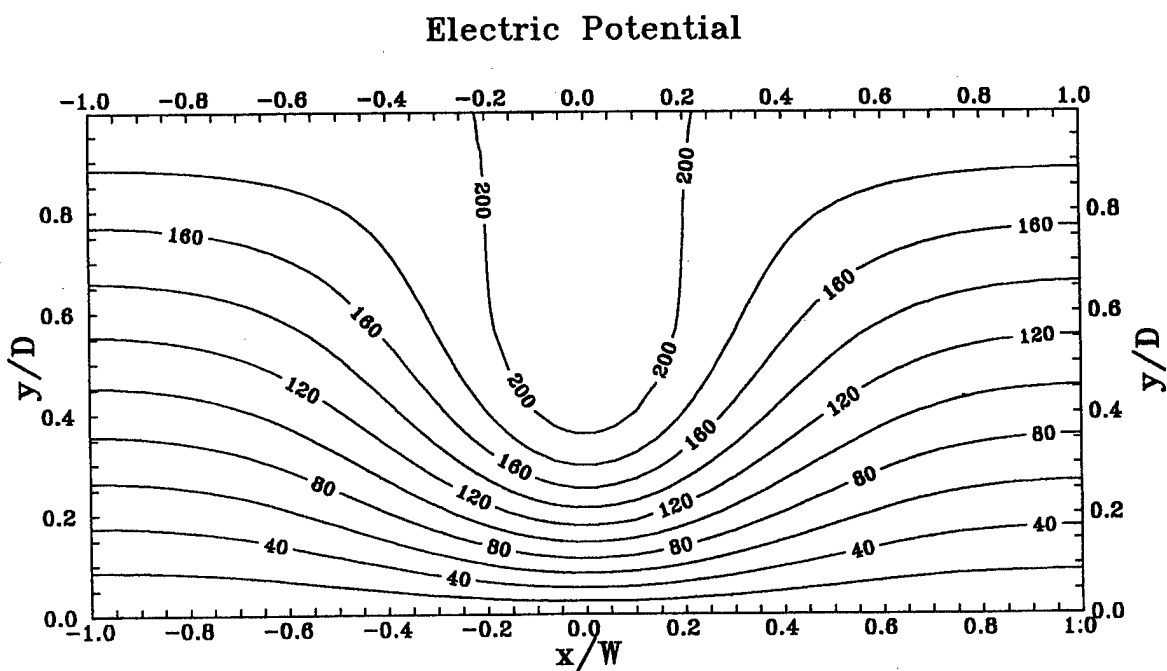
Figure 4. Calculated electric potential distribution (in Volts) in the DC discharge in the optically pumped CO/Ar plasma. $S_0 = 1.0 \cdot 10^{15}$ $cm^{-3}sec^{-1}$, $\beta = 2 \cdot 10^{-6}$ cm^3/sec, U=200 V

Centerline electron concentration, cm^{-3}
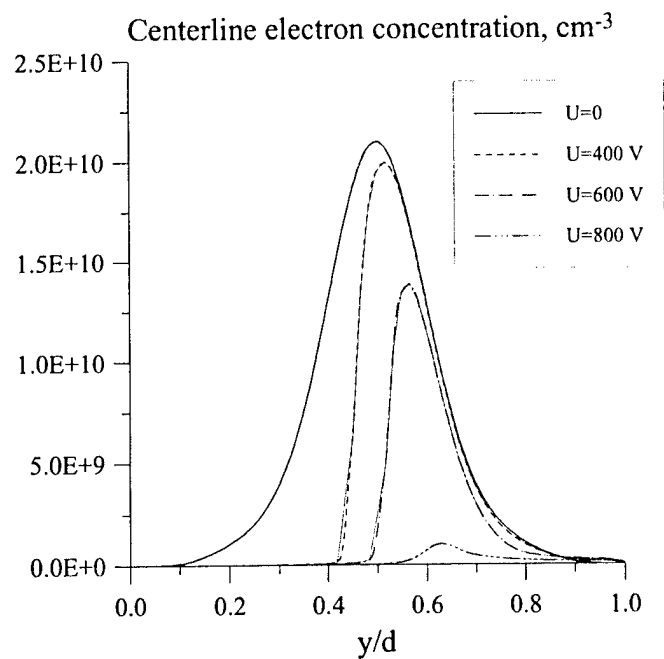
Figure 5. Calculated electron concentration in the CO/Ar plasma at the axis of symmetry of the discharge (x=0) for the conditions of Fig. 2

Ion Concentration   Electron Concentration
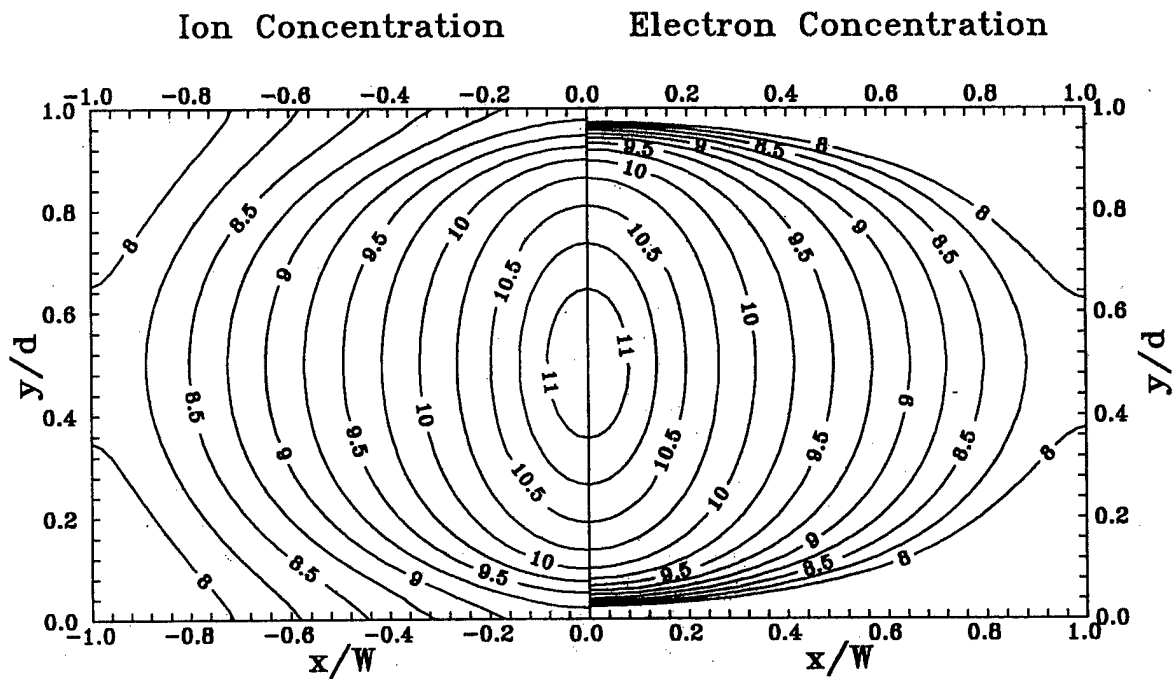
Figure 6. Calculated period-averaged electron and ion concentration distributions (log scale, cm^{-3}) in the RF discharge in the optically pumped CO/Ar plasma. S_0=1.0·10^{15} cm^{-3}sec^{-1}, β=2·10^{-8} cm^3/sec

Electric Potential
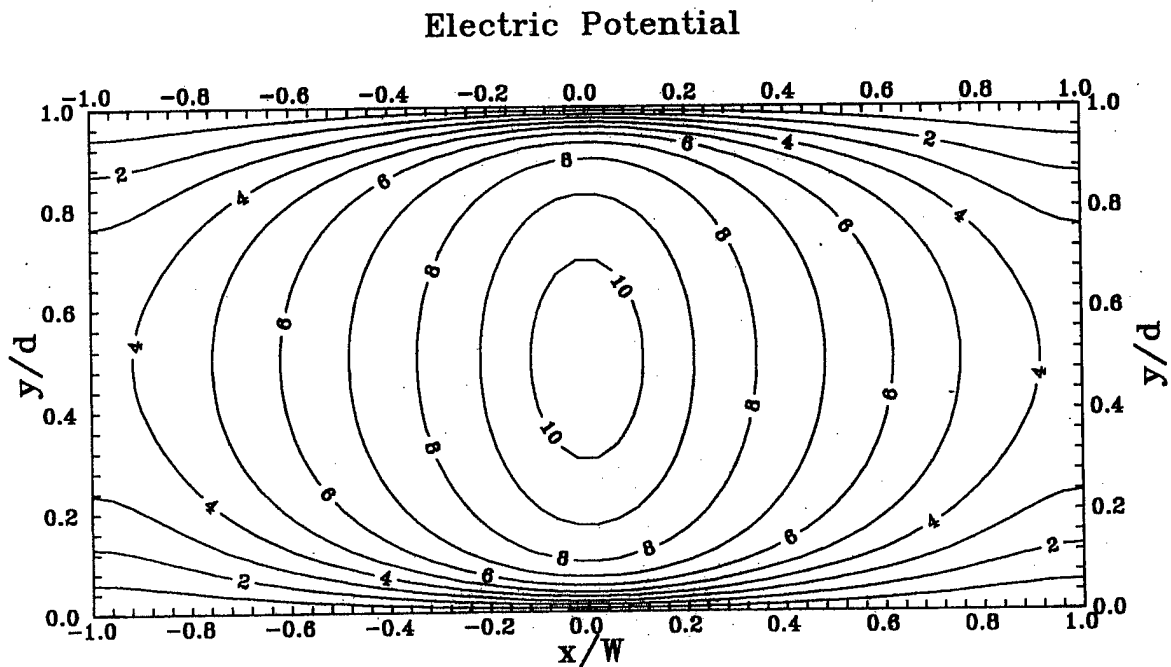
Figure 7. Calculated period-averaged electric potential distribution (in Volts) in the RF discharge in the optically pumped CO/Ar plasma. S_0=1.0·10^{15} cm^{-3}sec^{-1}, β=2·10^{-8} cm^3/sec
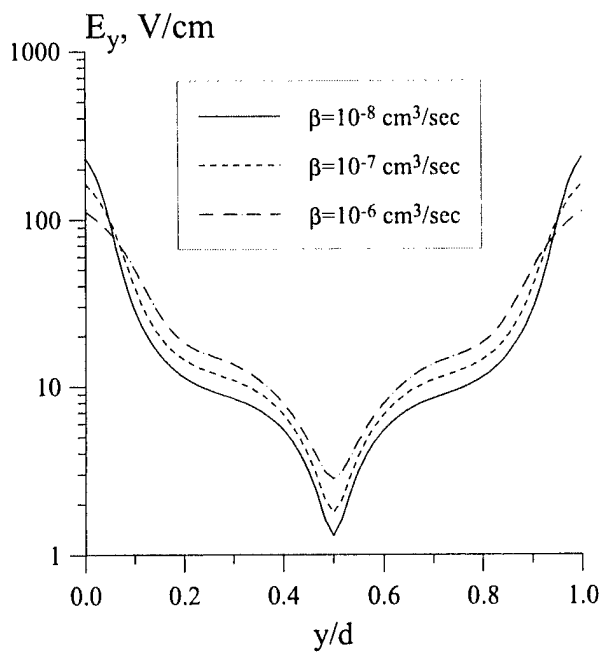
Figure 8. Calculated y-component of the RMS electric field in CO/Ar plasma at the axis of symmetry of the RF discharge (x=0).
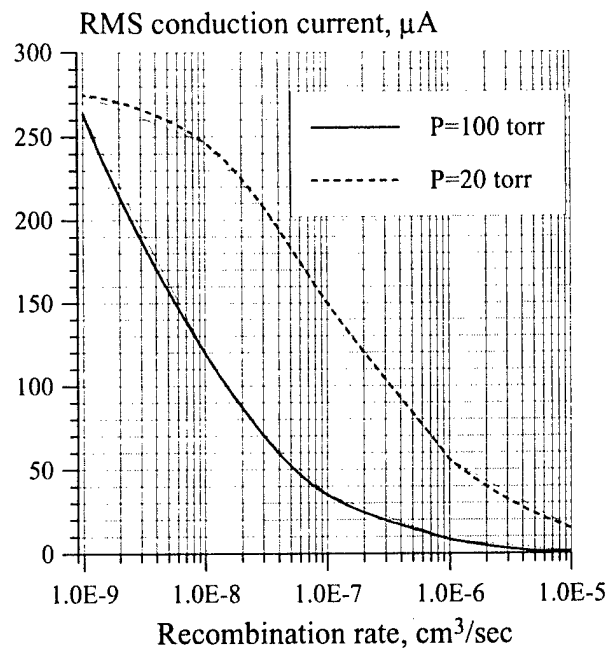
Figure 9. Calculated RMS conduction current of the RF discharge as a function of the recombination rate coefficient.
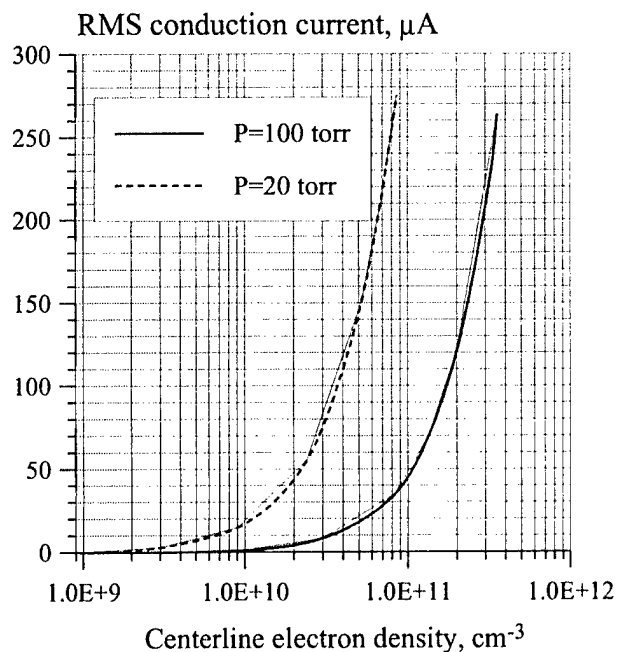
Figure 10. Calculated RMS conduction current of the RF discharge as a function of the electron density at the laser beam axis.

4. VIBRATIONAL ENERGY STORAGE IN HIGH-PRESSURE MIXTURES OF DIATOMIC MOLECULES

Elke Plönjes, Peter Palm, Wonchul Lee, Matthew D. Chidley, Igor V. Adamovich,

Walter R. Lempert, and J. William Rich

CO/N_2, $CO/Ar/O_2$, and $CO/N_2/O_2$ gas mixtures are optically pumped using a continuous wave CO laser. Carbon monoxide molecules absorb the laser radiation and transfer energy to nitrogen and oxygen by vibration-vibration energy exchange. Infrared emission and spontaneous Raman spectroscopy are used for diagnostics of optically pumped gases. The experiments demonstrate that strong vibrational disequilibrium can be sustained in diatomic gas mixtures at pressures up to 1 atm, with only a few Watts laser power available. At these conditions, measured vibrational temperatures of diatomic species are in the range T_v=1900-2300 K for N_2, T_v=2600-3800 K for CO, and T_v=2200-2800 K for O_2. Translational-rotational temperature of the gases does not exceed T=700 K. Line-of-sight averaged CO vibrational level populations up to v=40 are inferred from infrared emission spectra. Vibrational level populations of CO(v=0-8), N_2(v=0-4), and O_2(v=0-8) near the axis of the focused CO laser beam are inferred from the Raman spectra of these species. The results demonstrate a possibility of sustaining stable nonequilibrium plasmas in atmospheric pressure air seeded with a few per cent of carbon monoxide. The obtained experimental data are compared with modeling calculations that incorporate both major processes of molecular energy transfer and diffusion of vibrationally excited species across the spatially nonuniform excitation region, showing reasonably good agreement.

1. Introduction

Nonequilibrium vibrational kinetics of diatomic molecules has been a focus of attention for many years in gas discharge plasmas, molecular lasers, pollution control, upper atmosphere chemistry, and gas dynamic flows [1,2]. The rate of energy transfer between the vibrational molecular modes and the "external" modes of rotation and translation is, in particular, a determining process in many high enthalpy fluid environments (such as in supersonic nozzles and behind shock waves). Furthermore, the details of energy distribution among the quantum states within the vibrational modes is a key issue in non-thermal plasma chemical reactor design, in predicting radiation from supersonic nozzle expansions, and in the design of a variety of molecular gas lasers [3]. This energy distribution is primarily controlled by vibration-to-vibration (V-V) energy exchange processes [4,5],

$$AB(v) + CD(w) \rightarrow AB(v-1) + CD(w+1),\tag{1}$$

which in a broad range of parameters are known to be much faster than vibration-to-translation (V-T) relaxation,

$$AB(v) + CD \rightarrow AB(v-1) + CD. \qquad (2)$$
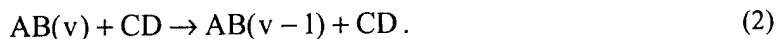
In Eqs. (1,2), AB and CD stand for diatomic molecules, v and w are vibrational quantum numbers. Near-resonance V-V exchange processes, such as $E_v(AB)-E_{v-1}(AB)\lambda E_{w+1}(CD)-E_w(CD)$ in Eq. (1), are of particular importance, since they can sequentially populate very high vibrational levels of the molecules [4,5], and thereby precipitate nonequilibrium chemical reactions, electronic excitation with subsequent visible and UV radiation, and ionization.

Methods of sustaining strong vibrational disequilibrium in gases include (i) rapid expansion in a supersonic nozzle, (ii) excitation of molecular vibrations in electric discharges, and (iii) optical pumping by laser radiation absorption. The use of the first approach is difficult due to the short available test time, while the second approach is limited to fairly low pressures (P~1 atm) and low energy loading per molecule because of rapid development of discharge instabilities [6,7]. In contrast to this, steady state optically pumped plasmas can be sustained at high pressures (up to 20 atm in CO-Ar mixtures) [8]. The main problem with optical pumping, however, is that the use of efficient resonance absorption provides access only to a very few heteropolar molecules (such as CO and NO with a CO laser [9-14], or CO with a frequency doubled CO_2 laser [15]). On the other hand, the use of nonlinear absorption techniques, such as PUMP-DUMP [16], RELIEF [17], spontaneous Raman absorption [18], etc., allows only pulsed mode operation and makes energy addition to vibrational modes of homopolar molecules, such as N_2 and O_2, extremely inefficient.

These obstacles prevent development of new promising applications of vibrationally nonequilibrium environments, including sustaining stable large-volume ionization in high-pressure air and energy efficient high-yield mode-selective chemical synthesis.

The present paper discusses a new method of vibrational excitation of high-pressure gases, including nitrogen and oxygen, by collision-dominated vibrational energy transfer of Eq. (1) from an infrared active species (carbon monoxide), optically pumped by resonance absorption of the CO laser radiation. This method combines the advantage of the use of an efficient gas laser with the capability of excitation of various species at high pressures, without using electron impact.

2. Experimental

2.1 Emission spectroscopy

Figure 1 shows a schematic of the experimental setup for the study of vibrational energy transfer in $CO/Ar/N_2/O_2$ mixtures. A carbon monoxide laser is used to irradiate a gas mixture, which is slowly flowing through the pyrex glass optical absorption cell shown. The residence time of the gases in the cell is about 1 sec. The liquid nitrogen cooled CO laser was designed in collaboration with the University of Bonn and fabricated at Ohio State. It produces a substantial fraction of its power output on the $v = 1 \rightarrow 0$ fundamental band component in the infrared. The laser can operate at more than 100 W continuous wave (c.w.) power. However, in the present experiment, the laser is typically operated at 15 W c.w. broadband power on the lowest ten fundamental bands, with up to ~0.3 W on the $v = 1 \rightarrow 0$ component. The output on the lowest bands ($1 \rightarrow 0$ and $2 \rightarrow 1$) is necessary to start the absorption process in cold CO (initially at 300 K) in the cell. The quantum efficiency of the CO pump laser approaches 90%, with the overall efficiency about 40%, which makes is the most efficient gas laser available. The present use of CO laser pumped absorption cells to study the V-V process is a further development of a technique with a considerable literature [9-14].

The emission spectroscopy measurements reported here are made at CO partial pressure of 2 torr and total gas pressure of 100-130 torr. At these conditions, the gas mixture is optically thick for the CO laser radiation. A substantial portion of the laser power (up to 5 W) is absorbed over the absorption distance of L=12.5 cm. The Gaussian laser beam, which has a diameter of ~0.5 cm, does not have to be focused to provide substantial vibrational mode energy in the cell gases. However, in the present experiments it is focused to increase the power loading per CO molecule, providing an excitation region in the cell of ~1 mm diameter.

After the laser is turned on, the lower states of CO, $v \leq 10$, are populated by direct resonance absorption of the pump radiation in combination with the much more rapid redistribution of population by the intramode V-V exchange processes CO-CO (see Eq. (1)). These V-V processes then continue to populate the higher vibrational levels of CO above $v = 10$, which are not directly coupled to the laser radiation. At the same time, the intermode V-V exchange processes CO-N_2 and CO-O_2 also populate the low vibrational levels of nitrogen and oxygen molecules. In particular, rapid vibrational energy transfer from highly excited CO molecules to oxygen is facilitated by the near-resonance process

$$CO(v) + O_2(0) \rightarrow CO(v-1) + O_2(1), \quad v \sim 25 \qquad (3)$$
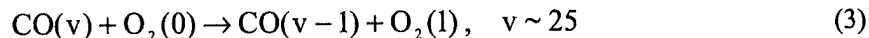
If the vibrational energy storage per N_2 or O_2 molecule becomes sufficiently high, the high vibrational levels of these molecules will be also populated by the intramode V-V exchange N_2-N_2 and O_2-O_2. It is well known [19] that until vibrationally excited molecules start producing rapid V-T relaxers in chemical

reactions (such as N and O atoms, CO_2, etc.), the overall rate of V-T relaxation in the gas mixture remains slow. Therefore, a substantial fraction of the energy added to the vibrational mode of CO by the laser remains stored in vibrational modes of N_2 and O_2.

When the laser is turned off, the vibrational levels are depopulated, again mainly by the V-V energy transfer, and the vibrational energy distribution approaches the Boltzmann distribution at the translational temperature. In the steady-state measurements reported in the present paper, the laser remains on all the time, so that a complete steady state is reached. Note that the vibrational energy stored in the diatomic molecules is constantly converted into heat both in V-V and V-T processes. However, the large heat capacity of the gases (including the vibrational modes), as well as conductive and convective cooling of the gas flow, allow us to control the translational/rotational mode temperature in the cell. Even in steady-state conditions, when the average vibrational mode energy of the CO would correspond to a few thousand degrees Kelvin, the temperature does not rise above a few hundred degrees. Thus a strong disequipartition of energy can be maintained in the cell, characterized by very high vibrational mode energy and a low translational/rotational mode temperature. As discussed in Section 1, similar nonequilibrium conditions exist in a variety of rapid supersonic expansions, in glow plasma discharges, and in a number of other thermodynamic environments. The present setup allows us to study the energy transfer and kinetic processes in a closely controlled environment, without the complications of electron impact processes and instabilities, which occur in electric discharges, or the experimental difficulties of creating and controlling a supersonic flow.

As shown in Fig. 1, the population of the vibrational states of the CO in the cell is monitored by infrared emission spectroscopy. For this purpose, a Bruker Fourier transform (FT) IFS 66 spectrometer is used to record the spontaneous emission from the CO fundamental, first and second overtone bands through a window on the side of the cell. The emission spectra are recorded at both high spectral resolution of 0.25 cm^{-1} and low resolution of 8.0 cm^{-1}. The translational-rotational temperature of the cell gases is determined from the rotational structure of the R-branch of the CO fundamental band $1 \rightarrow 0$.

2.2. Raman spectroscopy

To measure vibrational populations of N_2 and O_2 molecules in optically pumped gas mixtures, spontaneous Raman spectroscopy is used. Laser Raman diagnostics were performed by combining the CO laser beam and a pulsed Nd:YAG Raman pump laser beam using a 90^0 CaF_2 dichroic mirror, which transmits the CO laser, while reflecting the Nd:YAG laser (see Fig. 2). Raman spectra were obtained using the second harmonic output of the Nd:YAG laser in combination with an Optical Multichannel Analyzer (OMA) detector. The Nd:YAG laser was focused coaxial to the CO pump laser and Raman scattering in a volume element approximately 0.100 mm in diameter x 2 mm long was captured at 90^0. A

simple long wavelength pass (OG – 570) colored glass filter was used to attenuate the elastic scattering at 0.532 microns and transmit the Stokes shifted scattering, which was in the range 0.570 – 0.615 microns. The OMA consists of a 1/4 meter grating spectrometer with a micro-channel plate intensified CCD camera as the detector. The intensifier allowed a fast (~10 nsec) gate so that spontaneous emission from the optically pumped gas, which was much brighter than the detected Raman signal, could be minimized. The signal was integrated for time duration in the range 1-10 minutes. The resolution of the spectrometer was sufficient to resolve individual Q-branch vibrational bands but could not resolve any rotational fine structure. The wavelength coverage enabled the capture of approximately 15 vibrational bands simultaneously. Determining the complete N_2, O_2, and CO vibrational distributions required merging of 3 spectra, which were obtained sequentially with identical experimental conditions. More experimental detail can be found in our separate publication [20].

Note that inference of the vibrational level populations from Raman spectra requires knowledge of the Raman cross section dependence on the vibrational quantum number. For all data presented in this paper, we assume that the Stokes scattering cross sections scale as v+1, which is rigorously true only for a harmonic potential [21]. The measurements are made in CO/N_2 and $CO/N_2/O_2$ mixtures at total gas pressures of P=400 torr up to 1 atm, with 2-5% fraction of CO and up to 16% of O_2 in the cell.

3. Kinetic Model and the V-V Rate Parametrization

To interpret the results of the measurements, we use a state-specific kinetic model of excitation and relaxation of optically pumped anharmonic oscillators in inhomogeneous media. It is based on the master equation model described in detail in [10]; a significant upgrade is the incorporation of laser power distribution profile and transport processes (diffusion and heat conduction) across the Gaussian laser beam, which become of crucial importance when the beam is focused. The model evaluates the time-dependent vibrational level populations in $CO-N_2-O_2-Ar$ mixtures excited by a laser beam:

$$\frac{\partial n_{v,i}(r,t)}{\partial t} = \frac{1}{r}\frac{\partial}{\partial r}\left[rD_i\frac{\partial n_{v,i}(r,t)}{\partial r}\right] + VV_{v,i} + VT_{v,i} + SRD_{v,i} + VE_{v,i} + PL_{v,i}$$

$$\left.\frac{\partial n_{v,i}(r,t)}{\partial r}\right|_{r=0} = 0; \quad n_{v,i}(r,t)\big|_{r=\infty} = n_{v,i}(r,t)\big|_{t=0} = n_{v,i}(T_0) \tag{4}$$

$$v = 0, v_{max,i}$$

$$\rho c_p \frac{\partial T(r,t)}{\partial t} = \frac{1}{r} \frac{\partial}{\partial r} \left[r\lambda \frac{\partial T(r,t)}{\partial r} \right] + HVR$$

(5)

$$\frac{\partial T(r,t)}{\partial r}\bigg|_{r-0} = 0 \ ; \quad T(r,t)\big|_{r=\infty} = T(r,t)\big|_{t=0} = T_0$$

In Eqs. (4,5), $n_{v,i}(r,t)$ is the population of vibrational level v of species i, $n_{v,i}(T_0)$ is the initial equilibrium population at $T_0=300$ K, n_i are the species concentrations, r is the distance from the beam axis, D_i and λ are the diffusion and heat transfer coefficients, respectively, ρ and c_p are density and specific heat of the gas mixture at constant pressure. The rest of the notation is the same as in [10]: VV, vibration-vibration term; VT, vibration-translation term; SRD, spontaneous radiative decay (infrared); VE, vibration-electronic coupling; PL, laser pumping; HVR, gas heating by vibrational relaxation. The explicit expressions for these terms are given in [10].

The V-V rates for CO-CO, the V-T rates for CO-Ar, and the vibration-to-electronic (V-E) energy transfer rates $CO(X^1\Sigma)+CO \rightarrow CO(A^1\Pi)+CO$, used in the present model, were inferred from previous time-resolved optical pumping experiments [9,22]. The V-V rate parametrizations for CO-N_2, N_2-N_2, O_2-O_2, and N_2-O_2 are based on the results of the close-coupled trajectory calculations by Billing et al. [23-26]. Since the V-V rates for CO-O_2 are not available, they are evaluated by replacing the vibrational quantum of N_2 for that of O_2 in the CO-N_2 rate parametrization (see Appendix). The rationale for this assumption is that the near-resonance V-V exchange in both CO-N_2 and CO-O_2 collisions is primarily induced by the dipole-quadrupole interaction. The V-T rate parametrizations for CO-CO, N_2-N_2, and O_2-O_2 are also based on the results of calculations [23-26]; the remaining molecule-molecule V-T rates AB-M are considered to be independent of the collision partner M. Note that the V-T relaxation on molecules and on argon atoms is not expected to play an important part in the vibrational energy balance, because at the relatively low gas temperatures involved these V-T rates are very slow. The present version of the model does not incorporate V-T relaxation on reactive atoms such as N and O, because of the large uncertainty in prediction of chemical reaction rates of vibrationally excited molecules. The explicit analytic rate expressions used can be found in Appendix.

The system of equations (4,5) for 40 vibrational levels of CO, N_2, and O_2 is solved using a standard solver for stiff partial differential equations, PDECOL [27]. In the calculations, a 21-point nonuniform grid, with most points located near the laser beam axis, is used. The laser line intensity distributions are given by the equation $I_i(r)=I_{0i} \cdot [2/\pi R^2 \cdot \exp(-2r^2/R^2)]$, where I_{0i} are the incident line intensities in W, and parameter $R=0.56$ mm in the Gaussian intensity distribution across the focused laser beam is calculated by the code STRAHL developed at University of Bonn [28]. The present code uses the spectroscopic data

66

for the CO molecule [29] and accurate Einstein coefficients for spontaneous emission and absorption coefficients for the CO infrared bands [30] as inputs.

4. Results and Discussion

4.1. Emission Spectroscopy Results

Under the conditions described in Section 2, a highly nonequilibrium distribution of vibrational energy is created in the cell. Figure 3 shows the CO infrared emission from the CO-Ar mixture excited by the focused laser beam, as recorded by the FT spectrometer at a resolution of 0.25 cm^{-1}. The second overtone bands can be seen at the highest frequencies on the left (v>4300 cm^{-1}), the first overtone bands dominate at the lower frequencies (2250 cm^{-1}<v<4300 cm^{-1}), and the high frequency tail of the R-branch of the v = 1→ 0 fundamental is the tall peak on the right. A long wavelength cut-off filter is used to prevent any more of the very intense fundamental band emission at frequencies v<1950 cm^{-1} from entering the instrument, and swamping the overall signal. While this resolution is approximately 1/10 the rotational spacing of the CO molecule, there is a dense array of individual vibrational-rotational lines, due to the overlapping of the various band components.

The CO vibrational distribution functions (VDF) inferred from such high-resolution spectra using the standard technique [31], as well as theoretical line-of-sight averaged VDFs, are shown in Fig. 3 for two different gas mixtures, CO/Ar=2/100 and CO/N$_2$=2/100, at P=100 torr. The measured translational-rotational temperatures for these two cases are T=600 K and 450 K, respectively. The distributions shown in Fig. 4 are the well-known "V-V pumped" distributions [4,5], maintained by the rapid redistribution of vibrational energy by the V-V processes, which pump energy into the higher vibrational levels. They are obviously extremely non-Boltzmann, and characterized by high population of the upper vibrational levels. Note that replacing argon with nitrogen in the cell somewhat reduces the measured CO vibrational level populations, since some vibrational energy is transferred from CO to N$_2$. This effect is somewhat less pronounced in the calculations (see Fig. 4), which suggests that the theoretical V-V rates for CO-N$_2$ [23] used in the present calculations are underestimated. Figure 4 also shows the calculated centerline CO and N$_2$ VDFs in the CO/N$_2$ mixture. One can see that carbon monoxide at the beam center is in extreme vibrational disequilibrium. Furthermore, modeling calculations suggest that nitrogen also becomes strongly V-V pumped by vibrational energy transfer from CO, as discussed in Section 3. Calculated radial distributions of the first level vibrational temperature T$_v$(r), shown in Fig. 5, predict the centerline values of T$_v$(CO)=12,000 K in the CO/Ar mixture, and T$_v$(CO)=8500 K, T$_v$(N$_2$)=2400 K in the CO/N$_2$ mixture. For comparison, the apparent CO vibrational temperatures inferred from the line-of-sight averaged VDFs of Fig. 4 are T$_v$(CO)=3300 K and 2700 K, respectively. Figure 6 plots the calculated CO distribution

functions in the CO/Ar mixture at different distances from the laser beam axis. From Figs. 5,6, one can see that the optically pumped region is strongly nonuniform in the radial direction.

Figure 7 shows the experimental and the theoretical VDFs in $CO/Ar/O_2$ mixtures at different oxygen concentrations. One can see that the increase of O_2 partial pressure results in truncation of the CO VDF due to the V-V energy transfer from CO to O_2. However, even with 30 torr of O_2 in the cell, CO is still V-V pumped up to the level v~20. The model predictions do not fully reproduce the observed CO VDF fall-off at v>25 (see Fig. 7) unless the V-V rates for $CO-O_2$ at high vibrational levels (see Eq. (3)), varied in the calculations, considerably exceed the gas kinetic collision frequency. We believe this discrepancy to be due to (i) possible contribution of a fast nonadiabatic (reactive) channel of the V-V exchange between highly excited CO and O_2, and (ii) the effect of rapid V-T relaxation of CO on O atoms, both not incorporated into the model. An indirect evidence of these effects is the CO_2 infrared spectrum observed in $CO/Ar/O_2$ mixtures (see Fig. 8). CO_2 radiation, which could not be detected in CO/Ar and CO/N_2 mixtures, is most intense at oxygen partial pressures of 0.1-1.0 torr and becomes weaker as the O_2 concentration increases. CO_2 and oxygen atoms in the cell are likely to be produced in vibrationally stimulated chemical reaction $CO(v)+O_2(w) \rightarrow CO_2+O$. This scenario is consistent with the modeling calculations which predict strong vibrational excitation of diatomic species at the low O_2 partial pressures (see Fig. 9). For the conditions of Fig. 8, centerline vibrational temperatures are $T_v(CO)=13,000$ K, $T_v(O_2)=7000$ K and $T_v(CO)=9500$ K, $T_v(O_2)=3000$ K for 1 torr and 30 torr of O_2 in the cell, respectively.

4.2. Raman Spectroscopy Results

Spontaneous Raman spectroscopy allows access to vibrational levels of homopolar molecules and thereby provides powerful diagnostics of nonequilibrium gases. It also gives an opportunity for comparing predictions of modeling calculations discussed in Section 4.1 with the experimental data. In the experiments described in Section 3.2, Raman spectra of optically pumped CO, N_2, and O_2 are recorded in the pressure range P=400-760 torr. Figure 10 displays Raman spectra of these species measured in a $CO/N_2/O_2$ mixture at P=740 torr, with CO and O_2 partial pressures of 40 torr and 30 torr, respectively. In these spectra, one can easily identify a few low vibrational levels of CO, N_2, and O_2. However, Raman vibrational spectra of CO in CO/N_2 mixtures also show multiple peaks corresponding to about 40 first vibrational states of carbon monoxide [20]. This makes inference of vibrational populations of all these levels possible, provided that the Raman cross sections for highly vibrationally excited molecules are known with reasonable accuracy. As discussed in Section 3.2, Raman spectroscopy is essentially a point measurement. This means that if the focused Nd:YAG laser is aligned along the axis of the CO pump laser (see Fig. 2), the Raman spectra would provide vibrational level populations in the vicinity of the centerline of the excited region.

Figure 11 displays vibrational level populations of CO, N_2, and O_2 inferred from the Raman spectra such as shown in Fig. 10, at P=740 torr, with CO and O_2 partial pressures of 40 torr and 120 torr, respectively. Figure 12 shows vibrational level populations of CO and N_2 inferred from the Raman spectra of the optically pumped CO/N_2=3/100 mixture, at P=1 atm. At these conditions, the incident CO laser power of 10-13 W was about the same as in the experiments discussed in Section 4.1, while the gas pressure in the cell was much higher (~1 atm vs. 100 torr). Therefore vibrational energy loading per molecule in this second series of experiments is also much lower than in the first series. Indeed, the first level vibrational temperature of CO near the centerline, where vibrational disequilibirum is the strongest (T_v=2600-3000 K, see Figs. 11, 12), is in the same range as apparent values inferred from the line-of-sight averaged CO VDF in emission spectroscopy measurements (T_v=2700-3300 K, see Figs. 4,8). In other words, vibrational disequilibrium becomes weaker at higher pressures. However, even at P=1 atm it remains very strong. This is consistent with modeling calculations, also shown in Figs. 11, 12. Calculated centerline VDFs of the three diatomic species are in reasonable agreement with the data. Comparing the results of calculations in Figs. 11, 12, one can see that addition of oxygen to optically pumped gases results in depletion of the high vibrational levels of CO, as has been also observed in the emission spectroscopy experiments (see Fig. 6). From Fig. 11 one can see that the model somewhat overestimates the vibrational temperature of oxygen. We believe this to be an in indication of an additional energy sink from the vibrational mode of O_2, possibly due to V-T relaxation on O atoms.

Translational temperature in this series of experiments is evaluated from comparison of two Raman spectra of nitrogen, one with the CO laser on (e.g. see Fig. 10(a)), and the other with the laser turned off, i.e. in an equilibrium gas mixture at T_0=300 K. In the latter case, as expected, only the signal from v=0 is measured. Since the Raman signal intensity, I_v, is proportional to the product of the absolute population of a vibrational level, n_v, and the Raman cross section, σ_v~(v+1), this allowed inference of the number density of N_2 molecules, as well as the translational temperature, on the centerline of the excited region,

$$\frac{T}{T_0} = \frac{n_{N_2}(T_0)}{n_{N_2}(T)} = \frac{I_0}{\sum_v I_v / (v+1)} \qquad (6)$$

Nitrogen spectra have been used for the temperature inference for two reasons, (i) in the present experiments it is the most abundant species (78-98% of the gas mixture), so that vibrationally-stimulated chemical reactions are least likely to affect its concentration, and (ii) it has the fewest number of vibrational levels excited. From Eq. (6), the centerline translational temperature of the optically pumped gases for the conditions of Figs. 10-12 is inferred to be T≡500 K. Additional experiments [20]

demonstrate that the rotational structure of the S-branch Raman spectra can also be resolved, which allows inference of the translational-rotational temperature of the optically pumped gas.

These experimental results confirm the predictions of modeling calculations (see Section 4.1) and demonstrate that strong vibrational disequilibrium can be sustained by a c.w. CO laser in relatively cold molecular gas mixtures at atmospheric pressure. Among the numerous implications of this major result is the possibility of sustaining cold stable plasma in atmospheric pressure air (with CO used as an additive). Associative ionization of carbon monoxide in strongly vibrationally excited CO/N_2, $CO/Ar/O_2$, and $CO/Ar/NO$ mixtures already been demonstrated in our previous work [11,32,33]. The unconditional stability of these optically pumped plasmas is ensured by the absence of external electric field and electron impact ionization. The present data (in particular, strong vibrational excitation of O_2), suggest that oxygen might also play an important role in vibrationally stimulated ionization kinetics. In addition, high concentrations of vibrationally excited molecules in optically pumped air plasmas might also affect the rates of electron removal rates, i.e. recombination and attachment. Discussion of these issues is beyond the scope of the present paper. Recent studies of rates and mechanisms of ionization, recombination, and electron attachment in optically pumped air plasmas, as well as their stability, are discussed in our separate publication [33].

Comparison of the experimental data with the modeling calculations provides insight into kinetics of vibrational energy transfer among diatomic species and energy transport in nonuniform optically pumped gases. However, the results suggest that the rates of V-V exchange for $CO-N_2$, and especially those for $CO-O_2$, are not known with sufficient accuracy. Further optical pumping experiments using complementary infrared and Raman diagnostics would allow inference of the rates of these key energy transfer processes.

5. Summary

CO/N_2, $CO/Ar/O_2$, and CO/air gas mixtures are optically pumped using a low-power c.w. CO laser. Carbon monoxide molecules absorb the focused laser radiation and transfer vibrational energy to nitrogen and oxygen by V-V energy exchange. Infrared emission and spontaneous Raman spectroscopy are used for diagnostics of optically pumped gases. The results of experiments demonstrate that strong vibrational disequilibrium can be sustained in diatomic gas mixtures at atmospheric pressure. At these conditions, experimental vibrational temperatures of diatomic species at the laser beam axis are in the range T_v=1900-2300 K for N_2, T_v=2600-3800 K for CO, and T_v=2200-2800 K for O_2. At the same time, translational-rotational temperature of the gases does not exceed T=700 K. Line-of-sight averaged CO vibrational level populations up to v~40 are inferred from infrared emission spectroscopy. Centerline vibrational level populations of CO(v=0-8), N_2(v=0-4), and O_2(v=0-8) are inferred from the Raman

spectra of these species. The results demonstrate a possibility of sustaining stable nonequilibrium plasmas in atmospheric pressure air seeded with a few per cent of carbon monoxide. The obtained experimental data are compared with kinetic modeling calculations showing reasonable agreement.

6. Appendix

V-T rate parametrization:

$$P_{ij}^{v,v-1} = P_{ij}(T)\frac{v}{1-x_{ei}v}F(\lambda_{ij}^{v,v-1})$$

$$F(\lambda) = \frac{1}{2}(3-e^{-2\lambda/3})e^{-2\lambda/3}, \quad \lambda_{ij}^{v,v-1} = 2^{-3/2}\sqrt{\frac{c_{ij}}{T}}|\Delta E_i|, \quad \Delta E = 2\omega_{ei}x_{ei}(v-w)$$

$$P_{ij}(T) = \frac{10^{-7}kT}{(\tau_{ij}P)F(\lambda_{ij}^{1,0})[1-\exp(-\omega_{ei}/T)]}$$

$$\tau_{ij}P = \exp(A_{ij} + B_{ij}T^{-1/3} + C_{ij}T^{-2/3}) \text{ atm·}\mu\text{sec}$$

Species	c_{ij}	A_{ij}	B_{ij}	C_{ij}
CO-Ar, N₂-Ar, O2-Ar	1.335e-3	10.38	0	0
CO-M	0.25	-15.23	280.5	-549.6
N₂-M	0.25	-12.54	258.9	-390.9
O₂-M	0.25	-14.0	205	-295

V-V rate parametrization:

$$Q(v, w-1 \rightarrow v-1, w) = Z(S_{w-1,w}^{v,v-1} + L_{w-1,w}^{v,v-1})e^{-\Delta E/2T}, \quad \Delta E = 2\omega_e x_e(v-w)$$

$$S_{w-1,w}^{v,v-1} = S \cdot T\frac{v}{1-x_e v}\frac{w}{1-x_e w}F(\lambda_{w-1,w}^{v,v-1})$$

$$F(\lambda) = \frac{1}{2}(3-e^{-2\lambda/3})e^{-2\lambda/3}, \quad \lambda_{w-1,w}^{v,v-1} = 2^{-3/2}\sqrt{\frac{c}{T}}|\Delta E|$$

$$L_{w-1,w}^{v,v-1} = \frac{L}{T}\left(\frac{g^{v,v-1}}{g^{1,0}}\right)^2\left(\frac{g^{w-1,w}}{g^{1,0}}\right)^2\exp\left(-\frac{\Delta E^2}{bT}\right)$$

$$\left(\frac{g^{v,v-1}}{g^{1,0}}\right)^2 = \left(\frac{a+1}{a+3-2v}\right)^2 \frac{v(a+2-2v)(a+4-2v)}{a(a+3-v)} , \quad a = 1/x_e$$

Species	S	L	c, K^{-1}	b, K
CO-CO	1.64e-6	1.614	0.456	40.36
N$_2$-N$_2$	1.0e-7	-	0.120	-
O$_2$-O$_2$	7.0e-8	-	0.185	-
CO-N$_2$	7.0e-8	0.03	0.185	87.67
N$_2$-O$_2$	1.0e-7	-	0.120	-
CO-O$_2$	7.0e-8	0.03	0.185	87.67

Gas-kinetic collision frequency, $Z = 3 \cdot 10^{-10} (T/300)^{1/2}$ cm^3/s

V-E rate CO(X$^1\Sigma$)+M→CO(A$^1\Pi$)+M:

$k_{VE} = 10^{-12}$ cm^3/s

References

1. "Nonequilibrium Vibrational Kinetics", ed. M. Capitelli, Springer, Berlin, 1986

2. C. Park, "Nonequilibrium Hypersonic Aerodynamics", Wiley, New York, 1990

3. J. W. Rich, S.O. Macheret, and I.V. Adamovich, "Aerothermodynamics of Vibrationally Nonequilibrium Gas", Experimental Thermal and Fluid Science, Vol. 13, 1996, p. 1

4. J. W. Rich, "Relaxation of Molecules Exchanging Vibrational Energy", in "Applied Atomic Collision Physics", Vol. 3, "Gas Lasers", ed. E.W. McDaniel and W.L. Nighan, Academic Press, New York, 1982, pp. 99-140

5. B.F. Gordiets, V.A. Osipov, and L.A. Shelepin, "Kinetic Processes in Gases and Molecular Lasers", Gordon and Breach, London, 1988

6. E.P. Velikhov, A.S. Kovalev, and A.T. Rakhimov, "Physical Phenomena in Gas Discharge Plasmas", Moscow, Nauka, 1987

7. Raizer, Y.P., "Gas Discharge Physics", Springer-Verlag, Berlin, 1991

8. J.W. Rich, R.C. Bergman, and M.J. Williams, Measurement of Kinetic Rates for Carbon Monoxide Laser Systems, Final Contract report AFOSR F49620-77-C-0020 (November 1979)

9. R.L. DeLeon and J.W. Rich, "Vibrational Energy Exchange Rates in Carbon Monoxide", Chemical Physics, Vol. 107, 1986, p. 283

10. C. Flament, T. George, K.A. Meister, J.C. Tufts, J.W. Rich, V.V. Subramaniam, J.-P. Martin, B. Piar, and M.-Y. Perrin, "Nonequilibrium Vibrational Kinetics of Carbon Monoxide at High Translational Mode Temperatures", Chemical Physics, Vol. 163, 1992, p. 241

11. I. Adamovich, S. Saupe, M.J. Grassi, O. Shulz, S. Macheret, and J.W. Rich, "Vibrationally Stimulated Ionization of Carbon Monoxide in Optical Pumping Experiments", Chemical Physics, Vol. 173, 1993, p. 491

12. H.L. Wallaart, B. Piar, M.Y. Perrin, and J.P. Martin, "Transfer of Vibrational Energy to Electronic Excited States and Vibration Enhanced Carbon Production in optically pumped CO", Chemical Physics, Vol. 196, 1995, p. 149

13. H. Dunnwald, E. Siegel, W. Urban, J.W. Rich, G.F. Homicz, and M.J. Williams, "Anharmonic Vibration-Vibratino Pumping in Nitric Oxide by Resonant IR-Laser Irradiation", Chemical Physics, Vol. 94, 1985, p. 195

14. S. Saupe, I. Adamovich, M.J. Grassi, and J.W. Rich, "Vibrational and Electronic Excitation of Nitric Oxide in Optical Pumping Experiments", Chemical Physics, Vol. 174, 1993, p. 219

15. N.M. Gorshunov, private communication, 1990

16. Price, J.M., Mack, J.A., Rogaski, C.A., and Wodtke, A.M., "Vibrational-State-Specific Self-Relaxation Rate Constant Measurements of Highly Excited $O_2(v=19-28)$", Chemical Physics, Vol. 175, No. 1, 1993, p. 83

17. A. Noullez, G. Wallace, W. Lempert, R.B. Miles, and U. Frisch, "Transverse Velocity Increments in Turbulent Flow Using the RELIEF Technique," Journal of Fluid Mechanics, Vol. 339, p. 287, 1997.

18. N.G. Basov, E.M. Belenov, V.A. Isakov, E.P. Markin, A.N. Oraevskii, V.I. Romanenko, and N.B. Ferapontov, "Laser-Induced Chemical Reactions and Isotope Separation", Soviet Journal of Quantum Electronics, Vol. 2, p. 938, 1975

19. Billing, G.D., "Vibration-Vibration and Vibration-Translation Energy Transfer, Including Multiquantum Transitions in Atom-Diatom and Diatom-Diatom Collisions", Nonequilibrium Vibrational Kinetics, Springer-Verlag, Berlin, 1986, Chap. 4, pp. 85-111

20. W. Lee, M. Chidley, R. Leiweke, I. Adamovich, and W.R. Lempert, "Determination of O_2 and N_2 Vibrational State Distributions in CO Laser-Sustained Plasmas", AIAA Paper 99-3723, 30th Plasmadynamics and Lasers Conference, Norfolk, VA, June 28 – July 1, 1999

21. A. Eckbreth, "Laser Diagnostics for Combustion Temperature and Species", Gordon and Breach, Amsterdam , 1996.

22. E. Ploenjes, P. Palm, A.P. Chernukho, I.V. Adamovich, and J.W. Rich, "Time-Resolved Fourier Transform Infrared Spectroscopy of Optically Pumped Carbon Monoxide", AIAA Paper 99-3479, 30th Plasmadynamics and Lasers Conference, Norfolk, VA, June 28 – July 1, 1999

23. Cacciatore, M., Capitelli, M., and Billing, G.D., "Theoretical Semiclassical Investigation of the Vibrational Relaxation of CO Colliding with $^{14}N_2$", Chemical Physics, Vol. 89, No. 1, 1984, p. 17

24. Billing, G.D., and Fisher, E.R., "VV and VT Rate Coefficients in N_2 by a Quantum-Classical Model", Chemical Physics, Vol. 43, No.3, 1979, p. 395

25. Billing, G.D., and Kolesnick, R.E., "Vibrational Relaxation of Oxygen. State to State Rate Constants", Chemical Physics Letters, Vol. 200, No. 4, 1992, p. 382

26. Billing, G.D., "VV and VT Rates in N_2-O_2 Collisions", Chemical Physics, Vol. 179, No. 3, 1994, p. 463

27. N.K. Madsen and R.F. Sincovec, "Algorithm 540: PDECOL, General Collocation Software for Partial Differential Equations", ACM Transactions on Mathematical Software, Vol. 5, 1979, p. 326

28. A. Yariv and P. Yeh, "Optical Waves in Crystals: Propagation and Control of Laser Radiation", Wiley, New York, 1984; U. Sterr and W. Ertmer (Univ. Of Bonn, Germany), private communication

29. K.P. Huber and G. Herzberg, "Molecular Spectra and Molecular Structure", Vol. 4, "Constants of Diatomic Molecules", New York, Van Nostrand, 1979

30. C. Chackerian, Jr., R. Farrenq, G. Guelachvili, C. Rosetti, and W. Urban, Canadian Journal of Physics, Vol. 62, 1984, p. 1579

31. K.P. Horn and P.E. Oettinger, Journal of Chemical Physics, Vol. 54, 1971, p. 3040

32. I.V. Adamovich and J.W. Rich, "The Effect of Superelastic Electron-Molecules Collisions on the Vibrational Energy Distribution Function", Journal of Physics D: Applied Physics, Vol. 30, 1997, p. 1741

33. E. Plönjes, P. Palm, I.V. Adamovich, and J. W. Rich, "Control of Stability and Electron Removal Rate in Optically Pumped RF Discharges", AIAA Paper 99-3665, 30th Plasmadynamics and Lasers Conference, Norfolk, VA, June 28 – July 1, 1999
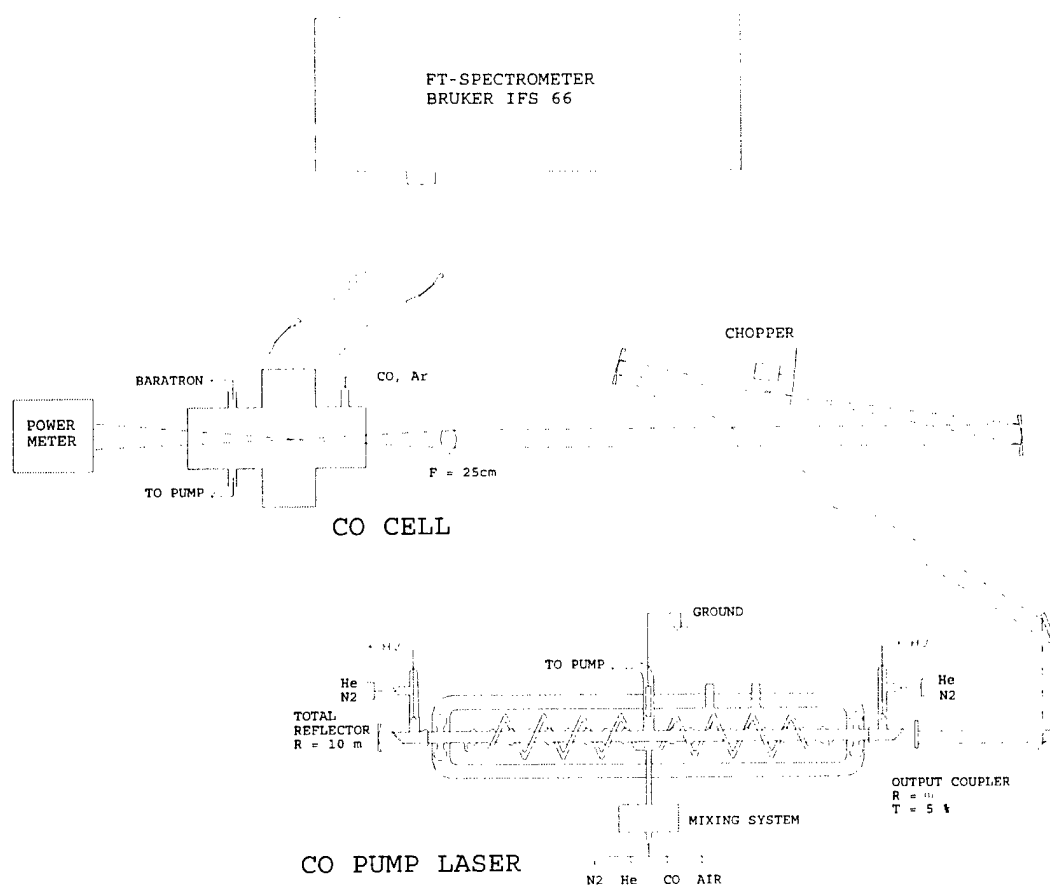
FT-SPECTROMETER
BRUKER IFS 66

CHOPPER

BARATRON CO, Ar

POWER
METER

F = 25cm

TO PUMP

CO CELL

GROUND

TO PUMP

He   He
N2   N2

TOTAL
REFLECTOR
R = 10 m

OUTPUT COUPLER
R =
T = 5 %

MIXING SYSTEM

CO PUMP LASER

N2   He   CO   AIR

Figure 1. Schematic of the experimental setup for emission spectroscopy

Computer   Pulser

ICCD

Monochromator

Power Meter
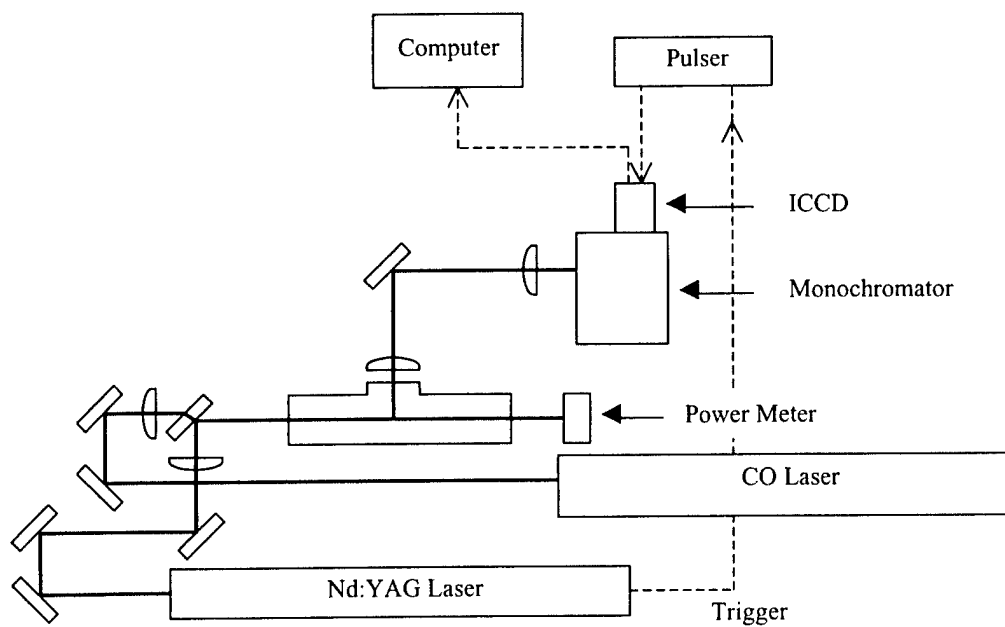
CO Laser

Nd:YAG Laser

Trigger

Fi

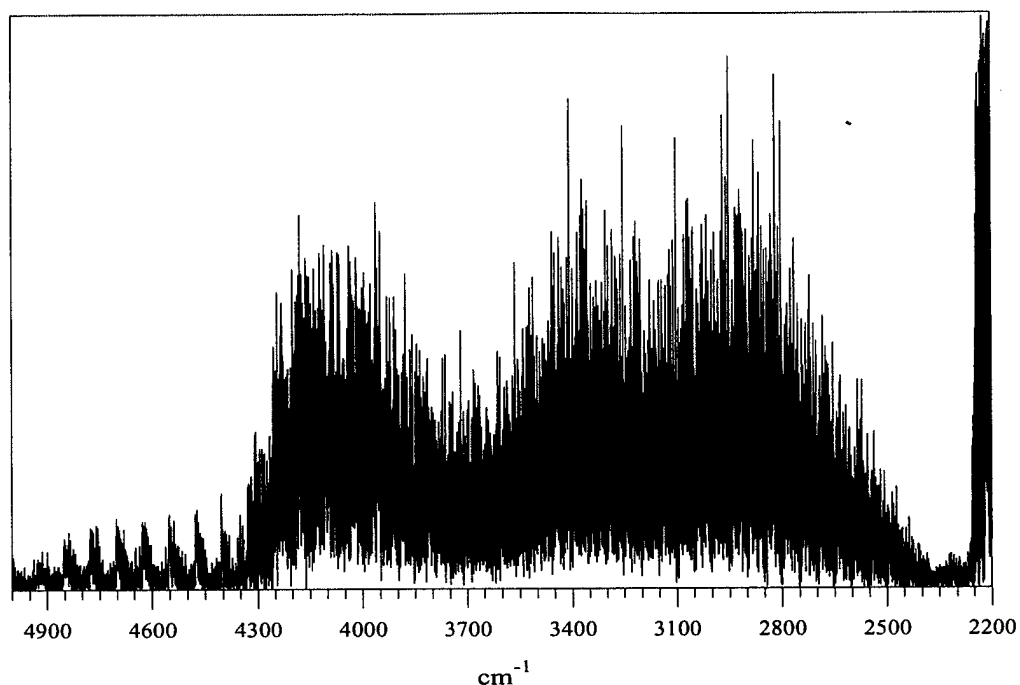Figure 2. Schematic of the experimental setup for Raman spectroscopy

Intensity

Figure 3. High-resolution (0.25 cm^{-1}) CO infrared spectrum. CO/Ar=2/100, P=100 torr
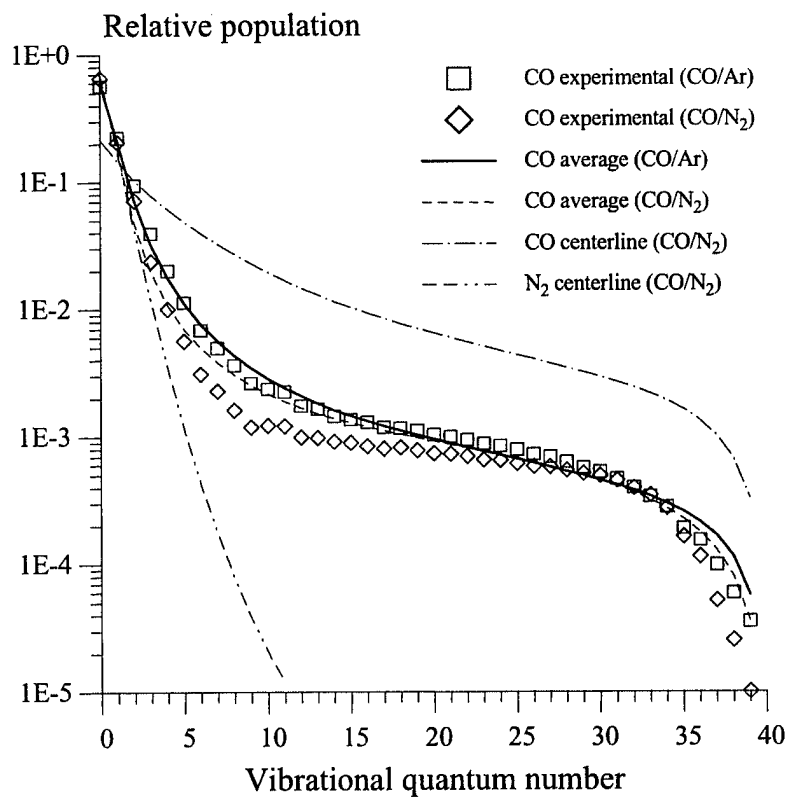

Figure 4. Experimental (CO) and theoretical (CO and N$_2$) distribution functions in CO/Ar=2/100 (T=600 K) and CO/N$_2$=2/100 (T=450 K) mixtures. P=100 torr, laser power is 15 W
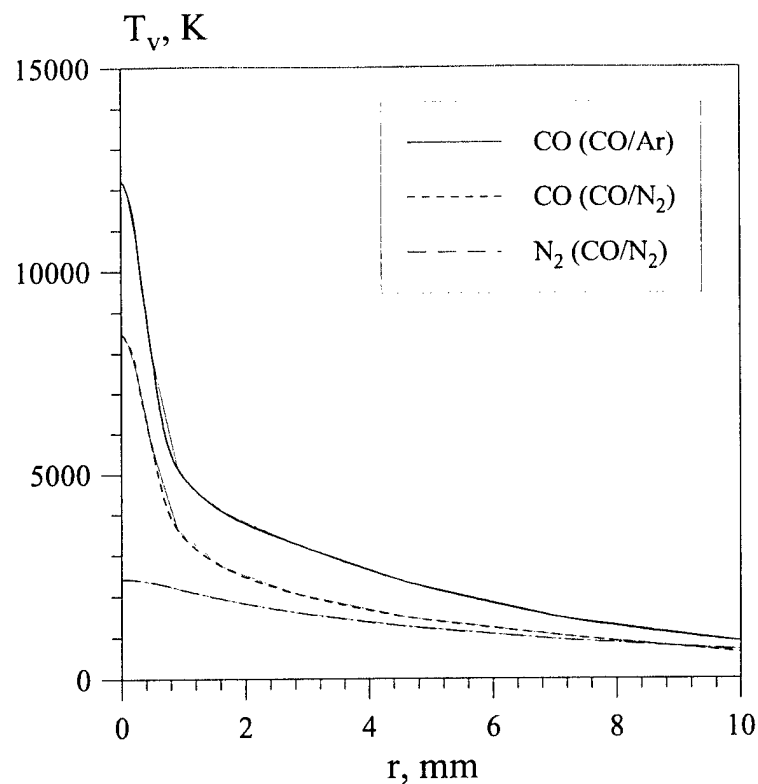
Figure 5. Calculated radial profiles of vibrational temperatures of CO and N_2 in CO/Ar=2/100 and CO/N_2=2/100 mixtures. P=100 torr.
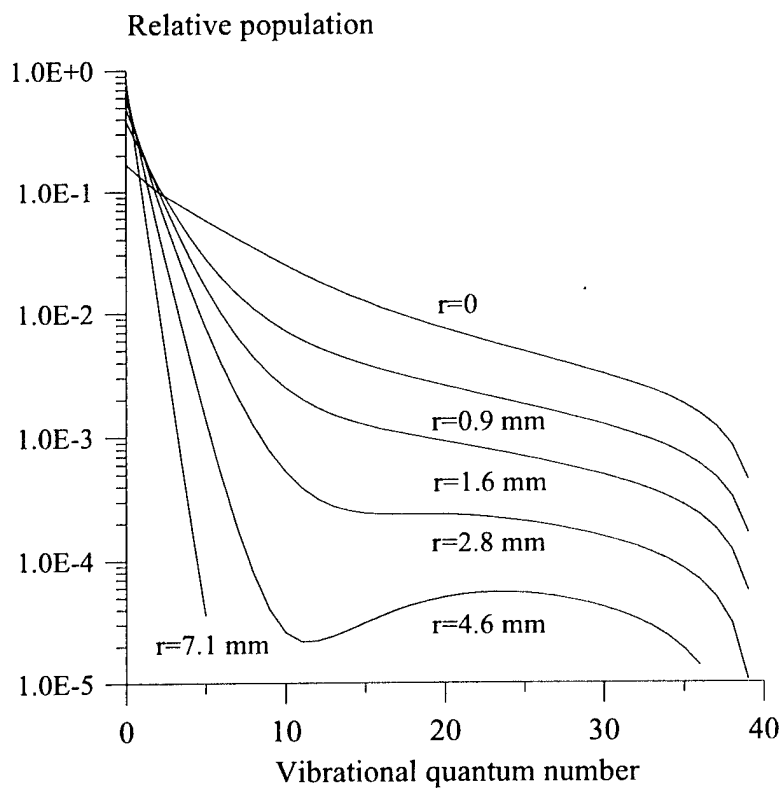
Figure 6. Calculated vibrational distribution functions in CO/Ar=2/100 mixture. P=100 torr.
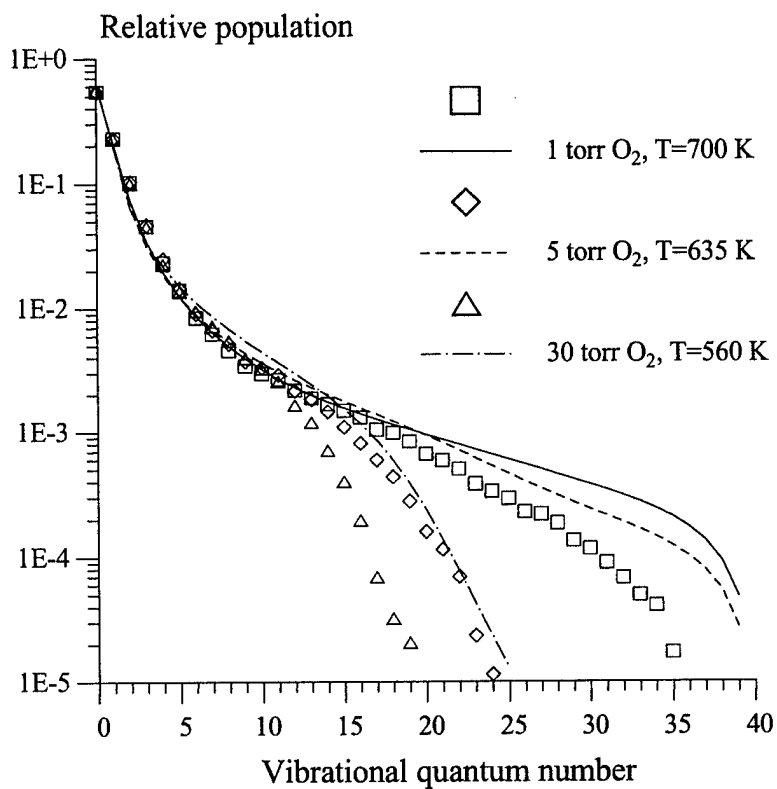
Figure 7. Experimental and theoretical CO distribution functions in CO/Ar/O$_2$ mixtures. P$_{CO}$=2 torr, P$_{Ar}$=100 torr, laser power is 15 W.
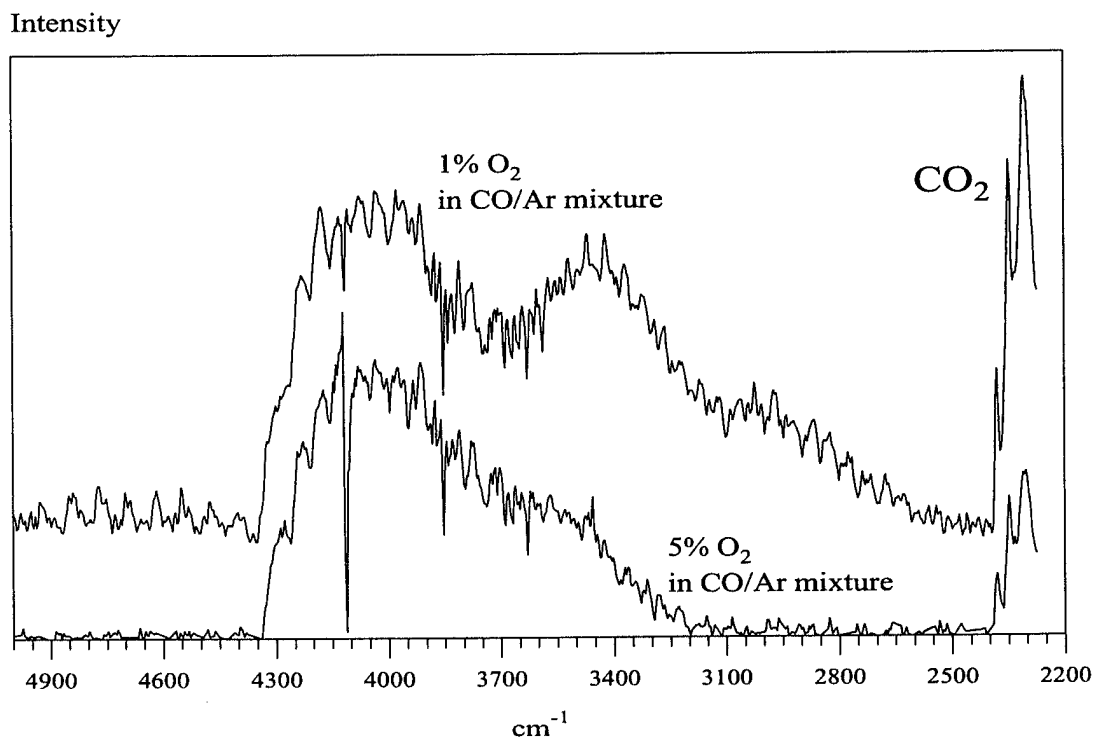
Figure 8. Low-resolution (8.0 cm^{-1}) CO infrared spectra for the conditions of Fig. 6
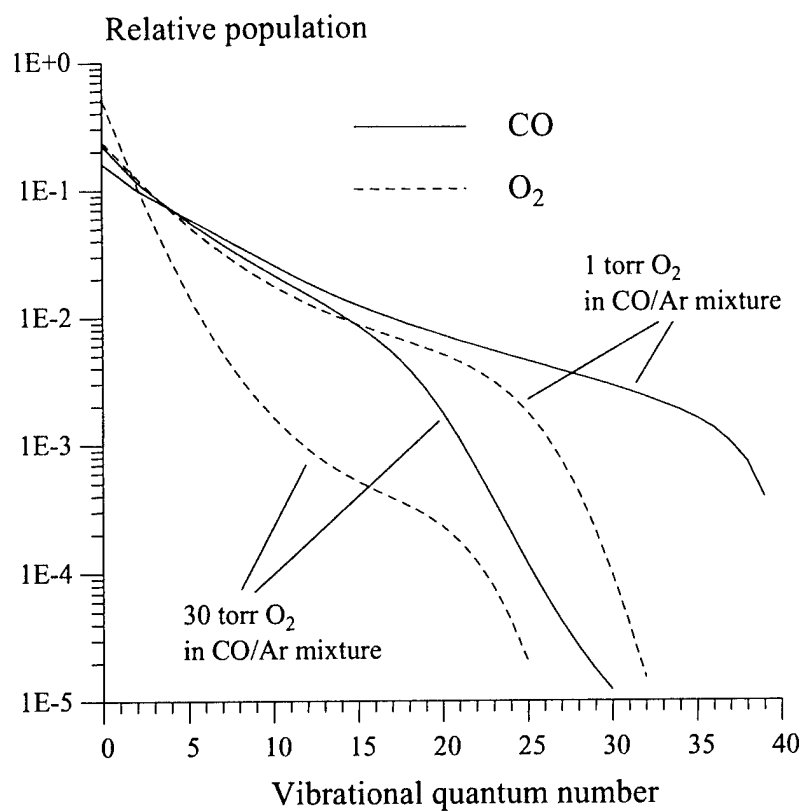
Figure 9. Calculated centerline vibrational distribution functions of CO and O_2 for the conditions of Fig. 7
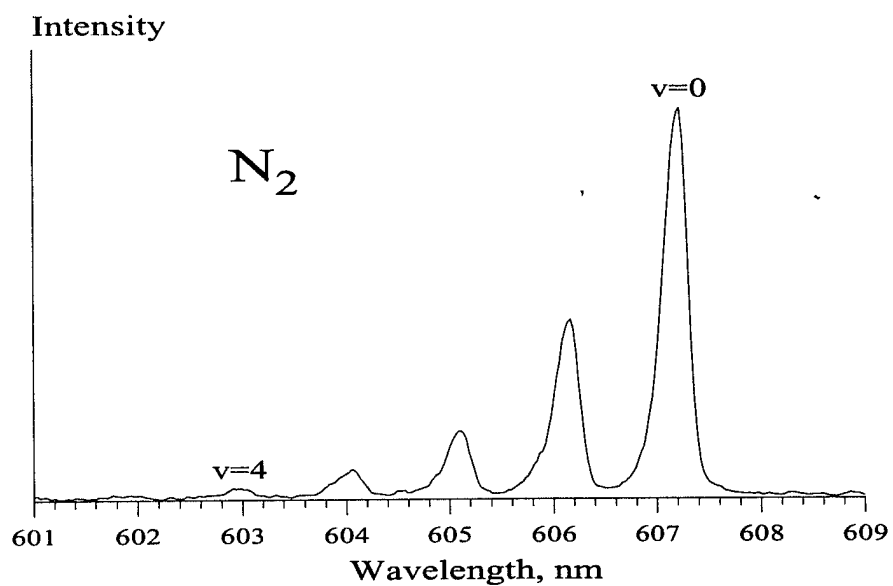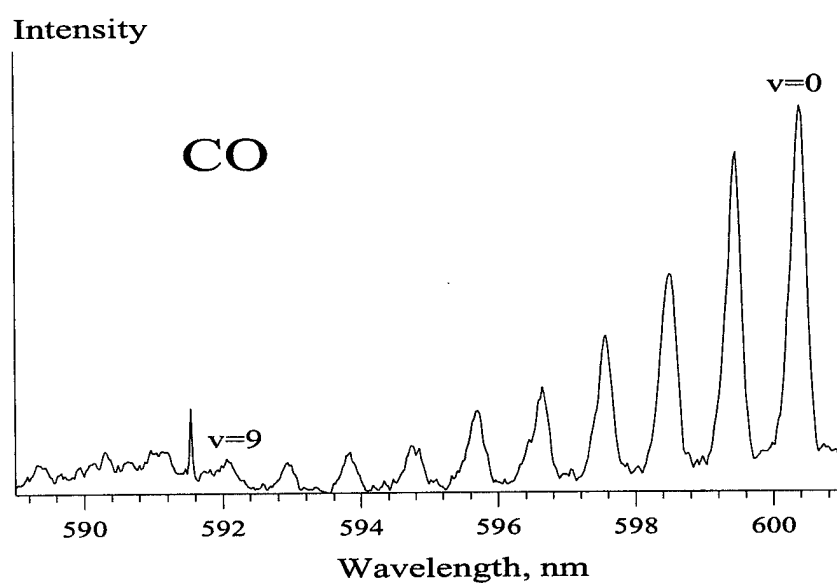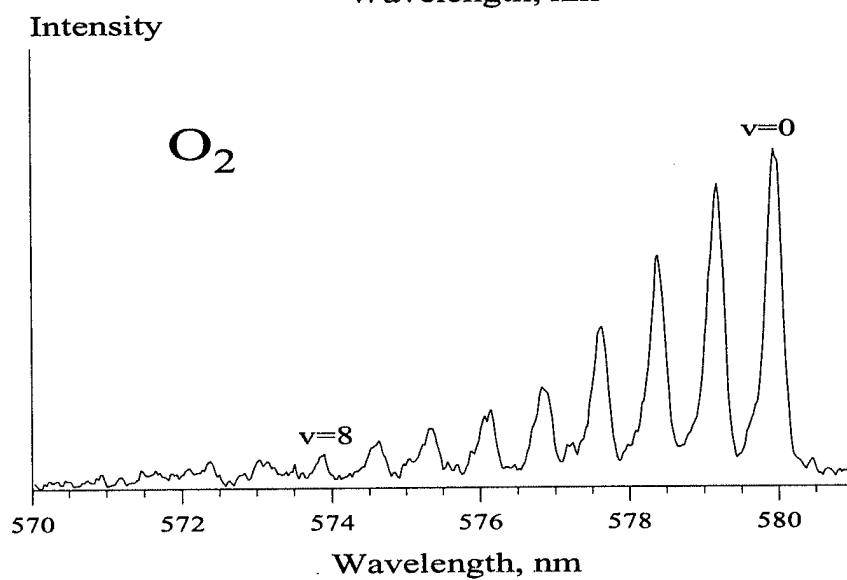
Figure 10. Raman spectra of N_2, CO, and O_2. $P(N_2)$=670 torr, $P(CO)$=40 torr, $P(O_2)$=30 torr
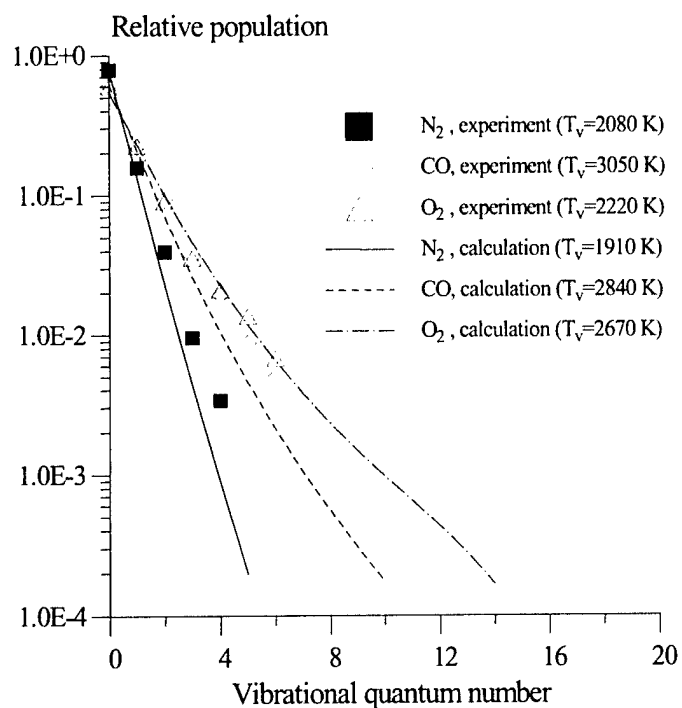
Figure 11. Experimental (symbols) and calculated (lines) centerline vibrational populations of N_2, CO, and O_2. $P(N_2)=580$ torr, $P(CO)=40$ torr, $P(O_2)=120$ torr
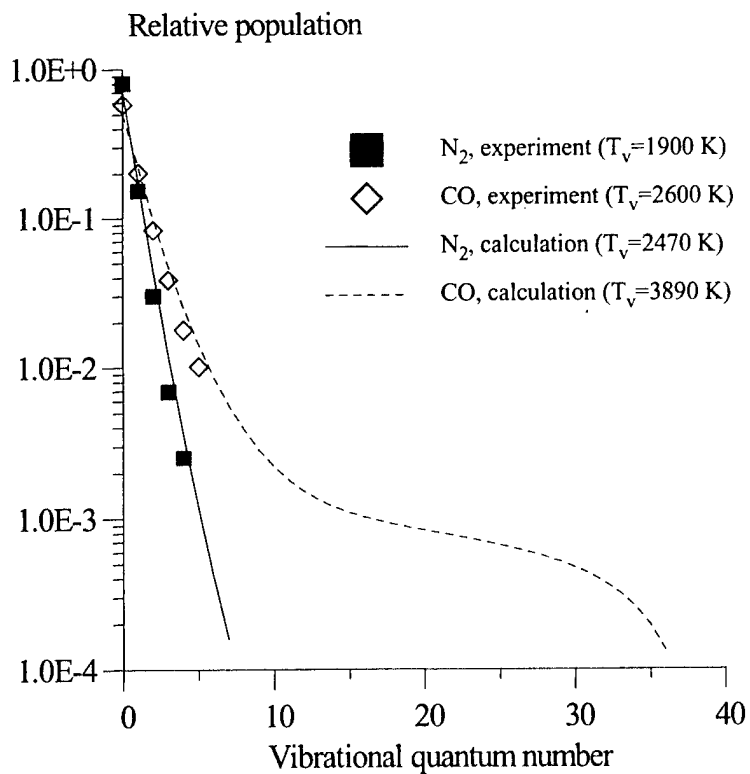
Figure 12. Experimental (symbols) and calculated (lines) centerline vibrational populations of CO and N_2. $CO/N_2=3/100$, $P=1$ atm

5. OPTICAL PUMPING STUDIES OF VIBRATIONAL ENERGY TRANSFER IN HIGH-PRESSURE DIATOMIC GASES

Wonchul Lee, Igor V. Adamovich, and Walter R. Lempert

Spontaneous Raman scattering is used to experimentally determine the vibrational distribution functions of diatomic species in N_2/CO and $N_2/CO/O_2$ gas mixtures optically pumped by a CO laser in the pressure range 410-760 torr. In N_2/CO mixtures, as many as 38 vibrational levels of CO are observed, in addition to 6 levels of N_2. The CO vibrational distribution function is highly non-Boltzmann, exhibiting the well-known Treanor plateau. In $N_2/CO/O_2$ mixtures, up to 13 vibrational levels of O_2 are observed, which also exhibit a highly non-Boltzmann distribution. Experimental data are compared to predictions of a master equation kinetic model, which incorporates absorption of the laser radiation, species and quantum state-specific vibration-vibration and vibration-translation energy exchange, as well as diffusion of vibrationally excited species out of the laser-excited volume. It is shown for the first time that modest power continuous wave lasers can be used to establish highly excited steady-state vibrational distributions of all three major diatomic species in CO-seeded atmospheric pressure dry air. This has implications for the energy-efficient creation of low-temperature, high-pressure air plasmas, in which the principal free electron loss mechanism is known to be three-body attachment to molecular oxygen.

1. INTRODUCTION

Knowledge of detailed nonequilibrium vibrational kinetics of diatomic molecules is essential for accurate prediction of behavior of low-temperature molecular plasmas for a wide variety of practical applications, including gas discharges, plasma chemical reactors, molecular lasers, upper atmosphere chemistry, and pollution control[1,2]. In a series of previous studies, it has been shown that the CO laser can be used to initiate and sustain highly nonequilibrium vibrational energy distributions in pure carbon monoxide and in mixtures of CO in noble gas buffers, such as helium and argon[3,4]. This, in turn, can induce a number of nonequilibrium collision-induced processes, such as energy transfer to high electronic states[5,6], ionization[7,8], and low-temperature free carbon production[9,10]. However, in the presence of common diatomic buffer gases, such as N_2 and O_2, rapid inter-species vibration-to-vibration (V-V) energy transfer is likely to quench highly vibrationally excited CO molecules, thereby reducing vibrational disequilibrium. This disequilibrium is critical for the production of free electrons, atoms, and chemically active metastable species[5-10]. The rate of vibrational energy loss from CO to N_2 and O_2 becomes especially critical at high partial pressures of the air species. While V-V exchange processes in pure CO are well understood[5,11], V-V exchange rates between high vibrational levels of CO and air species have not been experimentally measured. In this paper we present measurements of the vibrational state

distribution functions (VDFs) of N_2, O_2, and CO in gas mixtures optically pumped by a CO laser at pressures up to 1 atm.

The process here referred to as "optical pumping" consists of two distinct stages. Stage one is the direct laser excitation of a suitable target species to a low-lying vibrational level (or levels). In the work to be presented here the CO molecule is the target, which is directly excited to vibrational levels v<10 by resonance absorption of a broadband, continuous wave (cw), liquid nitrogen cooled, mid-IR CO laser radiation, in a single photon stepwise process

$$CO(v-1) + h\nu \rightarrow CO(v) \tag{1}$$

Cooling the laser allows emission on low vibrational transitions of CO, down to 2→1 (and, in some cases, 1→0), which are essential for triggering radiation absorption by cold CO (initially at room temperature). The second stage is the anharmonic collisional V-V up-pumping process:

$$CO(v) + CO(w) \rightleftarrows CO(v-1) + CO(w+1) \tag{2}$$
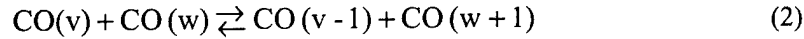
where v and w are vibrational quantum numbers such as w>v[3]. The up-pumping is driven by the anharmonicity of the intramolecular potential, which results in process (2) being exothermic in the forward direction. Detailed balance then requires that the forward rate of process (2) exceed the reverse rate, so that the molecule with the larger initial quantum number, w, is preferentially excited by the forward V-V energy transfer process. Ultimately, the degree of vibrational excitation is limited by vibration-to-translation (V-T) relaxation, the rate of which increases with vibrational quantum number[3], or, in some special cases, by vibration-to-electronic (V-E) coupling[5,11].

In pure CO, or in mixtures of CO and inert gas buffers such as argon and/or helium, previous work[3-9,11] has shown that at pressures in the range 0.1 - 1.0 atm., optical pumping driven by a modest intensity (~10 W/cm^2) cw CO laser produces steady-state vibrational distribution functions (VDFs) with significant fractional population in levels as high as v=30-40 (f_v~10^{-3} and above) while maintaining relatively low translational/rotational temperature (T=300-750K). Under these conditions, a variety of nonequilibrium processes can occur. For example, when up-pumping is sufficient to populate CO vibrational levels higher than v~33, so that the sum of the vibrational energies of binary collision partners exceeds the ionization potential, $\varepsilon_v + \varepsilon_w > \phi_{ion} = 14\ eV$, ionization occurs by associative ionization mechanisms[7,8] such as

$$CO(v) + CO(w) \rightarrow (CO)_2^+ + e^- \tag{3}$$

In addition, if vibrational levels higher than v~25 are populated, the total vibrational energy of the collision partners may exceed the activation energy of disproportionation reaction, ε~5.5eV, which produces free carbon[9],

$$CO(v) + CO(w) \rightarrow C + CO_2 \qquad (4)$$

Since the overall rate of energy relaxation from the vibrational mode of CO due to both V-T, V-E, and non-resonance V-V processes is fairly slow, vibrational up-pumping (1,2), associative ionization (3), and free carbon production (4) can all be generated in a low translational temperature, high-pressure, steady-state plasma sustained by continuous wave CO laser irradiation.

Adding air species to the optically pumped CO plasma initiates V-V energy transfer to nitrogen and oxygen,

$$CO(v) + N_2(w) \rightleftarrows CO(v-1) + N_2(w+1) \qquad (5)$$

$$CO(v) + O_2(w) \rightleftarrows CO(v-1) + O_2(w+1) \qquad (6)$$
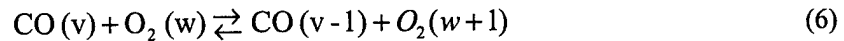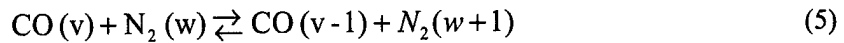
If the energy relaxation rate from the vibrational modes of all three diatomic species remains sufficiently slow, these processes may produce strong vibrational excitation of N_2 and O_2, and even lead to ionization of these species by association mechanisms such as that given by Eq. (3). Additionally, it is well known that the rate of electron detachment from O_2^- ions increases by several orders of magnitude as the temperature is increased from ~300 K to ~ 1500 K[12] (electron affinity of the O_2^- ion is about 0.43 eV). It is plausible, albeit speculative, that vibrational excitation of O_2 at low translational/rotational temperature, with subsequent rapid resonance charge transfer from O_2^- to $O_2(v)$ may produce vibrationally excited ions and thereby also result in an increased electron detachment rate. Since electron attachment to O_2 is the dominant mechanism of electron removal in cold air plasmas[12], this would provide a possibility of sustaining cold, nonequilibrium, low power budget air plasmas, which is the principal motivation of the present study.

To summarize, optical pumping in air can be thought of as occurring in two steps. Step one is the direct laser excitation of CO vibrational levels 1 to ~9 by absorption of continuous wave CO laser radiation. Step two, which consists of both inter- and intra- species collisional V-V transfer, then excites

higher levels of CO (up to v~40), as well as multiple vibrational levels of N_2 (up to v~5) and O_2 (up to v~12).

The present paper presents spontaneous Raman scattering measurements which we believe constitute the first determination of steady-state vibrational state populations of N_2 and O_2 in optically pumped gas mixtures, as well as the first spatially resolved vibrational level population measurements of CO. Comparison of experimental data with predictions of a detailed master equation kinetic model,[11,13] incorporating effects of V-V, V-T, and V-E energy transfer, as well as thermal and mass diffusion, is also presented.

1. EXPERIMENTAL

A schematic diagram of the optical cell and Raman instrumentation is illustrated in Fig. 1. Optically pumped gas mixtures are formed by loose focusing of a continuous wave (cw) CO laser into a flowing Pyrex glass cylindrical cell of approximate dimensions 0.60 m long × 0.050 m diameter. The cell is equipped with 1" diameter calcium fluoride (CaF_2) windows in order to provide optical access in the five-micron region. A gas manifold delivers room temperature mixtures of any combination of N_2, O_2, and CO, with composition controlled by individual flow meters. Total pressure is monitored with a Baratron pressure gauge.

The CO pump laser employed in this study has been described in greater detail previously[11,13]. By suitable choice of gas composition, flow rate, and temperature, lasing can be induced on a wide variety of different fundamental vibrational transitions in the vicinity of 5 microns. For the work to be presented here, the laser was operated with approximately 160 Watts of input electrical power and flow rates of 2000, 200, and 16 ml/min of helium, nitrogen, and carbon monoxide, respectively. The gain region is approximately 1 m in length, and was cryogenically cooled with liquid nitrogen. Figure 2 shows an experimental emission spectrum of the laser. It can be seen that a significant fraction of the total CO laser output power is on the 2→1 vibrational band. This is designed to trigger the collisional up-pumping process (see Section 1). Significant power is also seen on transitions 3 → 2 through 9 → 8. For the 3 → 2, 4 → 3, 5 → 4, 6 → 5, and 7 → 6 transitions, lasing occurs on two rotational lines, while for the other vibrational bands, lasing occurs on a single rotational line. The total laser output power employed in these studies is approximately 12 Watts.

Laser Raman diagnostics were performed by combining the CO laser and second harmonic output of a pulsed Nd:YAG Raman pump laser with a 90° CaF_2 dichroic mirror. The mirror was coated to transmit the CO laser, while reflecting the Nd:YAG laser. Q-branch spectra were obtained using the Nd:YAG laser in combination with an Optical Multichannel Analyzer (OMA) detector. The Nd:YAG laser had a single pulse output energy of 200 mJ at the second harmonic wavelength of 0.532 microns, and was operated at

a repetition rate of 10 Hz. The individual pulse duration was approximately 10 nsec. In order to provide spatial resolution in the radial direction, the Nd:YAG laser was focused coaxially to the CO pump laser (with a 0.40 m focal length lens) and Raman scattering captured at 90°. The focal length of the lens was chosen as a compromise which avoids both window/mirror damage and dielectric breakdown of the gas mixture. A simple long wavelength pass (OG – 570) colored glass filter was used to attenuate the elastic scattering at 0.532 microns and transmit the Stokes shifted scattering, which was in the range 0.570 – 0.615 microns. To maximize signal to noise, a pair of f/4 lenses and 2" diameter mirrors were used to rotate the image of the focused laser beam parallel to the vertically oriented input slit of the OMA spectrometer. The effect was to capture a solid angle of approximately 0.049 sr (corresponding to f/4 optics), while spatially averaging the signal over a cylindrical volume of approximate dimensions 2 mm in length × 100 microns in diameter. The OMA consisted of a 1/4 meter f/4 spectrometer with a micro-channel plate intensified CCD camera for the detector. The purpose of the intensifier was to provide a fast (order 10 nsec) gate so that spontaneous emission from the optically pumped cell, which in some circumstances was much brighter than the detected Raman signal, could be minimized. The quantum efficiency of the detector was approximately 6% at the Stokes wavelength, and the signal was integrated for time durations in the range 20 seconds - 10 minutes. For all Raman measurements reported here, the spectrometer was used with a 1800 line/mm grating which resulted in a spectral resolution of approximately 1.5 Angstroms, and a spectral coverage of 16 nm. The resolution was sufficient to resolve individual Q-branch vibrational bands but not to resolve any rotational fine structure. The wavelength coverage enabled the capture of approximately 15 vibrational bands simultaneously. Determining the complete N_2, O_2, and CO vibrational distribution functions required merging of 3 spectra, which were obtained sequentially with identical optical conditions.

Vibrational level populations were obtained directly from the integrated intensity of each unresolved Q-branch band profile. Due to problems with wavelength calibration of the spectrometer, integrated intensities were extracted by hand from the raw data. Raw intensity data was corrected for the wavelength dependence of the detector quantum efficiency, the filter transmission, and the well known inverse fourth power dependence off the scattering cross section. It should also be noted that extraction of the vibrational distribution function from the raw Raman data requires knowledge of the vibrational level dependence of the Raman cross section. For all data presented in this paper, we assume that the Stokes scattering cross section scales as the square of the matrix element, $M_{mn}^1 = \langle m \mid r - r_e \mid n \rangle$, where $m+1 = n$ represent Morse potential wave functions. The matrix elements were evaluated using an analytical expression given by Callas[14]. As an example, Fig. 3 shows the vibrational quantum number (v) dependence of the relative CO cross section, normalized by division by v+1, the well known harmonic oscillator result. It can be seen that for v = 40, the Morse potential cross section exceeds the harmonic

oscillator prediction by approximately 35%. A very similar dependence was found for N_2 and O_2. It should be noted, however, that this procedure assumes that the polarizability derivative, $\left(\partial\alpha / \partial Q\right)_0$, is independent of v. It also ignores matrix element terms higher than first order.

Uncertainty in the relative intensities from which the experimental vibrational level populations are derived is estimated to be 10-20%. Uncertainty in the ratio of vibrational populations of levels v=0 and v=1, which is used to determine the effective vibrational temperatures of the species (see Section 3), is estimated to be 5% for N_2 and 7% for CO and O_2. The uncertainty in this ratio is lower than that of the relative populations due to significant cancellation in systematic uncertainties in baseline and linewidth.

2. EXPERIMENTAL RESULTS

Figure 4 shows a Raman spectrum obtained from a 4% mixture of CO in N_2 at a total pressure of 410 torr, acquired with an integration time of 1 minute. The six peaks on the right, in the wavelength range between 608 and 602 nm correspond to the Stokes shifted transitions from vibrational states v=0-5 of N_2, respectively. While the vibrational level populations cannot be described by a Boltzmann distribution it is useful, for illustrative and comparison purposes, to define a "first level vibrational temperature" as

$$T_v = \frac{\theta_1}{\ln\left[f_0 / f_1\right]}, \tag{7}$$

where θ_1=3353 K is the energy of the first vibrational level of N_2, and f_0 and f_1 are the relative populations of vibrational levels v=0 and v=1, respectively. With this definition, the "vibrational temperature" of N_2 obtained from the data of Fig. 4 is approximately T_v = 2200 +/- 70 K. The expanded intensity scale on the left side of Fig. 4 shows vibrational levels v=0-37 (from left to right) of CO, illustrating that in this case a clear "Treanor plateau"[3] has been achieved in the CO population distribution. While this distribution is highly non-Boltzmann, an effective vibrational temperature of T_v=3500±250 K can still be defined by considering the first two level populations, using Eq. (7). The apparent relative populations range from f_0=0.4 for the ground vibrational level to f_{37}=2.5·10^{-3} for the highest observed level, v=37. Similar to that which has been observed in CO/Ar mixtures using IR emission spectroscopy[3-9,11], the relative population drops precipitously at v~40. This sudden drop-off in the VDF has been attributed in the past to near-resonance collisional energy transfer between v~40 of the ground electronic state, $X^1\Sigma^+$, and low vibrational levels of the $A^1\Pi$ excited state[5] (the upper state of the well-known 4th positive system of CO). Translational/rotational temperature, although not measured for conditions identical to that of Fig. 4, is

estimated to be less than T≅600 K, based on previous rotationally resolved CO IR emission spectra measured in optically pumped Ar/CO mixtures[11] and S-branch N_2 Raman spectra (see Fig. 7) obtained for other gas compositions as part of this work.

Figure 5 shows typical Raman spectra obtained from a mixture of 40 torr CO, 15 torr O_2, and 700 torr N_2. Similar to Fig. 4, the top spectrum shows six N_2 vibrational levels, v=0-5, with corresponding first level vibrational temperature of approximately T_v=2500±100 K. The middle spectrum shows the v=0-8 bands of CO, with T_v=3400±250 K. The bottom spectrum contains vibrational states of O_2, which shows significant population in levels v=0-12, with T_v=3660±400 K. Note, again, that the full vibrational distributions of CO and O_2 are strongly non-Boltzmann and cannot be truly characterized by a single vibrational temperature. Figure 6 shows experimental spectra taken under similar conditions to that of Fig. 5 except that the mole fraction of oxygen has been increased from 2% to 16%, and the total pressure slightly dropped, from 755 to 740 torr. In this case the effective N_2 and CO vibrational temperatures somewhat decrease (from T_v=2500±100 K to 2100±70 K, and from T_v=3400±250 K to 3050±200 K, respectively), whereas the effective O_2 vibrational temperature drop is even more significant (from T_v=3660±400K to 2200±150 K).

The data of Figs. 4-6 represent, to our knowledge, the first steady-state optical pumping experiments performed in high pressure (up to 1 atm) mixtures of diatomic gases. In particular, it is clear from the data of Fig. 6 that a relatively low intensity (~100 W/cm^2) CO laser can be used to produce steady state optical pumping in atmospheric pressure air with effective vibrational temperatures exceeding 2000 K for all three major diatomic species. As will be discussed in the next section, this has the potential to significantly impact the ability to create volume ionization in air.

Comparison of predicted and observed VDFs requires a reasonable (+/- 100 K) estimate of the rotational/translational temperature. For the data given in Figs. 5 and 6 this is accomplished using rotationally resolved S-branch Raman spectra of N_2. As an example, Fig. 7 shows an experimental Stokes S-branch spectrum of N_2 in an optically pumped mixture at the same experimental conditions as those used to obtain the Q-branch spectra of Fig. 5. The relatively weak S-branch spectrum "sits" on top of the long wavelength wing of the N_2 Q-branch, complicating extraction of an accurate rotational temperature. Nonetheless, an estimate of the rotational temperature can be made, based on the observation that the rotational population is maximum at approximately level 8 or 10, leading to an inferred temperature in the range T≅420 – 640 K.

3. COMPARISON TO KINETIC MODELING CALCULATIONS

To model the results of the experiments, a state-specific master equation model[4,11,13] has been used, which evaluates the radial and time dependence of vibrational populations of diatomic species in

CO/N_2/O_2 mixtures optically pumped by a CO laser. The model has been described in detail previously, and will be only summarized here. The basic governing equations are given by:

$$\frac{\partial n_{v,i}(r,t)}{\partial t} = \frac{1}{r}\frac{\partial}{\partial r}\left[rD_i\frac{\partial n_{v,i}(r,t)}{\partial r}\right] + VV_{v,i} + VT_{v,i} + SRD_{v,i} + VE_{v,i} + PL_{v,i} \qquad (8)$$

$$\rho c_p \frac{\partial T(r,t)}{\partial t} = \frac{1}{r}\frac{\partial}{\partial r}\left[r\lambda\frac{\partial T(r,t)}{\partial r}\right] + HVR \qquad (9)$$

where $n_{v,i}(r,t)$ is the time and space dependent population of vibrational level v of species i, r is the distance from the laser beam axis, D_i and λ are the mass diffusion and heat conduction coefficients, respectively, and ρ and c_p are density and specific heat of the gas mixture at constant pressure. The rest of the notation is the same as in Refs. [4,11,13]: $VV_{v,i}$ represents the species and v level-dependent vibration-vibration energy transfer term; $VT_{v,i}$ represents the species and v level-dependent vibration-translation relaxation term; SRD_v represents the v level dependent CO spontaneous radiative decay (infrared) term; $VE_{v,i}$ represents vibration-electronic coupling terms, principally the coupling between the $X^1\Sigma$ and $A^1\Pi$ states of CO; $PL_{v,i}$ represents the laser absorption term; and HVR represents the term describing gas heating by vibrational relaxation (both in V-T and in non-resonance V-V processes). Equations (8,9) are primarily coupled through the strong temperature dependence of the V-T relaxation and V-V transfer rates, as well as somewhat weaker temperature dependence of the laser radiation absorption cross sections. The explicit expressions for each of the terms in Eqs. (8,9) are given in Ref. [4].

With the exception of CO-CO V-V rates, for which extensive state-specific experimental data have been previously obtained[5,11], V-V and V-T rates incorporated into Eqs. (8,9) are based both on the results of semiclassical close-coupled trajectory calculations[15-18] by Billing et al. and state-specific experiments, where available[19-21]. Note that the semiclassical V-V and V-T rates for O_2-O_2 and O_2-N_2 used in the present paper[17] are in good agreement both with the experiments[19-21] and with the fully quantum calculations[22]. The model also uses accurate Einstein coefficients for spontaneous emission for the CO infrared bands[23] and assumes Gaussian intensity distribution of the CO excitation laser with beam waist of 1 mm. The resulting system of equations describing forty vibrational levels of CO, N_2, and O_2 is solved using a standard stiff partial differential equation solver[24]. More detailed discussion of the model can be found in Refs. [11,13]. In the present paper, the vibrational distribution functions inferred from the Raman spectra are compared with the calculated vibrational level populations on the centerline of the

laser beam. The validity of this approach is justified by the previous modeling calculations[13] which show that the change of the populations across the Raman pump laser beam of ~0.1 mm diameter is very weak.

Figure 8 shows experimental and predicted vibrational distribution functions inferred from the Raman spectra of Fig. 4. The modeling predictions were performed assuming a steady-state rotational/translational temperature of 500 K, which, as discussed previously, is near the middle of the range of temperatures inferred from the rotational Raman spectra of Fig 7 and previous IR emission spectra[11]. Qualitatively, the general features of the steady-state CO and N_2 vibrational energy distributions can be understood by comparison, on the one hand, of the rates of inter- and intra-species V-V exchange and, on the other hand, the rates of inter- and intra-species V-T relaxation. It is well known[25] that in the absence of significant concentrations of atoms and/or polyatomic molecules, such as O, N, CO_2, and H_2O, the overall rate of V-T and vibration-to-rotation (V-R) relaxation in diatomic gases such as CO and N_2 is extremely slow. In fact, the dominant vibrational energy relaxation mechanism in this case is the non-resonant V-V exchange of Eqs. (2,5). In addition, diffusion of vibrationally excited molecules out of the laser beam path (with characteristic time τ_{diff}~0.01-0.1 sec) and convection through the absorption cell (with characteristic time τ_{conv}~1 sec) are both far too slow to be significant vibrational energy sinks. Therefore, as illustrated in Fig. 8, a substantial fraction of the laser energy initially deposited into the CO vibrational mode remains stored in vibrations of CO and N_2. Furthermore, from simple detailed balance arguments (see discussion in Section 1), the larger vibrational mode spacing of N_2 (2330 cm^{-1}) compared to CO (2143 cm^{-1}) results in preferential $N_2 \rightarrow$ CO energy transfer by the V-V process of Eq. (5), which becomes exothermic in the reverse direction. The combined effect is to establish, in the steady state, highly nonequilibrium VDFs for both diatomic species, but in which the average vibrational energy in CO strongly exceeds that of N_2.

Quantitatively, it can be seen that for N_2, the experimental and predicted distributions agree very well. In the case of CO, while the experimental VDF agrees reasonably well with the prediction (within about 50%), there is a rather consistent disagreement among the highest observed levels. While the cause of this disagreement is not completely understood, there are several possible sources of experimental error. In particular, it should be noted that the individual Q-branch CO bands in Fig. 4 are not completely resolved. This can lead to uncertainty in the baseline, and some resulting uncertainty in the populations. This is aggravated by the fact that for the highest vibrational levels, the dark current in the ICCD camera was a substantial fraction of the total detected signal. While the dark current is reasonably constant, any background drift would lead to a not insignificant error. In addition, some of the discrepancy could be due to inaccuracy in the assumed rotational/translational temperature. This effect will be estimated below, using the data of Fig. 5.

Figure 9 shows the comparison of experimental and calculated vibrational distribution functions inferred from the $N_2/CO/O_2$ Raman spectra of Fig. 5. Again, a rotational/translational temperature of 500 K is assumed, based on the approximate temperature inferred from the S-branch spectrum of Fig. 7. It can be seen that, in contrast to N_2, the main effect of adding even relatively small amounts of O_2 to the mixture (here oxygen partial pressure is 15 torr) is to significantly reduce the vibrational level populations of CO. Again, this can be understood qualitatively by consideration of detailed balance of inter-species V-V transfer. Since the vibrational mode spacing of oxygen (1556 cm^{-1}) is considerably less than that of CO, the forward rate for CO $\rightarrow$ O_2 V-V exchange (see Eq. (6)) exceeds the backward rate, resulting in steady-state vibrational distributions in which the populations of CO are lower than those of O_2. Here again non-resonant V-V exchange processes such as those given by Eqs. (2,5,6) control the overall vibrational energy relaxation rate.

More quantitatively, it can be seen that for this gas composition, the model predicts the first level vibrational temperature of O_2 to be considerably higher ($T_v \cong 5600$ K) than that of CO ($T_v \cong 3900$) or nitrogen ($T_v \cong 2500$ K). While the ordering of the experimental first level vibrational temperatures is qualitatively consistent with this prediction, the quantitative agreement is rather poor. In particular, the experimental O_2 vibrational populations are significantly lower than predicted by the model, and, referring back to Fig. 5, appear to drop dramatically for levels higher than approximately twelve. Again, some of this discrepancy could be due to uncertainty in the rotational/translational temperature. Figure 10 shows the model predictions for the CO, N_2, and O_2 VDFs at T = 400K, 500 K, and 600 K, for the conditions corresponding to the spectra of Fig. 5. It can be seen that the predictions for the O_2 populations for levels higher than approximately eight exhibit considerable temperature dependence, even over this rather restricted range. The temperature dependence of the CO and N_2 VDFs is considerably smaller.

In addition, the discrepancy between the experiment and the prediction could indicate the presence of an additional rapid energy sink for the oxygen vibrational mode. One possibility is a vibrationally stimulated chemical reaction between carbon monoxide and oxygen,

$$CO(v) + O_2(w) \rightarrow CO_2 + O , \qquad (10)$$
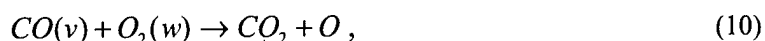
not incorporated into the model. Note that this reaction also produces oxygen atoms, which are known to be very efficient V-T relaxers of O_2, N_2, and CO[26]. Therefore V-T relaxation of O_2 by O atoms might well contribute to this vibrational energy sink. These arguments are consistent with the results of previous infrared emission spectroscopy studies[13] which show significant emission from carbon dioxide in optically pumped CO/Ar/O_2 mixtures with similar partial pressures of O_2 (~1 torr).

Finally, Fig. 11 shows the comparison of calculated (at T=500 K) and experimental VDFs corresponding to the data of Fig. 6. It can be seen that increasing the mole fraction of O_2 from 2% to 16% results in a further substantial drop in the vibrational level populations of both O_2 and CO. It is clear that in this mixture, the fixed power of the excitation laser, in combination with the increased net rate of CO-O_2 V-V transfer (due to the higher concentration of O_2) is responsible for the drop in the CO and O_2 vibrational energy loading. Significant systematic deviation between the experimental populations and the modeling predictions is also quite evident, with the experimental CO and O_2 VDFs being much closer to each other than predicted by the model. The precipitous drop-off in the VDFs of both species for vibrational levels greater than approximately 6 provides further evidence of the presence of an additional rapid relaxation process which is not accounted for in the model.

Nonetheless, the main result of Fig. 11 is that it demonstrates, for the first time, that optical pumping can be used to obtain highly excited vibrational distributions of all three major diatomic species in CO-seeded atmospheric pressure dry air. Among the implications of this result is a possibility for efficient generation of low temperature nonequilibrium air plasmas. In particular, it is well known that in low to moderate temperature air plasmas (T<1500 K) the principal mechanism for loss of free electrons is three-body attachment to molecular oxygen[12]:

$$O_2 + e^- + O_2 \rightleftarrows O_2^- + O_2 \tag{11}$$

The forward rate of this process, $k_{att} \cong 2 \cdot 10^{-30}$ cm^6/s, is nearly temperature-independent, while the reverse rate increases exponentially with temperature[27], $k_{det} \cong 10^{-10}$ exp(-ε_{aff}/T) cm^3/sec, where ε_{aff}=0.43 eV is electron affinity of oxygen molecule. Note that ε_{aff} is approximately equal to two vibrational quanta of O_2. Therefore vibrational excitation of O_2 up to levels v>2, with subsequent rapid resonance charge transfer from O_2^- to O_2(v) is potentially capable of accelerating electron detachment from O_2^- ions, thereby shifting the equilibrium of process (11) toward the left. The results shown in Figs. 6 and 10 suggest that this major loss mechanism can be mitigated at low translational temperature using a modest intensity, energy-efficient CO laser. This suggests a potential strategy for efficient generation of large-volume, nonequilibrium atmospheric pressure air plasmas at low power budget. We are currently pursuing this approach using a 80 KeV electron beam as a source of efficient volume ionization.

4. SUMMARY

Experimental Raman Q-branch spectra have been obtained in optically pumped mixtures of diatomic gases under a variety of conditions, with total pressure up to 1 atm. In N_2/CO mixtures, quantitative vibrational population fractions have been determined for levels v=0-5 and v=0-37 for N_2 and CO,

respectively. At P=410 torr, the first level vibrational temperatures of N_2 and CO are approximately T_v=2200K and T_v=3500K, respectively. In atmospheric pressure N_2/CO/O_2 mixtures, 6 vibrational levels of N_2, up to 13 levels of O_2, and up to 9 levels of CO are observed. At these conditions, first level vibrational temperatures of these three species are in the approximate range T_v=2100-2500 K, T_v=2200-3700 K, and T_v=3000-3400 K, respectively.

Experimental vibrational level populations have been compared to predictions of a master equation kinetic model, which incorporates absorption of laser radiation, species and quantum state-specific vibration-vibration and vibration-translation energy exchange, as well as diffusion of vibrationally excited species out of the excited volume. In the case of N_2/CO, the experimental and calculated vibrational distribution functions agree rather well (within 50%). It is believed that the remaining disagreement can be attributed to a combination of experimental uncertainty in the integrated spectral Raman intensities, as well as systematic uncertainty in the rotational/translational temperature. In N_2/O_2/CO mixtures, the agreement between the experiment and the calculations becomes somewhat worse. In particular, the model tends to overpredict the high vibrational level populations of O_2. This could be indicative of the presence of a fast O_2(v) relaxation process, not incorporated into the model, such as vibrationally-simulated chemical reaction $CO+O_2(v) \rightarrow O+CO_2$. Other possibilities include rapid V-T relaxation of O_2 on oxygen atoms formed in this reaction, or a systematic error in rotational/translational temperature.

Finally, it has been demonstrated that modest intensity ($\sim$100 W/cm^2) continuous CO lasers can be used to establish highly excited steady-state vibrational distributions of all three major diatomic species in CO-seeded atmospheric pressure dry air. This offers a possibility for efficient generation of low-temperature nonequilibrium air plasmas in which the principal free electron loss mechanism is known to be three-body attachment to molecular oxygen.

REFERENCES

1. B.F. Gordiets, V.A. Osipov, and L.A. Shelepin, "Kinetic Processes in Gases and Molecular Lasers", Gordon and Breach, London, 1988

2. "Nonequilibrium Vibrational Kinetics", ed. M. Capitelli, Springer, Berlin, 1986

3. J. W. Rich, "Relaxation of Molecules Exchanging Vibrational Energy", in "Applied Atomic Collision Physics", Vol. 3, "Gas Lasers", ed. E.W. McDaniel and W.L. Nighan, Academic Press, New York, 1982, pp. 99-140

4. C. Flament, T. George, K.A. Meister, J.C. Tufts, J.W. Rich, V.V. Subramaniam, J.-P. Martin, B. Piar, and M.-Y. Perrin, "Nonequilibrium Vibrational Kinetics of Carbon Monoxide at High Translational Mode Temperatures", Chemical Physics, Vol. 163, 1992, p. 241

5. R.L. DeLeon and J.W. Rich, "Vibrational Energy Exchange Rates in Carbon Monoxide", Chemical Physisc, vol. 107, 1986, p. 283

6. H.L. Wallaart, B. Piar, M.Y. Perrin, and J.P. Martin, Chem. Phys., "Transfer of Vibrational Energy to Electronic Excited States and Vibration Enhanced Carbon Production in Optically Pumped CO", Chemical Physics Vol. 196, 1995, p. 149

7. I. Adamovich, S. Saupe, M.J. G. Rassi, O. Shulz, S. Macheret, and J.W. Rich, "Vibrationally Stimulated Ionization of Carbon Monoxide in Optical Pumping Experiments", Chemical Physics, vol. 173, 1993, p. 491

8. I.V. Adamovich and J.W. Rich, "The Effect of Superelastic Electron-Molecule Collisions on the Vibrational Energy Distribution Function", Journal of Physics D: Applied Physics, vol. 30, No. 12, 1997, pp. 1741-1745

9. J.W. Rich and R.C. Bergman, "Isotope Separation by Vibration-Vibration Pumping", Chap. 9 in "Nonequilibrium Vibrational Kinetics", Springer, Berlin, 1986

10. J. Rebello, D. Straub, and V.V. Subramaniam, "Diamond Growth from a CO/CH_4 Mixture by Laser Excitation of CO: Laser Excited Chemical Vapor Deposition", J. of Applied Physics, Vol. 72, 1992, pp. 1133-1136

11. E. Ploenjes, P. Palm, A.P. Chernukho, I.V. Adamovich, and J.W. Rich, "Time-Resolved Fourier Transform Infrared Spectroscopy of Optically Pumped Carbon Monoxide", Chemical Physics, vol. 256, 2000, pp. 315-331

12. Y.P. Raizer, "Gas Discharge Physics", Springer, Berlin, 1991

13. E. Ploenjes, P. Palm, W. Lee, M. D. Chidley, I. V. Adamovich, W. R. Lempert, and J.W. Rich, "Vibrational Energy Storage in High Pressure Mixtures of Diatomic Gases," accepted for publication in Chemical Physics, May 2000

14. J.A.C. Gallas, "Some matrix elements for Morse oscillators," Phys. Rev. A, Vol 21, No. 6, 1980, p. 1829.

15. M. Cacciatore, M. Capitelli, and G.D. Billing, "Theoretical Semiclassical Investigation of the Vibrational Relaxation of CO Colliding with $^{14}N_2$", Chemical Physics, Vol. 89, No. 1, 1984, p. 17

16. G.D. Billing, and E.R. Fisher, "VV and VT Rate Coefficients in N_2 by a Quantum-Classical Model", Chemical Physics, Vol. 43, No.3, 1979, p. 395

17. G.D. Billing, and R.E. Kolesnick, "Vibrational Relaxation of Oxygen. State to State Rate Constants", Chemical Physics Letters, Vol. 200, No. 4, 1992, p. 382

18. G.D. Billing, "VV and VT Rates in N_2-O_2 Collisions", Chemical Physics, Vol. 179, No. 3, 1994, p. 463

19. Price, J.M., Mack, J.A., Rogaski, C.A., and Wodtke, A.M., "Vibrational-State-Specific Self-Relaxation Rate Constant Measurements of Highly Excited $O_2(v=19-28)$", Chemical Physics, Vol. 175, No. 1, 1993, pp. 83-98

20. Park, H., and Slanger, T.G., "O (X, v=8-22) 300 K Quenching Rate Coefficients for O_2 and N_2, and $O_2(X)$ Vibrational Distribution from 248 nm O_3 Photo-dissociation", Journal of Chemical Physics, Vol. 100, No. 1, 1994, pp. 287-300

21. Klatt, M., Smith, I.W.M., Tuckett, R.P., and Ward, G.N., "State-Specific Rate Constants for the Relaxation of $O_2(X^3\Sigma_g^-)$ from Vibrational Levels v=8 to 11 by Collisions with NO and O ", Chemical Physics Letters, Vol. 224, Nos. 3,4, 1994, pp. 253-257

22. R. Hernandez, R.Toumi, and D.C. Clary, "State-Selected Vibrational Relaxation Rates for Highly Vibrationally Excited Oxygen Molecules", Journal of Chemical Physics, Vol. 102, No. 24, 1995, pp. 9544-9558

23. C. Chackerian, Jr., R. Farrenq, G. Guelachvili, C. Rosetti, and W. Urban, Canadian Journal of Physics, Vol. 62, 1984, p. 1579

24. N.K. Madsen and R.F. Sincovec, "Algorithm 540: PDECOL, General Collocation Software for Partial Differential Equations", ACM Transactions on Mathematical Software, Vol. 5, 1979, p. 326

25. G. D., Billing., "Vibration-Vibration and Vibration-Translation Energy Transfer, Including Multiquantum Transitions in Atom-Diatom and Diatom-Diatom Collisions", Nonequilibrium Vibrational Kinetics, Springer-Verlag, Berlin, 1986, Chap. 4, pp. 85-111

26. E.A. Andreev, and E.E. Nikitin, "Vibrational and Electronic Energy Transfer in Atom-Molecule Collisions", in "Khimiya Plasmy" (Plasma Chemistry), ed. by B.M. Smirnov, Vol. 3, Moscow, Atomizdat, 1976, pp. 28-94

27. H.S.W. Massey, E.H.S. Burhop, and H.B. Gilbody, "Electronic and Ionic Impact Phenomena", Vol. III, "Slow Collisions of Heavy Particles", Oxford, Clarendon Press, 1971

List of Figures

Computer
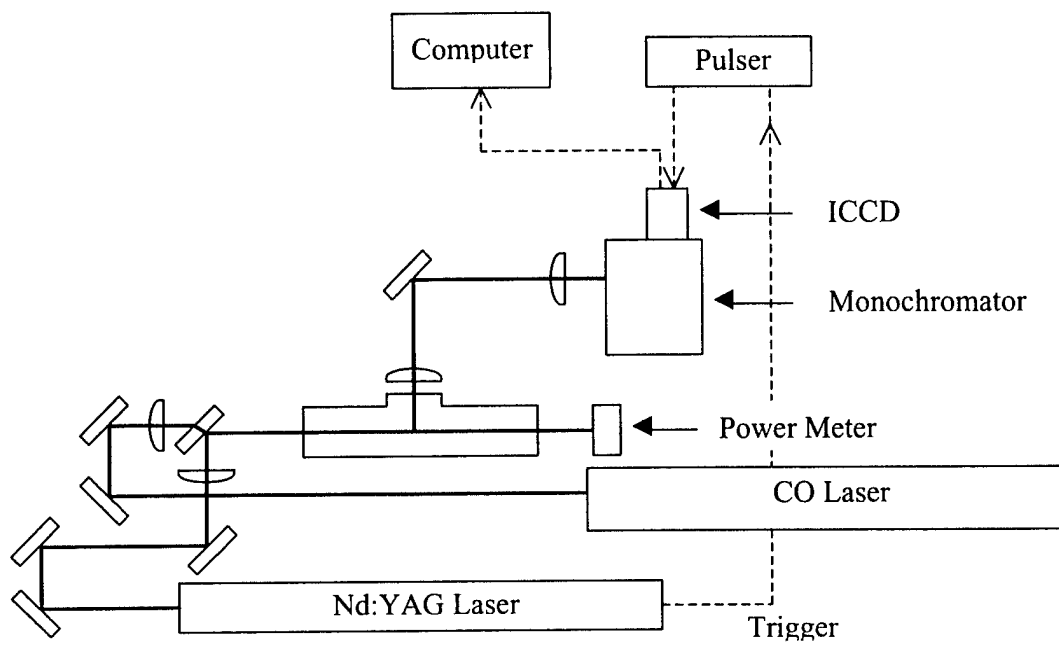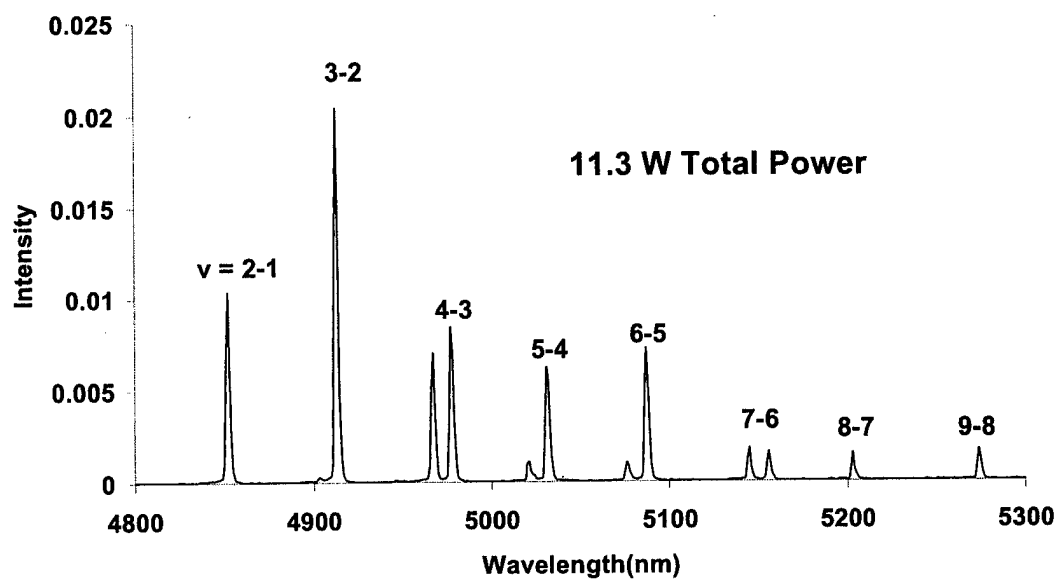
Pulser

ICCD

Monochromator

Power Meter

CO Laser

Nd:YAG Laser

Trigger

Figure 1

Figure 2

Figure 3

Figure 4

Figure 5

Figure 6

Figure 7

Relative population

CO, experiment (T_v=3500 K)

N_2, experiment (T_v=2200 K)

CO, calculation (T_v=4900 K)

N_2, calculation (T_v=2600 K)

Vibrational quantum number

Figure 8

Figure 9

Fig 10.

Figure 11

6. ELECTRON DENSITY AND RECOMBINATION RATE MEASUREMENTS IN CO-SEEDED OPTICALLY PUMPED PLASMAS

Peter Palm, Elke Plönjes, Matt Buoni, Vish V. Subramaniam, and Igor V. Adamovich

Electron production rate and electron density in cold optically pumped CO-Ar and CO-N$_2$ plasmas in the presence of small amounts of O$_2$ and NO have been measured using a Thomson discharge probe and microwave attenuation. Nonequilibrium ionization in the plasmas is produced by an associative ionization mechanism in collisions of highly vibrationally excited CO molecules. It is shown that adding small amounts of O$_2$ or NO (50-100 mtorr) to the baseline gas mixtures at P=100 torr results in an increase of the electron density by up to a factor of 20-40 (from $n_e < 10^{10}$ cm^{-3} to $n_e = (1.5-3.0) \cdot 10^{11}$ cm^{-3}). This occurs while the electron production rate either decreases (as in the presence of O$_2$) or remains nearly constant within a factor of 2 (as in the presence of NO). It is also shown that the electron-ion recombination rates inferred from these measurements decrease by 2 to 3 orders of magnitude compared to their baseline values (with no additives in the cell), down to $\beta \cong 1.5 \cdot 10^{-8}$ cm^3/sec with 50-100 mtorr of oxygen or nitric oxide added to the baseline CO-Ar mixture, and $\beta \cong (2-3) \cdot 10^{-7}$ cm^3/sec with 75-100 mtorr of O$_2$ or NO added to the baseline CO-N$_2$ mixture. The overall electron-ion removal rates in the presence of equal amounts of O$_2$ or NO additives turn out to be very close, which shows that the effect of electron attachment to oxygen at these conditions is negligible. These results suggest a novel method of electron density control in cold laser-sustained steady-state plasmas and open a possibility of sustaining stable high-pressure nonequilibrium plasmas at high electron densities and low plasma power budget.
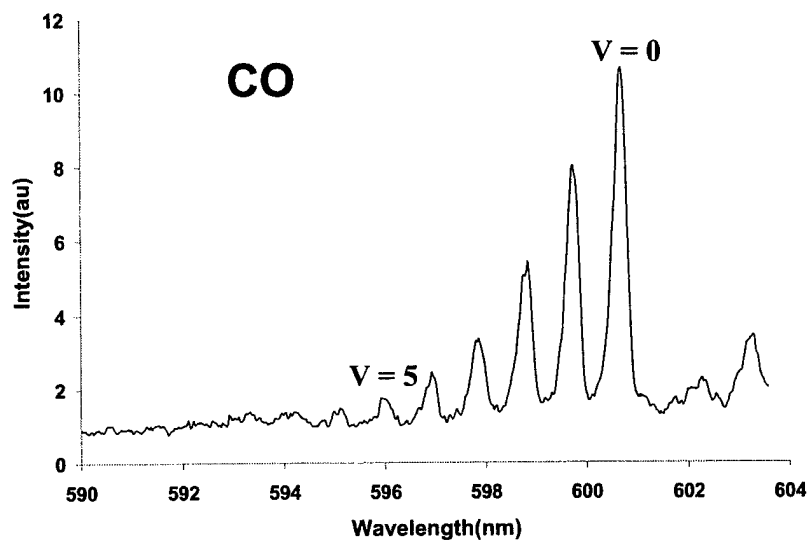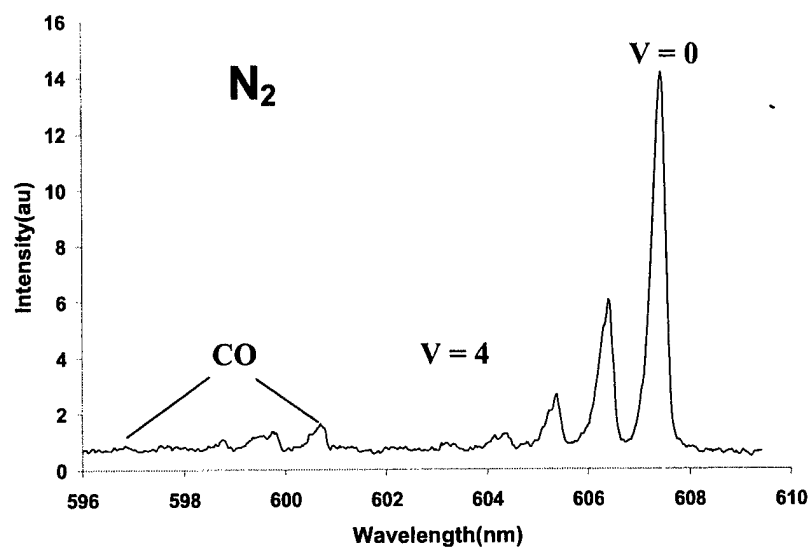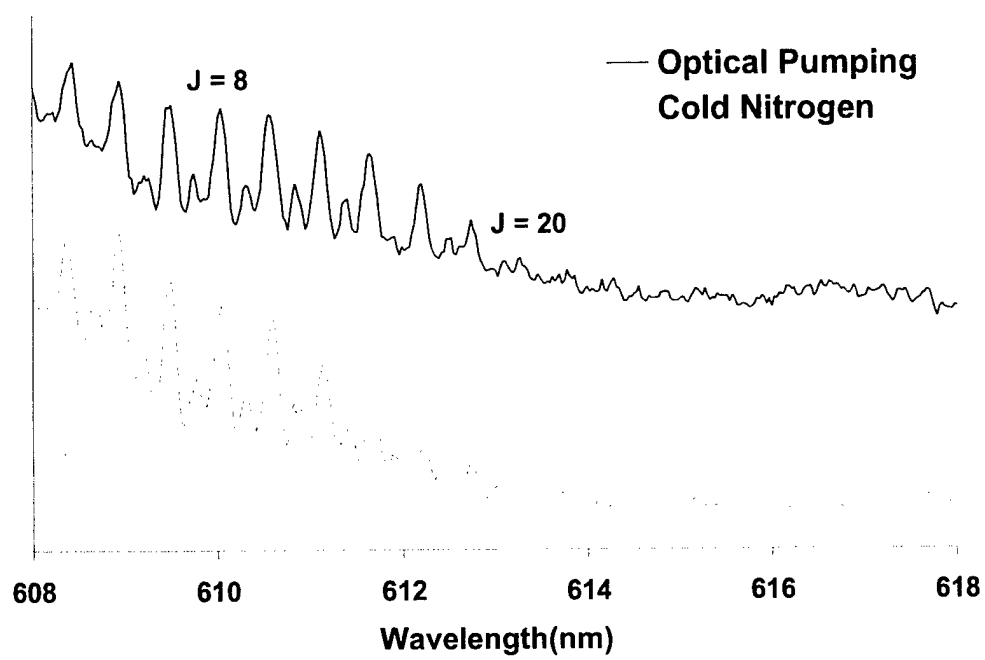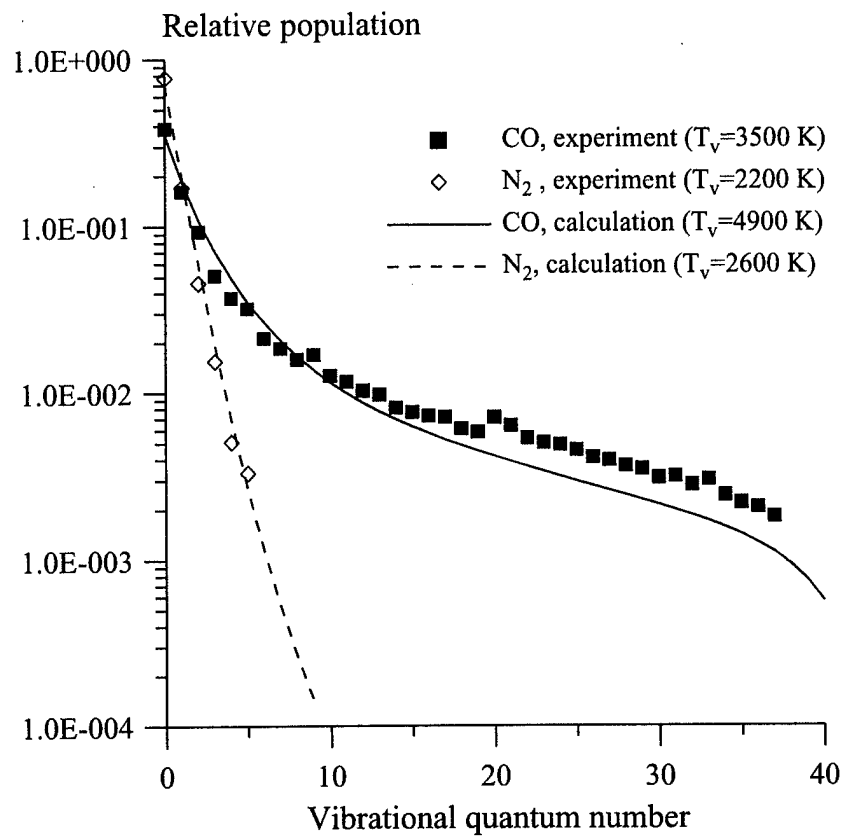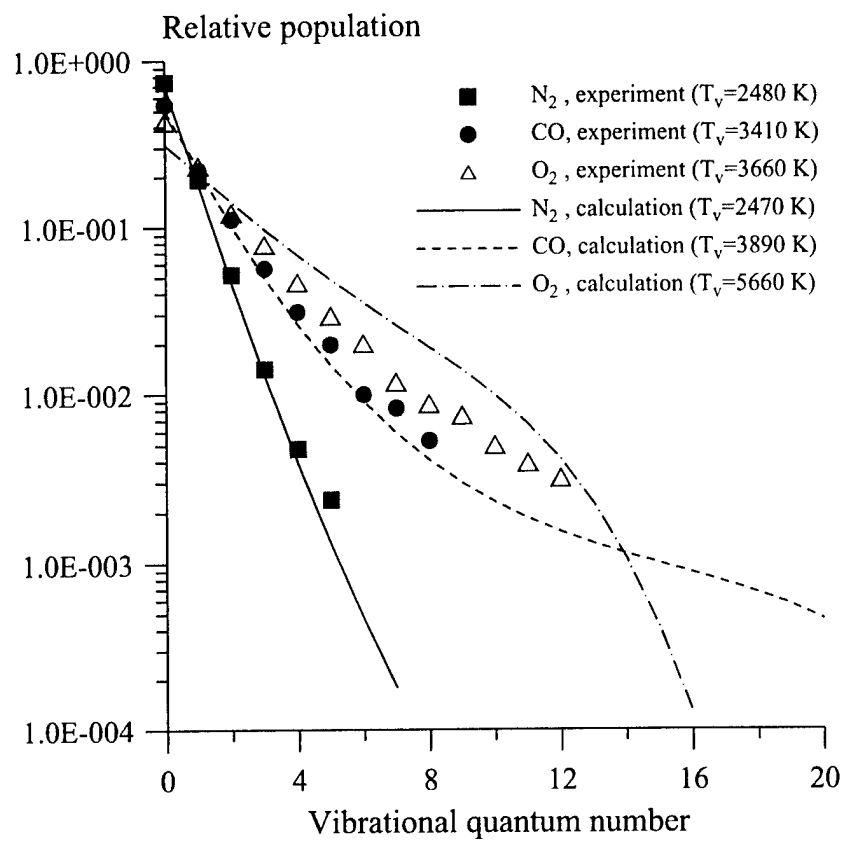
1. Introduction

Steady-state nonequilibrium optically pumped environments are produced by resonance absorption of infrared laser radiation by molecules in low vibrational quantum states, with subsequent collisional vibration-to-vibration (V-V) pumping up to high vibrational levels [1,2],

$$AB(v) + AB(w) \rightarrow AB(v-1) + AB(w+1) \qquad (1)$$
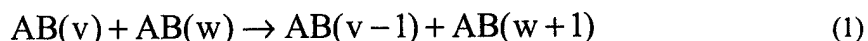
In Eq. (1), AB stands for a diatomic molecule, and v and w are vibrational quantum numbers. This method creates strong vibrational disequilibrium at high densities (up to a few atm in the gas phase), wide temperature range (T=100-1500 K), and a low power budget (~1-10 W/cm^3). In particular, optical pumping by a CO laser has been previously achieved in gas phase CO/Ar/He mixtures [3-8] at pressures of up to 10 atm [3], gas phase nitric oxide [9,10], liquid phase CO [11,12], and solid CO and NO matrices

[13,14]. Recently, optical pumping has also been demonstrated in mixtures of CO with infrared inactive gases, such as nitrogen and air, at atmospheric pressure [15,16]. In this case, N_2 and O_2 molecules become vibrationally excited by near-resonance V-V energy transfer from CO,

$$CO(v) + N_2(w) \rightarrow CO(v-1) + N_2(w+1) \tag{2}$$

$$CO(v) + O_2(w) \rightarrow CO(v-1) + O_2(w+1) \tag{3}$$
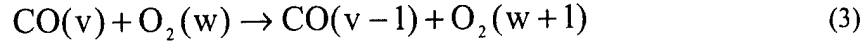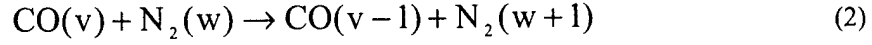
In the experiments of Refs. [2-16], the CO laser power was fairly low, ranging from a few Watts to 200 W c.w.

Ionization in optically pumped gases is produced by an associative ionization mechanism, in collisions of two highly vibrationally excited molecules when the sum of their vibrational energies exceeds the ionization potential [17-20],

$$AB(v) + AB(w) \rightarrow (AB)_2^+ + e^-,$$
$$E_v + E_w > E_{ion} \tag{4}$$
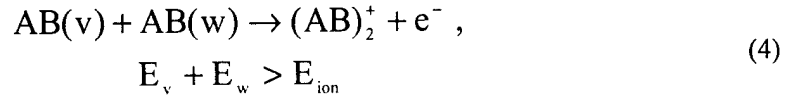
Ionization of carbon monoxide by this mechanism has been previously observed in CO/Ar/He gas mixtures optically pumped by resonance absorption of CO laser radiation [18-20]. The estimated steady-state electron density sustained by a 10 W CO laser in optically pumped CO/Ar/He plasmas with high vibrational level populations of $n_{CO}(v\sim30)\sim10^{15}$ cm^{-3} is $n_e\sim10^{10}$-10^{11} cm^{-3} [19]. Note that unlike electron impact ionization, the ionization mechanism of Eq. (4) is not susceptible to ionization heating instability, which is responsible for filamentation and the glow-to-arc collapse in high-pressure nonequilibrium plasmas, where ionization is primarily produced by electron impact [21]. Indeed, since the high vibrational level populations of diatomic molecules decrease with temperature due to an exponential rise of the vibration-translation (V-T) relaxation rates [22], there is a negative feedback between the gas heating and the rate of associative ionization. This precludes the ionization instability development and provides a possibility for the use of associative ionization for sustaining unconditionally stable optically pumped nonequilibrium plasmas at high gas pressures (1 atm and above).

The present paper addresses the effect of adding air species, such as O_2 and NO, to optically pumped CO/Ar and CO/N_2 plasmas on the electron production and removal kinetics. Previous results [20] suggest that adding these species produces a significant electron density rise in these plasmas at a nearly constant plasma power budget and electron production rate. Therefore, the main objective of the present study is to investigate the role of these additives on the electron density and on the electron removal rate in the

plasma. This would provide insight into the feasibility of sustaining large-volume atmospheric pressure nonequilibrium air plasmas at a minimum power budget.

2. Experimental

The overall schematic of the experimental setup is shown in Fig.1. A carbon monoxide laser is used to excite CO/Ar and CO/N$_2$ gas mixtures, with additives such as O$_2$ or NO, slowly flowing through the pyrex glass optical absorption cell shown. The residence time of the gas mixture in the cell is of the order of a few seconds. The liquid nitrogen cooled CO laser [8] is designed in collaboration with the University of Bonn and fabricated at Ohio State. It produces a substantial fraction of its power output on the v = 1→0 fundamental band component in the infrared. In the present experiment, the laser is typically operated at 10-13 W c.w. broadband power on the lowest ten vibrational bands. The output on the lowest bands (1→0 and 2→1) is necessary to start the absorption process in cold CO (initially at 300 K) in the cell. The laser beam can be focused to a focal area of ~1 mm diameter to increase the power loading per CO molecule, producing an excited region 10-20 cm long and 2-3 mm in diameter.

The lower vibrational states of CO, v≤10, are populated by direct resonance absorption of the pump laser radiation in combination with rapid redistribution of population by V-V exchange processes. The V-V processes then continue to populate higher vibrational levels above v=10, which are not directly coupled to the laser radiation (see Eq. (1)). The large heat capacity of the Ar and N$_2$ diluents, as well as conductive and convective cooling of the gas flow, enables control over the translational/rotational mode temperature in the cell. At steady-state conditions, when the average vibrational mode energy of the CO would correspond to a few thousand degrees Kelvin, the temperature never rises above a few hundred degrees. Thus a strong disequipartition of energy can be maintained in the cell, characterized by very high vibrational mode energy and a low translational/rotational mode temperature. As shown in Fig. 1, the population of the vibrational states of CO in the cell is monitored using a Biorad FTS 175C Fourier transform infrared spectrometer, which records spontaneous emission from the CO fundamental, first and second overtone bands through a CaF$_2$ window on the side of the cell.

Ionization of highly excited CO molecules in the cell occurs by the associative ionization mechanism of Eq. (4). The electron production rate in this optically pumped plasma is determined from the saturation current of the non-self-sustained DC Thomson discharge [18-20] between two 3 cm diameter brass plate electrodes located in the absorption cell as shown in Fig. 2. Two infrared transparent CaF$_2$ windows were placed upstream and downstream of the plates (see Fig. 2), so that the laser beam creates a nearly cylindrical excited region between the windows. Thus the plasma generated in the interelectrode space is isolated from the plasma sustained in the remainder of the cell, which significantly reduces the charged species drift and diffusion into the interelectrode space. This allows reaching a well-

pronounced current saturation. The electrodes, which are typically 10 to 20 mm apart, are connected to a reversible polarity DC power supply (Thorn EMI GENCOM Inc., Model 3000R), which produces voltage in the range 0-3000 V. The induced current is measured with a Keithley 2001 multimeter, with a 1 MΩ resistor connected in series with the cell to protect the multimeter in case of breakdown. The applied DC voltage is deliberately kept sufficiently low to preclude electron impact ionization. Therefore, in the saturation regime of the Thomson discharge, the applied electric field, which does not produce any ionization by itself, removes as many electrons per second as are produced in the entire discharge volume. The electron production rate per unit volume of the plasma is found from the saturation current as follows [20],

$$S \cong \frac{I_s}{e\pi d^2 D / 4},$$ (5)

where d is the diameter of the ionized region created by the focused laser beam, D is the electrode diameter, and $\pi d^2 D/4$ is the volume occupied by the plasma. The plasma diameter, $d = 2.5 \pm 0.5$ mm, is estimated from the diameter of the visible blue glow of the C_2 Swan band radiation, which is strongly coupled with the high vibrational level populations of CO [7].

The electron density in the optically pumped plasma is independently measured by microwave attenuation. The microwave experimental apparatus consists of an oscillator, a transmitting and receiving antenna / waveguide system, and transmitted and reflected microwave power detectors. The phase-locked dialectrically stabilized oscillator generates 20 mW (13 dBm) of microwave radiation at a frequency $v = 10$ GHz, which is transmitted via SMA-type semi-rigid cable to an antenna within the transmission waveguide. The gap between the waveguides is 1 cm. The receiving waveguide is positioned directly opposite the transmitting waveguide, with the laser-generated plasma located between them (see Fig. 2). The signal transmitted through the plasma is received by an antenna at the back of the receiving waveguide and sent to a tunnel diode detector with a low-noise preamplifier. The detector produces a low-noise DC voltage proportional to the received microwave power, ranging from 0 to 15 V for the transmitted power in the range from −60 dBm to −30 dBm. The voltage noise level is typically 1-2 mV, so that the resultant signal-to-noise ratio is $\sim 10^4$. Power reflected by the plasma is detected by a zero-bias Schottky diode detector through an isolator in the line between the oscillator and transmitting antenna. This detector produces a DC voltage in the mV range proportional to the reflected microwave power in the range from 0 to 20 mW. In the present experiments, the measured change in reflected power between the laser on and laser off conditions is negligible.

Typical microwave power levels transmitted across the 1 cm gap between the waveguides were in the range of −10 dBm to 0 dBm, decreasing by up to 1 dB when the plasma was generated. To scale the transmitted signal down to the power range over which the detector has the highest sensitivity (that is, down to −60 dBm to −30 dBm range), attenuators were inserted in the line between the receiving antenna and the transmitted power detector. From the relative difference of the transmitted power with and without a plasma the attenuation of the microwave signal across the plasma was determined with an uncertainty of 0.002 dB. This assumes a negligible difference in the power radiated from the gap between the waveguides, with and without the plasma present, which is justified by the negligible change in the measured reflected power at these conditions.

During the microwave attenuation measurements, the laser beam was chopped at a frequency of 57 Hz, providing a square wave laser input into the cell. The laser remained on and off for approximately 8 msec. Our previous time-resolved Fourier transform infrared spectroscopy measurements [8] showed that at CO partial pressures $P_{CO}>0.5$ torr this time is sufficiently long to reach both the quasi-steady state fully V-V pumped distribution and the complete vibrational relaxation of CO in the cell. In addition, the characteristic time scales for associative ionization and for electron-ion recombination, $\tau_{ion}\sim n_e/(k_{ion}n_{CO}^2 f_{v>30}^2)\sim 0.1$ msec and $\tau_{rec}\sim 1/\beta n_e\sim 0.1$-1.0 msec are both much shorter than the chopper cycle duration. Here $k_{ion}=1.5\cdot 10^{-13}$ cm^3/sec is the associative ionization rate coefficient [20], $n_{CO}=10^{17}$ cm^{-3} is the CO concentration in the cell (at $P_{CO}=3$ torr), $f_{v>30}\sim 10^{-3}$ is the fraction of the CO molecules participating in the associative ionization process of Eq. (4) [20], $\beta=10^{-8}$-10^{-7} cm^3/sec is the electron-ion dissociative recombination rate, and $n_e=10^{11}$ cm^{-3} is the estimated maximum electron density [20]. Therefore the laser on and laser off conditions correspond to the quasi-steady state weakly ionized plasma and nearly fully recombined plasma conditions, respectively. The difference between the incident and transmitted microwave powers between the plasma on and plasma off conditions was determined from the amplitude of the resultant nearly square wave forward power detector signal, $\delta V = V_{inc} - V_{trans}$, modulated by the chopper, and averaged by a Textronix TDS380 oscilloscope over 256 averages. The average electron density in the plasma was inferred from these measurements using the following relation [21],

$$ n_e = \frac{m_e c \varepsilon_0}{e^2} v_{coll} \frac{\delta V}{V_{inc}} \frac{1}{d} \frac{W}{d}, \tag{6} $$

where v_{coll} is the electron-neutral collision frequency, $\dfrac{\delta V}{V_{inc}} = \dfrac{V_{trans} - V_{inc}}{V_{inc}}$ is the relative attenuation factor

in terms of the forward power detector voltage proportional to the incident and the transmitted microwave

power, W=1 cm is the waveguide width, and d=2.5±0.5 mm is the diameter of the ionized region. The electron-neutral collision frequency in CO-Ar and CO-N_2 mixtures at P=100 torr and T=600 K, $v_{coll}=1.1\cdot10^{12}$ cm^3/sec and $v_{coll}=2.1\cdot10^{12}$ cm^3/sec, respectively, was obtained from the Boltzmann equation solution [19] using the experimental cross-sections of elastic and inelastic electron collision processes available in the literature.

O_2 or NO were both diluted in nitrogen at the 5000 ppm level to add controlled small amounts (from a few millitorr to a few hundred millitorr) of these species to the cell. The resultant O_2/N_2 and NO/N_2 gas mixtures have been added to the baseline CO/Ar and CO/N_2 gas mixtures. The baseline pressure in the cell was P=100 torr, with the CO partial pressure of P_{CO}=3 torr. The O_2/N_2 and NO/N_2 mixture partial pressure was varied from 1 torr to 100 torr. Note that adding the same amounts of pure nitrogen (without the additives) to the baseline gas mixtures did not produce significant changes in the measured electron density.

3. Results and Discussion

Figure 3 shows the low-resolution (8 cm^{-1}) CO first overtone infrared emission spectra measured in the optically pumped CO-Ar plasmas with O_2 and NO additives. At these conditions, vibrational levels up to v~35-40 are populated and radiating. From Fig. 3, one can see that adding small amounts (~0.1%) of oxygen to the cell gases results in the depopulation of the high vibrational levels of CO (v>15-20), without producing significant changes in the low vibrational level populations. This is most likely due to the rapid near-resonance V-V energy transfer from highly excited CO to O_2,

$$CO(v) + O_2(0) \rightarrow CO(v-1) + O_2(1), \quad v \sim 25 \qquad (7)$$
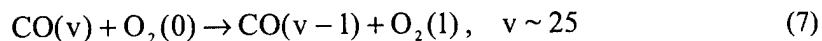
as discussed in our previous publication [15]. On the other hand, adding comparable amounts of nitric oxide to the baseline CO-Ar mixture, in addition to reducing the intensities of the high vibrational bands (v'=20-30) compared to the low bands (v'=2-5), decreases the absolute intensity of the entire spectrum (see Fig. 3). This indicates that the populations of all CO vibrational levels in the range v~2-35 are substantially reduced in the presence of NO. This is consistent with the fact that compared to CO and O_2, NO is a much faster V-T relaxer [23], so that even the low vibrational levels of CO are depopulated by the rapid V-T relaxation processes such as

$$CO(v = 1) + NO \rightarrow CO(v = 0) + NO, \qquad (8)$$

114
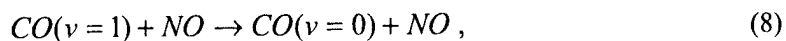
which are competing with the V-V pumping process of Eq. (1). Thus, in both these cases, the concentration of the highly vibrationally excited CO molecules in the cell is reduced. Indeed, Fig. 4 illustrates this effect showing CO vibrational distribution functions inferred from the high-resolution (0.25 cm^{-1}) CO infrared spectra in CO-Ar-O$_2$ mixtures. Similar behavior has been previously observed from the CO distribution function measurements in CO-Ar-NO mixtures [20]. At these experimental conditions (P=100 torr, P$_{CO}$=3 torr), the translational/rotational mode temperature inferred from the high-resolution (0.25 cm^{-1}) infrared spectra is in the range of T=500-700 K [8,18,20].

Figure 5 displays the microwave signal intensity transmitted through an optically pumped CO-Ar-NO plasma. As discussed in Section 2, the signal is modulated by a chopper providing a square wave laser input into the cell. It can be seen from Fig. 5 that turning on the laser results in the well-pronounced attenuation of the transmitted signal due to the vibrationally stimulated ionization in the cell.

Figures 6 and 7 show the average electron density in the optically pumped CO-Ar plasmas with small admixtures of O$_2$ and NO, respectively. One can see that in both cases adding 50-75 mtorr of oxygen or nitric oxide to the cell gases increases the electron density by about a factor 20-40, up to n$_e$=(1.5-3.0)$\cdot$10^{11} cm^{-3}, compared with the baseline case with only CO and Ar in the cell, n$_e$=(3-6)$\cdot$10^9 cm^{-3}. This type of behavior is somewhat unexpected since oxygen is known to be an efficient electron attacher by a three-body process,

$$e^- + O_2 + M \rightarrow O_2^- + M \qquad (9)$$

with a rate of k$_{att}$N=10^{-11} cm^3/s [24], which is likely to reduce the electron density. Further increase of the additive partial pressure up to 400-500 mtorr resulted in the gradual reduction of the electron density back to to n$_e$=(1-2)$\cdot$10^{10} cm^{-3} (see Figs. 6,7). The uncertainty in the measured electron density, indicated by the error bars in Figs. 6,7 is mostly due to uncertainty in the diameter of the ionized region, estimated to be in the range between 2.0 and 3.0 mm (see Section 2). The measured maximum electron densities are consistent both with the values predicted by coupled master equation / Boltzmann equation modeling calculations [19] and inferred from RF probe conductivity measurements [20]. Similar behavior of electron density as a function of additive partial pressure was observed in CO/N$_2$/O$_2$ and CO/N$_2$/NO mixtures (see Fig. 8), where the electron density also increased by about a factor of 10-20 in the presence of 25-75 mtorr O$_2$ or NO.

The observed sharp electron density rise with the additive partial pressure between 0 and 100 mtorr (see Figs. 6,7) occurs despite the fact that the CO vibrational level populations have been found to monotonously decrease when oxygen or nitric oxide are added to the cell (see Figs. 3,4 and Ref. [20]).

This rise might be interpreted by the participation of O_2 and NO molecules, which both have lower ionization potentials than CO (12.1 eV, 9.6 eV, and 14.0 eV, respectively), in the vibrationally stimulated ionization process of Eq. (4). However, measurements of the net electron production rate at these conditions turn out to be inconsistent with this suggestion. Figure 9 shows current-voltage characteristics of the Thomson discharge sustained between two DC electrodes in the CO-Ar-O_2 plasma (see Fig. 2). One can see that the saturation current of this discharge, proportional to the electron production rate in the plasma, is actually dropping with the O_2 concentration. As discussed in Section 2, in the saturation regime, the applied electric field removes as many electrons per second as are produced in the entire discharge volume. This is illustrated by the measurements of electron density in the Thomson discharge as a function of the applied voltage (see Fig. 10). The fact that the electron density in the plasma drops by about an order of magnitude as the discharge approaches saturation confirms that the saturation current indeed approaches the net electron production rate (within about 10%).

The independent measurements of the electron density and the electron production rate lead us to conclude that the simultaneous electron production rate drop and electron density rise with the additive partial pressure can be only due to the net electron removal rate reduction in the presence of small amounts of O_2 or NO (up to 100 mtorr) in the optically pumped CO-Ar and CO/N_2 plasmas.

To infer the electron removal rate in the optically pumped plasmas, we measured both the electron production rate and the electron density in the same experiment. At these conditions, the electron removal rate is essentially a sum of three processes, (i) ambipolar diffusion of charged species out of the ionized region, (ii) electron-ion recombination, and (iii) electron attachment to oxygen molecules. The time scales for the electron removal by the first two mechanisms differ by about an order of magnitude, $\tau_{diff} \sim d^2/D_a \sim 10$ msec and $\tau_{rec} \sim 1/\beta n_e \sim 0.1$-$1.0$ msec, where $d \sim 0.2$-0.3 cm is the diameter of the ionized region, $D_a \sim 5$ cm^2/sec is the ambipolar diffusion coefficient at P=100 torr [25], $\beta \sim 10^{-8}$-10^{-7} cm^3/sec is the dissociative recombination coefficient, and $n_e \sim 10^{11}$ cm^{-3} is the electron density. Therefore in the present work we neglect charge species loss by diffusion. Also, O_2^- ion formation by the three-body electron attachment process of Eq. (9) is neglected. The arguments in favor of this assumption are as follows: (i) adding small amounts of O_2 to the cell gases results in an increase of the electron density in the plasma, which suggests that rapid three-body elecron attachment to oxygen is mitigated to a large extent, (ii) similar results were obtained when comparable amounts of NO, which is not an efficient electron attacher, are added to the cell gases, and (iii) Raman spectroscopy measurements of the O_2 vibrational level populations (v=0-12) in the optically pumped CO/N_2/O_2 plasmas [15,16] show that O_2 in these mixtures becomes strongly vibrationally excited, reaching vibrational temperature of $T_v(O_2)$=2200-3600 K. In particular, the latter result suggests that strong vibrational excitation of O_2 might well stimulate detachment of electrons from the weakly bound O_2^- ions (with electron affininity of $\sim$0.43 eV).

116

With the dominant electron removal process being dissociative recombination, in the steady state its rate can be directly inferred from the electron production rate per unit volume, S, and the electron density, n_e,

$$\beta = \frac{S}{n_e^2} \qquad (10)$$

Figures 11, 12 show the results of simultaneous measurements of the electron production rate inferred from the Thomson discharge saturation current and the electron density in the optically pumped CO-Ar-O_2 and in CO-Ar-NO mixtures, respectively. From Fig. 11, one can see that the electron production rate drops with the O_2 partial pressure by about a factor 5, while electron density increases by approximately a factor of 30. Similarly, Fig. 12 shows that the electron production rate weakly changes (approximately within a factor of 2) depending on the NO partial pressure, while the electron density increases with the NO partial pressure almost by a factor of 50. Figure 13 shows the electron-ion recombination rate coefficients inferred from these data using Eq. (10). It can be seen that the recombination rate in CO-Ar-O_2 and in CO-Ar-NO mixtures decreases by about three orders of magnitude, from its baseline value of $\beta=2\cdot10^{-5}$ cm^3/sec (with no additives in the cell) to $\beta\sim1.5\cdot10^{-8}$ cm^3/sec with 50-100 mtorr oxygen or nitric oxide added (see Fig. 13). Interestingly, the electron-ion recombination coefficients in both mixtures (with 50-100 mtorr of O_2 or NO added) are very close, which shows that the contribution of electron attachment to oxygen at these conditions is negligible. Similarly, the recombination rate in CO-N_2-O_2 and CO-N_2-NO mixtures decreases by about two orders of magnitude, from $\beta=5\cdot10^{-5}$ cm^3/sec with no additives in the cell to $\beta\sim(2\text{-}3)\cdot10^{-7}$ cm^3/sec with 75-100 mtorr O_2 or NO added (see Fig. 14). Here again the difference between the recombination coefficients in O_2 and NO doped CO-N_2 mixtures is small.

Thus, adding small amounts (~0.05-0.1%) of O_2 and NO to the optically pumped CO-Ar and CO-N_2 plasmas allows control and considerable increase of the electron density (from $n_e=(6\text{-}8)\cdot10^9$ cm^{-3} up to $n_e=(1\text{-}3)\cdot10^{11}$ cm^{-3}) by reducing the electron-ion recombination rate (by up to 2-3 orders of magnitude). This result is consistent with the electron density and recombination rate inference from the RF probe plasma conductivity measurements [20].

Quantitative interpretation of the observed effect, i.e. identifying specific kinetic processes responsible for the electron recombination rate reduction, requires knowledge of the ion composition of the optically pumped plasma. However, a qualitative scenario can be suggested based on previous ion composition measurements in a glow discharge in CO-Ar-O_2 mixtures using in situ ion mass spectrometry [26]. The mass spectra taken in CO/Ar mixtures without oxygen show that the dominant ions in the

discharge are dimer ions $(CO)_2^+$ and cluster ions of the general form $C_n(CO)_2^+$, n=1-15. However, adding a few tens of millitorr of O_2 to these gas mixtures resulted in nearly complete disappearance of these ions and their replacement by the O_2^+ ions. Note that the electron-ion dissociative recombination rate of the dimer $(CO)_2^+$ ion, $\beta=2\cdot10^{-6}$ cm^3/s [27], greatly exceeds the rate of recombination of the monomer O_2^+ ion, $\beta=(3-5)\cdot10^{-8}$ cm^3/s at the electron temperature of $T_e\sim0.3-0.5$ eV [21]. The recombination rate of the large carbon cluster ions can possibly be even higher. A similar process, i.e. destruction of the rapidly recombining carbon-based cluster ions and their replacement by the slowly recombining monomer ions, such as O_2^+ and NO^+, might also occur in optically pumped plasmas. This might occur in rapid exothermic ion-molecules reactions, such as

$$(CO)_2^+ + O_2 \rightarrow CO + CO + O_2^+ \qquad (11)$$

$$(CO)_2^+ + NO \rightarrow CO + CO + NO^+ \qquad (12)$$
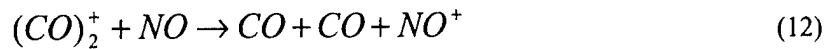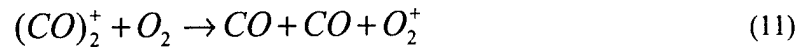
(both O_2 and NO have much lower ionization potential than CO). In addition, rapid resonance charge transfer from the vibrationally excited $O_2(v)$ and $NO(v)$ molecules to O_2^+ and NO^+ ions can produce vibrational excitation of these ions, which may further reduce the dissociative recombination rate [28]. More information on the detailed kinetic mechanism of the observed effect is expected to be obtained from ion mass spectrometry measurements in the optically pumped plasmas.

The observed effects also open a possibility of additional energy coupling to the vibrational modes of diatomic molecules in the optically pumped plasmas (such as CO and N_2). This process, which requires some initial ionization of the gas mixture, relies on free electron heating by an external sub-breakdown RF field with subsequent vibrational excitation by electron impact. Indeed, if the reduced electric field is in the range $E/N=(1-3)\cdot10^{-16}$ V·cm^2, which is about an order of magnitude lower than the breakdown threshold, up to 90% of the input electrical power coupled to the plasma goes to excitation of vibrational modes of molecules, such as CO and N_2 [29-31]. The use of this effect would allow sustaining large volumes of strongly nonequilibrium optically pumped gases without using a high-power pump laser.

4. Summary

Electron production rate and electron density in cold optically pumped CO-Ar and CO-N_2 plasmas in the presence of small amounts of O_2 and NO have been measured using a Thomson discharge probe and microwave attenuation. Nonequilibrium ionization in the plasmas is produced by an associative ionization mechanism in collisions of highly vibrationally excited CO molecules. It is shown that adding small amounts of O_2 or NO (50-100 mtorr) to the baseline gas mixtures at P=100 torr results in an

increase of the electron density by up to a factor of 20-40 (from $n_e < 10^{10}$ cm^{-3} to $n_e = (1.5-3.0) \cdot 10^{11}$ cm^{-3}). This occurs while the electron production rate either decreases (as in the presence of O_2) or remains nearly constant within a factor of 2 (as in the presence of NO). It is also shown that the electron-ion recombination rates inferred from these measurements decrease by 2 to 3 orders of magnitude compared to their baseline values (with no additives in the cell), down to $\beta \cong 1.5 \cdot 10^{-8}$ cm^3/sec with 50-100 mtorr of oxygen or nitric oxide added to the baseline CO-Ar mixture, or $\beta \cong (2-3) \cdot 10^{-7}$ cm^3/sec with 75-100 mtorr of O_2 or NO added to the baseline CO-N$_2$ mixture. The overall electron-ion removal rates in the presence of equal amounts of O_2 or NO additives turn out to be very close, which shows that the effect of electron attachment to oxygen at these conditions is negligible. These results suggest a novel method of electron density control in cold laser-sustained steady-state plasmas and open a possibility of sustaining of stable high-pressure nonequilibrium plasmas at high electron densities and low plasma power budget.

References

1. J. W. Rich, "Relaxation of Molecules Exchanging Vibrational Energy", in "Applied Atomic Collision Physics", vol. 3, "Gas Lasers", ed. E.W. McDaniel and W.L. Nighan, Academic Press, New York, 1982, pp. 99-1407

2. B.F. Gordiets, V.A. Osipov, and L.A. Shelepin, "Kinetic Processes in Gases and Molecular Lasers", Gordon and Breach, London, 1988

3. J.W. Rich, R.C. Bergman, and M.J. Williams, Measurement of Kinetic Rates for Carbon Monoxide Laser Systems, Final Contract report AFOSR F49620-77-C-0020 (November 1979)

4. J.W. Rich and R.C. Bergman, Chem. Phys., Vol. 44, 1979, p. 53

5. R.L. DeLeon and J.W. Rich, Chem. Phys., vol. 107, 1986, p. 283

6. C. Flament, T. George, K.A. Meister, J.C. Tufts, J.W. Rich, V.V. Subramaniam, J.-P. Martin, B. Piar, and M.-Y. Perrin, Chem. Phys., vol. 163, 1992, p. 241

7. H.L. Wallaart, B. Piar, M.Y. Perrin, and J.P. Martin, Chem. Phys., Vol. 196, 1995, p. 149

8. E. Plönjes, P. Palm, A.P. Chernukho, I.V. Adamovich, and J.W. Rich, Chem. Phys., vol. 256, 2000, p. 315

9. H. Dünnwald, E. Siegel, W. Urban, J.W. Rich, G.F. Homicz, and M.J. Williams, Chem. Phys., Vol. 94, 1985, p. 195

10. S. Saupe, I. Adamovich, M.J. Grassi, and J.W. Rich, Chem. Phys., vol. 174, 1993, p. 219

11. D.S. Anex and G.E. Ewing, J. Phys. Chem., Vol. 90, p. 1604, 1986

12. R.S. Disselkamp and G.E. Ewing, J. Phys. Chem., Vol. 93, p. 6334, 1989

13. J.P. Galaup, J.Y. Harbec, R. Charneau, and H. Dubost, Chem. Phys. Lett., Vol. 120, 1985, p. 188

14. I. Hadj Bachir, R. Charneau, and H. Dubost, Chem. Phys., Vol. 177, 1993, p. 675

15. E. Plönjes, P. Palm, W. Lee, M. D. Chidley, I.V. Adamovich, W.R. Lempert, and J. W. Rich, Chem. Phys., vol. 260, 2000, p. 353

16. W. Lee, I.V. Adamovich, and W.R. Lempert, "Optical Pumping Studies of Vibrational Energy Transfer in High-Pressure Diatomic Gases", Journal of Chemical Physics, vol. 114, 2001, p. 1178

17. L.S. Polak, P.A. Sergeev, and D.I. Slovetskii, Sov. High Temperature Physics, Vol. 15, 1977, p. 15

18. I. Adamovich, S. Saupe, M.J. Grassi, O. Schulz, S. Macheret, and J.W. Rich, Chem. Phys., vol. 173, 1993, p. 491

19. I.V. Adamovich and J.W. Rich, J. Phys. D: Appl. Phys., vol. 30, 1997, p. 1741

20. E. Plönjes, P. Palm, I.V. Adamovich, and J.W. Rich, J. Phys. D: Appl. Phys., vol. 33, 2000, p. 2049

21. Raizer, Y.P., "Gas Discharge Physics", Springer-Verlag, Berlin, 1991

22. Billing, G.D., "Vibration-Vibration and Vibration-Translation Energy Transfer, Including Multiquantum Transitions in Atom-Diatom and Diatom-Diatom Collisions", Nonequilibrium Vibrational Kinetics, Springer-Verlag, Berlin, 1986, Chap. 4, pp. 85-111

23. S. Saupe, I. Adamovich, M.J. Grassi, and J.W. Rich, Chem. Phys., vol. 174, 1993, p. 219

24. H.S.W. Massey, E.H.S. Burhop, and H.B. Gilbody, "Electronic and Ionic Impact Phenomena", Vol. III, "Slow Collisions of Heavy Particles", Oxford, Clarendon Press, 1971

25. E.W. McDaniel, "Collision Phenomena in Ionized Gases", Wiley, New York, 1964

26. Y. Kaufman, P. Avivi, F.Dothan, H. Keren, J. Malinowitz, J. Chem. Phys., Vol. 72, 1980, p. 2606

27. R. Johnsen, "Recombination of Cluster Ions", in B.R. Rowe et al. (eds.), "Dissociative Recombination", Plenum, New York, 1993

28. T. Mostefaoui, S. Laube, G. Gautier, C. rebrion-Rowe, B.R. Rowe, and J.B.A. Mitchell, J. Phys. B: At. Mol. Opt. Phys., Vol. 32, 1999, p. 5247

29. N.L. Aleksandrov, A.M. Konchakov, and E.E. Son, Sov. J. Plasma Physics, Vol. 4, 1978, p. 169

30. N.L. Aleksandrov, A.M. Konchakov, and E.E. Son, Sov. Phys. Tech. Phys., Vol. 49, 1979, p. 661

31. N.L. Aleksandrov, F.I. Vysikailo, R.Sh. Islamov, I.V. Kochetov, A.P. Napartovich, and V.G. Pevgov, Sov. High Temp. Phys., Vol. 19, 1981, p. 22

Figure Captions

Figure 1. Schematic of the experimental setup

Figure 2. Schematic of the Thomson discharge electrode and microwave waveguide arrangement in the absorption cell

Figure 3. First overtone CO emission spectra in optically pumped CO-Ar mixtures with small amounts of O_2 and NO added. P_{CO}=3 torr, P_{Ar}=100 torr

Figure 4. CO vibrational level populations for the conditions similar to those of Fig. 3. P_{CO}=2 torr, P_{Ar}=100 torr

Figure 5. Transmitted microwave signal with the pump CO laser turned on and off. P_{CO}=3 torr, P_{Ar}=100 torr, P_{NO}=50 mtorr

Figure 6. Electron density in CO-Ar-O_2 mixtures as a function of the O_2 partial pressure

Figure 7. Electron density in CO-Ar-NO mixtures as a function of the NO partial pressure

Figure 8. Electron density in CO-N_2 mixtures as a function of the NO partial pressure

Figure 9. Saturation of the Thomson discharge in the optically pumped CO-Ar-O_2 mixtures

Figure 10. Electron removal by the applied ffield in the Thomson discharge approaching saturation

Figure 11. Electron production rate and electron density in CO-Ar-O_2 mixtures as a function of O_2 partial pressure

Figure 12. Electron production rate and electron density in CO-Ar-NO mixtures as a function of NO partial pressure

Figure 13. Electron recombination rate coefficient in CO-Ar mixtures as a function of additive partial pressure

Figure 14. Electron recombination rate coefficient in CO-N_2 mixtures as a function of additive partial pressure

Figures

Figure 1.

Side View   **Top View**

Figure 2

Figure 3.
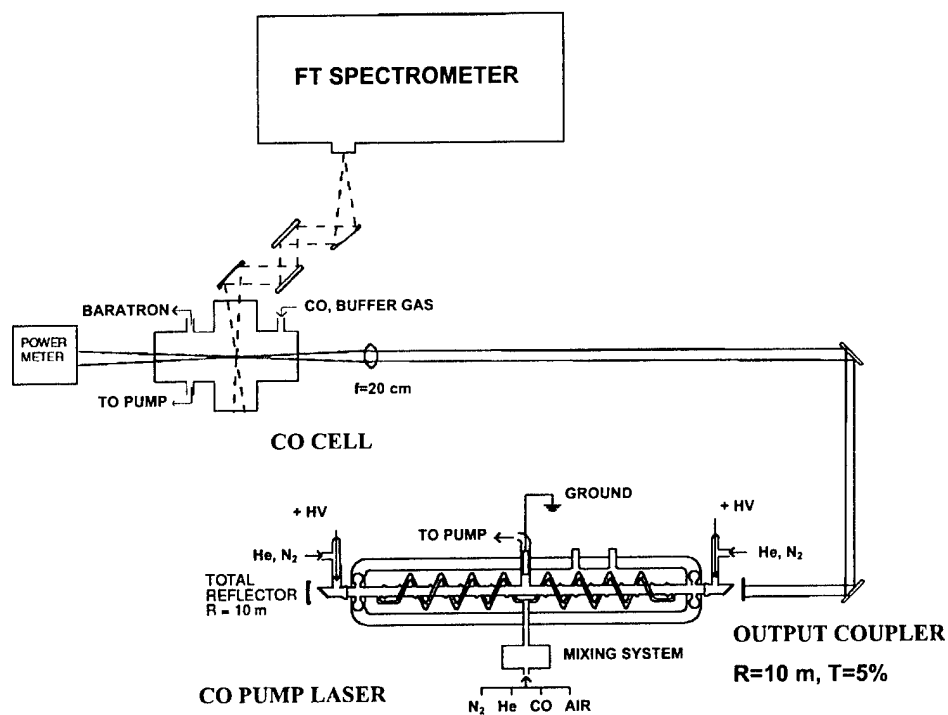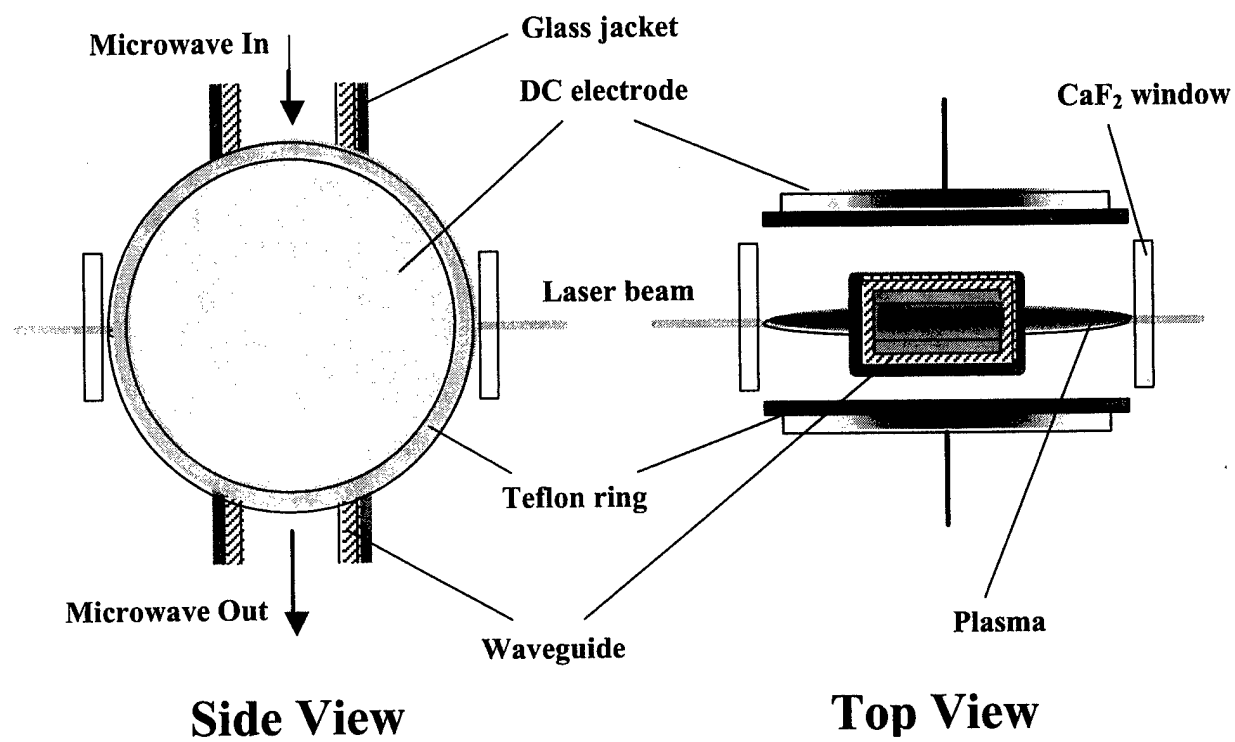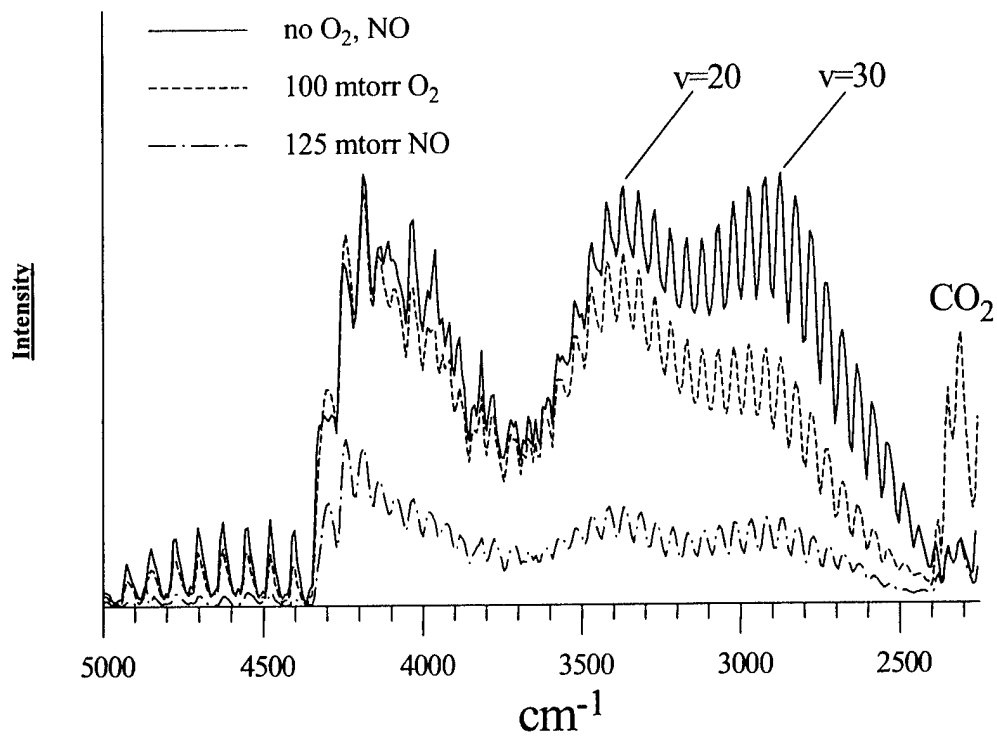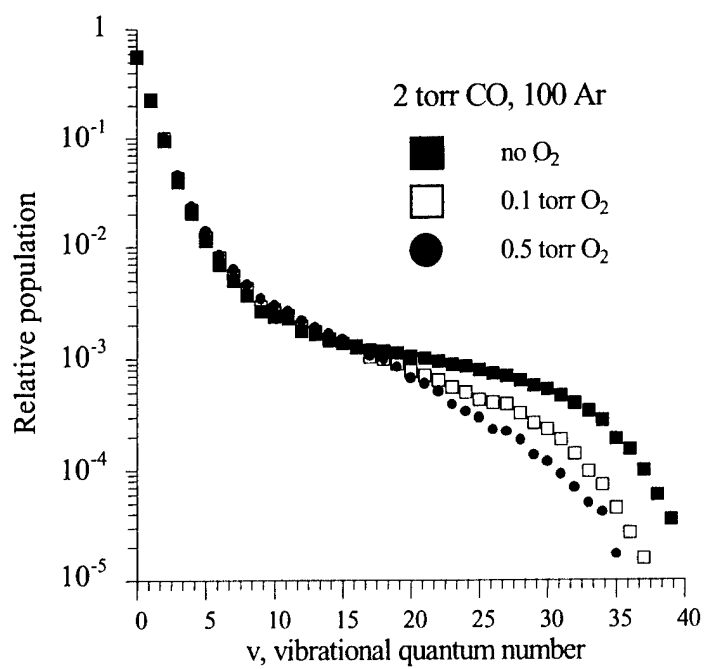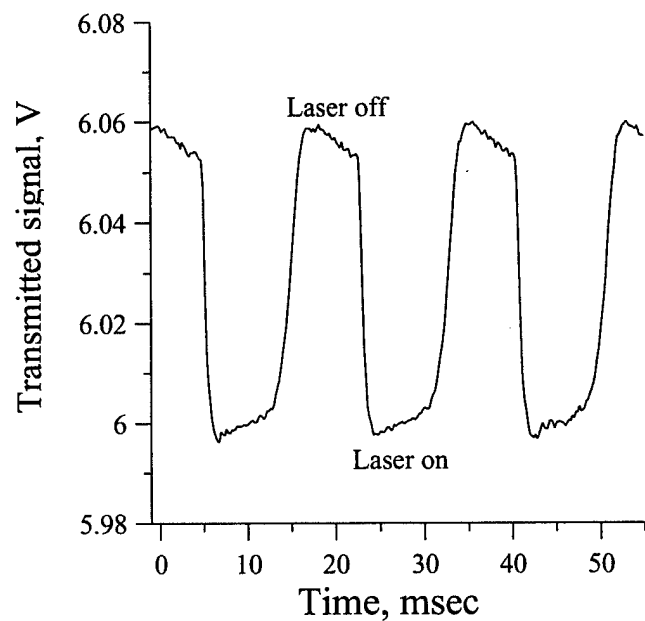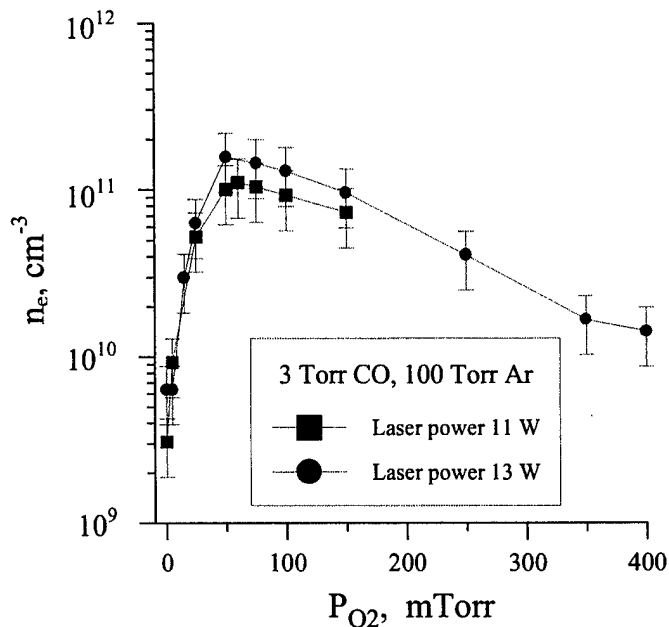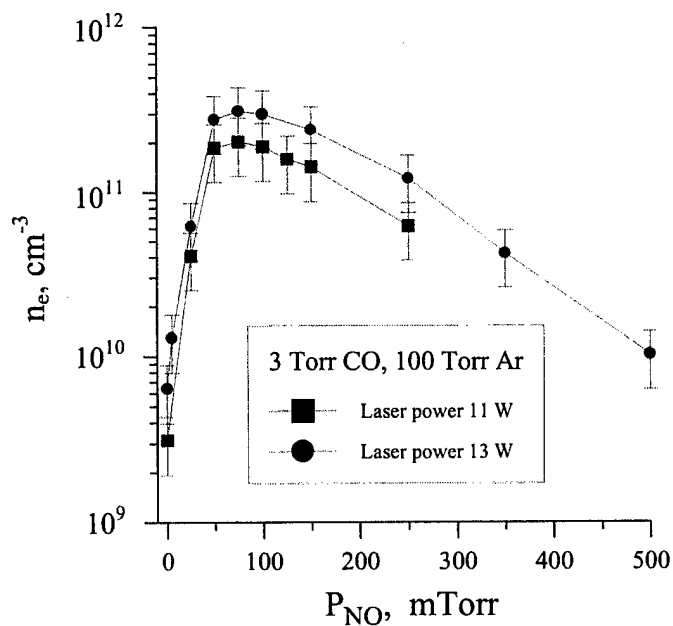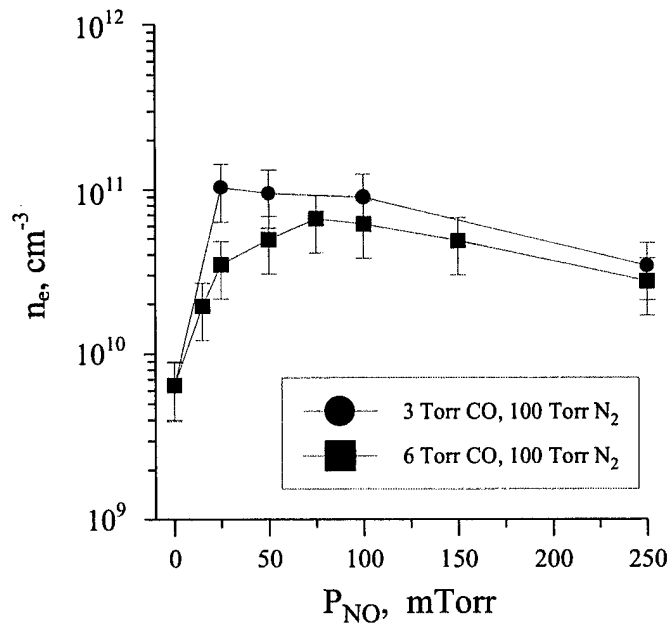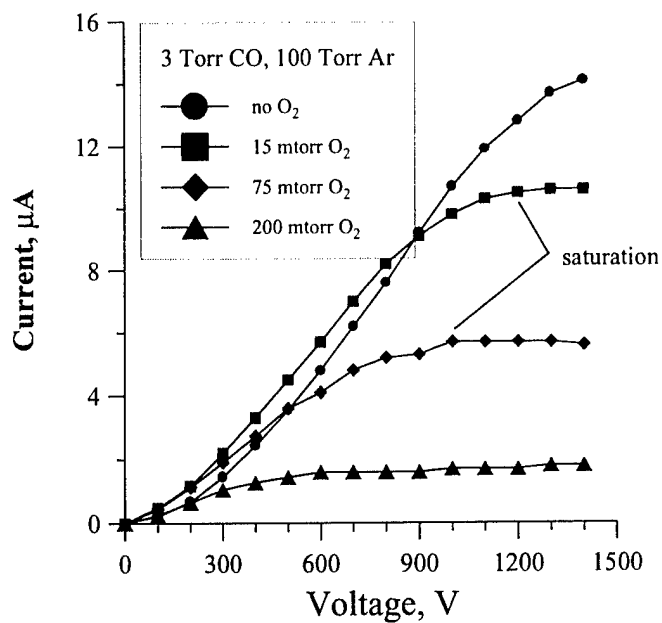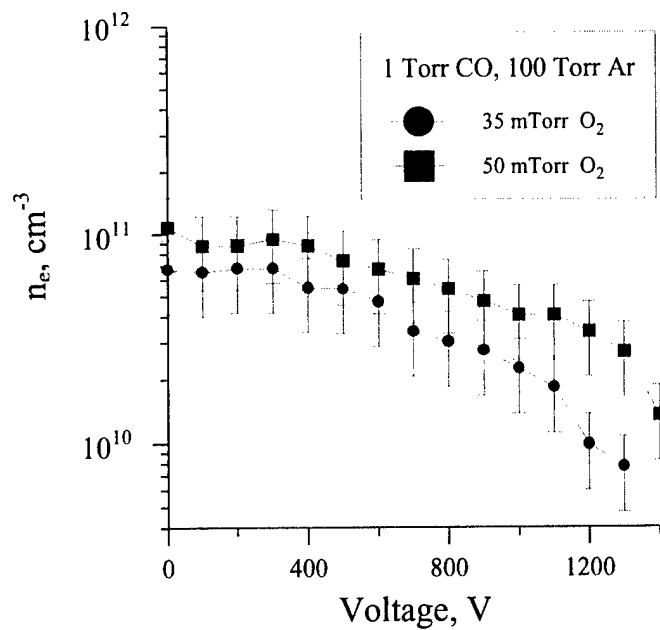

Figure 4.

Figure 5.

Figure 6.

Figure 7.

Figure 8.

125
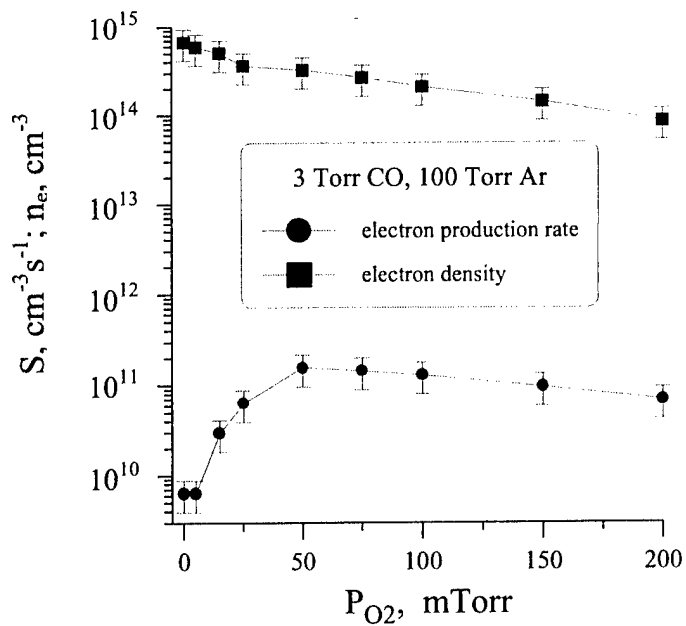
Figure 9.

Figure 10.

Figure 11.

Figure 12.

Figure 13.

β, cm^3/sec

Additive partial pressure, mTorr

3 Torr CO, 100 Torr Ar

Type of additive:

△ oxygen

□ nitric oxide

Figure 14.

β, cm^3/sec

Additive partial pressure, mTorr

6 Torr CO, 100 Torr N$_2$

Type of additive:

△ oxygen

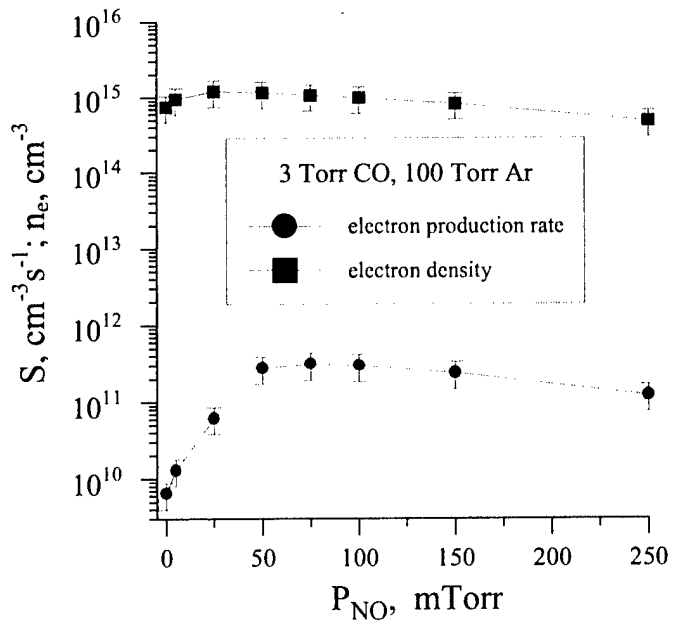□ nitric oxide
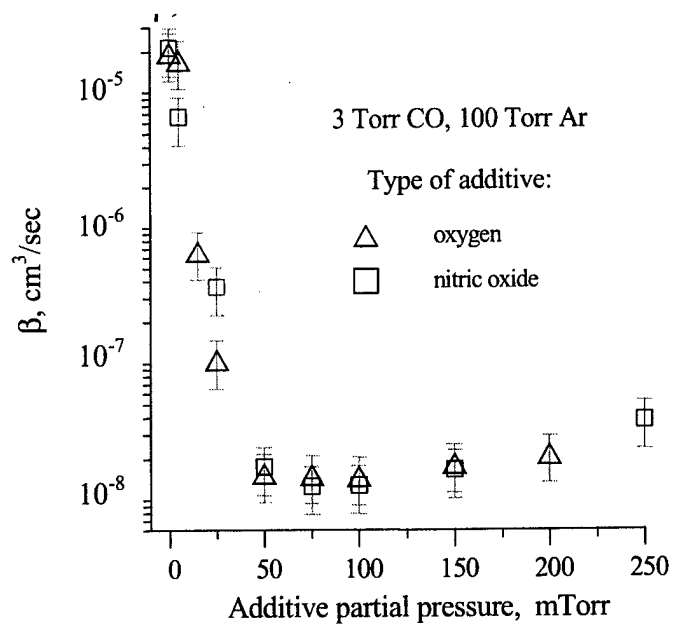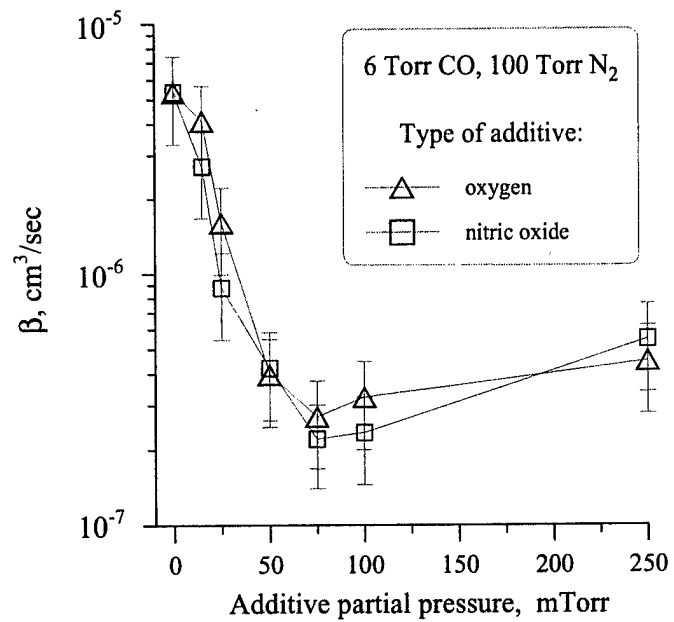
7. A COLD THERMIONICALLY-EMITTING DUSTY AIR PLASMA FORMED BY RADIATIVE HEATING OF GRAPHITE PARTICULATES

J. L. Lilly, and V. V. Subramaniam

Formation of an atmospheric pressure dusty air plasma is explored experimentally in this paper. The plasma is created by seeding an air flow with graphite particles and irradiating the particulates with a focused CO_2 laser beam. The graphite particles are thus heated to thermionically emitting temperatures, and average particle temperatures and average particle number densities are measured. The presence of charges is inferred both from these measured quantities using a simple theoretical transient model, and experimentally by applying a DC bias across the irradiated region. It is found that an electron density of $\sim 6.7 \times 10^5$ cm^{-3} (6.7×10^{11} m^{-3}) can be produced at steady state in the presence of O_2. This value can be increased to 3.6×10^7 cm^{-3} (3.6×10^{13} m^{-3}) in the ideal case where electron attachment to O_2 is suppressed and where a lower work function particulate is used.

I. Introduction

Dusty plasmas occur in nature as well as in many man-made devices and processes. In some cases, particulates are formed within the plasma itself while in others, the particulates may be introduced deliberately. For instance, in silicon etching plasmas, particulates are formed and suspended at sheath boundaries in rf discharges[1,2], and in other laboratory plasmas[3-5]. Dusty plasmas also occur naturally in space[6-9]. Further, the presence of particulates in a plasma can lead to formation of ordered structures, or Coulomb crystals, which can exhibit phenomena similar to phase transition depending on the Coulomb parameter[10, 11]. In all these dusty plasmas, the particulates or "dust" are generally negatively charged. More recently, dusty plasmas in which active electron emission occurs from the particulates themselves have been explored theoretically[12,13]. In such dusty plasmas, electrons may be emitted from the particulates by photoemission or thermionic emission, resulting in positively charged particulates. Dusty plasmas with thermionically emitting particulates have been studied previously, but in plasmas in thermal equilibrium[14, 15]. An advantage of plasmas with electron-emitting particulates is that electron production may depend on photoemission or thermionic emission, rather than on electron-impact ionization processes. Consequently, diffuse volumetric weakly ionized plasmas can be produced at higher pressures such as atmospheric pressure, where conventional methods involving application of electric fields result in constricted, filamentary discharges. Production of diffuse plasmas in atmospheric pressure air with sufficient electron concentration can have application as electromagnetic reflectors and absorbers[16]. In this work, a thermionically emitting dusty plasma is formed by heating graphite particles entrained in an air flow. The graphite particles are heated by irradiation from a focused CO_2

laser beam. The resulting plasma has a low average gas temperature (room temperature) while the grain temperatures are high (~ 2400 K) causing the graphite particles to emit electrons thermionically. This dusty plasma therefore differs from other thermal equilibrium dusty plasmas that have been studied previously[14, 15]. Experimental measurements of average particulate temperature and average particulate number density are reported, from which the steady state electron concentration can be inferred.

This paper is organized as follows. The experimental apparatus and procedure are described in section II, followed by the experimental results and discussion in section III. These results are summarized in section IV.

II. Experimental Apparatus and Procedure

A schematic of the experimental apparatus is shown in Fig. 1. It mainly comprises a fluidized bed (not shown in Fig. 1) where graphite particles are entrained in a flow of air supplied from a compressed air source, a main chamber with optical access and purges for the windows, a CO_2 laser source, and associated diagnostic equipment. The CO_2 laser (Apollo, model 3020) using a nominal gas mixture of 6%CO_2, 76%He, and 18% N_2, produces a maximum output of 25W cw. This beam is focused into the main chamber using a plano-convex ZnSe focusing lens (1 inch diameter, with focal length, f = 7.5 ins.). The focal point of the beam is at the center of the main chamber. Orthogonal to the axis of the laser beam, ports allow specific diagnostic apparatus to be placed. For example, copper electrodes can be placed on either side of the focal region as shown in the schematic in Fig. 1, enabling a DC bias to be applied to detect the presence of charged species. Alternatively, windows can be placed to allow the determination of average particulate temperature from radiative emission. Experiments are conducted using graphite powder (average particle diameter of 25 μm, Alpha Aesar) since it is readily obtainable and economical, although other materials such as oxides with lower work function are available. The sustained delivery of these particles to the experimental chamber requires the use of a fluidized bed to continuously entrain them in the gas flow. Utilizing a tangential flow emanating from the bottom of the fluidizer, the particulate is entrained within the gas flow (compressed air) and delivered to the experiment chamber. Because of the nature of the fluidizer, its size naturally limits the run time for an experiment. However, some control can be exercised over the flow rate and number density of the particulate delivered, so that operating conditions are repeatable. Thus for a given flow rate, a specific number density of particles is attained within the chamber.

A typical run begins by loading 4g of graphite particulate into the fluidizer. The flow rate through the fluidizer is increased to 4000 sccm, causing the particles to fluidize. Once fluidized, the particulate is delivered to the experiment chamber where it is irradiated by the focused CO_2 laser beam. In the

presence of this laser irradiation, the particulate begins to glow yellow to white along the axis of the laser beam, as can be seen in the photograph in Fig. 2. Although the laser beam is focused at the center of the chamber, a substantial portion of the beam is rendered visible along its axis by the glowing particles. It is important to note that the particulates are not stationary within the experiment chamber and are convected by the gas flow. Power measurements taken with and without the particulates indicate that approximately 10 W cw is absorbed. The typical duration of an experiment is less than 10 minutes with these conditions maintained, for the size of the fluidizer and amount of particulates used[17].

The average particle number density is separately determined for set run conditions using the attenuation of a 1mW HeNe laser source (Uniphase, 1508-0). Transmission of the laser through the chamber with and without the presence of the particulate flow is measured using a photodiode (Thor Labs, DET210) connected to a digital oscilloscope (Tektronix, TDS 360) at a 100Hz sampling frequency. However, due to the limitations of the oscilloscope, 45 seconds is required to save acquired data. Consequently, instantaneous data is collected over a 10 second time interval, followed by a period of 45 seconds during which the data is stored and no new data is acquired. When particulates are present, the laser beam is attenuated. Assuming the particles to be spherical, and the beam attenuation to be due to scattering by the particulates away from the detector, the average particle number density can be estimated from the signal recorded by the photodiode. This signal depends on the ratio of intensities recorded with ($V(t)$) and without the particles (V_o), the radius of the particles (r_p), and the length of the particle-laden flow that is traversed by the beam (l_L). Then the number density of the particulates, $n_p(t)$ is given by:

$$n_p(t) = \frac{1}{\pi r_p^2 l_L}\left[1 - \frac{V(t)}{V_o}\right] \qquad (1)$$

A normalized intensity ($V(t)/V_o$) is recorded by the photodiode during a typical 10 second trace of a run. Many such normalized traces are then obtained over the course of a run, each separated by the 45 seconds required to store the data. Each 10 second trace is averaged to yield a single representative value of the normalized intensity over that 55 second interval. This procedure is effective in yielding reproducible results for a given set of run conditions.

Visible emission from the particulate allows the average temperature of the particles to be determined using radiative emission. The particulate emission is collected onto the slits of a spectrometer (Instruments SA, Triax550 monochromator) using two glass (BK-7) plano-convex focusing lenses and two first surface mirrors (to match the f-number of the spectrometer). The intensity of the emitted radiation is recorded using a detector (Spectrum One – 2000 x 800 pixel, CCD3000D). The system is calibrated using a blackbody source (Infrared Industries, Inc. Model 563 blackbody cavity and model 201 temperature controller)[17]. The radiating particles are assumed to be diffuse gray emitters over the

130

wavelength range 500 nm – 700 nm (consistent with the radiative properties of carbon reported in ref.[18]). This enables an average particle temperature to be determined from the measured intensities. The intensities of particle emission are normalized by the intensity at a specified wavelength (690 nm) in order to eliminate the emissivity, corrected for the measurement system response, and compared with blackbody emission to yield the best fit temperature. Note that this method yields a single value for the average particulate temperature based on emission from all the radiating particles.

Verification of the presence of charges within the dusty plasma is achieved through the application of an external electric field. Copper electrodes are placed across the plasma with the center of the electrodes corresponding to the focal point of the laser beam. A DC voltage of 3 KV is applied to the electrodes, which are separated by a distance of 0.3 ins. (7.6 mm.). The current is measured by a pico-ammeter (Keithley, 2001 Multimeter) in the external circuit.

III.   Experimental Results & Discussion

There are several concurrent processes in the thermionically emitting dusty air plasma. These include absorption of laser radiation by the particulates, convective heat transfer between the particulates and the air flow, radiative heat transfer from the particulates, electron production by thermionic emission, electron attachment to oxygen, electron recombination on positively charged grains, and reaction between the carbon particulates and oxygen. In this section, characteristic times for several of these processes are considered in order to determine those that are dominant in the thermionically emitting dusty plasma. Estimates of these characteristic times depend upon certain experimentally measured quantities such as average particulate number density, n_P, and average particle temperature, T_P. These are measured using the techniques described in Section II, and are discussed first.

The particulate concentration is determined in a separate experiment by attenuation of a He-Ne laser beam, in the absence of CO_2 laser irradiation, as described in Section II. Using the normalized values of laser intensity transmitted through the dusty gas, transient normalized laser intensities averaged over 10 second intervals, are obtained over the duration of the experiment. From both these data, the particulate number density can be evaluated using equation (1). Figure 3 shows the time-varying particulate number density over a typical 10 second interval. As can be seen in Fig. 3, the particle-laden flow is highly unsteady and average particulate concentrations vary from 10^3 cm^{-3} to 10^4 cm^{-3}. Figure 4 shows the 10-second averaged particulate number densities over the course of an entire run, yielding particulate number densities that are unsteady and reaching values up to nearly $n_p \approx 10^4$ cm^{-3}.

The particulate temperature is measured using the radiation emitted from the heated particulates. As described in Section II, the measured intensities normalized by the intensity at a reference wavelength (690 nm), are used to infer the average particulate surface temperature. The average particulate

temperature measured over a 5 minute period during the steady state portion of a typical run is shown in Fig. 5. The average particulate temperature is found to be approximately $T_p \approx 2400K \pm 100K$, and is relatively constant during this time. It is likely that the particulate temperatures in the focal region of the laser beam are higher than this value, while those temperatures away from this region will be lower.

Using these measured values of n_p and T_p, characteristic times for the various processes in the thermionically emitting dusty plasma can be estimated. From Fig. 2, the size of the glowing region can be determined to be 0.5 mm. Assuming the velocity of the particulate is the same as the speed of the gas through the chamber, its velocity is estimated to be 6 cm/s from the measured gas flow rate of 4000 sccm. This yields a lower limit on the time required for the particles to traverse the glowing region. The residence time of a grain within the (glowing region) path of the laser beam can therefore be estimated to be $\tau_{res} \approx 8$ ms. Assuming that in the presence of fluidized graphite all the measured attenuation in laser power of 10 W is due to absorption by the particulate, the characteristic time required to heat the graphite particles ($C_V = 2043 J/kg/K$) from their initial room temperature to a final temperature of $T_p \approx 2400K$ can be determined to be $\tau_{heat} \approx 200$ μs. It can be seen that this characteristic time for heating is an order of magnitude less than the minimum time the particles are resident in the path of the laser beam. From the measured flow rate, a Reynolds number (based on particle diameter and a flow speed of 6 cm/s) of about 0.1 can be deduced. At such low Reynolds numbers, the convective heat transfer coefficient can be estimated to be $h = k \left(Nu_{r_p} \right) / r_p \approx 4200$ W/m^2/k. This yields a characteristic time for convection of τ_{conv} ≈ 4.5 ms. Similarly, assuming optically thin radiation, the characteristic time for heat loss by radiation can be estimated to be $\tau_{rad} \approx 21$ ms. It can be seen that for the particle sizes relevant to this work, convective loss dominates radiative loss. Moreover, the characteristic time required for convective cooling is on the order of the time the particle spends in the path of the laser beam. This suggests that the size of the glowing region is of the same order as the width of the focused laser beam, or larger.

When the hot graphite particles are exposed to the air, they can react with the gaseous oxygen to form CO_2 and CO. Assuming the graphitic carbon is reacted to form CO_2 ($C(s)+O_2 \rightarrow CO_2$), the loss of mass due to chemical reaction can be estimated. Using the calculated mass-based rate coefficient of $k = 1.12 \times 10^{-2}$ g/cm^{2}s for a particle temperature of 2400 K and atmospheric pressure from ref.[19], a residence time of 8 ms, and an initial particle size of 25 μm diameter, the net loss in mass of the particle can be estimated to be approximately 10%. Thus, the heated particle is not entirely consumed in the presence of oxygen.

At the measured average temperatures of 2400 K, it is expected that graphite emits electrons thermionically. However, direct measurement of electron concentration is difficult in such a weakly ionized plasma. Efforts were made to measure the average electron concentration across the laser-

irradiated region using attenuation of 10 GHz microwave radiation, but the attenuation was indistinguishable from background noise. The attenuation measurement was designed to nominally detect an electron concentration of 10^{13} cm^{-3}, and was sensitive to electron concentrations as low as 10^9 cm^{-3} [20]. The fact that no measurable attenuation could be observed with this diagnostic suggests that the average electron concentration in the thermionically emitting dusty plasma was less than 10^9 cm^{-3}. The presence of charges within the thermionically emitting dusty plasma was detected by applying a DC bias (3 kV) on electrodes (separated by a distance of 0.3 ins. or 7.6 mm) placed across the laser-irradiated region, as discussed previously in Section II. The electrodes were connected to an external circuit so that the presence of current flow could be measured. In the presence of both the applied DC bias and laser irradiation of the particulate, unsteady currents ranging from 0.1 μA to 0.6 μA were observed. The unsteady nature of the observed current flow is understandable given that the particulate number density was unsteady as well (see Fig. 4). As a control, current flow in the external circuit was also measured in the absence of laser irradiation but with the particulate flow present. No current flow was observed in this latter case.

Additional evidence of the presence of charges was found when the electrodes were examined upon completion of the experiment. With no laser irradiation of the particulate and in the presence of an applied 3 kV bias, both electrodes were completely covered with graphite particles. When the particulates were irradiated by the laser beam in the presence of the externally applied electric field, the particulates deposited onto the anode surface displayed a specific pattern (see Fig. 6a). The particulate deposits were observed at the edges of the positive electrode (anode) with a vertical stripe in the center devoid of any particulates (Fig. 6a). This can be explained by the fact that the positively charged graphite particles heated near the focal point of the laser (where the highest particulate temperatures are expected) are repelled by the anode thereby producing a particle-free region on the electrode surface. In contrast, the ground or negative electrode (cathode) was completely covered with particles (see Fig. 6b). This is exactly what would be expected when the laser heats those particles at the focal point in the center of the inter-electrode gap, up to temperatures where appreciable thermionic emission takes place. These particles should assume a positive charge after emitting electrons. Consequently, in the presence of an electric field, they would drift in the direction of the field toward the negative electrode. This explains why the cathode was completely covered with particulates and the anode coverage displayed a specific pattern. The amount of deposits was influenced by the ambient humidity, which affected agglomeration of the particles loaded into the fluidizer section. Nevertheless, the pattern of deposits on the electrodes was repeatable, and served to verify that electrical charges were indeed present while particulates were heated by the laser.

Direct measurement of the electron concentration in the thermionically emitting dusty plasma was not possible. However, an estimate of the electron concentration in the region of the focal point can be obtained using the experimentally measured n_p and T_p, as well as the operating conditions in the experiment. The electron production can be estimated from measured values of n_p and T_p, using the Richardson-Dushman equation, while electron loss rates depend on specific loss mechanisms. Electron loss mechanisms in the neighborhood of the focal point of the laser beam include two channels of electron attachment to oxygen species, and recombination with the positively charged grains:

$$e^- + O_2 + N_2 \xrightarrow{\ k_1\ } O_2^- + N_2 \qquad (2)$$

$$e^- + O_2 + O_2 \xrightarrow{\ k_2\ } O_2^- + O_2 \qquad (3)$$

$$e^- + O_2 \xrightarrow{\ k_3\ } O^- + O \qquad (4)$$

$$(dust)^+ + e^- \xrightarrow{\ k_4\ } (dust) \qquad (5)$$
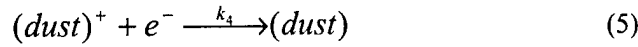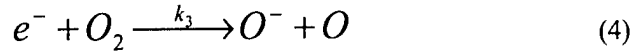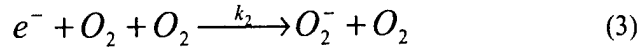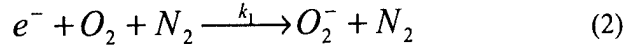
Assuming that $n_{O^-} \ll \left\{ n_e, n_{O_2^-} \right\}$, the net rate of production of electrons is then given by the difference between production and loss mechanisms:

$$\frac{dn_e}{dt} = \left(\frac{n_p}{e} \right) 4\pi r_p^2 A T_p^2 e^{(-(e\phi_w + e\phi_s)/k_B T_p)} - k_1 n_{O_2} n_{N_2} n_e - k_2 n_{O_2}^2 n_e - k_3 n_{O_2} n_e - k_4 n_p n_e \qquad (6)$$

where r_p is the radius of the particulate and is assumed to be constant (12.5 μm), A is the theoretical thermionic emission coefficient, k_B is Boltzmann's constant, e is the charge on an electron, k_1 is the rate coefficient for electron attachment via process (2), k_2 is the rate coefficient for electron attachment via process (3), k_3 is the rate coefficient for recombination via process (4), k_4 is the rate coefficient for recombination via process (5), ϕ_w is the work function of graphite, ϕ_s is the grain potential [13], and n_α is the concentration of species α. The work function of graphite depends on crystallographic orientation, and varies widely[21], but here we take it to be constant at 4.5 eV. The rate coefficients

$$k_1 = 1.07 \times 10^{-31} \times \left(\frac{300}{T_e} \right)^2 \times \exp\left(\frac{1430}{T} - \frac{1500}{T_e} \right) cm^6 s^{-1}$$

and

$$k_2 = 1.4 \times 10^{-29} \times \frac{300}{T_e} \times \exp\left(\frac{100}{T} - \frac{700}{T_e} \right) cm^6 s^{-1}$$

are obtained from ref.[22], and $k_3 = 8.8 \times 10^{-11} \times \exp\left(\dfrac{-51060}{T_e}\right) cm^3 s^{-1}$ is given in ref.[23]. In these

expressions for the rate coefficients, T is the gas temperature in K and T_e is the electron temperature in K. Here we take $T_e = T$. As an approximation for k_4, we assume the simplified model of a probe in a

collision-dominated sheath[24] holds, and is given by $k_4 = \dfrac{4}{3}\overline{C}_e \pi r_p \lambda_e$, where $\overline{C}_e$ is the mean thermal

speed of an electron, and λ_e is the mean free path of an electron. An independent equation for the rate of

change of the concentration of the O_2^- ion can also be written:

$$\frac{dn_{O_2^-}}{dt} = k_1 n_{O_2} n_{N_2} n_e + k_2 n_{O_2}^2 n_e + k_3 n_{O_2} n_e - k_5 n_p n_{O_2^-} \qquad (7)$$

where k_5 is the rate coefficient for recombination of O_2^- ions on positively charged grains. As before, we assume the simplified model of a probe in a collision-dominated sheath[24] holds for recombination

of O_2^- ions on the grains. Thus, $k_5 = \dfrac{4}{3}\overline{C}_{O_2^-} \pi r_p \lambda_{O_2^-}$, where $\overline{C}_{O_2^-}$ is the mean thermal speed of O_2^-

ions, and $\lambda_{O_2^-}$ is their mean free path. Equations (6) and (7) represent two equations in the three

unknowns n_e, $n_{O_2^-}$, and the grain potential ϕ_s. The third equation is obtained from charge neutrality:

$$n_{O_2^-} + n_e = \frac{4\pi\varepsilon_0}{e} n_p r_p \phi_s \qquad (8)$$

Equations (6) – (8) now represent a system of coupled ordinary differential equations that can be solved

for the temporal variation of n_e, $n_{O_2^-}$, and ϕ_s. We note that in the absence of oxygen (i.e.,

$n_{O_2} = n_{O_2^-} = 0$, $k_5 = 0$, and with k_4 replaced by the appropriate rate coefficient corresponding to the

electron collection current determined from the orbit-limited current to an attracting probe at low pressure (i.e. collisionless sheath limit), the present model reduces to that of ref.[13] identically, at steady state.

For the conditions determined from the present experiment ($T_p \approx 2400$ K, $n_p \sim (10^3$ cm^{-3}), $r_p = 12.5$ μm) and with $\phi_w = 4.5$ eV, equations (6) through (8) are solved numerically subject to the initial conditions

$n_e = n_{O_2^-} = 0$. The particle temperature of 2400 K is prescribed at t = 0 and maintained thereafter. The

calculated concentrations are shown in Fig. 7 for the range of times 0.1 ns to 10 μs. As can be seen, the electron concentration rises to a maximum of 5.2 x 10^6 cm^{-3} at about ten nanoseconds, after which it drops to a steady state value of 6.7 x 10^5 cm^{-3} due to attachment to O_2. It can be seen that at steady state,

the dominant negatively charged particle is the O_2^- ion with a concentration of 1.1×10^7 cm^{-3}. The grain potential is shown in Fig. 8 for this case, and asymptotes to a value of 1.4 V. Such low values of electron concentrations are consistent with experimental observations of fluctuating currents in the range of 0.1 μA – 0.6 μA when a 3 kV DC bias is applied across the irradiated region (see discussion earlier in this section).

Equations (6) through (8), when combined, reveal that the electron concentration n_e increases directly with the concentration of particulates n_p. The results shown in Figs. 7 and 8 are for a fixed value of $n_p = 10^3$ cm^{-3}. However, the dust density can be seen from Fig. 4 to vary up to an order of magnitude in the experiments, so that the electron concentration would also be expected to vary. For $n_p = 10^4$ cm^{-3}, equations (6) through (8) yield steady state values of $n_e = 6.7 \times 10^6$ cm^{-3} and $n_{O_2^-} = 1.1 \times 10^8$ cm^{-3}, while for $n_p = 10^2$ cm^{-3}, steady state values of $n_e = 6.7 \times 10^4$ cm^{-3} and $n_{O_2^-} = 1.1 \times 10^6$ cm^{-3} are found.

It is interesting to explore the ultimate electron concentration that can be attained in the thermionically emitting dusty plasma at atmospheric pressure, by lowering the work function to that of oxide particles (such as CeO_2 with $\phi_w = 2.5$ eV, and melting temperature of 2873 K), raising the particle temperature to 2800 K, and assuming the attachment process to O_2 to be inhibited (i.e. k_1, k_2, k_3, and k_5 equal 0). The latter can be achieved in principle under non-equilibrium conditions where O_2 is vibrationally excited in order to favor electron detachment (i.e. reverse of the processes (2) and (3))[25]. Figure 9 shows the resulting electron concentration as a function of time over the range of 0.1 ns to 10 μs after the particles have reached their steady state temperature of 2800 K. As expected, electron concentrations are much higher (maximum and steady state value of 3.6×10^7 cm^{-3}) than in the case where attachment processes to O_2 are active. The grain potential for this case is shown in Fig. 10, and can be seen to asymptote to $\phi_s = 4.2$ V. The higher value for the grain potential obtained in this case is consistent with higher electron concentrations in the absence of O_2 as can be seen from equation (8).

IV. Summary & Conclusions

A volumetric thermionically emitting dusty air plasma has been created at atmospheric pressure using CO_2 laser irradiation of graphite particles. Experimental measurements of the average particle temperature and the average particle number density are found to be $T_p \approx 2400$K and $n_p \approx O(10^3$ cm^{-3} or 10^9 m^{-3}) respectively. An analysis of the relevant time scales shows that the characteristic time for heating of the particles is an order of magnitude less than the minimum characteristic residence time in the irradiated region. As the graphite particles are heated in air, it is estimated that their average initial mass is reduced by approximately 10% because of chemical reaction with O_2. The presence of charges has

been verified both through observation of a current flow through an external circuit in the presence of an applied DC bias, and deduced from the specific pattern of particle deposits found on the electrodes. Using experimentally measured values of the average particle temperature and average particle number densities, a simple model is used to estimate the steady state concentrations of electrons and O_2^- ions in the thermionically emitting dusty air plasma. The steady values of $n_e \sim 6.7 \times 10^5$ cm^{-3} (6.7×10^{11} m^{-3}) and $n_{O_2^-} \sim 1.1 \times 10^7$ cm^{-3} (1.1×10^{13} m^{-3}) are consistent with the fact that 10 GHz microwave radiation could be transmitted through the thermionically emitting dusty plasma. For attenuation of microwave radiation of this frequency to be observable using our apparatus, electron concentrations in excess of 10^9 cm^{-3} (10^{15} m^{-3}) would have been necessary. Scaling to larger volumes and an order of magnitude higher electron concentration can be accomplished by increasing the particle number density and particle size, using a low work-function material, or by increasing the laser power irradiating the particulate (i.e. increasing the particle temperature).

References:

(1)   G. S. Selwyn, J. Singh, and R. S. Bennett, "*In Situ* laser diagnostic studies of plasma-generated particulate contamination", **J. Vac. Sci. Technol. A** 7 (4), pp. 2758-2765, July/August 1989.

(2)   G. S. Selwyn, K. L. Haller, and E. F. Patterson, "Trapping and behavior or particulates in a radio frequency magnetron plasma etching tool", **J. Vac. Sci. Technol. A** 11 (4), pp. 1132-1135, July/August 1993.

(3)   G. Praburam, and J. Goree, "Evolution of a Particulate Cloud in an RF Plasma", **IEEE Trans. Plasma Sci.**, Vol. 24, No. 1, pp. 97-98, February 1996.

(4)   R. C. Hazelton, and E. J. Yadlowsky, "Measurement of Dust Grain Charging in a Laboratory Plasma", **IEEE Trans. Plasma Sci.**, Vol. 22, No. 2, pp. 91-96, April 1994.

(5)   R. Walch, M. Horanyi, and S. Robertson, "Measurements of the Charging of Individual Dust Grains in a Plasma", **IEEE Trans. Plasma Sci.**, Vol. 22, No. 2, pp. 97-102, April 1994.

(6)   C. K. Goertz, "Dusty plasmas in the Solar System", **Rev. Geophys.**, Vol. 27, No. 2, pp. 271-292, 1989.

(7)   L. H. Shan, and C. K. Goertz, "On the Radial Structure of Saturn's B Ring", **Astrophys. J.** Vol. 367, p. 350, 1991.

(8)   D. A. Mendis, H. L. F. Houpis, and J. R. Hill, "The Gravito-Electrodynamics of Charged Dust in Planetary Magnetospheres", **J. Geophys. Res.**, Vol. 87, p.3449, 1982.

(9)   G. Praburam, and J. Goree, "Cosmic Dust Synthesis by Accretion and Coagulation", **Astrophys. J.**, Vol. 441, pp. 830-838, 1995.

(10)   H. Ikezi, "Coulomb solid of small particles in plasmas", **Phys. Fluids**, Vol. 29, No. 6, pp. 1764-1766, 1986.

(11)   J. H. Chu, and I. Lin, "Direct Observation of Coulomb Crystals and Liquids in Strongly Coupled RF Dusty Plasmas", **Phys. Rev. Lett.**, Vol. 72, No. 25, pp. 4009-4012, June 1994.

(12)   M. Rosenberg, D. A. Mendis, and D. P. Sheehan, "UV-Induced Coulomb Crystallization of Dust Grains in High Pressure Gas", **IEEE Trans. Plasma Sci.**, Vol. 24, No. 6, pp. 1422-1430, December 1996.

(13)   M. Rosenberg, D. A. Mendis, and D. P. Sheehan, "Positively Charged Dust Crystals Induced by Radiative Heating", **IEEE Trans. Plasma Sci.**, Vol. 27, No. 1, pp. 239-242, February 1999.

(14)   V. E. Fortov, A. P. Nefedov, O.F. Petrov, A. A. Samarian, and A. V. Chernyschev, "Emission Properties and Structural Ordering of Strongly Coupled Dust Particles in a Thermal Plasma", **Phys. Lett. A, 219**, pp. 89-94, August 1996.

(15)   V. E. Fortov, A. P. Nefedov, O.F. Petrov, A. A. Samarian, and A. V. Chernyschev, "Particle Ordered Structures in a Strongly Coupled Classical Thermal Plasma", **Phys. Rev. E**, Vol. 54, No. 3, pp. R2236-R2239, September 1996.

(16)   R. Vidmar, "On the Use of Atmospheric Pressure Plasmas as Electromagnetic Reflectors and Absorbers", **IEEE Trans. Plasma Sci.**, Vol. 18, No. 4, pp. 733-741, August 1990.

(17)   J. L. Lilly, *The Production of a Volumetric Dusty Plasma at Atmospheric Conditions*, Undergraduate Honors Thesis, Department of Mechanical Engineering, The Ohio State University, August 1999.

(18)   D.R. Lide, *Handbook of Chemistry and Physics*, 72nd Edition, CRC Press, Boston, 1991.

(19)   R.H. Essenhigh, "Rate equations for the carbon-oxygen reaction: An evaluation of the Langmuir absorption Isotherm at atmospheric pressure", **Energy and Fuels**, Vol. 5, No. 1, pp. 41-46, 1991.

(20)   P. Palm, E. Ploenjes, M. Buoni, V. V. Subramaniam, and I. V. Adamovich, "Electron Density and Recombination Rate Measurements in CO-Seeded Optically Pumped Plasmas", submitted to **J. Appl. Phys.**, (in press).

(21)   V. S. Fomenko, *Handbook of Thermionic Properties: Electronic Work Functions and Richardson Constants of Elements and Compounds*, G. V. Samsonov (Ed.), Plenum Press Data Division, New York, 1966.

(22)   I. A. Kossyi, A. Y. Kostinsky, A. A. Matveyev, and V. P. Silakov, "Kinetic scheme of the non-equilibrium discharge in nitrogen-oxygen mixtures", **Plasma Sources Sci. Technol.**, Vol. 1, pp. 207 - 220, 1992.

(23)   M. Lieberman, and A. Lichtenberg, *Principles of Plasma Discharges in Materials Processing*, John Wiley & Sons, New York, 1994.

(24)   F.F. Chen, *Plasma Diagnostic Techniques*, Chap. 4 in R.H. Huddlestone and S.L. Leonard (Ed.), Academic Press, New York, 1965.

(25)   W. C. Lee, I. V. Adamovich, and W. R. Lempert, "Optical Pumping Studies of Vibrational Energy Transfer in High-Pressure Diatomic Gases", **J. Chem. Phys.**, Vol. 114, No. 3, pp. 1178-1186, 15 January 2001.
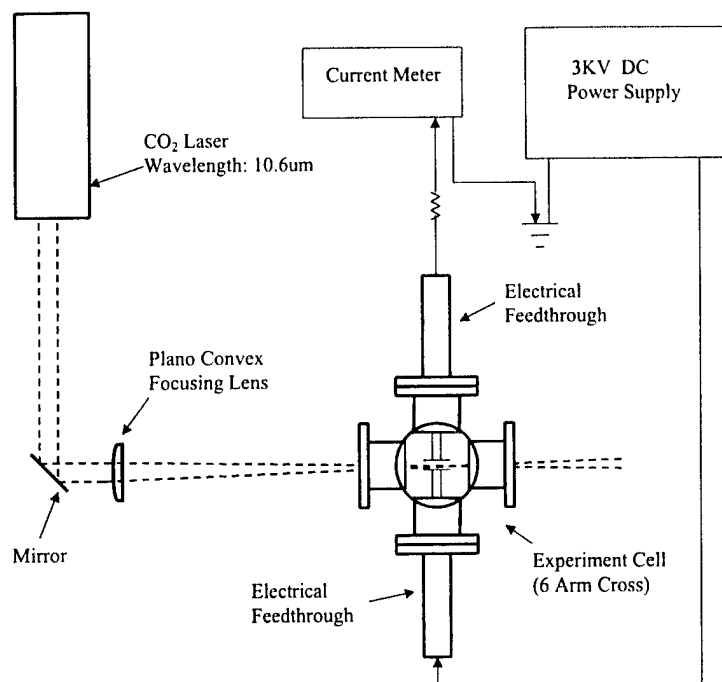
Figure 1: Schematic of the experimental apparatus showing the electrodes across the laser-irradiated region.
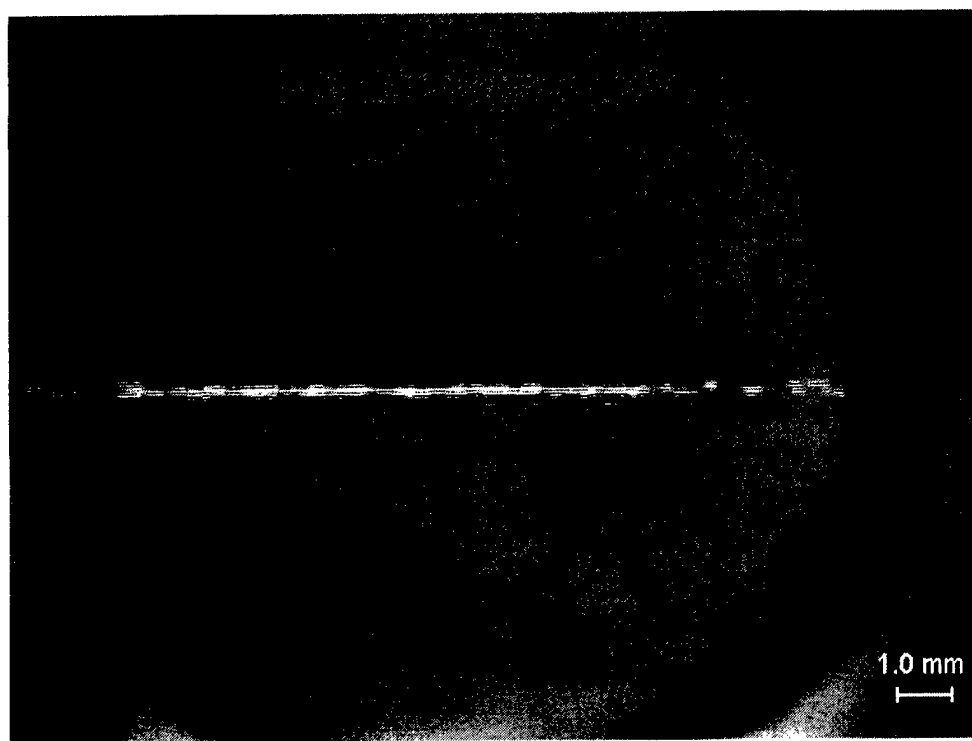
Figure 2: Graphite particulates in an air flow glowing while irradiated by a focused CO_2 laser beam.
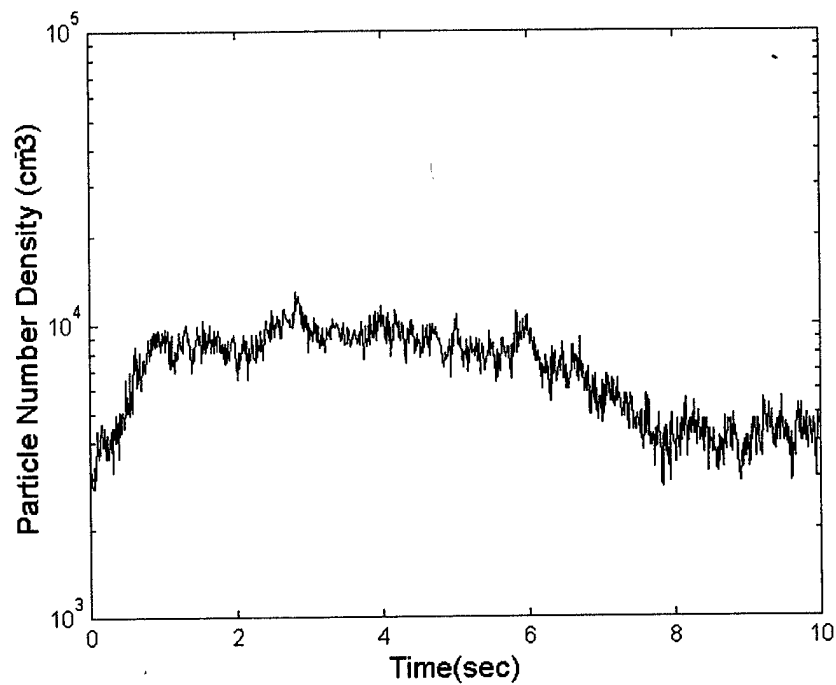
Figure 3: Time varying particle number density values over a 10 second time interval of a typical run.
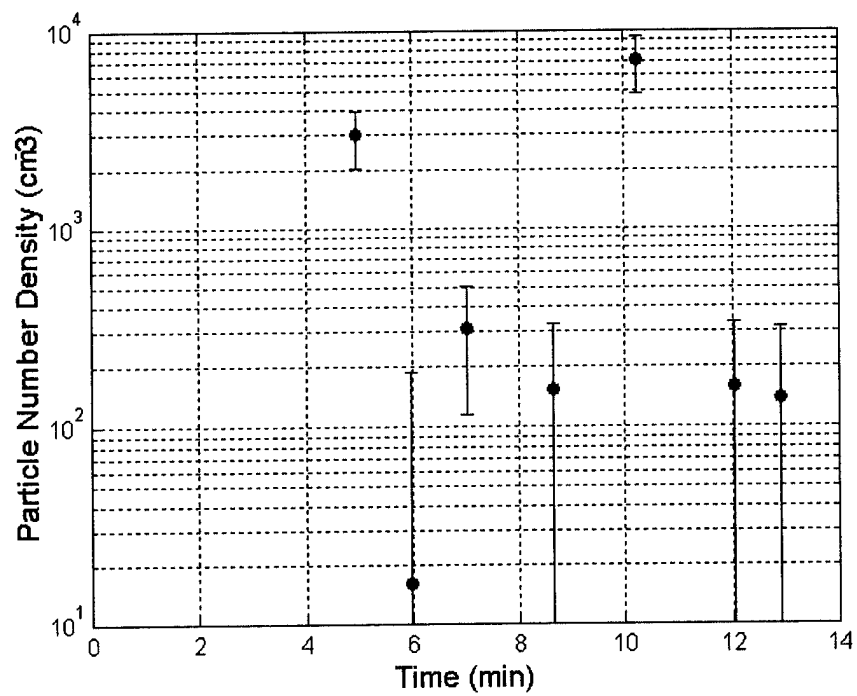
Figure 4: Particle number density values over a typical run obtained by averaging over multiple 10 second intervals (see Fig. 3).
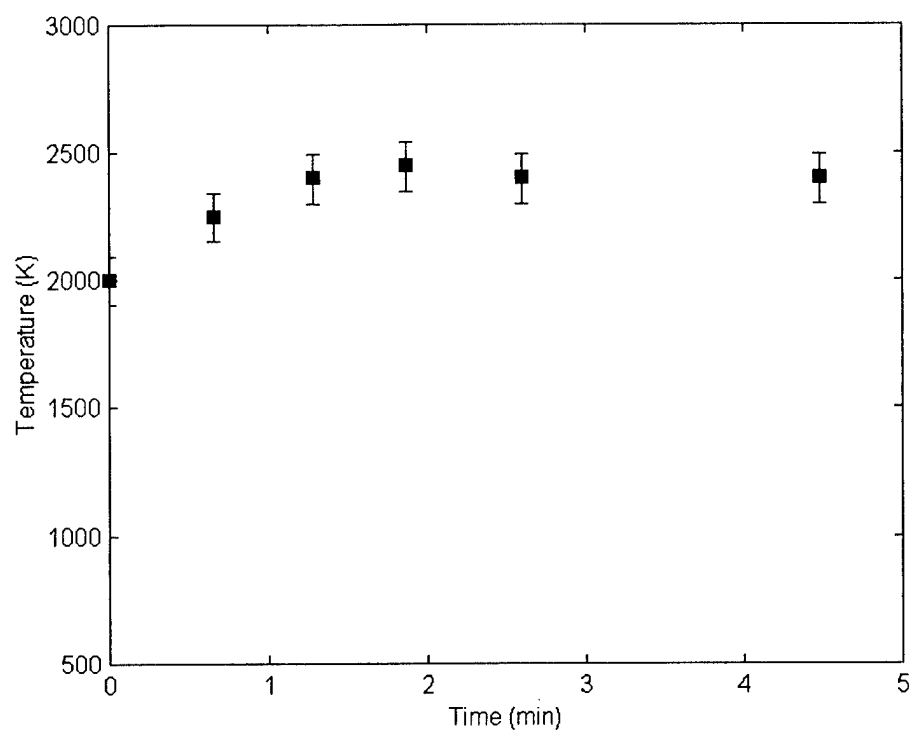
Figure 5: Average particle temperature over a 5 minute period of a typical run. Note that t = 0 on this figure is an arbitrary point as the flow conditions become established on average.

Flow Direction

Direction of laser beam
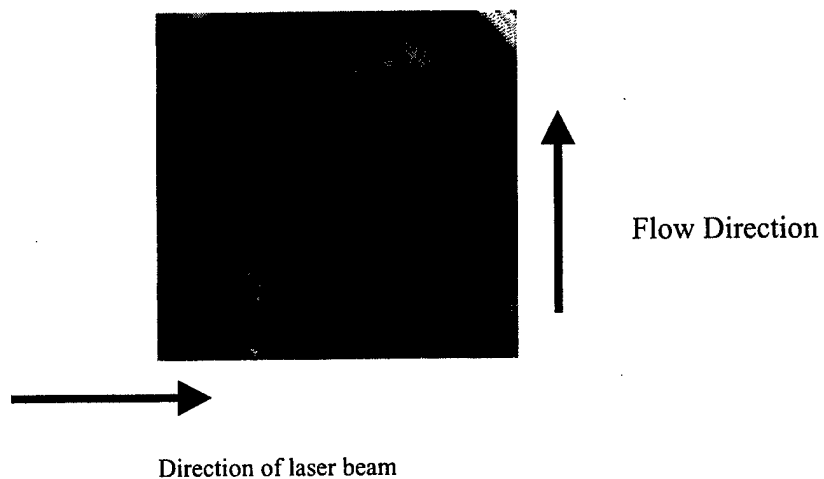
Figure 6a: Anode (positive) surface displaying a specific pattern of graphite particle deposits. The diameter of the electrode is 1 in. (2.54 cm), the inter-electrode gap spacing was 0.3 ins. and the applied bias was 3 kV.

Figure 6b: Cathode (ground) surface covered by graphitic particles. The diameter of the electrode is 1 in. (2.54 cm), the inter-electrode gap spacing was 0.3 ins. and the applied bias was 3 kV.
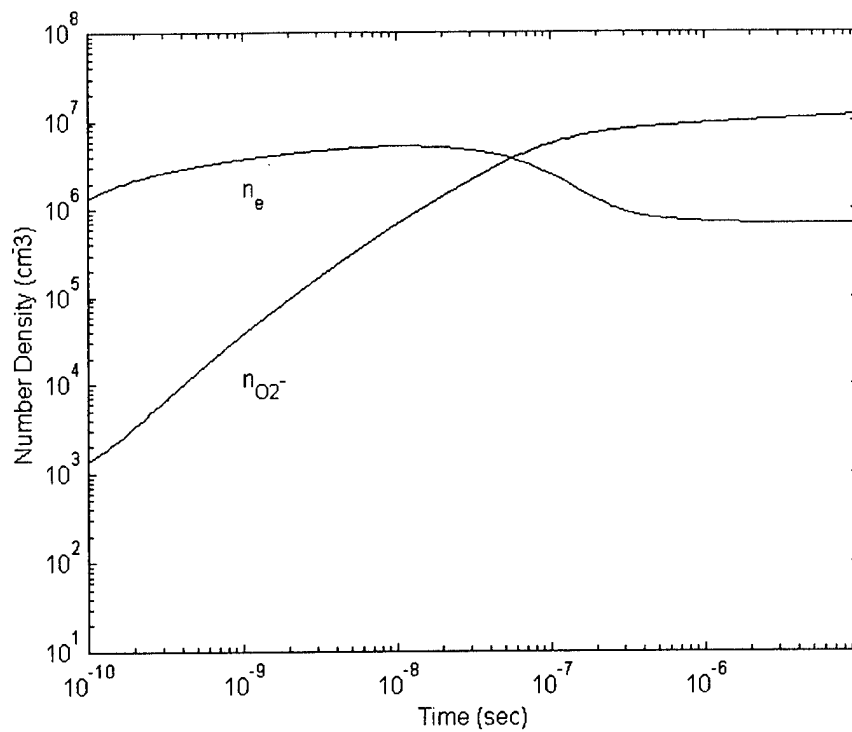
Figure 7: Electron concentrations in the atmospheric pressure dusty air plasma calculated as a function of time with particle radius (12.5 μm), temperature (2400 K), number density (10^3 cm^{-3} or 10^9 m^{-3}), and work function ($\phi_W = 4.5$ eV) prescribed.
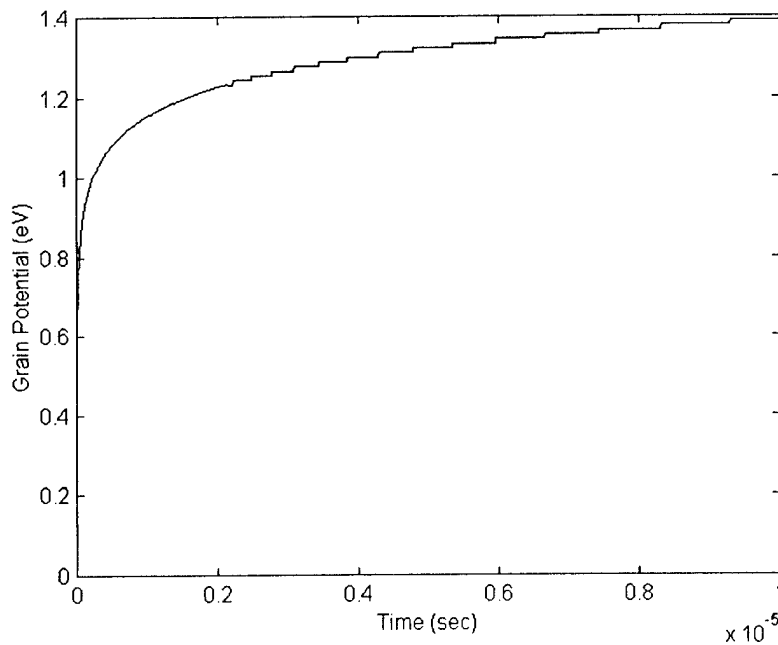
Figure 8: The grain potential calculated from equation (8) versus time is shown here for the same case as Fig. 7.
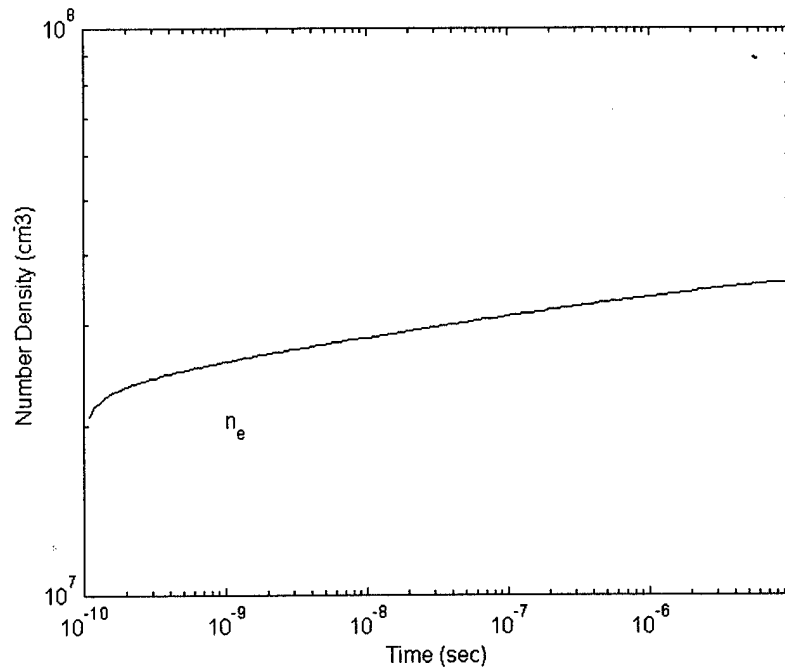
Figure 9: Best case electron concentrations in the atmospheric pressure dusty air plasma calculated as a function of time with electron attachment to O_2 inhibited, with particle radius (12.5 μm), temperature (2800 K), number density (10^3 cm^{-3} or 10^9 m^{-3}), and work function ($\phi_w = 2.5$ eV) prescribed. The work function corresponds to particles of CeO_2[13].
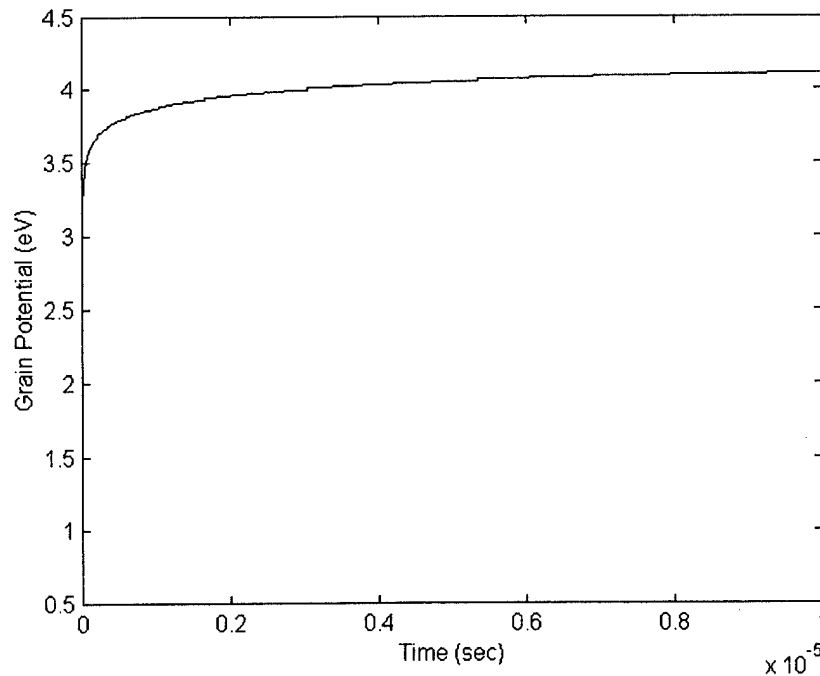
Figure 10: The grain potential calculated from equation (8) versus time is shown here for the same case as Fig. 9.

8. RF ENERGY COUPLING TO HIGH-PRESSURE OPTICALLY PUMPED NON-EQUILIBRIUM PLASMAS

Elke Plönjes, Peter Palm, Wonchul Lee, Walter R. Lempert, and Igor V. Adamovich

The paper presents an experimental demonstration of a high-pressure unconditionally stable nonequilibrium molecular plasma sustained by a combination of a continuous wave CO laser and a sub-breakdown radio frequency (RF) electric field. The plasma is sustained in a CO/N_2 mixture containing trace amounts of NO or O_2 at pressures of P=0.4-1.2 atm. The initial ionization of the gases is produced by an associative ionization mechanism in collisions of two CO molecules excited to high vibrational levels by resonance absorption of the CO laser radiation with subsequent vibration-vibration (V-V) pumping. Further vibrational excitation of both CO and N_2 is produced by free electrons heated by the applied RF field, which in turn produces additional ionization of these species by the associative ionization mechanism. In the present experiments, the reduced electric field, E/N, is sufficiently low to preclude field-induced electron impact ionization. Unconditional stability of the resultant cold molecular plasma is enabled by the negative feedback between gas heating and the associative ionization rate. Trace amounts of nitric oxide or oxygen added to the baseline CO/N_2 gas mixture considerably reduce the electron-ion dissociative recombination rate and thereby significantly increase the initial electron density. This allows triggering the RF power coupling to the vibrational energy modes of the gas mixture. Vibrational level populations of CO and N_2 are monitored by infrared emission spectroscopy and spontaneous Raman spectroscopy.

The experiments demonstrate that the use of a sub-breakdown RF field in addition to the CO laser allows an increase of the plasma volume by about an order of magnitude. Also, CO infrared emission spectra show that with the RF voltage turned on the number of vibrationally excited CO molecules along the line of sight increase by a factor of 3 to 7. Finally, spontaneous Raman spectra of N_2 show that with the RF voltage on the vibrational temperature of nitrogen increases by up to 30%. This novel energy efficient approach allows sustaining large-volume high-pressure molecular plasmas without the use of a high-power CO laser. This opens a possibility of using the present technique for high-yield plasma chemical synthesis and plasma material processing.

1. Introduction

Stability control of large-volume high-pressure nonequilibrium molecular plasmas has always been one of the most challenging problems of gas discharge physics and engineering. At high pressures, the most critical instability, which produces the collapse of a diffuse nonequilibrium self-sustained discharge

into a constricted hot arc, is the ionization heating instability. Basically, it develops due to a positive feedback between gas heating and electron impact ionization rate [1,2]. Therefore small electron density perturbations, producing excess Joule heat, result in a more rapid electron generation and eventually lead to runaway ionization. Among a few well known high-pressure plasma stabilization methods one can mention the use of separately ballasted multiple cathodes [1], aerodynamic stabilization [3], RF frequency high-voltage pulse stabilization [4], and external ionization by a high-energy electron beam [5].

The use of these techniques is tantamount to introduction of an additional damping factor into a conditionally stable system, which raises the instability growth threshold and allows sustaining a diffuse discharge at higher pressures and/or electron densities. However, they do not affect the original source of the ionization heating instability. For this reason, raising the gas pressure or discharge current eventually results in a glow-to-arc collapse. Even the non-self-sustained DC discharge with external ionization produced by an e-beam is in fact self-sustained in the unstable cathode layer, where ionization is primarily produced by secondary electron emission from the cathode [2]. Therefore instability growth in the cathode layer of high power discharges sustained by an e-beam results in the development of high current density cathode spots extending into the positive column and eventually causing its breakdown.

The cathode layer instability of the e-beam sustained discharge can be avoided by using an RF instead of a DC electric field to draw the discharge current between dielectric-covered electrodes. In this case, the secondary emission from the electrodes is precluded, the cathode regions do not form, and the current loop is closed by the displacement current in the near-electrode sheaths. This type of discharge remains non-self-sustained in the entire region between the electrodes and is therefore not susceptible to the cathode layer instability [2]. Indeed, experiments show that an RF beam-driven discharge remains stable at higher E/N and current densities than a DC discharge [6]. However, at high e-beam currents this type of discharge also becomes unstable since the rate of ionization by the beam is inversely proportional to the gas density, so that gas heating by the beam would eventually produce an ionization instability.

The above discussion shows that even the use of external ionization does not always allow unconditionally stable discharge operation at high currents and pressures. On the other hand, it suggests that a discharge system sustained by an external source with a negative feedback between gas heating and ionization rate, and using a sub-breakdown RF field to draw the discharge current might be unconditionally stable [7]. An ionization process that satisfies this condition is the associative ionization in collisions of two highly vibrationally excited molecules [7-12],

$$AB(v) + AB(w) \rightarrow (AB)_2^+ + e^- ,$$
$$E_v + E_w > E_{ion}$$

(1)
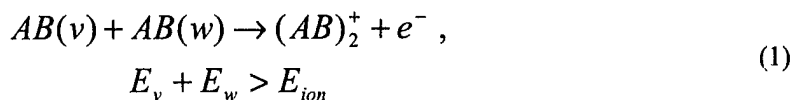
In Eq. (1), AB represents a diatomic molecule, and v and w are vibrational quantum numbers. Basically, ionization is produced in collisions of two highly vibrationally excited molecules when the sum of their vibrational energies exceeds the ionization energy. Ionization by this mechanism has been previously observed in CO-Ar and CO-N_2 gas mixtures optically pumped by resonance absorption of CO laser radiation at pressures of P=0.1-1.0 atm and temperatures of T=300-700 K [7,9-12]. In these optically pumped nonequilibrium plasmas, where high vibrational levels of CO are populated by near-resonance V-V exchange, a gas temperature rise results in rapid relaxation of the upper vibrational level populations because of the exponential rise of the vibration-translation (V-T) relaxation rates with temperature [13]. In other words, ionization by mechanism (1) can be limited and even terminated by the gas heating.

The main objective of the present paper is to experimentally demonstrate the feasibility of the unconditionally stable high-pressure molecular plasma concept. To accomplish this, carbon monoxide containing gas mixtures are vibrationally excited at high pressures using a combination of a CO laser and a sub-breakdown RF field.

2. Experimental

A schematic of the experimental setup is shown in Fig. 1. A continuous wave (c.w.) carbon monoxide laser is used to irradiate a high-pressure gas mixture, which is slowly flowing through a six-arm cross pyrex glass optical absorption cell. The gas mixture used in the present experiments is nitrogen containing 1% of carbon monoxide and trace amounts (~10-100 ppm) of nitric oxide or oxygen, at pressures of P=0.4-1.2 atm. The residence time of the gases in the cell is about 1 sec. The liquid nitrogen cooled CO laser was designed in collaboration with the University of Bonn and fabricated at Ohio State. It produces a substantial fraction of its power output on the v = 1→ 0 fundamental band component in the infrared. The laser can operate at more than 100 W c.w. power. However, in the present experiments, the laser is operated at 10-15 W c.w. broadband power on the lowest ten fundamental bands, with up to ~0.3 W on the v = 1→ 0 component. The output on the lowest bands (1→ 0 and 2→ 1) is necessary to start the absorption process in cold CO (initially at 300 K) in the cell. The quantum efficiency of the CO laser approaches 90%, with an overall efficiency of up to 40%, which makes it the most efficient gas laser available. The Gaussian laser beam of ~6 mm diameter is focused to increase the power loading per CO molecule, providing an excitation region of ~1-2 mm diameter and up to 10 cm long. The absorbed laser power is of the order of 1 W/cm over the absorption length of about 10 cm, which gives an absorbed power density of ~100 W/cm^3. The present use of the CO laser to excite high-pressure gas mixtures is a further development of a technique with a considerable literature [14-22].

The low vibrational states of CO, $v \leq 10$, are populated by direct resonance absorption of CO pump laser radiation in combination with rapid redistribution of population by vibration-vibration (V-V) exchange processes [23],

$$CO(v) + CO(w) \rightarrow CO(v-1) + CO(w+1) \qquad (2)$$
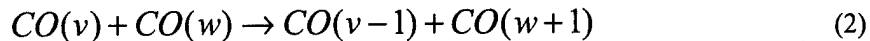
The V-V processes then continue to populate higher vibrational levels of CO as well as vibrational levels of N_2, which are not coupled to the laser radiation [20-22],

$$CO(v) + N_2(w) \rightarrow CO(v-1) + N_2(w+1) \qquad (3)$$
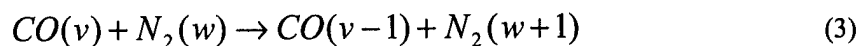
The large heat capacity of the gases, as well as conductive and convective cooling of the gas flow, allow control of the translational/rotational mode temperature in the cell. In steady-state conditions, when the average vibrational mode energy of the CO would correspond to several thousand degrees Kelvin, the temperature never rises above a few hundred degrees [20-22]. Thus a strong disequipartition of energy can be maintained in the cell, characterized by very high energy of the vibrational modes and a low translational/rotational mode temperature. The population of vibrational states of CO in the cell is monitored by infrared emission spectroscopy. For this purpose, a Bruker IFS 66 Fourier transform infrared (FTIR) spectrometer is used to record the line-of-sight integrated spontaneous emission from the CO fundamental, first and second overtone bands through a CaF_2 window in the side of the cell. Vibrational populations of N_2 molecules are measured by spontaneous Raman spectroscopy. For this, a pulsed Nd:YAG Raman probe laser beam is directed into the cell (see Fig. 1). In the present experiments, the Nd:YAG laser is focused coaxial to the CO pump laser, and Raman scattering signal from a volume element approximately 0.100 mm in diameter x 2 mm long is captured at 90^0. Raman spectra are obtained using the second harmonic output of the Nd:YAG laser in combination with an optical multichannel analyzer (OMA) detector. A detailed description of the emission spectroscopy and Raman spectroscopy diagnostics used in the present experiments can be found in [20-22].

At these highly nonequilibrium conditions, the optically pumped gas mixture becomes ionized by the associative ionization mechanism of Eq. (1). Ionization of carbon monoxide by this mechanism has been previously observed in CO-Ar and CO-N_2 gas mixtures optically pumped by resonance absorption of CO laser radiation [7,9-12]. The calculated [9-11] and measured [7,12] steady-state electron density sustained by a 10 W CO laser in these optically pumped plasmas is in the range of $n_e \sim 10^{10}$-10^{11} cm^{-3}.

Two 3 cm diameter brass plate electrodes are placed in the cell as shown in Fig. 1, so that the laser beam creates a roughly cylindrical excited region between the electrodes, 1-2 mm in diameter. The probe electrodes, 13.5 mm apart, are connected to a 13.56 MHz, 600 W ENI ACG-6B RF power supply via a modified MFJ-949E tuner used for plasma impedance matching. Typically, the reflected RF power does not exceed 5-10% of the forward power. The applied RF voltage amplitude, measured by a high voltage probe, is varied in the range of 2-3 kV at P=0.8-1.2 atm, so that the peak reduced electric field did not exceed $E/N \cong 1 \cdot 10^{-16}$ V·cm^2. We emphasize that this low value of E/N precludes electron impact ionization produced by the applied field, so that the associative ionization of Eq. (3) remains the only mechanism of electron production in the plasma. The applied RF field is primarily used to heat free electrons created by the associative ionization mechanism and to couple additional power to the vibrational modes of the gas mixture molecules by electron impact processes,

$$CO(v) + e^-(hot) \rightarrow CO(v + \Delta v) + e^-(cold) \qquad (4)$$

$$N_2(v) + e^-(hot) \rightarrow N_2(v + \Delta v) + e^-(cold) \qquad (5)$$
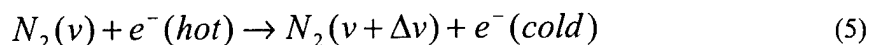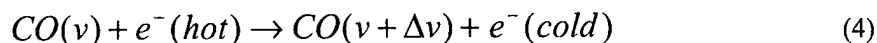
It is well known that in a wide range of the reduced electric field values, $E/N = (0.5\text{-}5.0) \cdot 10^{-16}$ V·cm^2, more than 90% of the input electrical power in nitrogen plasmas goes to vibrational excitation of N_2 by electron impact [1] (see Fig. 3). Combined with the high efficiency of the CO laser, this provides a very efficient method of sustaining extreme vibrational disequilibrium in high-pressure molecular gases without the use of a high-power pump laser.

Strong vibrational disequilibrium enhanced by the electron impact processes of Eqs. (4,5) results in a faster electron production by the associative ionization mechanism of Eq. (3). The resultant electron density increase in turn further accelerates the rate of energy addition to the vibrational modes of the molecules. However, this self-accelerating process does not produce an ionization instability such as occurs in other types of high-pressure nonequilibrium plasmas. The reason for this is a built-in self-stabilization mechanism existing in plasmas sustained by associative ionization. In high-pressure self-sustained discharge plasmas, excess Joule heating produced by a local electron density rise accelerates the rate of impact ionization and therefore results in a further increase of electron density (see Fig. 2), This is the well-known mechanism of ionization-heating instability development [1,2]. In a plasma sustained by associative ionization, excess Joule heating due to a local electron density rise sharply increases the vibration-translation (V-T) relaxation rates, which results in a rapid depopulation of high vibrational energy levels, slows down the ionization rate, and reduces the electron density (see Fig. 2). This provides

negative feedback between gas heating and the ionization rate and enables unconditional stability of the plasma at arbitrarily high pressures, for as long as the applied RF field does not produce any impact ionization. Obviously, optically pumped plasmas sustained by the CO laser alone (without the externally applied field) are always unconditionally stable. Indeed, stable and diffuse plasmas of this type have been sustained in CO-Ar mixtures at pressures up to 10 atm [14]. Figure 4 shows a schematic of the dominant kinetic processes in the CO laser / RF field sustained CO-N_2 plasma.

Triggering the RF power coupling to the vibrational modes of the cell gases requires the initial electron density, n_e, to exceed a certain threshold value. Our recent studies of associative ionization in CO laser pumped plasmas [7,11,12] showed that the electron density in these plasmas,

$$ n_e = \sqrt{\frac{S}{\beta}}, \quad where \quad S = k_{ion} \sum_{E_v + E_w > E_{ion}} n_{CO}(v) n_{CO}(w), \tag{6} $$

can be significantly increased (from $n_e < 10^{10}$ cm^{-3} to $n_e = (1.5\text{-}3.0) \cdot 10^{11}$ cm^{-3}) by adding trace amounts of species such as O_2 and NO to the baseline CO/Ar or CO/N_2 gas mixtures. In Eq. (6), S is the electron production rate by the mechanism of Eq. (3), $k_{ion} = (1.1\text{-}1.8) \cdot 10^{-13}$ cm^3/s is the associative ionization rate coefficient [7], β is the electron-ion dissociative recombination rate coefficient, and $n_{CO}(v)$ is the population of the vibrational level v of CO. Note that the observed electron density increase occurs at a nearly constant electron production rate S, which was measured independently [7,12]. In other words, adding small amounts of O_2 or NO to the gas mixture considerably reduces the dissociative recombination rate β. This result is consistent with previous measurements of the ion composition in glow discharges in CO-Ar-O_2 and CO-He-O_2 mixtures [24,25]. These previous studies showed that in a discharge in CO-Ar and CO-He mixtures without oxygen the dominant ions are rapidly recombining cluster ions such as $C_n(CO)_2^+$, n=1-12. However, adding a few tens of mtorr of O_2 resulted in a nearly complete destruction of the cluster ions and their replacement by the slowly recombining monomer O_2^+ ion. The recombination rate coefficients of $(CO)_2^+$ and O_2^+ ions in the presence of 1 eV electrons are $\beta = 2 \cdot 10^{-6}$ and $3 \cdot 10^{-8}$ cm^3/s, respectively [1,26]. Therefore, replacing the cluster ions with the monomer ions would increase the electron density at a constant electron production rate S by about an order of magnitude. For this reason, in the present experiments trace amounts of oxygen or nitric oxide have been added to the baseline CO/N_2 gas mixture.

3. Results and discussion

In a first series of experiments, the baseline 1% CO – 99% N_2 mixture was optically pumped by a CO laser at P=600 torr. The pump laser power was 10 W. Figures 5 and 6 show the CO first overtone emission spectrum and the N_2 spontaneous Raman spectrum at these conditions, respectively. One can see that about 35 vibrational levels of CO and 4 vibrational levels of N_2 are populated. The first level vibrational temperature of N_2 at the CO laser centerline was determined from the ratio of the v=0 and v=1 N_2 vibrational level relative populations, f_0 and f_1,

$$T_v = \frac{\theta_1}{\ln\left[f_0 / f_1\right]},$$ (7)

$T_v(N_2)$=1900 K. In equation (7), θ_1=3353 K is the energy of the first vibrational level of N_2. The translational temperature at the centerline was evaluated from comparison of two Raman spectra of nitrogen, shown in Fig. 6, one with the CO laser on, and the other with the laser turned off, i.e. in an equilibrium gas mixture at T_0=300 K. In the latter case, as expected, only the signal from v=0 is measured. Since the Raman signal intensity, I_v, is proportional to the product of the absolute population of a vibrational level, n_v, and the Raman cross section, $\sigma_v \sim (v+1)$, this allowed straightforward inference of the number density of N_2 molecules, $n_{N_2}(T)$, as well as the translational temperature,

$$\frac{T}{T_0} = \frac{n_{N_2}(T_0)}{n_{N_2}(T)} = \frac{I_0}{\sum_v I_v /(v+1)}$$ (8)

For the conditions of Figs. 5 and 6, the translational temperature of the optically pumped plasma is T=380 K.

Applying 2500 V peak RF voltage to the cell electrodes did not result in any detectable change in the plasma appearance or in the infrared and Raman spectra. We believe this to be due to the low electron density in the optically pumped CO/N_2 plasma without additives, because of the rapid recombination of electrons with the cluster ions [7,11,12] (see discussion in Section 2). Measurements in the same mixture at the lower cell pressure of P=300 torr and 100 torr also did not show any effect. In these low-pressure runs, the applied RF voltage was also lowered to keep the peak reduced electric field $E/N \cong 1 \cdot 10^{-16}$ $V \cdot cm^2$ well below the electron impact ionization threshold.

In the second series of measurements, 20 torr of NO/N_2 mixture containing 5000 ppm of NO was added to the cell gases at a total pressure of P=600 torr, so that the NO partial pressure in the cell was 100

152

mtorr. In this case, applying the same 2500 V peak RF voltage to the electrodes produced a dramatic change of the plasma (see Fig. 7). In the absence of the RF field, the cylindrical region excited by a focused CO laser can be easily seen due to a few cm long, 1 mm diameter violet-blue glow produced by radiation of electronically excited molecules (C_2 Swan and CN bands, see Fig. 7). Turning the RF field on produced a curtain-like glow about 1-2 mm thick, centered at the laser beam and filling nearly the entire distance between the electrodes (approximately 1 cm x 3 cm). In other words, the apparent plasma volume increased by about an order of magnitude. This curtain-like plasma looked diffuse and stable, with no hint of arc filaments.

The significance of this result is that the applied weak electric field, not capable of initiating electron impact ionization, nevertheless results in producing ionization up to 6-7 millimeters away from the CO laser beam which initiates the plasma. Note that at these conditions, the amplitude of the drift oscillations of the plasma electrons, induced by the RF field, is only about $\delta \sim w_{dr}/2\nu \sim 1$ mm. Here $w_{dr} \sim 2 \cdot 10^6$ cm/s is the electron drift velocity at $E/N \cong 1 \cdot 10^{-16}$ V·cm^2 [1] and $\nu = 13.56$ MHz is the RF field frequency. Therefore the present technique allows "propagation" of the coupled vibrational excitation and associative ionization over distances considerably exceeding the electron oscillation amplitude, thereby significantly increasing the volume occupied by the plasma. Turning the CO laser off with the RF field on resulted in a slow decay and eventual extinguishing of the plasma curtain (within a few seconds). Covering the RF electrodes with teflon layers did not change the appearance of the plasma curtain, which shows the effect of the secondary electron emission for the electrodes to be insignificant.

CO first overtone infrared emission spectra taken at these conditions with the RF voltage off and on show that the infrared signal intensity, integrated along the line of sight, increases by about a factor of 7 (see Fig. 8). Figure 8 also shows CO spectra obtained in the same gas mixture at a higher pressure of P=720 torr, a higher laser power of 15 W, and a somewhat lower RF voltage of 2200 V, which look similar to the 600 torr data. We believe that the signal intensity rise is primarily due to the plasma volume increase, although the FTIR line of sight is perpendicular to the plasma curtain. However, Raman spectra of nitrogen taken at the centerline of the CO laser beam with RF voltage off and on (see Fig. 9) show that the vibrational temperature of N_2 at P=600 torr increases from $T_v(N_2)$=1900 to 2500 K. This demonstrates that the RF field makes the vibrational disequilibrium at the CO laser beam axis considerably stronger. Comparison of these Raman spectra with the cold N_2 spectrum show that at P=600 torr the centerline translational temperature increases from T=380 K with the RF field off to the T=530 K with the RF on, which apparently self-limits further ionization by the associative ionization mechanism (see Section 2). Note that even at this somewhat higher gas temperature the peak reduced electric field does not exceed $E/N \cong 1.3 \cdot 10^{-16}$ V·cm^2.

We believe that the amount of RF power coupled to the vibrational modes of the cell gases can be considerably increased by increasing the mass flow rate through the cell. In this case, more efficient convective cooling of the flow would reduce the steady-state gas temperature so that the associative ionization process would terminate at a higher electron density.

Adding a small amount of oxygen to the baseline CO/N_2 mixture at the same pressure of P=600 torr produced similar results. Oxygen was added to the cell directly from a gas cylinder, and therefore its partial pressure could not be precisely controlled. We estimate the upper limit of the O_2 partial pressure in the cell at approximately 0.1 torr. Turning the RF field on (peak voltage 2750 V) with oxygen in the cell considerably increased the visible glow intensity and nearly doubled the glow diameter, although in this case the plasma curtain did not form. Figures 10, 11 show CO infrared spectra and N_2 Raman spectra at these conditions, taken with the RF voltage on and off. Figure 10 also shows CO spectra obtained in the same gas mixture at a high pressure of P=720 torr, a higher laser power of 15 W, and a higher RF voltage of 3150 V, which look similar to the 600 torr data. In this case, the infrared signal intensity increased by approximately a factor of 3, while the N_2 vibrational temperature at P=600 torr increased from $T_v(N_2)$=1850 to 2460 K. Translational temperature of the gas mixture at P=600 torr, inferred from the Raman spectra, increased from T=360 to 540 K.

Similar results have been obtained at several different cell pressures in the range P=0.4-1.2 atm. In this entire pressure range, the CO laser / RF field pumped plasma always looks stable and diffuse. At the highest pressures P>1 atm, the effect of the RF field on the vibrational populations of CO and N_2 becomes somewhat lower, since the pumping processes are limited by the RF voltage available. For the RF field pumping process to be efficient, the applied reduced electric field has to be in the range $E/N \cong (1-5) \cdot 10^{-16}$ $V \cdot cm^2$ (see Fig. 3). In this range, only a small fraction of the input electrical power goes into direct gas heating and electronic excitation. At P=1.2 atm, this condition requires the peak RF voltage to exceed 3000 V. Unfortunately, at these high voltages the MFJ tuner sometimes started arcing internally, which limited our ability to run at optimum conditions. Also, the design of the absorption cell available for these experiments did not allow measurements at higher pressures or higher flow rate. However, we expect the CO laser / RF field pumped plasmas to be unconditionally stable also at higher pressures, given enough laser and RF power to trigger the pumping.

In the present work, the electron density with the RF field turned off and on has not been measured. Electron density measurements using both microwave attenuation [12] and filtered Thomson scattering, as well as ion composition measurements using *in situ* ion mass spectrometry [24,25] would provide additional insight into the kinetics of these unique high-pressure nonequilibrium plasmas.

The high-pressure unconditionally stable CO-containing plasmas studied in the present paper may be used for high-yield single-wall carbon nanotube (SWNT) production. In particular, ordered arrays of 60-

70% pure SWNT material have been recently produced in optically pumped, chemically reacting, nonequilibrium CO/Ar/Fe(CO)$_5$ plasmas sustained by a 20 W CO laser [27]. In this process, strong vibrational excitation of CO molecules by V-V pumping drives the gas-phase CO disproportionation reaction,

$$CO(v) + CO(w) \rightarrow CO_2 + C \,, \tag{9}$$
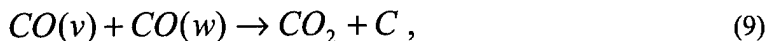
producing free carbon atoms at low gas temperatures, with subsequent SWNT formation on catalytic iron cluster surfaces. The yield of this process at a relatively low CO partial pressure of P$_{CO}$=50 torr (tens of milligrams per hour) is comparable with the yield of the high-pressure CO (HiPCO) SWNT synthesis process developed at Rice University [28]. Note that the CO reactant pressure in the HiPCO process is much higher (P$_{CO}$=1-10 atm). The RF energy coupling effect reported here is expected to be used to scale up the plasma volume and the SWNT yield at high CO pressures (P$_{CO}$≥1 atm), without producing ionization instabilities or the use of a high-power pump laser.

4. Summary

The results of the experiments demonstrate the feasibility of unconditionally stable high-pressure plasmas sustained by a combination of a continuous wave CO laser and a sub-breakdown RF field. The plasma is sustained in a CO/N$_2$ mixture containing trace amounts of NO or O$_2$ at pressures of P=0.4-1.2 atm. The initial ionization of the gases is produced by associative ionization in collisions of two CO molecules excited to high vibrational levels by resonance absorption of CO laser radiation with subsequent vibration-vibration (V-V) pumping. Further vibrational excitation of both CO and N$_2$ is produced by free electrons heated by the applied RF field, which in turn produces additional ionization of these species by the associative ionization mechanism. Vibrational level populations of CO and N$_2$ are monitored by infrared emission spectroscopy and spontaneous Raman spectroscopy. In the present experiments, the reduced electric field, E/N, is sufficiently low to preclude field-induced electron impact ionization. The unconditional stability of the resultant cold molecular plasma is enabled by the negative feedback between gas heating and the associative ionization rate. Trace amounts of nitric oxide or oxygen added to the baseline CO/N$_2$ gas mixture considerably reduce the electron-ion dissociative recombination rate and thereby significantly increase the initial electron density. This allows triggering the RF power coupling to the vibrational energy modes of the gas mixture.

The experiments demonstrate that the use of a sub-breakdown RF field in addition to the CO laser allows the increase of the plasma volume by about an order of magnitude. Also, CO infrared emission spectra show that with the RF voltage turned on the number of vibrationally excited CO molecules along

155

the line of sight increase by a factor of 3 to 7. Finally, spontaneous Raman spectra of N_2 showed that with the RF voltage on the vibrational temperature of nitrogen increases by about 30%. This novel energy efficient approach allows sustaining large-volume high-pressure molecular plasmas without the use of a high-power CO laser.

References

1. Raizer, Y.P., "Gas Discharge Physics", Springer-Verlag, Berlin, 1991

2. E.P. Velikhov, A.S. Kovalev, and A.T. Rakhimov, "Physical Phenomena in Gas Discharge Plasmas", Moscow, Nauka, 1987

3. W. Rich, R.C. Bergman, and J.A. Lordi, AIAA Journal, vol. 13, p. 95, 1975

4. Generalov, N.A., V.P. Zimakov, V.D. Kosynkin, Yu.P. Raizer, and D.I. Roitenburg, Technical Physics Letters, vol. 1, p. 431, 1975

5. Basov, N.G., Babaev, I.K., Danilychev, V.A., et al., Sov. Journal of Quantum Electronics, vol. 6, 1979, p. 772

6. A.S. Kovalev, E.A. Muratov, A.A. Ozerenko, A.T. Rakhimov, and N.V. Suetin, Sov. J. Plasma Physics, Vol. 11, 1985, p. 515

7. E. Plönjes, P. Palm, I.V. Adamovich, and J. W. Rich, "Ionization Measurements in Optically Pumped Discharges", Journal of Physics D: Applied Physics, vol. 33, No. 16, 2000, p. 2049

8. L.S. Polak, P.A. Sergeev, and D.I. Slovetskii, Sov. High Temperature Physics, Vol. 15, 1977, p. 15

9. I. Adamovich, S. Saupe, M.J. Grassi, O. Schulz, S. Macheret, and J.W. Rich, Chem. Phys., vol. 173, 1993, p. 491

10. I.V. Adamovich and J.W. Rich, J. Physics D: Applied Physics, vol. 30, 1997, p. 1741

11. I.V. Adamovich, "Control of Electron Recombination Rate and Electron Density in Optically Pumped Nonequilibrium Plasmas", Journal of Physics D: Applied Physics, vol. 34, 2001, p.319

12. P. Palm, E. Plönjes, M. Buoni, V.V. Subramaniam, and I.V. Adamovich, "Electron Density and Recombination Measurements in CO-seeded Optically Pumped Plasmas", accepted for publication in Journal of Applied Physics, 2001

13. Billing, G.D., "Vibration-Vibration and Vibration-Translation Energy Transfer, Including Multiquantum Transitions in Atom-Diatom and Diatom-Diatom Collisions", Nonequilibrium Vibrational Kinetics, Springer-Verlag, Berlin, 1986, Chap. 4, pp. 85-111

14. J.W. Rich, R.C. Bergman, and M.J. Williams, "Measurement of Kinetic Rates for Carbon Monoxide Laser Systems", Final Contract Report AFOSR F49620-77-C-0020 (November 1979)

15. R.L. DeLeon and J.W. Rich, "Vibrational Energy Exchange Rates in Carbon Monoxide", Chemical Physics, vol. 107, 1986, p. 283

16. C. Flament, T. George, K.A. Meister, J.C. Tufts, J.W. Rich, V.V. Subramaniam, J.-P. Martin, B. Piar, and M.-Y. Perrin, "Nonequilibrium Vibrational Kinetics of Carbon Monoxide at High Translational Mode Temperatures", Chemical Physics, vol. 163, 1992, p. 241

17. H.L. Wallaart, B. Piar, M.Y. Perrin, and J.P. Martin, "Transfer of Vibrational Energy to Electronic Excited States and Vibration Enhanced Carbon Production in optically pumped CO", Chemical Physics, vol. 196, 1995, p. 149

18. H. Dünnwald, E. Siegel, W. Urban, J.W. Rich, G.F. Homicz, and M.J. Williams, "Anharmonic Vibration-Vibration Pumping in Nitric Oxide by Resonant IR-Laser Irradiation", Chemical Physics, vol. 94, 1985, p. 195

19. S. Saupe, I. Adamovich, M.J. Grassi, and J.W. Rich, "Vibrational and Electronic Excitation of Nitric Oxide in Optical Pumping Experiments", Chemical Physics, vol. 174, 1993, p. 219

20. E. Plönjes, P. Palm, A.P. Chernukho, I.V. Adamovich, and J.W. Rich, "Time-Resolved Fourier Transform Infrared Spectroscopy of Optically Pumped Carbon Monoxide", Chemical Physics, vol. 256, 2000, p. 315

21. E. Plönjes, P. Palm, W. Lee, M. D. Chidley, I.V. Adamovich, W.R. Lempert, and J. William Rich, "Vibrational Energy Storage in High-Pressure Mixtures of Diatomic Molecules", Chemical Physics, vol. 260, 2000, pp. 353-366

22. W. Lee, I.V. Adamovich, and W.R. Lempert, "Optical Pumping Studies of Vibrational Energy Transfer in High-Pressure Diatomic Gases", Journal of Chemical Physics, vol. 114, 2001, p. 1178

23. J. W. Rich, "Relaxation of Molecules Exchanging Vibrational Energy", in "Applied Atomic Collision Physics", Vol. 3, "Gas Lasers", ed. E.W. McDaniel and W.L. Nighan, Academic Press, New York, 1982, pp. 99-140

24. Y. Kaufman, P. Avivi, F. Dothan, H. Keren, and J. Malinowitz, "Ion Clusters in He-CO and Ar-CO Glow Discharges", J. Chem. Phys., vol. 72, 1980, p. 2606

25. H. Keren, P. Avivi, and F. Dothan, "Positive Ion Spectra in He-CO-O_2-Laser Discharges", IEEE J. Quant. Electr., QE-12, 1976, p. 58

26. R. Johnsen, "Recombination of Cluster Ions", in B.R. Rowe et al. (eds.), "Dissociative Recombination", Plenum, New York, 1993

27. E. Plönjes, P. Palm, J.W. Rich, and V.V. Subramaniam, to be published

28. P. Nikolaev, M.J. Bronikowski, R.K. Bradley, F. Rohmund, D. T. Colbert, K.A. Smith, and R.E. Smalley, Chem. Phys. Lett., vol. 313, 1999, p. 91

Figure Captions

Figure 1. Schematic of the CO laser / RF field pumping experiment

Figure 2. Stability feedback loops for a self-sustained discharge plasma and for the CO laser / RF pumped plasma

Figure 3. Electron energy balance in a nonequilibrium nitrogen plasma

Figure 4. Schematic of the dominant kinetic processes in a CO/N_2 plasma pumped by a CO laser and a sub-breakdown RF field

Figure 5. CO first overtone infrared emission spectrum in the CO laser pumped baseline 1% CO – 99% N_2 gas mixture at P=600 torr.

Figure 6. Raman spectra of nitrogen in a cold (T= $T_v(N_2)$=300 K) and the CO laser pumped (T=380 K, $T_v(N_2)$=1900 K) baseline 1% CO – 99% N_2 gas mixture at P= 600 torr.

Figure 7. Photographs of the CO laser / RF field pumped 1% CO – 99% N_2 – 10 ppm NO gas mixture at P= 1 atm. Top, RF field turned off; bottom, RF field turned on.

Figure 8. CO first overtone infrared emission spectra in the CO laser / RF field pumped 1% CO – 99% N_2 – 150 ppm NO gas mixture at (a) P=600 torr, laser power 10 W, and (b) P=720 torr, laser power 15 W.

Figure 9. Raman spectra of nitrogen in the CO laser / RF field pumped 1% CO – 99% N_2 – 150 ppm NO gas mixture at P=600 torr. The spectra are normalized on the v=0 peak intensity.

Figure 10. CO first overtone infrared emission spectra in the CO laser / RF field pumped 1% CO – 99% N_2 gas mixture with about 0.01% O_2 at (a) P=600 torr, laser power 10 W, and (b) 720 torr, laser power 15 W.

Figure 11. Raman spectra of nitrogen in the CO laser / RF field pumped 1% CO – 99% N_2 gas mixture about 0.01% O_2 added at P=600 torr. The spectra are normalized on the v=0 peak intensity.

Figure 1.

Self-sustained discharge   **CO laser / RF pumped plasma**
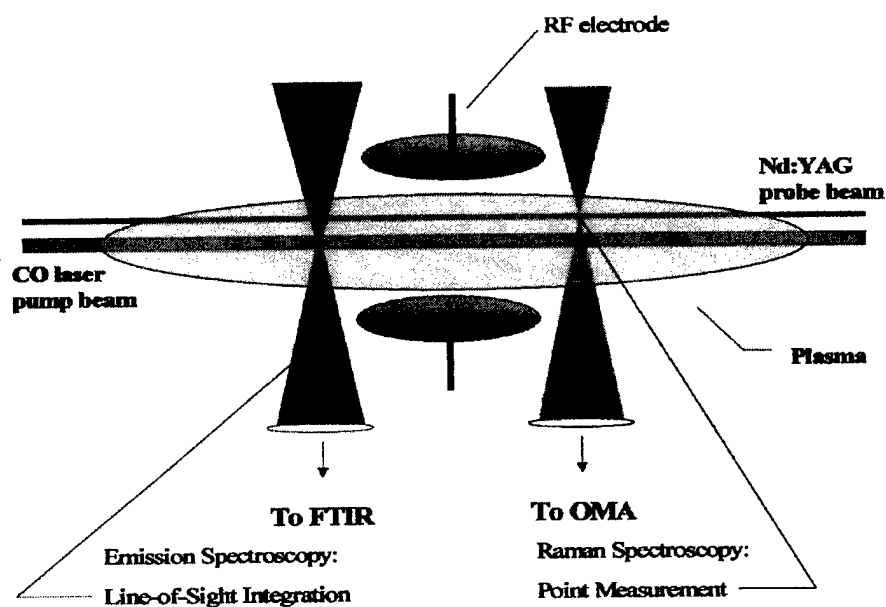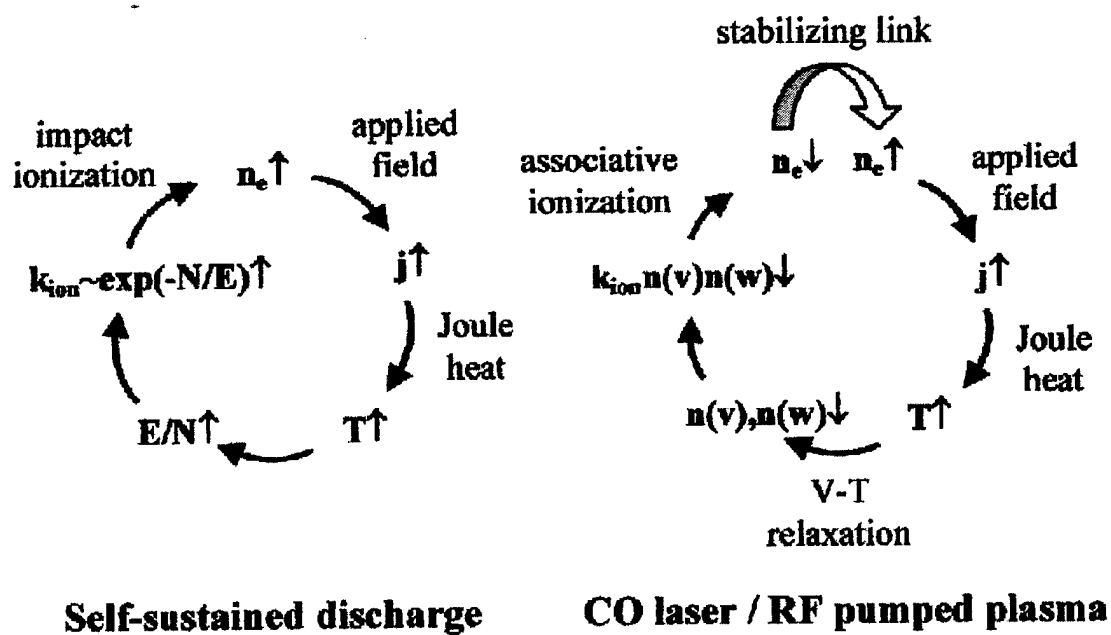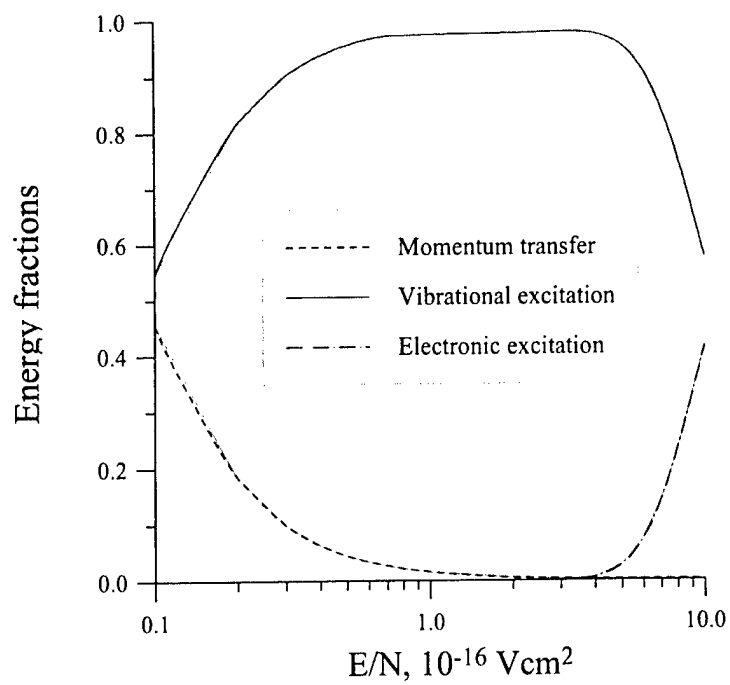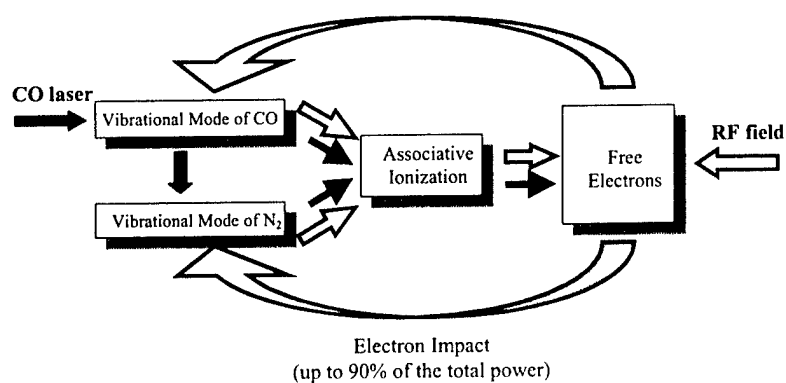
Figure 2.

Figure 3.

Electron Impact
(up to 90% of the total power)
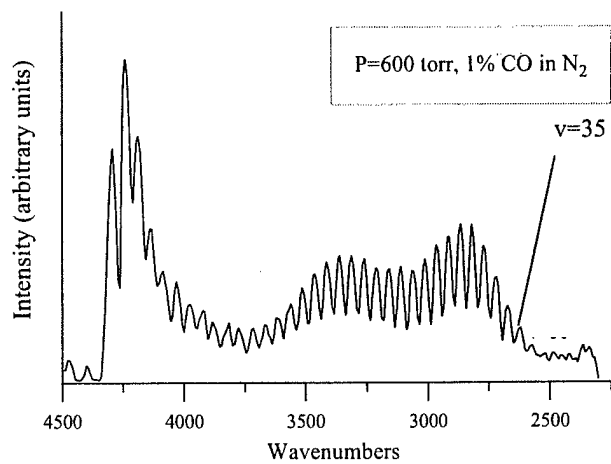
Figure 4.

Figure 5.

Figure 6.

Figure 7.
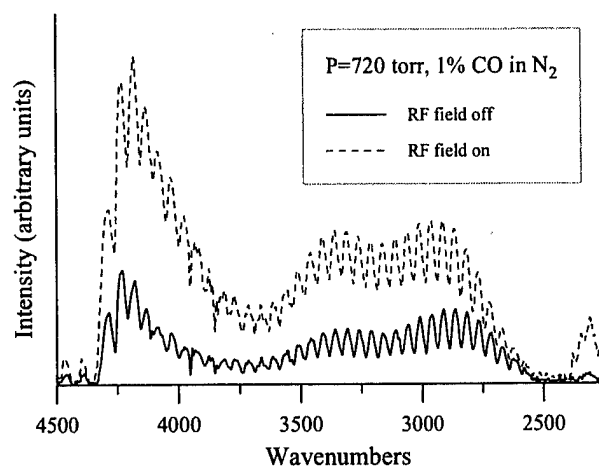
Figure 8.

Figure 9.

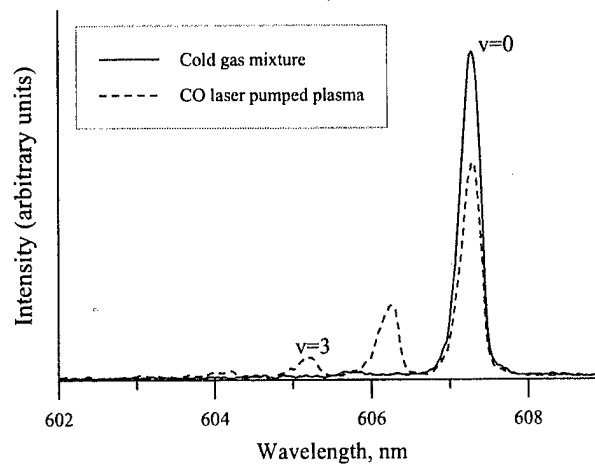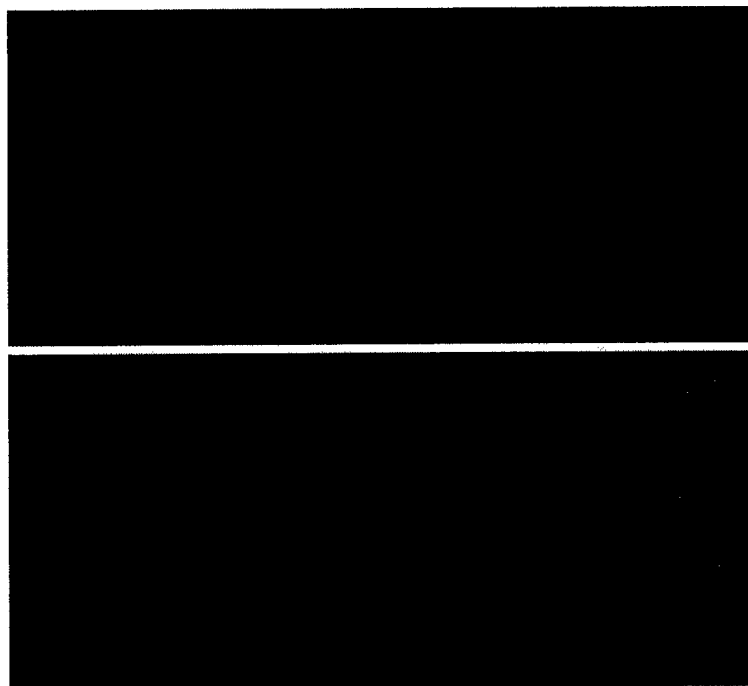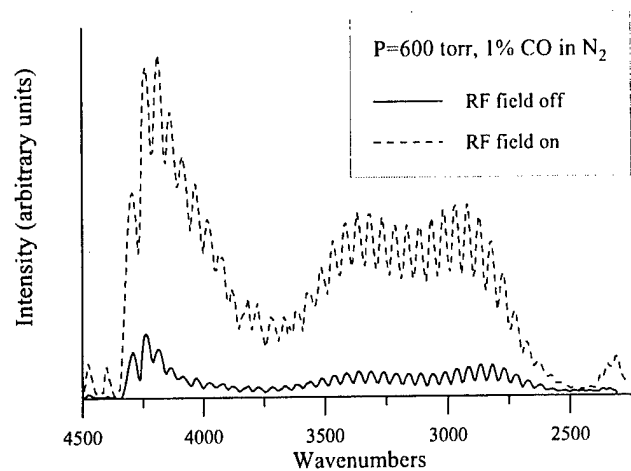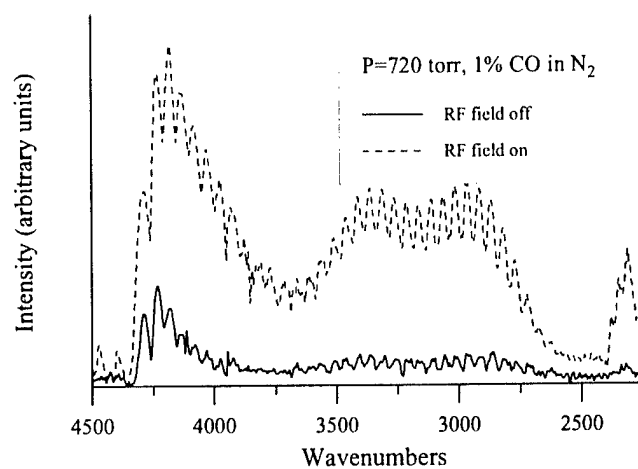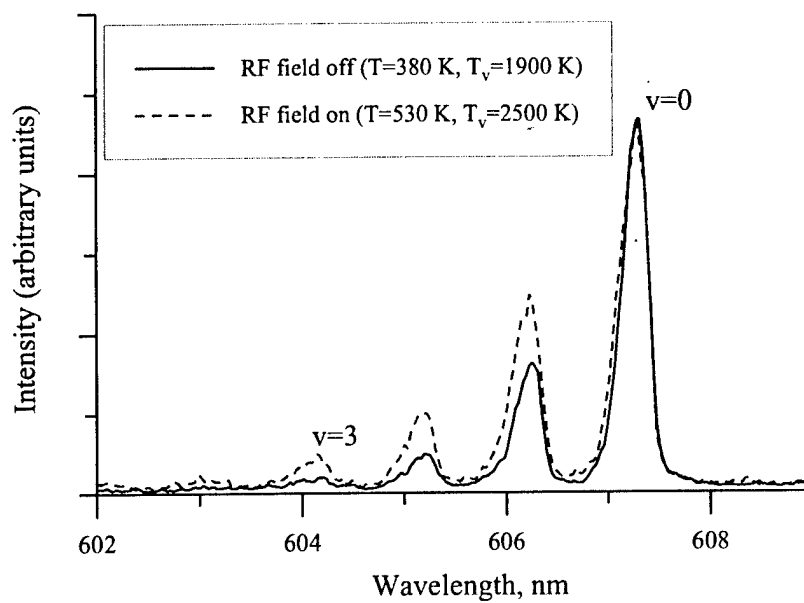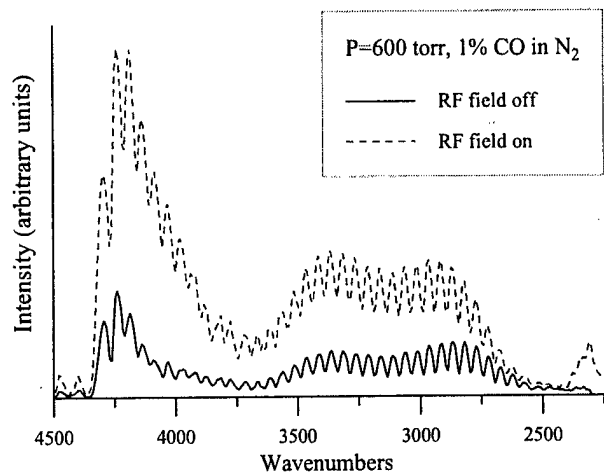(a)   (b)

Figure 10.

Figure 11.

163
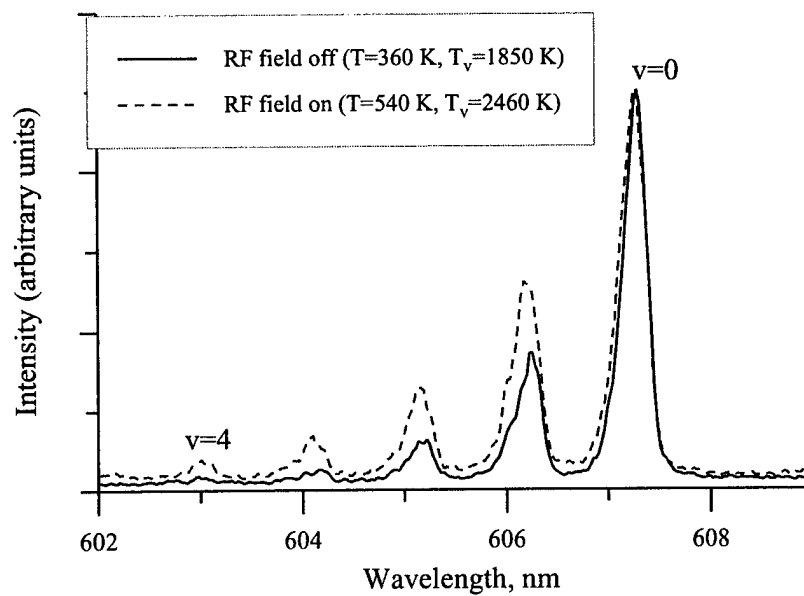
9. SPATIALLY RESOLVED RAMAN MEASUREMENTS OF N₂ VIBRATIONAL LEVEL POPULATIONS IN OPTICALLY/RF PUMPED PLASMAS

Kraig Frederickson, Peter Palm, Elke Ploenjes, Walter R. Lempert, and Igor V. Adamovich

This section presents the results of spatially resolved Raman measurements of nitrogen vibrational level populations in a nonequilibrium optically pumped plasma sustained by a combination of a continuous wave CO laser and a sub-breakdown radio frequency electric field. The plasma is created in a CO/N_2 environment, at a total pressure of 300 torr. Ionization of the gases occurs by an associative ionization mechanism, in collisions of two highly vibrationally excited molecules. These highly vibrationally excited states are populated by resonance absorption of the CO radiation followed by anharmonic (vibration-vibration) V-V pumping. Additionally, N_2 also becomes vibrationally excited due to collisions with vibrationally excited CO. When an RF field is applied to the plasma, collisions between the free electrons heated by the field and the diatomic species create additional vibrational excitation within the plasma region. Note that the reduced electric field, E/N, is sufficiently low to prevent electron impact ionization, which would lead to the glow-to-arc collapse. Vibrational level populations of N_2 are measured using spontaneous Raman spectroscopy. The results show that applying the RF field to an optically pumped CO/N_2 plasma produces stronger vibrational disequilibrium both in the region occupied by the CO laser beam and outside of this region. The experimental results are compared with kinetic modeling calculations showing a satisfactory agreement.

1. Introduction

Creating a high-pressure, low-temperature, large-volume plasma has been a challenge to the fields of gas discharge physics and engineering. Large-volume plasmas have traditionally been established at low pressure. At high pressures plasmas become constricted due to rapid instability development. While heating can increase the electron production and diffusion rates, it can quickly lead to runaway ionization due to the ionization heating instability. The runaway ionization causes the glow-to-arc collapse occurring in high-pressure plasmas. By utilizing an ionization method that does not rely on electron impact ionization, it is possible to prevent the thermal instability [1].

The associative ionization mechanism of Eq. (1) produces free electrons in collisions of two vibrationally excited molecules

$$AB(w) + AB(x) \rightarrow (AB)_2^+ + e^- \qquad (1)$$

$$E_w + E_x > E_{ion}$$
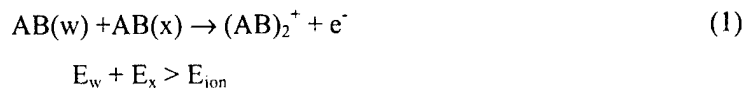
Here E_{ion} is the ionization potential for the molecule of interest. In the case of the CO molecule the ionization potential is on the order of 14 eV.

Associative ionization is produced by collisions of molecules with the total vibrational energy of the collision partners exceeding that of the ionization potential. This type of ionization has been previously observed in CO/Ar and CO/N_2 optically pumped plasmas [2-6]. It has been accomplished by resonance absorption of CO laser radiation followed by vibration-to-vibration (V-V) anharmonic up-pumping [7]. These processes are shown in Eq. (2,3), where v and w are vibrational quantum numbers.

$$CO(v) + h\nu \rightarrow CO(v+1) \tag{2}$$
$$CO(v) + CO(w) \rightarrow CO(v-1) + CO(w+1) \tag{3}$$
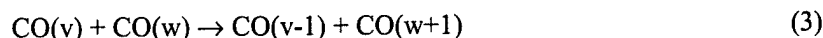
The result is a significant population of high vibrational levels of CO molecules. These molecules can then undergo the associative ionization mechanism illustrated by Eq. (1). It is important to note that while the CO vibrational mode energy at these conditions is a few thousand degrees Kelvin, the translational/rotational temperature never exceeds a few hundred degrees.

While this method can create high-pressure, low-temperature plasmas, it does not produce a large-volume discharge. The optically pumped plasma created by this method is confined to the volume defined by the incident CO laser beam. Outside of the CO laser beam the electrons rapidly recombine and diffusion of the vibrationally excited species is limited due to the high pressure of the system. Additionally, the vibrationally excited species diffusing out of the excitation volume quickly relax to the ground vibrational state.

The main objective of this paper is to demonstrate experimentally the volume increase of the optically pumped plasma outside of the region defined by the incident CO laser beam when an external sub-breakdown RF field is applied. When applied, the RF field couples additional power to the CO and N_2 vibrational energy modes by electron impact excitation. In this case, additional vibrational excitation of both CO and N_2 is produced by free electrons heated by the applied RF field [1]. This in turn produces additional ionization of these species by the associative ionization mechanism of Eq. (1). Note that in the present experiments, the reduced electric field, E/N, is sufficiently low to preclude field-induced electron impact ionization. In the present work, this effect is studied by measuring spatially resolved spontaneous Raman spectra of N_2 with and without an applied RF field.

2. Experimental

A schematic of the experimental set-up is shown in Figs. 1 and 2. A broadband continuous wave CO laser having output at the first 10-12 fundamental bands of CO is used to irradiate a gas mixture. The

mixture consists of nitrogen containing approximately 1.5% CO and trace amounts (approximately 300 ppm) of NO. The total pressure of the gas mixture is approximately 300 torr. The residence time of the gases in the cell is approximately 1 second. The cryogenically cooled CO laser was designed in collaboration with the University of Bonn and constructed at The Ohio State University. It is tuned to emit a substantial percentage of its power on the $v=1\rightarrow0$ and $v=2\rightarrow1$ fundamental transitions with the majority of the remaining power output in the next 10 vibrational bands. The total output of the laser is approximately 10-15 W.

The output of the CO laser is focused into a six arm cross pyrex absorption cell containing the gas mixture. Focusing the beam increases the power loading per CO molecule along the laser beam. This produces an optically pumped region approximately 2 mm in diameter and 10 cm long. Two circular copper electrodes (3 cm diameter) placed above and below the path of the CO laser beam are used to apply the RF field to the optically pumped plasma. The absorption cell is supported by a vertical translation stage fitted with a micrometer that produced precision movement on the order of ±0.005 mm. This setup permitted the movement of the Raman laser probe beam vertically with respect to the optically pumped plasma.

A nonequilibrium vibrational mode energy distribution of the cell gases is produced by anharmonic V-V up-pumping. In particular, irradiating the gas mixture with a CO laser tuned to the lowest 10-12 vibrational transitions leads to the vibrational excitation of CO molecules to vibrational levels from $v=1$ to $v=10$-12 by direct resonance absorption. Higher vibrational levels $v\sim10$-40, which are not accessible to the laser, are populated by V-V energy transfer.

In the laser excited CO/N_2 plasma, vibrational energy transfer in collisions between vibrationally excited CO molecules and N_2 molecules also causes vibrational excitation of nitrogen. As shown in Eq. (4)

$$CO(w) + N_2(v) \rightarrow CO(w-1) + N_2(v+1) \qquad (4)$$
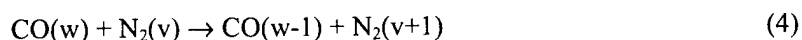
N_2 can be vibrationally excited although it is not directly coupled to the incident CO laser radiation.

Presence of free electrons in the gas mixture may also lead to vibrational excitation of molecular species by electron impact. Basically, free electrons heated by the applied electric field primarily lose their energy by collisional energy transfer to vibrational energy modes of the diatomic species.

$$CO(w) + e^- \rightarrow CO(w+\Delta w) + e^- \qquad (5)$$

$$N_2(w) + e^- \rightarrow N_2(w+\Delta w) + e^- \qquad (6)$$

By heating free electrons created by associative ionization of vibrationally excited molecules with an applied RF field, vibrational nonequilibrium can be attained outside of the volume occupied by the CO laser beam. In this experiment, two copper electrodes are placed above and below the optically pumped plasma with a separation of approximately 13 mm. Connected to these electrodes is a 13.56 MHz, 600W ENI ACG-6B RF power supply via a modified MFJ-949E tuner, which is used for plasma impedance matching. Tuning the impedance so that the reflected RF power does not exceed 5-10% of the forward power was typical for these experiments. Setting the output wattage of the RF power supply to 100 W produced a peak-to-peak voltage of 4 kV measured by a high voltage probe. At these conditions, the peak reduced electric field did not exceed $E/N \approx 1 \cdot 10^{-16}$ V·cm^2 [1]. This low value of the reduced electric field precludes electron impact ionization and ionization instability development. Therefore, electrons in the optically pumped plasma enhanced by the RF field are produced only by the associative ionization mechanism.

In these present experiments, the gas mixture in the cell contains approximately 300 ppm of nitric oxide. Addition of trace amounts of NO to the optically pumped plasma is necessary to increase the electron number density. Previous experiments in CO/Ar glow discharge plasmas [8] showed that the dominant ions in the discharge are dimer ions, $(CO)_2^+$, and cluster ions of the general form $C_n(CO)_2^+$, n=1-15. However, adding a few tens of millitorr of O_2 to these gas mixtures resulted in nearly complete disappearance of these ions and their replacement by O_2^+ ions. Note that the electron-ion dissociative recombination rate of the dimer $(CO)_2^+$ ion, $\beta = 2 \cdot 10^{-6}$ cm^3/s [9], greatly exceeds the rate of recombination of the monomer O_2^+ ion, $\beta = (3-5) \cdot 10^{-8}$ cm^3/s [10]. The recombination rate of the large carbon cluster ions can possibly be even higher. Our previous measurements [11] showed that electron density in the optically pumped CO/Ar and CO/N$_2$ plasmas can be considerably increased by adding small amounts of O_2 and NO. This might occur due to a similar process, i.e. destruction of the rapidly recombining carbon-based cluster ions and their replacement by the slowly recombining monomer ions, such as O_2^+ and NO$^+$.

To acquire spontaneous Raman spectra of the optically pumped plasma, a pulsed Nd:YAG laser tuned to the second harmonic (532 nm) and operated at 10 Hz was used to probe the gas mixture. Each laser pulse has an output energy of 200 mJ and a duration of approximately 10 ns. The Nd:YAG laser probe beam was combined with the CO laser pump beam using a 90° CaF$_2$ dichroic mirror which was coated to allow transmission of the CO laser beam while reflecting the Nd:YAG beam. Spatial resolution of the Raman spectra was enhanced by focusing of the probe beam using a 0.4 m focal length lens. A notch filter was used to attenuate the 532 nm line resulting from elastic scattering. The Stokes shifted signal was in the range of 600 to 612 nm, which is well outside the attenuation profile of the notch filter. To maximize the signal to noise the image of the plasma was rotated using 2 inch diameter mirrors so that the it was oriented parallel to the vertical input slit of the OMA spectrometer. In addition the signal was

focused with $f/4$ lenses to match the 0.25 meter $f/4$ spectrometer. This resulted in a solid angle of approximately 0.049 sr, corresponding to an area defined by the monochromator slits and probe beam of approximately 2mm in length by 100 μm in height. The detector used to acquire the Stokes shifted signal was a microchannel plate intensified charge-coupled device (ICCD) camera. By using a pulser to gate the intensifier the signal to noise increased by eliminating much of the spontaneous emission from the optically pumped cell. The quantum efficiency of the detector was on the order of 6% at the Stokes wavelength and the signal was integrated for a duration of 30s. Within the monochromator, a 1800 line/nm grating was used which resulted in a spectral resolution of approximately 1.5 $\Rightarrow$ and a spectral range of approximately 10 nm. The resolution was adequate to resolve the individual Q-branch vibrational bands, but insufficient to obtain any rotational fine structure.

Uncertainty in the relative band intensities of the Raman spectra of the laser-excited plasma from which the experimental vibrational level populations are derived is estimated to be 10%-20%. For Raman spectra of the optically pumped plasma enhanced by the RF field, the uncertainty is somewhat greater (20-25 %) due to a lower signal-to-noise ratio. Uncertainty in the ratio of vibrational populations of levels v=0 and v=1 is estimated to be 6%.

3. Kinetic model

The two-dimensional time-dependent model of the non-self-sustained RF discharge used in the present optical pumping experiments incorporates the equations for electron and positive ion concentrations, as well as the Poisson equation for the electric field:

$$\frac{\partial n_k(x,y,t)}{\partial t} + \nabla \vec{\Gamma}_k = Q_k ,$$

$$\vec{\Gamma}_k = D_k \nabla n_k(x,y,t) - \frac{q_k}{|e|} \mu_k \nabla \phi(x,y,t) n_k(x,y,t)$$

$$n_k(x,0,t) = n_k(x,d,t) = 0, \quad \frac{\partial n_k(0,y,t)}{\partial x} = \frac{\partial n_k(\pm W,y,t)}{\partial x} = 0$$

$$n_k(x,y,0) = 0$$

(7)

$$\nabla^2 \phi(x,y,t) = \frac{1}{\varepsilon_0} \sum_k q_k n_k(x,y,t) ,$$

$$\phi(x,0,t) = 0 , \quad \phi(x,d,t) = U_0 \cos(2\pi vt) , \quad \frac{\partial \phi(0,y,t)}{\partial x} = \frac{\partial \phi(\pm W,y,t)}{\partial x} = 0 \quad (8)$$

$$\phi(x,y,0) = U_0 y / d$$

$$Q_e = S - \beta n_e n_+$$
$$Q_+ = S - \beta n_e n_+ \tag{9}$$

In Eqs. (7-9), the index k stands for electrons and positive ions, e is the electron charge, n_k and $q_k = \pm e$ are the species concentrations and charges, D_k, μ_k, and $\bar{\Gamma}_k$ are the species diffusion coefficients, mobilities, and fluxes (conduction current density vectors), respectively, ϕ and $\bar{E} = -\nabla\phi$ are the electric potential and electric field, $\bar{j} = \sum q_k \bar{\Gamma}_k$ is the electric current, d is the separation between the electrodes, W is the electrode half-width, U_0 and ν are the applied voltage amplitude and frequency, S is the rate of electron production by the associative ionization mechanism of Eq. (1), and β is the electron-ion recombination coefficient.

Equations (7-9) are accompanied by equations for vibrational energies of two diatomic species, CO and N_2, as well as the translational-rotational energy equation:

$$\frac{\partial \varepsilon_{vib,j}(x,y,t)}{\partial t} + \nabla\left[D_j \nabla \varepsilon_{vib,j}(x,y,t)\right] = R_j^{las} + R_j^{field} - R_j^{rel},$$

$$\varepsilon_{vib,j}(x,0,t) = \varepsilon_{vib,j}(x,d,t) = \varepsilon_{vib,j}(\pm W,y,t) = \varepsilon_{vib,j}(T_o), \quad \frac{\partial \varepsilon_{vib,j}(0,y,t)}{\partial x} = 0 \tag{10}$$

$$\varepsilon_{vib,j}(x,y,0) = \varepsilon_{vib,j}(T_o)$$

$$\frac{5}{2}kN\frac{\partial T(x,y,t)}{\partial t} + \nabla\left[\lambda\nabla T(x,y,t)\right] = kN(y_{CO}R_{CO}^{rel} + y_{N_2}R_{N_2}^{rel}),$$

$$T(x,0,t) = T(x,d,t) = T(\pm W,y,t) = T_o, \quad \frac{\partial T(0,y,t)}{\partial x} = 0 \tag{11}$$

$$T(x,y,0) = T_o$$

In Eqs. (10,11), $\varepsilon_{vib,j}$ is the average vibrational energy per molecule, the index j stands for CO or N_2, k is the Boltzmann constant, N is the number density, y_{CO} and y_{N2} are mole fractions of CO and N_2 in the mixture, and R_j^{las}, R_j^{field}, R_j^{rel} are the rates of vibrational excitation by the laser and electron impact and vibrational energy relaxation, respectively.

169

It is well known that the vibrational distribution functions (VDF) of diatomic species at the conditions of extreme vibrational disequilibrium sustained by the combined laser and electric field excitation can be strongly non-Boltzmann. Determination of the vibrational level populations of CO and N_2 in such nonuniform plasmas, $f_{v,j}$, would require solution of master equation, i.e. approximately 100 coupled 2-D partial differential equations of the general form

$$\frac{\partial f_{v,j}(x,y,t)}{\partial t} + \nabla[D_j \nabla f_{v,j}] = \left(\begin{array}{c} Laser \\ Excitation \end{array}\right)_{v,j} + \left(\begin{array}{c} Electron \\ Impact \end{array}\right)_{v,j}$$
$$+ (V-T)_{v,j} + (V-V)_{v,j} + (V-E)_{v,j}, \tag{12}$$

which would be rather computationally intense. In Eq. (12), $f_{v,j}$ are the relative populations of vibrational levels (vibrational distribution function) and v is the vibrational quantum number. The explicit expressions for the terms in the right-hand-side of Eq. (12) can be found in [12]. The present kinetic model retains only two equations for the vibrational energy modes of CO and N_2 $\varepsilon_{vib,j}$ (Eqs. (10)), obtained from the master equation (12) using the relations

$$\varepsilon_{vib,j} = \sum_{v} \varepsilon_{v,j} f_{v,j}; \quad \varepsilon_{v,j} = \omega_{e,j} v\left[1 - x_{e,j}(v+1)\right], \tag{13}$$

where $\omega_{e,j}$ and $x_{e,j}$ are the vibrational frequency (in K) and the anharmonicity of the molecules. The vibrational distribution functions (VDFs) of CO and N_2, $f_{v,j}$, have been determined using analytical theory of vibration-vibration (V-V) pumped anharmonic oscillators [13], as a steady-state solution of master equation (12) without space diffusion terms,

$$\frac{f_v}{f_0} = \left\{\begin{array}{l} \exp\left(-\frac{E_1 v}{T_v} + \frac{\Delta E v(v-1)}{T}\right); \quad v \le v_0 = \frac{1}{2} + \frac{T}{2x_e T_v} \\ \\ \exp\left(-\frac{v_0^2 \Delta E}{T}\right)\left(\frac{v_a - v}{v_a - v_0}\right)^{1/2} \frac{v_0 + 1}{v+1} \\ \\ -\frac{T}{12\Delta E} \frac{\delta_{VV}^3}{y_j \widetilde{Q}_{10}} \sum_{M} \frac{y_M P_{10}^M \exp(\delta_{10}^M v)}{\delta_{10}^M} \frac{1}{v+1}; \quad v > v_0 \end{array}\right. \tag{14}$$

In Eq. (14), $E_1 = \omega_e(1-2x_e)$, $\Delta E = \omega_e x_e$, $T_v = E_1/\ln(f_1/f_0)$ is the first level vibrational temperature, P_{10}, $\tilde{Q}_{10}$, δ_{VT}, and δ_{VV} are the parameters in the expressions for the V-T and V-V rate coefficients,

$$P_{v+1,v}^{M} = P_{10}^{M}(v+1)\exp(\delta_{VT}^{M}v),$$ (15)

$$Q_{v+1,v}^{w,w+1} = (v+1)(w+1)\left\{Q_{10}^{S}\exp\left(-\delta_{VV}|v-w|\right)\left[\tfrac{3}{2}-\tfrac{1}{2}\exp\left(-\delta_{VV}|v-w|\right)\right] + Q_{10}^{L}\exp\left(-\Delta_{VV}(v-w)^2\right)\right\},$$ (16)

$$\tilde{Q}_{10} = Q_{10}^{S} + \frac{\delta_{VV}^{3}}{12\Delta_{VV}}\left(\frac{\pi}{\Delta_{VV}}\right)^{1/2}Q_{10}^{L},$$ (17)

y_M is the V-T relaxation collision partner mole fraction, and $v_a = E_a/E_1$ is the activation level of the vibration-to-electronic (V-E) energy transfer process,

$$CO(X^1\Sigma, v \sim 40) + CO \rightarrow CO(A^1\Pi, v \sim 0) + CO,$$ (18)
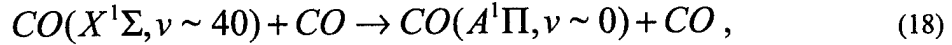
The analytic VDFs of Eq. (14) are in good agreement with steady-state distribution functions obtained by numerical integration of master equation with the V-T and V-V rates given by Eqs. (15,16) [14]. In the present calculations, the two VDFs have been determined iteratively from Eq. (13) using the functional dependence (14) on the first level vibrational temperatures, $T_{v,j}$, as adjustable parameters. This approach greatly reduces the number of equations solved while taking into account the key effect of strongly non-Boltzmann distribution function on the associative ionization rate in the plasma. Note that this approach assumes that both vibrational distributions are quasi-steady-state and that their perturbation by diffusion is weak.

The rate of CO vibrational excitation by resonance absorption of the CO laser radiation, used in Eq. (10), is evaluated as follows [12],

$$R_{CO}^{las} = \sum_{v,J}\frac{A_v B_v}{8\pi ckT}\left(\frac{c}{v}\right)^3 I_v\,\theta\,S_J\exp\left(-\frac{B_v J(J+1)}{T}\right)\varepsilon_v f_v,$$ (19)

where A_v is the Einstein coefficient for spontaneous radiation, B_v is the rotational constant, v is the laser line frequency, I_v is the laser line power density, θ is the absorption line shape factor, J is the rotational quantum number, and S_J is the Honl-London factor.

The rate of vibrational excitation of CO and N_2 molecules by electron impact in the presence of the RF field is approximated as

$$R_j^{field} = \frac{\vec{j} \cdot \vec{E}}{Nk} \tag{20}$$

The approximation of Eq. (20) is applicable in the range of the reduced electric field $E/N \cong (0.5\text{-}5.0)\cdot 10^{-16}$ V·cm^2, where more then 95% of the input electric power, $\vec{j} \cdot \vec{E}$, goes to vibrational excitation of CO and N_2 [10].

The rate of energy relaxation from the vibrational mode of each diatomic species with the vibrational distribution function (VDF) given by Eq. (14) is evaluated as follows [13],

$$R_j^{rel} = E_1 \frac{6\tilde{Q}_{10}\Delta E}{T\delta_{VV}^3}(v_0 + 1)^2 \exp\left(-\frac{2v_0^2 \Delta E}{T}\right)y_j N$$
$$+ E_1 Q_{10}^{(01)'} \exp\left(\frac{E_1 - E_1'}{T}\right)\left(f_1 f_0' - f_0 f_1'\right)y_j N, \tag{21}$$

In Eq. (21), the first term in the right-hand-side represents the intra-mode energy relaxation rate due to V-T, V-V, and V-E processes combined, while the second term is the energy relaxation rate due to the V-V' energy exchange between vibrational modes of CO and N_2,

$$CO(v) + N_2(v') \rightarrow CO(v-1) + N_2(v'+1) \tag{22}$$
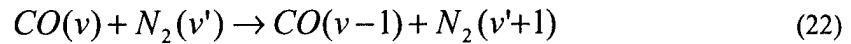
Again, Eq. (21) is in good agreement with the steady-state energy relaxation rate obtained from the numerical solution of the master equation [14].

The electron production rate by the associative ionization mechanism of Eq. (1), used in Eq. (9), is calculated as follows,

172

$$S = k_{ion} N^2 y_{CO}^2 \sum_{E_v + E_w > E_{ion}} f_{v,CO} f_{w,CO} \,, \tag{23}$$

The electron and ion mobilities and diffusion coefficients in a nitrogen plasma as functions of the reduced electric field E/N, where N=P/kT is the number density, are taken from [15,16]. The V-V and V-T rates in CO-N_2-He mixtures are taken from [12,17]. The CO pump laser spectum is taken to be the same as in [18].

Direct numerical solution of coupled partial differential equations (7,8,10,11) remains rather problematic due to the fact that the characteristic time scales for reaching the quasi-steady-state distributions of electric field, $\tau_{RF} \sim d/w_{dr}$, vibrational populations and electron density, $\tau_{vib} \sim \tau_{ion} \sim E_1 / R^{rel}$, and gas temperature, $\tau_{HT} \sim d^2/D$, are widely different,

$$\tau_{RF} \sim 10^{-6} \sec \quad << \quad \tau_{vib} \sim \tau_{ion} \sim 10^{-4} - 10^{-3} \sec \quad << \quad \tau_{HT} \sim 1 \sec \tag{24}$$

In the above estimates, $d \sim 1$ cm, $w_{dr} = \mu_e E \sim 10^6$ cm is the electron drift velocity, and $D \sim 1$ cm^2/s is the diffusion coefficient. The values of τ_{vib} for CO and N_2 are estimated from Eqs. (14,21) for $T \sim 300$ K, $T_v(CO) \sim 3000$ K, $N \sim 10^{18}$ cm^{-3}, $y_{CO} \sim 0.01$, and $y_{N2} \sim 1$. For this reason, the RMS electric field distribution has been evaluated by integrating Eqs. (7,8) separately, over the time period $\Delta t_1 \sim \tau_{RF}$, and then assumed to remain unchanged while integrating Eqs. (10,11) over $\Delta t_2 \sim \tau_{vib} \sim \tau_{ion}$. These two stages were repeated until the steady-state spatial distribution of RMS electric field, RMS charged species concentrations, vibrational level populations, and gas temperature was achieved over $\Delta t_3 \sim \tau_{HT}$.

In the calculations discussed in the following section, the 3 cm diameter circular electrodes (see Fig. 3) are modeled as square electrodes of the same surface area. The electrode separation and full width are d=1 cm and 2W=2.66 cm. The CO laser beam power distribution is assumed to be Gaussian with the $1/e^2$ radius of 1 mm. Calculations are made for a CO-N_2 mixture with 1.4% of CO at P=300 torr. To simulate the effect of additional V-T relaxation produced by addition of small amounts of NO to the plasma, the model gas mixture was also assumed to contain 1% helium. The RF voltage amplitude and frequency are U_0=1500 V and ν=10 MHz, respectively. The system of equations (7,8,10,11) is solved using standard stiff PDE solver PDECOL [19].

173

4. Results and Discussion

4.1. Experimental Measurements

Previously, it was shown that RF coupling to free electrons produced in an optically pumped CO plasma enhances the vibrational disequilibrium induced in the path of the laser excitation beam [1]. The current results show that this effect is not limited to the volume occupied by the CO laser beam, which is approximately 2 mm in diameter and 10 cm long. Indeed, as can be seen in Figs. 4 and 5, the N_2 Raman spectra band intensities (i.e. the fractional vibrational level populations) increase when the RF field is applied, both at the CO laser beam axis (see Fig. 4), and away from the CO laser beam (see Fig. 5). Note that the Raman spectra with the RF applied have been scaled and baseline corrected to match the intensity of the $v=0$ peak when the RF is off. This effect is also illustrated in Fig. 6, which shows fractional vibrational level populations. From Fig. 6, one can see that the vibrational level populations for $v=1-4$ become greater when the RF filed is applied. As discussed in Section 2, the RF power is coupled to the vibrational mode of the diatomic molecules via the free electrons produced in the laser-sustained plasma.

Analysis of the spontaneous Raman spectra of N_2 provides insights into the vibrational population distribution. The vibrational state fractional populations are proportional to the intensity of the corresponding peaks after scaling by $1/(v + 1)$. When the spectra of the RF and laser sustained plasmas for a coaxial alignment of the pump and probe beams are compared, the increase in fractional population of states with larger v becomes apparent. By comparing the relative peak heights a greater fractional population is found in states with larger v for the RF sustained plasma. This is illustrated in the Boltzmann plot for that case Fig. 6.

Similar analysis of the case in which the probe and pump beam are not coaxial show a similar result. At a vertical separation of 2.25 mm, when a RF field is not applied, the vibrational nonequilibrium is diminished. However, when a vertically aligned RF field is applied the vibrational loading of the molecule intensifies. This is demonstrated in the Raman spectra and fractional population analysis shown in Figs. 5 and 6. It is important to note that at each probe position the fractional population of states with higher v becomes greater when a RF field is applied. By subjecting the plasma to the RF field a wider distribution of vibrational states is obtained.

The broadening of the vibrational state distribution may be demonstrated quantitatively by defining an equivalent Boltzmann temperature. The equivalent Boltzmann temperature is the slope of the vibrational distribution function at $v=0$, defined as follows

$$T_v = \frac{\theta_v}{\ln\left(f_0 / f_1\right)} \qquad (25)$$

In Eq. (25), $\theta_v = 3353° K$ is the characteristic vibrational temperature for N_2 and f_0/f_1 is the ratio of the fractional populations for vibrational levels $v=0$ and $v=1$. Illustrated in Fig. 12 are the first level equivalent Boltzmann temperatures for varying degrees of separation between the probe and pump beam in the vertical plane. Note that with a vertical displacement between the probe and pump beam the equivalent Boltzmann temperatures never drop below 2000° K when the RF field is applied, even at a displacement of more than 5 mm. Examining the vibrational temperature at the maximum and minimum displacements exhibits this behavior. At coaxial alignment there is a percent gain of approximately 10%. However, at the maximum displacement the percent gain is almost 60%. It is important to note that the increase in vibrational temperature is not due to simple heating of the species present. The translational/rotational temperature does not approach the vibrational temperature in any of the cases presented.

The translational/rotational temperatures were inferred from the Raman spectra by comparing the peak intensities of a vibrationally pumped sample to that of a vibrationally cold sample. These temperatures were calculated as follows,

$$T_H = T_C * \left(\frac{I_C}{I_H}\right) \qquad (11)$$

where T_C is the cold gas temperature (300° K), I_C is the intensity of the cold peak and I_H is the integrated scaled intensity $[1/(v+1)]$ of the peaks in the vibrationally hot spectra. Temperatures inferred from the Raman spectra using this method can be found in Fig. 13. Note that this method provides only a rather crude estimate of the temperature since the rotational band structure is ignored. In addition, at large displacement between the pump and probe beam the probe beam path begins to become blocked, causing the probe beam to scatter. This might well introduce an additional error in the temperature inference. Note that the first level vibrational temperature remains much greater than the translational temperature at all data points measured (see in Figs. 12 and 13).

4.2. Modeling Calculations

Figures 7-10 show contour plots of the calculated first level vibrational temperatures of CO and N_2, as well as the translational temperature and the electron density in optically pumped CO/N_2/He

175

plasmas. The left half of each of these plots refers to the parameter distribution in the plasma sustained by a CO laser alone, while the right half shows distribution of the same parameters in the plasma sustained by a combination of the laser and the RF field. For the laser/RF sustained plasma, the parameters shown have been averaged over the RF field oscillation period. From Figs. 7 and 8, it can be seen that applying the RF field to the optically pumped plasma produces a stronger vibrational disequilibrium, with vibrational temperatures of both CO and N_2 considerably increasing (from $T_v(CO)=3700$ K to 4300 K and $T_v(N_2)=2500$ K to 2900 K on the laser beam centerline). Note that with the RF field turned on the size of the vibrationally nonequilibrium region also substantially increases (roughly by a factor of 2 in the x-direction).

Calculations of the energy balance in the plasma shows that the absorbed laser power in the region between the electrodes is 0.9 W, while the RF power coupled to the plasma is greater by approximately a factor of 2, 1.9 W. In other words, using the sub-breakdown RF field nearly triples the total power added to the plasma. More rapid vibrational energy relaxation in V-V exchange processes in the laser/RF sustained plasma produces additional heat removed from the plasma by conduction. Diffusion of vibrationally excited molecules provides another channel of energy removal from the plasma. In the present calculations, convective cooling of the gas mixture in the slow-flow absorption cell is neglected. From Fig. 9, one can see that the calculated translational temperature on the laser beam axis increases from T=470 K in the laser-sustained plasmas to T=600 K in the laser/RF sustained plasma.

Analysis of Fig. 10 shows that the electron density in the presence of the RF field is greatly reduced, from $n_e=0.8 \cdot 10^{11}$ cm^{-3} to $0.6 \cdot 10^{10}$ cm^{-3}. This result is not surprising since additional heating produced by relaxation processes in the presence of the RF field considerably increases the V-T rates (especially among the high vibrational levels of CO). This results in depletion of the high CO vibrational level populations (at v≥30-35), as shown in Fig. 11, and reduces the rate of ionization by the associative ionization mechanism. This effect, i.e. the negative feedback between the temperature rise and the ionization rate self-stabilizes the plasma and precludes the ionization-heating instability development. On the other hand, the same effect self-limits the amount of RF power coupled to the plasma. However, the electron density and consequently the power coupled to the plasma can both be increased by reducing the translational temperature (e.g. using convective cooling of the plasma in a fast-flow absorption cell). This may considerably increase energy stored in vibrational mode energies of CO-containing molecular gas mixtures at high pressures.

Figure 12 compares the measured and the calculated N_2 vibrational temperatures in the plasma along the line between the electrode centers. One can see that in the absence of the RF field the agreement is quite satisfactory. With the RF field turned on, the calculated vibrational temperature turns out to be somewhat lower than in the experiment. The difference between the experiment and the calculations is

176

within 20% except for one data point taken at y/d=0.94, or less than 1 mm away from the bottom electrode. We believe that at this location scattering of the probe Nd:YAG laser beam off the electrode surface might considerably increase the uncertainty in the measured vibrational level populations. Additional measurements with a smaller separation between the measurement points are necessary to estimate reproducibility of the data and the magnitude of this effect.

Figure 13 shows the measured and the calculated translational temperature of the plasma along the line between the electrode centers. Again, with the RF field turned off and far from the electrodes the agreement is satisfactory. However, temperature measured closer to the bottom electrode (within 2.5 mm) appears to be considerably higher than on the laser beam centerline. The same effect is observed with the RF field turned on (see Fig. 13). Again, probe laser beam scattering off the electrode surface might account for this counterintuitive behavior of the gas temperature in both these cases. With the RF field on, the discrepancy between the calculated and the measured temperature becomes quite substantial, up to 50-100% (see Fig. 13). There are two most likely reasons for such considerable disagreement. First, the translational temperature inferred from the intensities of the rotationally unresolved vibrational bands of the Raman spectra (see Section 2) can be considered only as a fairly crude estimate, since the individual rotational line contribution is not taken into account. Second, there is a considerable uncertainty in the pivotal parameter of the kinetic model controlling the steady-state ionization rate and therefore the RF power coupled to the plasma (as well as the gas temperature), i.e. the temperature dependence of the CO V-T rates among the high vibrational levels ($v \geq 30-35$). Weak V-T rate temperature dependence would produce a fairly strong gas heating before the CO vibrational populations would be depleted thereby slowing down the ionization. On the other hand, steep rise of the V-T rates with temperature would slow down the ionization at more moderate temperatures.

These V-T rates are most likely controlled by collisions of highly vibrationally excited CO molecules with fast relaxer trace species, such as products of the CO disproportionation reaction, including carbon clusters, or NO molecules present in the plasma. Currently, the data on the rates of these processes are not available. Therefore, in the present calculations, the self-termination of ionization by V-T relaxation is modeled semi-qualitatively, by adding 1% of helium to the baseline CO/N_2 mixture, which might well affect the accuracy of the model predictions. Additional temperature measurements in $CO/N_2/He$ optically pumped plasmas using the rotationally resolved Raman spectra [20] are needed to resolve this issue.

5. References

1. E. Ploenjes, P. Palm, W. Lee, W. R. Lempert, and I.V. Adamovich, "RF Energy Coupling to High-Pressure Optically Pumped Plasmas." Journal of Applied Physics, vol. 89, No. 11, 2001, pp. 5911-5918

2. W. Lee, I.V. Adamovich, and W.R. Lempert, "Optical Pumping Studies of Vibrational Energy Transfer in High-Pressure Diatomic Gases", Journal of Chemical Physics, vol. 114, 2001, p. 1178-1186

3. I. Adamovich, S. Saupe, M.J. Grassi, O. Schulz, S. Macheret, and J.W. Rich, Chem. Phys., vol. 173, 1993, p. 491

4. I.V. Adamovich and J.W. Rich, J. Physics D: Applied Physics, vol. 30, 1997, p. 1741

5. E. Plönjes, P. Palm, I.V. Adamovich, and J. W. Rich, "Ionization Measurements in Optically Pumped Discharges", Journal of Physics D: Applied Physics, vol. 33, No. 16, 2000, p. 2049

6. I.V. Adamovich, "Control of Electron Recombination Rate and Electron Density in Optically Pumped Nonequilibrium Plasmas", Journal of Physics D: Applied Physics, vol. 34, 2001, p.319

7. J. W. Rich, "Relaxation of Molecules Exchanging Vibrational Energy", in "Applied Atomic Collision Physics", vol. 3, "Gas Lasers", ed. E.W. McDaniel and W.L. Nighan, Academic Press, New York, 1982, pp. 99-140

8. Y. Kaufman, P. Avivi, F.Dothan, H. Keren, J. Malinowitz, J. Chem. Phys., Vol. 72, 1980, p. 2606

9. R. Johnsen, "Recombination of Cluster Ions", in B.R. Rowe et al. (eds.), "Dissociative Recombination", Plenum, New York, 1993

10. Raizer, Y.P., "Gas Discharge Physics", Springer-Verlag, Berlin, 1991

11. P. Palm, E. Plönjes, M. Buoni, V.V. Subramaniam, and I.V. Adamovich, "Electron Density and Recombination Rate Measurements in CO-Seeded Optically Pumped Plasmas", Journal of Applied Physics, vol. 89, No. 11, 2001, pp. 5903-5910

12. C. Flament, T. George, K.A. Meister, J.C. Tufts, J.W. Rich, V.V. Subramaniam, J.-P. Martin, B. Piar, and M.-Y. Perrin, "Nonequilibrium Vibrational Kinetics of Carbon Monoxide at High Translational Mode Temperatures", Chemical Physics, Vol. 163, 1992, p. 241

13. B.G. Gordiets and S.A. Zhdanok, "Analytic Theory of Ahnarmoinic Oscillators", in Nonequilibrium Vibrational Kinetics, "ed. by M. Capitelli, Springer, Berlin, 1986

14. I.V. Adamovich, S.O. Macheret, and J.W. Rich, "Spatial Nonhomogeneity Effects in Nonequilibrium Vibrational Kinetics", Chemical Physics, vol. 182, 1994, pp. 167-183

15. L.G.H Huxley and R.W. Crompton, "The Diffusion and Drift of Electrons in Gases", Wiley, New York, 1974

16. E.W. McDaniel, "Collision Phenomena in Ionized Gases", Wiley, New York, 1964

17. E. Ploenjes, P. Palm, W. Lee, M. D. Chidley, I.V. Adamovich, W.R. Lempert, and J. William Rich, "Vibrational Energy Storage in High-Pressure Mixtures of Diatomic Molecules", Chemical Physics, vol. 260, 2000, pp. 353-366

18. E. Ploenjes, P. Palm, A.P. Chernukho, I.V. Adamovich, and J.W. Rich, "Time-Resolved Fourier Transform Infrared Spectroscopy of Optically Pumped Carbon Monoxide", Chemical Physics, vol. 256, pp. 315-331, 2000

19. N.K. Madsen and R.F. Sincovec, ACM Trans. Math. Software, vol. 5, 1979, p. 326

20. W. Lee and W.R. Lempert, AIAA Paper 2002-0394
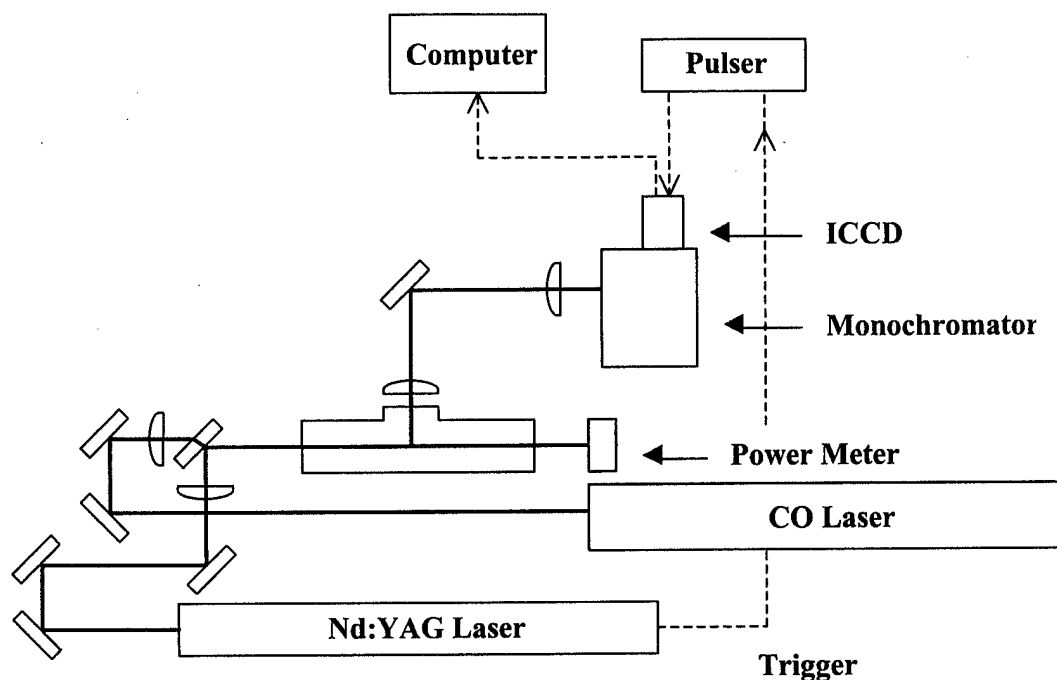
Figure 1. Experimental apparatus for spatially resolved Raman measurements.
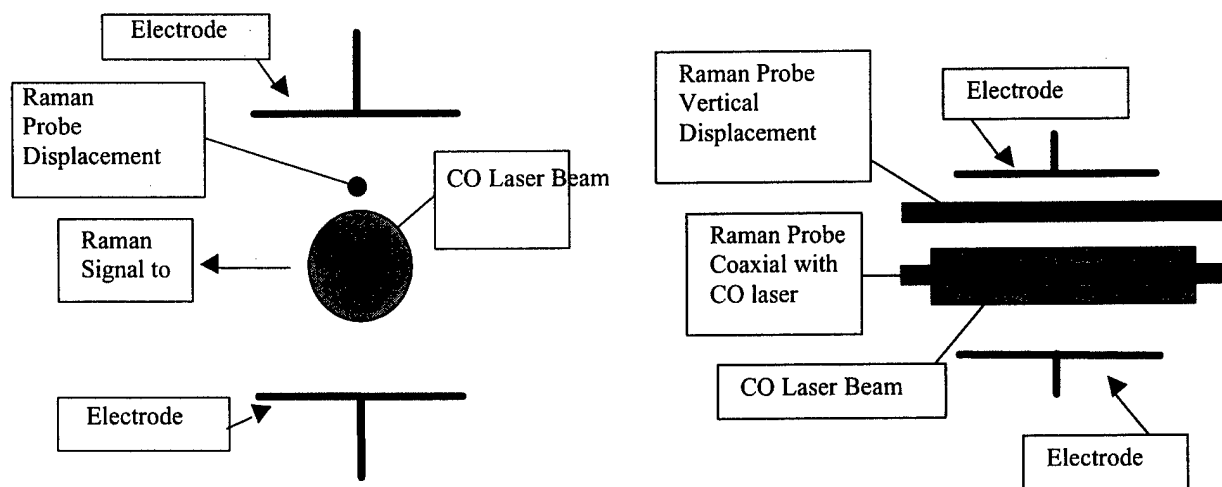
Figure 2. Schematic of electrode arrangement and CO laser and Nd:YAG laser beams at various measurement point locations.
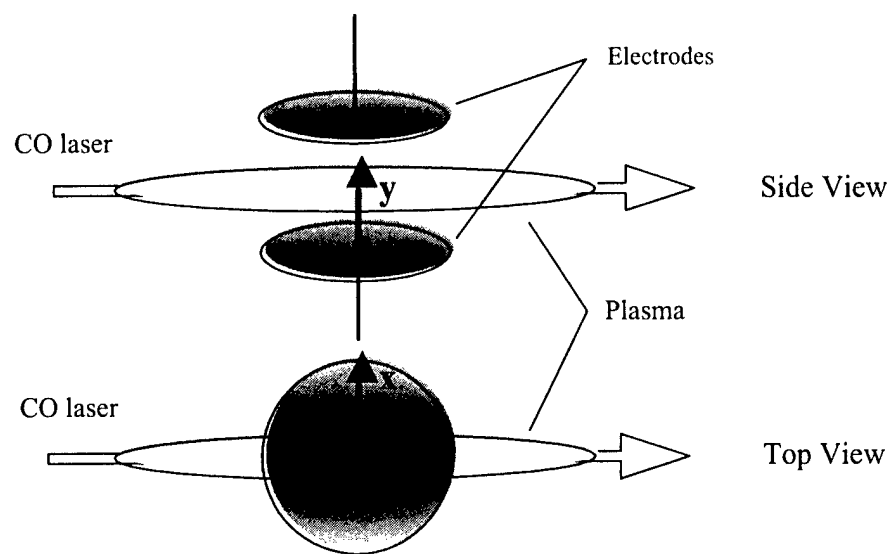
Figure 3. Schematic of electrodes in the cell and of the discharge geometry
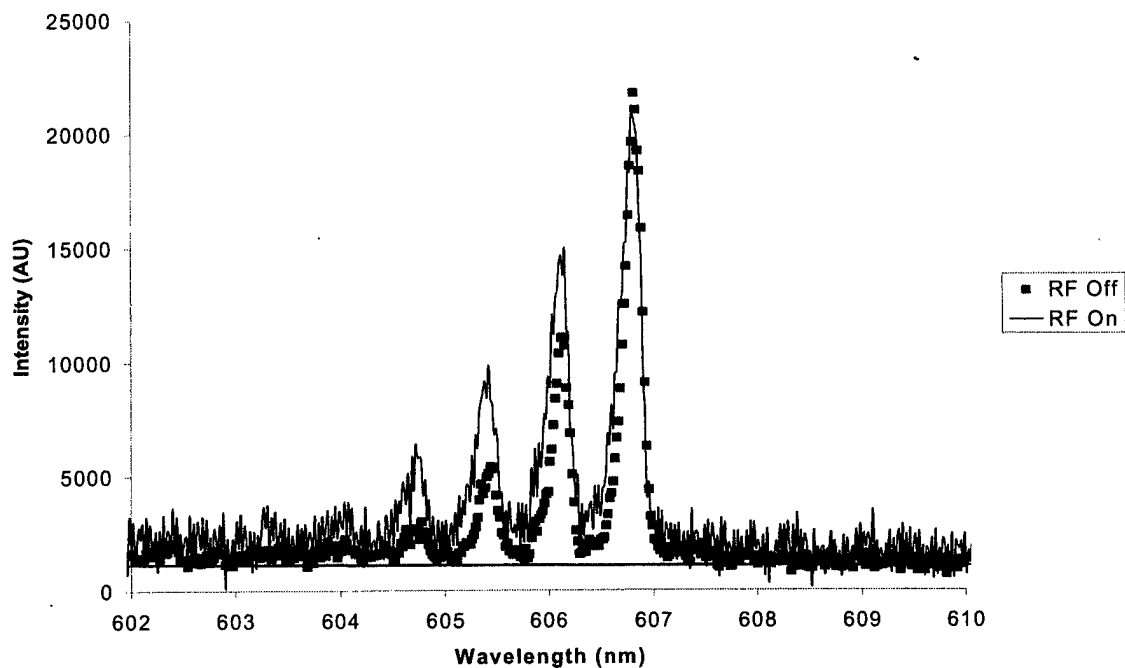
Figure 4. Raman spectra of vibrationally excited N_2 for the coaxial orientation of the pump and the probe laser beams, with the RF field on and off.
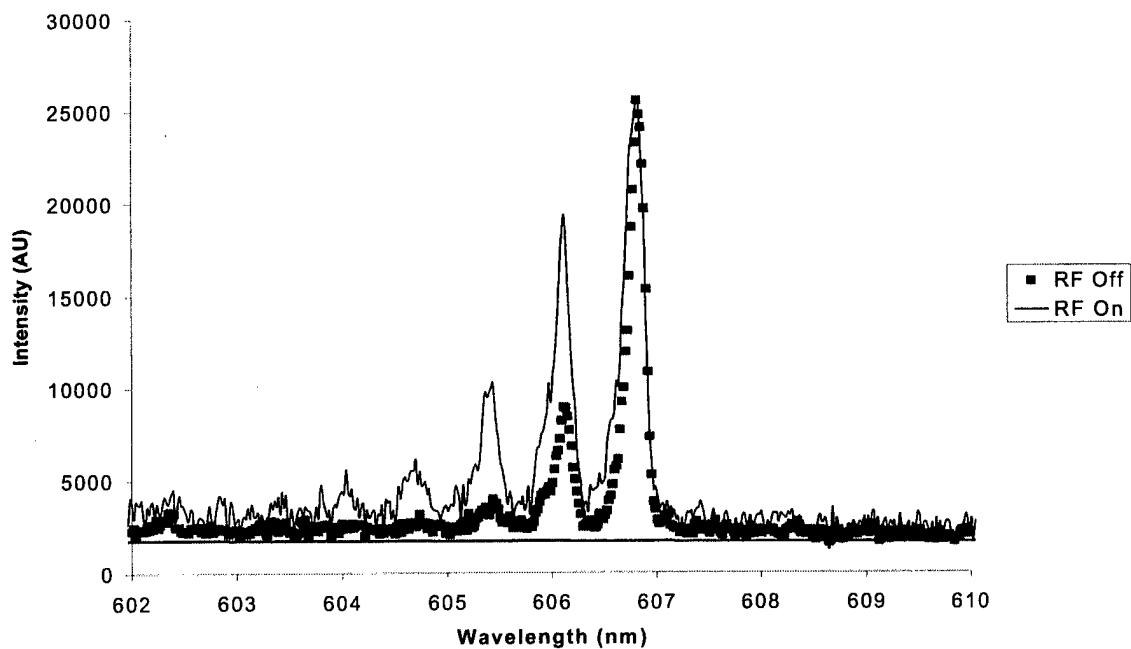
Figure 5. Raman spectra of vibrationally excited N_2 with a 2.25 mm vertical separation between the pump and the probe laser beams, with the RF field on and off.
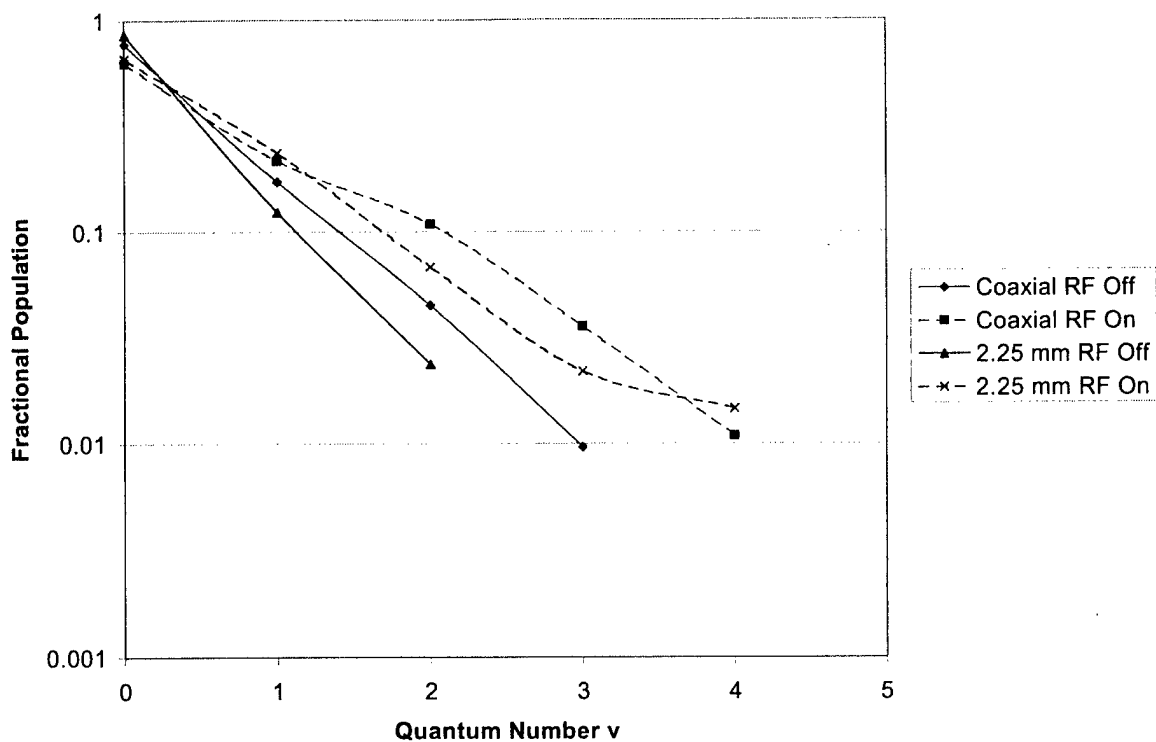
Figure 6. N_2 vibrational level populations for two different locations of the probe laser beam.

CO vibrational temperature, K
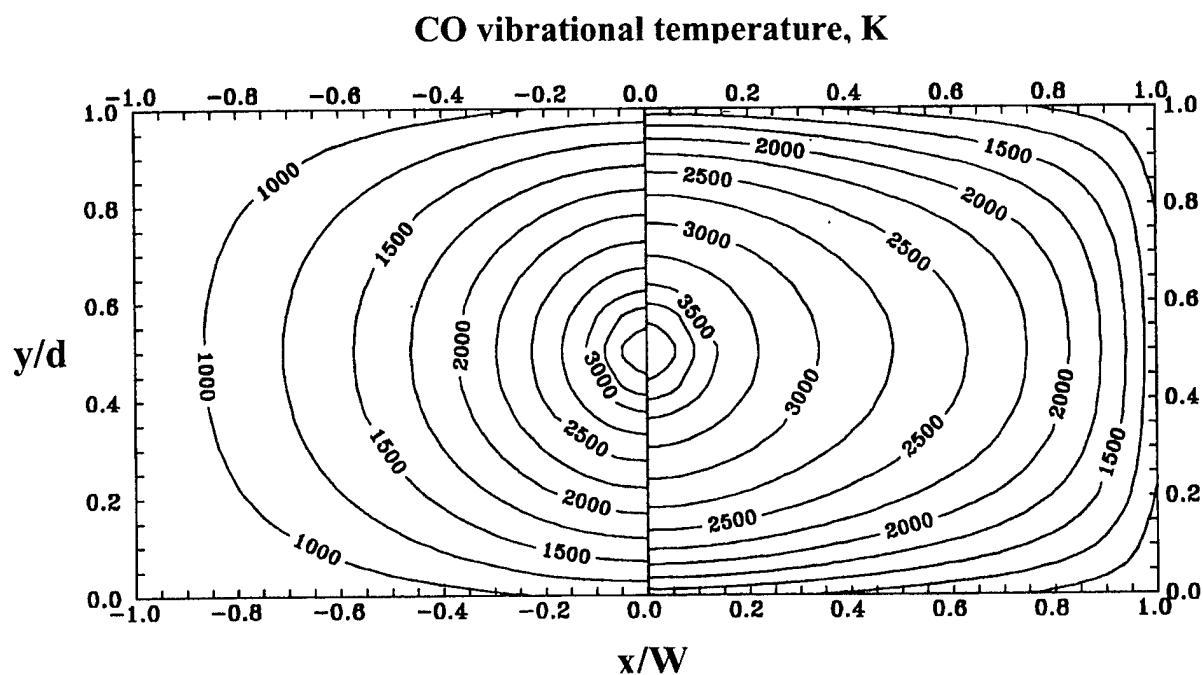
Figure 7. First level vibrational temperature of CO in the optically pumped CO/N_2 plasma without **(left)** and with **(right)** RF field applied.

N₂ vibrational temperature, K
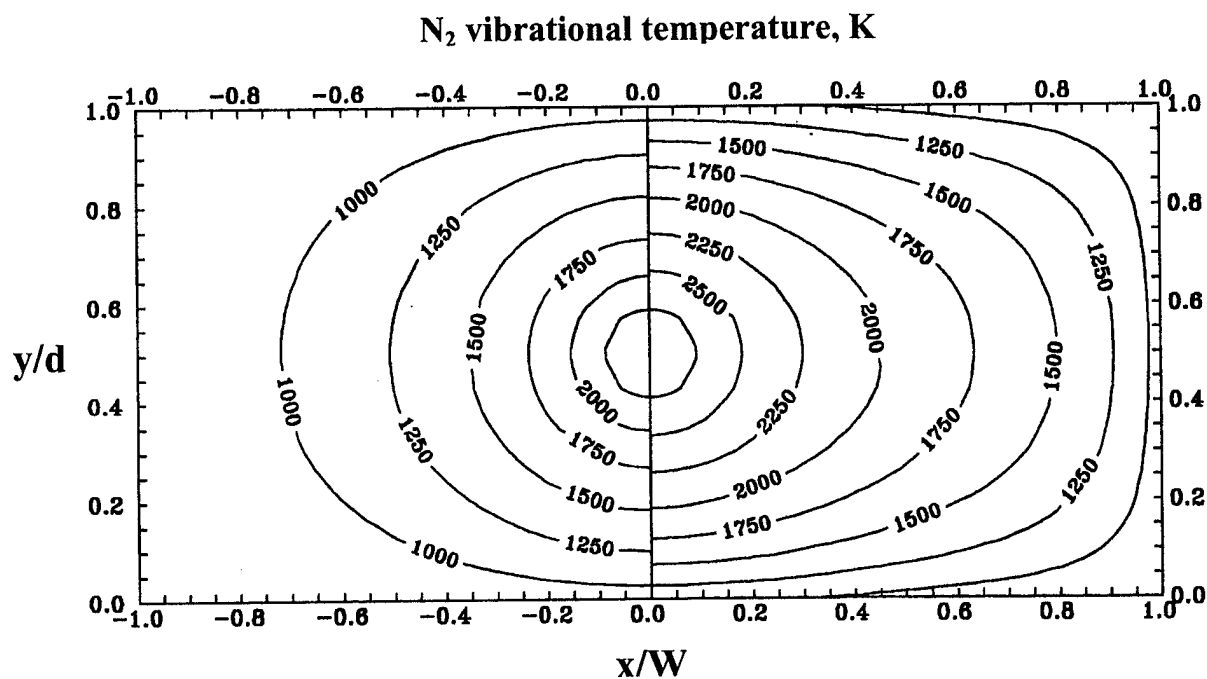
Figure 8. First level vibrational temperature of N_2 in the optically pumped CO/N_2 plasma without (**left**) and with (**right**) RF field applied.

Translational temperature, K
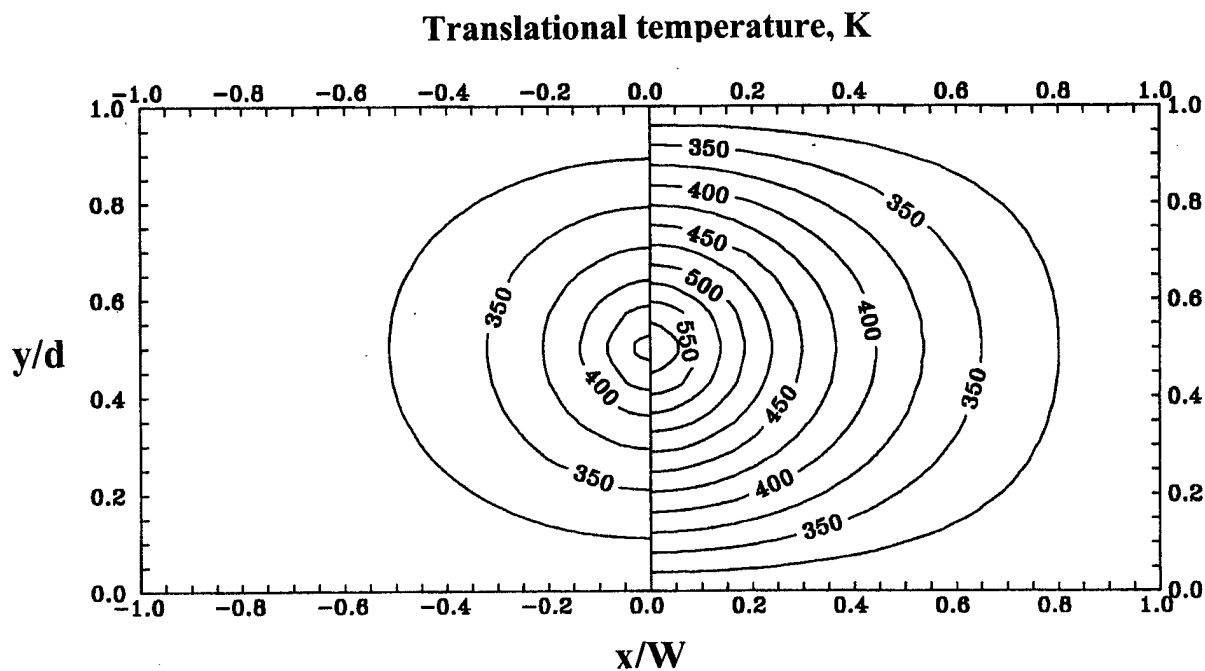
Figure 9. Translational temperature distribution in the optically pumped CO/N_2 plasma without (**left**) and with (**right**) RF field applied.

Electron density, log(cm³)
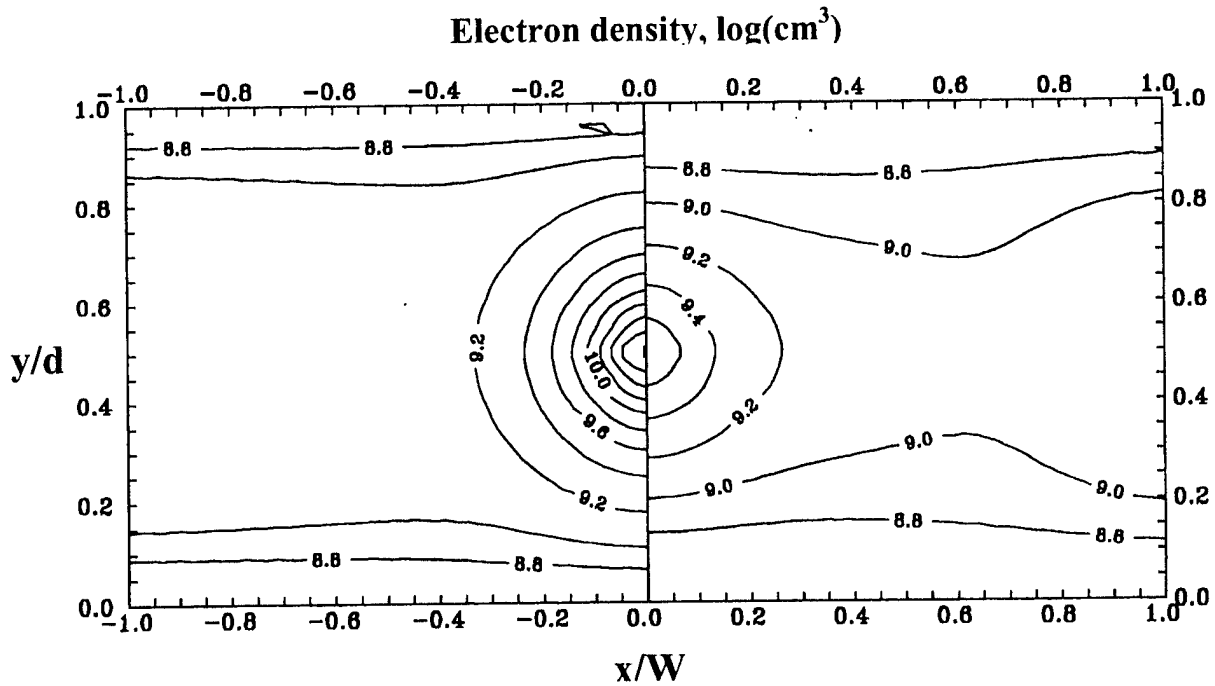
Figure 10. Electron density distribution in the optically pumped CO/N₂ plasma without (**left**) and with (**right**) RF field applied.

Relative population

x/W=
——— 0.00
——— 0.13
——— 0.30
——— 0.50
——— 0.74
——— 1.00

Vibrational quantum number

Relative population

x/W=
——— 0.00
——— 0.13
——— 0.30
——— 0.50
——— 0.74
——— 1.00

Vibrational quantum level
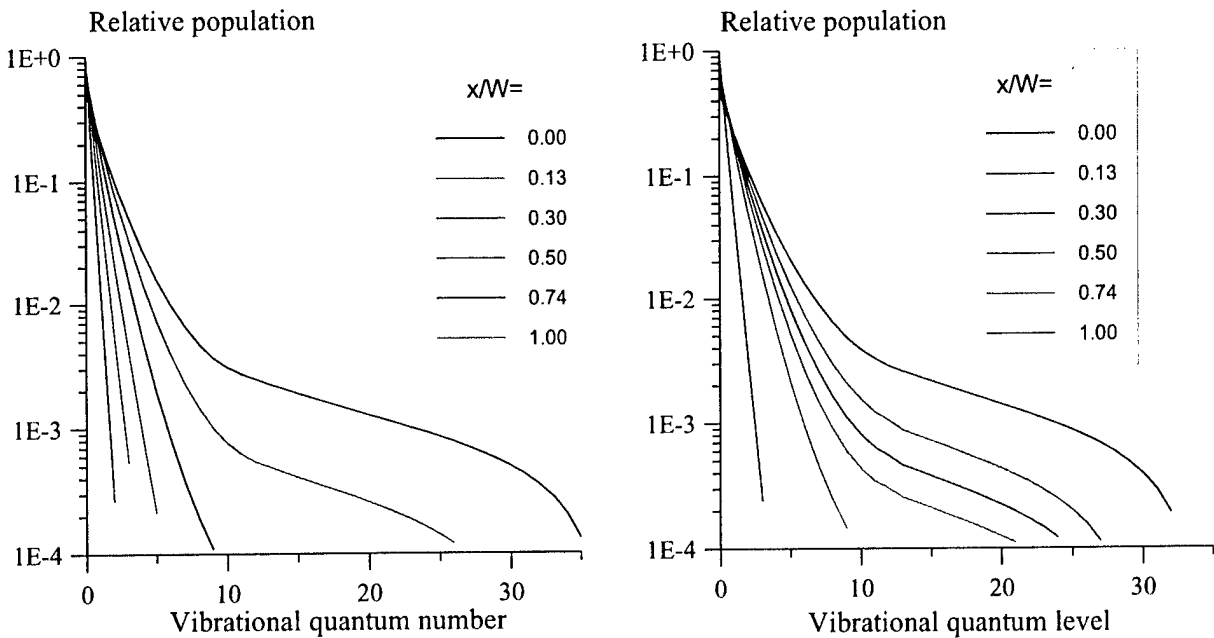
Figure 11. CO vibrational distribution functions along the centerline between the electrodes (at y=0.5) in the optically pumped CO/N₂ plasma without (**left**) and with (**right**) RF field applied.
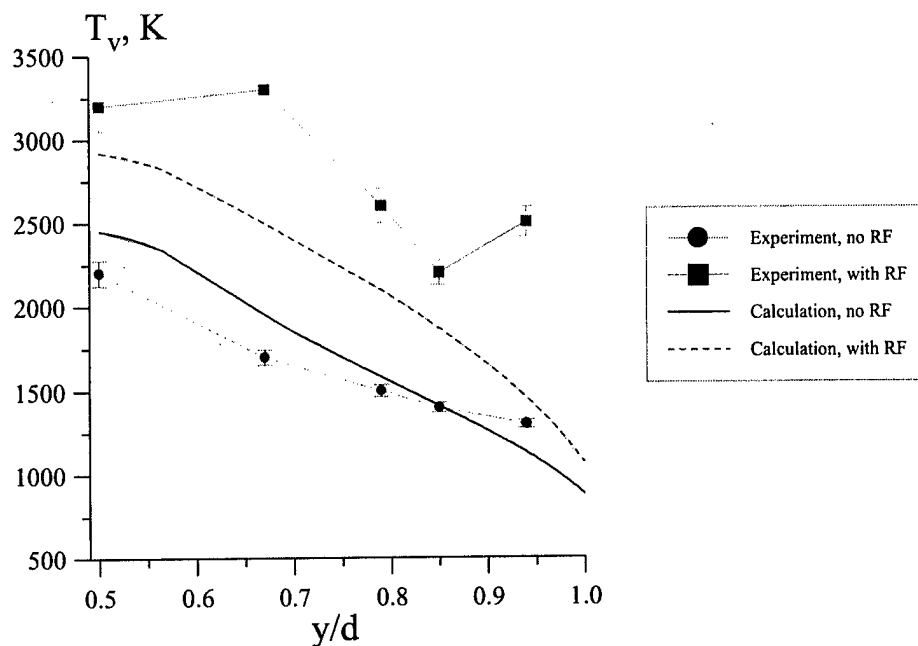
Figure 12. Comparison of the measured and calculated N_2 vibrational temperature in the optically pumped CO/N_2 plasma with and without RF field applied (at x=0).
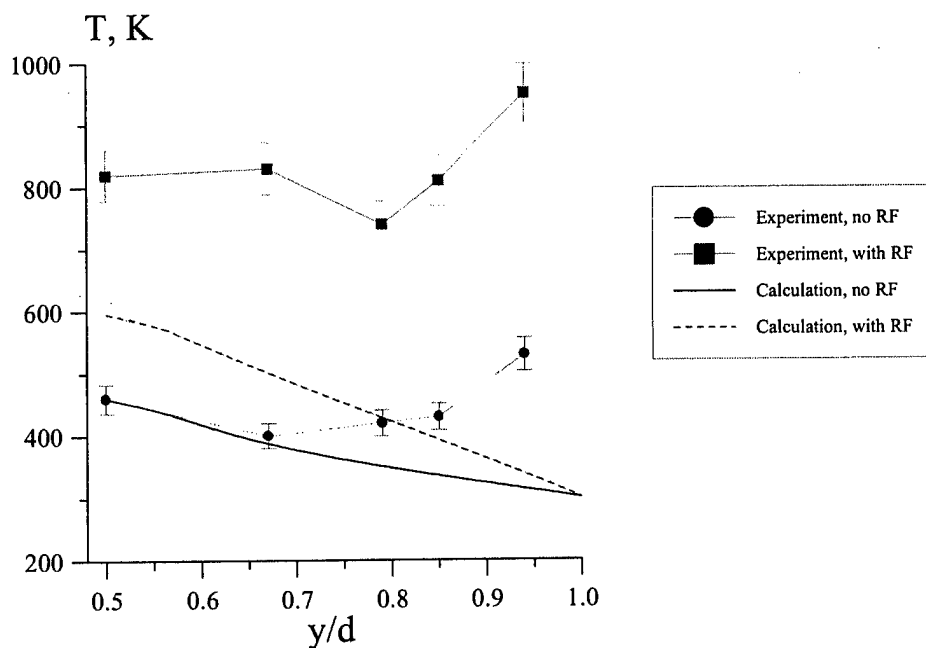
Figure 13. Comparison of the measured and calculated translational temperature in the optically pumped CO/N_2 plasma with and without RF field applied (at x=0).

10. HIGH PRESSURE AIR PLASMAS SUSTAINED BY AN ELECTRON BEAM AND ENHANCED BY OPTICAL PUMPING

Peter Palm, Elke Plönjes, Igor V. Adamovich, Vish V. Subramaniam, Walter R. Lempert,

and J. William Rich

This chapter presents experimental work on the concept of using an electron beam as an efficient volume ionization source combined with optical pumping. The optical pumping is used to vibrationally excite diatomic molecules in the plasma in order to reduce the overall electron removal rate. By this means, the power budget to sustain a stable plasma in low temperature, atmospheric pressure air is significantly reduced.

We present time-resolved electron density measurements in e-beam excited air plasmas. Vibrational excitation of the air species using optical pumping was found to reduce the electron recombination rate by more than one order of magnitude and the effective electron attachment rate by at least three orders of magnitude.

1. Introduction

Sustaining large-volume plasmas in atmospheric pressure air presents an extremely challenging problem. Among the most critical technical issues that have to be addressed to resolve this problem are the plasma power budget and stability. Numerous aerospace applications such as supersonic flow control, supersonic combustion control, and nonequilibrium MHD propulsion require an ability to initiate and sustain large volume (~1 m^3), relatively cold (T<2000 K) diffuse plasmas in atmospheric air, with electron density up to n_e~10^{13} cm^{-3}. For these applications, a power budget of the order of 1-10 MW/m^3 is desired. Finally, these plasma conditions are to be maintained for relatively long times, at least for 10 msec.

These goals define a highly nonequilibrium molecular plasma. The simultaneous requirement of electron densities of 10^{13} cm^{-3} and gas temperatures at or below 2000 K represent an enormous departure from thermodynamic equilibrium, and rule out the use of purely thermal plasmas, such as high temperature arc discharges, to achieve this result. This can be illustrated by simple estimates using the Saha equation for a thermal equilibrium air plasma. For example, to achieve the stated electron density by merely heating the air, a gas temperature of ~ 4300 K would have to be maintained. Conversely, if atmospheric-pressure air were maintained at only the desired maximum gas temperature of 2000 K, the equilibrium electron density would be only ~ 10^6 cm^{-3}, many orders of magnitude below the desired value.

The preceding requirements have mandated examination of approaches using low-temperature nonequilibrium plasmas, of the general type characterized as glow discharges. Such systems have long been demonstrated to provide highly nonequilibrium plasmas, with relatively high free electron densities, with the requisite lower gas temperatures. However, if self-sustained discharges, lacking an external ionization source, are used, such glows are usually only struck at low pressures, well below even 0.1 atm. Various methods have been used to extend the range of such self-sustained discharges to near atmospheric pressures, such as the use of individually ballasted multiple cathodes, short duration radio frequency high-voltage pulse stabilization, or aerodynamic stabilization [1-5]. Typically, however, the energy efficiency of such discharges is much lower than desired for the present goal, since only a small fraction of the input electrical power goes into ionization.

An alternative approach is the use of non-self-sustained glow discharges, in which some or all of the required volume ionization is provided by an external source, such as an electron beam [6,7]. Electron beams are identified as having by far the lowest power budget among all nonequilibrium ionization methods [8-10]. Further, reliance on an external ionization source mitigates another principal difficulty known to exist in high-pressure discharges at large current densities. The well-known glow-to-arc-transition, with subsequent plasma thermalization, can be significantly delayed or avoided altogether.

There is recent experimental evidence that vibrational excitation of diatomic species produced by a CO laser may reduce the rates of electron removal (dissociative recombination and attachment to oxygen) in nonequilibrium plasmas [11]. In the present work, we use the same approach as in Ref. [11], i.e. optical pumping by a CO laser, to modify the electron removal rates in the electron beam sustained, CO-seeded high-pressure air plasma.

First, electron impact ionization of vibrationally excited molecules produced by a CO laser can create vibrationally excited molecular ions such as N_2^+ and O_2^+,

$$N_2(v) + e_{beam}^- \rightarrow N_2^+(v) + e_{beam}^- + e_{secondary}^-. \tag{5}$$
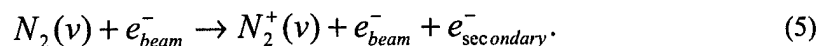
Vibrationally excited ions can also be created by a rapid resonance charge transfer from vibrationally excited parent molecules, such as

$$O_2^+ + O_2(v) \rightarrow O_2^+(v) + O_2. \tag{6}$$
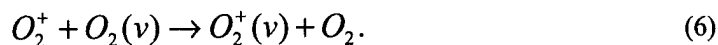
Recent experimental data [12] shows that vibrational excitation of molecular ions such as NO^+ or O_2^+ can considerably reduce the rate of their dissociative recombination, such as

187

$$O_2^+(v) + e^- \rightarrow O + O. \tag{7}$$

Secondly, three-body attachment of secondary electrons produced by the electron beam to vibrationally excited oxygen molecules created by a CO laser,

$$O_2(v) + e^- + M \rightarrow O_2^-(v) + M , \tag{8}$$

would produce vibrationally excited ions $O_2^-(v)$. Since the electron affinity of this ion is only about 0.4 eV [1], vibrational excitation of oxygen molecules to vibrational levels $v \geq 2$ might provide enough energy for auto-detachment of an electron,

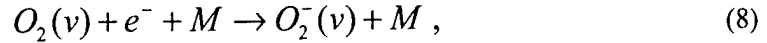$$O_2^-(v \geq 2) \rightarrow O_2 + e^-. \tag{9}$$

Since the three-body electron attachment to oxygen molecules is by far the most rapid mechanism of electron removal in cold, high-pressure air plasmas, reduction of the attachment rate would greatly reduce the plasma power budget.

Experimental investigation of this effect of electron removal rate reduction in electron beam sustained optically pumped air plasmas is the main objective of the present paper.

2. Experimental

Figs. 1,2 show schematics of the experimental setup. An electron gun (Kimball Physics EGH-8101) generates an electron beam with an energy of up to 80 keV and a beam current of up to 20 mA. The electron gun can be operated continuously or pulsed. From the vacuum inside the electron gun the electron beam passes through an aluminum foil window into a plasma cell that can be pressurized up to atmospheric pressure. The foil window with a thickness of 0.018 mm is glued onto a vacuum flange with an aperture of 6.4 mm. About 30 keV of the electron beam energy is lost in the window, which results in heating of the window. Pulsed operation of the electron gun at a low duty cycle prevents overheating and failure of the window. In the electron gun the electron beam has a relatively small divergence that increases significantly (~90° full angle) due to scattering in the foil window. A 12.7 mm diameter brass electrode faces the window at a distance of 10 mm. This defines a volume of the e-beam excited plasma of ~ 1 cm³ between the beam window and the electrode. The beam window together with the entire

chamber is grounded. For the current experiments the electrode was usually also grounded. The electron gun was typically operated at beam energies between 60 keV and 80 keV and different beam currents measured using an unbiased Faraday cup placed behind the beam window. The plasma cell is pressurized with air at pressures between 100 Torr and 1 atmosphere. A slow gas flow is maintained in the cell to provide flow convective cooling and to remove chemical products. The residence time of the gas mixture in the cell is of the order of a few seconds.

Perpendicular to the e-beam axis a CO laser beam is directed into the e-beam excited plasma. The laser is used to vibrationally excite the diatomic plasma constituents. The liquid nitrogen cooled CO laser [13] produces a substantial fraction of its power output on the v = 1? 0 fundamental band component in the infrared. In the present experiment, the laser is typically operated at ~10 W c.w. broadband p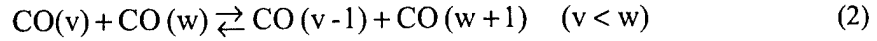ower on the lowest ten vibrational bands. The output on the lowest bands (1? 0 and 2? 1) is necessary to start the optical absorption process in cold CO at 300 K, which constitutes 1-5% of the gas mixture in the cell. The laser beam is focused by a 250 mm focal distance lens to a focal area of ~0.5 mm diameter to increase the power loading per CO molecule, producing an excited region ~5 cm long.

The electron density in the e-beam/optically sustained plasma is measured by microwave attenuation. The microwave experimental apparatus consists of an oscillator, a transmitting and receiving antenna/ waveguide system, oriented perpendicular to the e-beam axis and under an 45° angle to the laser axis (Fig. 2), and transmitted and reflected microwave power detectors. The phase-locked dialectrically stabilized oscillator generates 20 mW (13 dBm) of microwave radiation at a frequency ?=10 GHz, which is transmitted via SMA-type semi-rigid cable to an antenna within the transmission waveguide. The receiving waveguide is positioned directly opposite the transmitting waveguide, with the plasma located between them (Fig. 2). The signal transmitted through the plasma is received by an antenna at the back of the receiving waveguide and sent to a tunnel diode detector. The detector produces a DC voltage proportional to the received microwave power. To scale the transmitted signal down to the proper range for the detector, attenuators (10-20 dB) were inserted in the line between the receiving antenna and the transmitted power detector. From the relative difference of the transmitted power with and without a plasma the attenuation of the microwave signal across the plasma was determined. This assumes a negligible difference in the power radiated from the gap between the waveguides, with and without the plasma present, which is justified by the negligible change in the measured reflected power at these conditions.

In the optically pumped high-pressure gas mixture, the lower vibrational levels of CO, v≤10, are populated by direct resonance absorption of the CO laser radiation,
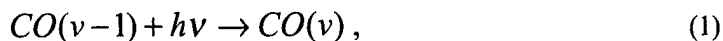
$$CO(v-1) + hv \rightarrow CO(v), \tag{1}$$

in combination with the much more rapid redistribution of population by the intramode vibration-to-vibration (V-V) exchange processes,

$$CO(v) + CO(w) \rightleftarrows CO(v-1) + CO(w+1) \quad (v < w) \tag{2}$$

These V-V processes then continue to populate the higher vibrational levels of CO above v=10, which are not directly coupled to the laser radiation. At the same time, the intermode V-V exchange processes,

$$CO(v) + N_2(w) \rightleftarrows CO(v-1) + N_2(w+1) \tag{3}$$

$$CO(v) + O_2(w) \rightleftarrows CO(v-1) + O_2(w+1) \tag{4}$$
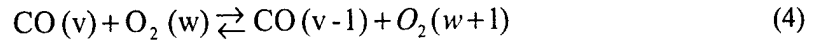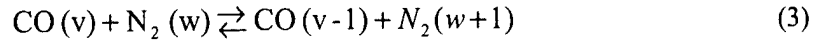
also populate the vibrational levels of nitrogen and oxygen molecules. Therefore, in the laser-excited region, the concentrations of the vibrationally excited CO, O_2, and N_2 molecules may be very high. Indeed, our previous experiments in high-pressure optically pumped plasmas [14-16] showed that in atmospheric pressure air seeded with 4% CO, a 10 W c.w. CO laser can sustain fairly high vibrational temperatures of all three major diatomic species, $T_v(CO) \cong 2700$ K, $T_v(O_2) \cong T_v(N_2) \cong 1900$ K, while keeping the gas temperature low, $T \cong 350$ K (e.g. see Fig. 3).

3. Results and discussion

If the electron removal rates (i.e. the electron-ion recombination rate and/or the electron attachment rate) in the laser-excited region are reduced, then (i) the steady-state electron density reached after an electron beam pulse is turned on should rise, and (ii) the electron density decay after the beam is turned off should become slower. In the present experiment, the average electron density in the e-beam sustained plasma is inferred from the microwave attenuation measurements using the following relation [11],

$$n_e^{baseline} = \frac{m_e c \varepsilon_0}{e^2} \nu_{coll} \frac{\delta V}{V_{inc}} \frac{1}{D}, \tag{10}$$

where v_{coll} is the electron-neutral collision frequency, $\dfrac{\delta V}{V_{inc}} = \dfrac{V_{trans} - V_{inc}}{V_{inc}}$ is the relative attenuation factor in terms of the forward power detector voltage proportional to the incident and the transmitted microwave power, and $D \cong 1.0$ cm is the size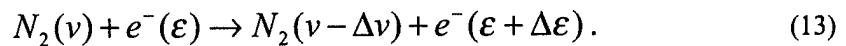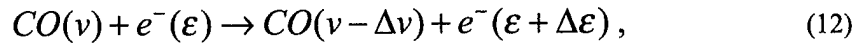 of the ionized region along the microwave signal propagation (see Fig. 2). Note that Eq. (10) assumes a uniform ionization across the plasma.

A CO laser beam propagating across the electron beam sustained plasma creates a cylindrical shape optically pumped region of $d \cong 2$ mm diameter (see Figs. 2,3 [16]). The analysis of the microwave absorption measurements in electron beam sustained plasmas enhanced by optical pumping is somewhat complicated by the fact that at the present time the plasma volume affected by a focused CO laser, $\sim \pi d^2 D/4 \sim 0.03$ cm^3, is considerably smaller than the volume ionized by the electron beam, $\sim 0.5 D^3 \sim 0.5$ cm^3. For this reason, Eq. (10) should be modified to take this effect into account. If one assumes that the electron removal rate modification due to vibrational excitation is significant, and that consequently the electron density in the optically pumped region, $n_e^{modified}$, is much higher than in the e-beam ionized region, $n_e^{baseline}$, Eq. (10) becomes

$$n_e^{modified} \cong \frac{m_e c \varepsilon_0}{e^2} v_{coll} \frac{\delta V}{V_{inc}} \frac{1}{d} \frac{W}{d}, \qquad (11)$$

where W is the width of the waveguide. In addition, inference of the electron density should account for the change of the electron-neutral collision frequency, v_{coll}, in the optically pumped plasma, which primarily depends on the electron temperature. In the present paper, the dependence of the collision frequency on the average electron energy is calculated by solving the coupled master equation for the vibrational level populations of CO, N_2, and O_2, and Boltzmann equation for the secondary (low-energy) plasma electrons [17]. In the optically pumped plasma, the electron temperature is strongly coupled to the vibrational temperatures of the diatomic species due to rapid energy transfer from vibrationally excited molecules to electrons in superelastic collisions [18-20],

$$CO(v) + e^-(\varepsilon) \rightarrow CO(v - \Delta v) + e^-(\varepsilon + \Delta \varepsilon), \qquad (12)$$

$$N_2(v) + e^-(\varepsilon) \rightarrow N_2(v - \Delta v) + e^-(\varepsilon + \Delta \varepsilon). \qquad (13)$$

191

In the present work, we assume the average electron energy in the optically pumped plasma to be about $\bar{\mathcal{E}}$ ~0.2 eV, which is close to the maximum measured vibrational temperature in optically pumped 1 atm air [15]. This gives the collision frequency of $v_{coll}=5\cdot10^{12}$ s^{-1} at P=1 atm, T=300 K. In the e-beam sustained plasma, the average electron energy is $\bar{\mathcal{E}}$ ~0.03 eV, and the collision frequency is $v_{coll}=2\cdot10^{11}$ s^{-1}. The collision frequency scales with the gas number density. Summarizing, the electron densities in the electron beam sustained plasma, $n_e^{baseline}$, and in the optically enhanced region, $n_e^{modified}$, are evaluated from Eqs. (10) and (11), respectively.

Fig. 4 shows time resolved measurements of the electron density during and after a 5 μsec e-beam pulse with and without optical pumping in CO seeded air at P=0.5 atm. A very fast rise and decay of the purely e-beam sustained plasma can be seen. The recorded rise and decay time is limited by the rise and decay time of the electron beam itself of ~ 200 nsec. The trace with the laser on comprises, as mentioned before, contributions from two plasma regions with very different characteristics. Fig. 5 illustrates how the equilibrium e-beam excited region and the nonequilibrium e-beam/laser excited region contribute to the overall signal recorded by the microwave system. The overall signal consists of an initial fast rise of the electron density in the e-beam sustained region outside of the laser pumped region when the e-beam is turned on. Due to strong electron attachment and recombination the steady state electron density in this region is relatively low, on the order of 10^{11} electron/cm^3, as determined from Eq. (10). The further rise of the overall signal after this initial rise is due to the continuing electron build-up in the e-beam ionized / laser excited region. In this region the overall electron loss rate becomes very low and even at the end of the e-beam pulsed the electron density has not reached a steady state, i.e. the electron loss rate has not reached the electron production rate. Similar to the signal evolution after the e-beam was switched on, switching off the e-beam is followed by an initial very fast decay of the overall signal due to the contribution from e-beam sustained plasma outside of the laser excited region. After this the plasma outside of the laser excited region is fully decayed and the observed slow decay of the microwave attenuation signal is solely due to the slowly decaying plasma in the laser excited region. The electron density in this final decay has to be determined according to Eq. (11).

Fig. 6 shows the electron density decay in the laser excited region of a 1 atm air plasma seeded with 5% of CO following a 30 μsec e-beam pulse. The e-beam was operated at an initial electron gun energy of 60 keV that decreased to ~30 keV due to losses in the beam window. The beam current behind the window was about 5 mA. The laser power absorbed in the e-beam plasma was approximately 1 W. In order to determine an upper limit (disregarding attachment) of the electron recombination rate ß in this plasma a recombination dominated electron density decay, $n_e=n_e^0/(1+n_e^0 ßt)$ [1], was fitted to the measurement. The obtained recombination rate ß=1.6x10^{-7} cm^3/sec is one order of magnitude smaller than

the rate $\beta=2\times10^{-6}$ cm^3/sec in cold e-beam sustained air plasma without vibrational disequilibrium [21]. This recombination rate agrees well with our earlier results in purely optically pumped $CO/N_2/O_2$ plasmas [11]. This indicates that vibrational excitation of the diatomic species can significantly reduce the electron recombination rate in cold high-pressure air plasmas.

The fit of the electron recombination rate shown in Fig. 6 agrees very well with the experimental data and therefore does not suggest significant contributions from other electron loss processes, most notable electron attachment to O_2. Nevertheless, since attachment is usually the dominant electron removal process in cold high-pressure air plasmas, an upper limit of the effective electron attachment rate, $k_{eff}=?_{eff}/[O_2]^2$, was determined by fitting a purely attachment caused electron density decay, $n_e=n_e^0\exp(-?_{eff}\,t)$, to the data of Fig. 6. This is shown in Fig. 7. Although the inferred effective attachment rate, $k_{eff}=2.3\times10^{-33}$cm^6/sec is an upper limit due to the neglect of electron loss by recombination it is three orders of magnitude smaller than the attachment rate in 1 atm equilibrium cold air, $k_a=2.5\times10^{-30}$cm^6/s. This suggests that electron attachment to O_2 in vibrationally excited cold air plasmas is very strongly, if not totally, mitigated. A fit of the experimental decay trace to the theoretical electron density decay curve with both recombination and attachment incorporated is expected to somewhat improve the accuracy of the inferred recombination and attachment rates.

The electron densities achieved within the 2 mm diameter e-beam ionized / CO laser excited region of CO-seeded air, determined from Eq. (11), are $n_e\cong4\cdot10^{12}$ cm^{-3} at P=0.5 atm and $n_e\cong2\cdot10^{12}$ cm^{-3} at P=1 atm. The plasma power budget at P=1 atm, which includes only the recombination and attachment losses, is $\dot{Q}=2$ W/cm^3. If the electron density in increase to $n_e=10^{13}$ cm^{-3}, the recombination/attachment power budget would increase up to $\dot{Q}=40$ W/cm^3. Taking into account the e-beam ionization efficiency ($\cong50\%$) and the CO laser power required to sustain vibrational disequilibrium (5-10 W/cm^3) would increase the power budget up to $\dot{Q}\cong10$ W/cm^3 at $n_e\cong2\cdot10^{12}$ cm^{-3} and $\dot{Q}\cong90$ W/cm^3 at $n_e=10^{13}$ cm^{-3}. Further plasma power budget reduction can only be achieved by further reducing the electron-ion recombination rate below the currently achieved value of $\beta=1.6\times10^{-7}$ cm^3/sec.

The optical pumping approach used in the present work to reduce the electron recombination rate and especially the attachment rate in high-pressure air plasmas has a distinct advantage over equilibrium gas heating. Indeed, if the CO-air mixture excited by a CO laser up to a vibrational temperature of $T_v=2000$ K completely relaxes, the gas mixture temperature would increase by only about $\Delta T\cong250$ K. Note that equivalent mitigation of electron attachment to oxygen in equilibrium high-temperature air would require gas heating by up to about $\Delta T\cong2000$ K.

4. Summary

Time resolved electron density measurements in electron beam sustained cold atmospheric pressure air plasmas were used to study the effect of vibrational excitation of the diatomic air species on electron removal processes, notably dissociative recombination and attachment to O_2. Vibrational excitation of the diatomics was efficiently produced by optical pumping of CO seeded into the air and subsequent vibration-vibration energy transfer within the CO vibrational mode and from the CO to O_2 and N_2. From the electron density decay after an e-beam pulse upper limits for the electron recombination rate and the electron attachment rate in these plasmas were determined. Compared to equilibrium cold air electron recombination and electron attachment in vibrationally excited cold air were found to be reduced to $\beta=1.6 \times 10^{-7}$ cm^3/sec and $k_{eff}=2.3 \times 10^{-33}$ cm^6/sec, i.e. by one and three orders of magnitude, respectively.

Since the three-body electron attachment to oxygen molecules is by far the most rapid mechanism of electron removal in cold, high-pressure air plasmas, reduction of the attachment rate together with the reduction of the dissociative recombination rate greatly reduces the plasma power budget.

References

1. Raizer, Y.P., "Gas Discharge Physics", Springer-Verlag, Berlin, 1991

2. E.P. Velikhov, A.S. Kovalev, and A.T. Rakhimov, "Physical Phenomena in Gas Discharge Plasmas", Moscow, Nauka, 1987

3. Generalov, N.A., V.P. Zimakov, V.D. Kosynkin, Yu.P. Raizer, and D.I. Roitenburg, Technical Physics Letters, vol. 1, p. 431, 1975

4. W. Rich, R.C. Bergman, and J.A. Lordi, AIAA J., vol. 13, p. 95, 1975

5. Zhdanok, S.A., Vasilieva, E.M., and Sergeeva, L.A., "Study of the High Voltage Atmospheric Pressure Discharge and its Application for Surface Treatment", Soviet J. of Engineering Physics, Vol. 58, No.1, pp.101-104, 1990

6. Basov, N.G., Babaev, I.K., Danilychev, V.A., et al., Sov. Journal of Quantum Electronics, vol. 6, 1979, p. 772

7. A.S. Kovalev, E.A. Muratov, A.A. Ozerenko, A.T. Rakhimov, and N.V. Suetin, Sov. J. Plasma Physics, Vol. 11, 1985, p. 515

8. I.V. Adamovich, J. W. Rich, A.P. Chernukho, and S.A. Zhdanok, "Analysis of the Power Budget and Stability of High-Pressure Nonequilibrium Air Plasmas", Paper 00-2418, presented at AIAA 31th Plasmadynamics and Lasers Conference, Denver, CO, June 19-22, 2000

9. S.O. Macheret, M.N. Shneider, and R.B. Miles, "Modeling of air plasma generation by electron beams and high-voltage pulses", AIAA Paper 2000-2569, 31st AIAA Plasmadynamics and Lasers Conference, Denver, CO, June 19-22, 2000

10. S.O. Macheret, M.N. Shneider, and R.B. Miles, "New types of electron beam generated electric

discharge in dense gases - A 'fountain' and a 'thunderstorm'", AIAA Paper 99-3721, 30th AIAA Plasmadynamics and Lasers Conference, Norfolk, VA, June 28 – July 1, 1999

11. P. Palm, E. Plönjes, M. Buoni, V.V. Subramaniam, and I.V. Adamovich, "Electron Density and Recombination Rate Measurements in CO-Seeded Optically Pumped Plasmas", Journal of Applied Physics, vol. 89, 2001, pp. 5903-5910

12. T. Mostefaoui, S. Laube, G. Gautier, C. rebrion-Rowe, B.R. Rowe, and J.B.A. Mitchell, J. Phys. B: At. Mol. Opt. Phys., Vol. 32, 1999, p. 5247

13. E. Plönjes, P. Palm, A.P. Chernukho, I.V. Adamovich, and J.W. Rich, Chem. Phys., vol. 256, 2000, p. 315

14. E. Ploenjes, P. Palm, W. Lee, M. D. Chidley, I.V. Adamovich, W.R. Lempert, and J. William Rich, "Vibrational Energy Storage in High-Pressure Mixtures of Diatomic Molecules", Chemical Physics, vol. 260, 2000, pp. 353-366

15. W. Lee, I.V. Adamovich, and W.R. Lempert, "Optical Pumping Studies of Vibrational Energy Transfer in High-Pressure Diatomic Gases", Journal of Chemical Physics, vol. 114, No. 3, 2001, pp. 1178-1186

16. W.R. Lempert, W. Lee, R. Leiweke, and I.V. Adamovich, "Spectroscopic Measurements of Temperature and Vibrational Distribution Function in Weakly Ionized Gases", Paper 00-2451, presented at 21st AIAA Aerodynamic Measurement Technology And Ground Testing Conference, Denver, CO,19 - 22 June 2000

17. I.V. Adamovich, J.W. Rich, and G.L. Nelson, "Feasibility Study of Magneto-hydrodynamics Acceleration of Unseeded and Seeded Air Flows", AIAA Journal, vol. 36, No. 4, 1998, pp. 590-597

18. N.L. Aleksandrov, A.M. Konchakov, and E.E. Son, Sov. J. Plasma Physics, Vol. 4, 1978, p. 169

19. N.L. Aleksandrov, A.M. Konchakov, and E.E. Son, Sov. Phys. Tech. Phys., Vol. 49, 1979, p. 661

20. I.V. Adamovich and J.W. Rich, "The Effect of Superelastic Electron-Molecule Collisions on the Vibrational Energy Distribution Function", Journal of Physics D: Applied Physics, vol. 30, No. 12, 1997, pp. 1741-1745

21. H. Matzing, "Chemical Kinetics of Flue Gas Cleaning by Irradiation with Electrons", Adv. in Chem. Phys., vol.80, pp. 315-403

Figures
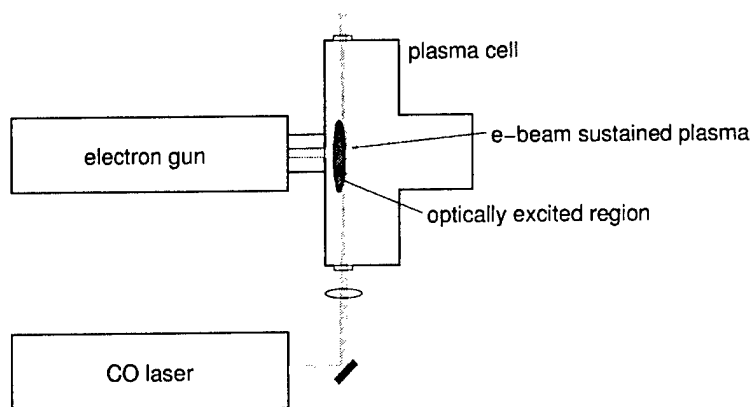
Figure 1. Schematic of the electron beam and laser setup.
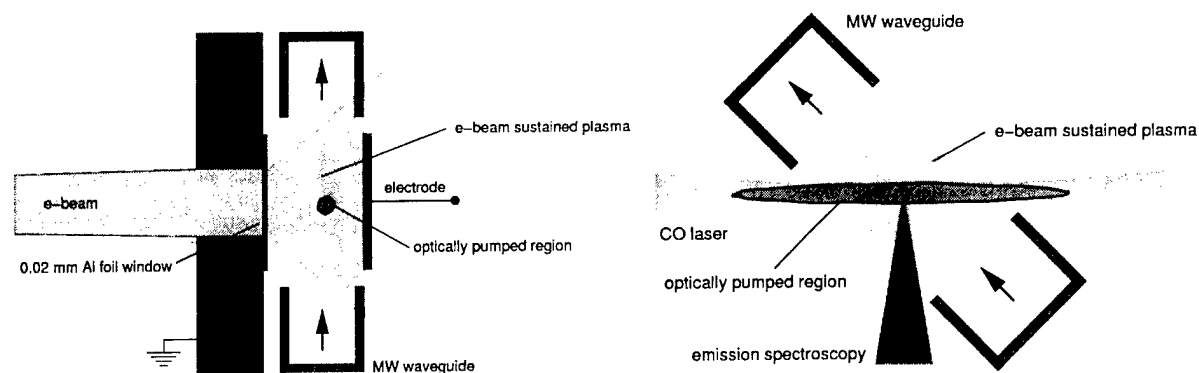
Figure 2. Schematic of the plasma cell.
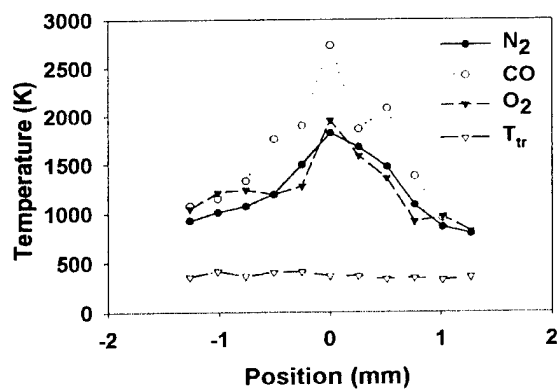
Figure 3. Radial dependence of vibrational and translational temperatures in optically pumped air at 1 atm [16].

1/2 atm air, 5 % CO

$P_{laser}^{absorbed} \sim 1W$

$E = 65\ keV,\ I = 5\ mA$
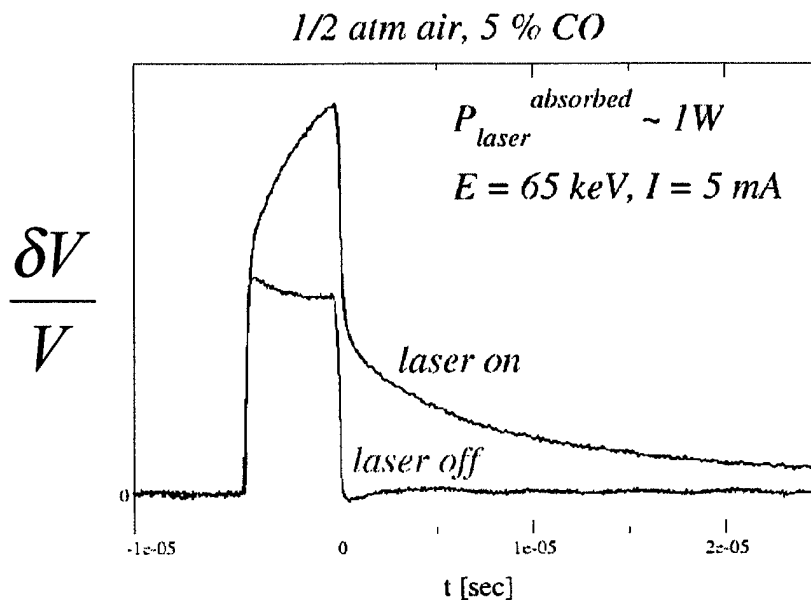
Figure 4. Time resolved measurements of microwave signal absorption during and after a 5μsec e-beam pulse with and without optical pumping in CO seeded air at p=0.5 atm.
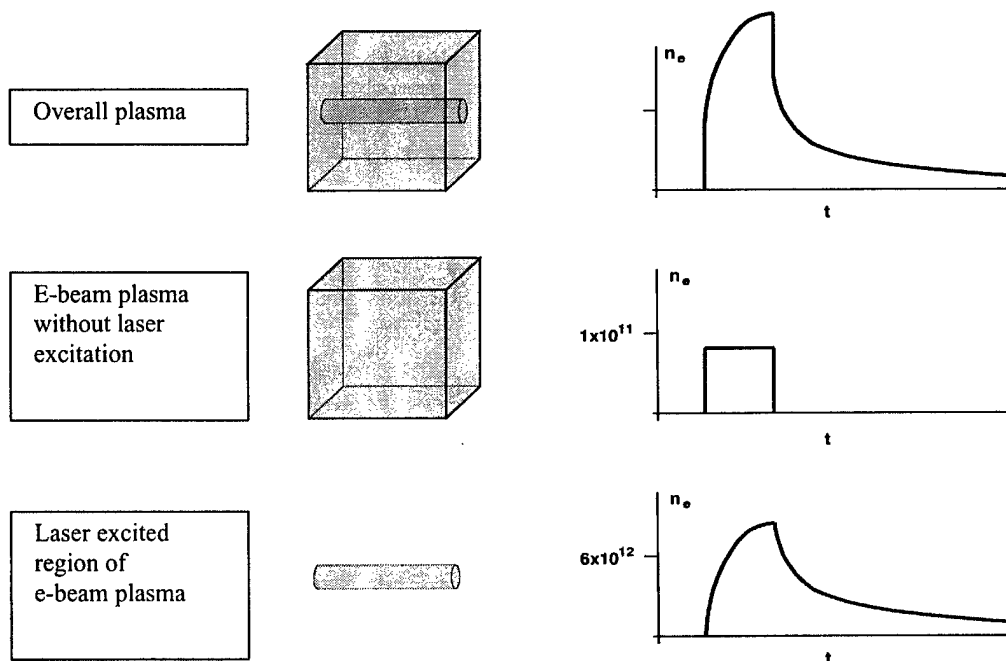
Figure 5. Illustration of how the e-beam ionized region and the e-beam ionized / laser vibrationally excited region contribute to the overall electron density signal recorded by the microwave system. Note the different scales on the n_e-axes.

1 atm air, 5 % CO

$$P_{laser}^{absorbed} \sim 1W$$

$$E = 60 \; keV, \; I = 5 \; mA$$

$$\beta = 1.6 x 10^{-7} \; cm^3 s^{-1}$$

t [sec]
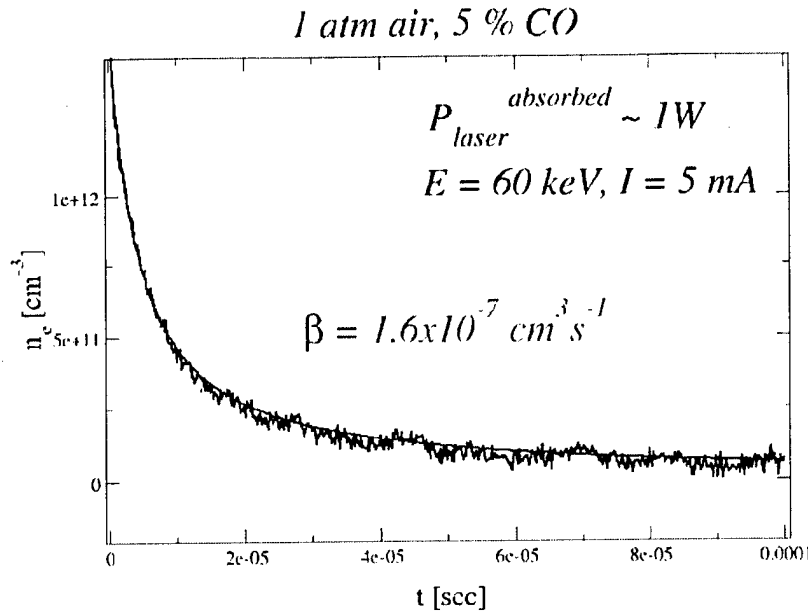
Figure 6. Electron density decay in 1 atm of optically pumped CO seeded air following a 30 μsec e-beam pulse. The e-beam was operated at an initial electron gun energy of 60 keV that decreased to ~30 keV due to losses in the beam window.

1 atm air, 5 % CO

$$P_{laser}^{absorbed} \sim 1W$$

$$E = 60 \; keV, \; I = 5 \; mA$$

$$k_{eff} = 2.3 x 10^{-33} \; cm^{-3} sec^{-1}$$

$$\tau = 19 \mu sec$$

t [sec]

Figure 7. Electron attachment rate in 1 atm of CO seeded optically pumped air determined from the electron density decay. The e-beam was operated at an initial electron gun energy of 60 keV that decreased to ~30 keV due to losses in the beam window. The top trace is with the laser pumping on, the bottom trace is without laser pumping. The electron density was determined from Eq. (10), i.e. the electron density averaged over the entire e-beam sustained region is shown.

11. MITIGATION OF ELECTRON ATTACHMENT AND RECOMBINATION IN ATMOSPHERIC PRESSURE AIR PLASMAS

Peter Palm, Elke Plönjes, Igor V. Adamovich, and J. William Rich

This section presents experimental data and kinetic modeling quantifying the effect of vibrationally driven mitigation of electron-ion recombination and electron attachment in electron beam sustained atmospheric pressure dry air plasmas. We present time-resolved electron density measurements in e-beam excited air plasmas accompanied by kinetic modeling of the electron production and removal processes. Nonequilibrium vibrational excitation is maintained by optical excitation of carbon monoxide, a few percent of which is seeded into the air, using a carbon monoxide laser and subsequent vibration-vibration energy transfer to oxygen and nitrogen. The experimental results are consistent with a model that assumes rapid vibrationally induced detachment of electrons from O_2^- and vibrationally induced heating of the electrons to temperatures on the order of 5000 K, thus effectively mitigating the effect of electron attachment and electron-ion recombination, respectively.
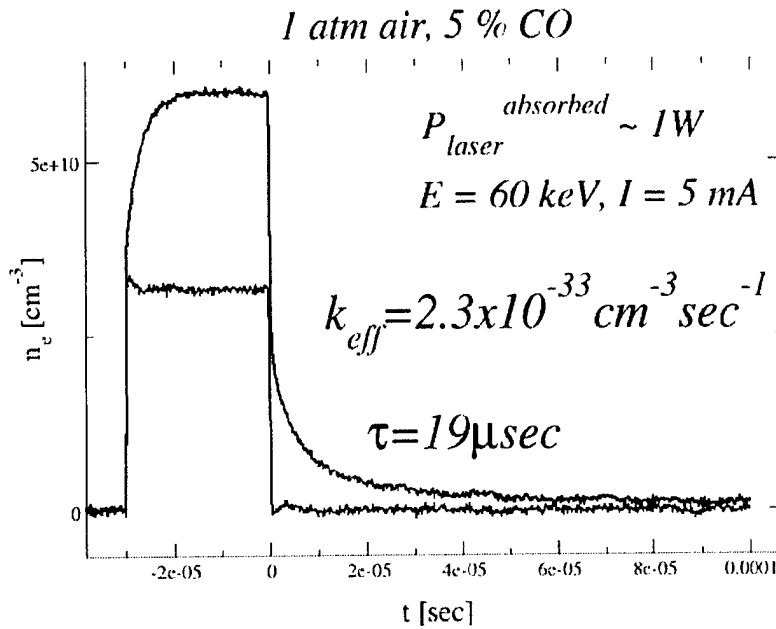
1. Introduction

Sustaining large-volume plasmas in atmospheric pressure air presents an extremely challenging problem. Among the most critical technical issues that have to be addressed to resolve this problem are the plasma power budget and stability. Numerous aerospace applications such as supersonic flow control, supersonic combustion control, and nonequilibrium MHD propulsion require an ability to initiate and sustain large volume (~1 m^3), relatively cold (T<2000 K) diffuse plasmas in atmospheric air, with electron density up to n_e~10^{13} cm^{-3}. For these applications, a power budget of the order of 1-10 MW/m^3 is desired.

The simultaneous requirement of electron densities of 10^{13} cm^{-3} and gas temperatures at or below 2000 K represent a strong departure from thermodynamic equilibrium, and rule out the use of purely thermal plasmas, such as high temperature arc discharges, to achieve this result. Electron beams are identified as having the lowest power budget among all nonequilibrium ionization methods [Ada00, Mac00, Mac99]. Further, an external ionization source mitigates another principal difficulty known to exist in high-pressure discharges at large current densities. The well-known glow-to-arc-transition, with subsequent plasma thermalization, can be significantly delayed or avoided altogether.

Even using an efficient ioniziation source the power budget required to sustain a relatively cold air plasmas is huge (>1 GW/m^3). This is predominantly due to rapid attachment of electrons to oxygen molecules. Consequently, reduction of the air plasma power budget mandates mitigation of electron attachment and, for further power reduction, lowering of the electron-ion recombination rate.

2. Experimental

Figs. 1 and 2 show schematics of the experimental setup. An electron gun (Kimball Physics EGH-8101) generates an electron beam with an energy of up to 80 keV and a beam current of up to 20 mA. The electron gun can be operated continuously or pulsed. From the high vacuum section inside the electron gun the electron beam passes through an aluminum foil window into a plasma cell that can be pressurized up to atmospheric pressure. About half of the electron beam energy is lost in the window. Pulsed operation of the electron gun at a low duty cycle prevents overheating and failure of the window. In the electron gun the electron beam has a relatively small divergence that increases significantly (~90° full angle) due to scattering in the foil window. The electron gun is typically operated at beam energy of 60 keV. A slow gas flow is maintained in the cell to provide flow convective cooling and to remove chemical products. The residence time of the gas mixture in the cell is on the order of a few seconds.

Perpendicular to the e-beam axis a CO laser beam can be directed into the e-beam excited plasma. The laser is used to vibrationally excite the diatomic plasma constituents. The liquid nitrogen cooled CO laser [Plo00] produces a substantial fraction of its power output on the $v = 1 \rightarrow 0$ fundamental band component in the infrared. In the present experiment, the laser is typically operated at ~10 W c.w. broadband power on the lowest ten vibrational bands. The output on the lowest bands ($1 \rightarrow 0$ and $2 \rightarrow 1$) is necessary to start the optical absorption process in cold CO at 300 K, which constitutes ~5% of the gas mixture in the cell. The laser beam is focused by a 250 mm focal distance lens to a focal area of ~0.5 mm diameter to increase the power loading per CO molecule, producing an excited region ~5 cm long.

The electron density in the e-beam sustained plasma is measured by microwave attenuation. The microwave measurement apparatus consists of an $v=40$ GHz oscillator, a transmitting and receiving antenna/waveguide system, oriented perpendicular to the e-beam and laser (Fig. 2), and transmitted microwave power detector. The receiving waveguide is positioned directly opposite the transmitting waveguide, with the e-beam plasma located between them (Fig. 2). The MW detector produces a DC voltage proportional to the received microwave power. From the relative difference of the transmitted power with and without a plasma the attenuation of the microwave signal across the plasma is determined.

With laser excitation, the lower ($v \leq 10$) vibrational levels of CO, seeded into the gas mixture, are populated by direct resonance absorption of the CO laser radiation,
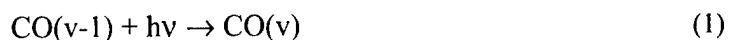
$$CO(v-1) + h\nu \rightarrow CO(v) \tag{1}$$

in combination with the much more rapid redistribution of population by the intramode vibration-to-vibration (V-V) exchange processes,

$$CO(v) + CO(w) \rightarrow CO(v-1) + CO(w+1) \quad (v<w) \tag{2}$$

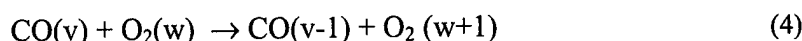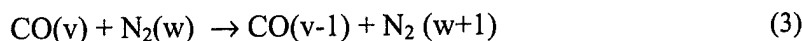These V-V processes then continue to populate the higher vibrational levels of CO above $v=10$, which are not directly coupled to the laser radiation. At the same time, the intermode V-V exchange processes,

$$CO(v) + N_2(w) \rightarrow CO(v-1) + N_2(w+1) \tag{3}$$

$$CO(v) + O_2(w) \rightarrow CO(v-1) + O_2(w+1) \tag{4}$$
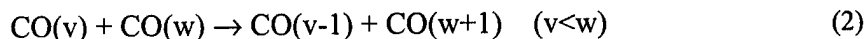
populate the vibrational levels of nitrogen and, due to the smaller vibrational quanta, preferentially to oxygen molecules. Therefore, in the laser-excited region, the concentrations of the vibrationally excited CO, O_2, and N_2 molecules is very high. Indeed, our previous experiments in high-pressure optically pumped plasmas [Plo00b, Lee01, Lem00] showed that in atmospheric pressure air seeded with 4% CO, a 10 W c.w. CO laser can sustain fairly high vibrational temperatures of all three major diatomic species, $T_v(CO) \cong 2700$ K, $T_v(O_2) \cong T_v(N_2) \cong 1900$ K, while keeping the gas temperature low (see also Fig. 4).

3. Results and discussion

A reduction of the electron removal rates (i.e. the electron-ion recombination rate and/or the electron attachment rate) in the vibrationally excited region should manifest itself in two experimental observations:(i) the steady-state electron density reached after an electron beam pulse is turned on should rise, and (ii) the electron density decay after the beam is turned off should become slower. In the present experiment, the average electron density in the e-beam sustained plasma is inferred from microwave attenuation measurements using the following relation [Pal01a],

$$n_e^{modified} = (m_e c \varepsilon_0 / e^2) \cdot v_{coll} \cdot (\delta V/V) \cdot 1/D \tag{5}$$

where v_{coll} is the electron-neutral collision frequency, $\delta V/V = (V_{trans} - V_{inc})/V_{inc}$ is the relative attenuation factor in terms of the forward power detector voltage proportional to the incident and the transmitted microwave power, and $D \cong 0.8$ cm is the size of the ionized region along the microwave signal propagation (see Fig. 2). Note that Eq. (5) assumes a uniform ionization across the plasma.

A CO laser beam propagating across the electron beam sustained plasma creates a cylindrically shaped vibrationally excited region of d≅2 mm diameter (see Fig. 2). The analysis of the microwave absorption measurements in electron beam sustained plasmas enhanced by laser excitation is somewhat complicated by the fact that at the present time the plasma volume affected by a focused CO laser, is considerably smaller than the volume ionized by the electron beam. For this reason, Eq. (5) should be modified to take this effect into account. If one assumes that the electron removal rate modification due to vibrational excitation is significant, and that consequently the electron density in the optically pumped region, $n_e^{modified}$, is much higher than in the e-beam ionized region, $n_e^{baseline}$, Eq. (5) becomes

$$n_e^{modified} = (m_e c \varepsilon_0 / e^{2)}) \cdot v_{coll} \cdot (\delta V / V) \cdot W / (\pi d^2 / 4) \qquad (6)$$

where W≅0.33 cm is the width of the waveguide perpendicular to the laser beam axis. In addition, inference of the electron density should account for the change of the electron-neutral collision frequency, v_{coll}, in the vibrationally excited plasma, which primarily depends on the electron temperature. In the present paper, the dependence of the collision frequency on the average electron energy is calculated by solving the coupled master equation for the vibrational level populations of CO, N_2, and O_2, and Boltzmann equation for the secondary (low-energy) plasma electrons [Ada98]. In the laser excited plasma, the electron temperature is strongly coupled to the vibrational temperatures of the diatomic species due to rapid energy transfer from vibrationally excited molecules to electrons in superelastic collisions [Ale78, Ale79, Ada97]. In the present work, we assume the average electron energy in the optically pumped plasma to be about 5000 K, which is higher than our earlier estimates of ~ 2300 K (i.e. the vibrational temperature) but in good agreement with the modeling calculations and recent Langmuir probe measurement in laser pumped plasmas [Plo02]. This gives a collision frequency of $v_{coll}=6.1 \cdot 10^{11}$ s^{-1} in air at p=1 atm and T=560 K. In the purely e-beam sustained plasma, the average electron energy is ~300 K, and the collision frequency is $v_{coll}=1.1 \cdot 10^{11}$ s^{-1} at p=1 atm and T=300 K. Summarizing, the electron densities in the electron beam sustained plasma and in the laser enhanced region are evaluated from Eqs. (5) and (6), respectively.

The experimental results are compared with a kinetic model of the electron production, electron removal, and charge transfer processes in the investigated air plasmas. The model takes into account rates for electron production by the e-beam, S, electron-ion recombination, β, 3-body ion-ion recombination k_R, electron attachment in 3-body collisions to O_2, k_a^{O2}, and to N_2, k_a^{N2}, electron detachment from O_2^- in collisions with O_2, k_d^{O2}, and in collisions with N_2, k_d^{N2}. Electron densities, n_e, positive ion densities, n^+, and O_2^- densities are calculated integrating the differential equations

$$dn_e/dt = S - k_a^{O2}\, n_e\, [O_2]^2 - k_a^{N2}\, n_e\, [O_2][N_2] - \beta\, n_e\, n^+ \qquad (7)$$
$$+ k_d^{O2}\, n_e\, [O_2^-][O_2] + k_d^{N2}\, n_e\, [O_2^-][N_2]$$

$$d[O_2^-]/dt = k_a^{O2}\, n_e\, [O_2]^2 + k_a^{N2}\, n_e\, [O_2][N_2] - k_R\, [O_2^-]\, n^+\, N \qquad (8)$$
$$- k_d^{O2}\, n_e\, [O_2^-][O_2] - k_d^{N2}\, n_e\, [O_2^-][N_2]$$

$$dn^+/dt = S - \beta\, n_e\, n^+ - k_R\, [O_2^-]\, n^+. \qquad (9)$$

In a first step, modeling results are fitted to the time resolved electron density in 1 atm of pure N_2 after a 20μs e-beam pulse. Fig. 4 shows the electron density measurement and the calculated electron density that best agrees in peak electron density and electron density decay. From the fit we obtain an electron production rate of $S=2.7 \times 10^{12} cm^{-3} s^{-1}$ and, since the decay in N_2 is dominated by electron-ion recombination, the effective dissociative electron-ion recombination rate for our e-beam ionized N_2 plasma. The determined recombination rate $\beta = 0.9 \times 10^{-6} cm^3 s^{-1}$ lies between the known recombination rates for the expected dominant ions N_4^+ ($\beta = 2 \times 10^{-7} cm^3 s^{-1}$) and N_2^+ ($\beta = 2 \times 10^{-6} cm^3 s^{-1}$). Consequently, the measurement suggest that about 50% of the positive ions in the plasma are the faster recombining N_4^+ that is produced in a conversion reaction.

Electron density measurements in the laser excited part of the e-beam plasma are somewhat more uncertain than measurements in purely e-beam sustained plasmas. This is due to i) the uncertainty in the diameter d of the laser excited region (see Eq. 6), ii) the uncertainty in the translational temperature in the laser excited region, and iii) the uncertainty in the electron temperature T_e in the laser excited region. From the size of the visible glow of a laser excited N_2/CO plasma at p=1 atm and from earlier Raman spectroscopic measurements [Lem00] the diameter of the laser excited region was estimated to be d=0.2 cm. The translational temperature in the laser region was measured spectroscopically from a Boltzmann plot of the infrared emission intensities of CO 1$\rightarrow$0 R-branch lines. For 1 atm of air seeded with 5% CO and optically excited by a 10 W CO laser the temperature was found to be 560 K.

Fig.5 shows the measured electron density assuming d=0.2 cm and T_e=5000 K and a calculated electron density pulse in N_2 at T=560 K. Assuming identical electron production rates in 1 atm of air and 1 atm of N_2 the slope of the initial electron density rise in laser excited air should be identical to the slope in N_2. Very good agreement is achieved by changing the diameter of the laser excited region in Eq. 6 from d=0.2 cm to d=0.185 cm, also shown in Fig. 5. The signal to noise ratios for electron density measurements in the laser excited region are much lower than purely e-beam excited plasmas. This is

caused by the much smaller size of the laser excited region and the consequently lower MW attenuation. In fact, a microwave attenuation measurement in the laser excited region is always accompanied by a measurement in the surrounding, purely e-beam excited region (Fig.6).

Fig.7 shows the calibrated electron density pulse from Fig.6 together with a calculated pulse in N_2 at T=560 K and the assumed T_e=5000 K. Both traces appear to be in very good agreement. Most notably, the decay of the electron density in laser excited air is equally slow as in N_2, i.e. attachment of electrons to O_2 does not seem to be a relevant process in vibrationally excited air. The importance of attachment to oxygen in cold equilibrium air can be seen in the dashed trace in Fig.7 showing the corresponding electron density measurement without laser excitation. Note the 200 fold higher peak electron density in laser excited air ($7.9 \times 10^{11} cm^{-3}/4.4 \times 10^9 cm^{-3}$).

As mentioned before, the CO laser excited air plasma is in a very strong vibrational nonequilibrium. The vibrational temperature of the diatomic species exceeds the translational temperature by at least a factor of 4. Nevertheless, the fraction of molecules in excited vibrational states is still small compared to the population of the vibrational ground state. Therefore, the apparent complete mitigation of electron attachment to oxygen in vibrationally excited air cannot be caused by a vibrationally induced modification of the attachment rate itself because the ground-state O_2 molecules (>50%) would still be exhibiting the full attachment rate, i.e. the total attachment rate could only be reduced by less than 50%. Consequently, the vibrational excitation has to be acting on the electron detachment side. On the other hand, the detachment rate shows a strong temperature dependence which raises the question of whether the observed effect might be due to the temperature rise (300 K $\rightarrow$ 560 K) associated with the optical excitation of our air plasma.

Fig. 8 shows the experimental electron density in a 30 μsec e-beam pulse in p=1 atm air at slightly higher beam current than in Fig 7. The modeling calculation, assuming $S=0.5 \times 10^{18} cm^{-3}s^{-1}$, $\beta=2 \times 10^{-6} cm^3 s^{-1}$, $k_a^{O2}=2.5 \times 10^{-30} cm^6 s^{-1}$, $k_a^{N2}=0.16 \times 10^{-30} cm^6 s^{-1}$, $k_d^{O2}=2.2 \times 10^{-18} cm^3 s^{-1}$, $k_d^{N2}=1.8 \times 10^{-20} cm^3 s^{-1}$, $k_R=1.55 \times 10^{-25} cm^3 s^{-1}$ [Rai91] and T=300K shown also in Fig. 8 agrees well with the experimental data. The two other traces in Fig. 8 show the calculated electron densities taking into account modified electron detachment, and electron-ion recombination rates due to increased electron and translational temperatures. The modified rates for increased translational temperature only and increased translational and electron temperature used are $\beta=1.5 \times 10^{-6} cm^3 s^{-1}$, $k_d^{O2}=2.2 \times 10^{-14} cm^3 s^{-1}$, $k_d^{N2}=1.8 \times 10^{-16} cm^3 s^{-1}$, and $\beta=6.3 \times 10^{-7} cm^3 s^{-1}$, $k_d^{O2}=2.2 \times 10^{-14} cm^3 s^{-1}$, $k_d^{N2}=1.8 \times 10^{-16} cm^3 s^{-1}$, respectively [Rai91]. It can be seen that the change of electron and translational temperatures associated with the laser excitation would not produce a very strong effect on the electron density (x2) and the plasma decay time. Therefore, the strong effect observed in the experimental data with laser excitation can be attributed to the vibrational excitation, not temperature effects.

Fig. 9 shows calculated electron densities for the conditions of Figs. 4,5,7 using hugely increased electron detachment rates. Increase of the detachment rates by 5 orders of magnitude fully mitigates the effect of attachment and the calculated trace for laser excited air practically coincides with the calculated trace for N_2. The change of the electron-ion recombination rate from $\beta=0.9\times10^{-6}$ cm^{3}s^{-1} to $\beta=2.2\times10^{-7}$ is due to the increase of the electron temperature from $T_e=300$ K in cold gas to $T_e=5000$ K in the vibrationally excited gas.

In Fig. 10 the calculated number densities for the negatively charged species e$^-$ and O_2^- are shown. Due to attachment, the dominant negative species in cold air is O_2^-, whereas in vibrationally excited air the O_2^- population is insignificant ($<2\times10^9$ cm^{-3}) and the dominant negative species is e$^-$. Note the higher total number density of charged species in vibrationally excited air which is due to the reduced ion-ion recombination channel.

The experimental results and modeling calculations are consistent with the following hypothesis for the effect of vibrational excitation on electron attachment to oxygen and electron-ion recombination in electron beam sustained atmospheric pressure air plasmas: i) since the electron affinity of O_2^- is only about 0.4 eV [Rai91], vibrational excitation of O_2^- to vibrational levels $v\geq2$ can provide sufficient energy for the detachment of the attached electron

$$O_2^- \ (v\geq2) \ [+ M \ ] \rightarrow O_2 + e^- \ [+ M \ ] \tag{10}$$

while charge transfer from O_2^- to vibrationally excited oxygen is sufficiently rapid to make this process very efficient and ii) superelastic collisions of the initially cold secondary electrons produced by the electron beam with highly vibrationally excited molecules increase the electron temperature significantly to $T_e\approx5000$ K which reduces the electron-ion recombination rate.

The overall influence of these effects on the plasma power budget can be estimated as follows. In cold air plasmas the dominant electron removal process is attachment to oxygen. The minimum power budget (assuming 100% ionization efficiency) to sustain a cold air plasma with an electron density of $n_e=10^{13}$cm^{-3} is therefore given by $P_a=E_{ion}k_a[O_2]^2$. For an average ionization energy in air of $E_{ion}\approx14$ eV this gives $P_a=1.4$ kW/cm^3=1.4GW/m^3. In the case of vibrationally excited air, the electron loss by attachment is replenished by detachment of electrons from O_2^- instead of O_2 in the case of cold air. With an electron affinity of $E_{det}\approx0.4$ eV the minimum power budget to overcome attachment decreases to $P_a=E_{det}k_a[O_2]^2=40$ W/cm^3 at T=300 K or $P_a=10$ W/cm^3 at the reduced gas density at T=560 K. In case of mitigated attachment the main electron removal process in an electron beam sustained air plasma is dissociative electron-ion recombination. The minimum power budget to overcome recombination is given

by $P_{rec}=E_{ion}\beta n_e^2$. With an electron-ion recombination rate of $\beta \approx 1 \times 10^{-6}$ cm^{3}s^{-1} we obtain $P_{rec}=225$ W/cm^3. With the measured recombination rate in vibrationally excited air, $\beta \approx 2 \times 10^{-7}$ cm^{3}s^{-1}, the minimum power budget to overcome recombination decreases to $P_{rec}=45$ W/cm^3. This, of course, does not yet include the efficiency of the laser excitation process and the efficiency of the electron beam ionization process.

4. Summary

Time-resolved electron density measurements in electron beam sustained cold atmospheric pressure air plasmas were used to study the effect of vibrational excitation of the diatomic air species on electron removal processes, notably dissociative recombination and attachment to O_2. Vibrational excitation of the diatomics was produced by laser excitation of CO seeded into the air and subsequent vibration-vibration energy transfer within the CO vibrational mode and from the CO to O_2 and N_2. The experimental results are consistent with a model that assumes rapid vibrationally induced detachment of electrons from O_2^- and vibrationally induced heating of the free electrons to temperatures on the order of $T_e \approx 5000$ K, thus effectively mitigating the effect of electron attachment and electron-ion recombination, respectively. The theoretical minimum power budget to overcome attachment and recombination in our vibrationally excited air plasmas was found to be approximately 50 W/cm^3 which represents a significant reduction compared to almost 2000 W/cm^3 in cold equilibrium air.

References

[Ada97] I.V. Adamovich and J.W. Rich, "The Effect of Superelastic Electron-Molecule Collisions on the Vibrational Energy Distribution Function", Journal of Physics D: Applied Physics, vol. 30, No. 12, 1997, pp. 1741-1745

[Ada98] I.V. Adamovich, J.W. Rich, and G.L. Nelson, "Feasibility Study of Magneto-hydrodynamics Acceleration of Unseeded and Seeded Air Flows", AIAA Journal, vol. 36, No. 4, 1998, pp. 590-597

[Ada00] I.V. Adamovich, J. W. Rich, A.P. Chernukho, and S.A. Zhdanok, "Analysis of the Power Budget and Stability of High-Pressure Nonequilibrium Air Plasmas", Paper 00-2418, 31th Plasmadynamics and Lasers Conference, Denver, CO, June 19-22, 2000

[Ale78] N.L. Aleksandrov, A.M. Konchakov, and E.E. Son, Sov. J. Plasma Physics, Vol. 4, 1978, p. 169

[Ale79] N.L. Aleksandrov, A.M. Konchakov, and E.E. Son, Sov. Phys. Tech. Phys., Vol. 49, 1979, p. 661

[Bas79] Basov, N.G., Babaev, I.K., Danilychev, V.A., et al., Sov. Journal of Quantum Electronics, vol. 6, 1979, p. 772

[Gen75] Generalov, N.A., V.P. Zimakov, V.D. Kosynkin, Yu.P. Raizer, and D.I. Roitenburg, Technical Physics Letters, vol. 1, p. 431, 1975

[Kov85] A.S. Kovalev, E.A. Muratov, A.A. Ozerenko, A.T. Rakhimov, and N.V. Suetin, Sov. J. Plasma Physics, Vol. 11, 1985, p. 515

[Lee01] W. Lee, I.V. Adamovich, and W.R. Lempert, "Optical Pumping Studies of Vibrational Energy Transfer in High-Pressure Diatomic Gases", Journal of Chemical Physics, vol. 114, No. 3, 2001, pp. 1178-1186

[Lem00] W.R. Lempert, W. Lee, R. Leiweke, and I.V. Adamovich, "Spectroscopic Measurements of Temperature and Vibrational Distribution Function in Weakly Ionized Gases", Paper 00-2451, presented at 21st AIAA Aerodynamic Measurement Technology And Ground Testing Conference, Denver, CO,19 - 22 June 2000

[Mac99] S.O. Macheret, M.N. Shneider, and R.B. Miles, AIAA Paper 99-3721, 30th AIAA Plasmadynamics and Lasers Conference, Norfolk, VA, June 28 - July 1, 1999

[Mac00] S.O. Macheret, M.N. Shneider, and R.B. Miles, "Modeling of air plasma generation by electron beams and high-voltage pulses", AIAA Paper 2000-2569, 31st AIAA Plasmadynamics and Lasers Conference, Denver, CO, June 19-22, 2000

[Mae91] H. Maetzing, "Chemical Kinetics of Flue Gas Cleaning by Irradiation with Electrons", Adv. in Chem. Phys., vol.80, pp. 315-40

[Mos99] T. Mostefaoui, S. Laube, G. Gautier, C. ebrion-Rowe, B.R. Rowe, and J.B.A. Mitchell, J. Phys. B: At. Mol. Opt. Phys., Vol. 32, 1999, p. 5247

[Pal01a] P. Palm, E. Plönjes, M. Buoni, V.V. Subramaniam, and I.V. Adamovich, "Electron Density and Recombination Rate Measurements in CO-Seeded Optically Pumped Plasmas", Journal of Applied Physics, vol. 89, 2001, pp. 5903-5910

[Pal01b] Peter Palm, Elke Plönjes, Igor V. Adamovich, Vish V. Subramaniam, Walter R. Lempert, and J. William Rich, "High pressure air plasmaS sustained by an electron beam and enhanced by optical pumping", AIAA-Paper 2001-2937, 32nd AIAA Plasmadynamics and Lasers Conference, 11-14 June 2001, Anaheim, CA

[Plo00a] E. Plönjes, P. Palm, A.P. Chernukho, I.V. Adamovich, and J.W. Rich, Chem. Phys., vol. 256, 2000, p. 315

[Plo00b] E. Ploenjes, P. Palm, W. Lee, M. D. Chidley, I.V. Adamovich, W.R. Lempert, and J. William Rich, "Vibrational Energy Storage in High-Pressure Mixtures of Diatomic Molecules", Chemical Physics, vol. 260, 2000, pp. 353-366

[Plo01]   E. Ploenjes, P. Palm, W. Lee, W.R. Lempert, and I.V. Adamovich, "RF Energy Coupling to High-Pressure Optically Pumped Nonequilibrium Plasmas", Journal of Applied Physics, vol. 89, No. 11, 2001, pp. 5911-5918

[Plo02] E. Plönjes, P. Palm, I.V. Adamovich, J.W. Rich, "Characterization of Electron-   Mediated Vibration-Electronic (V-E) Energy Transfer in Optically Pumped Plasmas Using Langmuir Probe Measurements", AIAA-Paper 2002-2243, 33rd AIAA Plasmadynamics and   Lasers Conference, 20-23 May 2002, Maui,Hawaii

[Rai91] Raizer, Y.P., "Gas Discharge Physics", Springer-Verlag, Berlin, 1991

Figures
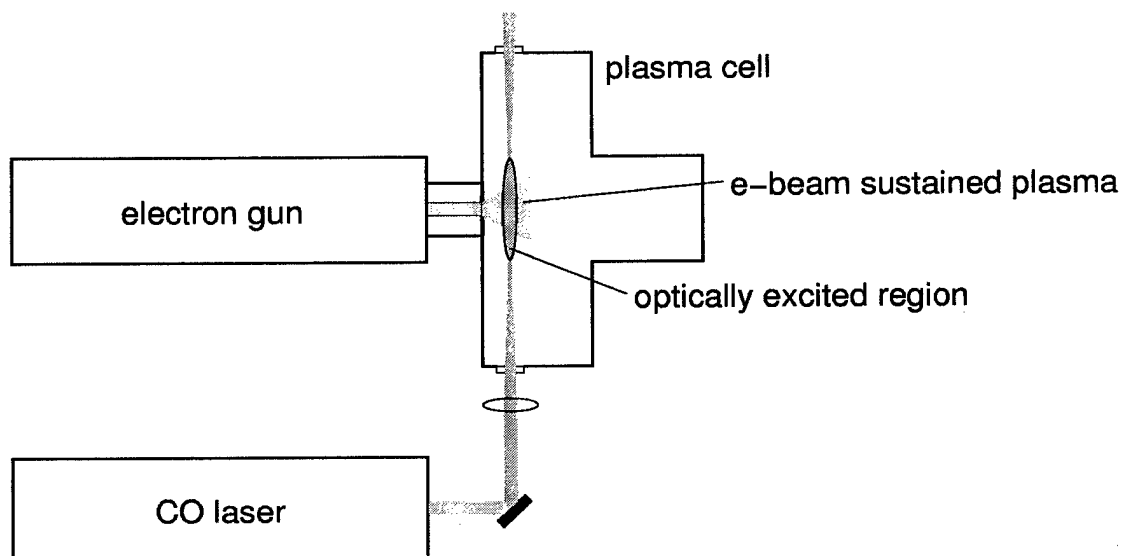
Figure 1. Schematic of the electron beam and laser setup.

Figure 2. Schematic of the plasma cell.

CO 1->0 R-Branch Emission
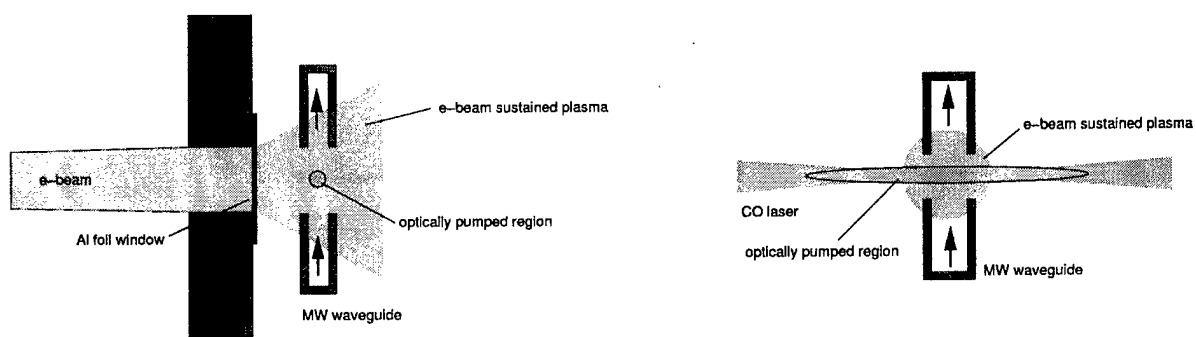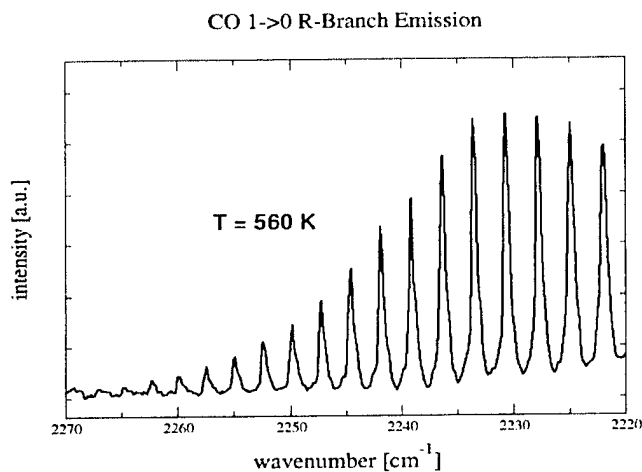
Figure 3. Translational temperature in vibrationally excited air at 1 atm measured by Fourier transform emission spectroscopy.
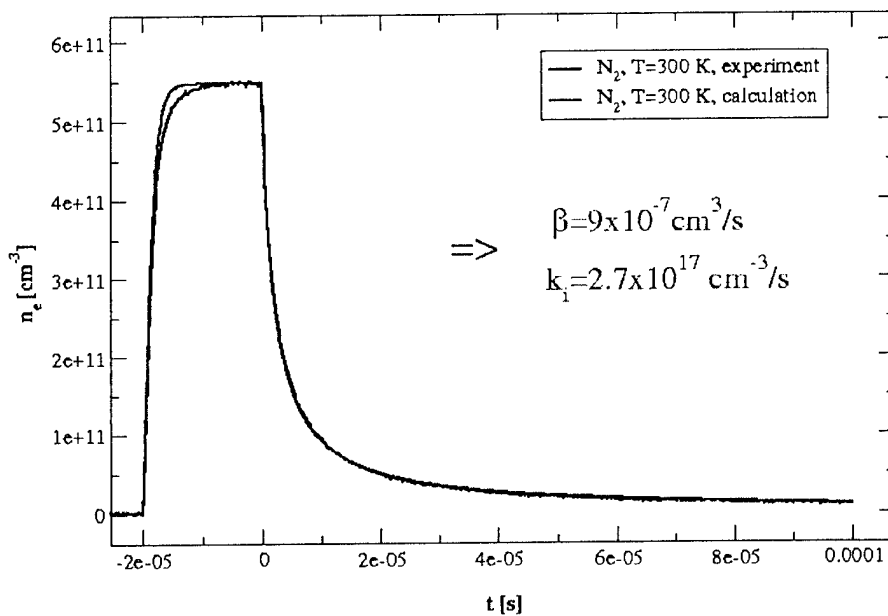
Figure 4. Measured and calculated electron densities during and after a 20μs e-beam pulse in 1 atm N_2. In the calculation the electron production rate k_i and recombination rate β were chosen to best fit the measurement.
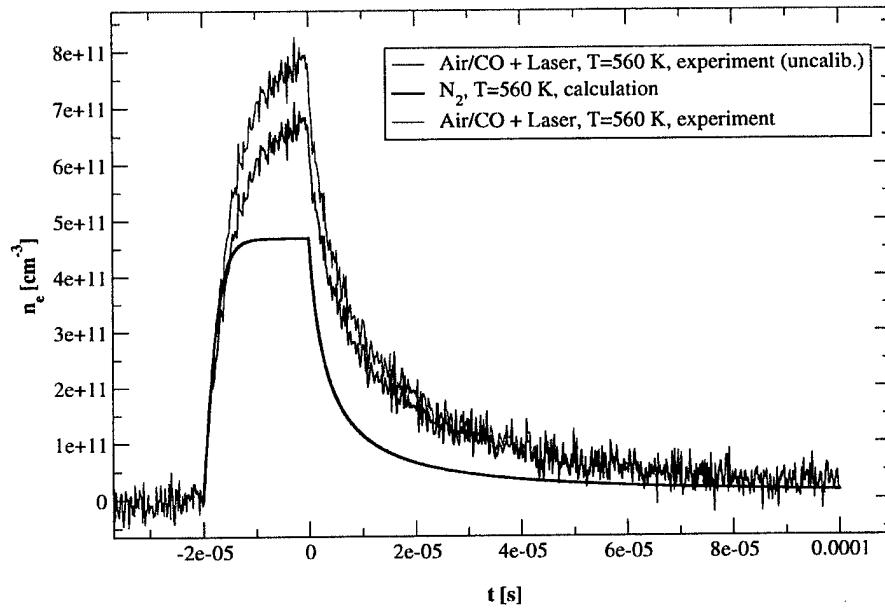
Figure 5. Measured electron densities in 1 atm of laser excited, CO seeded air before and after calibration by comparison with N_2. Assuming identical electron production rates in 1 atm of air and 1 atm of N_2 the slope of the initial electron density rise should be identical for air and N_2. Very good agreement is achieved by changing the diameter of the laser excited region from d=0.2 cm to d=0.185 cm (Eq. 6).
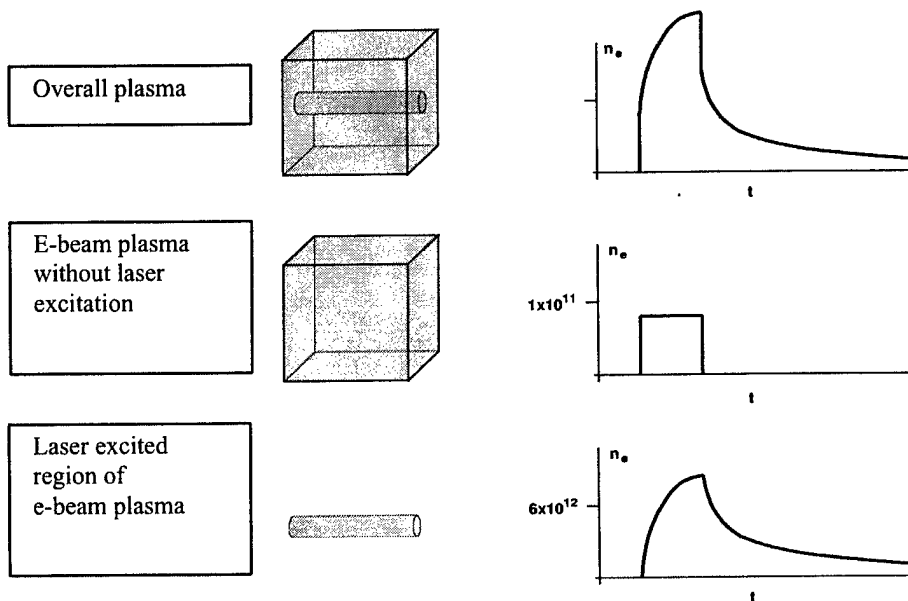
Figure 6. Illustration of how the e-beam ionized region and the e-beam ionized / laser excited region contribute to the overall electron density signal recorded by the microwave system. Note the different scales on the n_e-axes.
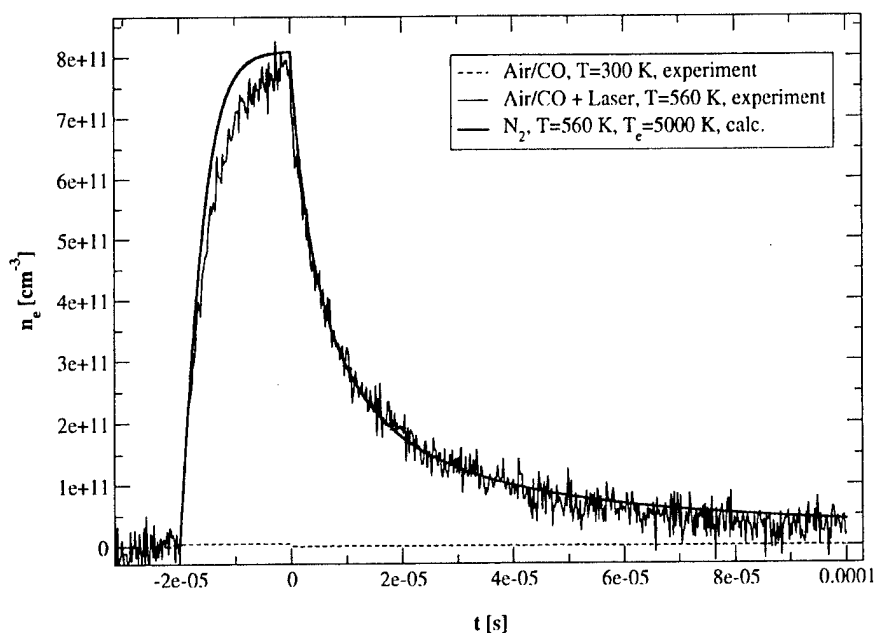
Figure 7. Measured electron density pulse in 1 atm of vibrationally excited air compared with calculated electron density in N_2. In strong contrast to a plasma in cold equilibrium air (dashed line) vibrationally excited air does not seem to exhibit any electron attachment to O_2, i.e. peak electron density and plasma decay in vibrationally excited air seem to be purely caused by electron-ion recombination.
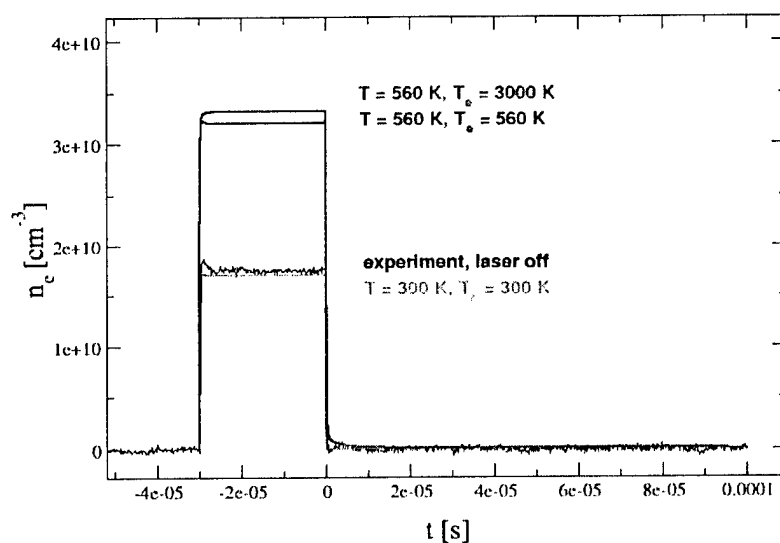
Figure 8. Comparison of experimental data and kinetic modeling for different translational and electron temperatures.
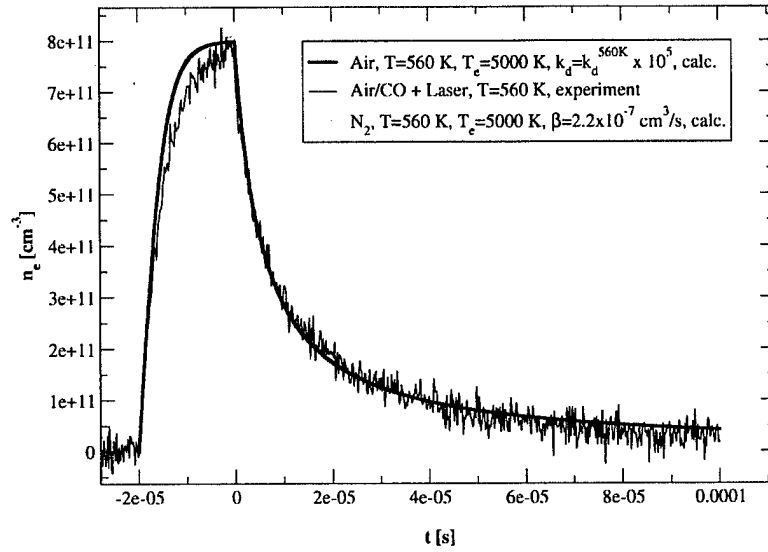
Figure 9. Experimental and calculated electron densities for the conditions of Figs. 4,5,7 using hugely increased electron detachment rates. Increase of the detachment rates by 5 orders of magnitude fully mitigates the effect of attachment and the calculated trace for laser excited air practically coincides with the calculated trace for N_2.
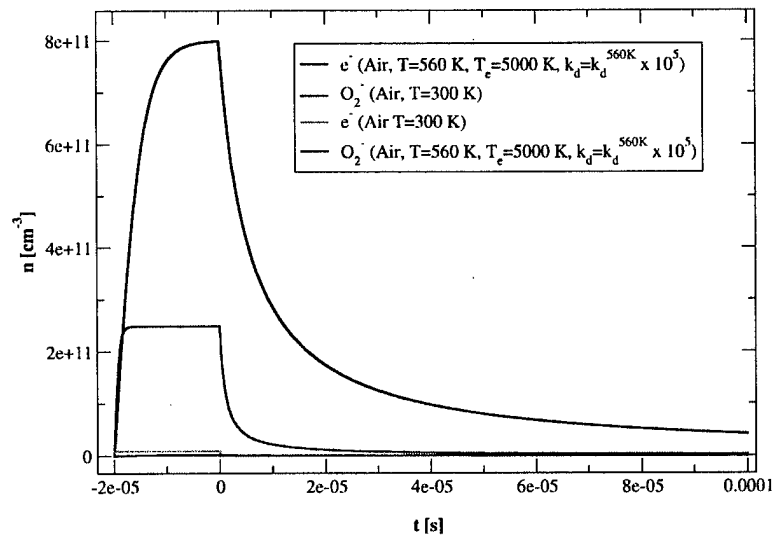
Figure 10. Calculated number densities for the negatively charged species e^- and O_2^-. Due to attachment, the dominant negative species in cold air is O_2^-, whereas in vibrationally excited air the O_2^- population is insignificant ($<2\times10^9$ cm^{-3}) and the dominant negative species is e^-. Note the higher total number density of charged species in vibrationally excited air which is due to the

12. SPECTRALLY FILTERED RAMAN/THOMSON SCATTERING USING A RUBIDIUM FILTER

Wonchul Lee and Walter R. Lempert

A new spectrally filtered light scattering apparatus is presented based on a diode laser injected seeded titanium:sapphire laser and rubidium vapor filter at 780 nm. It is shown that the realizable attenuation of quasi-elastically scattered light, limited by a residual broad spectral line width, unseeded, component to the laser output, is as high as 5×10^5 using the laser system alone. Preliminary measurements incorporating a set of dispersing prisms and a stimulated Brillouin scattering Phase Conjugate Mirror external to the laser appear to provide additional extinction. The utility of the system for measurement of electron density and temperature by Thomson scattering is demonstrated in a 30 torr argon dc discharge. At 100 mamps current an electron density of 5.52×10^{13} cm^{-3} is measured on the discharge center line with a 2σ value of statistical uncertainty equal to 1.2×10^{12} cm^{-3}. The corresponding electron temperature is 1.26 ± 0.05 eV.

INTRODUCTION

Recent advances in solid state laser technology have enabled a variety of new optical diagnostic techniques based on the use of atomic/molecular vapor filters as narrow bandwidth "notch" filters and/or as spectral discriminators[1-2]. In this paper we present new results obtained using a rubidium vapor filter in combination with a diode laser injection- seeded, narrow spectral bandwidth titanium:sapphire laser at 780 nm. The emphasis is to demonstrate the utility of the system for low wave number inelastic scattering diagnostics, such as pure rotational Raman and/or Thomson scattering. The laser system, based on that developed by Moulton and Rines,[3] and essentially identical to that previously used for filtered scattering diagnostics by Finkelstein, et al.[4], and Zaidi, et al.[5], consists of the following basic components. The second harmonic output of a commercial Q-switched Nd:YAG laser is used as a pump source for a bread board ti:sapphire laser, which is injection-seeded using a single frequency external cavity diode laser. The principal differences between this laser system and that reported by Finkelstein is the use of the diode laser seed source, which substitutes for an argon-ion pumped continuous wave ti:sapphire ring laser, and the use of injection seeding, as opposed to injection locking. This results in a significant decrease in cost and complexity, but has some disadvantages, which will be discussed in subsequent sections. The system is also conceptually similar to that recently described by Bakker, et al[6], who obtained Thomson scattering spectra in a glow discharge by combination of a grazing incidence dye laser with a sodium vapor filter. This system has the advantage that the laser is readily available commercially and is relatively simple. The filter, however, is somewhat more complex.

The above cited pulsed Raman/Thomson scattering systems are also similar, conceptually, to previously reported Raman systems which pair an alkali vapor filter with continuous wave lasers such as ti:sapphire[7], or semiconductor diode[8].

EXPERIMENTAL

Figure 1 shows a schematic diagram of the filtered scattering apparatus. The titanium sapphire laser cavity is essentially identical to that described in reference 3, but is pumped by the second harmonic output of a commercial (Continuum Powerlite Precision 8000) 10 Hz repetition rate Q-switched Nd:YAG laser. The pump laser output of approximately 260 mJ per pulse is split into four parts, each of which pumps a single surface of one of two ti:sapphire crystals. Each crystal surface is located in the intermediate field of a 130 cm focal length plano-convex lens (~ 60 cm before the waist), which partially focuses the ~ 8 mm diameter pump beam to a cross section of ~ 2-3 mm at the crystal surface. An ~ 8 mWatt external cavity diode laser (Newport Model 2010) is used for injection seeding, which has been performed in two configurations, labeled "A" and "B" in Fig. 1. Configuration A, similar to that described in reference 4, injects the seed laser using the very small (~ 1-2 %) reflection of horizontally polarized light at near Brewster's angle from a quartz flat inserted into the cavity. This has the advantage of simplicity, but poor coupling efficiency. Configuration B couples the seed laser through the cavity output coupler using a Faraday rotation optical isolator. In some experiments, the output of the injection seeded laser is externally dispersed using a "prism monochrometer", identical to that described by Bakker[6], followed by a Stimulated Brillouin Scattering (SBS) phase conjugate cell[9]. As will be described in the next section, the purpose of this is to minimize interference from a small residual broad-band, "non-seeded" component of the laser output. Ignoring this broad band component, the laser output energy is approximately 60 mJ per pulse, with spectral bandwidth of ~ 150 MHz (corresponding to 1 or 2 longitudinal modes). The individual pulse duration is ~ 30 nsec.

Scattering is 1:1 imaged at 90 degrees using a pair of mirrors and f/4 lenses to rotate the image of the Raman/Thomson scattering parallel to the entrance slit of an Optical Multichannel Analyzer (OMA) system, consisting of a 0.25 meter spectrometer and a GEN IV near IR microchannel plate Intensified CCD camera. Loose focusing of the pump laser (with a 40 cm focal length plano-convex lens) results in a cylindrical sampling volume 20-50 microns (defined by slit) in diameter by 5 mm in length. According to manufacturers specifications (which have not been verified), the ICCD has a quantum efficiency of order 25-30% at 780 nm, which greatly facilitates the scattering diagnostics. The spectrometer is operated with an input slit of between 20 and 50 microns. A 5 cm path length rubidium vapor cell, heated to a temperature of 320 °C, is placed in the detection path, between the scattering cell and the OMA. The vapor cell is quite simple, consisting of a single piece of 25.4 mm diameter quartz containing the

rubidium, with optical flats fused to each end. The cell is heated by wrapping with standard laboratory heating tape and is temperature controlled to +/- 1K using a thermocouple (placed on the outside of the cell) and a simple feed-back controller. To minimize condensation of rubidium vapor on the cell windows a pair of evacuated 25.4 mm diameter quartz extension tubes are fused to the ends of the cell. Heating of these tubes minimizes the temperature gradient at the cell windows and, therefore, rubidium vapor condensation. Some window degradation, presumably due to chemical reaction, is also observed. After approximately 200 hours of operation at high temperature, the cell transmission was measured to have dropped from approximately 0.85 (due to Fresnel losses) to approximately 0.50.

Rotational Raman spectra were obtained in a static cell, essentially identical to that used previously for Q-branch Raman spectra[10]. Thomson scattering spectra were obtained in a similar cell to which a pair of electrodes had been added. The electrodes were 0.25 inch diameter stainless steel rods, positioned in the center of the cell, separated by a spacing of 1 inch. All spectra were integrated on the ICCD sensor for a period of between 1 and 10 minutes.

RESULTS AND DISCUSSION

Characterization of System Extinction Without SBS Cell

Figure 2 shows a Fourier Transform transmission spectrum of the rubidium vapor cell at 320 °C, along with a least squares fit to a simple spectral model of the $5s\ ^2S_{1/2} - 5p\ ^2P_{3/2}$ transition at 780 nm. As can be seen Fig. 3, which is a calculation of the absorbance, the 780 nm transition is made up of 12 individual components, which result from a combination of hyperfine splitting and natural isotopic abundances[11]. While the theoretical absorption of the cell is exceedingly high, with calculated peak absorbance of ~3.5 x 10^6, the realizable attenuation of elastic and/or Rayleigh/Mie scattering is limited, as reported previously[5,12,13], by the existence of a small, but significant, broad spectral bandwidth (~ 1 nm) component to the narrow line width titanium:sapphire laser output. It should be pointed out that this component is not believed to be due to amplified spontaneous emission (ASE). Rather, it is believed to result from an unlocked component of the output intensity, which, as will be shown below, is dependent upon the injected seed laser power. This view is supported by the observation that insertion of a card directly in front of the high reflector in the rear of the ti:sapphire cavity completely eliminates the broad band component. (ie, it requires "lasing" feedback). To evaluate the realizable extinction of Rayleigh/Mie scattering, a detailed set of measurements have been performed using injection seeding configurations labeled "A" and "B" in Fig. 1, both with and without incorporation of the dispersing prisms and SBS cell.

216

As a baseline for comparison, Fig. 4a is a scattering spectrum from a static cell of 500 torr of nitrogen at room temperature, obtained without either injection seeding of the laser or insertion of the rudidium vapor filter into the detection path. It appears to be a single central component with line width of 0.56 nm Full Width at Half Maximum (FWHM) representing a convolution of the unseeded laser line width with the ~ 0.20 nm spectral resolution of the spectrometer. Fig. 4b is a 500 × blow up of the spectrum in Fig. 4a in which the intensity axis is normalized to the peak of the quasi-elastic Rayleigh/Mie scattering signal from Fig. 4a. It can be seen that the peak intensity of this central quasi-elastic scattering signal is a factor of ~ 5000 greater than that for the individual rotational Raman transitions (Note that a portion of the central scattering component is almost certainly due to stray elastic scattering from windows and surfaces). Moreover, it should also be noted that at our targeted conditions of ~ 10^{13} cm^{-3} electron density, the peak quasi-elastic Thomson scattering signal will be a factor of approximately twenty times lower than the peak Raman signal observed in Fig. 4b.

Figure 5 illustrates the attenuation of quasi-elastic scattering which was achieved using injection seeding alone. (Results obtained incorporating the SBS cell are presented subsequently). Figs 5 a-c illustrate the results of seeding configuration "A", in which the circulating seed power within the ti:sapphire cavity was measured to be ~ 50 - 100 microwatts (1-2% of the seed laser power). Figs 5a and b are identical to Fig 4a and b, except that injection seeding of the laser has resulted in a considerably narrowed spectral line width, with apparent FWHM, limited by the spectrometer resolution, of ~ 0.20 nm. In this case, it can be seen that the peak intensity of the central quasi-elastic scattering signal is a factor of ~ 2000 greater than the peak rotational Raman signal. Fig. 5c is another identical, similarly normalized spectrum, except that it was obtained using the rubidium filter. Comparison of Figs. 5b and 5c shows that the peak relative intensity of the central scattering component is reduced by a factor of ~ 4000 when the rubidium filter is employed. In addition, it can be seen from Fig. 5c that the residual transmitted central component has a "hole" in the center, corresponding to the narrow line width absorption cell. It should be noted that the spectra shown in Fig. 5b and 5c were obtained with a laser pulse energy incident to the scattering cell of ~ 50 mJ/pulse. The intensity was integrated on the ICCD detector for one minute.

Figure 5d shows the rotational Raman spectrum obtained employing seeding configuration "B". In this case, the circulating seed power in the ti:sapphire cavity is increased to ~ 1 mWatt, although the laser output is reduced by ~ 30% due to transmission losses in the optical isolator. It can be seen that the relative intensity of the central scattering component has been very greatly reduced, to the extent that it is difficult to determine from inspection. In fact, the peak residual fractional intensity, measured as described in a subsequent section (see Fig. 9), is ~ 2 ×10^{-6} so that the peak rotational Raman intensity is now ~ 100 times greater than the peak residual, transmitted central component scattering. It should also

217

be noted that the relative intensity of the unfiltered central component to which the data in Fig. 5d was normalized was approximately a factor of greater than that in Fig. 5c.

These results illustrate the well known fact that the spectral purity, P, defined as the ratio of the narrow band component of the injection seeded laser pulse to the total output, is a strong function of the circulating seed pulse energy. The injection seeding process is described in detail in Barnes and Barnes,[13] who show that the circulating seed energy required to achieve a given spectral purity scales as

$$E_{seed} \propto P/_{1-P} \qquad (1)$$

when other factors, such as the spatial and spectral overlap between the seed laser beam and the ti:sapphire cavity modes, are constant. Clearly, in the limit when P approaches one, the required seed energy increases rapidly. By the above definition, the spectral purity which we have achieved, employing seed configuration "B", is on the order of 0.99998. (Note that we arrive at this number by 1), assuming that the effective spectral line width of the residual transmitted light, which includes the spectrometer instrument function, is a factor of ~ 10 greater than that for the seeded light, and 2), that ~ half of the broad band component is absorbed by the filter). While we have not performed an exhaustive literature search, this represents, to our knowledge, an improvement of approximately three orders of magnitude over that reported in references 12 and 13 for cw injection seeding. Due to limits in the seed power of our external cavity laser system, it is not clear whether (or how close to) a practical limit we have achieved.

Thomson Scattering Spectra

Figure 6 shows a filtered Thomson scattering spectrum obtained from a dc argon "constricted" glow discharge also obtained without incorporation of the dispersing prisms and SBS cell. The argon pressure is 30 torr and the discharge current is 100 mamps. The constricted glow is ~ 2-3 mm in diameter and is stabilized by incorporation of a 500 ohm current limiting ballast resistor in series with the dc discharge. Approximately 25 % of the total applied 20 Watts is dissipated across the resistor. While this is somewhat inefficient, it provides a simple means to create a reasonably stable discharge with relatively high (~ 10^{13} cm^{-3}) electron density. Figure 6a shows the exceedingly weak Thomson scattering signal superimposed upon the relatively large argon spontaneous emission. Despite employing a gated ICCD camera, it can be seen that the spontaneous emission is many orders of magnitude more intense than the Thomson signal. This is confirmed in Fig. 6b, which is a 200 × blow-up of the spectrum in Fig. 6a.

Fig. 7 is a least squares fit of the experimental spectrum in Fig. 6b to a simple incoherent Thomson scattering model. The model assumes a Gaussian scattering spectrum, with Half Width at Half Maximum, γ, given by:

$$\gamma(\text{nm}) = \frac{\lambda_{780}}{c}\sqrt{\frac{2\ln(2)kT_e}{m_e}} = 1.285\sqrt{T_e} \qquad (2)$$

where T_e is the electron temperature in eV units. The model incorporates the measured transmission profile of the rubidium filter (Fig. 2), convolutes with the measured instrument response function of the OMA (similar to Fig. 5a), and calibrates the absolute intensity using the known rotational Raman cross section of 5.4×10^{-30} cm^2/sr for J = 6 → 8 transition of nitrogen at 488.0 nm [15] and Thomson scattering cross section of 5×10^{-26} cm^2/sr [16]. Note that while the Thomson scattering cross section is independent of wavelength, the rotational Raman cross section has been scaled to 780 nm assuming the well known v^4 dependence. From this procedure the inferred values of electron number density and temperature are 5.52×10^{13} cm^{-3} and 1.26 eV, respectfully. Corresponding values for the potential sensitivity, based on the statistical uncertainties (2σ) provided by the least squares fitting procedure[17] are 1.2×10^{12} cm^{-3} and 0.05 eV.

Evaluation of SBS Phase Conjugate Cell

Despite the significant reduction in stray scattering afforded by the rubidium vapor filter, spectra such as that shown in Fig. 7 are still subject to systematic error due to the small, but finite, non-rejected, residual stray light. For example, the data displayed in Fig. 7 is what results after subtraction of a small mean residual stray light component, the peak magnitude of which was measured to be ~ 10% of the net peak Thomson signal. At relatively high electron density, such as that measured in Fig. 7, the primary effect of this residual transmitted light is to introduce uncertainty in the inferred value of electron temperature. In order to assess this, we have altered the mean residual by $\pm$ 50 % and re-performed the least squares curve fits. As can be seen from Fig. 8, the fits themselves appear to be equally good as that displayed in Fig. 7. While there is virtually no effect on the inferred value of electron density, the values for electron temperature change slightly, by approximately +/- 0.05 eV, which is essentially the same as the 2σ value for the statistical uncertainty.

At lower values of electron density, where the signal is even weaker than that in Fig. 7, residual stray light is a more significant potential problem. We have performed some preliminary measurements employing the dispersing prisms and SBS cell to assess the potential to further reduce the residual broad band component of the seeded laser. This approach is similar to that described in reference 6 except that the pinhole spatial filter in that system has been replaced by the SBS cell. SBS is often employed to filter broad band ASE which is superimposed upon the narrow band output of dye and/or solid state lasers[14].

Its use, however, is based primarily on the increased divergence of the ASE component, which does not spatially overlap the focused "pump" beam in the SBS cell. (The increased line width of the ASE also plays a role, albeit a smaller one[14]). In a similar manner, the purpose of the prisms in our apparatus is to disperse the broad band unlocked component of the ti:sapphire laser so that after focusing into the SBS cell, its spatial overlap with the narrow band pump (and hence SBS reflection) will be reduced.

Inclusion of the SBS cell with seeding configuration "B", while reducing the available laser pulse energy by a factor of approximately, four (due to SBS losses), resulted in filter rejection which was sufficiently high that it was difficult to measure directly from rotational Raman spectra. However, some insight can be gained from Fig. 9, which shows the very weak residual transmitted light obtained from an evacuated cell with very long (10 minute) integration time. Figs. 9a/9b show the residual scattering without/with, respectfully, incorporation of the SBS cell. As alluded to in the previous section, Fig 9a shows that the peak residual transmission through the filter is $\sim 2 \times 10^{-6}$. While it is difficult to see by eye in Fig. 9b, the principal effect of the SBS cell is to reduce the line width, and therefore the integrated intensity, of the residual transmitted light. This can be seen much more clearly in Fig. 10, which is similar to Fig. 9 except that a small additional quantity of stray scattered light from optical elements has purposefully been allowed to "leak" into the spectrometer without being transmitted through the rubidium filter. It can be seen that when the SBS cell is employed, the residual light is spectrally more narrow, with line width essentially equal to the 0.20 nm resolution of the spectrometer. We conclude that the effective spectral purity of the entire system, laser and SBS cell, has been further improved to ~0.999998. We plan future measurements to determine this more accurately.

As a further test of the SBS cell, some preliminary Thomson spectra have been obtained. Figure 11 is a representative spectrum, along with least squares fit, obtained under identical conditions to that of Figs. 6 and 7 except that the dispersing prisms and SBS cell were employed and the electron density was lowered to a value of approximately 1.7×10^{13} cm^{-3}. It can be seen that the signal to noise ratio is reduced as a result of the factor of approximately four loss in the incident laser beam intensity (discussed above) and the approximate factor of three decrease in electron density. The least squares fitting procedure returns a value of 1.69×10^{13} +/- 1.4×10^{12} (2σ) cm^{-3} and 1.07 +/- .16 eV (2σ) for the electron number density and temperature, respectively.

It is stressed that sources of residual transmitted background signal are still being explored. In particular, it appears that a significant portion, if not the majority, is from stray light that is scattered from the numerous optical and other surfaces and is "seen" by the detector without following the principal imaging path. We have incorporated baffling and other approaches to minimize this, but it is not yet clear whether its contribution has been completely minimized. Nonetheless, these preliminary results appear to indicate that the incorporation of the prism-SBS cell does reduce the impact of residual stray light,

although this is achieved at the cost of reduced signal levels. We plan to evaluate the utility of the SBS cell in more detail in the near future, with emphasis on improving the net reflection efficiency.

CONCLUSIONS

A new spectrally filtered light scattering apparatus is presented which incorporates an external cavity diode laser injected seeded titanium:sapphire laser and an optically thick rubidium vapor filter at 780 nm. In a detailed set of measurements the realizable attenuation of quasi-elastically scattered light, which is limited by the existence of a broad spectral line width, unseeded, component to the laser output, has been determined. It is found that the magnitude of this broad band component is a strong function of the circulating power of the seed laser within the titanium:sapphire laser cavity. Injection of the seed laser through the ti:sapphire output coupler, employing a Faraday optical isolator, resulted in a measured peak transmission value of approximately 2×10^{-6}, corresponding to a spectral purity of 0.99998. Preliminary measurements indicate that incorporation of a set of dispersing prisms and a stimulated Brillouin scattering Phase Conjugate mirror appear to provide an additional factor of ten extinction.

The utility of the system for measurement of electron density and temperature by Thomson scattering was demonstrated in an argon dc constricted glow discharge. At 100 mamps current and 30 torr of argon an electron density of 5.52×10^{13} cm^{-3} was measured on the discharge center line with a 2σ value of statistical uncertainty equal to 1.2×10^{12} cm^{-3}. The corresponding electron temperature was measured to be 1.26 ± 0.05 eV.

REFERENCES

1. Miles, R.B., Yalin, A.P., Tang, Zhen, Zaidi, S.H., Forkey, J.N., "Flow field imaging through sharp-edged atomic and molecular 'notch' filters", Meas. Sci. Tech., Vol. 12, pp. 442-451, 2001.

2. Elliott, G.S., Glumac, N., Carter, C.D., "Molecular flitered Rayleigh scattering applied to combustion", Meas. Sci. Tech., Vol. 12, pp. 452-466, 2001.

3. Rines, G.A., and Moulton, P.F., "Performance of gain-switched Ti:Al$_2$O$_3$ unstable-resonator lasers", Opt. Lett., Vol. 15, pp. 434-436, 1990.

4. Finkelstein, N.D., W.R. Lempert, R.B. Miles, A. Finch, and G.A. Rines, "Cavity locked, injection seeded, titanium:sapphire laser and application to ultraviolet flow diagnostics", AIAA-96-0177, 34th AIAA Aerospace Sciences Meeting, Reno, NV, January 1996.

5. Zaidi, S., Z. Tang, A. Yalin, P. Barker, and R. Miles, 2000, "Filtered Thomson scattering in an argon plasma", AIAA-2001-0415, 39th AIAA Aerospace Sciences Meeting, Reno, NV, January 2001.

6.   Bakker, L.P., J.M. Freriks, F.J. deGroog, and G.M.W. Kroesen, "Thomson scattering using an atomic notch filter", Rev. Sci. Instrum., Vol. 71, pp. 2007-2014, 2000.

7.   Indralingan, R., Simeonsson, J.B., Petrucci, G.A., Smith, B.W., and Winefordner, J.D.W., "Raman spectrometry with metal vapor filters," Analytical Chemistry, Vol 64, pp. 964-967, 1992.

8.   Clops, R., Fink, M., Varghese, P.L., and Young, D., "Thermodynamic studies of subsonic gas flow using a laser diode Raman spectrometer," Applied Spectroscopy, Vol 54, no.9, pp. 1391 – 1398, 2000.

9.   Ni, C.K. and Kung, A.H, "Effective suppression of amplified spontaneous emission by stimulated Brillouin scattering phase conjugation", Optics Letters, Vol. 21, pp. 1673-1675, 1996.

10.   Lee, W., Adamovich, I. V., and Lempert, W. R., "Optical pumping studies of vibrational energy transfer in high-pressure diatomic gases", J. Chem. Phys., Vol. 114, pp. 1178-1186, 2001.

11.   Gustafsson, J., Rojas, D., and Axner, O., "The influence of hyperfine structure and isotope shift on the detection of Rb atoms in atmospheric pressure atomizers by the 2f-wavelength modulation technique", Spectrochim. Acta Part B Vol. 52, pp. 1937-1953, 1997.

12.   Yalin, A.P., Barker, P.F., and Miles, R.B., "Characterization of laser seeding by use of group-velocity dispersion in an atomic-vapor filter", Opt. Lett., Vol. 25, pp. 502-504, 2000.

13.   Barnes, J.C, Barnes, N.P., Wang, L.G., and Edwards, W., "Injection Seeding II: Ti:Al$_2$O$_3$ Experiments", IEEE J. Quant. Elec., Vol. 29, pp. 2684-2692, 1993.

14.   Ni, C.K. and Kung, A.H, "Amplified spontaneous emission reduction by use of stimulated Brillouin scattering: 2-ns pulses from Ti:Al$_2$O$_3$ amplifier chain", Applied Optics, Vol. 37, pp. 530-535, 1998.

15.   Penney, C. M., St. Peters, R. L., and Lapp, M., "Absolute rotational Raman cross sections for N$_2$, O$_2$ and CO$_2$", J. Opt. Soc. Am. Vol. 64, pp. 712-716, 1974.

16.   Hutchinson, I.H., *Principles of Plasma Diagnostics,* Cambridge University Press, Cambridge, 1990.

17.   Bevington, P. R., *Data Reduction and Error Analysis for the Physical Sciences,*" McGraw Hill, New York, 1969.

Figure Captions

Figure 1: Schematic Diagram of Filtered Thomson Scattering Apparatus

Figure 2: Experimental transmission of 5 cm path length rubididium vapor cell at 320 °C and least squares fit to spectral model.

Figure 3: Modeled absorbance of rubidium vapor cell including position and relative contribution of 12 hyperfine/isotope components

Figure 4: (a) Scattering spectrum of static cell of 500 torr of N_2 at room temperature. No vapor filter was employed.

(b) 500 X blowup of spectrum in Fig. 4a. Intensity axis is normalized to peak intensity in Fig. 4a.

Figure 5: (a) Scattering spectrum of static cell of 500 torr of N_2 at room temperature employing injection seeding configuration "A". No vapor filter was employed.

(b) 500 × blow up of Fig. 5a. Intensity axis is normalized to peak intensity in Fig. 5a.

(c) Pure rotational Raman spectrum of 500 torr of N2 at room temperature employing seeding configuration "A" without SBS cell. Intensity axis is normalized to peak intensity obtained without incorporation of vapor filter.

(d) Identical to Fig 5c except seeding configuration "B" employed.

Figure 6: Thomson scattering spectrum obtained using seeding configuration "B" from argon "constricted" glow dc discharge. Argon pressure is 30 Torr, discharge current is 100 mamps. Dispersing prisms and SBS cell were not employed.

Figure 7: Least squares fit to Thomson spectrum of Fig. 6b. Electron density is 5.52 cm-3 and electron temperature is 1.26 eV.

Figure 8: Least squares fits to spectrum of Fig 7 with residual background arbitrarily changed by plus (left) and minus (right) 50 %.

+50% : Te = 1.31 ± 0.07 (2σ), ρe = $5.53 \times 10^{13} \pm 1.4 \times 10^{12}$ (2σ)

-50% : Te = 1.21 ± 0.05 (2σ), ρe = $5.52 \times 10^{13} \pm 1.2 \times 10^{12}$ (2σ)

Figure 9: Residual transmitted scattering from evacuated cell using seeding configuration "B" without (left) and with (right) SBS cell.

Figure 10: Similar to Fig. 9 except that stray light has been purposefully allowed to "leak" into spectrometer in order to better illustrate line width difference between without SBS cell (left) and with SBS cell (right).

Figure 11: Thomson scattering spectrum and least squares fit obtained using dispersing prisms and SBS cell. Electron density is 1.69×10^{13} cm-3 and electron temperature is 1.07 eV.
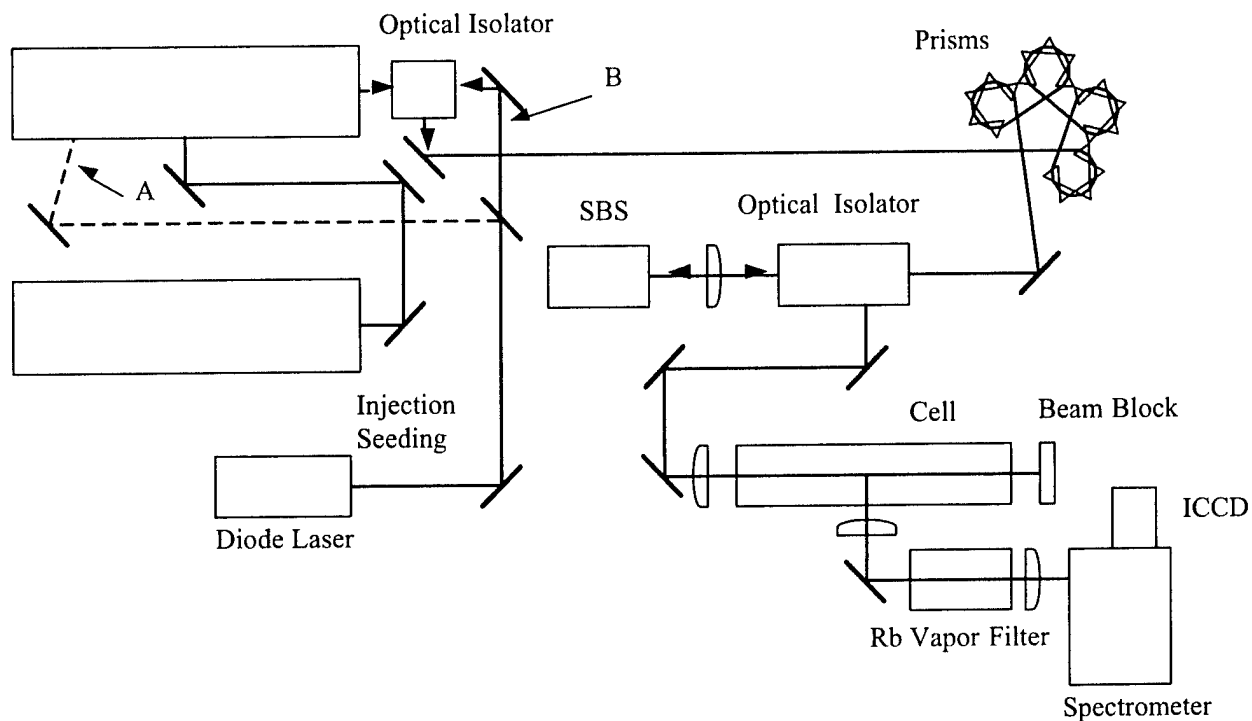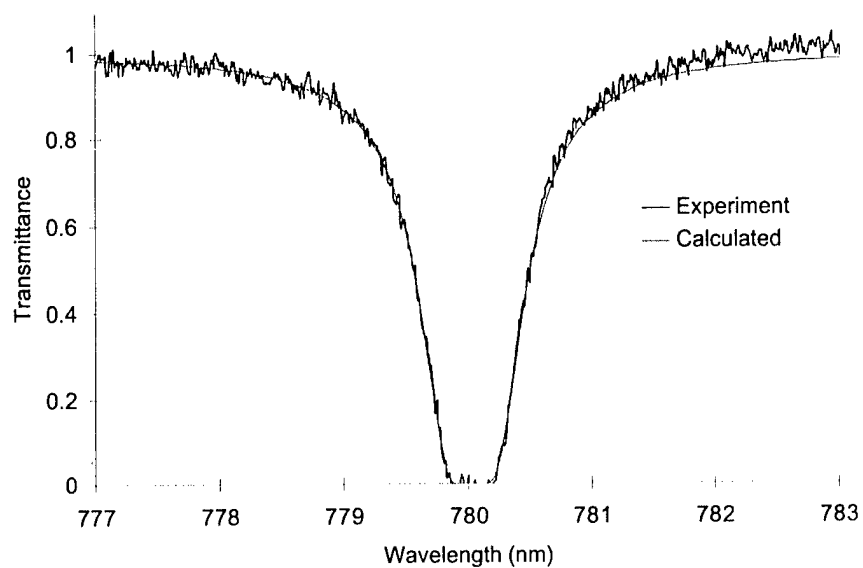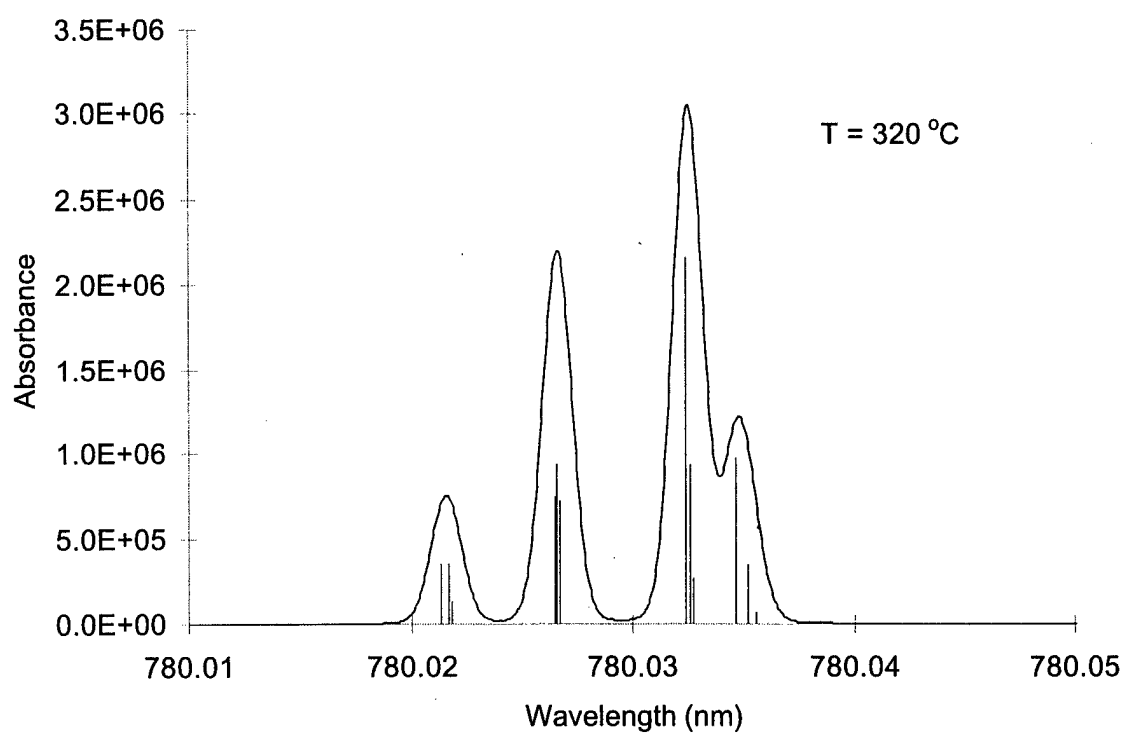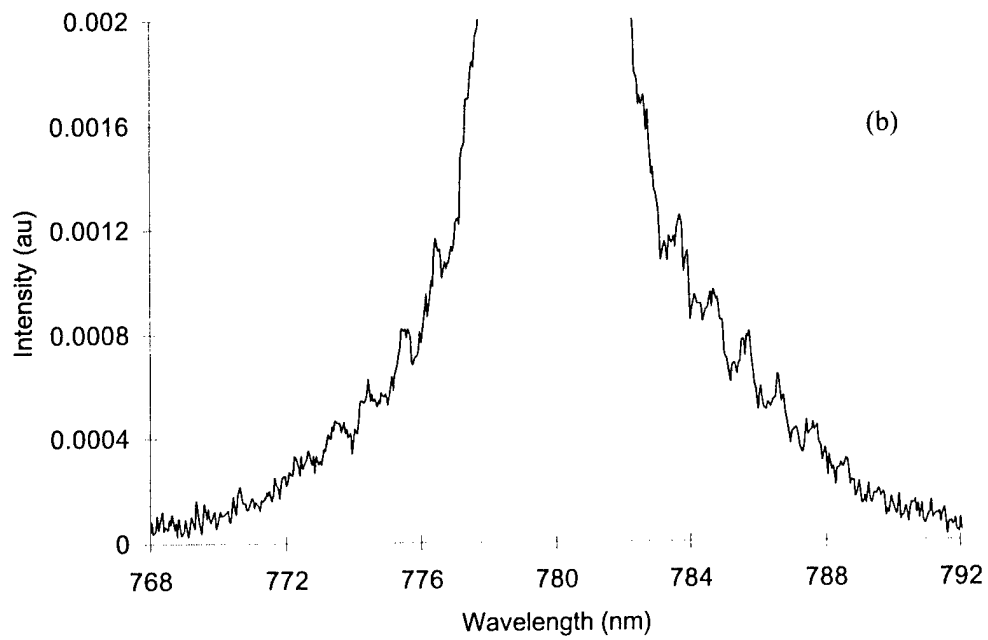
Figures

Figure 1

Figure 2

Figure 3
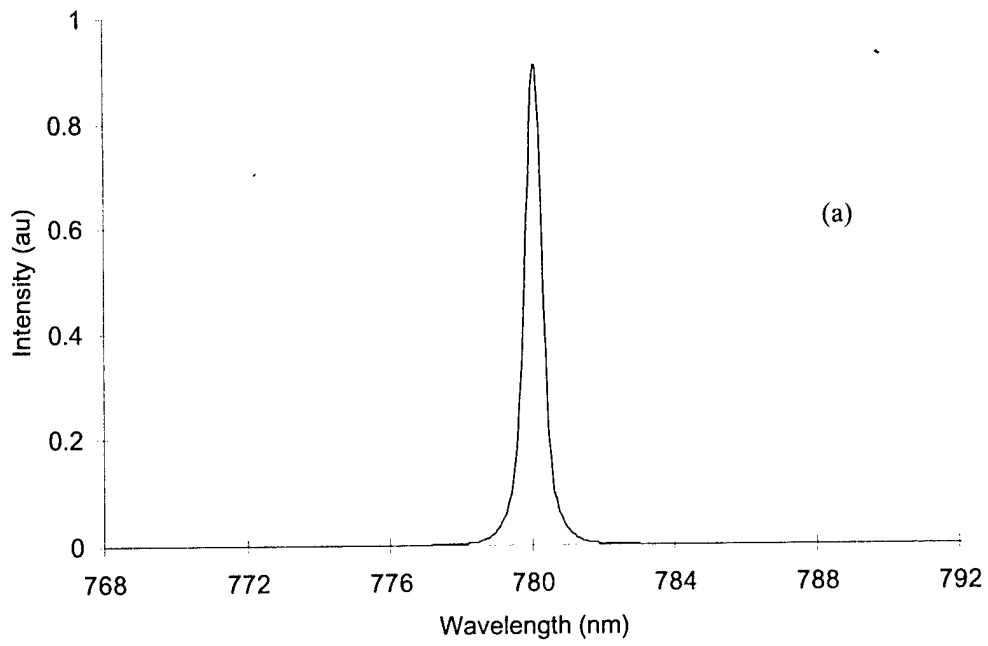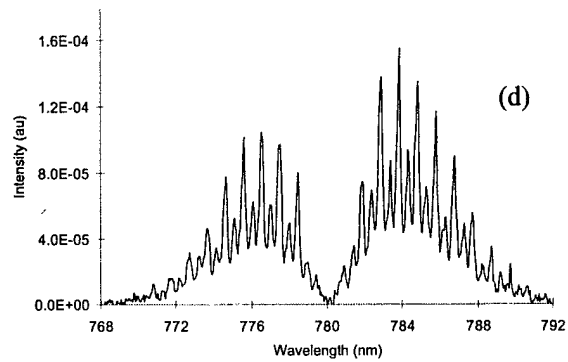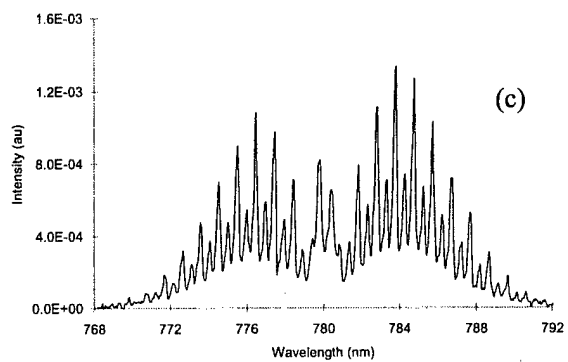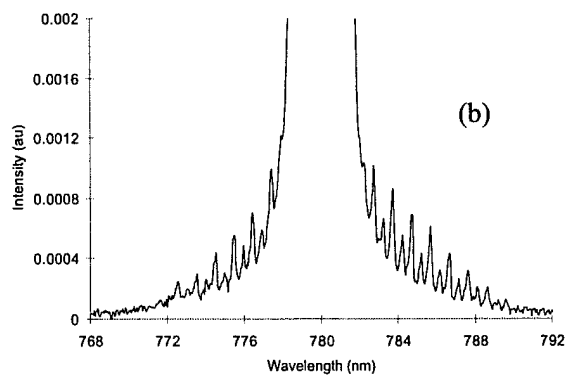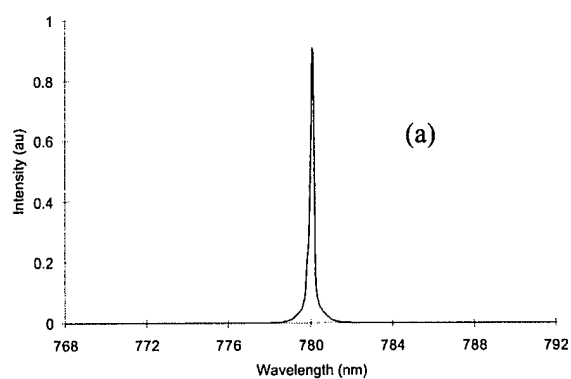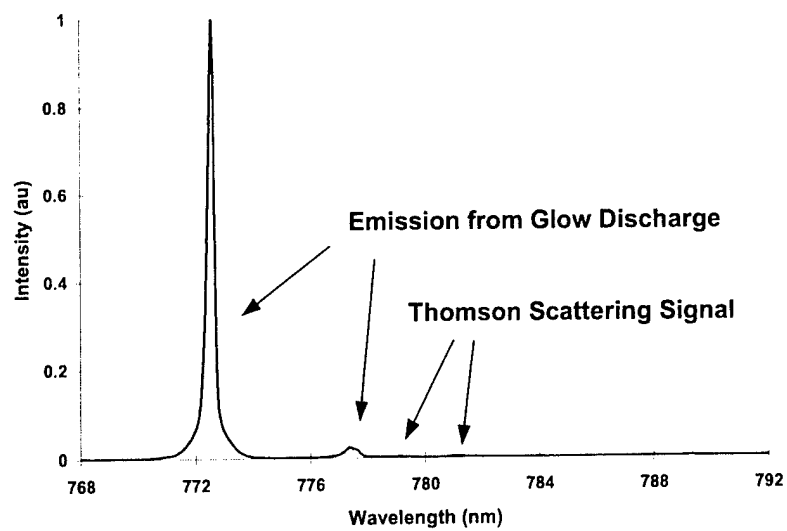
Figure 4

Figure 5

(a)
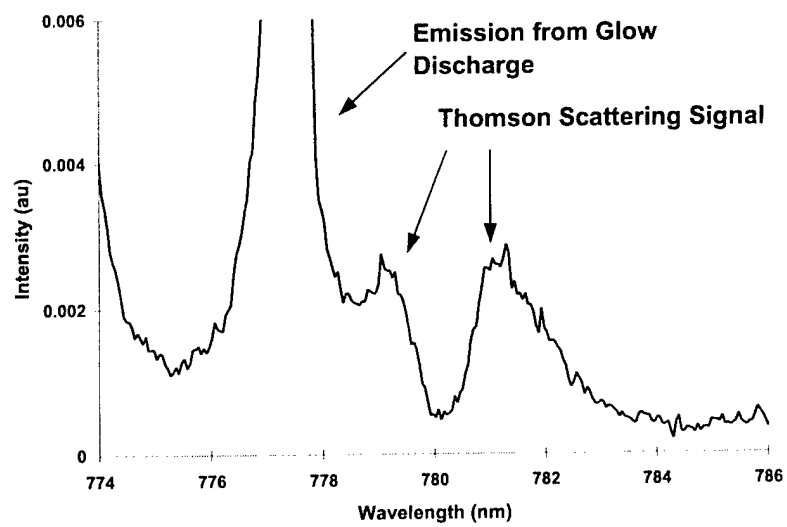
(b)

Figure 6
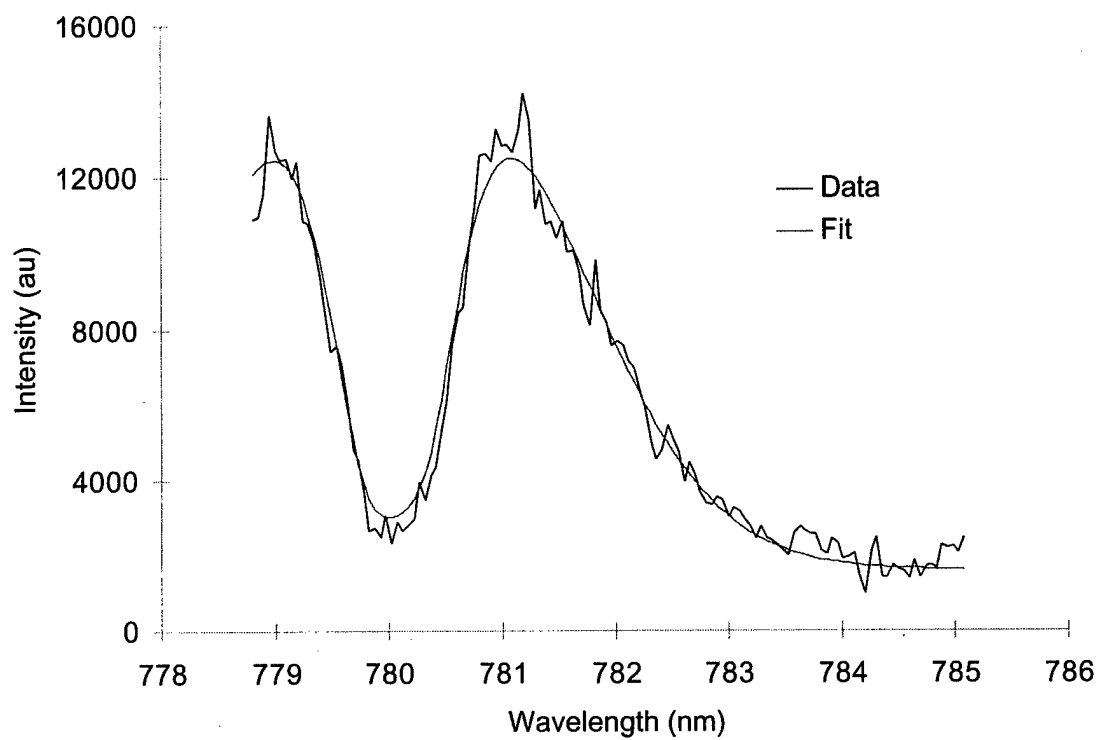
Figure 7
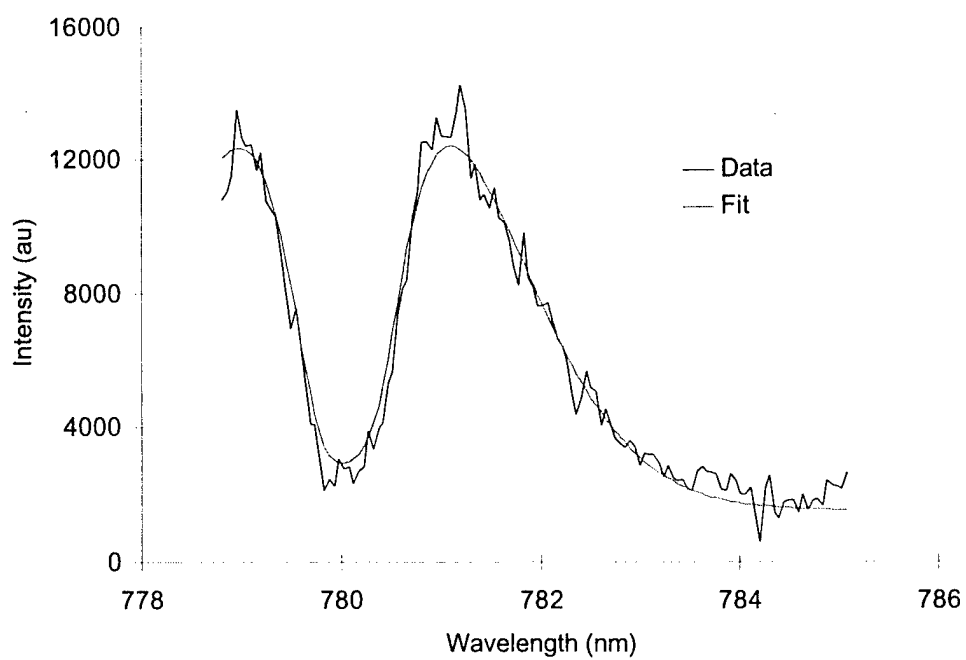
(a)
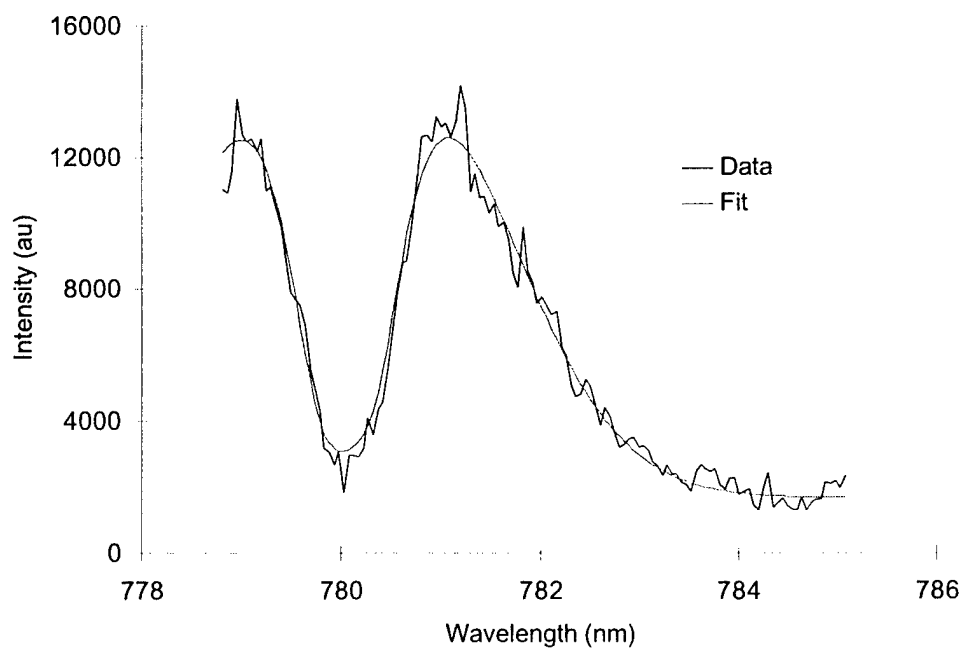
(b)

Figure 8
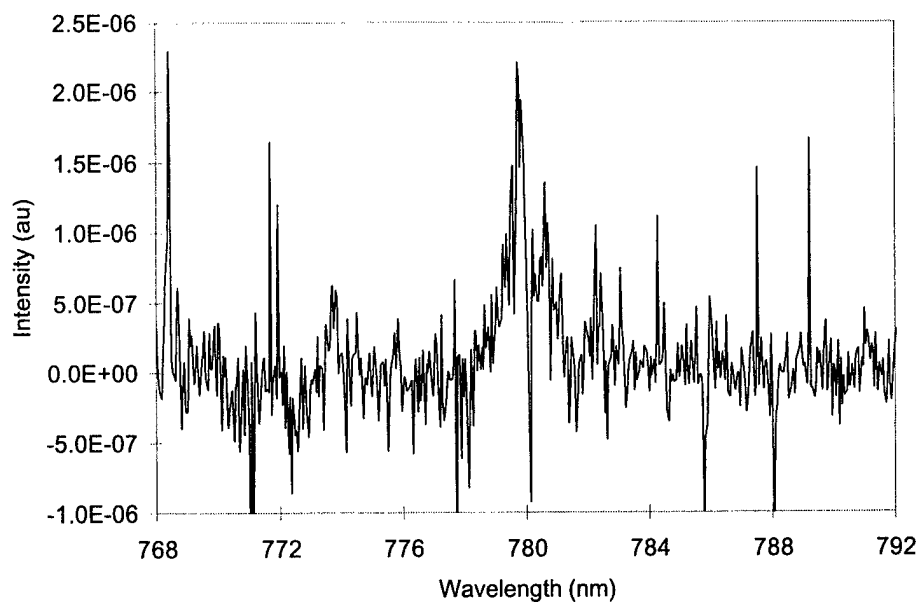
(a)
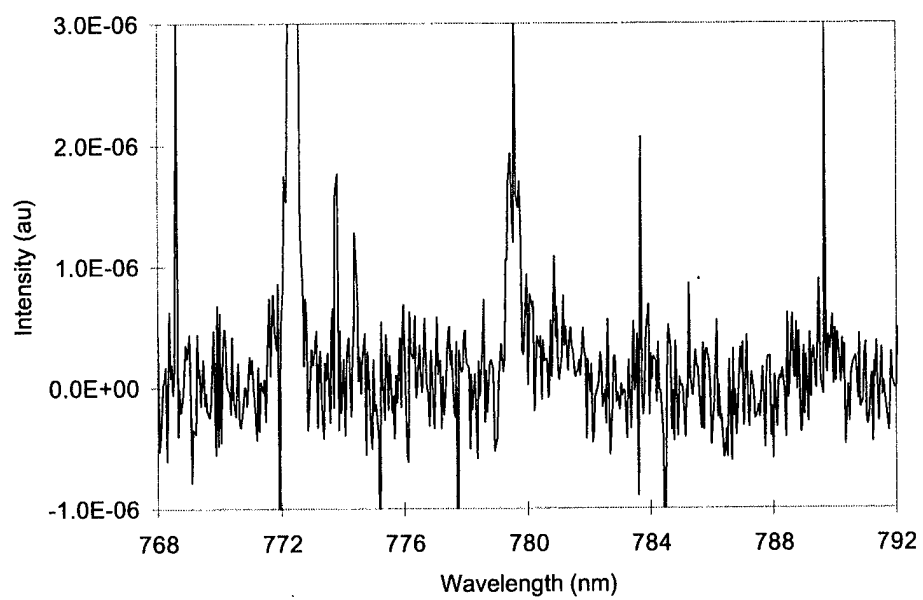
(b)

Figure 9
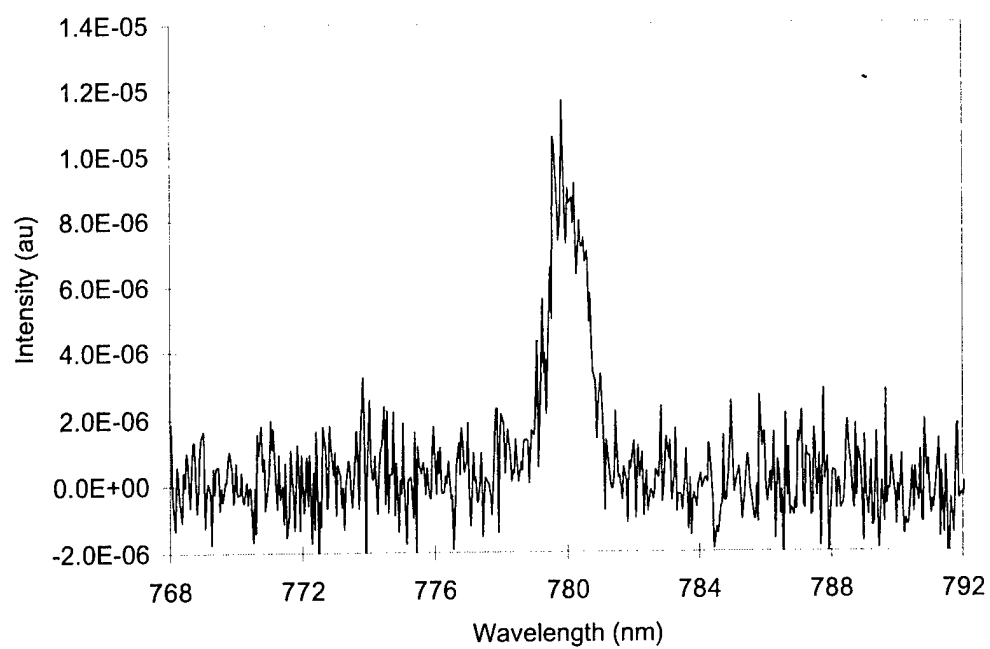
(a)
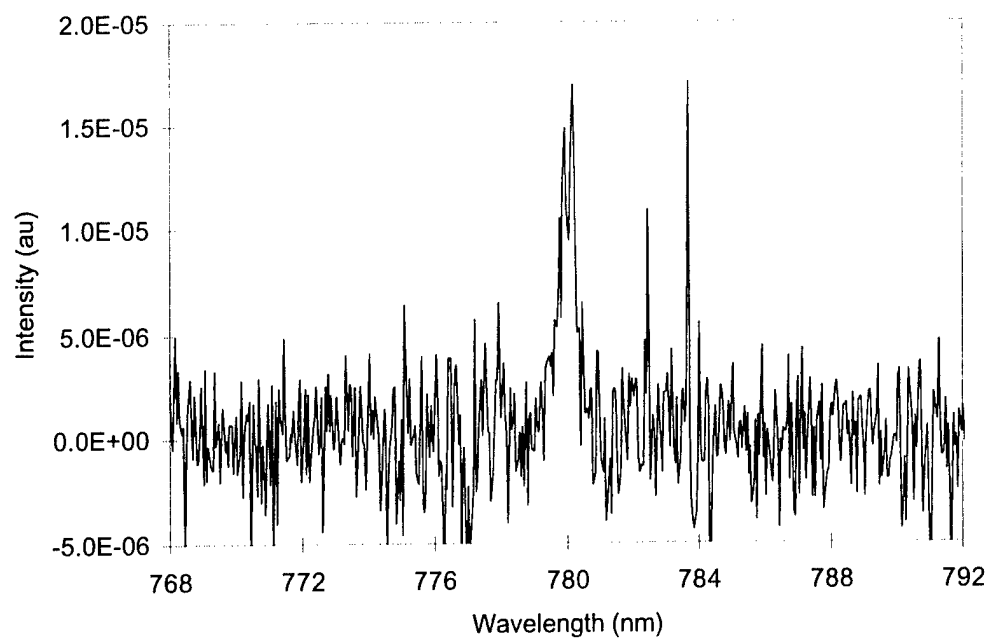
(b)

Figure 10
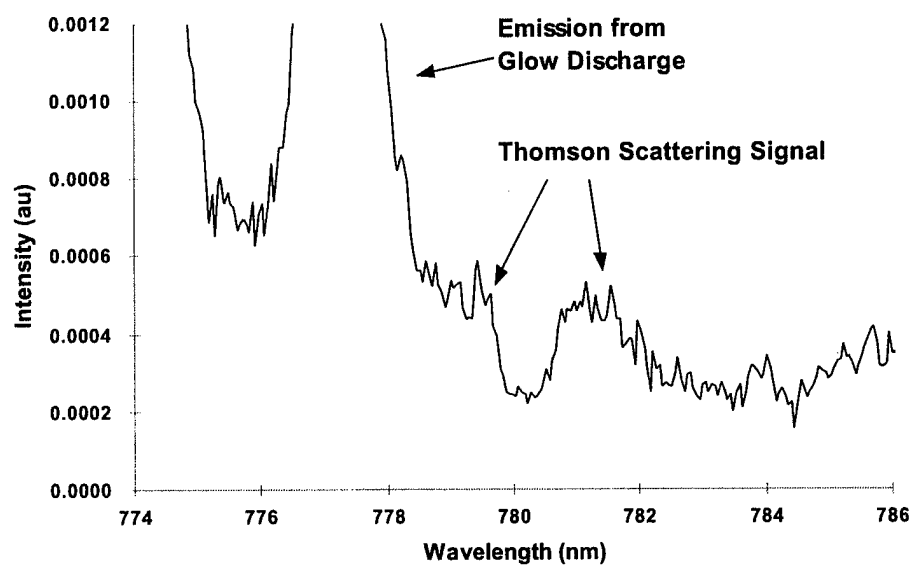
(a)
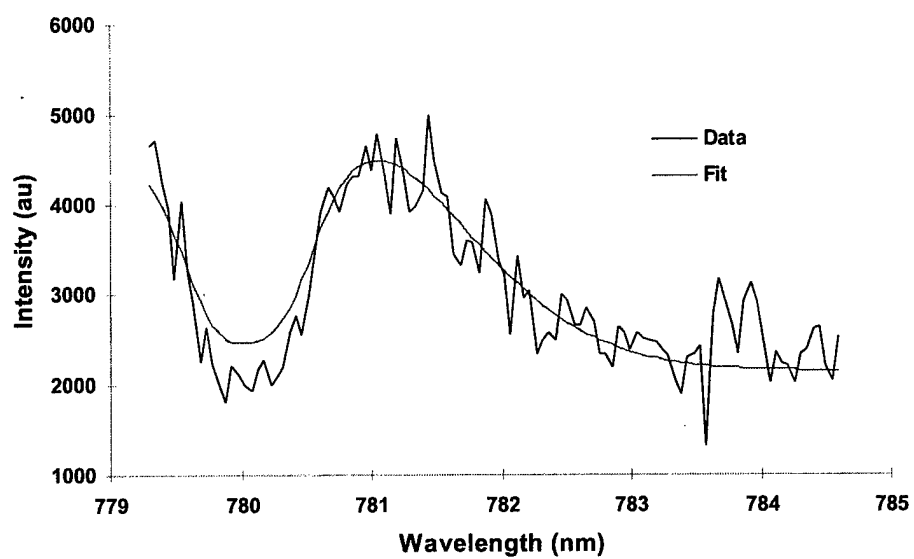
(b)

Figure 11

13. CO/HELIUM GLOW DISCHARGE TEMPERATURE MEASUREMENTS USING SINGLE PHOTON CO 4TH POSITIVE BAND LIF

Robert John Leiweke and Walter R. Lempert

Single-photon Laser Induced Fluorescence has been used to measure the trans-rotational temperature of mildly vibrationally excited carbon monoxide (v"≤9) within the positive column of a 3.6 % CO/He d.c. glow discharge at 1100 Pascal total pressure. A tunable, narrowband ArF excimer laser at 193nm was used to pump the strongly allowed CO $X^1\Sigma^+$(v"=7)→$A^1\Pi$(v'=1) transition with subsequent collection of the 200.8nm (1,8) 4th Positive emission. The resulting rotational spectral peaks were assigned and a subset was used to determine a rotational temperature of 432 ± 72K (3σ) on the discharge centerline. To provide a check on the accuracy of the LIF diagnostic, the results were compared to line of sight Fourier Transform – InfraRed emission measurements, which yielded a temperature of 395 ± 10K, in good agreement with the LIF. These results demonstrate that CO 4th Positive LIF is well suited as a spatially resolved temperature diagnostic for glow typical discharge environments.

I. INTRODUCTION

Laser Induced Fluorescence (LIF) has been proven to be a versatile and powerful tool for nonintrusive measurement of temperature and state selective species concentration in harsh environments, such as flames and other combustion systems, and plasmas.[1,2] Carbon monoxide is particularly attractive as a thermometric tracer due to factors such as ease of seeding, relative chemical inertness and thermal stability. To date, most reported CO LIF diagnostic schemes have centered on $X^1\Sigma^+$→$B^1\Sigma^+$ (Hopfield-Birge system) two-photon absorption using a tunable dye laser excitation source in the vicinity of 230nm, followed by $B^1\Sigma^+$→$A^1\Pi$ emission (Ångström system) in the range 450-750 nm.[3-6] Planar imaging employing this scheme, in combination with a cylindrical multi-pass cell, has been reported by Seitzman, *et al.*[4] Spontaneous $B^1\Sigma^+$→$X^1\Sigma^+$ fluorescence in the VUV (120nm) has been observed by populating the $B^1\Sigma^+$ after laser-assisted intermolecular collisional energy transfer.[7] Two photon $X^1\Sigma^+$-$A^1\Pi$ absorption (the well known 4th Positive band[8,9]) at 290nm has been used to excite the CO combustion products within an atmospheric flame to the v'=3 level with observed fluorescence in the (3,9) band near 197nm.[10-12]

In recent papers[13,14] we have demonstrated the ability to perform temperature measurements in highly vibrationally excited environments using single photon LIF of carbon monoxide.[15] Those studies employed a diagnostic strategy which takes advantage of a strong single-photon allowed absorption

between the $v''=20$ level of the $X^1\Sigma^+$ ground electronic state and the $v'=2$ level of the $D'^1\Sigma^+$ excited electronic state.[16] This scheme was found to have significant temperature measurement potential (+/-50K or better) in systems exhibiting extreme vibrational disequilibrium. However, many important engineering systems, such as glow discharge plasmas and dc and radio frequency (rf) sustained supersonic flows[17] are characterized by significant, yet more modest, levels of vibrational excitation.

In this paper, we demonstrate the potential of a new LIF diagnostic for determination of temperature in mildly nonequilibrium plasmas, based on the single photon allowed $X^1\Sigma^+(v''=7)\rightarrow A^1\Pi(v'=1)$ transition in CO. We have recently presented results[18] using this scheme in helium quenched, optically-pumped plasmas and here we present a proof-of-concept measurement in the positive column of a low pressure CO/He d.c. glow discharge. The CO $X^1\Sigma^+(v''=7)$ vibrational population fraction of this plasma has been estimated to be ~0.1% from FT-IR 1st overtone measurements. Temperature measurements by CO LIF are found to compare well (432 ± 72K, 3σ) with those determined by rotationally resolved Fourier Transform – InfraRed (FT-IR) spontaneous emission spectroscopy[19], 395±10 K.

II. BACKGROUND AND EXPERIMENTAL

Gas Conditions and Optical Access

Figure 1 is a side view illustration of the flow cell, electrode arrangement, and optical access ports used for all experiments described in this paper. A cylindrical Pyrex glass cell, 78cm long × 5.4cm (inner) diameter, is used to contain a slowly flowing (~0.5cm/s) gas mixture of 3.6% carbon monoxide (39.5 Pa) and helium at a total pressure of 1100 Pa. A gas manifold delivers mixtures of research-grade (99%) helium and iron-pentacarbonyl free, ultra-high purity (99.9%) CO, with composition and total pressure controlled by flow meters and a vacuum pump choke valve. The total cell pressure is monitored by a piezoelectric pressure transducer (Omega PX302-100A) and A/D meter (Omega DP25-S). Three perpendicular 5.1cm long × 5.1cm diameter glass arms provide optical access to the region of interest. Two of these arms are oriented with their axes out of the plane of the figure, while the third arm is directed vertically within the plane of the page. The cell ends and arms are equipped with flanges for mounting either 3.81cm dia. calcium fluoride (CaF_2) or UV-grade fused silica windows (UVFS) to provide spectral transmittance in the infrared and/or UV.

Electrical Conditions

Figure 1 also illustrates the geometry of the electrodes as well as the external power system. The annular stainless-steel electrodes are 1 mm thick and 3 cm in (outer) diameter. The anode is 1.3 cm long and the cathode is 5.0 cm long. These electrodes are spaced 19.5cm apart, concentric with the flow cell.

The asymmetry of the electrode placement with respect to the viewports insures optical access to the glow discharge positive column.

A 600 W d.c. power supply (Glassman High Voltage # EW10R60) was connected in series with a nominal 100 kΩ ballast resistor (measured to be 99.7 kΩ when hot) and the discharge plasma. The power supply was operated in positive-polarity, current-controlled mode. Supply voltages were measured using a 1000x (reducing) high-voltage probe (Fluke 80k-40). The d.c. discharge as reported in this paper required typical supply voltages of 3.1 kV (77W) for pure helium and 3.6 kV (90W) for the CO/He mixture. The total voltage drop across the electrodes was measured using a hand-held multimeter (BK Precision 389A) connected in parallel.

Figure 2 displays the resulting current-voltage (I-V) characteristic for both the pure helium discharge and the CO/He mixture taken on three different days. Note that while the addition of only 3% CO nearly doubles the interelectrode voltage (pure helium 500 V, mixture 900 V), it is still possible to maintain a stable, normal glow over the range of current supplied. For all experiments in this paper, the current was maintained at 25 mA, corresponding to the minimum observed in the CO/He I-V curve in Figure 2. Under this condition, the lumped resistance across the electrodes were ≈20 kΩ (pure He) and ≈40 kΩ (CO/He).

It should be noted that while there is slight variability of the I-V characteristic for the CO/He mixture (possibly due to electrode carbonization), these figures illustrate reasonable repeatability of the gas flow and discharge conditions.

Using the measured electrode voltage drop, we can make a rough estimate of the positive column reduced electric field (E/n)[20],

$$\frac{E}{n} \approx \frac{kT(V_p - V_{cf})}{pd} \tag{1}$$

where p is the total gas pressure, d, the inter-electrode spacing, k, Boltzmann's constant, T, the gas translational temperature, V_p is the measured electrode drop for the CO/He mixture ($V_p \approx 900V$), and V_{cf} is the cathode fall voltage.[20] Assuming $T \approx 500$ K and $V_{cf} \approx 450$ V, p=1050 Pa, and d=20 cm, we get $E/n \approx 1.5 \times 10^{-16}$ V-cm^2. It is well known[20] that the E/n required to maximize electron kinetic energy transfer to diatomic vibrational modes is approximately 3×10^{-16} V-cm^2.

FTIR Diagnostic Setup

An FTIR spectrometer (Bruker IFS66) incorporating a cryogenically cooled indium antimonide (InSb) detector was used with moderate resolution (8 cm^{-1}) to resolve the vibrational bands of the CO 1st overtone emission spectrum as well as with higher resolution (0.25 cm^{-1}) to resolve individual rotational transitions of the fundamental v=1→0 band.[19] As shown in Figure 3, the optical path was aligned to image the plasma emission directly through the side window using a 4 cm off-axis paraboloidal concave aluminum mirror. For all infrared measurements, a short-pass filter (Infrared Optical Products, Inc. #W03187) with a cutoff at ~4.9 μm (2040cm^{-1}) and ~3.1 μm (5500 cm^{-1}) bandwidth was used to attenuate the fundamental emission so as not to saturate the InSb detector. The experimentally determined filter response curve provided by the vendor was used to correct the FTIR measurements.

As mentioned previously, each viewport arm extends ~5 cm from the cell tube wall. It is known from prior experience that "colder" CO entrained within these arms absorbs I.R. emission to the extent that it suppresses the lower J levels of rotationally-resolved spectral peaks. While the exact thermal distribution of CO within the cell arms is unknown, we have used the HITRAN 2000 database[21] to characterize the effect of self-absorption in the process of extracting an average positive column temperature.

LIF Diagnostic Scheme

A simplified potential diagram for CO, illustrating the states most relevant to the present work, is given in Figure 4. The ground electronic state, $X^1\Sigma^+$, is characterized by a deep potential well with a dissociation energy[22] of ~11 eV (89460 cm^{-1}). Forty-two vibrational levels have been observed to date.[19] It is evident from Figure 4 that when CO is highly vibrationally excited, several single photon allowed transitions become energetically accessible, particularly at the ArF wavelength of 193 nm (51,800 cm^{-1}). For levels of approximately seven (or higher), absorption to the $A^1\Pi$ state becomes accessible[15,18], and for levels of approximately twenty (or higher), absorption to the $D'^1\Sigma^+$ becomes accessible.[13,14,16] As will be discussed in more detail below, all of these excitation possibilities (both single and two photon) are readily distinguishable by simple spectroscopic selection rules.

It is well known that the vibrational distribution function (VDF) of the ground electronic state, $X^1\Sigma^+$, of CO may attain a non-Boltzmann character within CO/He glow discharges.[23] Energy flows into the lower vibrational states (v≤8, especially v=1) via direct electron-vibration (e-V) excitation[24,25] with subsequent excitation to even higher levels (v< ~39) by means of vibration-vibration quantum exchange[26] processes (V-V "up-pumping"). At moderate translational temperatures, the forward rate of "up-pumping" begins to compete with the backward rate as well as vibration-translational (V-T) energy

exchange on helium atoms[27] and dissociation products[28] (*eg*. CO_2, C_2, C_2O, O) that tend to truncate the VDF. However, even with translational temperatures greater than 500K (5% CO/helium mixtures), significant $X(v=7)$ populations (0.4%) have been routinely observed.[23]

LIF Diagnostic Setup

LIF measurements were performed by wavelength scanning of a narrowband (linewidth $\leq$ 0.3Å) injection-locked 193 nm ArF excimer laser (Lambda Physik COMPex 150T) of 17 ns pulse duration. It is well known[29] that the fraction of laser power channeled into the narrowband varies widely over the ~1 nm ArF broadband gain profile, with the maximum occuring at the center wavelength ~193.3 nm. If not properly accounted for in the spectral analysis, this variation will systematically bias the temperature results. Thus, we have simultaneously measured the "locking efficiency" of the excimer laser as it is tuned through its' gain profile in conjuction with the LIF excitation spectra.

In a manner similar to that described by Wodtke, *et al.*[29], this measurement was achieved by monitoring a small portion (1mm pinhole aperture) of the excimer amplified spontaneous emission (ASE) with a medium resolution monochrometer (JobinYvon HR320, 30 cm, 2400 g/mm UV blaze) set to a bandpass of ~0.1 nm and PMT (Hamamatsu 1P28). The monochrometer grating was set to a spectral region corresponding to unlocked broadband emission (~195.1 nm) in order to avoid stray narrowband radiation. When the oscillator seed beam was blocked, the resulting broadband emission signal, V_b, provided a baseline. When the oscillator was unblocked and the laser was tuned into locking, this signal $V(\lambda)$ decreased. The locking efficiency was then computed over the tuning range using

$$\%Lock = 100 \cdot \left[1 - V(\lambda) / V_b \right] \qquad (2)$$

where λ is the excimer wavelength in nm. The locking signal from the PMT was fed into a 300 MHz, 5X preamplifier (Stanford Research Systems SR240) before being processed by a gated "boxcar" integrator (SRS SR250) with a time-constant of 100 shots (10s 10 Hz trigger rate).

Despite purging most of the beam path with dry nitrogen gas, the excimer beam power also varies with wavelength because of strong O_2 Schumann-Runge band absorption. We correct for this by simultaneously measuring the total excimer power at the cell exit window as a function of wavelength using a volumetric absorbing pyroelectric detector (Scientech Vector S310 Meter, AC50UV detector).

Using a 509 mm, cylindrical UVFS plano-convex lens, the excimer beam was focused (~100 μm waist) into a laser sheet intersecting the axial centerline of the glow discharge (see Figure 3 inset). Emission was collected (~f/10) through the top window (out of the plane of Figure 3) and 1:10 imaged ($M \approx 0.1$) onto the 0.10 mm entrance slit of a small, low resolution monochrometer (Jobin Yvon H10; 10 cm, f/3.5 aperture, UV 1200 g/mm). This monochrometer was set to 200.8 nm to collect the $A^1\Pi(v'=1) \rightarrow$

$X^1\Sigma^+(v''=8)$ vibrational emission band. A 0.10 mm exit slit (FWHM bandpass ~1.0 nm) was found to be adequate for rejection of Rayleigh scattering, stray excimer radiation, CO Resonance-Enhanced Multi-Photon Dissociation (REMPD) product emission[30], and extraneous 4th Positive ro-vibrational bands.

The total ambient air-path through which the 200.8 nm UV emission propagated was 25 cm. It should be noted that the intervening cold CO within the cell (5 cm path) does not self-absorb the 200.8 nm emission because the $v''=8$ is not populated along the path.

The monochrometer was mounted to a photomultiplier tube (PMT) housing containing a 250S (S-5) PMT (Hamamatsu R166UH) with ~35% quantum efficiency at 200 nm. The PMT voltage for all experiments in this paper was no greater than |-600| VDC. As shown in Figure 3, signals from the PMT were fed into a second boxcar with time constant of 30 shots. Boxcar averaged data (LIF, locking, and beam power) were plotted and stored on a PC computer.

Finally, note in Figure 3 that the entrance/exit monochrometer slits were oriented parallel to the cell principal axis to center the LIF collection on the discharge centerline. The inset displays the collocation of the area imaged by the slit, the plasma region, and the excimer laser sheet. The shaded region represents the ~0.9 mm×25 mm ≈ 22 mm² cross-sectional area of the plasma from which the LIF signal was obtained. Note that the laser sheet thickness within the imaging region is ≈100 μm.

III. RESULTS & DISCUSSION

VDF from the CO 1st Overtone Spectrum

To quantify the CO $X^1\Sigma^+(v''=7)$ population in the positive column of our CO/He d.c. glow discharge we have used FT-IR spectroscopy to vibrationally resolved (8 cm⁻¹) the CO first overtone emission, shown in Figure 5. Note in this figure that the signal from the $v''=7\rightarrow5$ is roughly the same magnitude as lower level transitions, an encouraging indication that the $v''=7$ is populated. To quantify the fractional vibrational populations, we have used the technique of Ref. [31] to iteratively extract the normalized VDF from the 1st overtone spectra shown in Figure 5. These results are shown in the Boltzmann plot of Figure 6. In this figure, the resulting vibrational level population fractions are overlayed with a best-fit Treanor distribution[26] at T_{rot}=400 K and T_{vib}=2500 K. It should be noted that the $v''=0$ and $v''=1$ populations are derived from this best-fit Treanor curve. Agreement with the Treanor distribution is good, and we see that under the conditions stated in Section II above, the $v''=7$ is ~0.1% populated.

CO Rotational Temperature from the IR Fundamental Spectrum

In order to provide a comparison for the LIF temperature measurements, we obtained rotationally resolved (0.25 cm⁻¹) R-branch FT-IR emission spectra of the CO fundamental, $v''=1\rightarrow0$ band, as shown in

Figure 7. This measurement was performed simultaneously with the 1st overtone spectral measurements. Thirty well resolved, high S/N peaks ranging between R(2)-R(7) and R(10)-R(30), can be distinguished. Also shown in Figure 7 is the combined FT-IR instrument and short-pass filter response derived from experimental blackbody calibration spectra at 16 cm⁻¹ resolution used to correct the peak values.

To attain the line-of-sight, spatially averaged temperature, these background subtracted and instrument-response corrected peaks were then mapped onto a Boltzmann plot, shown in   Figure 8. It is clear that a linear region exists from R(23) to R(31). Note that the region from R(19) to R(22) shows a pronounced non-linearity due to CO self-absorption caused by the intervening colder CO in the imaging arms (refer to Section II). In order to confirm that the plasma is optically thin in the spectral region used for the least-squares temperature estimate, we employed the HITRAN 2000 database[21] to model self-absorption at 290K. Figure 8 shows these results (dashed curve) overlayed on the Boltzmann plot. In this figure, we see that lines J'~23 to 31 coincide with a spectral region of negligable self-absorption (1% or less), indicating that we may use these points to extract the gas temperature. The least-squares slope indicates a line-of-site averaged CO rotational temperature of 395 ± 10K within the imaged region of positive column.

CO 4th Positive LIF Temperature

As alluded to previously, the X→A transition is easily distinguishable from either the X→B or X→D', based on simple selection rules.[32] In the case of single-photon X→D', the transition is $^1\Sigma \to {}^1\Sigma$ so that we expect a simple set of P/R branches while two-photon, X $^1\Sigma \to$ B $^1\Sigma$, will be dominated by an unresolved Q branch as described in detail in Ref. [3]. The single-photon A→X is $^1\Sigma \to {}^1\Pi$, so we expect to observe P, Q, and R branches, with the intensity of the Q branch being approximately double that of the P and R.

Using the molecular constants from Ref.[33] for the ground electronic state, Ref.[8] for the $A^1\Pi$, and transition probabilities from Ref.[34], it was predicted[18] that the dominant excitation band within the tuning range of the ArF laser would be the X(v''=7)→A(v'=1) with the strongest emission being from the A(v'=1)→X(v''=6) at 186 nm. However, it was found that this emission is absorbed by the ambient O_2 Schumann-Runge bands to the extent that dry N_2 purging becomes inadequate, thus requiring vacuum along the imaging path. For this reason we decided to use the A(v'=1)→X(v''=8) at 200.8nm which is not attenuated by O_2 absorption. It was found that this transition is sufficiently strong to obtain high signal/noise data.

The excimer radiation was focused into a 100 μm sheet (as opposed to a point) to mitigate potential saturation effects. This was investigated by tuning the excimer to the strong P(11) absorption line at

193.35 nm and collecting the emission while varying the laser power between 2 – 46 mJ/pulse (measured at the cell exit window). Signal saturation began to be detectable above ~35 mJ/pulse, so for all subsequent experiments the average energy at the power meter was limited to ~25 mJ/pulse.

Figure 9 shows typical experimental 4th Positive LIF and locking efficiency measurements. In this spectrum, the two most prominant features are the rotationally-resolved $v''=7\rightarrow v'=1$ (from $\lambda\approx193.05$ nm -193.56 nm) and $v''=12\rightarrow v'=8$ (from $\lambda\approx193.59$ nm -193.8 nm) absorption bands. The spectral region of the (7,1) band was selected for temperature extraction since it lies within the region of highest, and most constant, locking efficiency, and lowest O_2 Schumann-Runge absorption interference.

The experimental spectrum of Figure 9 was used, primarily, for calibrating peak positions and qualitatively displaying the sensitivity, since it was obtained at a relatively fast scan-rate such that peak intensities are not reproduced with sufficient accuracy to be used for quantitative analysis. As will be elaborated below, absolute peak heights used for temperature extraction in this paper were obtained using a slower scan rate over the relevant features

Closer inspection of Figure 9 within the wavelength range 193.3 nm -193.44 nm illustrates the lines used in this paper to extract a trans-rotational temperature, as shown in Figure 10. Note that the excimer locking efficiency and input laser power were nearly constant at ~62% and 25 mJ/pulse, respectively. For temperature estimation, absolute peak heights were obtained by slowly scanning *seven* times over each line; P(10), Q(16), P(11), Q(17), P(12), Q(18), P(13), and Q(19) at 4.71pm/min (0.4Hz grating rate) resulting in a total of 56 data points. The data analysis process included subtracting the broadband background from each peak, dividing by the measured locking efficiency to correct for narrowband power degradation, and finally dividing by the measured excimer energy to correct for ambient O_2 absorption in the beam path. Note in Figure 10 that the locking efficiency curve had a 2% periodic modulation during the scan due to vibrations within the grating control mechanism. The locking efficiency correction described above properly accounted for this systematic error.

The results were analyzed using the molecular constants mentioned above and small-sample statistics.[35] Figure 11 shows the resulting Boltzmann plot obtained from these 56 data points, 28 for each branch. Note that many of the data points lie quite close together, an indication of both the shot-to-shot stability of the excimer laser and the glow discharge environment. Also, it is apparent that the Q-branch is anomalously offset below the P-branch, but yielding qualitatively the same slope.

The least-squares slope for each branch yielded rotational temperatures of $T_P=441 \pm 89$K (3σ) and $T_Q=423 \pm 51$K using a rotational B-value[8,22] for the $v''=7$ vibrational level of 1.80 cm^{-1}. The average temperature of the combined branches is 432 ± 72K. These results compare favorably with our FT-IR result of 395 ± 10K. One possible source for discrepancy between these two results is the fact that the FT-

IR measurement is spacially averaged while the LIF is taken on the plasma centerline. Since the d.c. glow discharge positive column temperature is known to decrease with radial distance from centerline, this result of a slightly higher LIF temperature is not too surprising.

IV. CONCLUSIONS

Single photon LIF has been obtained within the positive column of a low pressure CO/He d.c. glow discharge using the 4th Positive bands originating from the $A^1\Pi$ electronic state. The rotationally resolved laser excitation spectra exhibit strong transitions originating from J" values between 8–20, which implies significant potential for rotational temperature measurement. Measurements using this LIF diagnostic technique indicate a 3σ temperature within the positive column of $432 \pm 72K$, in good agreement with the FTIR spectroscopic measurement of $395 \pm 10K$, as well as with prior research efforts.

REFERENCES

1. Eckbreth, A.C., *Laser Diagnostics for Combustion Temperature and Species*, Abacus Press, Cambridge, Mass., 1988.

2. Rothe, E.W. and Andresen, P., "Application of Tunable Excimer Lasers to Combustion Diagnostics: A Review", *Applied Optics*, Vol. 36, No. 18, 1997, pp. 3971-4033.

3. Everest, D.A., Shaddix, C.R., and Smyth, K.C., "Quantitative Two-Photon Laser-Induced Fluorescence Imaging of CO in Flickering CH_4 /Air Diffusion Flames", *Proceedings of the 26th International Symposium on Combustion*, The Combustion Institute, 1996, pp. 1161-1169.

4. Seitzman, J.M., Haumann, J., and Hanson, R.K., "Quantitative Two-Photon LIF Imaging of Carbon Monoxide in Combustion Gases", *Applied Optics*, Vol. 26, No. 14, 1987, pp. 2892-2899.

5. Aldén, M., Wallin, S., and Wendt, W., "Applications of Two-Photon Absorption for Detection of CO in Combustion Gases", *Applied Physics B.*, Vol. 33, 1984, pp. 205-208.

6. Haumann, J., Seitzman, J.M., and Hanson, R.K., "Two-Photon Digital Imaging of CO in Combustion Flows Using Planar Laser-Induced Fluorescence", *Optics Letters*, Vol 11, No. 12, 1986, pp. 776-778.

7. Lukasik, J. and Wallace, S.C., "Laser-Assisted Intermolecular Energy Transfer Between Electronic States of Carbon Monoxide in the Vacuum Ultraviolet", *Physical Review Letters* Vol. 47, No. 4, 1981, pp. 240-243.

8. Tilford, S.G. and Simmons, J.D., "Atlas of the Observed Absorption Spectrum of Carbon Monoxide Between 1060 and 1900 Å", *Journal of Physical Chemistry Reference Data*, Vol. 1, No. 1, 1972, pp. 147-187.

9. Beegle, L.W., Ajello, J.M., *et al.*, "High Resolution Emission Spectroscopy of the $A^1\Pi - X^1\Sigma^+$

Fourth Positive Band System of CO Excited by Electron Impact", *Astronomy and Astrophysics*, Vol. 347, 1999, pp. 375-390.

10. Sullivan, B.J. and Crosley, D.R., "Two-Photon Laser-Induced Fluorescence of CO in Flames", *Bulletin of the American Physical Society*, Vol. 27, 1982, pg 882.

11. Bernheim, R.A., Kittrell, C., and Veirs, D.K., "Two Photon Excitation of the Vacuum Ultraviolet Fluorescence of Carbon Monoxide", *Chemical Physics Letters*, Vol. 51, No. 2, October 15, 1977, pp. 325-328.

12. Filseth, S.V., Wallenstein, R., and Zacharias, H., "Two Photon Excitation of CO ($A^1\Pi$) and N_2 ($a^1\Pi_g$)", *Optics Communications*, Vol. 23, No.2, November 1977, pp. 231-235.

13. Leiweke, R.J. and Lempert, W.R., "Single-Photon PLIF Imaging of Vibrationally Excited Carbon Monoxide", AIAA paper 2000-0199, January, 2000.

14. Leiweke, R.J. and Lempert, W.R., "Rotational Temperature of Highly Vibrationally Excited CO Using $X^1\Sigma^+\leftarrow D'\,^1\Sigma^+$ Single-Photon LIF", submitted to *Applied Optics*, May 2002.

15. Wolk, G.L. and Rich, J.W., "Laser-Induced Fluorescence of Carbon Monoxide Under Extreme Vibrational Non-Equilibrium Conditions", *Chemical Physics Letters*, Vol. 87, No.2, 1982, pp. 117-122.

16. Wolk, G.L and Rich, J.W., "Observation of a New Electronic State of Carbon Monoxide Using LIF on Highly Vibrationally Excited CO($X^1\Sigma^+$)", *Journal of Chemical Physics*, Vol. 79, No. 1, 1983, pp. 12-18.

17. Yano, R., Contini, V., Plönjes, E., et al., "Supersonic Nonequilibrium Plasma Wind-Tunnel Measurements of Shock Modification and Flow Visualization", *AIAA Journal*, Vol. 38, No. 10, 2000, pp. 1879-1888.

18. Leiweke, R.J. and Lempert, W.R., "Optically-Pumped CO LIF Temperature Measurements Using the 4th Positive Bands", AIAA paper 2001-2936, June 2001.

19. Plönjes, E., Palm, P., Chernukho, A.P., Adamovich, I.V., and Rich, J.W., "Time-Resolved Fourier Transform Infrared Spectroscopy of Optically Pumped Carbon Monoxide", *Chemical Physics*, Vol. 256, 2000, pp. 315-331.

20. Raizer, Y.P., *Gas Discharge Physics, 2nd Edition*, Springer-Verlag, New York, 1997.

21. Rothman, L.S., Rinsland, C.P., Goldman, A., et al., "The HITRAN Molecular Spectroscopic Database and HAWKS 1996 Edition", *Journal of Quantitative Spectroscopy and Radiation Transfer*, Vol. 60, 1998, pp. 665-710.

22. Krupenie, P.H., "The Band Spectrum of Carbon Monoxide", *National Standard Reference Service, National Bureau of Standards (US)*, Vol. 5, 1966, pp. 1-87.

23. De Benedictis, S., D'Agostino, R., and Cramarossa, F., "Spectroscopic Analysis of the Vibrational Distributions in Dissociative CO-He RF Discharges", *Chemical Physics*, Vol. 71, 1982, pp. 247-256.

24. Aleksandrov, N.L., Konchakov, A.M., and Son, É.E., "Electron Energy Distribution and Kinetic Coefficients of a CO Plasma. I. Ground-State Molecules", *Soviet Physics Technical Physics*, Vol. 24, No. 6, 1979, pp. 661-664.

25. Aleksandrov, N.L., Konchakov, A.M., and Son, É.E., "Electron Energy Distribution and Kinetic Coefficients of a CO Plasma. II. Vibrationally Excited Molecules", *Soviet Physics Technical Physics*, Vol. 24, No. 6, 1979, pp. 664-666.

26. Treanor, C.E., Rich, J.W., and Rehm, R.G., "Vibrational Relaxation of Anharmonic Oscillators with Exchange-Dominated Collisions", *Journal of Chemical Physics*, Vol. 48, No. 4, 1968, pp. 1798-1807.

27. Yardley, J.T., *Introduction to Molecular Energy Transfer*, Academic Press, 1980.

28. De Benedictis, S., Cramarossa, F., and D'Agostino, R., "Residence Time Analysis of UV-Visible Emitting Species in CO-He Radiofrequency Discharges", *Chemical Physics*, Vol. 82, 1983, pp. 394-404.

29. Wodtke, A.M., Hüwel, L., Schlüter, H., and Andresen, P., "Simple Way to Improve a Tunable Argon Fluoride Laser", *Review of Scientific Instruments*, Vol. 60, No. 4, 1989, pp. 801-802.

30. Meijer, G., Wodtke, A.M., Heiner, V., Schlüter, H., and Andresen, P., "State-Selective Detection of CO Using a Tunable ArF Excimer Laser", *Journal of Chemical Physics*, Vol. 89, No. 4, 1988, pp. 2588-2589.

31. Horn, K.P. and Oettinger, P.E., "Vibrational Energy Transfer in Diatomic Gas Mixtures", *Journal of Chemical Physics*, Vol. 54, No. 7, 1971, pp. 3040-3046.

32. Herzberg, G., *Molecular Spectra and Molecular Structure I: Spectra of Diatomic Molecules, 2nd Edition*, Krieger Publishing, Malibar, FL, 1989.

33. Huber, K.P. and Herzberg, G., *Constants of Diatomic Molecules*, Van Nostrand, 1979.

34. Flament, C., George, T., Meister, K.A., et al., "Nonequilibrium Vibrational Kinetics of Carbon Monoxide at High Translational Mode Temperatures", *Chemical Physics*, Vol. 163, 1992, pp. 241-262.

35. Rabinovich, S., *Measurement Errors: Theory and Practice*, AIP Press, New York, 1995.

Figure Captions

Figure 1: Illustration of the flow cell geometry, gas flow, and electrical conditions for all experiments. All dimensions are in centimeters.

Figure 2: Current-Voltage (I-V) characteristic for the cases of pure helium and CO/He mixture. Different symbols reflect separate measurements performed under nominally indentical conditions.

Figure 3: Schematic diagram of experimental apparatus.

Figure 4: Simplified CO molecule potential energy diagram.

Figure 5: CO 1st overtone vibrational emission spectrum obtained by FT-IR spectroscopy.

Figure 6: Vibrational distribution function (VDF) derived from Figure 5 1st overtone spectra overlayed with a best-fit to Treanor distribution.

Figure 7: Rotationally resolved CO fundamental emission spectrum obtained by FT-IR spectroscopy and used to extract a line-of-sight average rotational temperature.

Figure 8: Boltzmann plot (left axis) and temperature obtained from the spectrum of Figure 7. Calculated "cold" CO self-absorption is also indicated (right axis).

Figure 9: CO 4th Positive LIF excitation spectrum collected at 200.8 nm. For clarity, only a few transitions are labeled (see Figure 10 below).

Figure 10: Magnified view of Figure 9 showing LIF transitions used for least-squares extraction of temperature.

Figure 11: Boltzmann plot of CO 4th Positive LIF peaks shown in Figure 10. Temperature is obtained for each branch separately, then averaged.
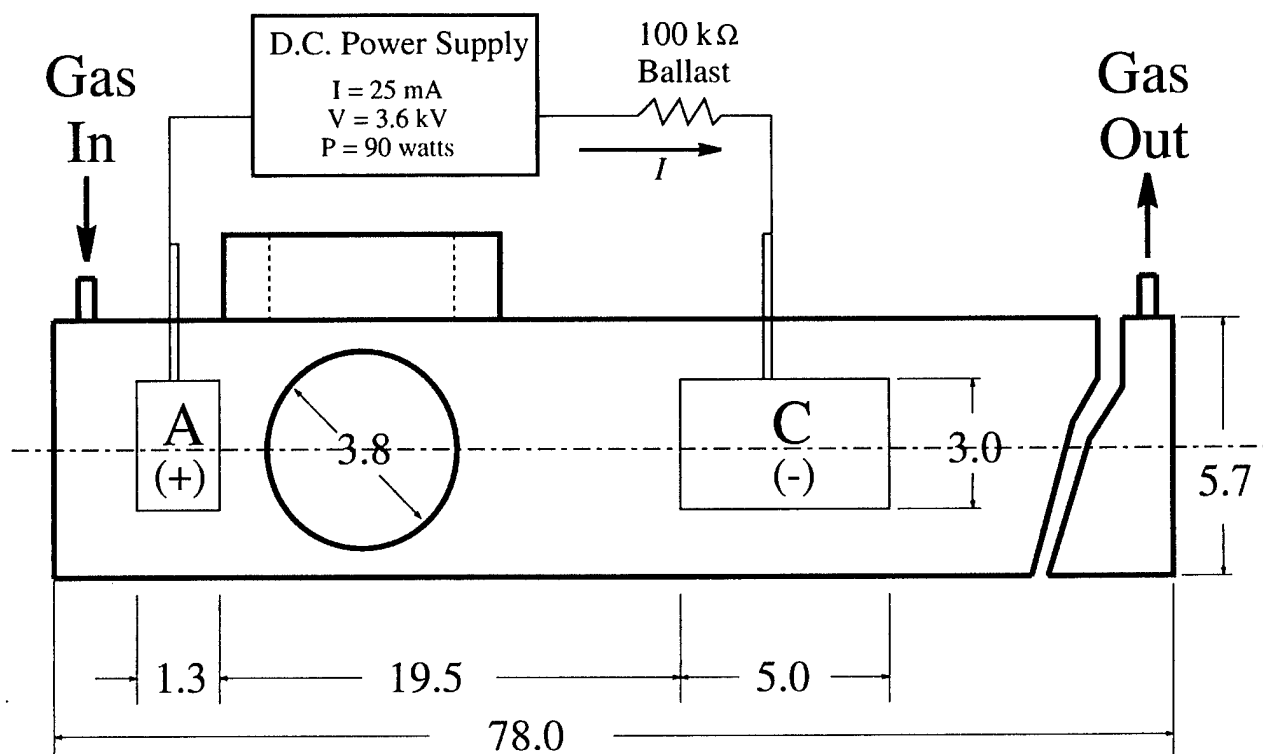
Figure 1

Figure 2

Figure 3

Figure 4

Figure 5

The plot shows Normalized Population, N_v / N_o, on the vertical axis (logarithmic scale from 10^{-4} to 10^0) versus Vibrational Quantum Number, v'', on the horizontal axis (0 to 9).

Legend:
- ● 1st Overtone Data
- —— Treanor Distribution
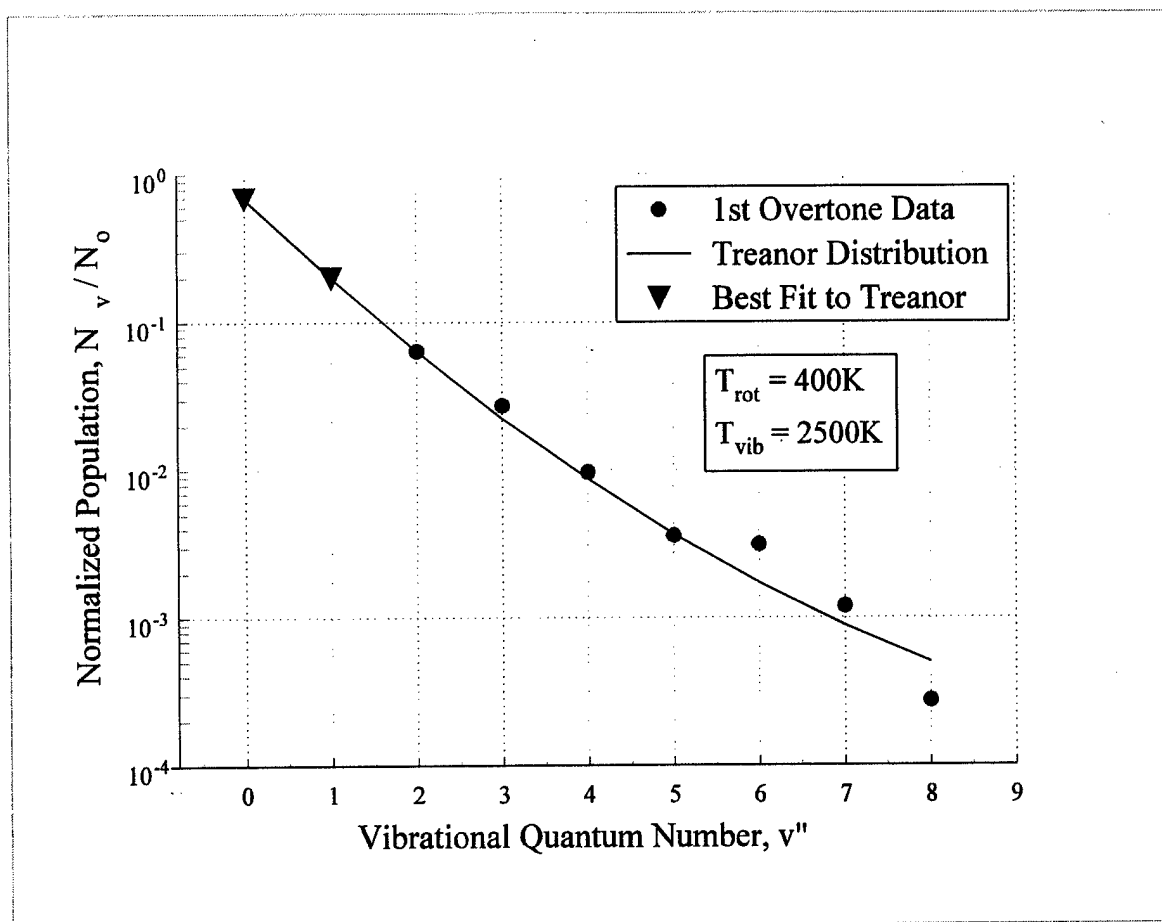- ▼ Best Fit to Treanor

$T_{rot} = 400K$
$T_{vib} = 2500K$

Figure 6

251

Figure 7

Figure 8

Figure 9

254
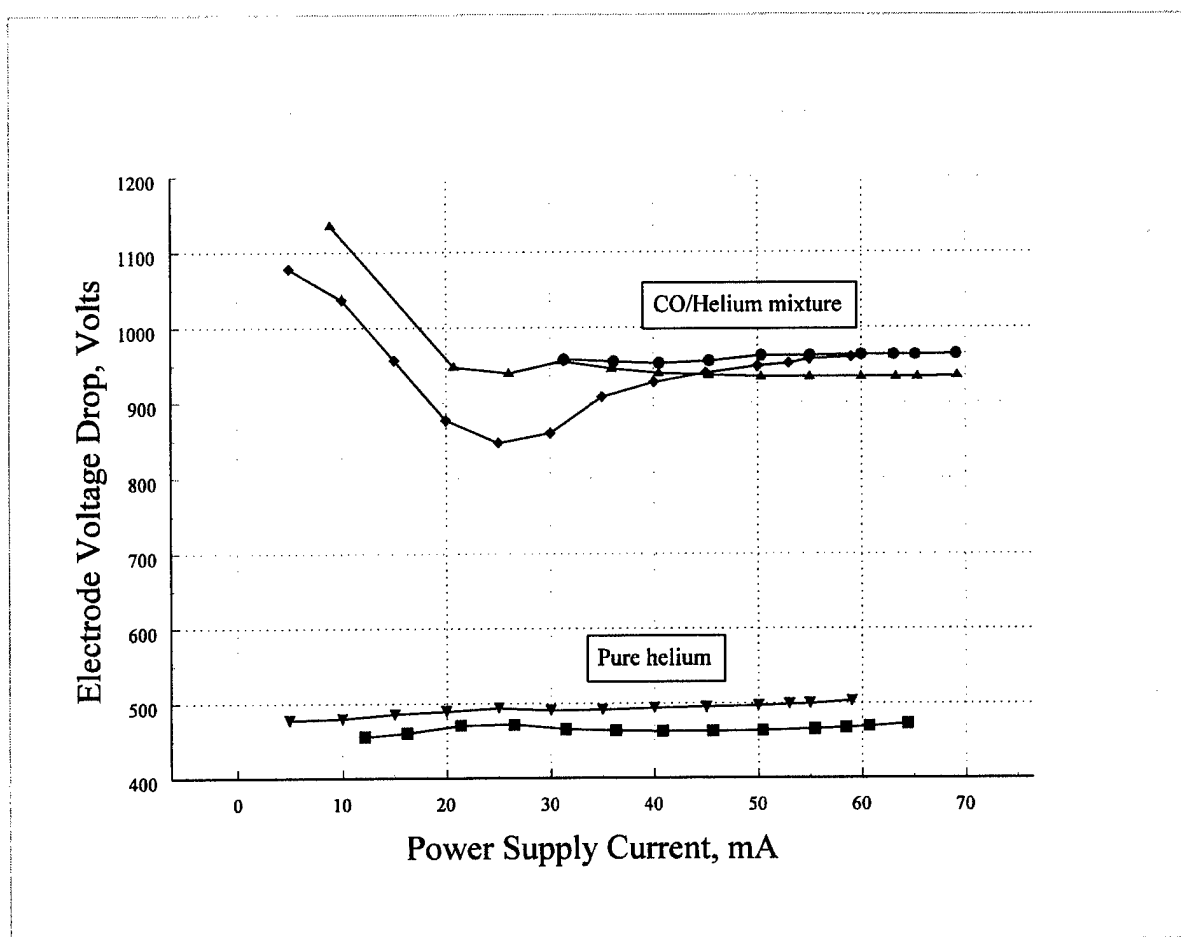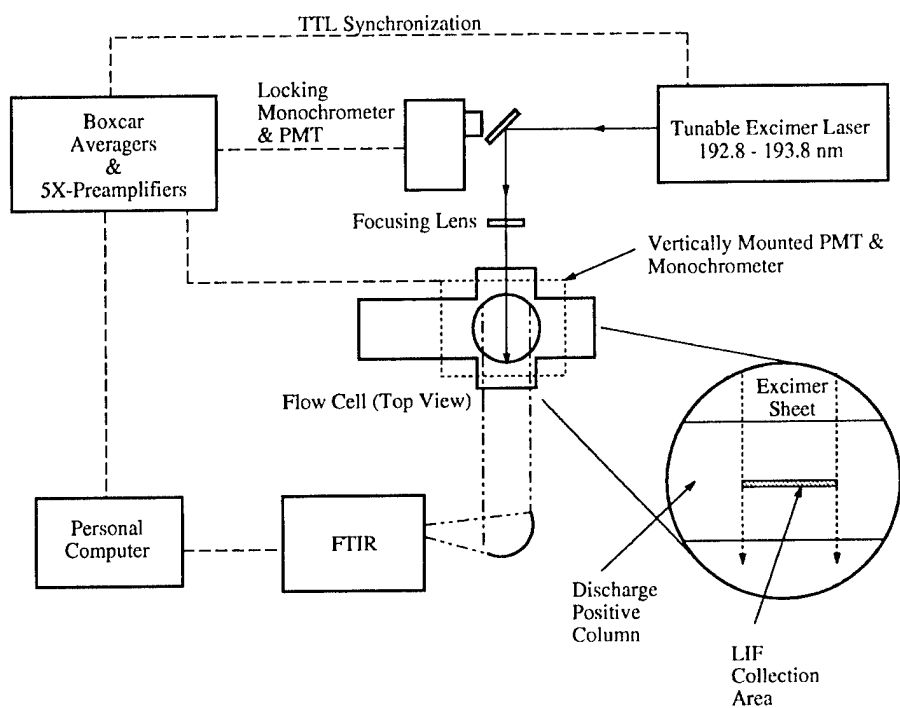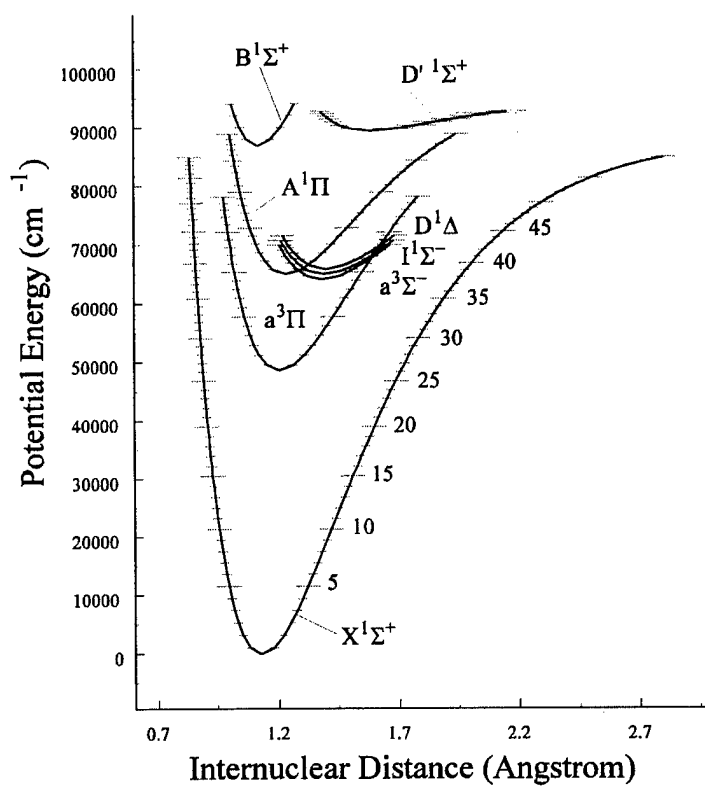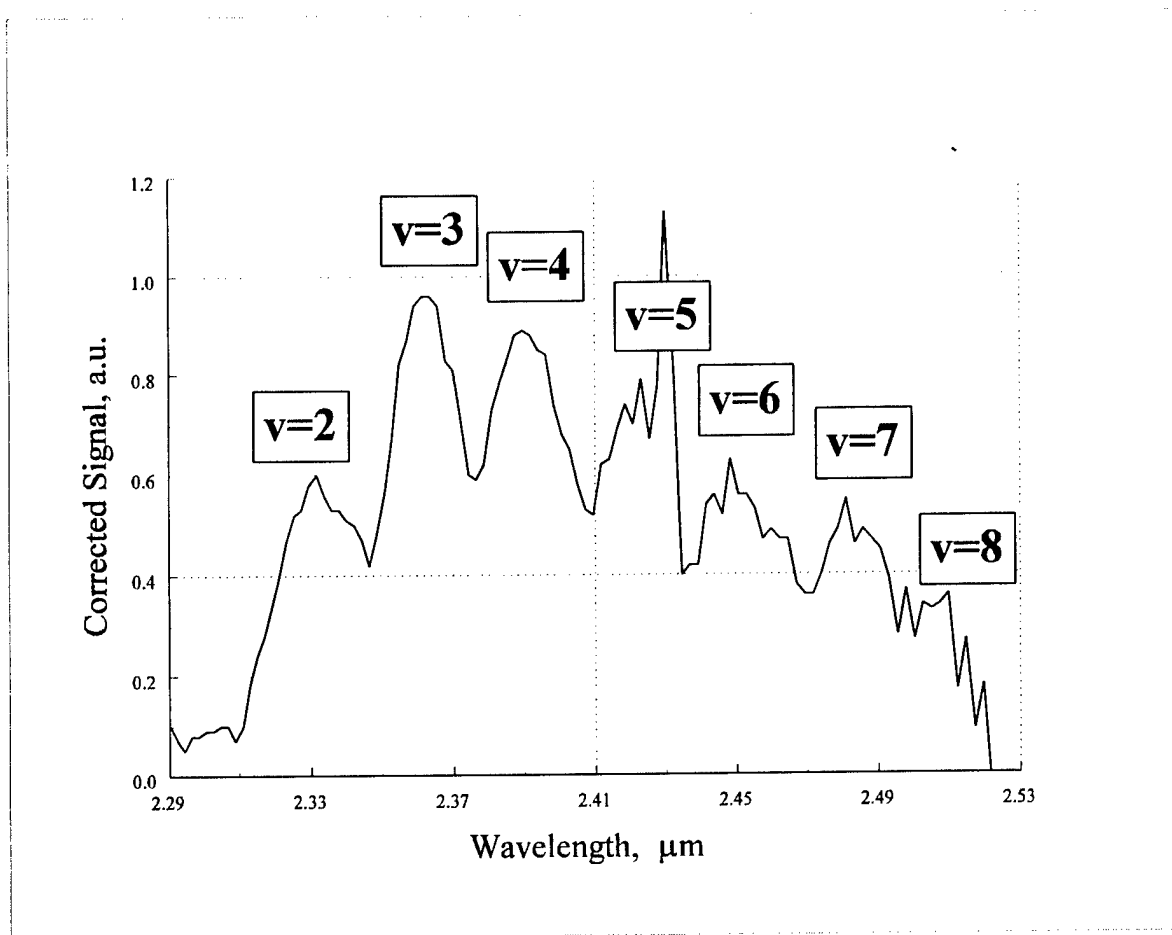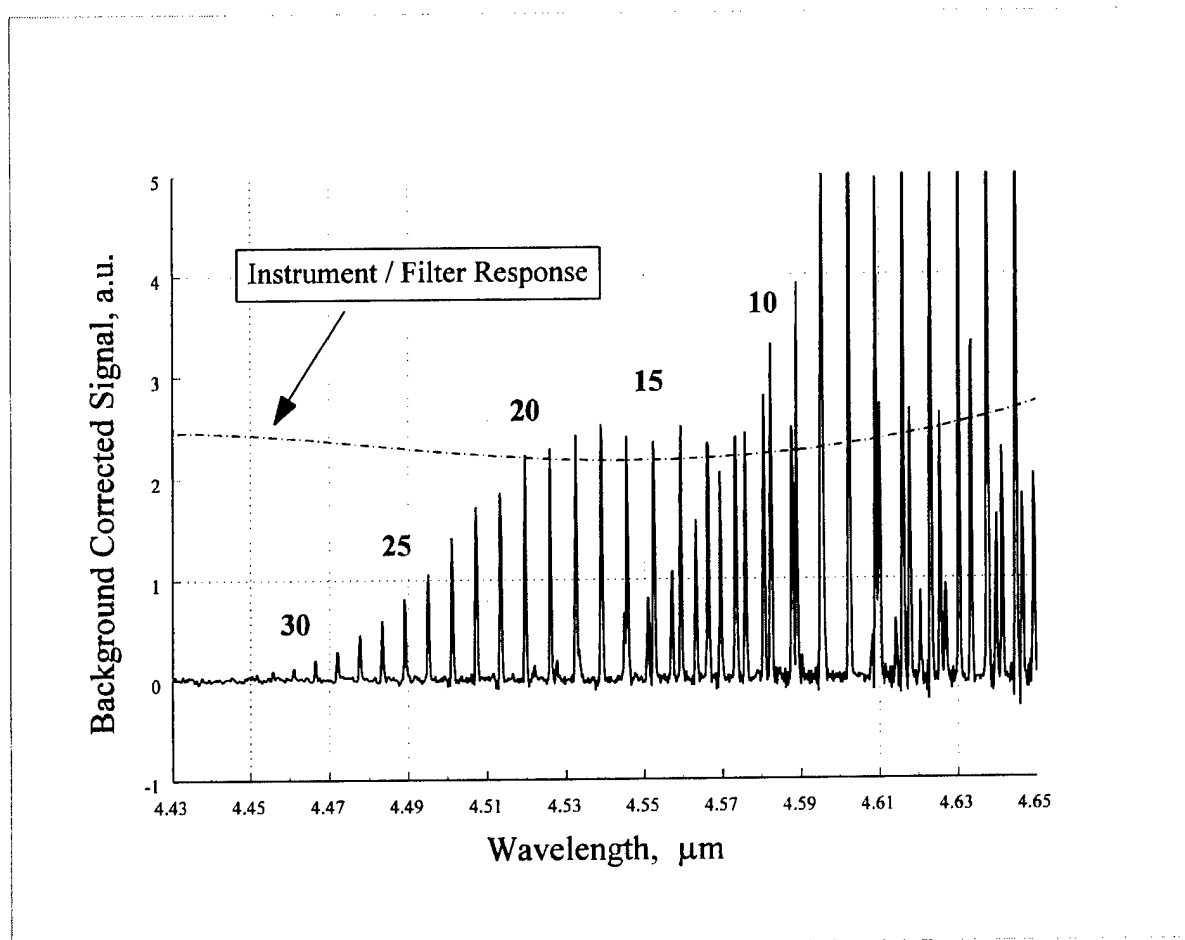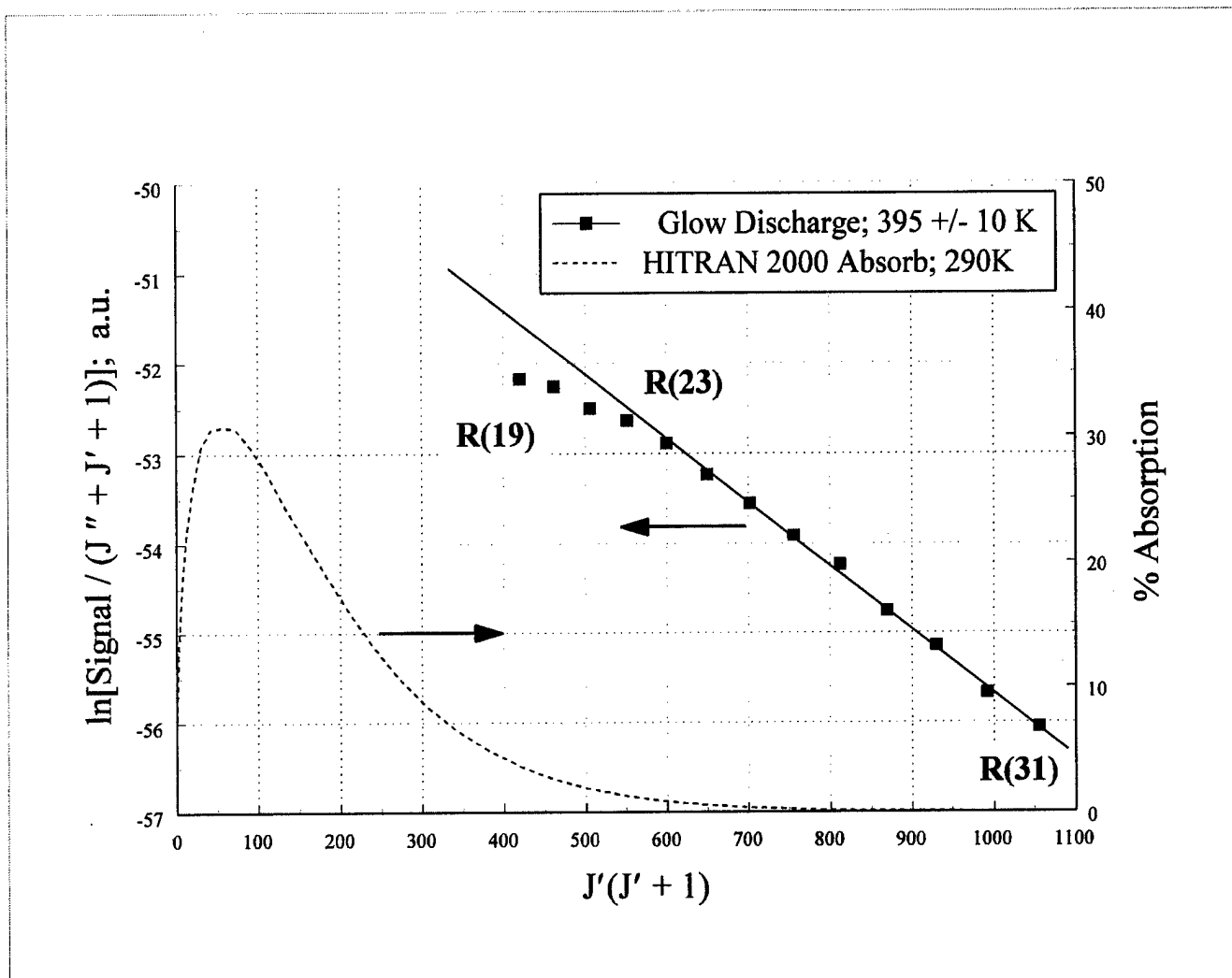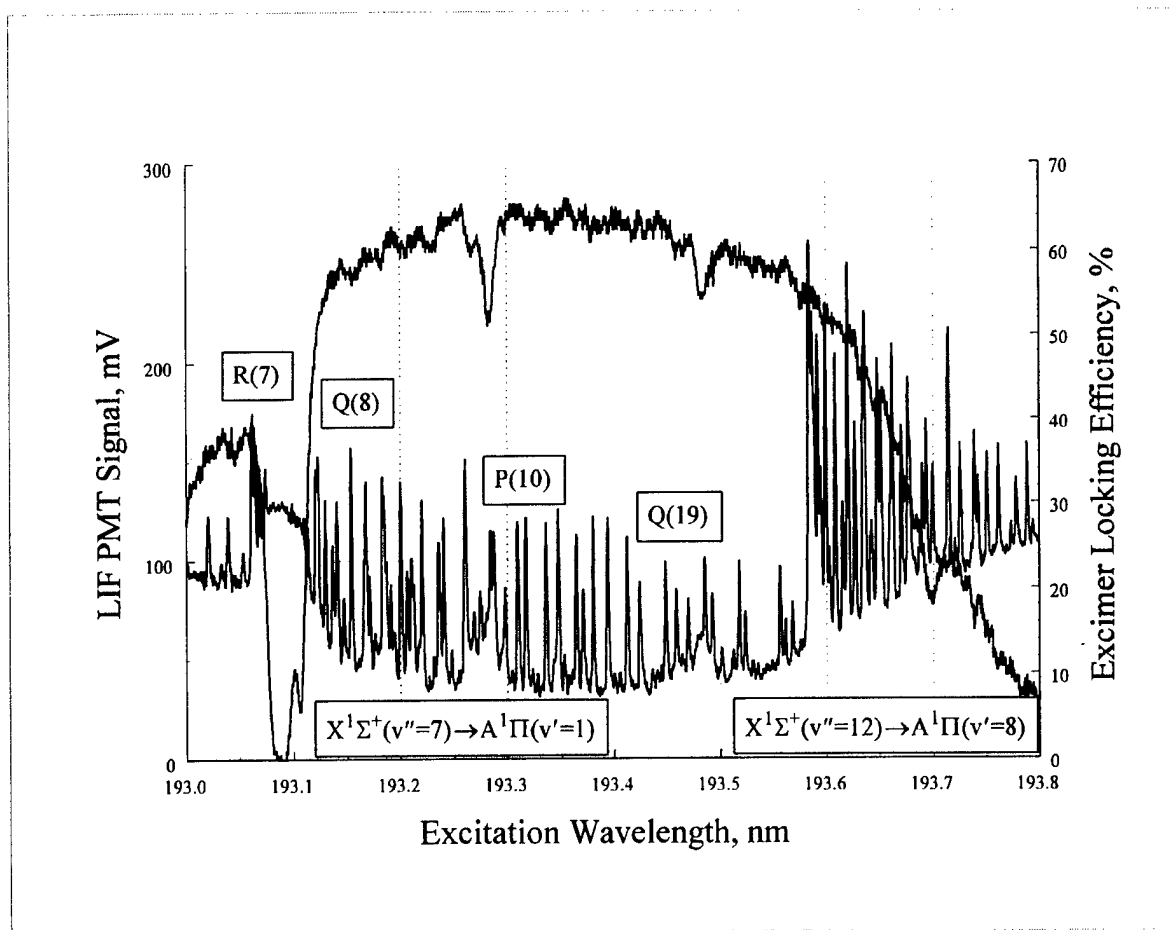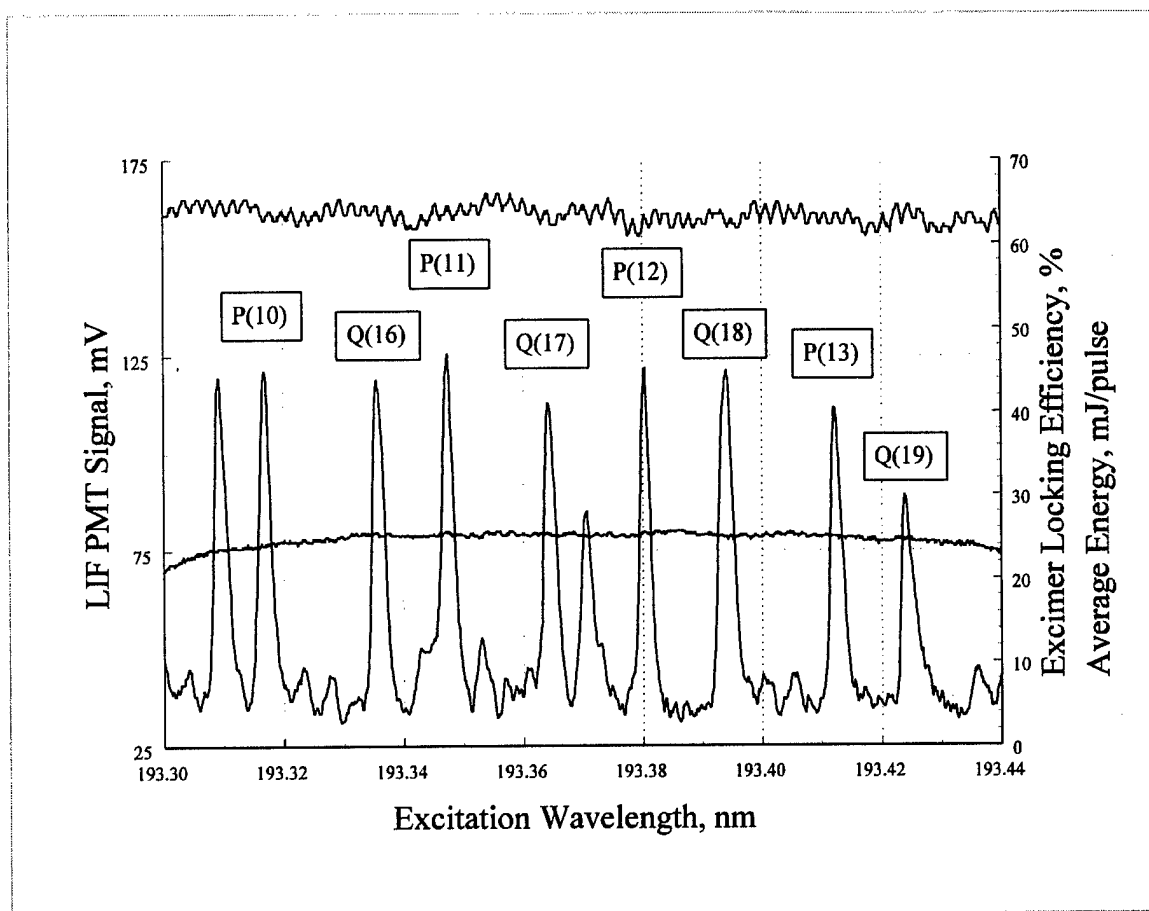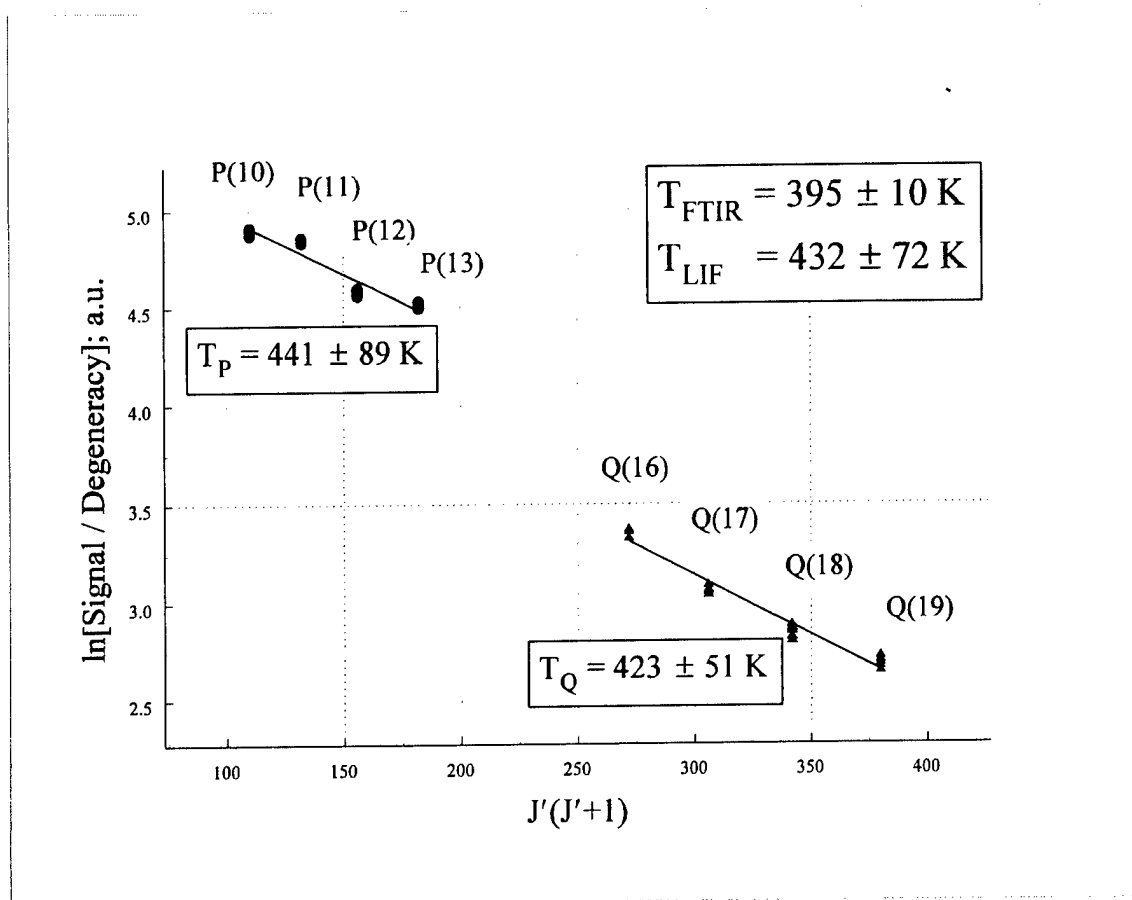
Figure 10

Figure 11

14. HIGH-VOLTAGE PULSER DEVELOPMENT FOR THE PLASMA RAMPARTS PROGRAM

E. Walton, B. Baertlein, S. Oh

1. INTRODUCTION

Under the AFOSR Plasma Ramparts MURI, The Ohio State University ElectroScience Laboratory (OSU-ESL) was tasked to develop high-voltage (HV) short-pulse generators, referred to hereafter simply as "pulsers." This report is a summary of that work. The details of our effort appear in a separate document [6], to which the reader may refer for more details.

The overall goal of this work was to generate plasma using a minimum of input power. Recent research [1] suggests that plasma can be initiated in air by a very short, HV electromagnetic pulse. The plasma then takes a few tens of nanoseconds to decay. Subsequent tests have shown that a sequence of such pulses having a low duty cycle can sustain the plasma, leading to a significant reduction in power requirements vis a vis continuous RF excitation. The required pulse voltage is very high (greater than 8,000 Volts) and the pulse duration is very short (less than 10 nanoseconds). The generation and transmission of such pulses offers some challenges, which were the subject of this study.

This research documented here has as its objective the generation of pulses that meets the following requirements:

- > 10,000 volts
- < 10 ns
- continuous, eternal pulse train with pulse repetition frequency near 1 MHz
- >400 ohm load impedance (at the plasma)
- balanced (e.g., 2-wire) output at the plasma excitation electrodes

The work described here was performed in two parts. In the first part, a quick-response approach was adopted to provide a pulser to plasma researchers as early as possible (i.e., to avoid being in the position of delivering the pulse generator on the last day of the program). A commercial pulse generator was leased for this portion of the project, but it was not entirely suitable for this application. Specifically, the commercial unit did not have enough voltage (by a factor of 2), and the output port was matched to an unbalanced (coaxial) 50 ohms impedance. These problems were overcome by the timely development of

a voltage-boosting balun transformer line. That transformer converted the unbalanced coaxial output line to a balanced twin-line feed. It also transformed the impedance from 50 ohms to 400 ohms to match the plasma electrodes, and it boosted the voltage from 5,000 volts to 12,000 volts at the plasma excitation point. The resulting device is described in Section 2.

In the second phase of the effort we studied pulse compression techniques. The goal of that task was to obtain pulse widths less than 2 ns for an eternal pulse train. This can be achieved by generating a sequence of low-voltage, long-duration pulses, amplifying them and feeding them to a passive dispersive network that compresses their time duration while simultaneously increasing their amplitude. The theory and development of that alternative pulser are described in Section 3.

2. WIDE BAND TAPERED BALUN

2.1. Objectives

As noted in Section 1, the initial objective of our effort was to meet short-term pulser needs using a commercial pulse generator. We leased a pulser (Bournlea Model 3162) that produced a burst of 1024 pulses of 5 kV amplitude, 10 ns duration and a pulse repetition frequency (PRF) of a few tens of kHz. To make this device useful, it was necessary to transform the pulser's 50 ohm coaxial output to approximately 400 Ohms on a twin line. A sketch of the relevant hardware appears in Figure 2.1.

Short pulses have very wide percentage bandwidths, and this issue complicates impedance transformations. Figure 2.2 shows the spectral content of a 10 ns pulse with 3 ns rise and fall time. An impedance transformer that will pass this pulse without distortion must operate non-dispersively from DC to more than 250 MHz. Classical approaches to impedance transformation, including transformers wound on air or ferrite cores, will not work because the high voltages will produce arc-over and ferrite saturation.

The large ratio of the input and output impedances (400:50 or 8:1) made it necessary to use a two-stage design for the impedance transformer. The first stage is based on a tapered transmission line concept [2] (the so-called "zipper line"). A tapered balun[1] transformer was fabricated by cutting a slot of increasing width in the outer shield of a coaxial line as shown in Figure 2.3. This process results in a twin-lead transmission line (a balanced structure) with a spacing of a few cm and an impedance of approximately 150 Ohms. For the second phase of this effort, the separation of the twin leads was increased to 10-cm to

---

[1] A "balun" (**bal**anced to **un**balanced) is a device for transforming an unbalanced transmission line (like a coaxial cable) to a balanced transmission line (line twin-lead line).

produce the desired final impedance. Using well-separated conductors allows HV operation while avoiding arcing.

2.2. Design and Fabrication

A key issue in the design of a tapered transmission line is the manner in which the impedance Z changes along its length z (see Figure 2.4). The function $Z(z)$ dictates the performance of the line by controlling the reflection of incident energy. A number of authors have studied methods of optimizing $Z(z)$ for best performance [2-4]. A Tchebysheff taper for Z has a number of attractive properties [3], and it is the point of departure for most studies. Unfortunately, a Tchebysheff taper that provides acceptable performance for the frequency band of interest here will have a length greater than 5
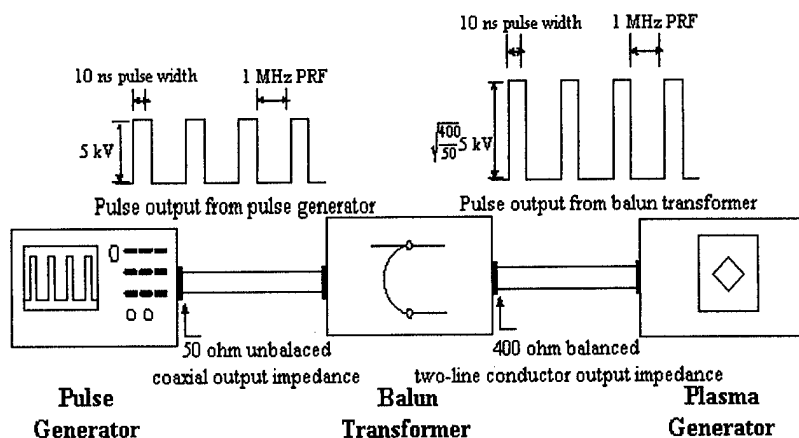

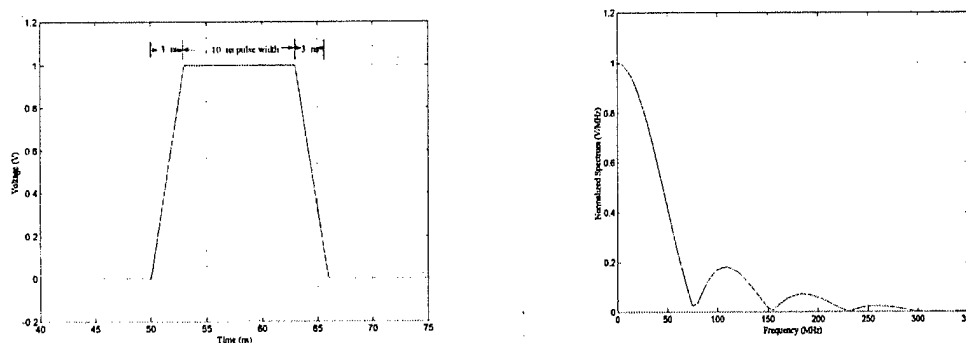**Figure 2.1.** Block diagram for use of a transformer with the commercial pulse generator

Figure 2.2. Bandwidth requirements of the balun transformer
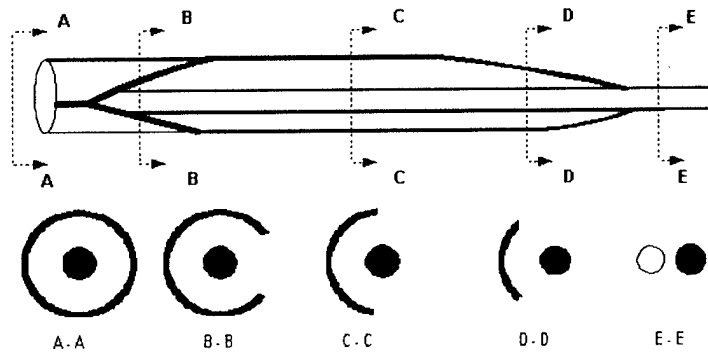
Figure 2.3. Coaxial implementation of tapered balun.
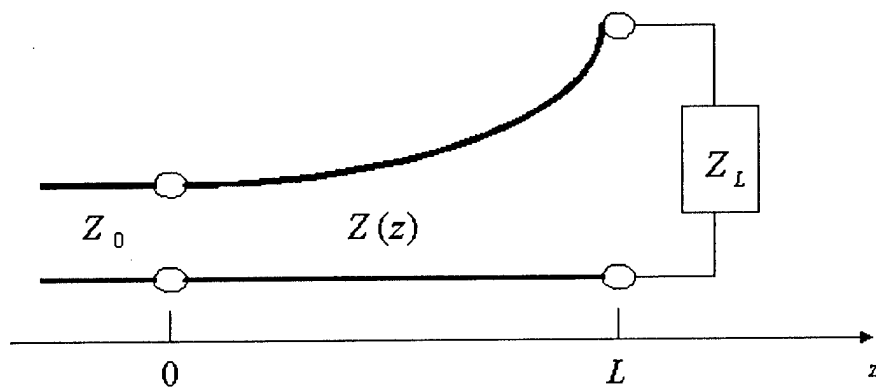
Figure 2.4. Impedance variation with distance (taper).

meters. One can achieve acceptable performance with a shorter line by using a Klopfenstein [3] taper, which gives the minimum reflection coefficient over a fixed passband for a given taper length. (This approach trades bandwidth for shorter line length.) The relation between the width of the slot and the impedance of the line is shown in Figure 2.5. Examples of the impedance taper appear in Figure 2.6.

Although the Klopfenstein design is optimal, a number of problems arise in practice. Specifically, the design involves an approximation that is only valid when the overall impedance change is small. In addition, it yields impedance discontinuities at each end of the line, even if the impedance mismatch is small (see Figure 2.6). A near-optimal design was proposed by Hecken [5] to avoid the impedance steps at the taper ends, but that approach results in a net increase in the line length. A comparison of the Klopfenstein and the near-optimum taper of Hecken is given in Figure 2.7. One finds that the low-frequency cutoff of the Klopfenstein taper is defined by $ßL = 4.6992$, but for the near-optimal (Hecken) taper, it is increased to $ßL = 5.3711$. (In these expressions, $\beta = 2\pi f/v$, where f is the frequency and v is the velocity of propagation.) In addition, the length of the latter design is increased by 14.29 %.

A fundamental challenge in this task is addressing the following conflicting issues:
- The majority of the pulse energy lies in the low-frequency regime.
- The transformer length is determined by the lowest frequency (i.e., lower frequencies require longer transformers)

As a result of these issues, neither the Klopfenstein nor the Hecken tapers lead to designs that have a reasonable length and, hence, we were led to investigate the following alternative design strategy.

We note in Figure 2.7 that the optimum tapers are close to linear (in impedance). Figure 2.5 implies that the slotted outer shield of the coaxial line is a narrow metal strip for most of its length. That configuration is fragile and it wastes physical line length. A more practical design is shown in Figure 2.8, where we use a slot angle that varies linearly with distance. This design was fabricated as shown in Figure 2.9. Two pieces of copper pipe were used to create the coaxial line, and the output is a twin=line pair. An impedance of approximately 150 Ohms can be achieved with only 2 meters of line. A two-meter extension of the twin-lead line was envisioned to provide the additional impedance change to 400 Ohms, but (as described below) was found to be unnecessary.

2.3. Testing and Performance Analysis

A network analyzer was used to measure the input impedance of this line. The network analyzer measures the complex reflection coefficient S_{11}, i.e., the reflected signal normalized to the transmitted signal. The measured reflection coefficient of this line as a function of frequency from nearly DC to 1,000 MHz is shown in Figure 2.10 for a 130 Ohm load. The reflected signal is more than 10 dB below the incident signal, which indicates good performance over the frequency band of interest. We require the balun to be non-dispersive or the output signal waveform will be distorted. The absence of
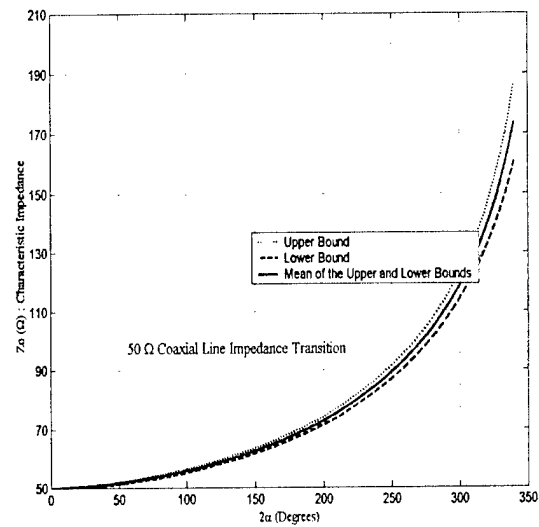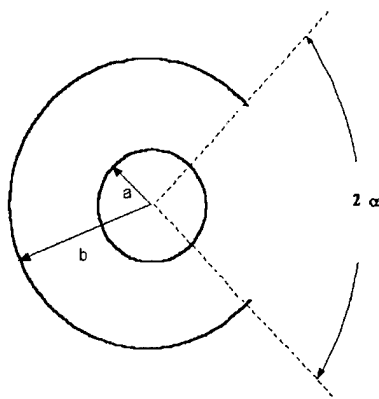
Figure 2.5 Relation between slot angle and impedance; .
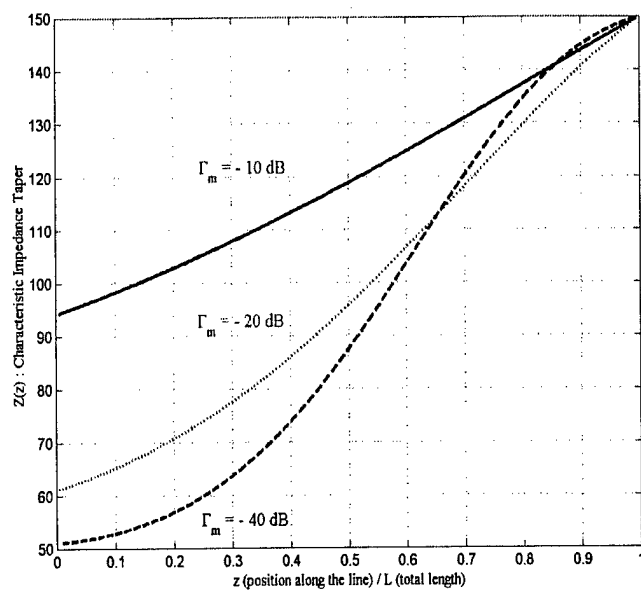
Figure 2.6. Examples of the Klopfenstein impedance tapered transition
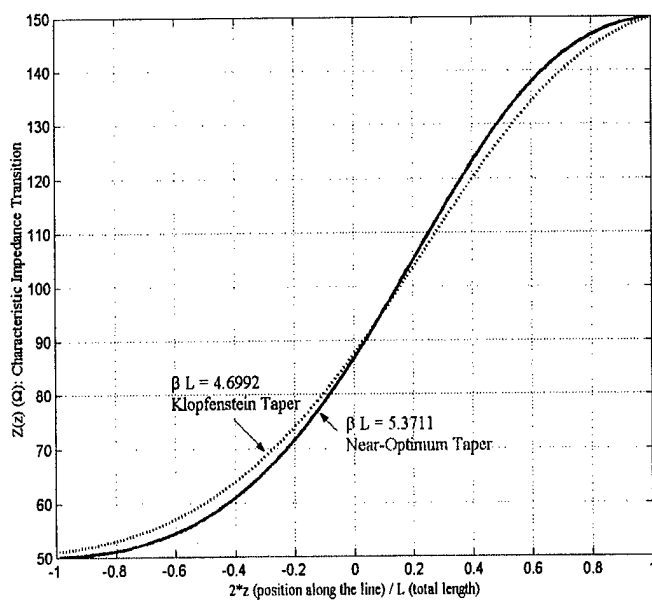
Figure 2.7. Comparison of Klopfenstein and near-optimum tapers
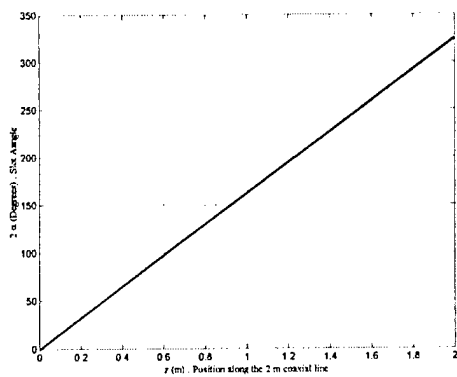
Slot angle along the taper length
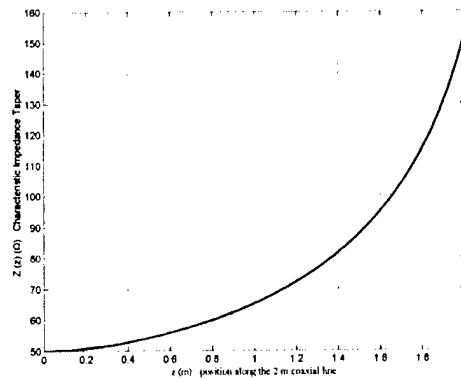
Characteristic impedance along the taper length

Figure 2.8. Slot angle versus length and resulting impedance profile.
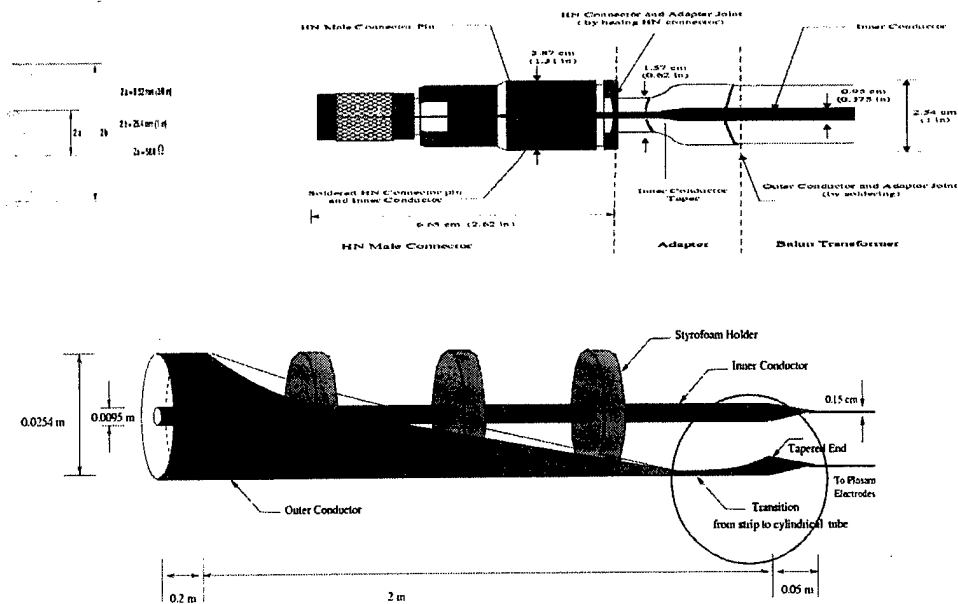
Figure 2.9. Fabrication of the balun transformer
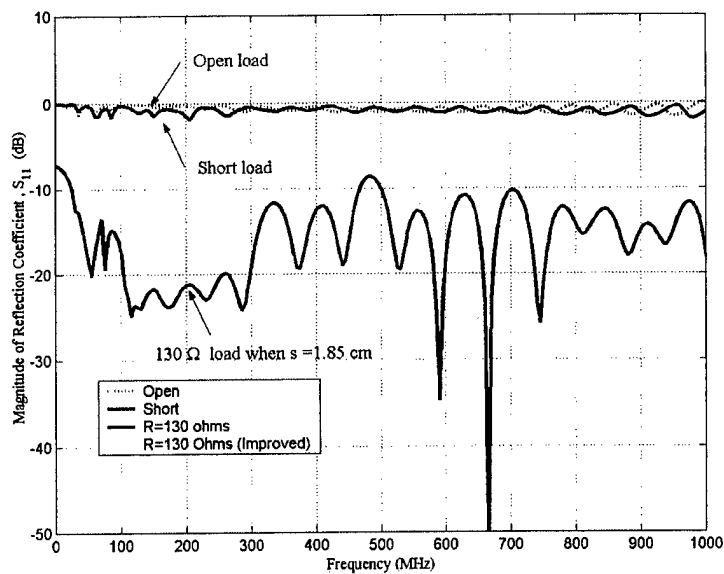
Figure 2.10. Response from 2 m balun

dispersion is indicated in Figure 2.11, in which the phase of the reflection coefficient is plotted as a function of frequency when the line is terminated with a short circuit, an open circuit and a 130 Ohm load

265

resistor. Note that the phase plot is a straight line for the open and short circuit cases (indicative of a non-dispersive line). The low value of S_{11} for the 130-ohm load further indicates that any dispersion is weak.

More insight into the behavior of the balun can be obtained by transforming the frequency-domain reflection data to the time domain. The time-domain results for open, short, and 130 Ohm loads are shown in Figure 2.12. The open circuit produces a positive pulse and the short circuit produces a negative pulse at a location corresponding to the end of the line, as required by the reflection coefficients of those loads (+1 and -1 respectively). The reflection from the matched load is significantly lower (note the change in scale), which confirms our earlier finding of good performance. Knowing the speed of propagation of the signal, we can plot this response as a function of distance along the line (see Figure 2.13). Note the connector response at the beginning of the line, and the response of the load resistor at the end of the line. Reflections from the load at the end of the line are greatly reduced and, in fact, are now comparable to reflections from the small imperfections in the connector at the input.

As indicated above, we planned to transform the line's 130 Ohm output impedance to the desired 400 Ohm impedance by extending the length of the line to four meters. Over the additional two meters, the impedance of the twin-lead line would be tapered by gradually spreading the distance between the lines. Reflection-coefficient results for the four meter line are shown in Figure 2.14. Note that the reflection coefficient is maintained below −10 dB for the band of interest with the 400 ohm load. Unfortunately, a four meter line is awkward to use in a laboratory setting. A number of experiments were performed, and it was found that comparable performance could be obtained with a two-meter transformer by simply spreading the ends of that line. The results, shown in Figure 2.15, indicate surprisingly good performance. The success of this approach can be attributed to interaction between the twin lead spacing at the end of the balun and a structural feature that also appears near the end of the balun, specifically, the transition from the thin remnant of the coaxial shell to a second cylindrical conductor (cf. the red circle in Figure 2.9). That transition introduces an additional reflection, which can be mitigated by spreading the leads. The action of spreading the leads also increases the impedance, which is precisely what is required to match the higher load impedance.

The two-meter balun was tested at high voltage. The experimental set-up, shown in Figure 2.16, uses a magnetic field probe placed some distance (about two inches) from the balun output to sense the current into the 400 Ohm resistor. We first calibrated the system at low voltage as shown in Figure 2.17, to relate the voltage across the resistor to the field probe measurement. When the system is operated at high voltage, the resistor current (and, hence, the output voltage) can then be inferred directly from the

266

magnetic field probe measurements. The high voltage results are shown in Figure 2.18. We confirm that the input to the balun line is 5 kV at 50 ohms, but at the output of the balun the voltage is approximately 10 kV. The width of the pulse (10 ns on input) has not been degraded.

2.4. Conclusions

We developed a balun transformer to permit 10 kV, 10 ns pulses to be driven into a 400 Ohm balanced load. The input to the balun is a commercial pulse generator producing 5 kV pulses into a 50 Ohms unbalanced (coaxial) load. No appreciable pulse degradation was observed in the output.
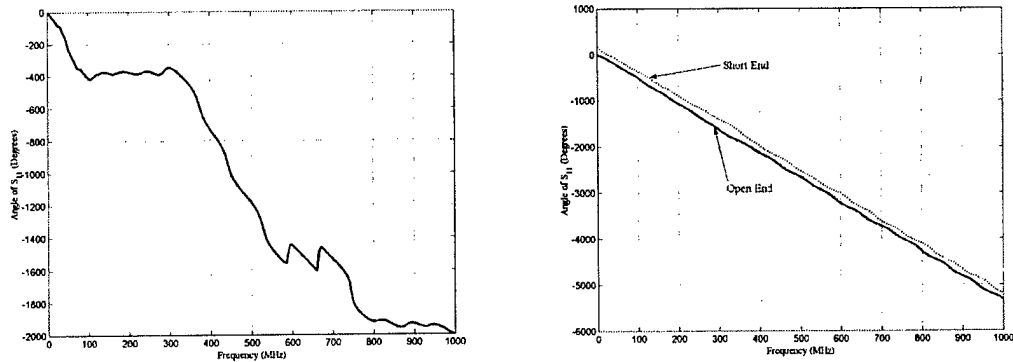
Figure 2.11. Phase response versus frequency for the 2 meter balun
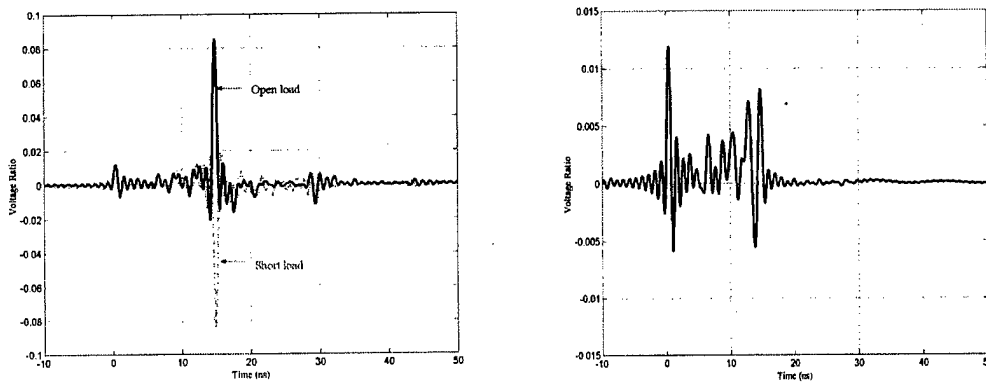
Time domain response of S11 with open and short loads

Time domain response with 130 O load

Figure 2.12. Time domain reflected response (S_{11}) of the 2 meter balun.

267
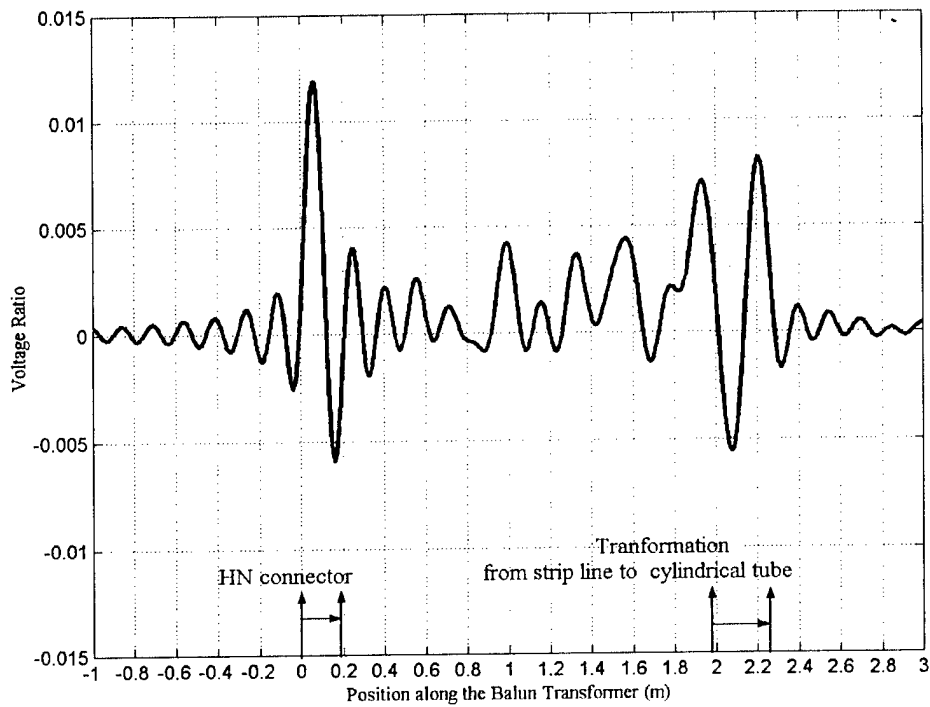
Figure 2.13. Time-domain reflected response (S_{11}) versus position along the balun with a 130 Ohm load.
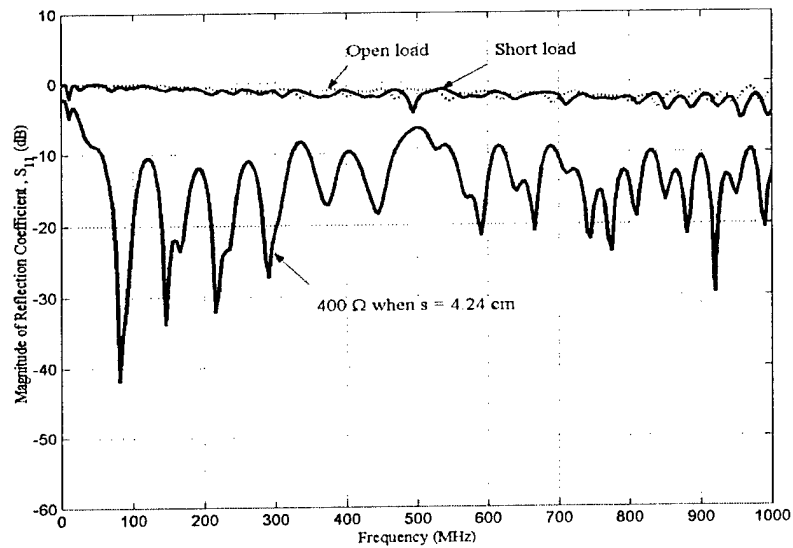
Figure 2.14. 4 meter balun response.
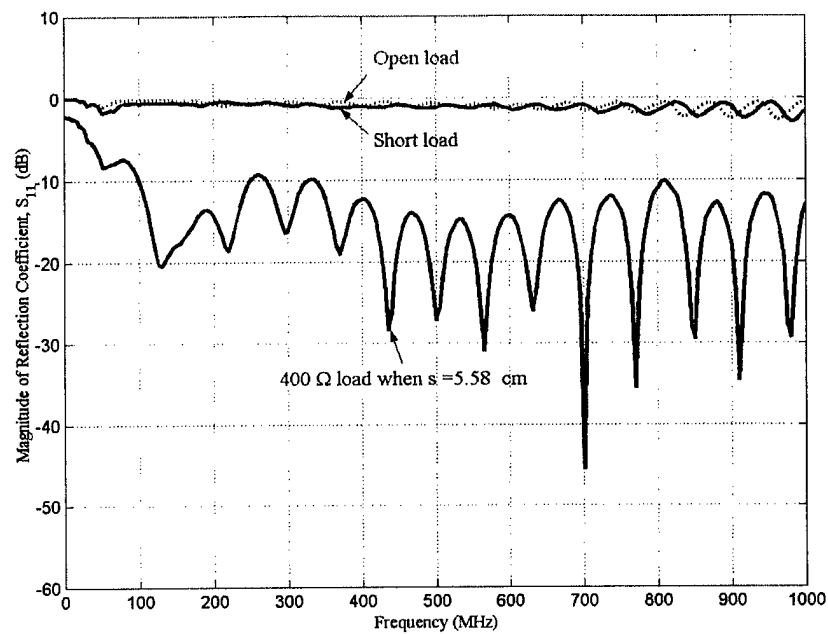
Figure 2.15. Response of the 2 m balun for the short, open, and 400 ohm loads
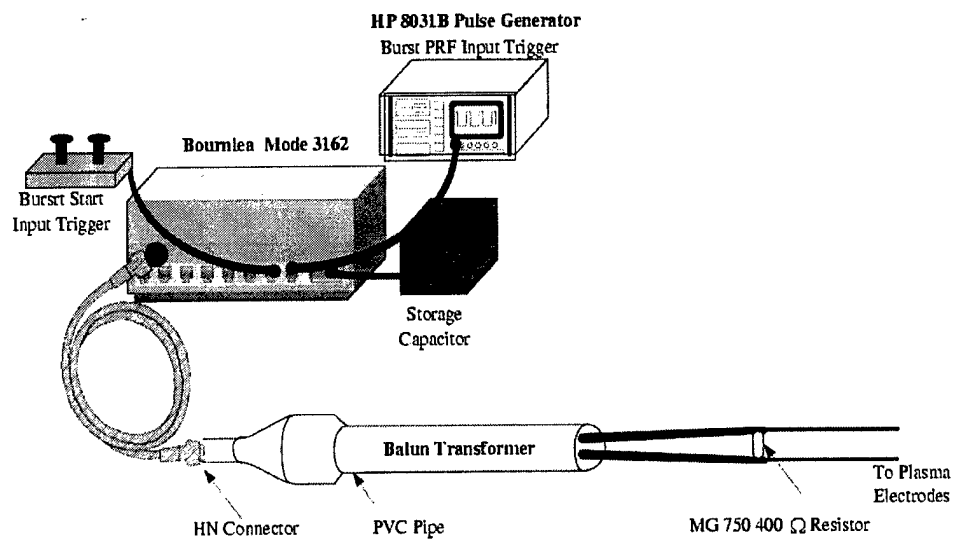
Figure 2.16. Set-up for the HV pulser system tests.

269
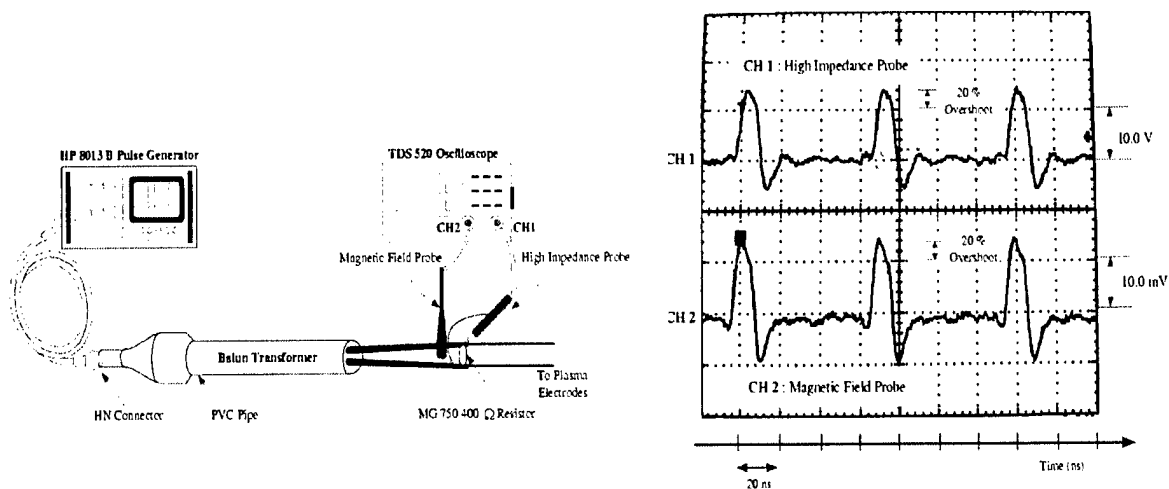
Figure 2.17. Verification measurements using a magnetic field probe.
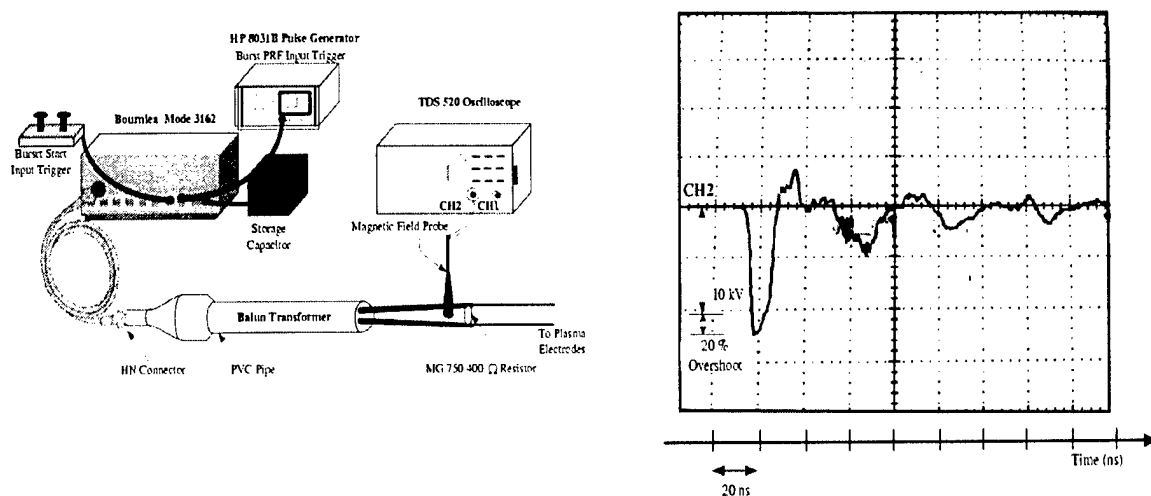
Figure 2.18. Test of the HV pulser system showing the pulse output from the balun when driven by the high-voltage pulser

270

3. PULSE COMPRESSION TECHNIQUES

In the second portion of the project OSU-ESL worked to develop a new, high-performance pulser. Many commercial pulsers use HV capacitors and high-speed switches to generate pulses with amplitudes of 10s of kV and pulse durations in the 10 ns range. At high (more than 100 kHz) pulse repetition frequencies (PRFs), the drive capacitors are rapidly depleted, and only a finite set of pulses (1024, for the Bournlea pulser) can be generated before they must be re-charged.

3.1. Objectives and General Approach

The objective of this work was to generate eternal trains of 1 ns, HV pulses at 1 MHz PRF. It is impractical to use HV high-speed switches for this task, because currently available switch speeds to not extend into the ns domain. Further, charging wide band capacitor lines (essentially transmission lines) requires high bandwidth (>1 GHz) capacitor systems.

The pulse generation approach investigated here involves waveform synthesis techniques at frequencies up to 1 GHz. We will generate a continuous waveform at lower voltages with a frequency bandwidth of roughly 1 GHz, and use frequency dispersion or synthesis techniques to form the desired impulse train.

3.2. Direct Fourier Synthesis

Our study began with an investigation of Fourier synthesis techniques. We explored the use of many (10s to 100s) coherent RF oscillators and power amplifiers to generate a set of harmonic sinusoids of modest voltage. Those sinusoid are then summed (with appropriate phases) to yield a function of the form $\sin(x)/(x)$ (also known as a "sinc" function). The sum of N harmonics having voltage V yields a sinc function with a PRF equal to the fundamental frequency and a peak voltage of NV. The pulse width is the period of the highest harmonic. This is illustrated in Figure 3.1. While this approach is theoretically sound, it is impractical because the required low-loss, HV, wideband RF combiner does not exist.

3.3. Matched Filter and Pulse Compression Techniques

A more practical approach to pulse synthesis involves so-called "pulse compression" techniques. In this approach a long-duration, wideband waveform is applied to a linear, dispersive device (the device is sometimes referred to as a "pulse compression line"). If the incident waveform is chosen appropriately, the amplitude of the output waveform will increase by v(BT), where B and T are respectively the

bandwidth and duration of the applied waveform. The applied waveform should be the result of deconvolving the device's impulse response from a bandlimited delta function. Thus, when the incident (low voltage) waveform is applied, a band-limited delta function of larger amplitude results. Similar techniques have been used for many years in radar systems as a means of obtaining high range resolution and large power on target from low-power waveforms. Radars typically transmit waveforms that are sinusoids whose frequency increases linearly with time (i.e., "chirps"). Suitable dispersive devices for these low-power, frequency-swept waveforms are available, and they effectively provide a frequency-dependent delay to the input waveform. For more general devices, an approximation to the optimum waveform is simply the device's time-reversed impulse response.
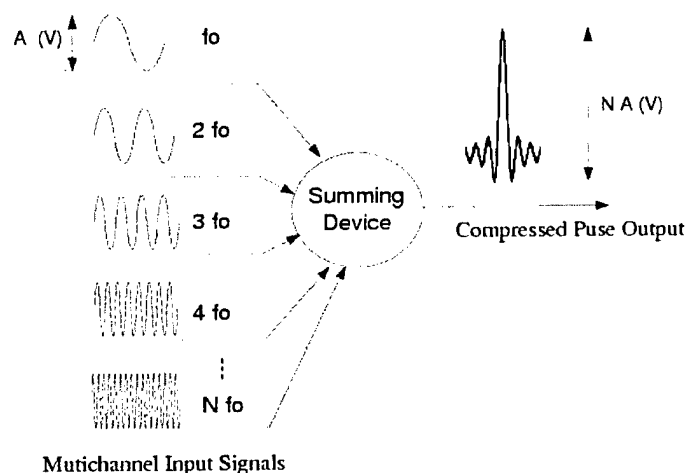
Figure 3.1. Direct Fourier synthesis using a summing network.

The chief technical challenge in using pulse compression concepts is to develop the dispersive delay line. OSU-ESL investigated several concepts including the "bridged-T" all-pass network and a reflective pulse forming line (PFL).

An "arbitrary waveform generator" (AWG or, more commonly, an "arb") is required to produce the specialized waveforms used in testing these devices. An AWG is essentially a very high-speed (roughly 1 GHz) digital memory with a computer interface. Arbitrary waveforms represented as a sequence of 32,000 16-bit numbers can be loaded into the memory from a computer (or even from a digital oscilloscope as the result of a measurement). Then, the AWG outputs these numbers at high speed via an internal D/A converter. The result is the desired output waveform.

272

3.3.1. Bridged-T All-Pass Network

A bridged-T all-pass network is shown in Figure 3.2. This is a circuit specifically designed to have a dispersive transmission coefficient, but low reflection (i.e., a good impedance match). A series of these filters can be used to form the dispersive transmission line required for pulse compression. Theoretically, the circuit has no loss, and a frequency-independent magnitude response. This technique has excellent theoretical properties, and OSU-ESL explored it in some detail (see [6]), but the loss per section was found to be prohibitive for real circuits. Ultimately, alternative methods had to be explored.

$Z_{IN}= Z_{OUT}$: Input and Output Characteristic Impedance
L1, L2 : Inductors
C1, C2 : Capacitors
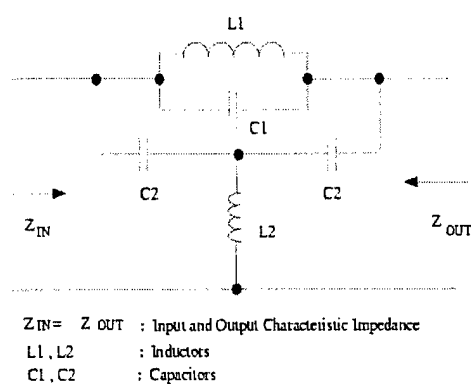
Figure 3.2. Bridged "T" all-pass network

3.3.2. Pulse Forming Line

Finally, pulse compression was explored using the PFL shown in Figure 3.3. The device uses a series of band-stop filters at harmonic frequencies f_0, $2f_0$, ...,Nf_0 separated by lossless transmission lines of time delay d. The input signal comprises CW tones at these frequencies of duration $2d$. Each input tone reflects from a different band-stop filter, thereby accumulating a different delay. At a time $N2d$ after the start of the input waveform, all harmonics arrive back at the device input and are superimposed coherently. (Note that each section of line is utilized twice, saving cable length.) A simulation of the concept using $N=4$ tones is shown in Figure 3.4. Note the increase in the peak voltage and the compression of the resulting impulse. For reasons that are beyond the scope of this discussion (see [6]) it is necessary to transmit waveforms that are discontinuous at tonal changes. These discontinuities introduced undesirable high-frequency content. A more practical input waveform using Hann windowing to smooth out these discontinuities is shown in Figure 3.5. The response is reduced in this case, but the transmitted energy is also reduced.

The band stop (or "reflective") filters can be implemented using coaxial lines, microstrip lines or lumped-element circuits. A lumped element design, the three section Tchebycheff bandstop filter shown in Figure 3.6, was used in our work. . We modeled the line and calculated the magnitudes and phases of the response. The group delay characteristics, which are critical to the line's performance, are shown in Figure 3.7. By adjusting the phases of the transmitted tones to account for shifts in the group delay, we can improve the performance of the system. This permits us to estimate the expected compressed pulse output as shown in Figure 3.8. We find that the pulse amplitude (3.3 V) is close to the ideal value (4V), and the pulse width (~2 ns) is comparable to the expected value ($1/Nf_0$=2.5 ns).

274
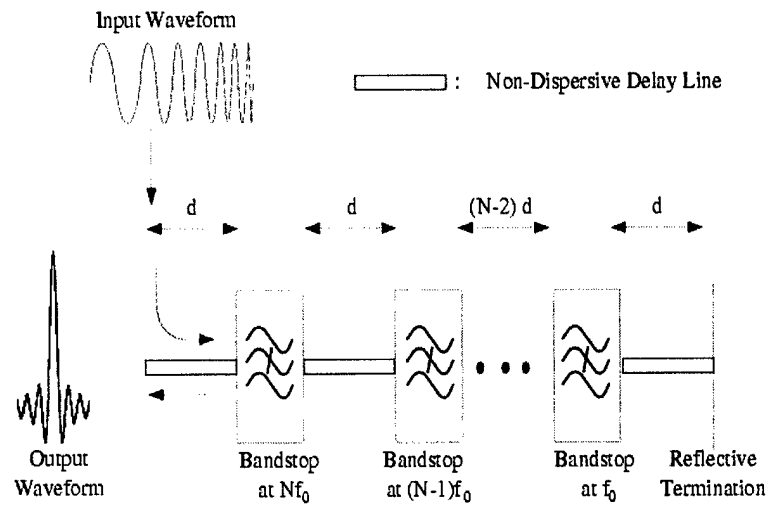
Figure 3.3. Pulse forming Line (PFL) with Reflective Filters
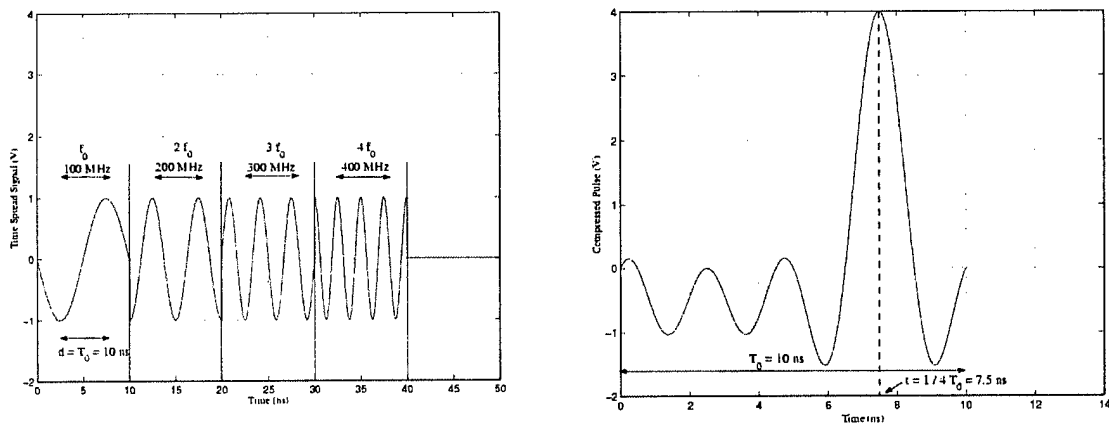
Figure 3.4. Time-spread signal and compressed pulse
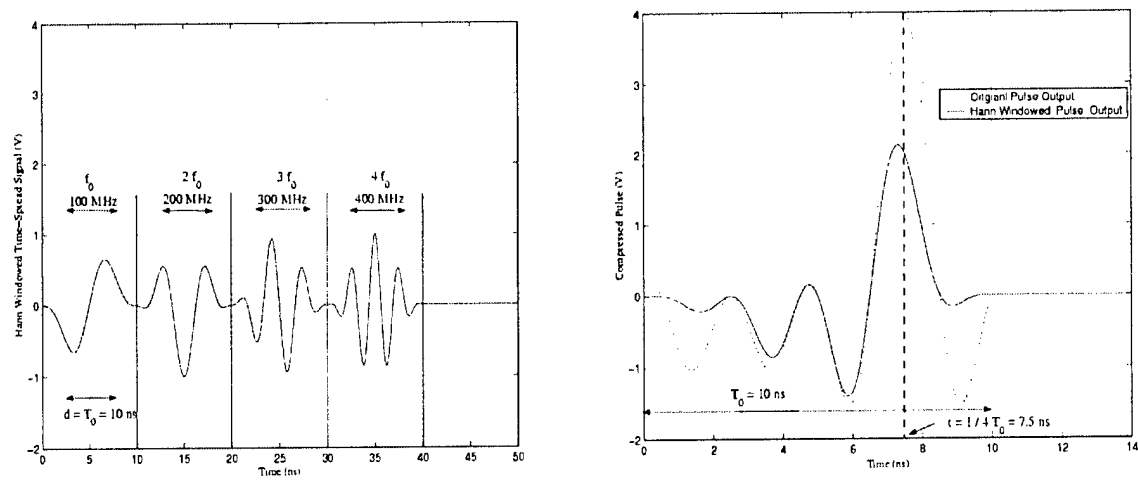
Figure 3.5. Hann-windowed time-spread signal eliminated discontinuities

Z_0 : Input and Output Characteristic Impedance

L_1, L_2 : Inductors

C_1, C_2 : Capacitors
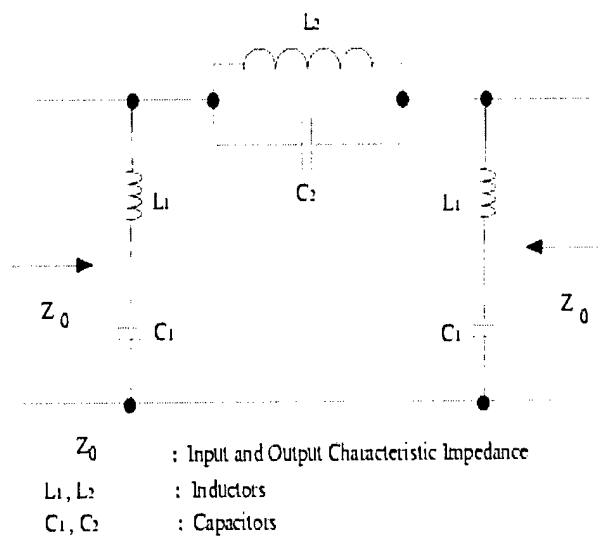
Figure 3.6. Implementation of reflective filter designs.

276
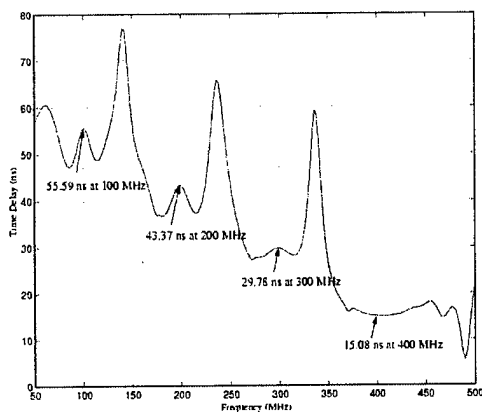
Time delay of the PFL
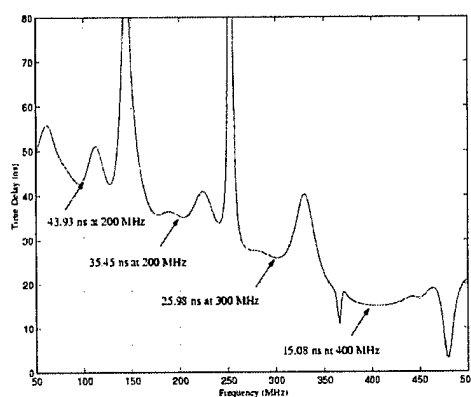
Time delay of the PFL with adjusted non-dispersive transmission lines

Figure 3.7. Group delay of the PFL for each frequency component.
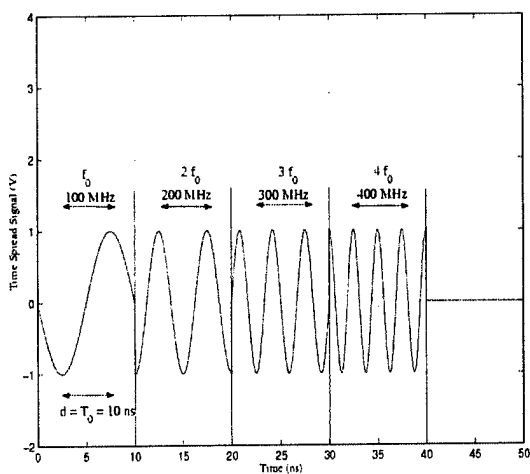
Time-spread signal
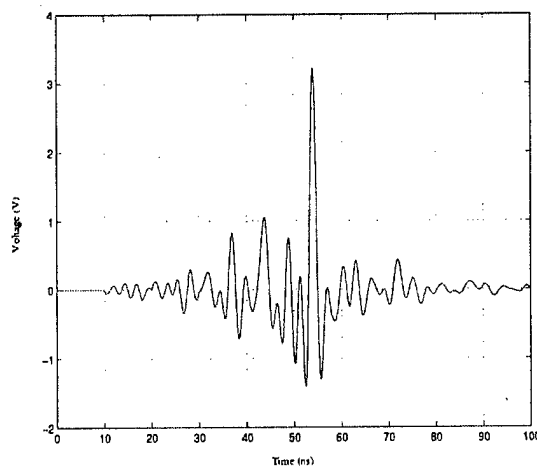
Compression pulse output

Figure 3.8. Compressed pulse output from the PFL

277

Additional tests (not shown) were done with the Hann-weighted input waveform to validate our modeled results by building a set of band-stop Tchebycheff filters as shown in Figure 3.6. The filters showed good stop-band performance, but loss and phase distortion for out-of-band signals was higher than anticipated. As a result, we were unable to replicate the performance shown in Figure 3.8.

An alternative approach (noted above) is to measure the impulse response of the PFL and apply the time-reversed impulse response as the PFL input. The resulting output is then the autocorrelation of the system response. Alternatively, one can view the system as a matched filter, for which the optimum input is the time-reversed impulse response. When this impulse response has a long duration and a wide bandwidth, the output is a short duration pulse with a large amplitude gain. This autocorrelation approach does not require careful control of the filter's out-of-band amplitudes and phases.

This matched-filter approach was explored using the PFL fabricated above. We first tested the concept using a semi-experimental approach. The impulse response of the line was captured by a digital oscilloscope. The response of the filter to the time-reversed input was then computed numerically. The measured impulse response is shown in Figure 3.9. In these results, a band-limited (50-450 MHz) impulse response is used. We see that response is very broadband, but there is excessive pass-band attenuation. Time-reversing this waveform and convolving it with itself yields the output waveform shown in Figure 3.10. Note that the resulting impulse has a time extent of less than two ns and a pulse amplitude of more than 4 times that of the original waveform. From Figure 3.9 we estimate a pulse duration of approximately 0.1 μs and a bandwidth of 400 MHz, which implies a maximum voltage gain on the order of v(BT)=6.3.

Based on the encouraging results in Figure 3.9, we tested the PFL by using the AWG to generate the input waveform from the time-reversed impulse response. The measured band-limited impulse response of this PFL is shown in Figure 3.11, and the measured output pulse is shown in Figure 3.12. A high-power circulator was not available for these tests, and a simple T-connector was used instead. This causes the input waveform to appear in the left portion of the output display in Figure 3.12, and it also produces a 6 dB loss in signal amplitude.

The results are encouraging. The resulting impulse is less than 2 ns in duration. The circuit used for this test is a low voltage surrogate for the amplified waveform that would be used in actual practice. In the final design, the initial waveform would be separated from the resulting impulse. The 6-dB loss in this type of tests system would also be eliminated.

278
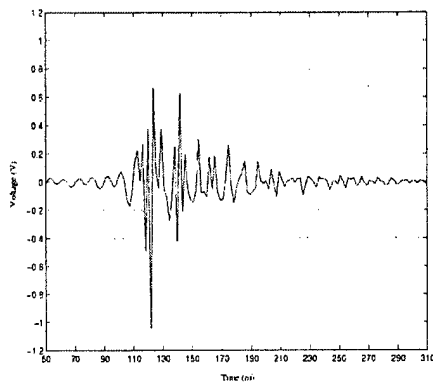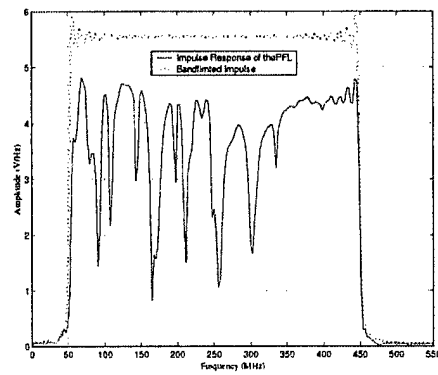
Time domain   Frequency Domain

Figure 3.9. Measured PFL impulse response and its frequency content.
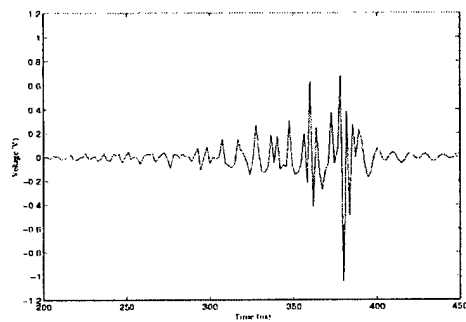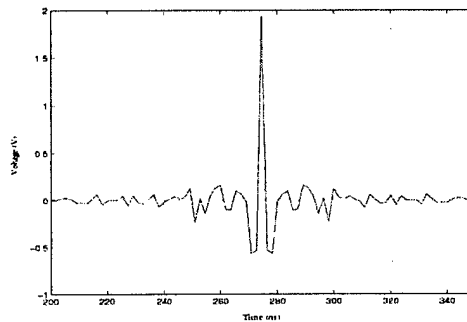
Time-reversed waveform   Frequency Domain

Figure 3.10. Measured, time-reversed impulse response and the numerically convolved PFL output.
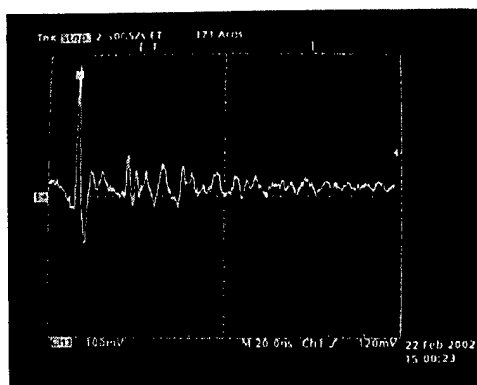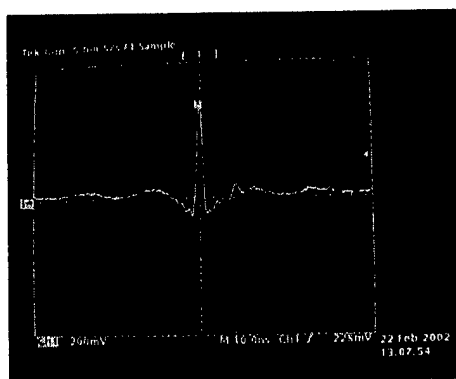
Figure 3.11. Band-limited impulse response and measured PFL output.
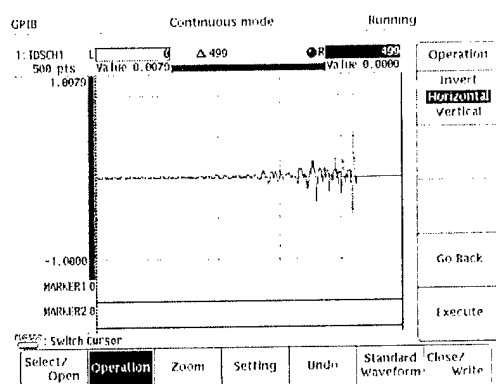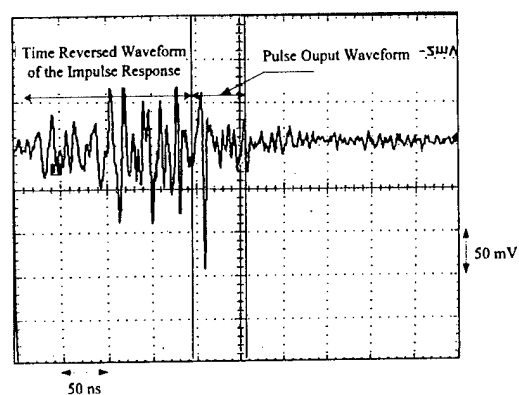
Time-reversed waveform   Ouput waveform

Figure 3.12. Time-reversed input waveform and output waveform from the PFL.

4. CONCLUSIONS

In this project the OSU ElectroScience Laboratory provided support to the AFOSR Plasma Ramparts program. The ESL task comprised development of "pulsers", i.e., generators of high-voltage, short-duration pulses.

280

The effort began with development of a device to convert the 5 kV, 50 Ohm coaxial output of a commercial pulse generator (the Bournlea Model 3162 pulser) to a 10 kV, 400 Ohm balanced output required for plasma experiments. The pulses produced by this device have a nominal duration of 10 ns, which implies a very broad frequency response. To meet these objectives we developed a balun transformer, which is essentially a specialized transmission line designed to produce an impedance transformation over a wide bandwidth. The balun was based on the tapered coaxial cable design studied by Hecken in 1956 [5] and optimized by Duncan and Minerva in 1960 [2] and by Hollman and Trankle in 1963 [4]. It was constructed using copper tubing that we fitted to a high voltage coaxial adapter. The outer conductor of the copper tubing was cut in a tapered slit based on design equations. The design has a minimum of dispersion, which avoids distortion in the pulse shape, and it includes a transformation from the unbalanced coaxial line to a balanced twin line to transform the impedance to the final required value. Testing showed that the transformer achieved the design objectives. We were able to deliver pulse voltages greater than 10 kV to a balanced load impedance of 400 Ohms.

In the second phase of our effort, we worked to develop an alternative pulser. The goal of that work was to generate an eternal train of 1 ns pulses with a pulse repetition frequency (PRF) greater than 1 MHz. A number of pulse compression techniques were investigated for this purpose. The underlying concept of all such techniques is to generate a wide band, long-duration waveform at relatively low voltages and then use a pulse-forming circuit to compress this waveform into a short high-voltage pulse. The original wide band waveform could be amplified using a 100 watt wide band (1 MHz to 1 GHz) power amplifier (such amplifiers are available commercially) and then compressed into the required high-voltage short pulses using the pulse-compression network.

We looked at various techniques for generating the required pulse train. Summation of harmonic, coherent sinusoids was one of the first concepts explored, but it was deemed impractical because of the requirement for a linear, high-voltage, wideband summation device that could combine 100 or more harmonics without significant loss. We next pursued pulse forming (transmission) lines (PFL's). It is well known that a frequency dispersive transmission line will transform a wide-band low-voltage waveform into a short-duration high-voltage output pulse. We tested several of these devices by building PFLs and exciting the lines using an arbitrary waveform generator (AWG). After experimenting with a number of approaches, the most successful technique was found to be autocorrelation of the system impulse response. In this technique, the time-reversed impulse response of the PFL is applied as the input, producing an output waveform which is the autocorrelation of the PFL's impulse response. (The concept is analogous to a matched filter.) For a wideband, dispersive line, the resulting pulse has a very

short duration. We used a digital oscilloscope to capture the impulse response and then delivered the waveform (digitally) to the AWG where it was time-reversed and stored in the AWG. This waveform was then applied to the test circuit, where it was shown to compress into the required pulse. Although significant pulse compression was achieved using this technique, we did not demonstrate an acceptable amplitude gain because of attenuation in the PFL. Another implementation of this concept using higher quality components should yield a reasonable voltage gain, but further development is required to demonstrate the 10 kV output voltages required for plasma generation.

5. REFERENCES

1. A. M. Hocutt and R. J. Barker, Air Plasma Ramparts Program Information Booklet, DC: Air Plasma Ramparts Program, 1997.
2. J. W. Duncan and V. P. Minerva, "100:1 bandwidth balun transformer," *Proc. IRE*, vol. 48, pp. 156-164, Feb. 1960.
3. R. W. Klopfenstein, "A transmission line taper of improved design," *Proc. IRE*, vol. 44, pp. 31-35, Jan 1956.
4. J. H. Hollman and F. A. Trankle, "Design of a high-power wide-band balun for the high frequency region," *IEEE Trans. Communication Electronics*, pp. 363-367, Jul 1963.
5. R. P. Hecken, "A near-optimum tapered transmission line matching section,' *Proc. IRE*, vol. 44, pp. 539-548, Apr 1956.
6. S-H Oh, "Generation of High Voltage Wideband Pulses for Plasma Experiments", MS Thesis, The Ohio State University Electrical Engineering Department, August, 2002.

15. SPIN-OFFS

Electron-Mediated Vibration-Electronic (V-E) Energy Transfer in Optically Pumped Plasmas

E. Plönjes, P. Palm, J.W. Rich, and I.V. Adamovich, **Chemical Physics**, Vol. 279, pp. 43-54, 2002

The paper discusses experiments on vibration-to-electronic energy transfer in CO laser pumped CO-Ar and CO-N_2 plasmas. Ionization in these strongly nonequilibrium plasmas occurs by an associative mechanism, in collisions of two highly vibrationally excited CO molecules. The experiments show that removal of the electrons from the optically pumped plasmas using a saturated Thomson discharge results in considerable reduction of the UV/visible radiation from the plasma (CO 4th positive bands, NO γ bands, CN violet bands, and C_2 Swan bands). At some conditions, the removal of electrons results in a nearly complete extinguishing of the UV/visible glow of the plasma. This effect occurs even though electron removal results in an increase of the high vibrational level populations of the ground electronic state $CO(X^1\Sigma, v\sim15-35)$. On the other hand, deliberate electron density increase by adding small amounts of O_2 or NO to the optically pumped CO-Ar plasmas produced substantial increase of the UV/visible radiation intensity, which strongly correlates with the electron density. The results of the present experiments indicate that the vibration-to-electronic (V-E) energy transfer process $CO(X^1\Sigma \rightarrow A^1\Pi)$, and, possibly, analogous processes populating radiating excited electronic states of NO, CN, and C_2, in optically pumped plasmas, may be mediated by the presence of electrons which are created in the absence of an electric field, with low initial energies. Most importantly, this effect occurs at ionization fractions as low as $n_e/N \sim 10^{-9}$-10^{-7}.

Supersonic Nonequilibium Plasma Wind Tunnel Measurements of Shock Modification and Flow Visualization

Yano. R., Contini, V., Ploenjes, E., Palm, P., Merriman, S., Aihal, S., Adamovich, I., Lempert. W., Subramaniam. V., and Rich, J.W, **AIAA Journal**, vol. 38, No. 10, 2000, pp. 1879-1888

The paper discusses experiments conducted in a new, small-scale, nonequilibrium plasma wind tunnel recently developed at Ohio State. The facility provides a steady-state supersonic flow of cold nonequilibrium plasma with well-characterized, near uniform, properties. The steady-state operation is an advantage compared with short runtime available in shock tubes and ballistic ranges. The plasma is produced in aerodynamically stabilized high-pressure glow discharge that forms the plenum of the supersonic nozzle. The possible modification of the supersonic flow due to ionization is studied by measuring the angle of oblique shocks attached to the wedge located in the nozzle test section. The results

do not show any detectable shock weakening or attenuation in weakly ionized nitrogen plasma, compared to the measurements in a non-ionized gas flow.

Experiments in supersonic flowing nitrogen and helium afterglow using this facility also demonstrate a novel technique for high-density supersonic flow visualization. It allows identifying all key features of the supersonic flow, including shocks, boundary layers, flow separation regions, and wakes by recording intense visible radiation of the weakly ionized plasmas. Interpretation of radiation intensity distributions in nonequilibrium supersonic flowing afterglow may provide information on key mechanisms of energy storage and ultraviolet radiation in high-altitude rocket plumes. In addition, these flow visualization experiments can be used for validation of multidimensional computer flow codes used for internal flow simulation.

Synthesis of single-walled carbon nanotubes in vibrationally nonequilibrium carbon monoxide

E. Plönjes, P. Palm, G.B. Viswanathan, V.V. Subramaniam, I.V. Adamovich, W.R. Lempert, H.L. Fraser, J.W. Rich, **Chemical Physics Letters**, vol. 352, No. 5-6, pp. 342-347, 2002

Single-walled carbon nanotubes (SWNTs) are synthesized in a gas-phase nonequilibrium plasma process. The carbon producing CO disproportionation reaction is driven very efficiently in a flow reactor, in which extreme disequilibrium between the vibrational and translational mode of the carbon monoxide gas is maintained even at low translational temperatures by using a powerful and efficient carbon monoxide gas laser. In the presence of metal catalysts, the vibrationally excited CO reacts to form CO_2 and structured carbon molecules, notably SWNTs. The individual tubes form ropes or flat ribbons and these are aligned parallel to each other into larger structures of SWNT material without any post-synthesis treatment.

16. DEVELOPMENT OF RUBIDIUM FILTERED THOMSON SCATTERING MASUREMENTS

S.H. Zaidi, Z. Tang, A.P. Yalin, P. Barker, and R.B. Miles

1 Introduction

Experimental diagnostic techniques play a significant role for the understanding of plasma properties and the validation of theoretical predictions. These diagnostics are in high demand in plasma aerodynamics where both intrusive and non-intrusive techniques are used to conduct plasma studies. The use of Langmuir probes is the most popular method for the measurement of electron temperature and electron density in low temperature and weakly ionized plasmas [1]. In spite of their usefulness, the intrusive nature and their restricted application to the low temperature plasmas make these probes unsuitable for high temperature plasma studies.

Among the non-intrusive techniques, Thomson scattering has emerged as an important diagnostic tool which can be used to make unambiguous measurements of electron temperature and electron number density in plasmas [2]. Experiments in plasmas with electron densities in the range of 10^{17} to 10^{21} cm^{-3} and electron temperatures in the range of 1eV to 5eV are now being performed [3]. Recent attempts have been made to lower limit for Thomson scattering measurements to below 10^{12} cm^{-3}. This density regime is commonly found in glow discharges which are used in industrial application including etching and depositions.

In spite of several advantages, Thomson scattering technique does have few limitations which mainly come from the plasma luminosity and the Rayleigh light which is scattered by the system as a back ground light. The Thomson signal has to compete with plasma emission and the elastic background radiation, both of which can mask the Thomson signal. To overcome the problem of interference from the undesired radiation, atomic dispersive resonance filters can be employed. In the present work a Rubidium filter along with a narrow width, frequency-tunable, pulsed Ti:Sapphire laser was used. The laser was tuned to the 780 nm absorption line of Rb vapor. The Rb filter was made optically thick at the laser wavelength, so that the light that is Rayleigh scattered from the neutral species in the plasma and background scattering are filtered out. As the Thomson signal is frequency broadened by the thermal motion and the ion acoustic coherent motion of the electrons, its linewidth becomes much greater than the absorption linewidth of the rubidium. This way the Thomson signal passes through the Rb filter whereas the undesired Rayleigh and background radiation is blocked. Further details of the Thomson technique and the related apparatus are presented below.

2 Thomson Scattering

When a laser beam is passed through a plasma, the Thomson component of the scattered light arises form free electrons. The bound electrons scatter the Rayleigh component whereas the stray light comes from elastic scattering from various surfaces in the system. Thomson and Rayleigh components are Doppler broadened but have very different spectral widths because electrons are much lighter than atoms.

The line shape of the Thomson scattering profile is a complicated function of the parameter α which, in turn, is a function of the scattering angle and the plasma characteristics (electron number density and electron temperature). The parameter α is defined as:

$$\alpha = 1/k\lambda_D \approx \lambda_0/(4\pi\lambda_D \sin (\theta/2)) \tag{1}$$

where λ_D is the Debye's length in the plasma and k is the magnitude of the difference between the scattered wave vector K_S and the incident wave vector K_O. Since the Thomson scattering is elastic, $|K_S| = |K_O|$. If $\alpha \ll 1$, the scattering comes from the uncorrelated electron motion and leads to incoherent Thomson scattering whereas for $\alpha > 1$ collective electron motion plays a dominant role and leads to coherent Thomson scattering.

The factor governing the spectral profile of the Thomson scattering is referred to as the form factor and is denoted by $S(K,\omega)$. The simplified expression for the form factor can be obtained by using the Salpeter's approximations [4] which assume that for most of the practical cases, the electron mass is much less than that of the ion and the electron temperature and the ion temperature are comparable.

The experimental detection of the line shapes provides information on plasma temperature and electron number and ion number densities. It would be worth mentioning that the frequency spectrum of the scattered light is strongly dependent on the scattering angle and the motion of the charged particles in the plasma. As compared to large scattering angles, spectral features at small scattering angles are compressed. In this regime stray light is a major interference that must be rejected and attenuated for accurate measurement of the scattering profile. This rejection can be achieved by employing atomic vapor filters as is explained n the next section.

3 Atomic Vapor Filters

Atomic vapor filters have been widely used to suppress Rayleigh signals and the back ground noise which arises from the elastic scattering from medium particles and surfaces. The initial applications involve the successful measurement of Raman intensities of gases only a few GHz away from the Rayleigh line [5]. Recently atomic filters have also been used in Thomson scattering measurements for the same reason. Bakker et. al. [6] used a sodium notch filter to suppress the stray light intensity in performing 90° Thomson scattering experiments in a low density plasma. In the current work an optically thick Rb filter has been employed in the system.
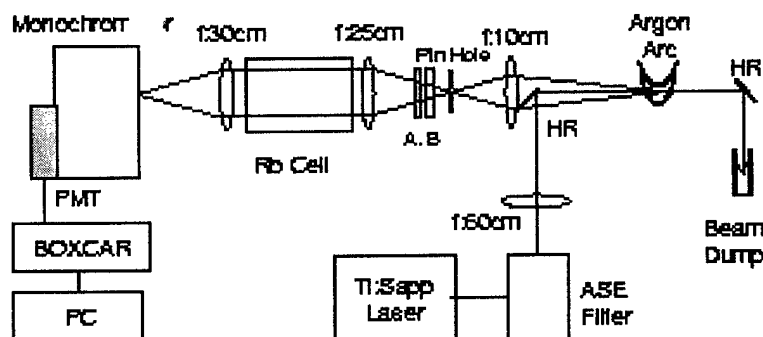
Figure 1: A schematic of the experimental arrangement.

4 Experimental Results

Figure 1 describes a schematic diagram of the experimental setup. The arc source plasma was an atmospheric argon MAXI-ARC lamp form NIST. In this water-cooled lamp, the arc constricting section is 6.3 mm long with a 4.0 mm diameter disk. The design of the lamp ensures stable burning of the argon flow. Pure atmospheric argon was supplied to the arc chamber. From the emission spectrum of the lamp it was found that the emission in the infra-red was significantly lower than in the visible region. Hence, it was advantageous to use the infra-red radiation source for Thomson scattering to reduce noise from the plasma emission background.

In contrast to Snyder et. al. [7], Bentley [8] and Bakker et. al [6] who performed 90° Thomson experiments, a backward layout has been adopted in this work. With the restricted optical access of the structure of the argon arc lamp, only the forward or backward scattering experiments were possible. The advantages of backward layout lie in a relatively less stray light radiation and the appropriate α

parameter for plasma diagnostics. As mentioned earlier, a narrow linewidth pulsed injection seeded Ti: Sapphire laser was used as the light source. The output of the laser was about 50-60 mj/pulse with a line-width of and about 100 MHz which made it an ideal choice for Thomson scattering. However the optical purity of this laser system was only about 99%. Besides the injection seed component, laser emission also consists of a broad ASE component. The elastic scattering from this ASE was found much stronger than the weak Thomson scattering. An ASE reduction filtered was constructed to overcome this problem. This filter consists of two spatial filters and 20-fold prisms which are used as the dispersive elements. Figure 2 shows both the ASE and the filtered ASE emission spectrum when the laser was tuned to the Rb D_2 line. The full width at half maximum of the ASE component is about at 2.0 nm whereas the corresponding value for the filtered ASE is about 0.7 nm which is spectrally narrow enough and can be suppressed by an optically thick Rb filter.
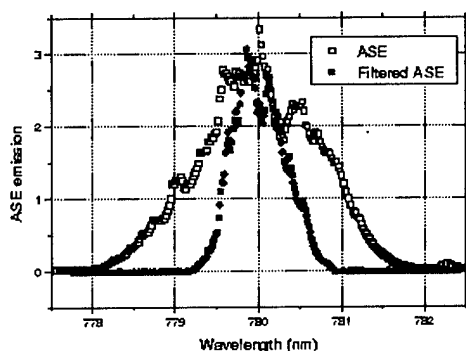
Figure 2: The ASE and the filtered ASE spectrum of the Ti:Sapphire laser.

It is worth mentioning that the Thomson scattering is linearly polarized whereas the plasma radiation is un-polarized. Therefore a Glan-Taylor polarizer was employed to pass the light which was polarized parallel to the electric field of the incident laser. The backward scattered light from the argon arc was spatially filtered and was passed through the Rb filter which absorbed the elastic and Rayleigh scattered light. The Thomson component of the scattered light was focused into a monochromator for spectral analysis where a photomultiplier tube (PMT) detected the required signal. The PMT was time gated synchronously with the laser to suppress the plasma luminosity. The signal was BOXCAR averaged, A/D converted, and was recorded by a computer.

Before making any Thomson measurements, the detection system was aligned by capturing the Raman features of the carbon oxide gas. Once the satisfactory Raman signals were obtained, the system was ready to measure the Thomson signal. The monochromator was set to 783.7 nm and the laser was tuned to 780.02 nm. Firstly, when the lamp was off, the laser radiation was blocked to check the zero level. Then the arc was ignited and the emission signal strength was monitored. The laser light was again blocked to check the zero drift, and the time gate of the BOXCAR was checked to make sure that the gate captured all the scattered light from the laser radiation. When the laser was focused into the arc, a big signal due to Thomson scattering was observed. The signal was reduced dramatically when the laser arc was extinguished. Once the Thomson signal was observed, a scan of its spectrum was obtained. The measurement results have been shown in figure 3 which also included the plasma emission spectrum without the laser and the laser emission spectrum without the plasma. The electron number density and the electron temperature was extracted from the Thomson scattering by matching   the   experimental line   profile   with the
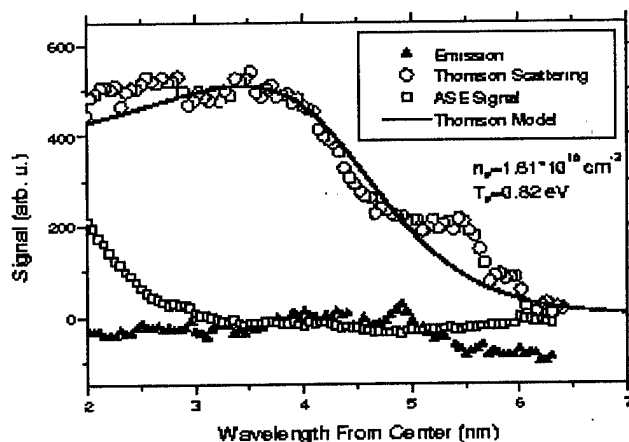
Figure 3: The plot of the measured Thomson scattering spectrum along with the fitted model.

theoretical models. The α parameter was 1.17 and the measurement results gave an electron temperature of 0.82 ± 0.06 eV, and an electron number density of $1.61 \times 10^{16} \pm 0.05 \times 10^{16}$ electrons /cm^3. The errors were estimated by the asymptotic standard errors from the fitting. It must be noted that all the Thomson scattering electron features observed so far were asymmetrical. The blue-wing hump was more than 10% to 30% larger than the red-wing hump. This asymmetry feature has also been observed by Snyder and

Bentley [7,8]. An example of such a Thomson scattering line profile is shown in figure 4. Although the integrated scattered light intensity is stronger in the blue wing than I the red wing, they have comparable spectral line-shapes and the same value of electron number density and electron temperature can be extracted from both sides. I n the graph, the two sides are separately fitted. The arc lamp was operated at an operating condition different from that used in figure 3. In this case the electron number density was found 5.48×10^{15} cm^{-3} whereas the electron temperature was about 2.42 eV.
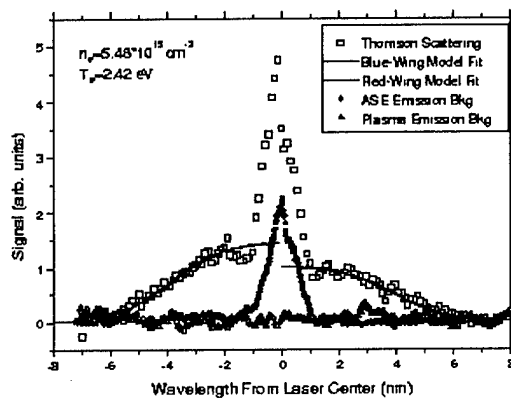
Figure 4: The plot of the measured Thomson signal along with the fitted model.

5 Summary

An optically thick Rb filter has been successfully used to suppress the elastic and Rayleigh scattering background while measuring a Thomson signal from an argon arc plasma which was operating at an atmospheric pressure. The spectral purity of a narrow linewidth Ti:Sapphire laser was achieved by using an ASE filter. The information on the electron temperature and the electron number density was extracted from the Thomson signal by fitting a model curve to the data.

References

[1] D. Batani, S. Alba, P. Lombardi, A. Glassi, Use of Langmuir probes in a weakly ionized, steady state plasma with strong magnetic field, Rev. Sci. Instrum. 68 (11), Nov. 1997.

[2] J. Sheffield, Plasma scattering of electromagnetic radiation, Academic Press, New York, 1975.

[3] C.J. Barth, M.N.A. Beurskens, C.C Chu, A.J.H. Donne, N.J.L. Cardozo, J. Herranz, H.J.V.D. Meiden, F.J. Pijper, A high resolution multiposition Thomson scattering system for the Rijnhuizen Tokamak Project, Rev. Sci. Instrum. 68 (9), Sep. 1997.

[4] E.E. Salpetter, Electron Density Fluctuations in a plasma, Physical Review, Vol. 120, No. 5, Dec. 1960, pp 1528-1535.

[5] Tang Z., Zaidi S.H., Miles R.B., Density gradient rubidium dispersive absorption filter for low wave number Raman and Thomson scattering, AIAA 2000-0644, 38th Aero. Scien. Meeting and Exhib., 10-13 January, 2000, Reno, NV.

[6]: Bakker L.P., Kroesen G.M.W., Thomson scattering using an atomic notch filter, Review of scientific instruments, Vol. 71, No 5, May 2000, pp 2007-2014.

[7] S.C. Snyder, L.D. Reynolds, J.R. Fincke, G.D. Lassahn, J.D. Grandy, T.E. Repetti, Electron temperature and electron number density profiles in an atmospheric press argon plasma jet. Phys. Rev. E., 50:519, 1994.

[8] R.E. Bentley, A departure from local thermodynamic equilibrium within a freely burning arc and asymmetrical Thomson electron features, J. Phys. D: Appl. Phys., 30:2880, 1997.

17. PRINCIPLES AND IMPLEMENTATION OF COHERENT RAYLEIGH SCATTERING

X. Pan, P.F. Barker, A. Meschanov, J.H. Grinstead, M.N. Shneider, and R.B. Miles

1. Introduction

Reliable measurements of plasma and flow properties are of fundamental importance, in particular spatially resolved measurements of translational temperature and electron number density [1]. In this paper, we present our work on plasma neutral temperature measurements using ponderomotive forces. Experiment using coherent Rayleigh scattering (CRS) to measure the gas temperature in a glow discharge is described. This localized measurement has high signal to noise ratio due to the fact that CRS is a coherent process. We also present the numerical calculation of photoacoustic detection of the energy deposition by optical lattice. Such a measurement also reveals the thermal energy distribution of atoms or molecules. Ponderomotive forces are key factors in both processes.

Ponderomotive force is usually defined as the force acting on individual particles (electrons, atoms, and molecules) due to the inhomogeneity of the fields. Consider a particle with charge q in an oscillating electromagnetic field, its Hamiltonian is given by

$$H(r,p;t) = \frac{1}{2m}\left[P - qA(r,t)\right]^2 + qU(r,t) \tag{1}$$

where P is the particle's momentum, A(r,t) and U(r,t) are the vector and scalar potentials at space vector r and time t . Averaging over time, the first order effects become zero, and we have

$$\langle H(r,p;t)\rangle = -\frac{\hbar^2}{2m}\nabla^2 - \frac{q^2}{2m}\langle A^2(r,t)\rangle \tag{2}$$

The second term on the right hand side of Eq. 2 is generally called ponderomotive potential. In a field gradient, a charged particle tends to minimize its potential energy by moving translationally. The force associated with this moving tendency equals the negative gradient of the ponderomotive pontential and is called ponderomotive force, with

$$f_{pond} = -\nabla U_{pond}(r,t) \tag{3}$$

In this report, however, we will mainly discuss the ponderomotive forces on atoms and molecules, which become induced dipoles in the electromagnetic field.

2 Temperature Measurement by coherent Rayleigh Scattering

Coherent Rayleigh scattering has recently been studied both theoretically and experimentally [2]. When two lasers beams, with electric field E_1 and E_2 at frequencies ω_1 and ω_2, cross each other, they form a traveling interference pattern in space. The pattern travels at speed $v=\Omega/q$, where $\Omega=\omega_1-\omega_2$ is the frequency difference, and $q = |k_1-k_2|$ is the wave vector difference of the two laser beams. If the laser light frequencies are far from gas resonant frequencies, a classical description will be sufficient. A polarizable atom or molecule in this region becomes an induced dipole with dipole momentum $p = \alpha E$, where α is the particle's polarizability and $E=E_1+E_2$ is the electric field. The potential energy of the induced dipole is

$$U = -\frac{1}{2}p.E = -\frac{1}{2}\alpha E^2 \qquad (4)$$

and the ponderomotive force

$$f_{pond} = -\nabla U_{pond}(r,t) = \frac{1}{2}\alpha\nabla E^2 \qquad (5)$$

tends to move the particle toward the region where the field intensity is stronger. For atoms that move at a velocity close to that of the interference pattern, this force will effectively modify their translational motion. Atoms moving much slower or faster will experience periodical forces and therefore won't be perturbed much. Another perspective points out that the traveling interference pattern forms a traveling and periodical potential well. Atoms and molecules with velocity close to that of the potential well will be attracted and trapped in the potential well and move with it.

The gas atoms in the crossed region of two laser beams will then redistribute and form a traveling density grating, which, in turn, form a traveling periodical refractive index field. If we shine a third laser beam onto this refractive index field, it can be Bragg reflected. We call this third beam probe beam and its Bragg reflected light coherent Rayleigh scattering signal. As in other coherent processes, it requires frequency matching and phase matching. The Maxwell-Boltzmann distribution function determines how many gas atoms move close to the velocity of the traveling interference pattern, and will be perturbed by it. Therefore the intensity of the coherent Rayleigh scattering signal is a function of the gas's Maxwell-Boltzmann distribution, i.e., the gas temperature.

A simple kinetic model ignoring collisions shows that, at low pressure, the spectral profile of the coherently scattered light is very well approximated by a Gaussian curve with a full width half maximum 10% wider than the spontaneous Rayleigh scattering profile, and that the width of the profile is

proportional to $\sqrt{T/m}$. Thus, a simple Gaussian profile analysis of experiment data is valid to calculate the gas temperature. Since collisions are ignored, the above analysis only applies in the Knudsen regime, where the Knudsen number, $Kn=l_m q/2p,$ is greater than unity.

We have used CRS to measure the temperature of an argon glow discharge. The experimental setup is shown in Fig. 1. A frequency-doubled Q-switched Nd:YAG laser (Continuum YG661-10) was used in the experiment to produce two broad band pump beams. The linewidth of the pump laser was approximately 60 GHz at the frequency doubled wavelength of 532 nm. The output from the laser was split into two beams using a 50/50 beam splitter. These two beams were focused and crossed at the center of the plasma at an angle of 178°. Each beam was approximately 20 mJ per pulse and the polarization of each beam was perpendicular to the plane of the page. The second harmonic output of an injection-seeded, frequency-doubled, Q-switched Nd:YAG laser (Spectra-Phyiscs Quantum-Ray laser) was used to produce the probe beam. This laser is seeded by a cw temperature-tuned Nd:YAG laser. The host laser can be tuned over a frequency range of about 9 GHz at the second harmonic at 532 nm. The tuning range and linearity of the laser were calibrated by a plane-parallel air spaced etalon. The polarization of the probe beam was perpendicular to that of the pump beams. This enabled us to pick out the CRS signal by polarization, since the signal had same polarization as the probe beam.

Care was taken to make sure the three laser pulses overlap both spatially and temporally in the plasma. The CRS signal was intense. When aligning in room air, one could see the coherently reflected beam with naked eyes. When phase matched, the CRS signal beam traced back along one of the pump beam's path, i.e., pump beam 2 indicated in Fig. 1. It was then separated from that path by a thin film polarizer. The beam was propagated for about 7 meters to photo detectors.
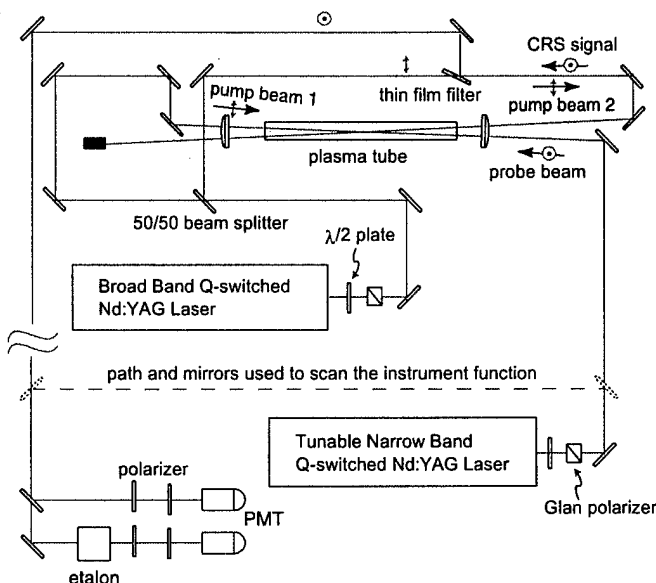
Figure 1. The optical setup using the coherent Rayleigh scattering to measurement temperature in a weakly ionized plasma.

Two photomultiplier tubes (PMTs) were used to collect the signal. Part of the beam passed through a solid plane-parallel etalon to a PMT. The etalon has a free spectral range of 15 GHz and was temperature stabilized to within 50 mK. Only light with frequency falling in the etalon's Airy function pass band was received by the PMT behind it. The convolution of the etalon's pass band and the probe laser's lineshape determined the frequency resolvability of our setup, i.e., the instrument function. The measured instrument function is 150 MHz FWHM. The other PMT without the etalon received all frequency component of the CRS signal. The etalon and two PMTs worked as a spectrometer. As our pump laser was broadband, the excited gas density grating has all frequency components that span the Maxwell-Boltzmann distribution. Scanning the narrow band probe laser, one then got the coherent Rayleigh scattering profile.

The plasma tube in Fig. 1 was 2 cm in diameter. The positive column of the argon glow discharge was about 25 cm. The pressure is 50 mb, and the current through the discharge is 10 mA. The crossing region of the lasers beams was aligned along the axis of the discharge. The region was about 100 μm in diameter and 1 cm long. This represented the spatial resolvability of our measurements. The ionization ratio of the glow discharge was fairly low, so the scatterers were atoms instead of electrons. Therefore the measure temperature was of the neutral gas.
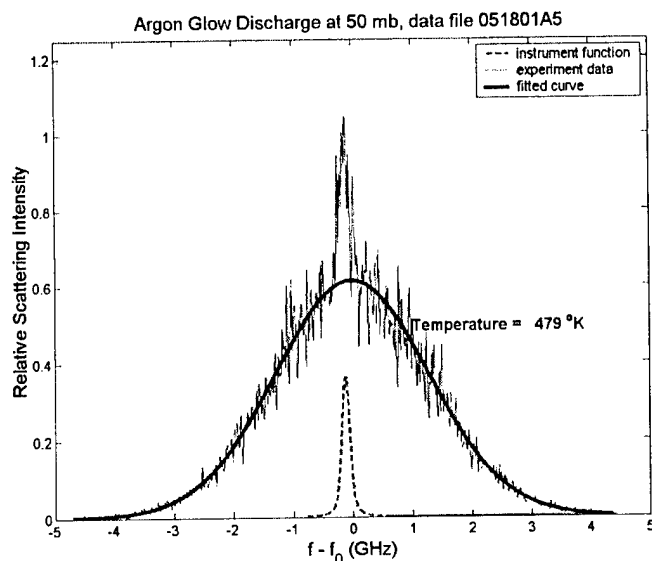
Figure 2. Profile of a coherent Rayleigh scattering signal from an argon glow discharge. The plasma is at 50 mb and the current is 10 mA.

Fig. 2 shows a sample measurement. The dashed curve is the instrument function. The thin solid curve is the measured signal profile. The raw data has a 250 MHz modulation due to the mode structure of the pump laser. It has been filtered out for the curve shown in Fig. 2. The sharp peak near $f\text{-}f_0$=0 GHz is due to the elastic scattering of the probe laser. It is not quite centered because the elastic scattering source was at a different place than the crossing volume of the laser beams. The fitted curve is a convolution of a Gaussian curve and the instrument function. The neutral temperature of the plasma was derived to be 479 K with 2% error.

Measurements were also performed in neutral argon gas under same condition. The CRS measurements agree with the temperature measured by thermocouple to within several degrees. This confirmed the validity of the CRS measurements.

Generally, CRS requires a greater experimental complexity than spontaneous Rayleigh scattering. However, its advantage justifies the efforts. The plasma environment, with its luminosity, low particle density, and close confinement geometry, is often harsh for optical diagnostics. The CRS signal is beam like, therefore it has the properties of a beam, e.g., highly directional, polarized, and highly bright. These properties lead to high signal to noise ration of the measurements.

3 Photoacoustic detection of energy deposition by optical lattice

In the simplified analysis of coherent Rayleigh scattering above, we ignored collision. Without collision, the dipoles will be set to drift by the optical lattice [3]. With collision at work, the optical interference lattice created by the crossing pump beams can deposit energy into the gas. While the atoms or molecules moving synchronously with the optical lattice are perturbed, their kinetic energy changes, and the Maxwell-Boltzmann distribution function is perturbed accordingly. Through collision, the perturbed distribution function relaxes. During this process, energy is exchanged between the optical lattice and the gas. Acoustic signal generated by this process will provide information of the gas thermal distribution, i.e., the gas temperature.

We numerically solved the one-dimensional kinetic equation to analyze this process. The kinetic equation with Bhatnagar, Gross and Krook (BGK) collision integral approximation is given by [4]

$$\frac{\partial f}{\partial t} + v\frac{\partial f}{\partial x} + \frac{F}{M}\frac{\partial f}{\partial v} = \frac{f - f_0}{\tau} \tag{6}$$

where F is ponderomotive force given by Eq. 5, M is the mass of the dipoles. The unperturbed gas has a MB velocity distribution function f_0, and $f = f(x,v,t)$ is the real time distribution function.
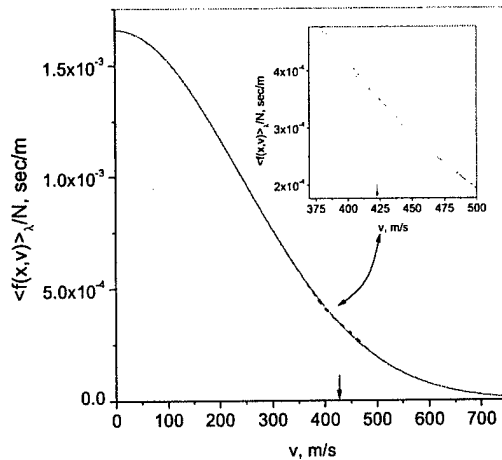
Figure 3. Gas distribution function as perturbed by a traveling optical lattice generated by two laser beams with frequency difference $\Delta\omega = 7.5$ GHz. The solid curve is the unperturbed MB distribution. The dotted curve is the perturbed MB distribution.

Our calculation condition is for two laser beams crossing in CO_2. Each beam is 100 mJ/pulse, 10 ns pulse duration and with a focal regime diameter of 100 μm. The CO_2 gas temperature is 300 °K and its pressure is 50 Torr.

Fig. 3 shows the calculated perturbation on the MB distribution. The perturbed distribution is able to reach a steady state during the laser pulses are on (10 ns). Later on, the gas relaxes to its new equilibrium state. Since more slow molecules have been attracted to the potential well than faster molecules, the energy is generally transferred from the optical lattice into the gas. Our calculation shows that the energy deposition is significant. The power absorption is shown in Fig. 4. Gas temperature can be derived from such a curve. The peak absorption happens near the molecule thermal velocity, which is 379 m/s. Interestingly, a standing optically lattice, with $\Delta\omega = 0$ GHz, does not add much energy into the gas. In fact, if there is no collision, one should expect the optical lattice to cool the gas down: this is essentially laser trapping of cold molecules [5].
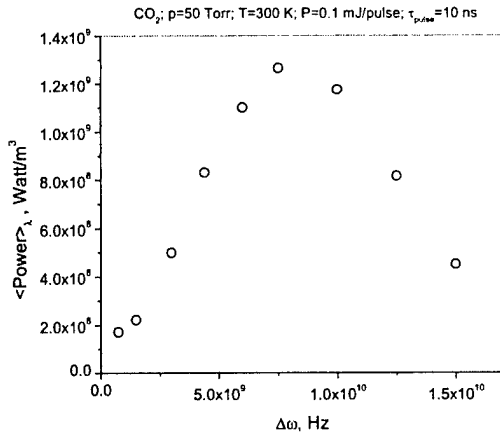
Figure 4. Calculated power deposition into CO_2 gas by an optical lattice.

We expect that such a fast energy deposition will generate detectable acoustic signal. The experiment uses two injection-seeded lasers. Microphones are used to detect the acoustic signal. If such a technique is experimentally demonstrated, the elastic scattering of optical measurements can be much less concerned. However, several issues should be addressed for its application in weakly ionized plasma, e.g., the influence of the plasma by the presence of a microphone.

4 Conclusions and Discussion

We have demonstrated that coherent Rayleigh scattering can be used to make accurate measurements of temperature in weakly ionized plasmas. We conclude that it is particularly suited to measurements in low density plasmas where the Knudsen regime can be met with available laser sources and geometries. The coherence nature of the signal means that high signal to noise ratio measurements can be done using CRS. As for the error sources, elastically scattered light remains one of the limiting interferences in this technique at very low gas densities. In our experiments both the multimode nature of the pump lasers and the temporal jitter of the probe laser meant long integration times were required to reduce measurement uncertainty to an acceptable level. Single shot measurements with similar accuracy, could be obtained if the spectral profile of the CRS signal, transmitted through the etalon was recorded on a two dimensional device such as a CCD. In this case, the broadband multimode laser that we used in our experiments would need to be replaced by a modeless laser. Such laser systems have been developed for CARS measurements.

We also investigated the possibility of an acoustic detection of the energy dumped in the gas by traveling optical lattice. This occurs when the Maxwell-Boltzmann distribution is perturbed by the ponderomotive forces. In this process, energy is transferred from the laser beams to the gas and an acoustic disturbance will be created. Measurement of the acoustic intensity from this interaction should yield information about the molecules energy distribution function, while completely eliminating gas luminosity and elastic laser scattering.

The force that perturbs the gas density is the electrostrictive force, it is also known as the dipole force, and more generally is a ponderomotive force. The ponderomotive force bridges the high frequency laser light with the translational motion of atoms, molecules and electrons. Researchers working with highly ionized plasmas also used it to accelerate electrons and generate plasma waves [6].

References

[1] Y. Z. Ionikh, N. V. Cherrnysheva, A.V. Meschanov, A.P. Yalin, R.B. Miles, Direct evidence for thermal mechanism of plasma influence on shock wave propagation, *Phys. Lett. A.*, **259**, 387, 1999

[2] J. H. Grinstead, P. F. Barker Coherent Rayleigh Scattering, *Phys. Rev. Lett.*, **85**, 1222, 2000

[3] P. F. Barker and M. N. Shneider, "Drift and Optical Landau Damping with Periodic Dipole Forces," accepted by *Phys. Rev. A*, 2001

[4] P. Bhatnagar, E. P. Gross, M.Krook, *Phys. Rev. A*, **94,** pp. 511, 1959

[5] V. I. Balykin, V. G. Minogin, and Letokhov, Electromagnetic trapping of cold atoms, *Rep. on Prog. in Phys.*, **63**, 9, 1429-1510, Sep. 2000.

[6] B. Amini and F. F. Chen, Thompson-Scattering Detection of Plasma Waves Excited by Two Laser Beams, *Phys. Rev. Lett.*, **53**, 15, 1984

18. COHERENT RAYLEIGH-BRILLOUIN SCATTERING

Xingguo Pan, Mikhail N. Shneider, and Richard B. Miles

Coherent Rayleigh-Brillouin scattering in gases has been studied experimentally for the first time in the kinetic regime and shown to give lineshapes that differ significantly from the spontaneous Rayleigh-Brillouin scattering. A kinetic model was developed to obtain an analytic solution of the lineshape for monatomic gases and good agreement with the experimental data was achieved.

Spontaneous Rayleigh-Brillouin scattering in gases originates from gas density fluctuations [1]. Its spectrum can be characterized using a uniformity parameter y, which is on the order of the ratio between the scattering wavelength and the gas mean free path. In the kinetic regime, corresponding to y ranging from 0 to around 3, theoretical studies [2-4] usually solve for the gas density fluctuations from kinetic equations. Excellent agreement between experimental data [5-7] and theory has been achieved. It was shown that when $y \to 0$ the scattering light power spectrum is a Gaussian curve corresponding to the Maxwellian distribution function of the gas molecules. As y increases to around one and greater, two shifted peaks appear. Their frequency corresponds to the sound velocity. Recently, efforts have been made to generate perturbations and then probe them with lasers [8-13]. As closely related, coherent Rayleigh scattering studied by Grinstead and Barker [13] is the collisionless limit of the work reported in this Letter. In this Letter, we report the experimental observation of coherent Rayleigh-Brillouin scattering (CRBS) in gases in the kinetic regime. Data obtained in argon and krypton at room temperature and various pressures will be presented. We also propose a simple kinetic model that yields good agreement with the experimental data of monatomic gases. We point out that the generated gas density perturbation in our configuration is intrinsically different from the spontaneous fluctuations.

The physical process of CRBS is illustrated in Fig1. Two pump beams, $\vec{E}_1 = \vec{E}_{10}\exp(i\vec{k}_1\vec{r} - \omega_1 t)$ and $\vec{E}_2 = \vec{E}_{20}\exp(i\vec{k}_2\vec{r} - \omega_2 t)$ with same polarization, are focused and crossed at their foci in the gas. Gas molecules inside the cross region experience dipole forces generated by the inhomogeneity of the intensity field [14]. We choose the x axis along $\vec{k}$, which is perpendicular to the fringes. The acceleration $a(x,t)$ of an individual molecule generated by the two single-mode beams is along the x axis and has a magnitude of

$$a = \frac{\alpha}{2M}\nabla(\vec{E}_1 + \vec{E}_2)^2 = -\frac{\alpha k E_{10} E_{20}}{M}\sin(kx - \omega t),\qquad(1)$$

where M and α are the mass and polarizability of the gas molecule, respectively; $k = |\vec{k}_1 - \vec{k}_2|$ and

$\omega = \omega_1 - \omega_2$ are the wave number and angular frequency of the dipole force field, respectively. The dipole forces create a wavelike density perturbation in the gas. A third, probe beam is counterpropagated against pump beam 2 and is Bragg scattered off the gas density perturbation. The scattered beam is the CRBS signal. By the phase matching condition, the signal beam follows, in reverse, the path of pump beam 1. The signal maintains the probe beam's polarization and is phase conjugated to pump beam 1. The signal beam's frequency is shifted from the probe beam's by the frequency of the traveling density perturbation wave.

The experimental setup was a modified version of that reported in [15]. In the experiment, a Q-switched, frequency doubled, broadband, pulsed Nd:YAG laser was used to produce the two pump beams. The power spectrum of the laser has a full-width-half-maximum of 26.5 GHz with a 250 MHz mode structure modulation. The laser's broadband means that the generated density perturbation is also broadband, i.e., a superposition of waves illustrated in Fig.1. Therefore, the acceleration $a(x,t)$ of each molecule due to the pump beams is broadband, i.e., a summation of a_s of all ω. The pump pulse had a duration of about 10 ns and the pulse energy directed into the cross region was around 6 mJ/pulse for each beam. The probe laser was an injection seeded, frequency doubled, pulsed Nd:YAG laser, operated in a single longitudinal mode. Its frequency could be scanned over a range of 20 GHz without mode hopping, and its pulse duration is 7 ns. It was easy to align the optics in the experiment, because the signal is relatively strong. For example, in room air, the signal could be clearly seen by eye on a white card with a 1 mJ probe beam pulse energy when the room was dark. The measured signal beam intensity at these conditions was less than 5 μJ. To avoid the complexity of fluctuations generated by the probe and signal beams' interaction, we tuned the probe beam to minimum level in the experiment.

The two pump beams were crossed at their foci inside a gas cell with a 178^0 angle. The diameter of the focal region was about 200 μm. The paths of the pump beams were carefully arranged so that they arrived at the interaction region simultaneously. The arrival of the probe pulse was adjusted relative to that of the pump pulses so that maximum signal was obtained. The optimal delay was about 1 ns. The jitter of the two lasers was each about 2 ns.

The signal beam was separated from the path of pump beam 1 using a thin film polarizer. It was then propagated for 7 meters in the lab to be detected. At this distance, the background ambient scattering of laser light from optical elements was greatly attenuated. About 4\% of the signal was directed to a photodetector for normalizing purpose, the rest was detected by another photodetector after passing through an etalon with a free spectra range of 11.85 GHz. The etalon was put in an enclosure whose temperature was stabilized to within $\pm0.1^0$ K. In the experiment, the probe laser's frequency was scanned.

For each frequency step, the ratio of the signal intensity detected by the photodetector after the etalon to that by the normalizing photodetector made a data point of the lineshape. Thirty shots were averaged for each frequency step. The recorded lineshape was a convolution of the CRBS lineshape and the instrument function. The instrument function was measured by sending the probe laser beam to the detector system and scanning the laser frequency. Shown in the argon 1 atm panel of Fig.2 is a fitted curve to the average of three measured instrument functions. Also, in each scan, a small portion of the probe laser beam was passed through another 900 MHz etalon to monitor the laser frequency and stability.

Fig.2 shows typical scans in argon and krypton at different pressures, at a temperature of $T_0 = 292^0$ K. Also indicated is the y parameter for each pressure. The definition of the y parameter is model dependent [3,4]. In this Letter, we use a kinetic model that assumes a constant collision time τ for molecules with different velocities, and the y parameter is defined as

$$y = \frac{1}{kv_0\tau} = \frac{8}{3\sqrt{2\pi}} \frac{\rho_0\sqrt{k_bT_0/M}}{\eta k}, \qquad (2)$$

where k_b is the Boltzmann constant, $v_0 = \sqrt{2k_bT_0/M}$, ρ_0 is the average gas density, and $\eta = (1/3)\rho_0\tau(8k_bT_0/\pi M)$ is the shear viscosity [16]. For the experimental data, y was calculated using the second expression of (2). The pressure of krypton was chosen to match the y parameter with the argon data. In the context of CRBS lineshape, the only significant difference between argon and krypton is their atomic mass. It is expected that the krypton lineshape is scalable to the argon lineshape for the same y parameter. Our experiment results show that it is indeed the case.

The raw profile for each graph has a 250 MHz modulation due to the pump laser's longitudinal mode structure. As an example, the raw data in krypton at 0.77 atm is shown by the vertically offset green curve. This modulation was observed as a well-defined, isolated, frequency component in the power spectrum of the recorded profile, and it was filtered out in the frequency domain of the Fourier transform of the recorded data. Data corresponding to smaller y parameters can be found in [13,15], which showed that the $y \sim 0.02$ curve is about 10% wider than the spontaneous Rayleigh scattering curve. For $y \geq 1$, the coherent Rayleigh-Brillouin spectrum show two strong shifted peaks in addition to the unshifted central peak. The central peak becomes relatively lower as y increases. The shifted peaks correspond to $\omega = kv_s$, where $v_s = \sqrt{\gamma k_b T_0/M}$ is the speed of sound of the gas. The same shape and evolution have also been observed for neon, nitrogen, and carbon dioxide.

We propose a simple kinetic model to explain the observed power spectrum. Since the CRBS is due to the gas density waves driven by the pump beams, its power spectrum is related to the density perturbation by

$$S(k,\omega) \propto \delta\bar{\rho}^*(k,\omega)\delta\bar{\rho}(k,\omega), \qquad (3)$$

303

where k is the wave vector, ω is the angular frequency, and

$$\delta\bar{\rho}(k,\omega) = \frac{1}{2\pi}\int\int_{-\infty}^{\infty} e^{-i(kx-\omega t)}\delta\rho(x,t)dtdx, \qquad (4)$$

is the space-time Fourier transform of the gas density perturbation.

The gas density perturbation is solved from kinetic equation

$$\frac{\partial f_1}{\partial t} + \vec{v}\nabla f_1 + a\frac{\partial}{\partial v_x}(\rho_0 f_0 + f_1) = \frac{1}{\tau}[f_0\delta\rho - f_1 + \frac{2\rho_0 f_0}{v_0^2}\vec{q}\vec{v} + \rho_0 f_0 \frac{\delta T}{T_0}(\frac{v^2}{v_0^2} - \frac{3}{2})], \qquad (5)$$

where $f_1 = f_1(\vec{x},\vec{v},t)$ is the deviation from the equilibrium distribution function with $f(\vec{x},\vec{v},t) = \rho_0 f_0(v) + f_1(\vec{x},\vec{v},t)$. Other symbols in (5) are:

$$f_0(v) = \frac{1}{\pi^{3/2}v_0^3}\exp(-\frac{v^2}{v_0^2}),$$

$$\delta\rho(\vec{x},t) = \int f_1 d^3v,$$

$$\vec{q}(\vec{x},t) = \frac{1}{\rho_0}\int \vec{v}f_1 d^3v, \qquad (6)$$

$$\delta T(\vec{x},t) = T_0[\frac{2}{3\rho_0 v_0^2}\int v^2 f_1 d^3v - \frac{1}{\rho_0}\delta\rho(\vec{x},t)].$$

The collision term, i.e., the right hand side of Eqn(5), is the linearized BGK [17] kinetic model. It has been shown that this model satisfies mass, momentum and energy conservation and the H-theorem. Yip and Nelkin [2] first used this kinetic model to derive an analytic solution of the spontaneous Rayleigh-Brillouin scattering. We take advantage of its simplicity in this study of the CRBS power spectrum. This model only considers the translational movement of the gas molecules, therefore, only monatomic gases will be modeled. The cylindrically symmetric configuration of the experiment allows us to assume along the radial axes a uniform Gaussian distribution that is maintained at the local temperature. The important difference from previous spontaneous scattering consideration is the term $a\frac{\partial}{\partial v_x}(\rho_0 f_0 + f_1)$ in (5). This term is the forcing term of the gas density perturbation in CRBS and is the key to explain the experimental data. When the perturbation is small, we can simplify (5) using

$$a\frac{\partial}{\partial v_x}(\rho_0 f_0 + f_1) \approx a\rho_0 \frac{\partial f}{\partial v_x}. \qquad (7)$$

The wavelike steady state solution in the form of $\exp(i(kx-\omega t))$ can then be found from (5). Following a procedure similar to that of [17] and using the traditional dimensionless parameters $\xi = \omega/kv_0$ and y, one obtains the density perturbation as

$$\delta\bar{\rho}(\xi,y) = \frac{i2\rho_0\bar{a}}{kv_0^2}\frac{E(1-iyD)+iyBF}{(1-iyA)(1-iyD)+iyB(1-iyC)}, \qquad (8)$$

where $\bar{a} = \bar{a}(\xi,y)$ is the space-time Fourier transform of the acceleration $a(x,t)$, and

$$A = (1/\sqrt{\pi})(\varpi_0 + 2\xi\varpi_1),$$
$$B = (1/2\sqrt{\pi})(-\varpi_0 + 2\varpi_2),$$
$$C = (2/3\sqrt{\pi})(\varpi_0 + 2\xi\varpi_1 + \varpi_2 + 2\xi\varpi_3),$$
$$D = (1/3\sqrt{\pi})(\varpi_0 + \varpi_2 + 2\varpi_4),$$
$$E = (1/\sqrt{\pi})\varpi_1,$$
$$F = (2/3\sqrt{\pi})(\varpi_1 + \varpi_3),$$

$$\varpi_4 = (\xi + iy)\varpi_3,$$
$$\varpi_3 = -\sqrt{\pi}/2 + (\xi + iy)\varpi_2,$$
$$\varpi_2 = (\xi + iy)\varpi_1,$$
$$\varpi_1 = -\sqrt{\pi} + (\xi + iy)\varpi_0,$$

and

$$\varpi_0(\xi, iy) = \int_{-\infty}^{\infty} \frac{\exp(-\eta_x^2)}{\xi + iy - \eta_x} d\eta_x$$

is the plasma dispersion function multiplied by $(-\sqrt{\pi})$.

The power spectrum $S(\xi, y)$ can then be calculated from (3) and (8). The intensity of coherent Rayleigh-Brillouin scattering signal is proportional to $(\rho_0 a)^2 / (kv_0^2)^2$. Its lineshape, when the power spectrum of the pump beams is fixed, is independent of the pump beams' intensity in the regime of small perturbation, i.e., when (7) holds.

With a 26.5 GHz pump laser bandwidth in our experiments, $\bar{a}$ varies less than 2% over the 6 GHz range of interest and can be considered as a constant, except for the pump laser's mode structure. In Fig.2, the spectra calculated from (3) and (8) for a constant $\bar{a}$ are compared with the filtered experimental data. The only adjustment was to match the height at the center of the experimental and theoretical lineshapes. Satisfactory agreement was achieved for $y<1$ At larger y values, the model correctly predicts the position of the Brillouin peaks, but slightly overestimates their height. The position of the shifted peaks is correctly predicted. The scalability of the argon and krypton data and the agreement between theory and experiment show that the physics of CRBS is well described in this regime.

In Fig.3, we compare the coherent and spontaneous spectra. The difference between the coherent and spontaneous scattering lineshapes is because the gas density perturbation in CRBS is generated by a wavelike dipole force field, rather than spontaneous fluctuations. The coherent $y \rightarrow 0$ curve is identical to that in [13], where the curve was obtained by solving a collisionless kinetic equation. The $y=3$ spontaneous curve was calculated using Yip and Nelkin's [2] formula, which has the same y definition. The important difference at $y \geq 1$ is that the coherent power spectrum has stronger Brillouin peaks and much weaker Rayleigh peak, indicating that the isentropic sound waves are resonantly pumped by the optical dipole force field. Furthermore, the relative intensity of the Rayleigh peak to the Brillouin doublets becomes smaller as y increases. This is different from the spontaneous case, where the ratio tends to a limit of $(c_p - c_v)/c_v$ [1].

305

We have shown that the CRBS power spectrum is different from that of the spontaneous scattering. The reason is that the generation of the gas density perturbation has a different mechanism. Our analytical solution of the spectrum based on the kinetic equation agrees well with the experimental data. A more accurate solution of the the Boltzmann equation with molecule internal energy considered is desirable for modeling molecular gases as well as a better agreement with atomic gases experiments. In the kinetic regime, CRBS lineshape can be used to measure gas properties and to study gas kinetic processes. It allows us to access gas kinetic processes, previously reached by spontaneous scattering, with a signal that is orders of magnitude stronger. It might also enable us to access new regimes. CRBS has the potential of becoming a new member of Rayleigh scattering based diagnostic methods [18] with the advantages of localized measurement and high signal-to-noise ratio. Interactions between the laser produced dipole force field and the gas molecules provide a possibility of perturbing or transporting ensembles of gas molecules [19].

References:
1. L. D. Landau and E. M. Lifshitz, Electrodynamics of Continuous Media (Addison-Wesley, 1966).
2. S. Yip and M. Nelkin, Phys. Rev. 135, A1241 (1964).
3. A.Sugawara, S.Yip and L. Sirovich, Phys. Fluids 11, 925 (1968).
4. G. Tenti, C. D. Boley, and R. C. Desai, Can. J. Phys. 52, 285 (1974).
5. T. J. Greytak and G. B. Benedek, Phys. Rev. Lett. 17, 179 (1966).
6. N. A. Clark, Phys. Rev. A 12, 232 (1975).
7. V. Ghaem-Maghami and A. D. May, Phys. Rev. A 22, 692 (1980).
8. C. Y. She et al., Phys. Rev. Lett. 51, 1648 (1983).
9. W. A. Schroeder, M. J. Damzen, and M. H. R. Hutchinson, IEEE J. of Quantum Electronics 25, 460 (1989).
10. S. Williams et al., Opt. Lett. 19, 1681 (1994).
11. W. Hubschmid, B. Hemmerling and A. Stampanoni-Panariello, J. Opt. Soc. Am. B 12, 1850 (1995).
12. H. Tanaka, T. Sonehata, and S. Takagi, Phys.Rev.Lett. 79, 881 (1997).
13. J. Grinstead and P. F. Barker, Phys.Rev.Lett. 85, 1222 (2000).
14. R. W. Boyd, Nonlinear Optics, (Academic Press, Boston, 1992).

15. X. Pan, P.F.Barker, A.Meschanov, J.H.Grinstead, M.N.Shneider, R.B.Miles, Opt.Lett. 27, 161 (2002).

16. L. B. Loeb, Kinetic Theory of Gases (Dover, New York, 1961).

17. P. L. Bhatnagar, E. P. Gross, and M. Krook, Phys. Rev. 94, 511 (1954).

18. R. B. Miles, W. N. Lempert, and J. Forkey, Meas. Sci. Tech. 12, 442 (2001).

19. P. F. Barker and M. N. Shneider, Phys. Rev. A 64, 033408 (2001).
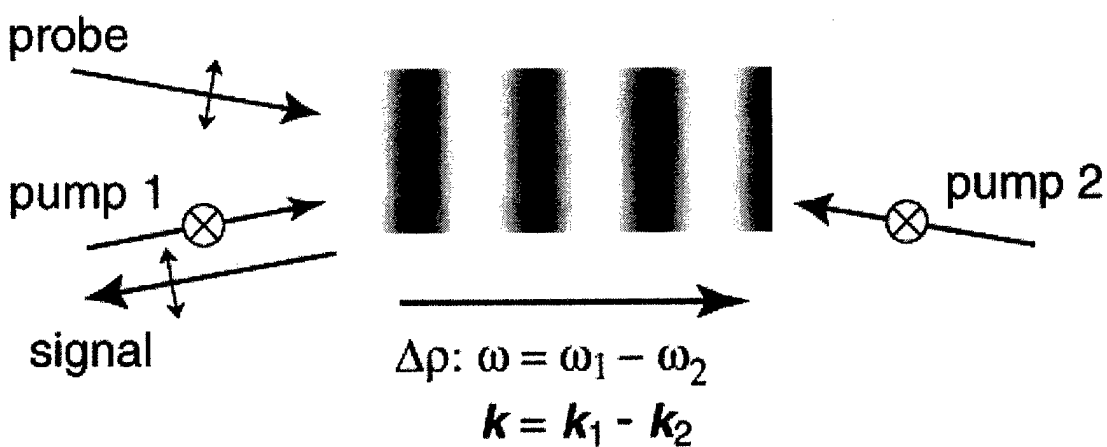
Fig.1. Coherent Rayleigh-Brillouin scattering in gases.
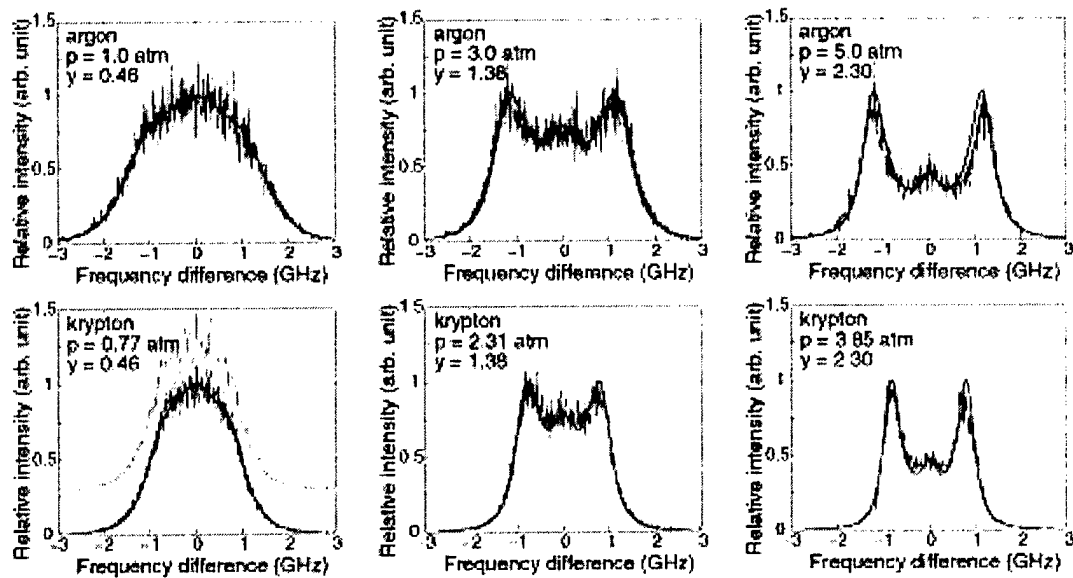
Fig.2. Power spectrum of coherent Rayleigh-Brillouin scattering at $T = 292^0$ K in argon and krypton. The blue curve is the experiment data with the pump laser's mode structure filtered out. The red solid curve is a convolution of the theoretical lineshape and the instrument function (shown in the argon 1 atm panel by the dashed red curve). The green curve in the krypton 0.77 atm panel is the raw data, offset by 0.3 vertically, displaying the pump laser's mode structure.
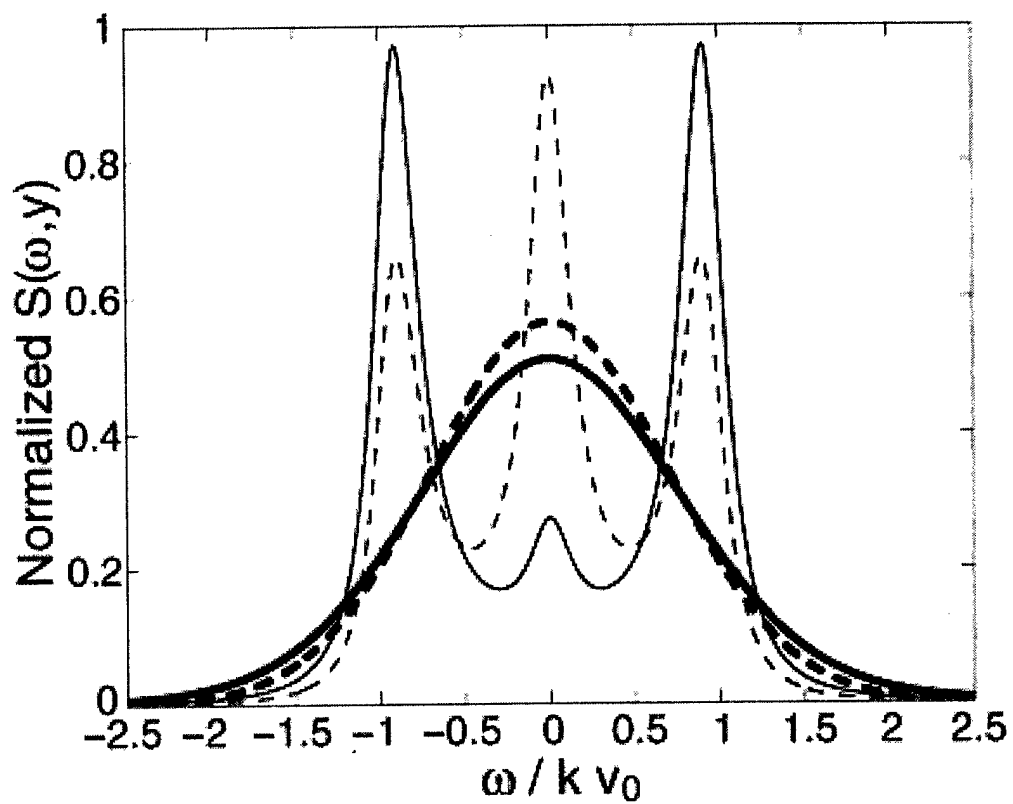
Fig.3. A comparison between the coherent and spontaneous Rayleigh-Brillouin power spectra calculated from linearized kinetic model, at $y \rightarrow 0$ (spontaneous: thick dashed curve, coherent: thick solid curve) and at $y = 3$ (spontaneous: thin dashed curve, coherent: thin solid curve). Area under each curve is normalized to 1.

19. MODELING OF PLASMA GENERATION IN REPETITIVE ULTRA-SHORT DC, MICROWAVE, AND LASER PULSES

S.O. Macheret and M.N. Shneider

1 Introduction

A number of both traditional and newly emerging applications of weakly ionized plasmas require that large volumes of air be ionized at relatively high pressures, from a few Torr to 1 atm, and low temperatures, from 230 K to about $1,000 - 2,000$ K, with ionization fraction of 10^{-6}-10^{-4}.[1-11] In many of these applications, such as absorption/reflection of electromagnetic waves, supersonic flow control, and supersonic/hypersonic MHD generators and accelerators, it is the ionization fraction and electrical conductivity related to it that are of principal interest.[3-11] Practicality of such uses of plasmas critically depends on the ability to generate and sustain the ionization with the lowest power input. Power budget reduction – the principal goal of this MURI program – was analyzed theoretically in our work.

The power budget of sustaining a nonequilibrium plasma with a prescribed electron number density n_e is proportional to the energy cost, W_i, of creating a new electron in the plasma.[11] When nonequilibrium plasma is sustained by a DC or oscillating electric field, electron energy balance is determined by electron energy gain from the field in collisions and energy losses in various inelastic and elastic processes.[12] Thus, electron temperature, T_e, or, more exactly, electron energy distribution function, EEDF (the latter is typically non-Maxwellian), is defined, for a given set of gas parameters, by the ratio of electric field strength to the gas number density, E/N, or, at low densities, by the ratio of electric field strength to the field oscillation frequency, E/ω.[12] Typical values of E/N in nonequilibrium discharges in molecular gases lie in the range $(1-6)\times10^{-16}$ $V \cdot cm^2$, and electron temperatures defined by the EEDF slope at low energy are in the range 1-3 eV.[12] Under these conditions, only a small fraction of plasma electrons are capable of ionization that requires at least 10-15 eV energy. Almost all collisions of plasma electrons with molecules result in inelastic or elastic energy losses. Especially strong in the electron energy range of 1-3 eV is resonant excitation of molecular vibrational states, consuming in typical glow or RF discharges more than 90% of the discharge power.[12] Thus, only a very small fraction, less than 0.1%, of the power is actually spent on ionization, corresponding to the energy cost W_i of at least several tens of keV per electron.[11]

From the point of view of ionization efficiency, it would be desirable to have electrons of very high energy, hundreds and thousands of electronvolts, that would be immediately capable of ionization. This would increase the ionization rate and its efficiency. In this regard, high-energy electron beams are a natural choice.[3-11] Indeed, electron acceleration in a vacuum, as opposed to a gas, environment is not

accompanied by large inelastic losses. Injection of the electrons accelerated to keV and higher energies into the gas results in ionization cascades, as beam electrons propagate and lose their energy. The resulting energy cost of plasma electron is $W_i = 34\ eV$ for air,[12, 13, 14] which is only a few times greater than the ionization energy of air molecules.

Earlier, we developed models and analyzed dynamics of plasmas generated by high-energy electron beams,[8] and also applied the models to supersonic MHD power generation and flow control.[3-7, 9-11] Although e-beams are undoubtedly the most efficient way of creating nonequilibrium plasmas, there are some inherent practical difficulties associated with e-beams. Among those difficulties are: problems related to mechanical and thermal strength of injection foils or windows, and beam scattering in high-density gases that would not allow the beam to penetrate far.

For this reason, we explored an alternative approach: producing high-energy electrons *in situ* by applying a strong electric field. This field would be substantially stronger not only than the field needed to sustain a steady plasma with the given electron density, but also than the field required for initial electrical breakdown of the gas. To maintain a prescribed level of ionization, strong electric field should be applied for only a short time, then the plasma should be allowed to somewhat decay, after which a new ionizing pulse would be applied, etc. Thus, a desired average n_e would be sustained by separating electron generation and removal processes in time, with pulse repetition rate matched to the rate of recombination or attachment. An important factor in assessing performance of the repetitive-pulse approach is that the reduced energy cost due to strong electric field in the pulse is somewhat offset by the need to produce more electrons in the pulse than the required average n_e.

In our earlier paper,[11] we have analyzed plasma generation by high-voltage DC pulses. The modeling included ionization and electron removal kinetics, full non-local kinetics of electrons, with EEDF evolution in time and space treated in "forward-back" approximation, dynamics of the self-consistent electric field. Calculations showed that increased electric field in the pulse would indeed lead to formation of a large group of high-energy electrons in high-voltage nanosecond pulse and dramatic increase in ionization rate.

In this section, we address further aspects of ionization with high-voltage pulses, including non-local nature of plasma dynamics and the effect of ionization between the pulses. The latter effect consists in high-energy electrons produced during the pulse generating additional ionization while moving and losing their energy after the pulse.

We also explore efficient plasma generation by ultrashort, high-power, repetitive electromagnetic pulses. One advantage of using laser or microwave beams, compared with e-beams or DC pulses, is that plasmas can be created in a remote location. Other advantages include the availability of ultrashort-pulse (nanosecond-range in the case of microwaves, and subpicosecond – in the case of lasers) sources with extremely strong peak power densities, and the absence of electrodes. At the same time, as will be shown in the paper, proper selection of parameters could make the ionization almost as efficient as that by e-beams, in contrast to conventional laser and microwave plasmas.

2 Estimates of power budget for ionization by ideal high-voltage repetitive pulses

To evaluate performance limits of ionization by high-voltage repetitive pulses, the following assumptions were made in order to permit an analytical or semianalytical solution:

- Ideal rectangular voltage pulses, that is, infinitesimally short rise and fall, with a constant voltage during the pulse
- Uniform plasma column both during and between the pulses
- No cathode voltage fall
- Ideal impedance matching between the source and the plasma: all the voltage falls on plasma, with no loss on ballast resistors
- The pulse is assumed to be very short, so that recombination and attachment processes can be neglected during the pulse.

Note that each of these assumptions means that ionization occurs under most favorable conditions, and violation of these assumptions would increase the power required to sustain a given average electron density.

We will denote the pulse duration as τ_1, and the time interval between the start of two consecutive pulses as τ_2, so that the pulse repetition rate is $f = 1/\tau_2$. During the pulse, electric field is constant, and so is the ionization frequency $v_i = v_i(E/N)$. The pulse is assumed to be very short, so that recombination and attachment processes can be neglected during the pulse. Therefore, electron density grows exponentially during the pulse, and the minimum and maximum electron densities are related by the equation

$$n_{e,\max} = n_{e,\min} \exp\left[\left(v_i(E/N)\tau_1\right)\right] \qquad (1)$$

Since the rate of work done by electric field on an electron is $eE \cdot v_{dr}$, where v_{dr} is the field-dependent drift velocity, the ionization cost per electron is

$$W_i = eEv_{dr}/v_i ,\tag{2}$$

and the power budget per unit volume is

$$P = \frac{1}{\tau_2}\int_0^{\tau_2} jEdt = W_i (n_{e,\max} - n_{e,\min})/\tau_2 \tag{3}$$

If attachment processes can be neglected, then electron kinetics between the pulses $(\tau_1 \le t \le \tau_2)$ is determined by electron-ion recombination: $dn_e/dt = -\beta n_e^2$, so that

$$n_e = n_{e,\max}/(1 + \beta n_{e,\max}(t - \tau_1)) , \quad \tau_1 \le t \le \tau_2 \tag{4}$$

The average number density of electrons is, therefore:

$$<n_e> = \frac{1}{\tau_2}\int_0^{\tau_2} n_e dt = \frac{n_{e,\min}}{v_i \tau_2}(\exp(v_i \tau_1) - 1) + \frac{1}{\beta \tau_2}\ln\left[1 + \beta n_{e,\max}(\tau_2 - \tau_1)\right] \tag{5}$$

From Eq. (1) and (4) we get:

$$n_{e,\min} = \frac{\exp(v_i \tau_1) - 1}{\beta \exp(v_i \tau_1)(\tau_2 - \tau_1)} \tag{6}$$

If attachment is significant in plasma decay between the pulses, then we have:

$$dn_e/dt = -\beta n_e^2 - v_a n_e ; \quad n_e = \frac{n_{e,\max} e^{-v_a(t-\tau_1)}}{1 + \frac{\beta n_{e,\max}}{v_a}\left(1 - e^{-v_a(t-\tau_1)}\right)} , \quad \tau_1 \le t \le \tau_2 \tag{7}$$

where the attachment frequency is $v_a = k_a N_{O_2} N + k_{da} N_{O_2}$. The average electron density is in this case:

$$<n_e> = \frac{1}{\tau_2}\int_0^{\tau_2} n_e dt = \frac{n_{e,\min}}{v_i \tau_2}\left(e^{v_i \tau_1} - 1\right) + \frac{1}{\beta \tau_2}\ln\left[1 + \frac{\beta n_{e,\max}}{v_a}\left(1 - e^{-v_a(\tau_2 - \tau_1)}\right)\right], \tag{8}$$

and Eq. (6) should be substituted by

$$n_{e,\min} = \frac{e^{v_i \tau_1 - v_a(\tau_2 - \tau_1)} - 1}{\beta \frac{e^{v_i \tau_1}}{v_a}\left(1 - e^{-v_a(\tau_2 - \tau_1)}\right)} \tag{9}$$

In calculations, we used drift velocities $v_{dr}(E/N)$ in the range $3 \cdot 10^{-19} \le E/N \le 10^{-14}$ V cm^2 interpolated from experimental data compiled in Ref. 15.

Ionization frequency required for calculations can be expressed as a product of Townsend ionization coefficient α and the drift velocity: $v_i = \alpha v_{dr}$. We used the following three expressions for Townsend coefficients representing interpolated experimental data in different ranges of E/p:

$$\alpha = 2.7 \cdot 10^{-8} p \exp(+0.35 E/p), \quad 1/\text{cm}, \quad 20 < E/p < 36 \text{ V/(cm·Torr)} \qquad (10a)$$

$$\alpha = 1.17 \cdot 10^{-4} p(E/p - 32.2)^2, \quad 1/\text{cm}, \quad 44 < E/p < 176 \text{ V/(cm·Torr)} \qquad (10b)$$

$$\alpha = 15 p \exp(-365 E/p), \quad 1/\text{cm}, \quad 100 < E/p < 800 \text{ V/(cm·Torr)} \qquad (10c)$$

Eq. (10a) was taken from Ref. 16, and Eqs. (10b) and (10c) – from Ref. 12. In E/p ranges where there is an overlap between any two of the equations (10a-c), a cubic polynomial interpolation for α was used to provide smooth transition between the formulas. Ionization rates numerically close to those of Eqs. (10a)-(10c) are obtained with the ionization rate representing an interpolation[17] of data from Refs. 18 and 19:

$$v_i/N = 10^{-8.25} \cdot 10^{-36.5/\theta} \text{ cm}^3/s, \quad 3 \le \theta \le 30, \text{ where } \theta = E/N \text{ in } 10^{-16} \text{ V·cm}^2. \qquad (10d)$$

Formulas (10a-c), valid at room temperature, were corrected for $T \ne 300 \ K$ by multiplying the pressure p by $(300/T)$. An additional correction was made for vibrational excitation of molecules. Although very little vibrational disequilibrium can be expected for very short pulses of very strong electric field and high gas densities, at temperatures of about 2000 K thermal vibrational excitation can contribute to ionization enhancement, due primarily to superelastic collisions that enhance high-energy tail of EEDF. This effect was taken into account by the multiplying $v_i(E/N)$ by a factor $k_v = 10^{Cz/\theta^2}$ as in Refs. 17, 20, 21, where $C = 28.3$, $z = \exp(-\hbar\omega_0/kT)$, and $\hbar\omega_0$ is the energy of the first vibrational level (for nitrogen, $\hbar\omega_0/k = 3353 \ K$).

Electron-ion dissociative recombination coefficient was taken as:[22]

$$\beta = 2 \cdot 10^{-7} (300/T_e)^{1/2} \text{ cm}^3/s. \qquad (11)$$

Since recombination only occurs between the pulses, with no electric field, electrons were assumed to thermalize rapidly, and their temperature T_e was assumed to be equal to the gas temperature: $T_e = T$ between the pulses. However, in the case of steady-state DC discharge, an electron temperature close to 1 eV, $T_e = 11560$ K, was assumed, in accordance with experimental and computational data.[12, 23] When calculating power budget for electron beam-produced plasmas, described in the previous section and shown in Figs.1 and 2, the rate at which energy is pumped into the plasma electrons due to beam relaxation was assumed to be slower than the collisional thermalization rate, so that only a small nonequilibrium takes place, with $T_e = 2T$.

In calculating attachment frequency, the low electron temperature between the pulses was taken into account, which permitted neglecting dissociative attachment. The three-body electron attachment rate coefficients were taken from Ref. 22:

$$e + O_2 + O_2 \rightarrow O_2^- + O_2 \; ; \; k_{a1} = 1.4 \cdot 10^{-29} \left(\frac{300}{T_e} \right) \exp\left(-\frac{600}{T} \right) \exp\left(\frac{700(T_e - T)}{T_e T} \right), \, cm^6/s$$

$$e + O_2 + N_2 \rightarrow O_2^- + N_2 \; ; \; k_{a2} = 1.07 \cdot 10^{-31} \left(\frac{300}{T_e} \right)^2 \exp\left(-\frac{70}{T} \right) \exp\left(\frac{1500(T_e - T)}{T_e T} \right), \, cm^6/s \qquad (12)$$

Representative results of the calculations with formulas and rates (1)-(12) are shown in Fig.1. The upper plot in Fig. 1 shows the power budget required to sustain the prescribed average electron density versus E/N in the pulse, with the pulse duration τ_1 as a parameter. The lower plot in Fig. 1 shows the required pulse repetition rate. For comparison, power requirement for steady-state plasmas sustained by DC field and electron beams is also shown in the figure. The DC power requirements were calculated in the following way. First, by equating the ionization frequency $v_i(E/N)$ to the sum of recombination and attachment frequencies, the value of E/N required to sustain the DC discharge was determined. Then the drift velocity $v_{dr}(E/N)$ and the current density $j = en_e v_{dr}$ was calculated, which then gave the power requirements $P = jE$.

As seen in Fig.1, very short high-voltage pulses with very high repetition rate could sustain a prescribed average ionization level in air with power input much lower than that in a DC discharge. The power savings come from the fact that during the ionization electric field and ionization rate are quite high, reducing the energy cost W_i of newly produced electrons. As seen in Fig. 2, the energy cost per electron decreases with E/N, reaching 66 eV at $E/N = 1.1 \times 10^{-14} \, V \cdot cm^2$, corresponding to the threshold field for electron runaway effect. However, Fig. 1 clearly shows that the power budget passes through a minimum and increases again at very high E/N. This is due to the fact the ionization rate in strong fields becomes excessively high, and too many electrons are produced during the pulse, wasting power. With shorter pulses, the excessive ionization is limited, permitting to better take advantage of the reduced energy cost per electron.

As seen in Fig. 1, even the minimum power budget achievable with high-voltage pulses is substantially higher than that for e-beam-sustained plasmas. Indeed, when plasma with $\langle n_e \rangle = 10^{13} \, cm^{-3}$ is sustained in 1 atm, 2000 K air by 10-nanosecond pulses at the optimum value of E/N and pulse repetition rate of about 500 kHz, the lowest power budget is about a factor of 50 lower than that in the DC discharge. However,

this power budget is still very high, close to 1 kW/cm^3, and is about a factor of 30 higher than that in electron beam-sustained plasma. The power budget can be improved with shorter pulses and higher values of E/N, provided that it is technical feasible to build a source of multikilovolt sub-nanosecond pulses with repetition rate of about 0.5 MHz, ideally matched to variable-impedance plasma has to be explored.

Fig. 1 and similar plots obtained by us for other values of average electron density can serve as a guide to anticipated overall performance of repetitive-pulse ionization. However, dynamics of these plasmas, even with ideally matched pulse source, is quite complex. With 10-nanosecond pulses, the optimum value of E/N is not much greater than the breakdown value $(E/N)_{br} = 1.1 \times 10^{-15}$ V·cm^2. At these values of E/N, the mean electron energy is still only several eV, and no substantial high-energy "tail" can be expected in EEDF. In this regime, ionization rate is determined by the local value of E/N. Additionally, at high gas density and at long interelectrode distances, cathode voltage fall and sheath dynamics should not play an important role. Therefore, the discharge can be adequately modeled in "hydrodynamic" approximation, and semi-analytical estimates of the power budget should be reasonably accurate.

With use of much shorter pulses and higher values of E/N, which is necessary to improve the power budget, the "hydrodynamic" approximation may fail, especially at low gas densities. As the mean energy gained by an electron between collisions increases, a growing number of electrons will acquire very high energy, so that a substantial high-energy tail in EEDF will be formed. This high-energy tail may become essentially a beam of "ballistic", or "runaway", electrons that keep gaining energy from the electric field while the cross-sections of their collisions with molecules is decreasing. This regime obviously requires full kinetic description of EEDF coupled with plasma kinetics and electric field dynamics. Very importantly, the ionization rate and rates of other electron-molecule inelastic processes at a given location are expected to be non-local: the rates of excitation and ionization will be due largely to high-energy ballistic electrons that were not born at this location but rather arrived from a location closer to the cathode, having acquired high energy in their path. Thus, plasmas sustained in low-density gases by repetitive ultrahigh-voltage pulses with pulse length of the order of 1 ns or shorter should be described with full non-local kinetic description of EEDF, coupled with dynamics of plasmas and electric field.

3 Kinetic modeling of spatio-temporal dynamics of nanosecond high-voltage discharges

For a deeper insight into dynamics of high-voltage nanosecond discharges, one needs to analyze behavior of electron energy distribution function (EEDF). In the kinetic model, we consider a one-dimensional process. We direct the x-axis from the grounded electrode (cathode, x=0) to the positively biased electrode (anode, x=L). All electrons in the model are considered on the basis of kinetic equation in the

so-called 'forward-back' approximation.[24] The major approximation is that in the course of elastic collisions with molecules electrons are scattered either strictly forward or strictly backward, with no lateral scattering. Ion motion, production, and losses were considered in the drift approximation. Poisson equation for electric field was fully coupled with plasma equations.

Details of computations with the kinetic model can be found in Ref. 11. A sample calculation with the kinetic model was performed for nanosecond pulse in air plasma at 1 Torr, 300 K. An initial electron and ion density of 10^9 cm^{-3} was assumed. The discharge gap was $L=3$ cm wide. The voltage pulse was triangular, with 1-ns rise time and 2-ns fall-off time, with amplitude of about 1100 V. 4. The peak voltage was that required for electron runaway effect in air at 1 Torr if the electric field in the discharge were uniform. However, electric field during the pulse is very nonuniform, as illustrated in Fig. 3. A large cathode sheath is formed, and most of the voltage is concentrated there (Fig. 3c, d). The very strong electric field (above the runaway threshold) in the sheath accelerates electrons to hundreds of eV (Fig. 4), with the mean energy reaching about 100 eV (Fig. 3e). These high-energy electrons are injected into the plasma and produce very strong ionization (Fig. 3a, f), which is similar to the negative glow region of glow discharges.

An interesting phenomenon occurs near the end of the pulse. The decreasing potential of the anode becomes lower than the electric potential in the middle of the plasma. The plasma cannot adjust instantaneously because of ion inertia, and a non-monotonic profile of the potential, with a maximum in the middle of the plasma, appears (Fig. 3c). Thus, during the second half of the pulse, electric field in the entire near-anode half of the plasma actually has the 'wrong' direction (Fig. 3d).

As seen in Fig. 3e and 4, the wave of high-energy electrons propagates towards the anode, so that the second peak in the profile of mean electron energy (Fig. 3e) appears in the second half of the pulse, when the group of high-energy electrons reaches the anode. The high-energy electron wave produces the wave of ionization propagating towards the anode. Again, in the second half of the pulse the ionization rate profile acquires a second maximum – near the anode. The reversal of electric field in the anode half of the discharge prevents low-energy electrons from reaching the anode and somewhat slows the high-energy electrons, which increases ionization cross sections and ionization rate near the anode. The spatio-temporal evolution of EEDF shown in Fig. 4 demonstrates the presence of a very large plateau extending to about 1 keV. At locations relatively far from the cathode, the high-energy plateau appears only at later times, when electrons accelerated near the cathode arrive at this location.

Overall, the calculations clearly show a very complex spatio-temporal evolution of the plasma. During the pulse, all plasma parameters are quite non-uniform, and ionization kinetics is non-local, being determined by high-energy ballistic electrons. This dynamics cannot be modeled by conventional "hydrodynamic" approach.

The non-uniformity of electron density seen in Fig. 3c and very high mean energy seen in Fig. 3e have interesting implications for plasma kinetics between the pulses. When the voltage is turned off, there will be a substantial number of electrons capable of ionization (Fig. 4). Even the mean electron energy ranges from about 40 eV to more than 100 eV (Fig. 3e). Therefore, a considerable additional ionization will occur after the pulse, and the number of electrons can increase by as much as a factor of 2-3. The profile of ionization rate after the pulse will not follow the mean energy profile of Fig. 3e, because high-energy electrons will move to a different location and ionize molecules there. The newly produced electrons, together with electrons already generated by the end of the pulse (Fig. 3a) will form the final profile of electron density which then will relax by diffusion and recombination with ions.

Simple estimates show that ambipolar diffusion cannot substantially change the n_e profile during the characteristic recombination time $(\beta n_e)^{-1}$ for typical values of plasma parameters considered here. Therefore, it is recombination that will be responsible for the relaxation of n_e profile. Since recombination rate βn_e^2 is non-linear with respect to n_e, the recombination will not only reduce n_e, but would also make its profile more uniform. Nevertheless, some non-uniformity of n_e profile will exist by the beginning of the next pulse. This non-uniformity can affect the dynamics of the next pulse. Note that in the present case, a uniform n_e profile at the beginning of the pulse was assumed. What the actual n_e profile at the beginning of the pulse would be after many pulses, and whether or not some associated oscillations or instabilities can occur remains to be explored. In any case, with repetitive-pulse method of plasma generation, electron density will not only oscillate in time, but will also be non-uniform in space.

Note that nanosecond high-voltage breakdown in dense gases was experimentally and theoretically investigated by several groups (see Refs. 25-27 and references therein). However, in those studies, the gas was either not preionized, or preionized very weakly by the beginning of the pulse. In contrast, we consider dynamics of nanosecond discharges that begin with pre-existing plasma with relatively high electron density. It is because of this pre-existing plasma that a very strong current instantaneously develops in the entire discharge volume, leading to the formation of the cathode sheath, so that the

electron runaway effect can exist only in the sheath. Thus, dynamics of nanosecond discharges with pre-existing plasma differs both qualitatively and quantitatively from nanosecond high-voltage breakdown.

At least some of the qualitative effects observed in high-voltage nanosecond pulses at low pressure should exist at higher pressures. Quantitative scaling, however, is not trivial. For gas discharge processes in the local approximation, when EEDF and rates of electron-impact processes are determined by the local field strength, the scaling to higher pressures would be straightforward. Since it is the parameter E/N that determines EEDF, all voltages and field would have to be scaled in direct proportionality to N. Also, since rates of all electron-impact processes are proportional to N, the scaling would involve reducing all time scales in inverse proportionality to N. However, kinetic effects observed in high-voltage nanosecond pulses are quite non-local: for instance, the growth of mean electron energy and ionization rate inside the plasma is due not to increase in local E/N, but to arrival of high-energy electrons from the cathode region to this location. Also, runaway (ballistic) electrons move and accelerate in electric field with very little effect of collisions, and the scaling for them would involve time and length scales different from those for low-energy electrons.

To check how important kinetic and non-local effects are in modeling plasmas sustained by high-voltage nanosecond pulses at higher pressures, we have computed the case when the plasma is sustained in air at 10 Torr, 300 K by triangular pulses with 1 ns rise time and 2 ns fall-off. The distance between the electrodes was set as L=5 cm, and the peak voltage was set at $V_{max} = 0.5E_cL$, where E_c is the electron runaway threshold field, $E_c/p = 365$ V/(cm·Torr).[28] This choice of V_{max} was made because it corresponds to the E/N value close to that giving the minimum power budget. In order to check how significant kinetic and non-local effects are, and to make computations doable within a reasonable time frame, plasma kinetics was uncoupled from dynamics of electric field by disregarding plasma polarization and formation of the cathode sheath.

Results of the calculations are shown in Figs. 5-7. Since the calculations assumed the initial electron density of 10^{11} cm^{-3}, in order to generalize the results, Fig. 7 shows the computations for the dimensionless ration of electron number density to its value at the beginning of the pulse. As seen in Fig. 7, mean electron energy reaches about 9 eV by the end of the pulse. This value is substantially higher than in continuous DC or RF discharges, but still not high enough to substantially enhance ionization after the pulse. Indeed, Fig. 7 shows that the electron density does increase during 1 ns after the pulse, but the increase is small, only about 10%. Fig. 5 demonstrates that EEDFs do have high-energy tails well resolved in our calculations, but the fraction of electrons having high energies is very small. Thus, kinetic

and non-local effects are quite small, which is confirmed in Fig. 6 where electron density is seen to be uniform in almost the entire discharge region. The only region where electron density is non-uniform is the 1-cm thick region near the cathode. This is the region where electrons are accelerated and electron avalanches are generated, bringing the conductivity current to its value in the bulk plasma. Thus, the non-uniform region essentially plays a role of cathode sheath. Since, however, real sheath dynamics was excluded from our computations by uncoupling plasma and electric field equations, the existence of the thick "sheath" in the calculations is an artifact. In reality, the sheath thickness under these conditions is expected to be much smaller, only about 0.05 cm.[11] We conclude that while hydrodynamic approach fails at pressures on the order of 1 Torr and E/N close to the runaway threshold, this approach is works well for nanosecond-scale pulses at pressure of about 10 Torr and higher, at E/N up to at least ½ of the runaway threshold. Thus, hydrodynamic modeling of pulsed discharges at 10 Torr and 1 atm in Ref. 11 is adequate.

4 Plasma sustained by repetitive high-power ultrashort electromagnetic pulses

4.1 The basic concept.

When an oscillating electric field with amplitude E_0 and frequency ω is turned on, free electrons placed in the field start oscillatory, or quiver, motion with the average energy[12]

$$\langle \varepsilon \rangle = \frac{e^2 E_0^2}{4m\omega^2} . \tag{13}$$

In conventional gas discharges, the quiver energy is on the order of 0.1 eV, that is, much lower than the ionization energy E_i of the molecules. Therefore, ionization in conventional discharges is due to inverse bremsstrahlung heating of electrons: between collisions, electrons gain velocity from the field, collisions randomize the velocity, transferring the quiver energy into 'electron heat' and increasing electron temperature.[12] When T_e reaches 1-3 eV, there is a sufficient 'tail' of EEDF (>10-15 eV) to sustain breakdown or steady-state discharge. This mechanism is responsible for microwave and laser breakdown and steady-state plasmas, permitting ionization in relatively weak fields.[12] However, large power dissipation in inelastic collisions that electrons experience while accelerating to ionization energies results in very low overall ionization efficiency, similar to that in DC discharges.

In contrast, free electrons could be accelerated not only to 10-15 eV, but to a few keV of quiver energy, if the ratio E_0/ω is large enough. According to Eq. (13), electric field amplitudes of the order of 10^6-10^8 V/cm would be needed to obtain 3 keV of collisionless quiver energy at wavelengths from a few

millimeters down to tens of microns. In these strong fields, free electrons remaining from the previous pulse can be accelerated to keV-range energy before they can collide with molecules, and thus electromagnetic energy would be converted into what could be described as *in situ* generation of electron beams without electrodes. The keV electrons would ionize the gas very efficiently, so that the efficiency of electromagnetic energy transformation into ionization of low-temperature gas can be, in principle, made very high.

Physics of microwave breakdown and plasma generation in short high-power pulses at low gas density was extensively studied, both theoretically and experimentally, in a number of previously published works.[29-34] In those studies, EEDF and ionization rate in strong oscillating fields at low gas density were computed. The idea that accelerated electrons can produce an additional ionization after the pulse was also expressed, and the relative increase in electron density after the pulse was estimated as the mean electron energy acquired by the end of the pulse divided by the energy cost of ionization for high-energy electrons.

In this section, we build upon the results previously obtained elsewhere, and extend those results, focusing specifically on two issues: modeling of ionization after the pulse and the principal possibility to extend the efficient ionization in high-power electromagnetic fields to higher gas densities.

4.2 Ionization in high-power short electromagnetic pulses. Extremely high E/ω.

For free electrons to gain high oscillatory energy between collisions, the electromagnetic wave frequency, ω, must be much higher than the frequency of both ionizing (ν_i) and elastic momentum-transfer (ν_m) collisions:

$$\omega >> \nu_i, \nu_m. \tag{14}$$

The electric field amplitude must also be high, certainly higher than E_c - the critical breakdown field in air:[29]

$$E_c = 28(N/2.7 \cdot 10^{19} \text{ cm}^{-3})\sqrt{1 + \omega^2/\nu_m^2} \text{ kV/cm}. \tag{15}$$

The average momentum-transfer frequency is[29]

$$\nu_m = 1.7 \cdot 10^{-7} N, \text{ cm}^3/\text{sec}, \tag{16}$$

where N is the air molecules number density.

Depending on the field amplitude, two distinct regimes are possible. If the field amplitude does not exceed about 100 E_c, then, although electrons can acquire quiver energy above the ionization potential and therefore can ionize molecules in every collision, the quiver energy still does not exceed about 100

eV where ionization cross-sections have their maxima. If, however, the field amplitude is extremely high, above 100 E_c, then the quiver energy is greater than about 100 eV, and all electrons become runaway, ballistic ones.[29]

The case of moderately high fields:

$$E_c \ll E_0 \ll 100E_c \qquad (17)$$

was analyzed in our AIAA Paper 2001-2940. Electron velocity distribution functions in this case were found to have strong low-energy core, and the fraction of high-velocity ballistic electrons was very small. Because of this, the additional ionization after the pulse was found not to be significant.

In the case $E_0 > 100E_c$, electron velocity distribution function, $f(v,t)$, differs strongly from a spherically symmetric distribution function. In the simplest approximation, all electrons, including new ones produced in ionization events, oscillate in the same phase. A more realistic approximation is the assumption of equidistribution of electrons over the "initial phases".[32, 34] In this paper, we adopt the simplest approximation:[29]

$$f(v,t) = n_e(t)\delta(v\text{-}v_0\cos\omega t), \qquad (18)$$

where $n_e(t)$ is the time-dependent electron density and $v_0 = eE_0/m\omega$ is the velocity amplitude. Ionization frequency oscillates with the field, and the ionization frequency averaged over the period is:[29]

$$v_i = \frac{\omega}{2\pi}\int_0^{2\pi/\omega} v_i(t)dt = v_{i,m}\psi_m(v_0/v_m), \qquad (19)$$

where $v_{i,m} = N\sigma_{i,m}v_m \approx 1.81\cdot10^{-7}N$ cm^3/sec, $\sigma_{i,m} = 2.9\cdot10^{-16}$ cm^2 is the maximum ionization cross-section in air (corresponding to the energy $\varepsilon = \varepsilon_m \approx 110$ eV), $v_m = \sqrt{2\varepsilon_m/m} = 6.25\cdot10^8$ cm/sec is the electron velocity corresponding to the maximum of ionization cross-section, and $\xi = v_0/v_m = 1.72\cdot10^{-2}E_0/E_c$. In our calculations, we used the dimensionless function $\psi(\xi)$ tabulated in Ref. 29 to compute the ionization rate and the evolution of electron density for a given set of parameters of the microwave pulse (ω, E_0), initial electron number density, $n_e(0)$, and gas parameters (pressure p and temperature T):

$$n_e(t) = n_e(0)\exp(v_i t) . \qquad (20)$$

The final electron energy and velocity distributions at the end of the pulse and the subsequent ionization process depend strongly on the way the pulse is turned off and on collisional phase randomization during the pulse. Indeed, in the absence of collisions, if the field is turned off gradually, over a number of

oscillations, then the electrons will lose their oscillatory energy, so that $\langle \varepsilon \rangle$ will be close to zero by the end of the pulse, and no additional after-pulse ionization will occur. For $\langle \varepsilon \rangle$ to be large by the end of the pulse, the pulse must end abruptly compared with the oscillation period.

Technical feasibility of producing such sharp, picosecond-scale, cut-offs is an important issue. If the almost-instantaneous cut-off is possible, the oscillation phase at the pulse end becomes important. If during the pulse there are no phase-randomizing collisions, and also if all newly produced electrons are born in the same oscillation phase, then, depending on the phase at the pulse end, electron energy and velocity can range anywhere from zero to their amplitude oscillatory values. As a consequence, if in this case the pulse duration has a slight scatter, after-pulse ionization can be expected to vary substantially from pulse to pulse. However, in reality, new electrons are produced in different oscillation phases. This, and a few phase-randomizing collisions during the pulse can result in a broad distribution of phases and velocities at the end of the pulse.

Leaving exploration of details of these complex processes for future work, we shall assume here that the mean electron energy by the end of the pulse is equal to the mean oscillatory energy of Eq. (13).

The energy absorbed by the plasma (per 1 cm^3) during the pulse would, in the absence of ionization and other collisional energy losses, be determined by

$$W = n_e(0)(<\varepsilon> - \tfrac{3}{2}T_e(0)) \approx n_e(0)<\varepsilon> . \qquad (21)$$

If, however, ionization and other collisional losses occurred during the pulse, then the absorbed energy per unit volume can be estimated roughly as

$$W = n_e(\tau_1)<\varepsilon> + (n_e(\tau_1) - n_e(0))Y_i, \quad n_e(\tau_1) = n_e(0)\exp(v_i t), \qquad (22)$$

where Y_i is the ionization cost. Calculation of time-average ionization cost in this case, when relatively infrequent ionizing collisions occur randomly, with the ionizing electron's velocity spanning the entire range from the ionization threshold to the amplitude oscillatory velocity, is a problem to be addressed in future. In this paper, we used the value $Y_i = 34$ eV equal to the well-known value for high-energy electron beams.[13, 14] Some justification for this value is provided by the fact that the mean energy $\langle \varepsilon \rangle$ is in the keV range.

Although a substantial scatter of oscillation phases and velocities of electrons can be expected by the end of the pulse, as discussed above, for qualitative and semi-quantitative analysis of the afterglow we shall assume that all electrons have the same phase and velocity corresponding to the energy $\langle \varepsilon \rangle$ of Eq. (13) by

the end of the pulse, $t = \tau_1$. In other words, we shall follow the motion and relaxation of an "average" electron. Since in extremely strong fields, $E_0 > 100E_c$, at $\omega \gg v_i, v_m$, the oscillatory energy is very high, $<\varepsilon> \cong 1$ keV, a substantial growth of electron density can occur in the afterglow, and the maximum achievable electron density is:

$$n_{e,max} \approx n_e(\tau_1) \frac{<\varepsilon>(\tau_1)}{Y_i}.$$

(23)

Since there are very fast electrons by the end of the pulse, one might think that these electrons would leave the plasma and ionize the surrounding gas. However, positive space charge that these electrons would leave behind can provide a strong retarding force. Since powerful microwave discharges occur in practice in relatively small volumes with the thickness on the order $\lambda / 4$, where $\lambda = 2\pi c / \omega$ is the wavelength, consider a plasma slab with a thickness $\delta x = \lambda / 4$. For $\omega = 2\pi \cdot 1.1 \cdot 10^{11}$ rad/s, $\delta x \approx 6.8 \cdot 10^{-2}$ cm; and for $\omega = 2\pi \cdot 10^{10}$ rad/s, $\delta x \approx 0.68$ cm. From one-dimensional Poisson equation, maximum values of electric field strength and potential that could be reached if all electrons leave the plasma are:

$$E_{max} = \frac{e}{\varepsilon_0} n_+ \delta x, \; V_{max} = \frac{e}{2\varepsilon_0} n_+ \delta x^2.$$

(24)

For example, for a plasma density $n_+ = 10^{12}$ cm^{-3} at the end of the pulse, maximum field and potential that would retard escaping electrons are: $1.23 \cdot 10^5 / 1.23 \cdot 10^6$ V/cm and $4.1 \times 10^3 / 4.1 \times 10^5$ V for microwave frequency $\omega = 2\pi \cdot 1.1 \cdot 10^{11} / 2\pi \cdot 10^{10}$ rad/s.

Therefore, even keV-energy electrons cannot move in significant numbers far outside the initial plasma volume. The flight of high-velocity electrons out of the plasma creates an ambipolar field that traps the rest of the electrons in a potential well. The depth of the potential well is on the order of the energy of high-velocity electrons. Therefore, in our model, after the pulse electrons oscillate in potential well, the depth of which is determined by the maximum electron energy. As electrons lose their energy in ionizing and other inelastic collisions, both mean electron energy and the depth of the well decrease. Newly produced low-energy electrons congregate near the bottom of the well and thermalize there. This model is illustrated in Fig. 8.

Neglecting phase randomization, fast electrons' motion can be described as damped oscillations. These are essentially Langmuir oscillations damped because inelastic collisions with gas molecules. In the first approximation, the oscillations occur on the background of plasma with electron and ion density $n_e(\tau_1)$.

324

The amplitude of the oscillations is equal to the Debye radius for the plasma with density $n_e(\tau_1)$ and mean electron energy $<\varepsilon>(t)$:

$$r_d = \sqrt{2\varepsilon_0 <\varepsilon>(t)/en_e(\tau_1)} \ . \tag{25}$$

For $n_e(\tau_1) = 10^{11} \ cm^{-3}$ and $<\varepsilon> = 1 \ keV$, $r_d \approx 5 \cdot 10^{-2} \ cm$. Since the electric field created when electrons are displaced by x from equilibrium is

$$E = \frac{e}{\varepsilon_0} n_e(\tau_1) x \ , \tag{26}$$

the equation of motion for the "average" fast electron is:

$$\ddot{x} = -\frac{e^2}{\varepsilon_0} \frac{n_e(\tau_1)}{m} x - \frac{F_{coll}}{m} \ , \tag{27}$$

where $F_{coll} = m(dv/dt)_{coll}$ is the collisional friction force. Taking into account only ionizing collisions that do not change the direction of velocity, only changing its magnitude by

$$\delta v = \left| \dot{x} - \sqrt{\dot{x}^2 - 2Y_i/m} \right|, \ \dot{x}^2 > 2Y_i/m \ ,$$

$$\delta v = 0, \ \dot{x}^2 \le 2Y_i/m \ . \tag{28}$$

the friction force can be written as

$$F_{coll} = m \cdot \text{sign}(\dot{x}) v_i(|\dot{x}|) \delta v \ , \tag{29}$$

and Eq. (27) takes the form:

$$\ddot{x} = -\frac{e^2}{\varepsilon_0} \frac{n_e(\tau_1)}{m} x - \text{sign}(\dot{x}) v_i(|\dot{x}|) \delta v \ . \tag{30}$$

Eq. (30) is the equation of motion for an oscillator with friction. The oscillation frequency

$$\Omega = \sqrt{\frac{e^2 n_e(\tau_1)}{\varepsilon_0 m}} \tag{31}$$

is the Langmuir frequency for plasma with electron density $n_e(\tau_1)$, and the damping is determined by the ionization rate.

Initial conditions for Eq. (30) are:

$$x(\tau_1) = 0 \ ? \ \dot{x}(\tau_1) = \sqrt{2 <\varepsilon>(\tau_1)/m} \ . \tag{32}$$

Electron density grows with time according to the equation:

$$dn_e/dt = n_e(\tau_1) v_i(|\dot{x}|) \ . \tag{33}$$

Fig. 9 shows phase diagram (velocity-coordinate) of the motion of "average" electron and the evolution of electron energy and number density after 1-nanosecond pulse of 110 GHz microwaves with amplitude $E_0 = 250E_c$ at gas pressure of 1 Torr, with electron density 10^9 cm^{-3} at the start of the pulse. The damped oscillatory motion and the strong expected growth of electron density in the "afterglow" are clearly seen in the figures. Note that experimental observations of the after-pulse ionization at low gas pressures were reported in Ref. 32.

Note that some phase randomization is expected to occur in collisions. Especially "dangerous" in this regard are elastic collisions occurring near the turning points, when electron velocity becomes low. This phase randomization will have to be included in more sophisticated models. Another factor to be included in subsequent calculations is a change in the Langmuir oscillation frequency with time, as electron density changes. Therefore, the present calculations should be viewed as a first estimate.

Based on these calculations, Fig. 10a shows the average electron energy at the end of the pulse, electron number density at the end of the pulse, and the maximum electron density between the pulses for different values of the microwave field amplitude. As in Fig. 9, the microwave frequency was 110 GHz, gas pressure – 1 Torr, but the electron density at the start of the pulse was chosen as 10^{10} cm^{-3}. Fig. 10b shows the computed power budgets and pulse repetition rates required to sustain time-average electron densities of 10^{12} cm^{-3} and 10^{13} cm^{-3} with these high-power microwave pulses.

4.3 Can the efficient ionization in high-power ultrashort electromagnetic pulses be extended to high pressures?

The two conditions necessary for energy-efficient ionization in electromagnetic fields are:

- Very high, keV-range electron quiver energy (13). This requires the ratio E/ω to be high enough.
- The pulse length must be shorter than the time interval between electron-molecule collisions.

The second condition puts an upper limit to the pulse length, and a lower limit to the frequency of the electromagnetic wave (at a given pressure). For example, the time interval between electron-molecule collisions in air is 0.2 ps at STP, or 5 ps at 30 Torr. Thus, 1-picosecond or shorter pulses would be required, and the frequency would have to be higher than 1 Terahertz (wavelength shorter than 300 microns). Provided that such a high-power, short-pulse, high repetition rate source can be developed, the basic physics of ionization due to high-energy electrons in and after the pulse will be mostly the same as in the high-power microwave plasma at low gas density that was analyzed in the previous section.

One important additional factor is multiphoton/tunneling ionization that should be suppressed: otherwise the laser pulse would ionize atoms in the focal region producing many low-energy electrons there, instead of high-energy electrons capable of ionizing the surrounding gas. The multiphoton/tunneling ionization can be significant, because, according to Eq. (13), to achieve the desired mean electron quiver energy $\langle \varepsilon \rangle \square 1$ keV at frequencies 1-2 orders of magnitude higher than the microwave frequencies considered in the previous section, the electric field of the laser beam should also be 1-2 orders of magnitude higher, bringing this field close to electric fields inside atoms and molecules.

Quantitative analysis of tunneling ionization in oscillating electric fields (a combination of tunneling and multiphoton ionization) is based upon Keldysh theory. For the probability of ionization per unit time $w(t)$ in a field $E(t)$ we have:[36]

$$w(t) = 4w_0 \left(\frac{E_i}{E_H} \right)^{5/2} \frac{E_a}{E(t)} \exp\left[-\frac{2}{3} \left(\frac{E_i}{E_H} \right)^{3/2} \frac{E_a}{E(t)} \right],$$ (34)

and the ionization probability per unit time averaged over the field oscillation is:

$$\langle w \rangle = 4w_0 \left(\frac{E_i}{E_H} \right)^{5/2} \frac{E_a}{E_0} \sqrt{\frac{2E_0}{\pi E_a}} \exp\left[-\frac{2}{3} \left(\frac{E_i}{E_H} \right)^{3/2} \frac{E_a}{E_0} \right]$$ (35)

where $w_0 = \frac{me^4}{\hbar^3} = 4.112 \times 10^{16} \ s^{-1}$; $E_a = \frac{m^2 e^5}{\hbar^4} = 5.12 \times 10^9 \ V/cm$; $E_H = 13.6 \ eV$.

The tunneling ionization rate (35) increases exponentially with electric field strength. On the other hand, to obtain a desired collisionless quiver energy, according to Eq. (13), a certain ratio E_0/ω is needed. This determines requirements for laser wavelength and power; longer wavelengths would allow us to reduce field strength needed to get high quiver energy and to suppress tunneling/multiphoton processes. On the other hand, very long wavelengths correspond to long oscillation periods that could exceed the time interval between electron-molecule collisions.

Specific estimates were performed for air and other gases in a wide pressure range. For air, assuming ionization energy of 12.6 eV (oxygen), laser wavelength of about 30 micron is needed. Then the quiver energy of 3 keV would require field amplitude of 164 MV/cm, or peak energy flux of 35.7 TW/cm^2. With 300-micron focal spot, the peak power should be 25.3 GW. The energy per 0.3 ps pulse should be 7.6 mJ. The probability of tunneling ionization during the pulse with these parameters is relatively small, about

10^{-6}. Thus, is the ionization fraction is greater than 10^{-6}, tunneling ionization can be, in the first approximation, neglected.

Pulse repetition rate should match the rate of recombination. For example, to sustain 10^{12}-10^{13} electrons/cm^3, repetition rate of the order of 100 kHz is necessary.

In He, where ionization energy is quite high, 24.6 eV, suppression of tunneling ionization could be accomplished at shorter wavelengths, about 10 microns or shorter.

Preliminary survey of currently and potentially available sources indicates that free-electron lasers and masers are attractive candidates for the repetitive-short-pulse method of efficient generation of plasmas at high gas pressures.

5 Conclusions

Ionization efficiency increases, and the power budget for sustaining a prescribed electron density decreases in plasmas generated by DC or oscillating electric fields if high-energy electrons are generated in these plasmas. High-energy electrons are produced if the ratio E/N in the DC case, or the ratio E/ω in low-pressure microwave or laser plasmas, can be made very high. To avoid overproduction of electrons and excess heating, the strong field should be turned on for only a short time, and then the plasma should be allowed to decay to the initial ionization level. This is the essence of the ultra-short repetitive pulse ionization method explored in our work.

Calculations of the power requirements for plasmas sustained by repetitive nanosecond pulses show that there is an optimum electric field that minimizes the power budget. This minimum power budget is much lower than that in a continuous DC or RF plasma, but still substantially higher than in a plasma sustained by electron beams.

Modeling of spatio-temporal dynamics of plasmas in nanosecond pulses shows strong coupling between non-local dynamics of high-energy electrons, ionization kinetics, and evolution of electric field. Cathode sheath phenomena are critical at low gas density, and ionization is essentially determined by acceleration of electrons in the sheath and their subsequent injection into the bulk plasma, leading to non-uniform and evolving in time electron energy and ionization degree profiles. At high gas pressures, sheath phenomena, non-local ionization, and ionization non-uniformity are suppressed, and plasma dynamics can be modeled in a macroscopic, "hydrodynamic" approximation.

With an appropriate choice of frequency and amplitude, the efficient repetitive-pulse ionization method can be extended to electromagnetic waves, i.e., to electrodeless systems. At low gas density, high-power nanosecond microwave pulses at frequency 10-100 GHz can accelerate electrons to ~ 1 keV energy, resulting in much more efficient ionization than that in conventional low-power systems. Moreover, most of the ionization would occur after the pulse, as the high-energy electrons produced during the pulse lose their energy on ionization.

In principle, the method of plasma generation by ultrashort repetitive high-power electromagnetic pulses can be extended to high gas densities. Technical feasibility of developing appropriate laser sources with parameters estimated in this paper remains to be studied.

REFERENCES

[1] Fraishtadt, V.L., Kuranov, A.L., and Sheikin, E.G., "Use of MHD Systems in Hypersonic Aircraft," *Technical Physics*, Vol. 43, 1998, p.1309.

[2] Gurijanov, E.P., and Harsha, P.T., "AJAX: New Directions in Hypersonic Technology," Paper AIAA-96-4609, 1996.

[3] Macheret, S.O., Shneider, M.N., and Miles, R.B., "Electron Beam Generated Plasmas in Hypersonic MHD Channels," Paper AIAA-99-3635, June 1999.

[4] Macheret, S.O., Shneider, M.N., Miles, R.B., and Lipinski, R.J., "Electron Beam Generated Plasmas in Hypersonic Magnetohydrodynamic Channels", *AIAA Journal*, 2001, Vol. 39, No. 7.

[5] Macheret, S.O., Shneider, M.N., and Miles, R.B., "MHD Power Extraction From Cold Hypersonic Air Flows with External Ionizers," AIAA Paper 99-4800, November 1999.

[6] Macheret, S.O., Shneider, M.N., and Miles, R.B., "Potential Performance of Supersonic MHD Power Generators," AIAA Paper 2001-0785, January 2001.

[7] Macheret, S.O., Shneider, M.N., and Miles, R.B., "External Supersonic Flow and Scramjet Inlet Control by MHD with Electron Beam Ionization," AIAA Paper 2001-0492, January 2001.

[8] Macheret, S.O., Shneider, M.N., and Miles, R.B., "Modeling of Discharges Generated by Electron Beams in Dense Gases: Fountain and Thunderstorm Regimes," *Physics of Plasmas*, Vol. 8, No. 5, 2001, pp. 1518-1528.

[9] Macheret, S.O., Miles, R.B., and Nelson, G.L., "Feasibility Study of a Hybrid MHD/Radiatively Driven Facility for Hypersonic Ground Testing," Paper AIAA 97-2429, June 1997.

[10] Macheret, S.O., Shneider, M.N., Miles, R.B., Lipinski, R.J., and Nelson, G.L., "MHD acceleration of supersonic air flows using electron beam enhanced conductivity," Paper AIAA-98-2922, June 1998.

[11] Macheret, S.O., Shneider, M.N., and Miles, R.B., "Modeling of Air Plasma Generation by Electron Beams and High-Voltage Pulses," AIAA Paper 2000-2569, June 2000.

[12] Raizer, Yu.P., "Gas Discharge Physics," Springer, Berlin, 1991.

[13] Bychkov, Yu.I., Korolev, Yu.D., and Mesyats, G.A., "Injection Gaseous Electronics" ["Inzhektsionnaia Gazovaia Elektronika", in Russian], Nauka, Moscow, 1982.

[14] Berger, M.J. and Seltzer, S.M., "Tables of Energy Losses and Ranges of Electrons and Positrons," NASA SP-3012, 1964.

[15] Handbook of Physical Quantities, ed. by I.S.Grigoriev and E.Z.Meilikhov, CRC Press, Boca Raton, Florida, 1997, Ch.21.

[16] V.A. Granovskii, Elektricheskii Tok v Gaze [Electrical Current in a Gas, in Russian], Nauka, Moscow, 1971, Ch.2 and references therein.

[17] A.Kh.Mnatsakanyan and G.V.Naidis, "Processes of Formation and Decay of Charged Particles in Nitrogen-Oxygen Plasmas," in: Khimiia Plazmy [Plasma Chemistry], Vol. 14, ed. by B.M.Smirnov. Energoatomizdat, Moscow, 1987, pp. 227-255. [In Russian].

[18] J.Dutton, *J. Phys. Chem. Ref. Data*, v.4, 1975, pp.577-856.

[19] J.W.Gallagher, E.C.Beaty, J.Dutton, and L.C.Pitchford, *J. Phys. Chem. Ref. Data.*, v.12, 1983, pp.109-152.

[20] N.L.Aleksandrov, A.M.Konchakov, and E.E.Son, *Sov. J. Plasma Physics*, Vol. 4, 1978, pp. 169-175, 1182-1186.

[21] E.E.Son, *High Temperature*, Vol. 16, 1978, pp. 1162-1166.

[22] I.A.Kossyi, A.Yu.Kostinsky, A.A.Matveyev, V.P.Silakov, "Kinetic Scheme of the Non-Equilibrium Discharge in Nitrogen-Oxygen Mixtures," *Plasma Sources Sci. Technol.*, Vol. 1, 1992, pp.207-220.

[23] Aleksandrov, N.L., Vysikailo, F.I., Islamov, R.Sh., Kochetov, I.V., Napartovich, A.P., and Pevgov, V.G., "Electron distribution function in 4:1 N_2-O_2 mixture," *High Temperature*, Vol. 19, 1981, p. 17.

[24] Yu.P.Raizer and M.N.Shneider, "Simplified Kinetic Equation for Electrons in Nonuniform Fields of Arbitrary Strength in Connection with the Cathode Sheath of a Glow Discharge," *Sov. J. Plasma Phys.*, Vol. 15, No. 3, 1989, pp.184-189.

[25] S.M.Starikovskaia, A.Yu.Starikovskii, and D.V.Zatsepin, "Development of a Spatially Uniform Fast Ionization Wave in a Large Discharge Volume", *J. Phys. D.: Appl. Phys.*, v. 31(5), 1998, pp.1118-1125.

[26] L.P.Babich, T.V.Loiko, and V.A.Tsukerman, "High-Voltage Nanosecond Discharge in a Dense Gas at a High Overvoltage With Runaway Electrons," *Sov. Phys. Uspekhi*, Vol. 33 (7), 1990, pp.521-540.

[27] L.P.Babich and L.M.Kutsyk, "Numerical Simulation of a Nanosecond Discharge in Helium at Atmospheric Pressure, Developing in the Regime of Runaway of Electrons" *High. Temp.*, v. 33(2), 1995, pp.190-197.

[28] E.M.Bazelyan and Yu.P.Raizer, Spark Discharge. CRC Press, Boca Raton, Florida, 1997.

[29] Borisov, N.D., Gurevich, A.V., and Milikh, G.M., Isskusstvennaia Ionizovannaia Oblast' v Atmosfere [Artificially Ionized Region in the Atmosphere, in Russian], IZMIRAN, USSR Academy of Sciences, Moscow, 1985.

[30] Vysokochastotnyi Razriad v Volnovykh Poliakh [High-Frequency Discharge in Wave Fields, in Russian], ed. by A.G.Litvak, Institute of Applied Physics of the USSR Academy of Sciences, Gorkiy, 1988.

[31] A.G.Litvak, "Freely Localized Gas Discharge in Microwave Beams," Chapter 4 in: Applications of High-Power Microwaves, A.V.Gaponov-Grekhov and V.L.Granatstein, editors, Artech House, Boston and London, 1994.

[32] Brizhinev, M.P., Vikharev, A.L., Golubyatnikov, G.Yu., Eremin, B.G., Ivanov, O.A., Litvak, A.G., Lirin, S.F., Plotnikov, I.V., Soluyanov, E.I., Semenov, V.E., Tolkacheva, O.N., and Shevchenko, O.V., "Ionization of a Low-Pressure Gas in a Very Intense Microwave Field," *Sov. Phys. JETP*, Vol. 71, No. 2, 1990, pp. 242-247.

[33] Arutyunyan, S.G., and Rukhadze, A.A., *Sov. J. Plasma Phys.*, Vol. 5, 1979, p. 395.

[34] Glazov, L.G., and Rukhadze, A.A., *Sov. J. Plasma Phys.*, Vol. 15, 1989, p. 863.

[34] Vikharev, A.L., Gil'denburg, V.B., Ivanov, O.A., *et. al.*, *Sov. J. Plasma Phys.*, Vol. 12, 1986, p. 870.

[35] http://physics.nist.gov/PhysRefData/Ionization/EII_table.html.

[36] Landau, L.D., and Lifshitz, E.M., Quantum Mechanics, Pergamon, London, 1978.
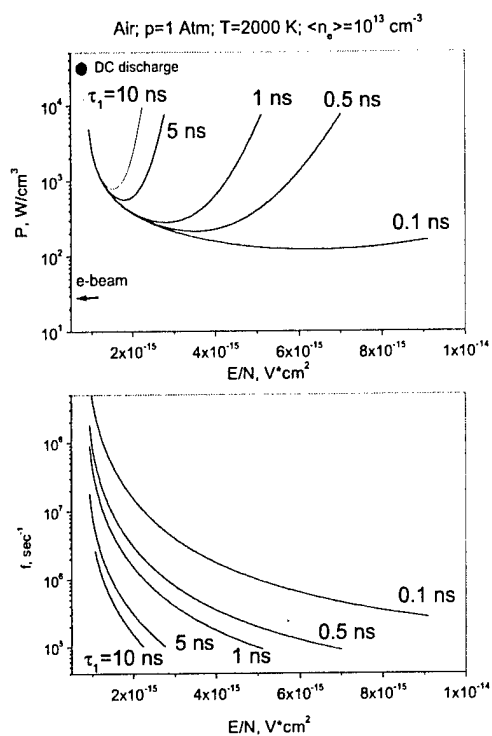
Fig.1. Power input (upper plot) and pulse repetition rate (lower plot) required to sustain a time-averaged electron number density of 10^{13} cm^{-3} in air at 1 atm, 2000 K, by repetitive ideal rectangular voltage pulses as functions of *E/N* (the ratio of the electric field in the pulse to the gas number density) at various pulse lengths τ_1. Power inputs required to sustain the same electron density at steady state by DC discharge and high-energy electron beams are also indicated on the upper plot.
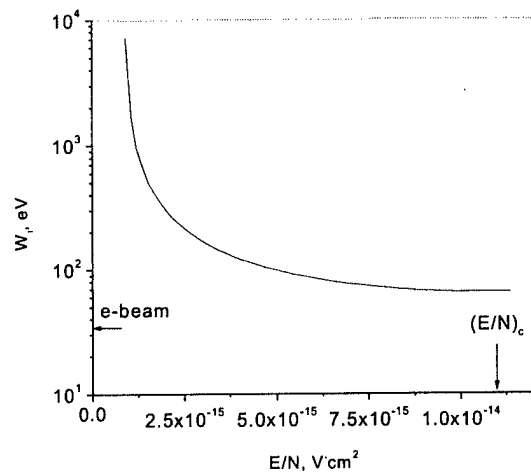
Fig. 2. Energy cost of ionization, in eV per newly produced electron, in air as a function of E/N (the ratio of electric field in the plasma to the gas number density). Energy cost of ionization by high-energy electron beams (34 eV) is also indicated. The critical value $E/N = (E/N)_c \approx 1.1 \times 10^{-14}$ $V \cdot cm^2$ corresponds to the threshold of electron runaway.
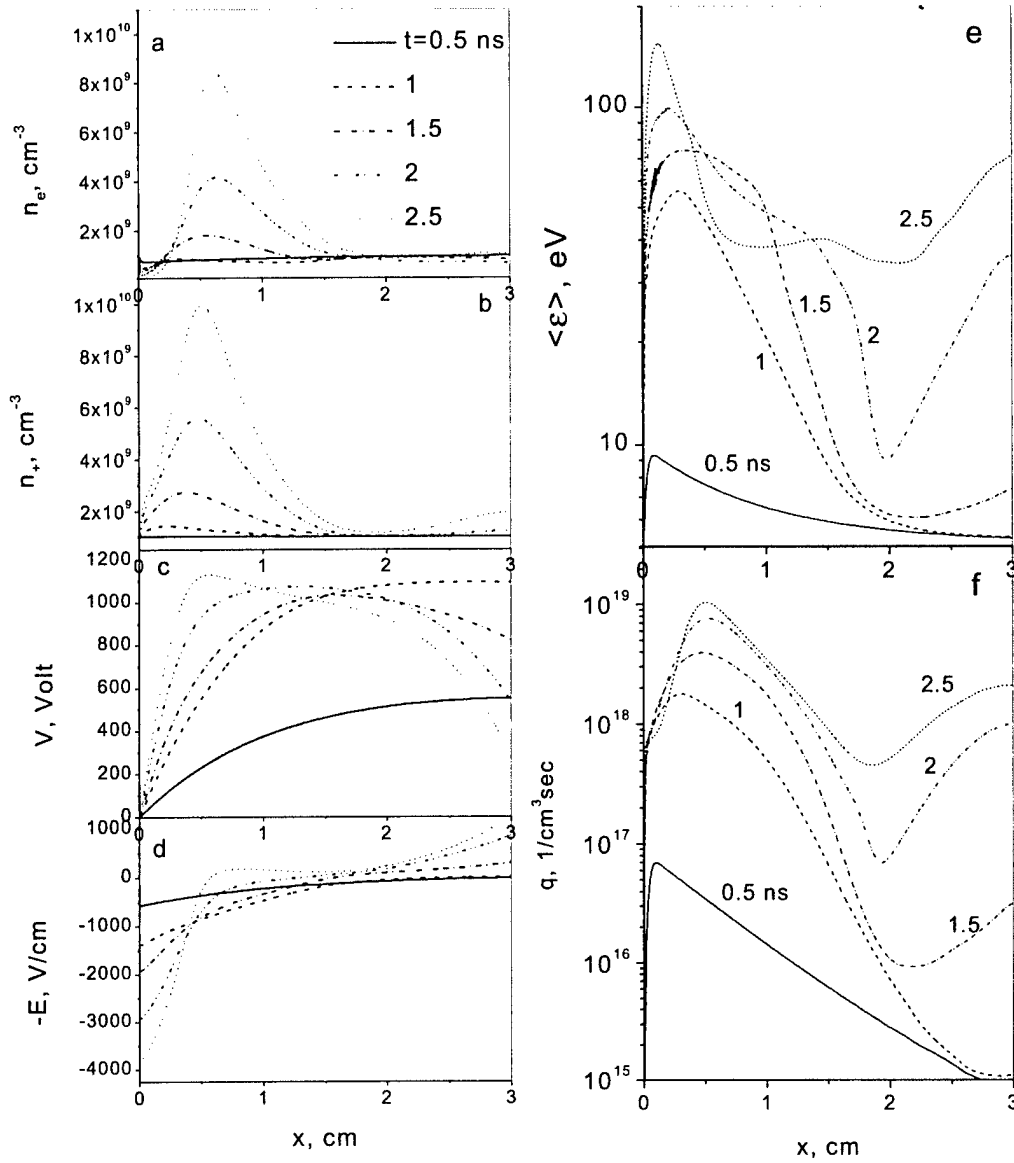
Fig. 3. Kinetic modeling of pulsed discharge in air: p=1 Torr; T=300 K, L=3 cm. Secondary electron emission coefficient γ=0.1; initial electron and ion number density is 10^9 cm^{-3}. Peak voltage is V_{max}=365pL Volts. Shown are spatial profiles of: a – electron and b – ion densities; c – electric potential; d – electric field; e – mean electron energy; and f – ionization rate, at different moments of time during the pulse
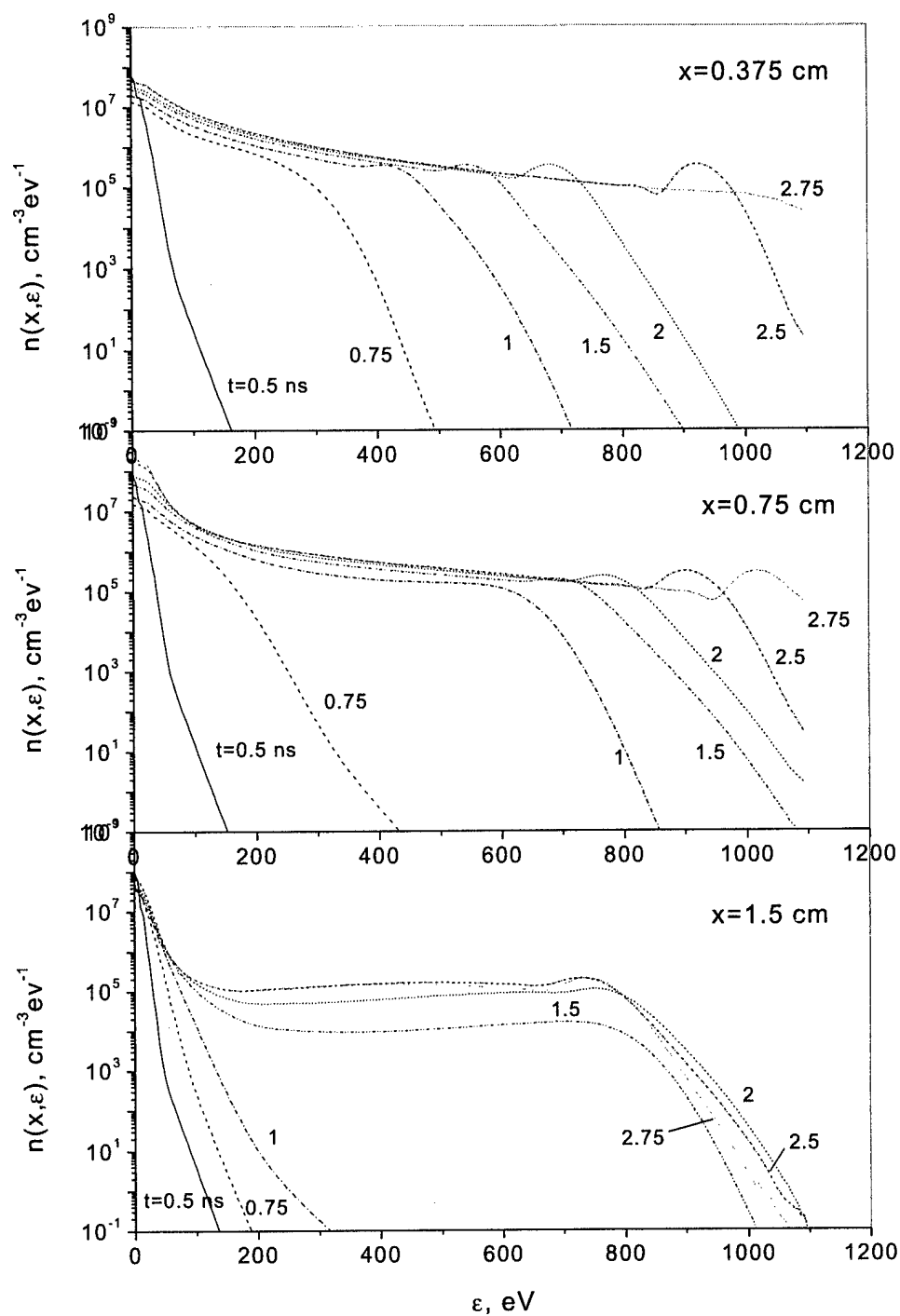
Fig. 4. Kinetic modeling of pulsed discharge in air at the same conditions as in Fig. 3: electron energy distribution function (EEDF) in different locations at various moments of time during the pulse.
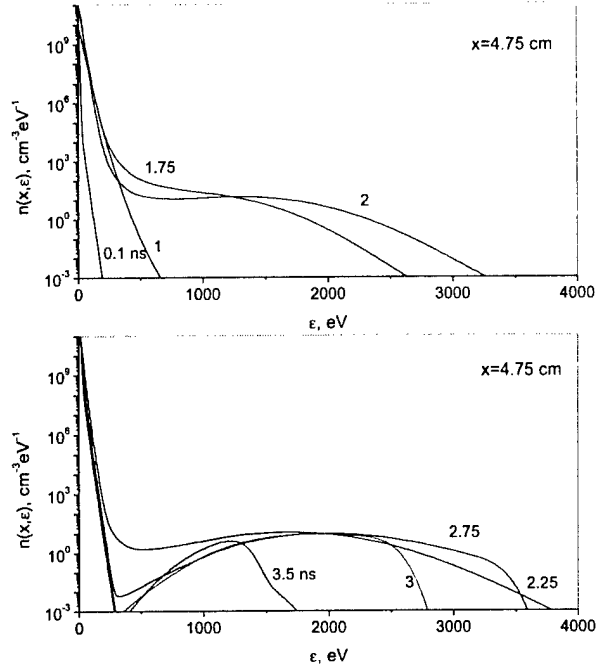
Fig. 5. Kinetic modeling of a pulsed discharge without near-electrode sheaths: electron energy distribution function (EEDF) at different time moments in the location x=4.75 cm. P=10 Torr; L=5 cm; $V_{max}=0.5E_{cr}L$; $E_{cr}/p=365$ V/(cm·Torr). Initial electron and ion number density is 10^{11} cm^{-3}.
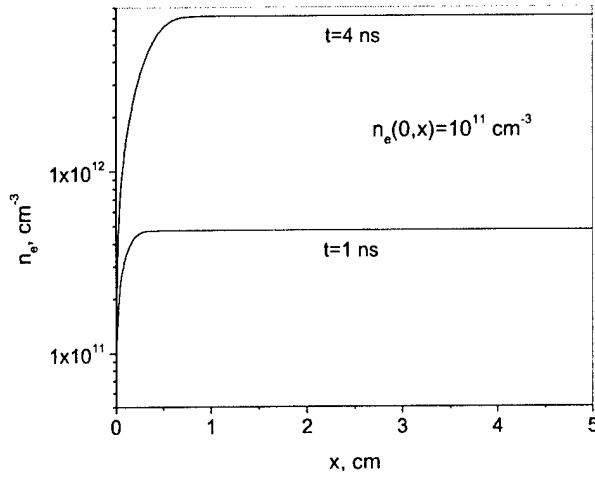
Fig. 6. Kinetic modeling of a pulsed discharge without near-electrode sheaths: longitudinal profiles of electron density. Conditions are the same as in Fig. 5.

336
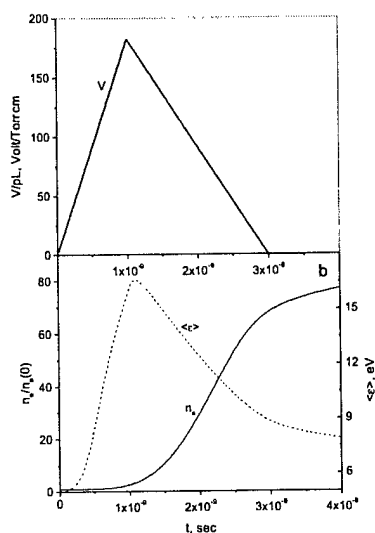
Fig. 7. Kinetic modeling of a pulsed discharge without electrode sheaths: evolution of mean electron energy and electron density with an arbitrary initial electron density. Other conditions are the same as in Fig. 5.
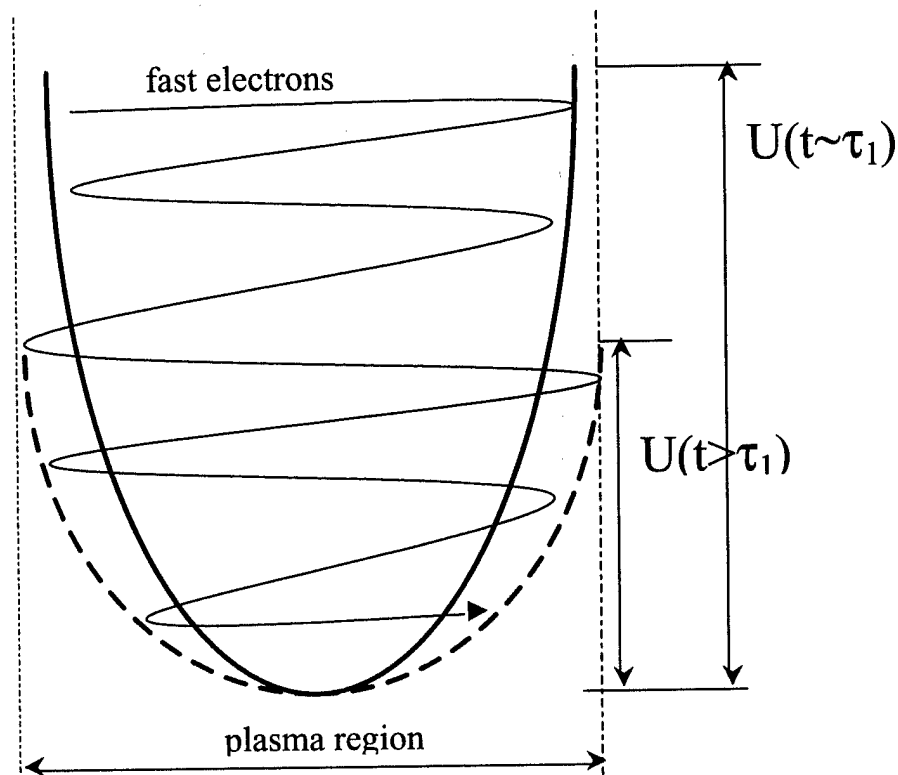
Fig. 8. Schematic illustration of the model of processes after an ultrahigh-power electromagnetic pulse: damped oscillatory motion of a high-energy electron in decreasing-depth ambipolar potential well.

E_0=250 E_k; ω=2πx1.1 10^{11} rad/s; n_e(0)=10^9 cm^{-3};n_e(τ$_1$)=2.18 10^{11} cm^{-3},p=1 Torr
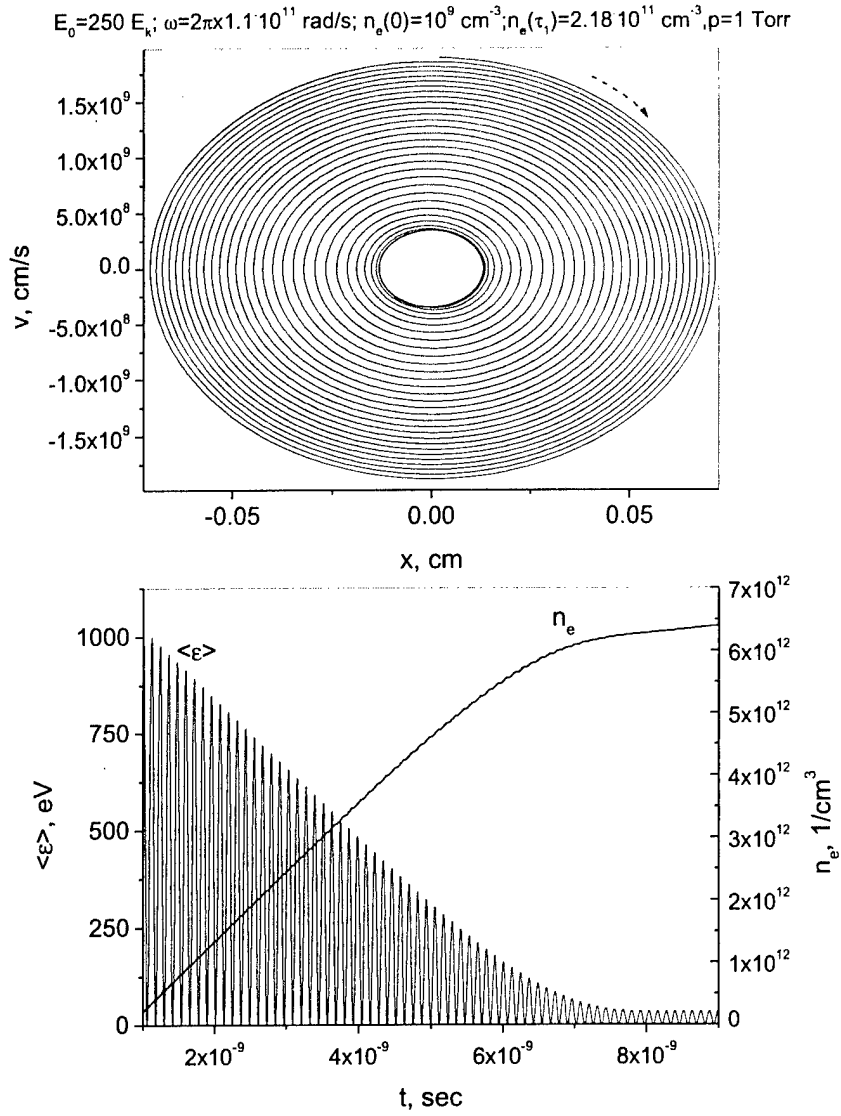
Fig. 9. Phase diagram (velocity-coordinate) of the motion of "average" electron and the evolution of electron energy and number density after 1-nanosecond pulse of 110 GHz microwaves with amplitude $E_0 = 250E_c$ at gas pressure of 1 Torr, with electron density 10^9 cm^{-3} at the start of the pulse.
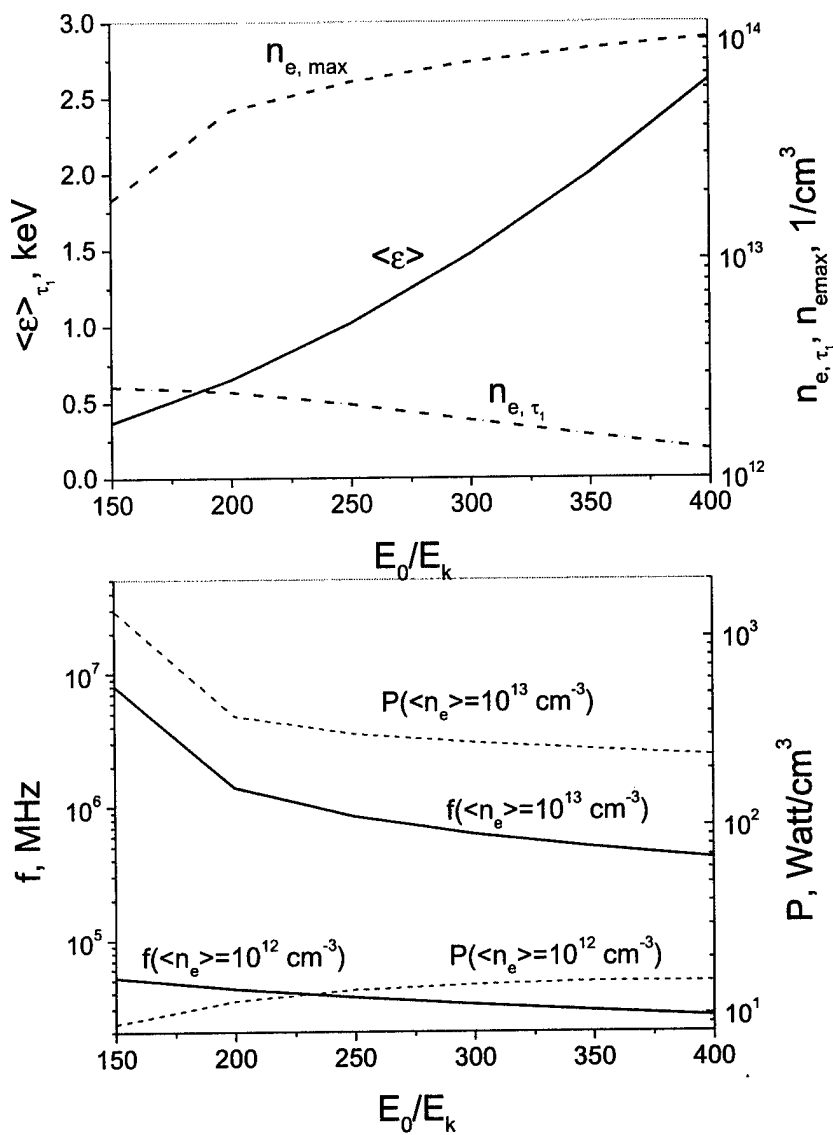
Fig. 10. a - average electron energy at the end of the pulse, electron number density at the end of the pulse, and the maximum electron density between the pulses at different values of microwave field amplitude.

b – computed power budgets and pulse repetition rates required to sustain time-average electron densities of 10^{12} cm^{-3} and 10^{13} cm^{-3}. Microwave frequency – 110 GHz, gas pressure – 1 Torr, electron density at the start of the pulse – 10^{10} cm^{-3}.

20. PRELIMINARY EXPERIMENTAL STUDIES OF AIR PLASMAS SUSTAINED BY REPETITIVE HIGH-VOLTAGE NANOSECOND PULSES

R. Murray, S. Zaidi, S.O. Macheret, M.N. Shneider, and R.B. Miles

To verify the theoretical predictions of dynamics, kinetic, and power budget of plasma sustained by high-voltage, high repetition rate, nanosecond pulses, Princeton University has recently purchased (from Moose Hill Enterprises, Inc.) and made operational a system generating 2-ns, 30 kV pulses at up to 100 kHz repetition rate.

To quantify the efficiency of the high voltage pulser as an ionization source, a static discharge cell has been designed and built.

Images of the resultant discharge in air at pressures of 20 Torr, 10 Torr, 5 Torr, and 1.5 Torr are shown in Figure 2. For the images in Figure 2, the pulser was operated at a repetition rate of 100 kHz with 30 kV, 2.5 FWHM ns pulses. At the higher pressures, the plasma is seen to contract somewhat.

Electron density in the plasmas was investigated using a 7.5 GHz microwave source. Based on absorption measurements, the time-averaged electron density is on the order of 10^{12} cm^{-3}.

Figure 1. Static discharge cell. The aluminum electrodes are clearly visible on the right side of the cell.

Figure 2. Images of the discharge in the static cell in air at pressures (clockwise from the top left) of 20 Torr, 10 Torr, 5 Torr, and 1.5 Torr. The discharge is sustained by a 30 kV, 2 ns pulse at a repetition rate of 100 kHz.

21. MODELING OF DISCHARGES GENERATED BY ELECTRON BEAMS IN DENSE GASES: "FOUNTAIN" AND "THUNDERSTORM" REGIMES

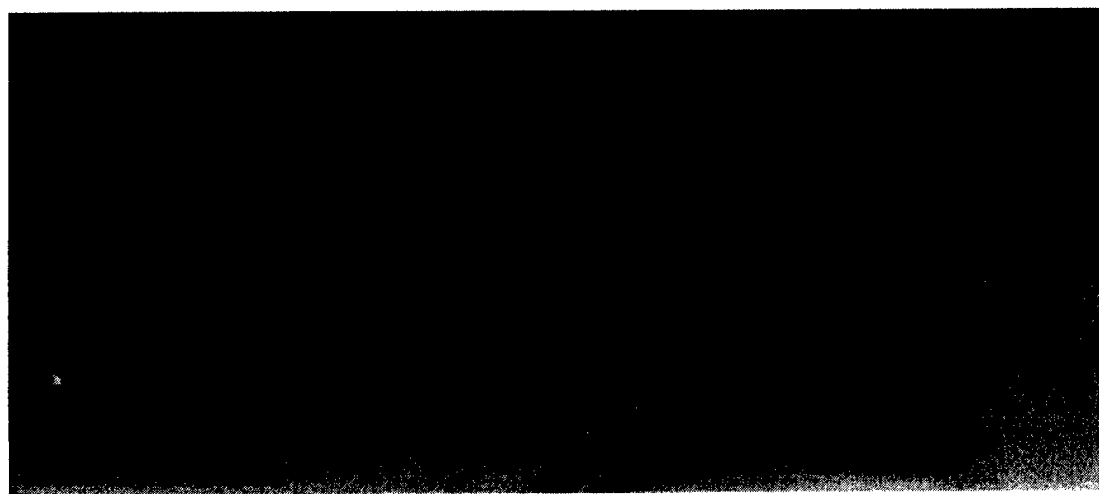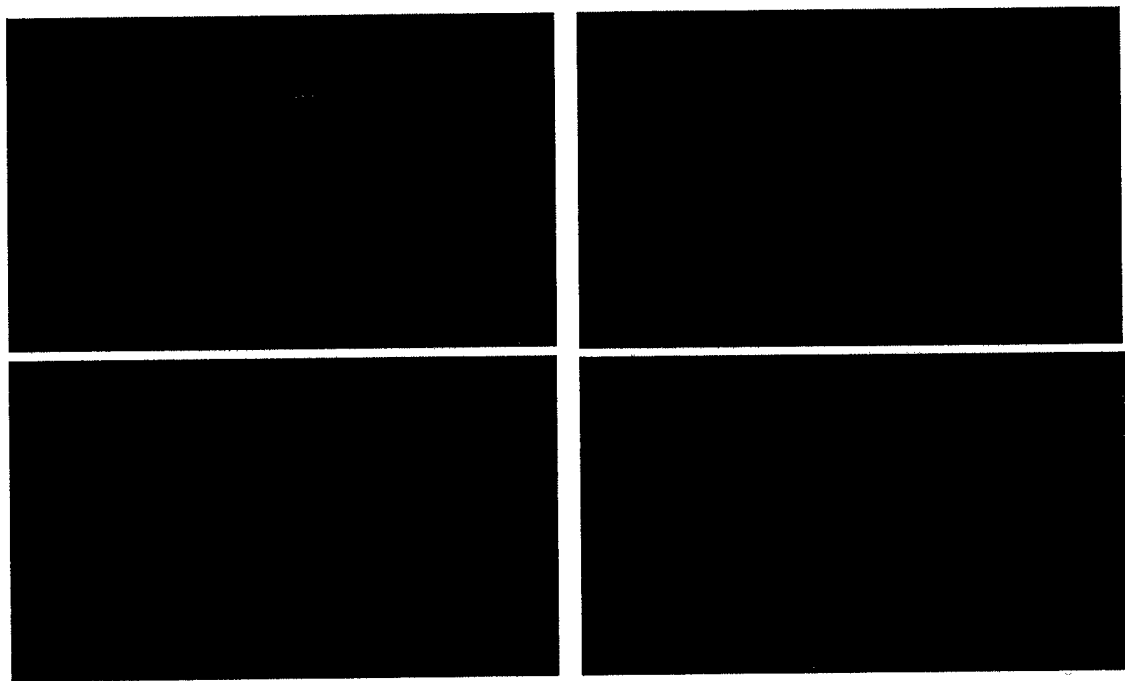*S.O. Macheret, M.N. Shneider and R.B. Miles*

Analysis is presented of the predicted dynamics of plasmas generated in air and other gases by injecting beams of high-energy electrons. Two distinct regimes are found, differing in the way that the excess negative charge brought in by the ionizing electron beam is removed. In the first regime, called a "fountain", the charge is removed by the back current of plasma electrons towards the injection foil. In the second, called a "thunderstorm", a substantial cloud of negative charge accumulates, and the increased electric field near the cloud causes a streamer to strike between the cloud and a positive or grounded electrode, or between two clouds created by two different beams. A quantitative analysis, including electron beam propagation, electrodynamics, charge particle kinetics, and a simplified heat balance, is performed in a 1D approximation.

Introduction

When beams of energetic electrons propagate into a gas, they lose their energy by ionizing and exciting the gas molecules, with 30-50% of the beam energy spent directly on ionization. Use of electron beams as an efficient ionization source to stabilize electric discharges is well known and widely used, in particular, in electric discharge lasers.[2]

The propagation of an electron beam injected into a background, initially neutral, gas is a complex and multiparametric problem.[3] Considerable experimental and theoretical work has been done on the interaction of electron beams with gases, where beam-induced ionization, return current, and charge neutralization strongly affect the propagation of the beam.[2, 4, 5, 6] Theoretical work on beam-gas interactions performed to date can be divided into three principal categories.

The first category, represented, *e.g.*, by Ref. 3, addresses relativistic (MeV-class) high-current (kiloamperes) pulsed beams. Because of the high currents and fast (nanosecond) transients, self-induced

---

[1] Yu.I.Bychkov, Yu.D.Korolev, and G.A.Mesyats, *Inzhektsionnaia Gazovaia Elektronika* [*Injection Gaseous Electronics*, In Russian] (Nauka, Novosibirsk, 1982).

[2] R.B.Miller, *An Introduction to the Physics of Intense Charged Particle Beams* (Plenum Press, New York and London, 1982).

[3] D.W.Swain, J. Appl. Phys. **43**, 396 (1972).

[4] P.A.Miller and J.B.Gerardo, J. Appl. Phys. **43**, 3008 (1972).

[5] D.A.McArthur and J.W.Poukey, Phys. Rev. Lett. **27**, 1765 (1971).

magnetic and electromagnetic effects, coupled with plasma generation, are of primary importance. However, the beam is assumed to be unaffected by its passage through the gas. This assumption is valid when the beam relaxation length is very large, which is the case for an MeV-class beam propagating into a low-to-moderate pressure gas, so that the beam energy is almost constant within the spatial region of interest.

The second category of papers addresses diffuse electric discharges supported by electron beams with applications to high-power lasers and fast switches,[1, 7] or to plasma reflectors of electromagnetic waves.[8, 9, 10, 11] The main requirement for the electron beam (injected from the cathode to the anode) in those discharges is to provide a uniform ionization throughout the volume. For this, the beam relaxation length should exceed the interelectrode gap, $l_r > L$. In this situation, variation of beam energy and current along its path is again quite small, simplifying theoretical analysis.

The third group of papers on electron beam interactions with gases addresses details of energy distribution of electrons in beam-produced plasmas.[12, 13, 14] Because of complexity of the problem, those analyses are zero-dimensional, i.e., uncoupled from beam propagation and beam-produced ionization.

In this paper, we consider beams with initial energy of between 1 keV to a few hundred keV and a current density of 1-100 mA/cm^2 propagating into a gas at a pressure from about 1 Torr to several atmospheres. We will be interested in a situation where the beam loses its energy and ionizes the gas far from the walls, and where the tip of the beam-produced plasma does not reach the anode. The low beam current allows us to neglect self-induced magnetic and electromagnetic effects. On the other hand, the relatively low beam energy and high gas density result in a relatively short beam penetration length, from a few centimeters to perhaps a few meters. Over this length, the energy of beam electrons varies quite significantly, so that the beam propagation is coupled with plasma generation, motion of charged

[6] S.A.Genkin, Yu.D.Korolyov, G.A.Mesyats, and V.B.Ponomarev, Pis'ma Zh.Tech. Fiz. **8**, 641 (1982).

[7] R.F.Fernsler, W.M.Manheimer, R.A.Meger, J.Mathew, D.P.Murphy, R.E.Pechacek, and J.A.Gregor, Phys. Plasmas **5**, 2137 (1998).

[8] J.Mathew, R.F.Fernsler, R.A.Meger, J.A.Gregor, D.P.Murphy, R.E.Pechacek, and W.M.Manheimer, Phys. Rev. Lett. **77**, 1982 (1996).

[9] W.M.Manheimer, IEEE Trans. Plasma Sci. **PS-19**, 1228 (1991).

[10] R.A.Meger, J.Mathew, J.A.Gregor, R.E.Pechacek, R.F.Fernsler, W.M.Manheimer, and A.E.Robson, Phys. Plasmas **2**, 2532 (1995).

[11] D.R.Suhre and J.T.Verdeyen, J. Appl. Phys. **47**, 4484 (1976).

[12] V.P.Konovalov and E.E.Son, Sov. Phys. Tech. Phys. **25**(2), 178 (1980).

[13] G.B.Lappo, M.M.Prudnikov, and V.G.Chicherin, High Temperature **18**, 527 (1980).

particles, gas heating, and spatio-temporal evolution of the electric field. In this paper, we develop a model for these coupled phenomena.

One of the main issues in the case where a beam loses its energy before reaching any wall or an anode is the mechanism of charge neutralization. When injected into a gas through a cathode toward an anode, an electron beam generates both a plasma and a "cloud" of negative space charge. As a result, the electric potential inside the gap becomes lower than the potential of either of the two electrodes. If the preexisting anode voltage is high, and the beam stops close to the anode without actually "touching" it, then the electron beam can quickly bring negative potential close to the anode, and the "cloud" will quickly accumulate such a charge that electric field near it can exceed the breakdown threshold of the ambient gas, creating either a streamer ?r Townsend breakdown between the "cloud" and the positively biased anode plate (Fig.1,a).

The sparks, or streamers, can be generated at high repetition rate by using a repetitive-pulse electron beam. With multiple electron beams, sparks will occur between the "clouds" as well as between each "cloud" and the "earth" (grounded plate). Since this process of removal of the excess negative charge is similar to lightning between thunderclouds and the earth and between the thunderclouds, we shall call the process a "thunderstorm".

One can also envisage a very different mechanism of charge neutralization: a quasistationary discharge between the virtual cathode at the tip of the beam-produced "cloud" and the metallic foil through which the beam is injected into the gas. In such a "fountain" discharge, the return current of plasma electrons will balance the forward current of high-energy beam electrons. In principle, to sustain such a discharge at steady state, the second electrode (the anode to which the voltage is applied) is not necessary. Thus, a quasisteady-state, stable, high-pressure discharge could be created with a single electrode (Fig.1, b). In its structure and properties, electron beam-sustained "single-electrode" discharge should be similar to conventional glow discharge (except that the electron temperature in beam-produced plasmas could be very low – see Sections II and III). The beam injection foil acts as an anode, and the tip of the cloud of injected negative charge serves as a virtual cathode for the "fountain" discharge. Of course, the cathode of the electron gun where the beam originates is the real cathode for the system as a whole.

One-dimensional modeling of electron beam injection, distortion of electric field, and plasma generation

To analyze the dynamics of beam-generated plasmas, let us consider a 1D model of a non-self-sustained high-pressure gas discharge, supported by an electron beam whose relaxation length, l_r, is shorter than the interelectrode gap L (Fig.1). The foil through which the beam is injected is considered as

one of the electrodes. In reality, a metallic holder electrically insulated from the foil by dielectric seals can have a potential applied to it and serve as an electrode. In the simple 1D model, though, the holder-electrode is indistinguishable from the foil-electrode.

Of course, 1D modeling could be quite restrictive. Even if the original electron beam is unidirectional and monoenergetic, scattering inside the foil and in the dense gas could make the problem three-dimensional. The problem would be close to one-dimensional one if the injection foil is very thin, or if a differentially pumped port is used instead of a foil for beam injection. Additionally, a strong magnetic field could be used to inhibit beam and plasma expansion. Thus, the following 1D analysis could be viewed as a first approximation in the case of beam injection through a thin foil or a differentially pumped port , with a strong guiding magnetic field.

There are two groups of electrons in the system: plasma electrons, with the number density n_e, and beam electrons, with the number density n_b. The latter group is described by a simplified kinetic equation in the so-called "forward" approximation.[15] The approximation takes into account only inelastic electron-molecule collisions that are assumed not to change the direction of electron motion. This approximation is well justified in our case, since for the most relevant, ionizing, high-energy part of the degradation spectrum of the beam, inelastic cross sections considerably exceed the momentum-transfer cross section: $\sigma_k^n(\varepsilon) \gg \sigma_m(\varepsilon)$, when $\varepsilon > 1000$ eV. The subscript k denotes various chemical constituents of the gas. Thus, the contribution of elastic collisions is small and we shall neglect them, assuming that all electrons move only in the direction normal to the foil (x-direction) at a speed of $v = (2\varepsilon/m)^{1/2}$. (This expression for the velocity is valid, of course, only for nonrelativistic electrons). Then the spectral density of the electron flux, $\Gamma(\varepsilon, x)$ is determined directly by the coordinate-dependent electron energy distribution function $n(\varepsilon, x)$: $\Gamma(\varepsilon, x) = v n(\varepsilon, x)$. Making the transformation from 1D velocity distribution function ($v_x \equiv v$) to the energy distribution function, with $f(v, x)dv = n(\varepsilon, x)d\varepsilon$, we obtain the equation[14]

$$\frac{\partial \Gamma}{\partial x} - eE(x,t)\frac{\partial \Gamma}{\partial \varepsilon} = Q(\Gamma)$$
$$= -\sum_{n,k} N_k \Gamma(x,\varepsilon)\sigma_k^n(\varepsilon) + \sum_{n,k} N_k \Gamma(x,\varepsilon + I_k^n)\sigma_k^n(\varepsilon + I_k^n) \qquad (1)$$

Here, excitation of the n-th quantum state of the molecule of k-th component, requiring electron energy I_k^n, and electron-impact ionization, requiring, in the first approximation, energy equal to the ionization potential I_k, contribute to the inelastic collision term Q. $\sigma_k^n(\varepsilon)$ are the excitation and ionization (in the

[14] Yu.P.Raizer and M.N.Shneider, High Temperature **27**, 329 (1989).

case of ionization, superscript $n=i$) cross sections, and N_k is the number density of the k-th chemical component of the gas.

Total beam electron number density at a given location is:

$$n_b(x) = \int_{\min I_k}^{\infty} \frac{\Gamma(x,\varepsilon)d\varepsilon}{\sqrt{2\varepsilon/m}}. \qquad (2)$$

The net flux, that is, the net number of beam electrons passing through unit area per unit time in the x direction, is:

$$\Gamma_b(x) = \int_{\min I_k}^{\infty} \Gamma(x,\varepsilon)d\varepsilon. \qquad (3)$$

Local ionization rate, that is, the number of ionization events in 1 cm^3 per 1 second at a given location x, is:

$$q(x) = \sum_k N_k \int_{I_k}^{\infty} \Gamma(x,\varepsilon)\sigma_k^i(\varepsilon)d\varepsilon. \qquad (4)$$

In an electron-impact ionization event, a part of energy ε of the impinging electron goes into production of the secondary electron, and a part goes into kinetic energy ε' of that electron. Details of the energy spectrum of secondary electrons, described by differential ionization cross sections, and the effect of that spectrum on electron energy distribution, excitation, and ionization rates, have been studied elsewhere.[11-13, 16, 17] The nascent spectrum of secondary electrons has a sharp maximum at about 5 eV, which is substantially lower than the ionization energy, and the probability for the secondary electron to immediately ionize a molecule is quite small. [11-13, 15, 16] At pressures of hundreds of Torr, secondary electrons will rapidly lose the memory of their nascent distribution and form the energy distribution function corresponding to the local value of E/N. [11-13, 15, 16] Because of this, details of the nascent spectrum were found to be unimportant, [11-13, 15] and simply assuming that new electrons are produced with either zero energy or with a mean energy corresponding to the local plasma electron temperature, $T_e(x)$, turned out to yield reasonably accurate energy distribution functions and kinetic rates. [11-13, 15, 16] The contribution of secondary (plasma) electrons to the total ionization rate is, therefore, determined by the electron temperature, or, more exactly, by the value E/N (see Eqs. (6)-(8) below).

One of the well-known parameters of electron beam interaction with gases is the so-called ionization cost, Y_k, that is, the mean energy of production of an electron-ion pair in beam electron collisions with molecules of the k-th component. At primary electron energies above a few hundred

[15] S.Yoshida, A.V.Phelps, and L.C.Pitchford, Phys. Rev. A **27**, 2858 (1983).

[16] V.P.Konovalov and E.E.Son, Sov. Phys. Tech. Phys. **26** (3), 328 (1981).

eV, Y_k is virtually independent of the beam energy, and is determined by the gas composition only. For example, in air, pure nitrogen, and oxygen, Y_k=34 eV, 35 eV, and 30.9 eV, respectively.[1] Therefore, in the inelastic collision integral Q for fast electrons, the term corresponding to the source of electrons of energy ε due to ionization can be written approximately as:

$$\sum_k N_k \Gamma(x, \varepsilon + Y_k) \sigma_k^i (\varepsilon + Y_k), \quad \varepsilon + Y_k \leq \varepsilon_b, \text{ where } \varepsilon_b \text{ is the beam electron energy.}$$

For simplicity, we shall assume that the injected beam is monoenergetic, so that the boundary condition for the beam is:

$$\Gamma(0, \varepsilon) = \left(\left|j_b\right|/e\right) \delta(\varepsilon - \varepsilon_b), \quad\quad\quad\quad (5)$$

where j_b is the electron beam current density, and ε_b is the energy of the injected electrons. Obviously, by modifying this boundary condition, effects of injection of a beam that is not monoenergetic can be easily accounted for.

Note that the "forward" approximation for kinetic equation was used here only to shorten the computations. There are no principal difficulties, except making computations longer, in using a more complete "forward-back" approximation accounting for backscattering and elastic collisions. Importantly, integral parameters of the beam-gas interaction, such as the relaxation length, $l_r = l_r(\varepsilon_b, N(x))$, the total rate of production of electron-ion pairs, $\text{Int}_1 = \int q dx = \text{Int}_1[\varepsilon_b, j_b, N(x)]$, and the total gas heating rate, $\text{Int}_2 = \int Q_b dx = \text{Int}_2[\varepsilon_b, j_b, N(x)]$, are independent of the type of kinetic equation used.

An example of the computed relaxation of a beam with an energy $\varepsilon_b = 15$ keV injected into a room air at $p = 1$ a??, $T(x) = 300$ K = const is shown in Fig. 2.

To describe the beam-generated plasma and the discharge, we used the following set of continuity equations for plasma electrons, n_e, and positive, n_+, and negative, n_-, ions, plus the Poisson equation for the potential:

$$\frac{\partial n_e}{\partial t} + \frac{\partial \Gamma_e}{\partial x} = q + \alpha \left|\Gamma_e\right| + k_d N n_- - v_a n_e - \beta n_e n_+ - \frac{\delta n_b}{\delta t},$$

$$\Gamma_e = -\mu_e n_e E - D_e \frac{\partial n_e}{\partial x} - k_T D_e \frac{n_e}{T_e} \frac{dT_e}{dx} \quad\quad (6)$$

$$\frac{\partial n_+}{\partial t} + \frac{\partial \Gamma_+}{\partial x} = q + \alpha \left|\Gamma_e\right| - \beta_{ii} n_- n_+ - \beta n_e n_+, \quad \Gamma_+ = \mu_+ n_+ E - D_+ \frac{\partial n_+}{\partial x}, \quad\quad (7)$$

$$\frac{\partial n_-}{\partial t} + \frac{\partial \Gamma_-}{\partial x} = -k_d N n_- + v_a n_e - \beta_{ii} n_- n_+, \quad \Gamma_- = -\mu_- n_- E - D_- \frac{\partial n_-}{\partial x} \quad\quad (8)$$

$$\frac{\partial^2 \varphi}{\partial x^2} = -\frac{e}{\varepsilon_0}(n_+ - n_e - n_- - n_b), \quad E = -\frac{\partial \varphi}{\partial x}. \tag{9}$$

In Eqs. (6)-(9), q is the beam-induced ionization rate determined by Eq. (4), and $\alpha = \alpha(E/N)$ is the first Townsend ionization coefficient[18] that describes avalanching, i.e., further ionization of the background gas by secondary (plasma) electrons. An additional source term due to thermalization of beam electrons, $-\delta n_b / \delta t = -d\Gamma_b / dx$, is also included in Eq. (6). To correctly describe charge transport in regions with very low electric field, the expressions for the fluxes Γ_e, Γ_+, and Γ_- include both drift (with mobilities μ_e, μ_+, and μ_-) and diffusion (with electron, positive ion, and negative ion diffusion coefficients D_e, D_+, and D_-, respectively) terms, as in modeling the negative glow of conventional glow discharges.[19] Electron temperature and mobility were taken as functions of the local value of E/N, $T_e(E/N)$, and $\mu_e(E/N)$. These functions were taken from the tabulated results of direct solution of Boltzmann kinetic equation for air.[20] At very low E/N, $E/N < 1$ Td, where the approximation for μ_e given in Ref. 19 is not valid, we used the approximation $\mu_e(T_e) = \tilde{\mu}_e(\tilde{T}_e / T_e)^{0.5}$, where $\tilde{\mu}_e, \tilde{T}_e$ are the values at $E/N = 1$ Td. The last approximation follows from the definition of electron mobility and the approximation of energy-independent mean free path:[17] $\mu_e = \frac{e}{m v_m} \approx \frac{e l_m}{m v(T_e)}$, where v_m is the momentum-transfer collision frequency, and l_m is the mean free path of electrons. The approximate values of mobility for both positive and negative ions were taken from Ref. 17: $\mu_{+,-} = 1.75 \cdot 10^3 / (p \cdot 300/T)$ cm²/V·s, where pressure p is in Torr. The diffusion coefficients were determined from the respective mobilities using the Einstein relation: $D_e = \mu_e T_e$; $D_{+,-} = \mu_{+,-} T$.

The value of electron temperature at very low E/N, $E/N \leq 1$ Td, where the approximation for μ_e given in Ref. 19 is not valid, is expected to be quite low, 0.1 eV or lower, i.e., within a factor of 2 of gas temperature. This follows from the electron energy distributions in beam-produced plasmas without electric field. [11-13, 15, 16] Note also that the plasma in the electron beam generated "cloud" should have properties close to those of negative glow plasmas of conventional glow discharges. Electrons in negative

[17] Yu.P.Raizer, *Gas Discharge Physics* (Springer, Berlin, 1991).

[18] Yu.P.Raizer and M.N.Shneider, High Temperature **29**, 833 (1991).

[19] N.L.Alexandrov, F.I.Vysikailo, R.Sh.Islamov, I.V.Kochetov, A.P.Napartovich, and V.G.Pevgov, High Temperature, **19** (1), 17 (1981).

glow plasmas are known to have low temperatures, down to the neutral gas temperature.[21] Therefore, in our computations, we assumed that $T_e(x,t) = 2T(x,t)$ whenever E/N is of the order of 1 Td or lower.

We used standard boundary conditions at the electrodes. These conditions are commonly used to model gas discharges with cold cathodes. For example, at $x = 0$, in the absence of negative ions ($n_- = 0$),

$$\Gamma_e = -\gamma\Gamma_+; \quad \partial n_+/\partial x = 0 \text{ if } E(0,t) \leq 0 \qquad (10a)$$

$$\Gamma_+ = 0; \quad \partial n_e/\partial x = 0 \text{ if } E(0,t) > 0, \qquad (10b)$$

where γ is the effective secondary emission coefficient, that is, the average number of electrons emitted for each ion impinging on the surface.

Boundary conditions for the Poisson equation are:

$$\varphi(0) = 0, \quad \varphi(L) = V. \qquad (11)$$

Relaxation of an electron beam results in gas heating. This decreases the gas density, affecting beam-induced ionization rate and the beam penetration depth. To model processes coupled with the heating, principal mechanisms of heating and cooling have to be identified. Energy is added to the plasma by both the electron beam and Joule dissipation. A part of the added energy goes directly into heat, while some energy is spent on excitation of vibrational and electronic molecular states. What part of the Joule dissipation rate jE goes into vibrational and electronic excitation is determined by the value of E/N,[17, 19] and at $E/N = 1 - 70$ Td vibrational excitation of oxygen and nitrogen consumes about 50-90% of jE. However, in all cases computed in this paper, the rate of energy addition by the beam turned out to be more than an order of magnitude higher than the Joule dissipation rate (see below), and thus the Joule dissipation could be neglected. As to the beam energy dissipation, only about 5% of it goes into vibrational excitation of nitrogen and oxygen,[11-13] and about 30-40% of the beam energy goes into excitation of electronic states. The electronic states can be expected to quench rapidly at high pressures (hundreds of Torr). About 10-30% of the energy released in quenching can end up in vibrational modes of molecules, thus increasing the fraction of beam energy spent on vibrational excitation to perhaps 10-15%. Some of the electronic states excited by the beam are radiative, however, a 1-cm wide column of high-density gas is optically thick for many of those radiative transitions. As a result, most of the energy dissipated by the beam is spent on gas heating, and the rate of energy loss by the beam can be, with an accuracy of 10-20%, considered equal to the gas heating rate. Thus, to model gas heating, we need to add to the set of equations (6) – (9) the equation of state,

[20] J.M.Anderson, J. Appl. Phys. **31**, 511 (1960).

$$p = R\rho T = R\rho_0 T_0 = \text{const}, \tag{12}$$

and heat balance:

$$\rho c_p \frac{dT}{dt} = q_h - \Theta, \tag{13}$$

where

$$q_h = -\frac{\partial \left[\Gamma_b(x) \cdot \langle \varepsilon_b(x) \rangle \right]}{\partial x} \tag{14}$$

is the rate of gas heating by the relaxing beam,[22]

$$\langle \varepsilon_b(x) \rangle = \frac{\displaystyle\int_{\min(I_k)}^{\infty} \frac{\Gamma(x,\varepsilon)}{\sqrt{2\varepsilon/m}} \varepsilon \, d\varepsilon}{\displaystyle\int_{\min(I_k)}^{\infty} \frac{\Gamma(x,\varepsilon)}{\sqrt{2\varepsilon/m}} \, d\varepsilon} \tag{15}$$

is the mean energy of the beam electrons, and Θ is the rate of heat removal by all mechanisms (thermal diffusion, convection, etc.) combined.

Initial conditions used in the computations were: $T(x,0) = T_0 = 300$ K; $n_e(x,0) = n_+(x,0) = n_-(x,0) = 0$.

The collision cross sections necessary for calculations of electron beam propagation and beam-induced ionization rates were taken from the literature.[23, 24, 25] For charge particle kinetics in the plasma, the following set of processes and their rate coefficients was used. (In all the following expressions for rate coefficients, pressure p is in *Torr*, and temperatures T_e and T are in *K*).

Electron-ion dissociative recombination rate coefficient is:[26, 17]

$$\beta = 2 \cdot 10^{-7} (300/T_e)^{1/2}, \text{cm}^3/\text{s}.$$

[21] S.O.Macheret, M.N.Shneider, R.B.Miles, R.J.Lipinski, and G.L.Nelson, Paper AIAA-98-2922 (1998).

[22] Y.Itikawa, M.Hayashi, A.Ichimura, K.Onda, K.Sakimoto, K.Takayanagi, M.Nakamura, H.Nishimura, and T.Takayanagi, J. Phys. Chem. Ref. Data **15**, 985 (1986).

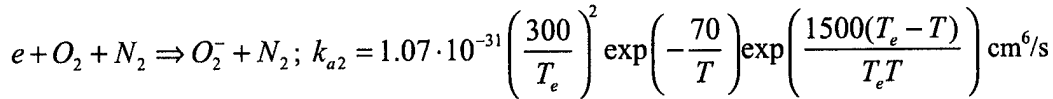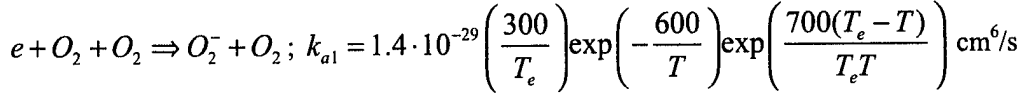[23] Y.Itikawa, M.Hayashi, A.Ichimura, K.Onda, K.Sakimoto, K.Takayanagi, Y.Hatano, M.Hayashi, H.Nishimura, and S.Tsurubuchi, J. Phys. Chem. Ref. Data **18**, 23 (1989).

[24] Y.Itikawa, Electron Collisions with N_2, O_2, and O: What We Do and Do Not Know (ISAS Research Note 526, 1993).

[25] I.A.Kossyi, A.Yu.Kostinsky, A.A.Matveyev, and V.P.Silakov, Plasma Sources Sci. Technol. **1**, 207 1992).
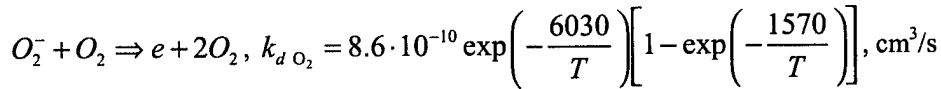
Ion-ion recombination rate coefficient (dependent on the gas density) is expressed as:[17]

$$\beta_{ii} = 1 \cdot 10^{-6}(0.5 + 1.5p/760) \cdot 300/T \text{ , cm}^3/\text{s.}$$

Three-body attachment processes and their rates are:[25]

$$e + O_2 + O_2 \Rightarrow O_2^- + O_2 \text{ ; } k_{a1} = 1.4 \cdot 10^{-29}\left(\frac{300}{T_e}\right)\exp\left(-\frac{600}{T}\right)\exp\left(\frac{700(T_e - T)}{T_e T}\right) \text{cm}^6/\text{s}$$

$$e + O_2 + N_2 \Rightarrow O_2^- + N_2 \text{ ; } k_{a2} = 1.07 \cdot 10^{-31}\left(\frac{300}{T_e}\right)^2 \exp\left(-\frac{70}{T}\right)\exp\left(\frac{1500(T_e - T)}{T_e T}\right) \text{cm}^6/\text{s}$$

Analysis shows that because of the substantial threshold energy for the dissociative attachment, $e + O_2 + 3.6 \text{ eV} \Rightarrow O + O^-$, at very low E/N typical for the plasmas that we consider, the dissociative attachment can be neglected

Thermal detachment and its rate coefficient are:[27]

$$O_2^- + O_2 \Rightarrow e + 2O_2 \text{ , } k_{d\,O_2} = 8.6 \cdot 10^{-10}\exp\left(-\frac{6030}{T}\right)\left[1 - \exp\left(-\frac{1570}{T}\right)\right] \text{, cm}^3/\text{s}$$

If active particles, such as electronically excited or radical species, are present in the plasma in large numbers, they can cause electron detachment from negative ions, e.g.

$$O_2^- + O_2(a^1\Delta_g) \Rightarrow e + 2O_2 \text{ , } k_{dA} = 2 \cdot 10^{-10} \text{ cm}^3/\text{s.}$$
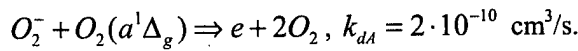
Because of these detachment processes, the detachment frequency can be generally written as: $v_d = k_{dO_2}N_{O_2} + k_{dA}N_A$, where N_{O_2} and N_A are the number densities of oxygen molecules and active (excited or radical) particles, respectively.

Results of the modeling

A. "Fountain"

Comparison of the computational results for cold ($T(x)$=300 K=const) nitrogen (Figs. 3 and 4) and air (Figs. 5, 6, and 7), with the same electron beam parameters ($j_b = 10$ mA/cm^2, $\varepsilon_b = 15$ keV) clearly demonstrates the role of electron attachment to oxygen that generates negative ions, reducing the maximum electron density at steady state.

Despite the difference between nitrogen and air, in both cases the injection of the beam leads to accumulation of negative charge and to growth of plasma conductivity. The process continues until a quasiequilibrium is reached: the charge that the beam brings in per unit time is fully balanced by the back

[26] E.M.Bazelyan and Yu.P.Raizer, *Spark Discharge* (CRC Press, Boca Raton, Florida, 1997).

flux of negative charge due to the drift of plasma electrons. The time scale of reaching the quasiequilibrium is $t \approx 0.1$ μs.

Profiles of the power deposited by electron beam, q_h, Joule dissipation due to plasma electrons, $j_e E$, and the reduced electric field, E/N, at $t= 10$ μs from the start of beam injection in the "fountain" regime in air initially at STP are shown in Fig. 7. As seen in Fig. 7, electric field in the plasma is very weak, $E/N \leq 1.5$ Td. Thus, plasma electron temperature should be close to the gas temperature, and the Joule dissipation rate is much lower than the rate of beam energy losses. According to the data of Ref. 19, at E/N=1.5 Td: $\eta_{v,N_2} < 0.05$; $\eta_{v,O_2} \approx 0.65$; where η_{v,N_2} is the fraction of the Joule dissipation spent on excitation of N_2 vibrational mode, and η_{v,O_2} is the same for the O_2 vibrational mode. Thus, although about two thirds of the Joule dissipation goes into vibrational excitation, the Joule dissipation itself is only a small part of the energy addition rate (upper plot in Fig. 7), which justifies disregard of vibrational excitation in the energy balance.

Calculations were also performed for air heated to T=2000 K, by postulating a model temperature profile shown in the caption to Fig. 8 (the temperature was uncoupled from beam and plasma equations). At this temperature and p=1 atm, the electron attachment frequency is $v_a \approx 4.37 \cdot 10^6$ s^{-1}, and the detachment frequency is $k_d N_{O_2} \approx 1.93 \cdot 10^7$ s^{-1}, so that the attachment is fully balanced by detachment, and electron number density of $n_e \approx 10^{13}$ cm^{-3} is achieved in air with relatively low electron beam current (Figs. 8 and 9).

Ionization and gas heating rates increase with the beam current density. Heating of the gas leads to its expansion and density reduction. This increases the beam relaxation length, so that the beam ionizes and heats the gas farther from the injection foil, burning its way through the gas. This is demonstrated in Figs. 10 and 11 for the beam with $j_b = 50$ mA/cm^2 and $\varepsilon_b = 15$ keV. These calculations were coupled with a heat balance equation. For the short time after the start of the process, t<1 ms, heat conduction losses are negligible. The characteristic time τ of the onset of natural convection can be estimated from the simple equation $g\tau^2/2 \approx h$, where h is the length scale of thermal nonuniformity, and g is the acceleration of gravity. Even with $h \approx 1$ mm, the onset of natural convection would take $\tau \square 10$ ms. Another well known mechanism of cooling hot channels is turbulent mixing. When heating of the channel ceases, which is the case, for example, in lightning channels, cold surrounding air moves into the channels, and the fast turbulent cooling ensues. In our case, though, heating continues inside the channel, causing temperature increase and gas expansion, so that the cold surrounding gas cannot move into the channel, thus preventing the onset of turbulent cooling. Thus, the calculations at t<1 ms can be done neglecting

352

heat transfer. As seen from Fig. 10a, by the time $t \approx 300~\mu s$ the electron density reaches $10^{13}~cm^{-3}$. Maximum gas temperature at this moment is $T \approx 700$ K (Fig. 10d). As shown in Fig. 12, electric field in this regime is very weak, with E/N of less than 1.5 Td. Thus, plasma electron temperature should be low, close to the gas temperature, and the Joule dissipation rate is much lower than the rate of beam energy losses (upper plot in Fig. 12), thus justifying disregard of vibrational excitation in the energy balance.

With increasing energy of electrons in the beam, both their penetration depth and the magnitude of negative charge accumulated in the gas grow. However, this does not result in qualitative changes, unless the electric field in non-ionized part of the volume reaches a threshold for breakdown.

B. "Thunderstorm"

Suppose that a high positive voltage is applied to the anode, and the beam relaxation length is shorter than the distance to the anode. Then, even if the potential at the tip of beam-produced plasma column were equal to that of the injection foil, the electric field between the plasma column and the anode is stronger than the field prior to beam injection. This stronger field can cause a breakdown between the tip of the plasma and the anode. Additionally, negative charge brought in by the beam distorts the distribution of electric potential, resulting in an increase of electric field between the plasma and the anode, and increasing chances for breakdown (see Fig.1). Whether the breakdown will be of Townsend or streamer type, depends on gas pressure and the spacing between the plasma and the anode, $d = L - l_r$. Townsend mechanism of electric breakdown is known to occur typically at $pd < 200$ Torr·cm, while at $pd > 10^3$ Torr·cm streamer mechanism takes over.[17, 26]

Time required to reach the breakdown field E_{br} can be estimated from the equation:

$$\frac{V_a}{L - l_r} + \frac{\left[j_b - j_e(t) \right]t}{2\varepsilon_0} = E_{br} \qquad (16)$$

Clearly, increasing the anode voltage V_a and making the beam relaxation length close to the distance to the anode helps the breakdown. The second term in the left-hand side of Eq. (16) is negative charge at the tip of beam-generated plasma column. Higher beam currents shorten the time t needed to reach breakdown. The return current of plasma electrons to the cathode (foil), $j_e(t)$, slows down the accumulation of negative charge at the tip of the plasma column, and under some conditions can prevent the breakdown. In other words, if a "fountain" develops rapidly, a "thunderstorm" is prevented. In this paper, we present results of one computed "thunderstorm" case. More detailed analysis, including regimes transitional between the "fountain" and the "thunderstorm", are to be performed in future.

An example of the "thunderstorm" regime is shown in Figs. 13 and 14. The calculations were done for the following set of parameters: j_b = 50 mA/cm^2, ε_b = 15 keV; L=1.75 cm, and $V(L)$=10 kV. As seen in Fig. 13, it takes t=7 ns for the electric field between the plasma and the anode to reach about 17 kV/cm, which is higher than 50% of the breakdown field in atmospheric air.[17] One-dimensional modeling is certainly not adequate for analysis of streamer development.[26] Indeed, the very reason for streamer breakdown in electric fields weaker than the critical breakdown field is that near the tip of the streamer the electric field is amplified because of the electrostatic polarization and the tip curvature.[13] The curvature radius is obviously very important for the streamer initiation and growth. Leaving the task of developing a more comprehensive model of the "thunderstorm" for the future, we can for now use a "rule of thumb" that the electric field is typically amplified by a factor of 2-3 because of the curvature. Therefore, exceeding an electric field of 15 kV/cm in 1D model, as shown in Fig. 13, would mean that the actual field at the tip would exceed 30 kV/cm, starting a streamer.

The behavior of the return current of plasma electrons, j_e (the middle plot in Fig. 14), is explained by the evolution of electric potential and field strength (the middle and the bottom plots in Fig. 13). Initially, potential throughout the gap is higher than the potential at the injection foil, and plasma electrons drift towards the anode rather than back to the foil. As the beam brings more negative space charge, the magnitude of the negative electric field in the plasma is reduced, while the field is amplified in front of the plasma tip. However, it would take almost 9 ns for the potential anywhere inside the gap to become negative, and for the field near the foil to reverse its direction, at which moment there exists a plasma cathode inside the gap and two anodes, the foil and the "original" anode. As seen in Fig. 14, even at t=9 ns the return current at the foil does not fully balance the beam current. Since the breakdown criterion is reached between 5 and 7 ns, the return current does not even start until the streamer onset, and in this case, $j_e = 0$ in Eq. (18). Since in this paper, we only predict the onset of breakdown without modeling the subsequent dynamics of the streamer, it is difficult to say what role, if any, the return current might play in the streamer development. Also, with set of parameters other than that in the present case, the return current could have been more significant. For example, lower initial anode voltage would have required more time to reach the breakdown field, and during that time, electric field could have reversed its direction, thus creating the return current and affecting the breakdown criterion (18).

Note that the main requirement for electron beams injected from the cathode to the anode in high-power lasers and fast switches is to provide a uniform ionization throughout the volume. If, however, the energy of beam electrons is not high enough, so that $l_r < L$, the plasma becomes non-uniform, and electric field is distorted, resulting in some cases in sparking near the anode. This breakdown instability

was experimentally observed.[6, 28] Since the instability is related to parameters of the injected beam, it has been dubbed an "injection instability".[1, 6, 27]

It is interesting to note that the electric current in the "thunderstorm" streamer is fully controlled by the current of the electron beam. Since the latter is, or can be made, quite low, Joule heating in the streamer can be weak, so that the streamer may not develop into a hot channel similar to lightning. In other words, a "cold thunderstorm" appears possible with electron beams.

Power requirements for plasma generation

The present simplified 1D model cannot fully describe the process of establishment of steady state, including heat transfer. Nevertheless, estimates of power requirements for plasma generation and of the necessary cooling rate can be done for a given temperature and pressure.

For example, suppose that the gas temperature is maintained at T=2000 K, and that an electron beam generates a plasma with $n_e \approx n_+ \approx 10^{13}$ cm^{-3}. If the recombination rate coefficient is about $\beta \approx 10^{-7}$ cm$^3/s$, then the required ionization rate is $q = \beta n_e^2 \approx 10^{19}$ cm^{-3}s^{-1}. The power needed to sustain the ionization is then $q_h = q Y_i e \approx 55$ W/cm^3, which also represents the gas heating rate. Since the ionization rate averaged over the beam relaxation length is $q = \dfrac{j_b \varepsilon_b}{e l_r Y_i}$, and the relaxation length is inversely proportional to the gas density, $l_r \approx l_r^0 N_0 / N \approx l_r^0 T / T_0$, we find the required beam current density: $j_b \approx \dfrac{e q l_r^0 Y_i T}{\varepsilon_b T_0}$. For example, for $\varepsilon_b = 15$ keV we get $j_b \approx 23$ mA/cm^2. These estimates agree well with the calculations depicted in Fig. 8 that show that the power required to sustain 1 cm^3 of plasma with electron density of about 10^{13} cm^{-3} is on the order of 100 W. Increasing the energy of beam electrons moves the ionization peak farther from the injection point, but the width of the peak region does not change much, still being a few centimeters. If a wider region of high electron density is desired, one way to achieve it is to use a beam with some spread of electron energies which translates to a spread of penetration depths. Note also that the power requirement of about 50-100 W/cm^3 does not include a significant energy loss in the beam injection foil. In a typical metallic foil, electron lose about 10-50 keV. Thus, the full cost of sustaining the plasma region with 10^{13} electrons/cm^3 could be a few times higher than the 50-100 W/cm^3 required for ionization.

A temperature of 2000 K virtually eliminated electron attachment, reducing the energy cost to that needed to balance the dissociative recombination. This temperature, however, does not need to be

---

[27] G.A.Mesyats, Sov. Tech. Phys. Letters **1**, 292 (1975).

artificially maintained by a heater, since the heating rate provided by the ionizing beam is high enough. Moreover, a substantial cooling is required to keep temperature from increasing above the 2000 K. A crude estimate of the cooling requirements can be done for convective cooling where heat is removed with the flow. The effective frequency of heat removal is roughly $v_u = 2u/D$, where u is the gas velocity, and D is the length of hot region. At steady state, $\rho c_p (T - T_0) v_u = Q_h$. From this simple formula, to sustain a temperature differential of $T - T_0 = 1700$ K in a 10-cm long (D=0.1 m) gas layer near the surface at the heating rate $q_h \approx 100$ W/cm^3, flow velocity should be about 15 m/s. If the plasma length along the flow is 1 m, then a 150 m/s flow will keep the temperature from increasing above the 2000 K limit.

Concluding remarks

Electron beams represent perhaps the most energy-efficient way to ionize gases at relatively low temperatures, when thermal ionization is negligible. Injecting beams of appropriate energy and current density, stable and controlled plasmas with high electron number density can be created in high-pressure gases. It turns out that dynamics of electron beam generated plasmas, when the beam relaxation length is shorter than the distance to the anode or other metallic objects, is quite interesting. In this paper, we pointed out and analyzed two distinct regimes of beam-produced plasmas: a "fountain" and a "thunderstorm". The two regimes differ in the way the negative space charge brought in by the beam is removed: by the return current of plasma electrons to the injection foil ("fountain") or by streamer breakdown ("thunderstorm"). It is interesting to note that the "fountain" regime is, in a sense, similar to the so-called negative glow part of glow discharge,[5, 12] where high-energy electrons arriving from the cathode sheath generate very efficient ionization, although the "fountain" has much larger spatial dimensions than those of negative glow at high gas density.

In our modeling, we considered an idealized one-dimensional problem. As discussed in Section II, 1D analysis can be viewed as a first approximation if the beam is injected through either a very thin foil or a differentially pumped port, and if a strong magnetic field is used for guiding and confining the beam and the plasma. Additionally, our analysis was limited to beams that are originally monoenergetic. By modifying the boundary condition (5), energy spread of the injected beam can be easily accounted for.

In two and three dimensions, the dynamics of both "fountain" and "thunderstorm" discharges may be quite interesting. As was already mentioned, a "thunderstorm", that is, a breakdown between the negatively charged cloud and the anode, could occur at a substantially lower anode voltage than that expected from 1D modeling. The effect is due to electric field amplification at the tip of the plasma column, similar to conventional streamers.[26] In principle, a streamer breakdown, or a "thunderstorm", is

also possible between different plasma clouds created by different electron beams, since the clouds may have different electric potentials. This breakdown will be facilitated by photoionization of gas between the clouds.

In the "fountain" regime, one consequence of the non-one-dimensionality of the problem is that electric field in and around the plasma column has not only axial, but also a radial component. Plasma electrons not only drift towards the foil, but also move outside the column, making the comparison with fountain even stronger. This electron motion decreases electric field in the plasma. Additionally, when electrons move from the heated plasma column to cold peripheral regions, they will rapidly attach to oxygen, forming a layer of ion-ion plasma around the heated electron-ion plasma column.

The "fountain" regime could be subject to various oscillations and instabilities. For example, perturbations of the plasma boundary could create local curved regions where electric field amplification would be strong enough to result in streamers.

Another group of phenomena could result from the effect of electron beam burning its way through the gas, as discussed earlier in this paper. Gas heating produced by the electron beam results in density decrease, allowing the beam to penetrate deeper. New portions of the gas are then heated, and the beam can penetrate still farther. In the case computed in this paper, portions of the gas left behind continue to be heated, preventing the surrounding cold gas from moving into the channel. If, however, the heating stops, so that the channel begins to cool, a radial flow of cold gas from peripheral to the central regions would start. This may eventually result in turbulence generation, oscillations of the beam penetration depth and of the local ionization fraction. Phenomena as complex as these certainly call for a more sophisticated 2D or 3D model to be developed in future.
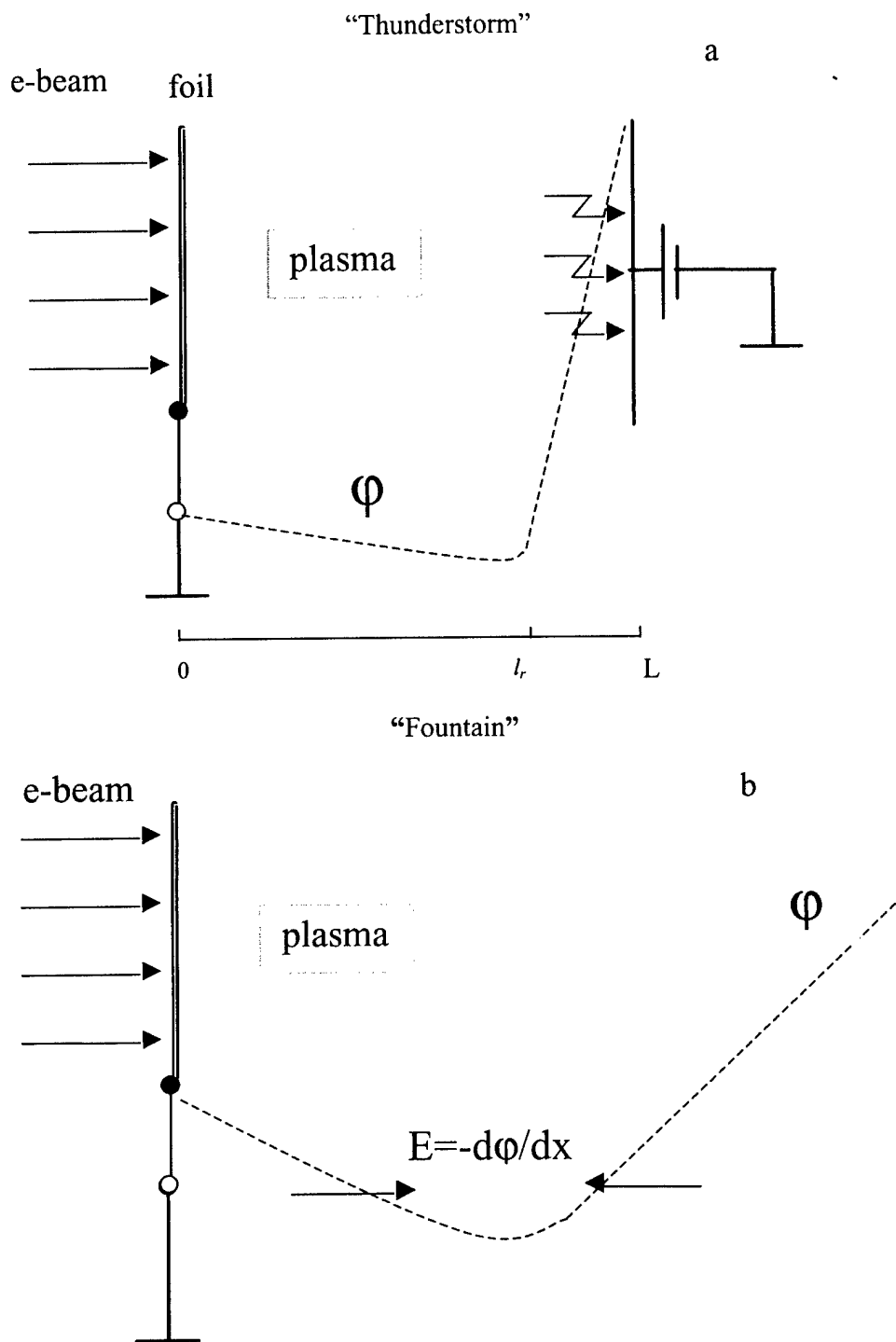
Fig.1. Schematic of "fountain" and "thunderstorm" regimes. The electron beam is injected through into the gas from left to right. φ is the electric potential, and E is the field.
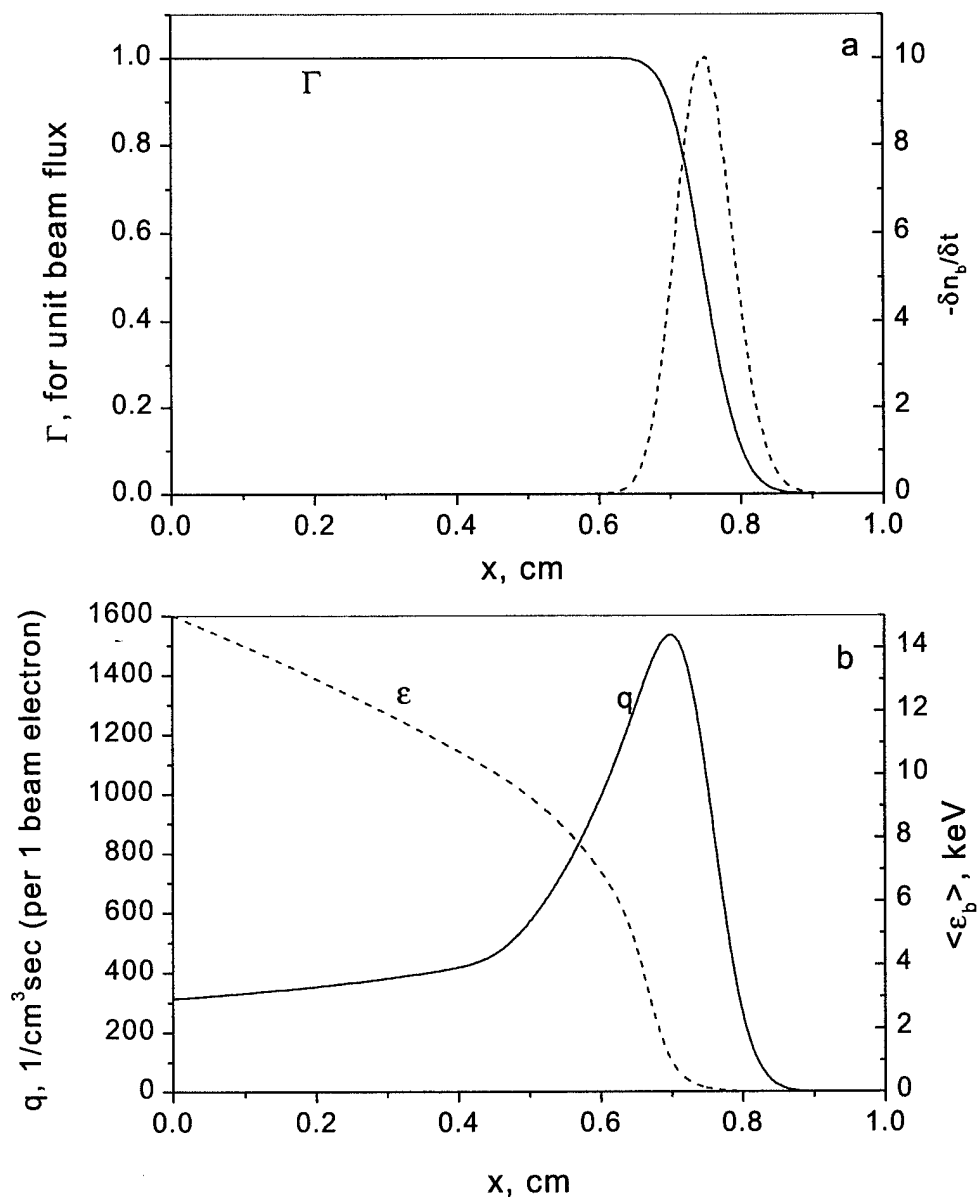
Fig.2. Computed steady-state relaxation of an electron beam injected parallel to the x coordinate at $x=0$ into room-temperature air at p=1 atm. Beam energy is $\varepsilon_b = 15$ keV. a – flux of beam electrons, Γ, and beam thermalization rate, $\delta n / \delta t = d\Gamma / dx$; b – mean electron energy, $< \varepsilon >$, and ionization rate, q.

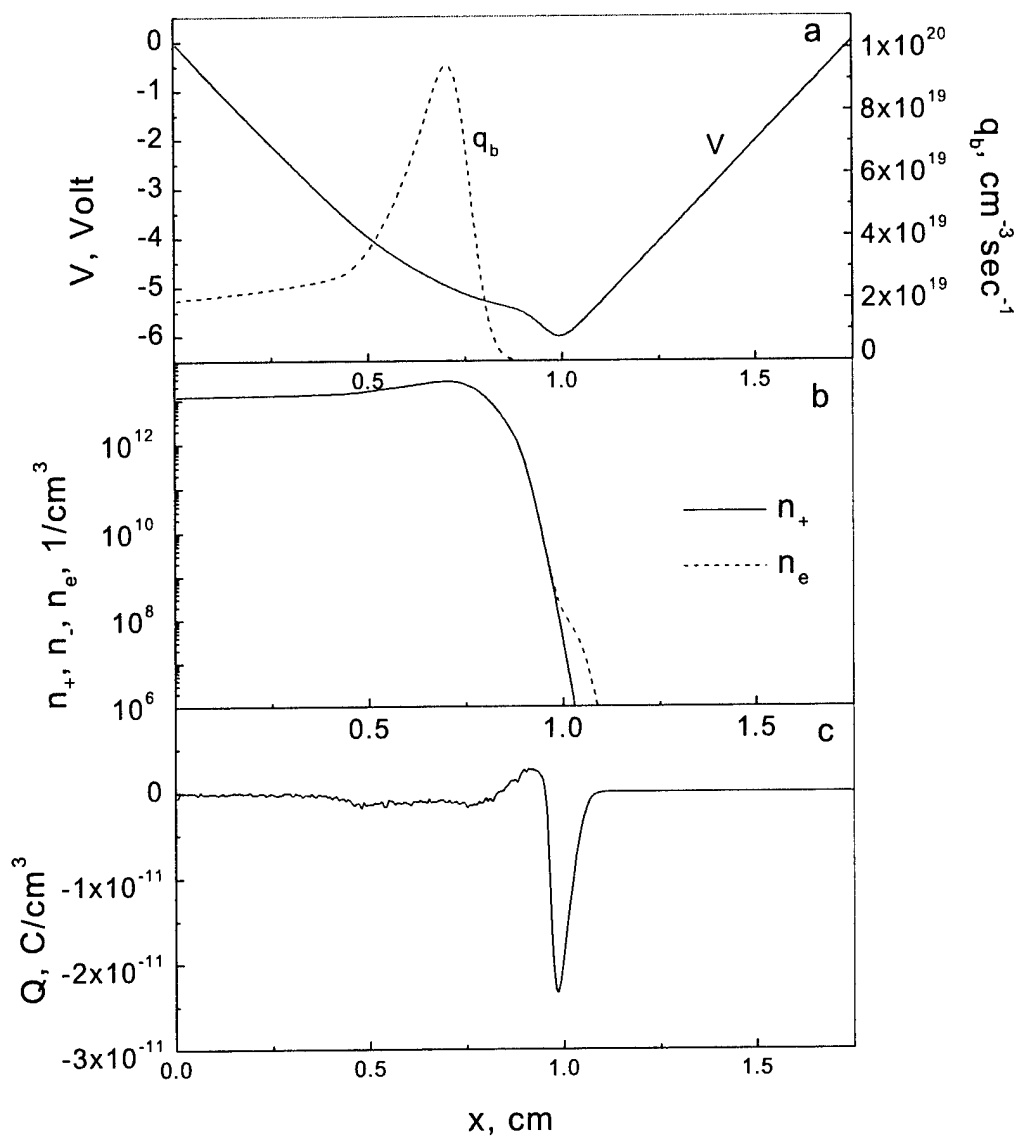**Fig.3.** Computed quasi-steady-state (t= 10 μs from the start of beam injection) profiles of plasma parameters along x coordinate in the "fountain" regime in room-temperature nitrogen at p=1 atm. Electron beam current density is 10 mA/cm^2, and the energy of beam electrons is ε_b =15 keV. (?) – electric potential, V, and ionization rate, q$_b$; (b) – electron and ion number densities; (e) – electric charge density, Q.
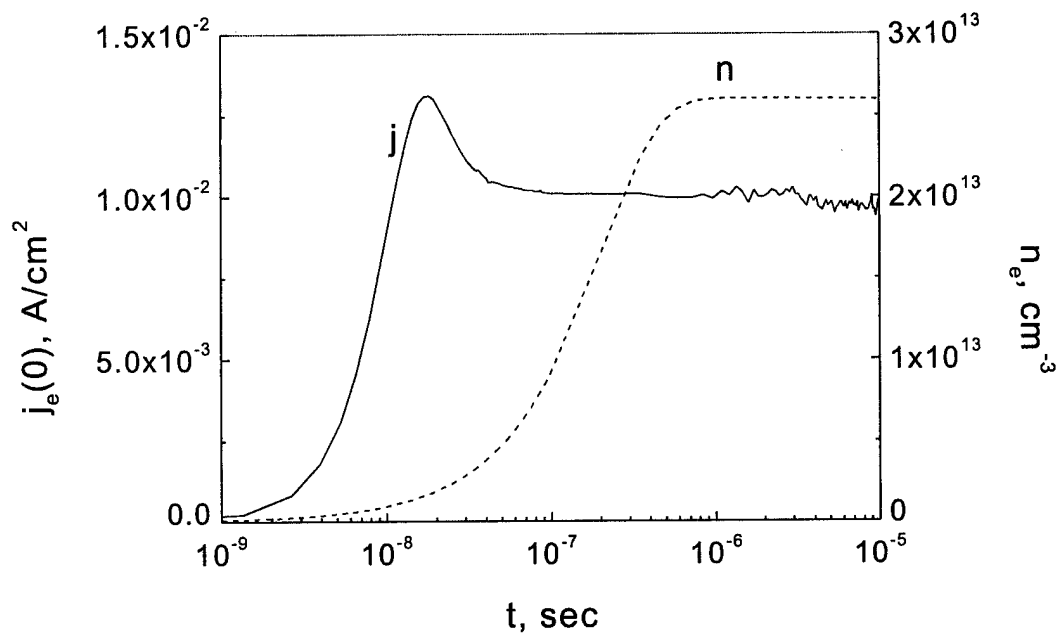
Fig.4. Back current of plasma electrons to the foil, $j_e(0)$, and peak electron density in the plasma, n_e, versus time from the start of beam injection in the "fountain" regime. The gas and beam parameters are the same as in Fig.3.
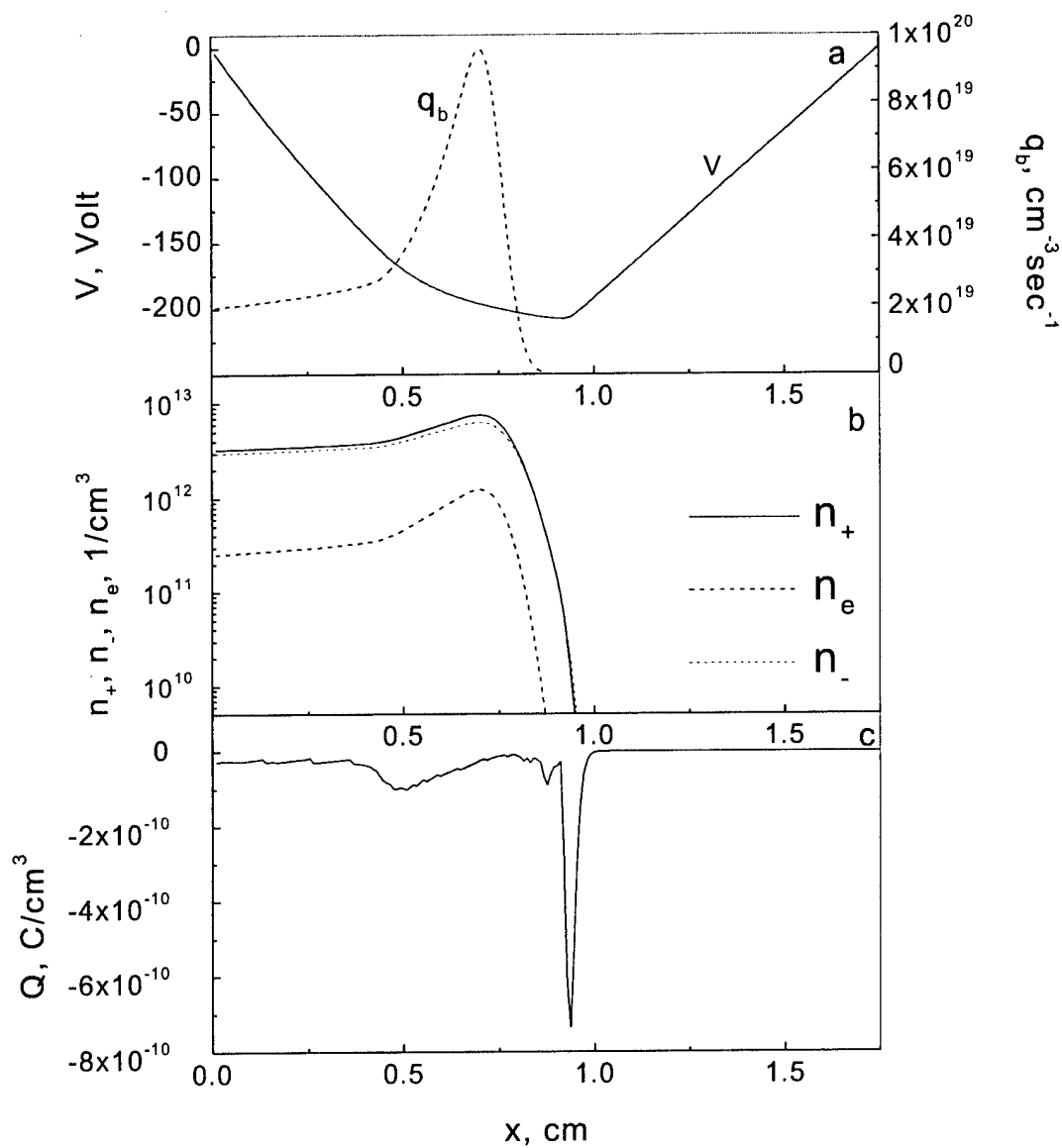
Fig.5. Computed quasi-steady-state ($t=10$ μs from the start of beam injection) profiles of plasma parameters along the x coordinate in the "fountain" regime in air at STP. Electron beam current density is 10 mA/cm^2, and the energy of beam electrons is $\varepsilon_b = 15$ keV. (?) – electric potential, V, and ionization rate, q_b; (b) – electron and ion number densities; (e) – electric charge density, Q.
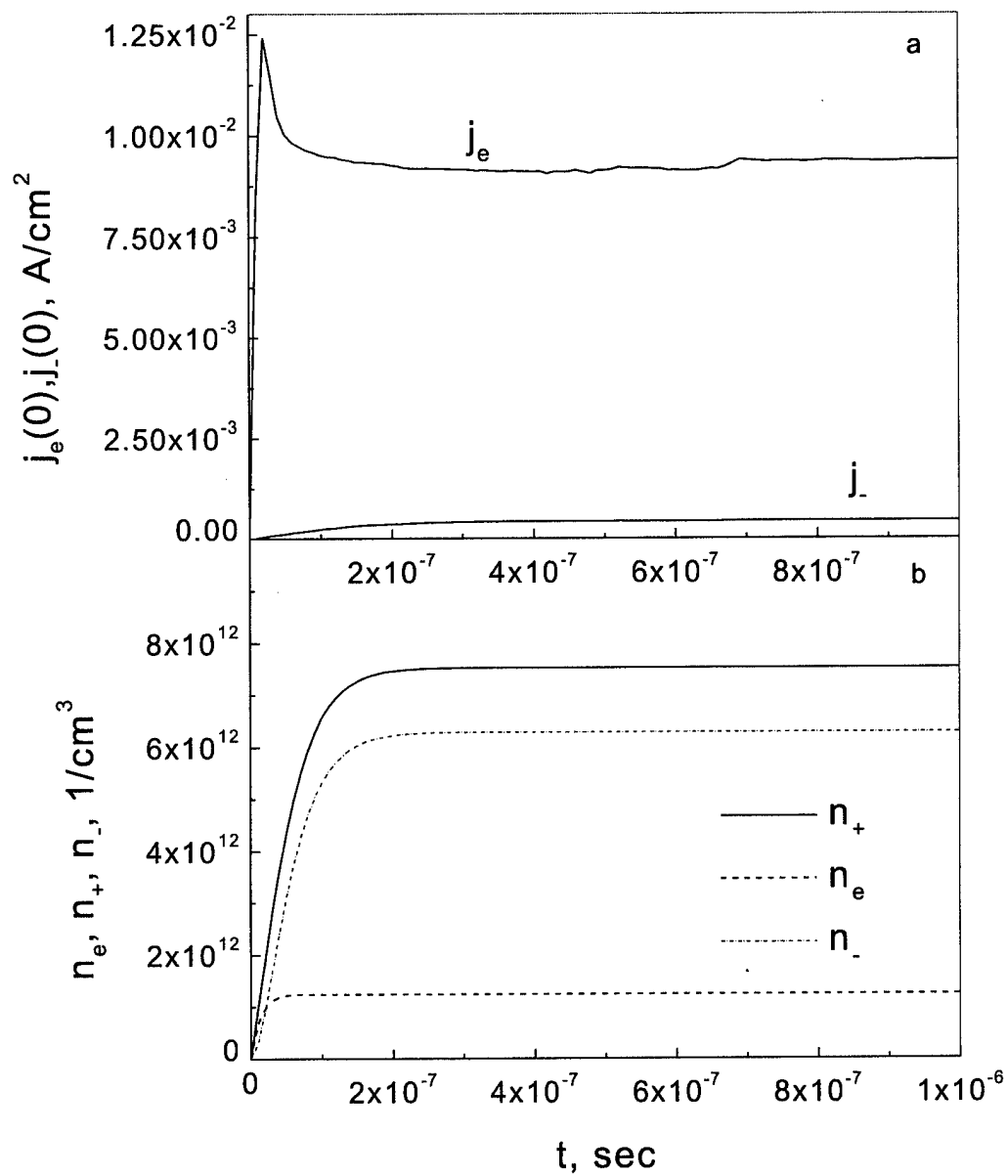
Fig.6. Back current of plasma electrons to the foil, $j_e(0)$, and peak electron and positive and negative ion densities in the plasma, n_e, n_+, and n_-, versus time from the start of beam injection in the "fountain" regime. The gas and electron beam parameters are the same as in Fig.5.
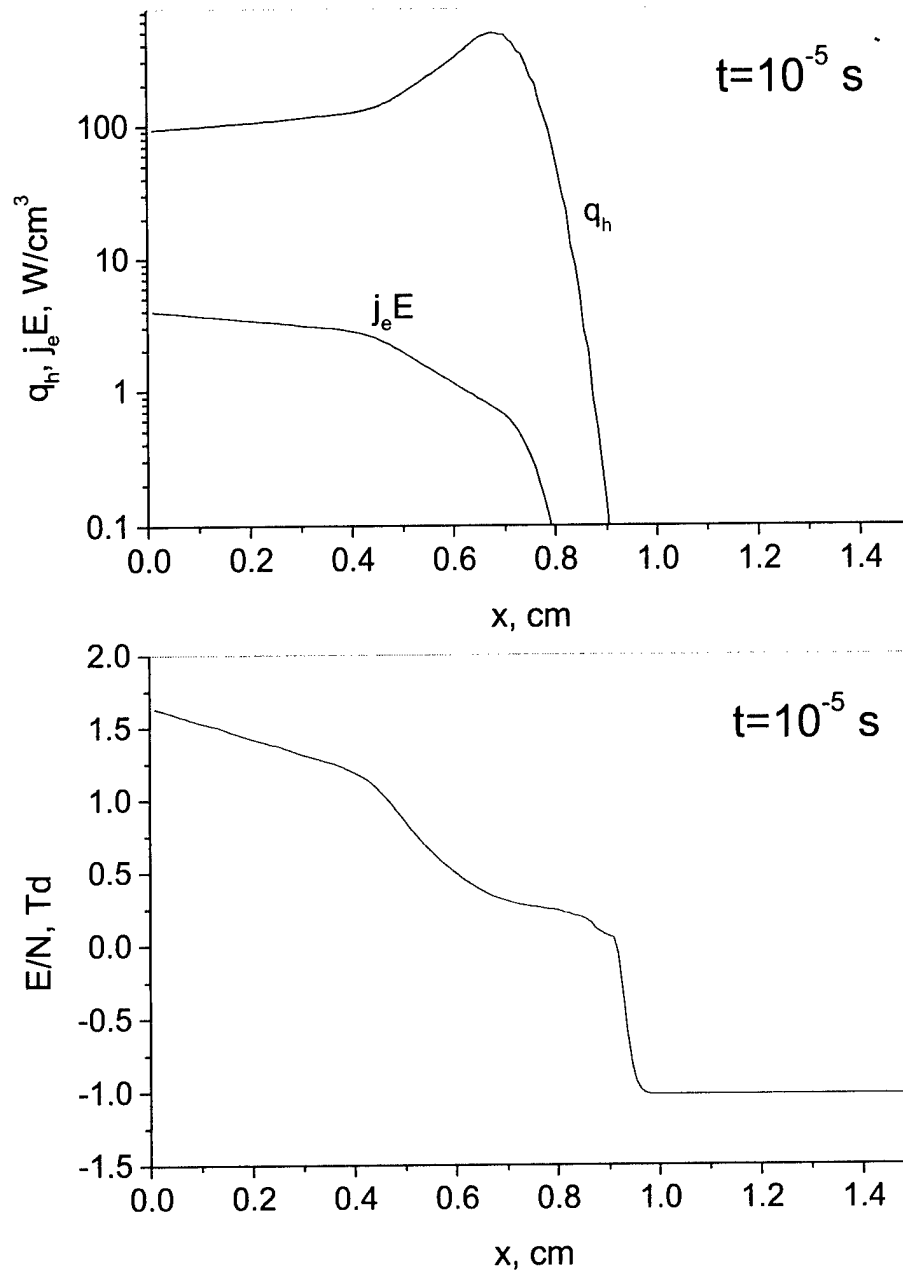
Fig.7. Profiles of the power deposited by electron beam, q_h, Joule dissipation due to plasma electrons, $j_e E$, and the reduced electric field, E/N, at $t= 10$ μs from the start of beam injection in the "fountain" regime in air at STP. Beam parameters are the same as in Fig.5.
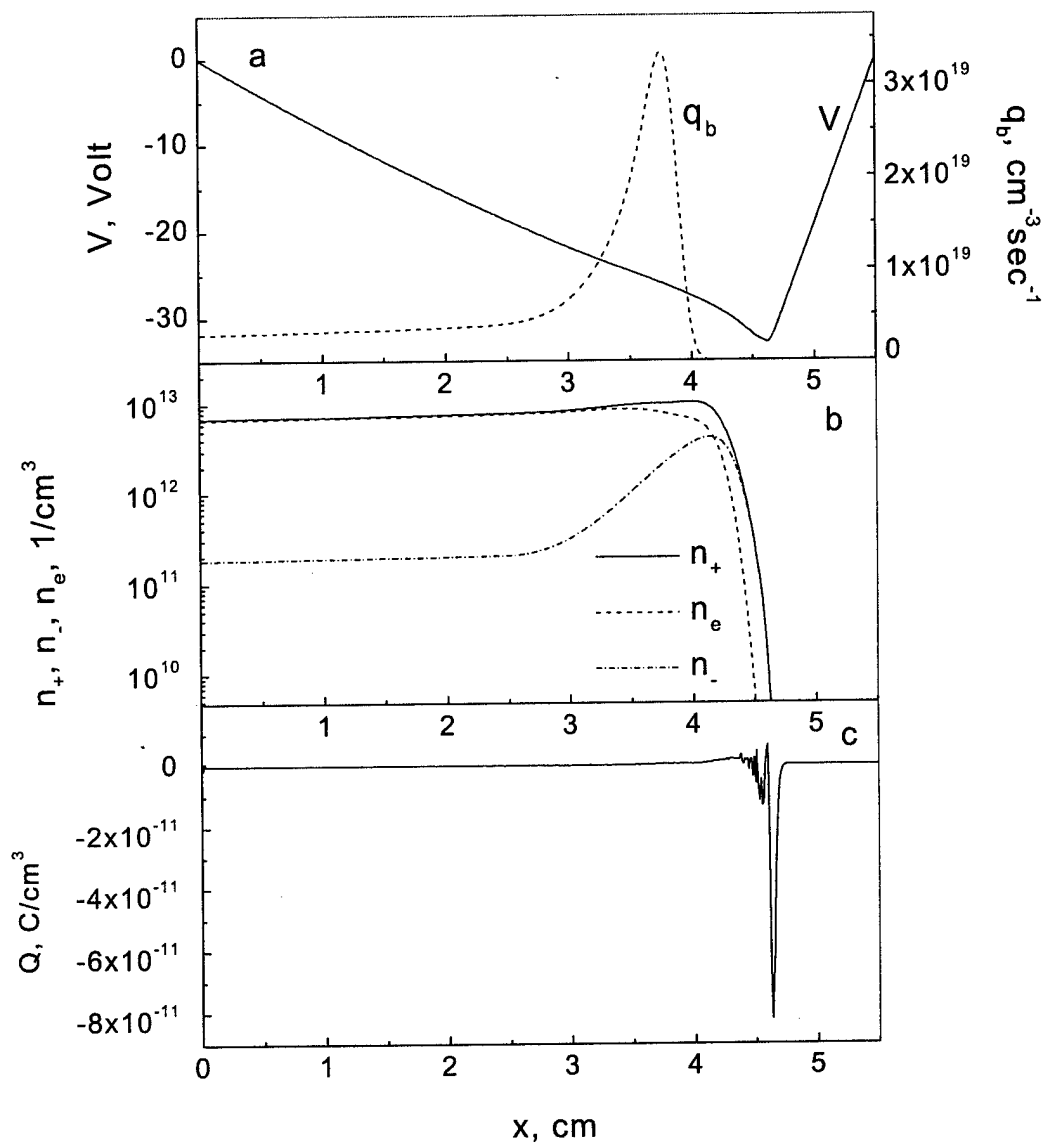
Fig.8. Computed quasi-steady-state ($t=$ 20 μs from the start of beam injection) profiles of plasma parameters along x coordinate in the "fountain" regime in air at $p=1$ atm. Electron beam current density is 10 mA/cm^2, and the energy of beam electrons is $\varepsilon_b = 15$ keV. The temperature profile is

$$T(x) = \begin{cases} 2000 \text{ K}, x < 3 \text{ cm} \\ 1700\exp(-((x-3)/1.5)^2) + 300 \text{ K}, x \geq 3 \text{ cm} \end{cases}$$

(?) – electric potential, V, and ionization rate, q_b; (b) – electron and ion number densities; (e) – electric charge density, Q.
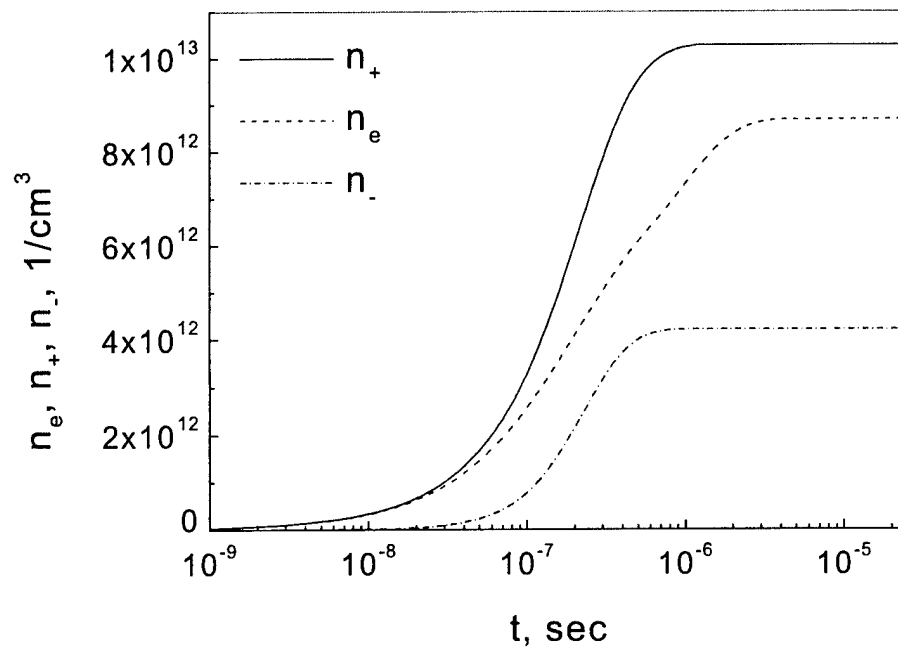
365

Fig.9. Peak number densities of electrons, n_e, positive, n_+, and negative, n_-, ions versus time from the start of beam injection in air. All parameters, including temperature profile, are the same as in Fig.8.
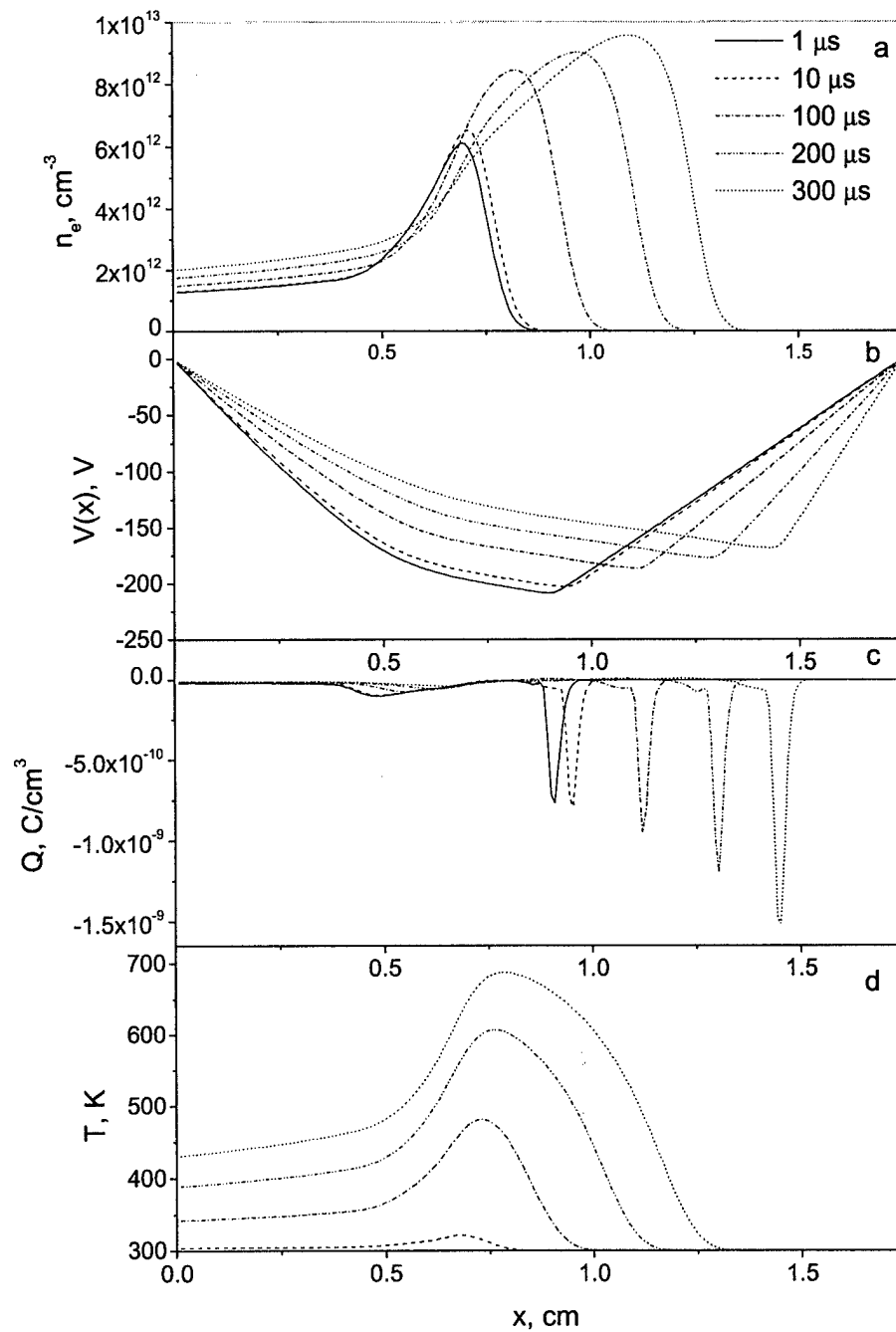
Fig.10. Time evolution of profiles of plasma parameters in the "fountain" regime in air initially at STP. Electron beam current density is 50 mA/cm², and the energy of beam electrons is $\varepsilon_b = 15$ keV. (?) – electron number density; (b) – electric potential; (c) – electric charge, Q; (d) – gas temperature.
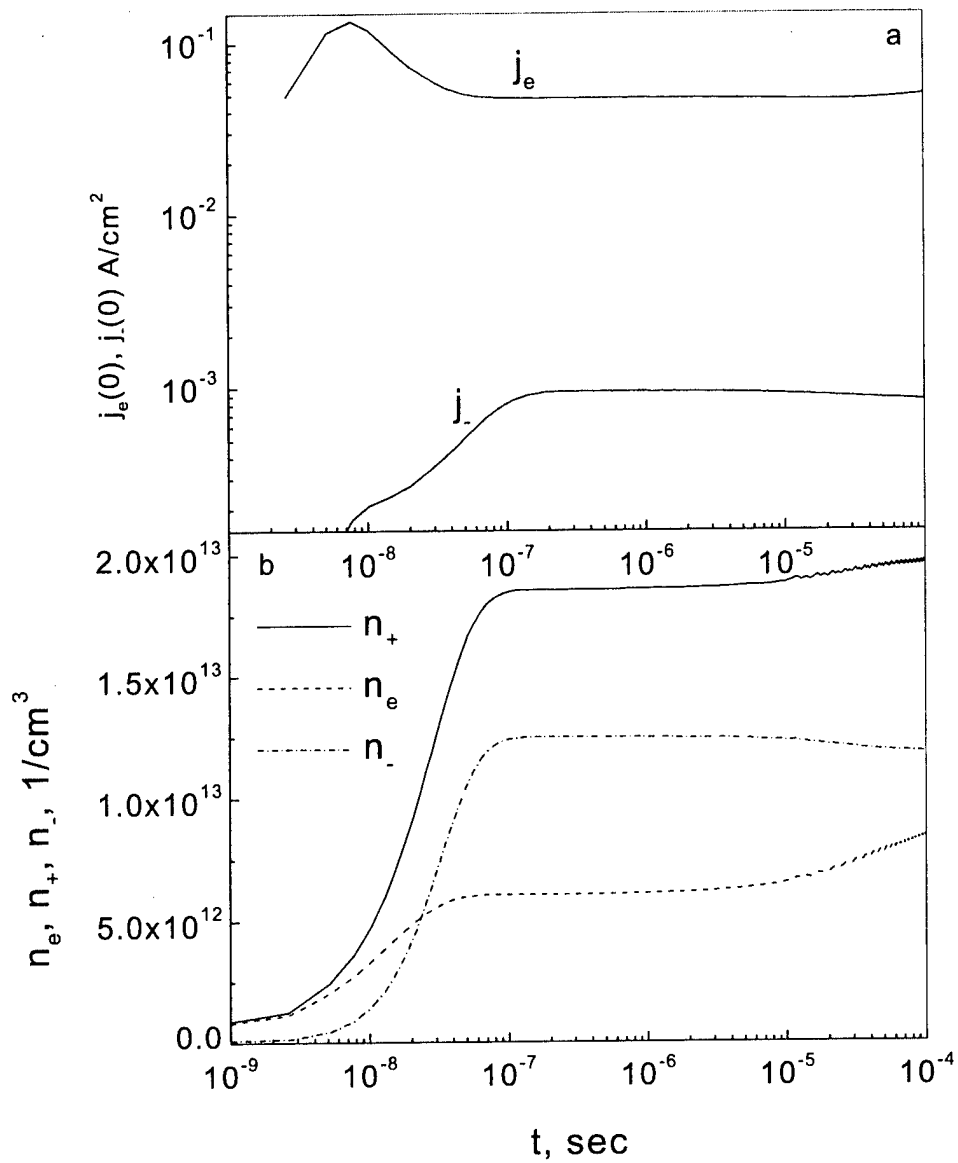
Fig.11. (a) Back current of plasma electrons, $j_e(0)$, and negative ions, $j_-(0)$, to the foil, and (b) peak electron and positive and negative ion densities in the plasma, n_e, n_+, and n_-, versus time from the start of beam injection in the "fountain" regime. The gas and electron beam parameters are the same as in Fig.10.
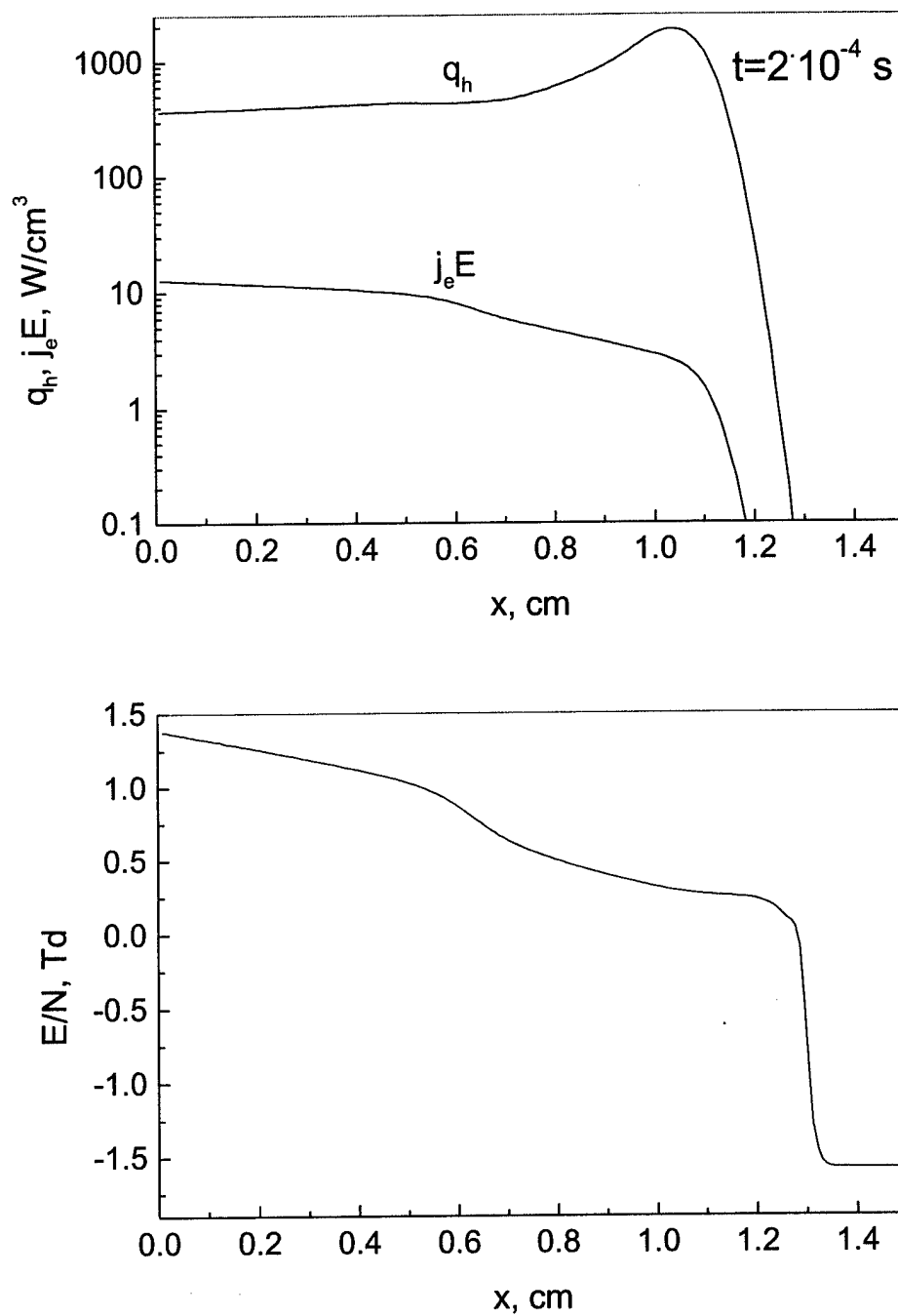
Fig.12. Profiles of the power deposited by electron beam, q_h, Joule dissipation due to plasma electrons, $j_e E$, and the reduced electric field, E/N, at t= 200 μs from the start of beam injection in the "fountain" regime in air at STP. Beam parameters are the same as in Fig.10.
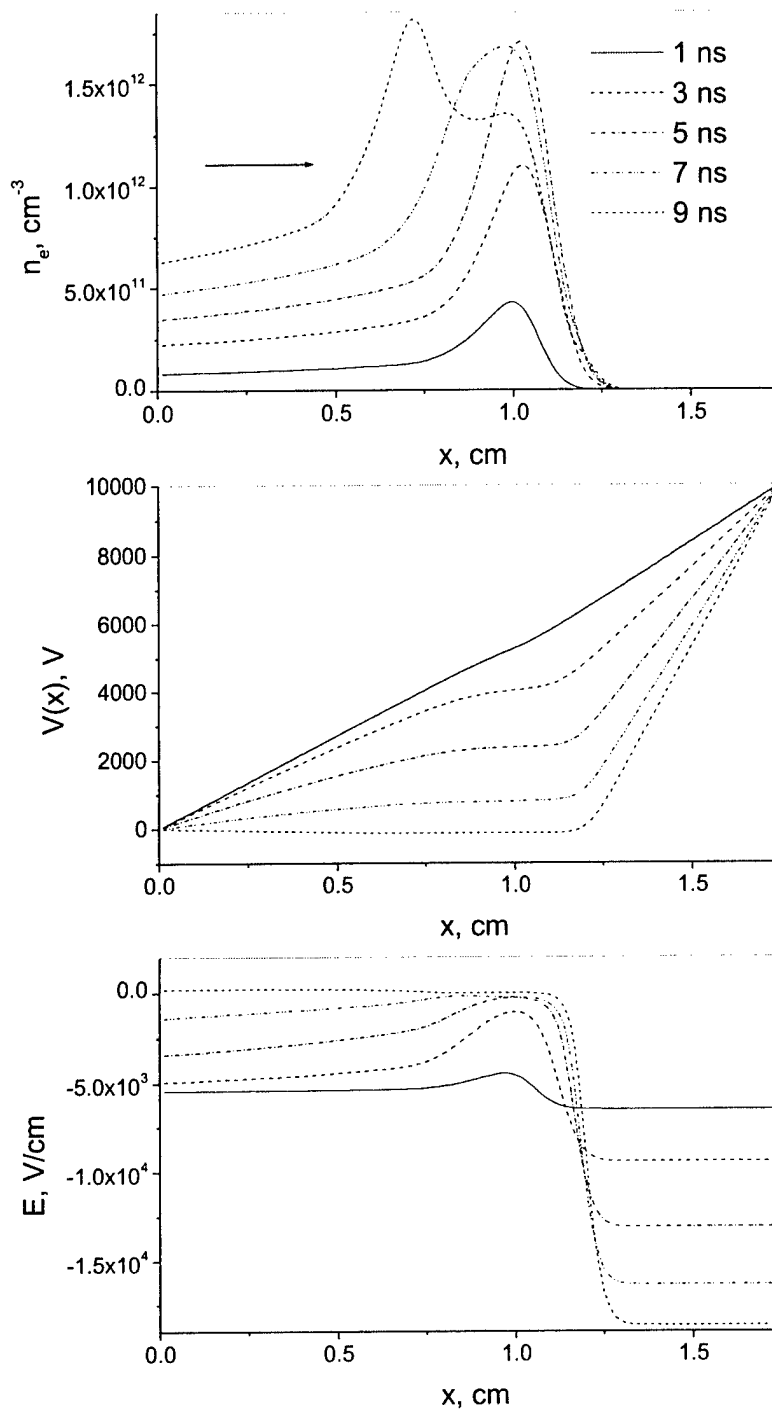
Fig.13. Time evolution of profiles of electron number density, n_e, electric potential, $V(x)$, and electric field, E, in the "thunderstorm" regime in air initially at STP. Electron beam current density is 50 mA/cm², and the energy of beam electrons is $\varepsilon_b = 15$ keV.
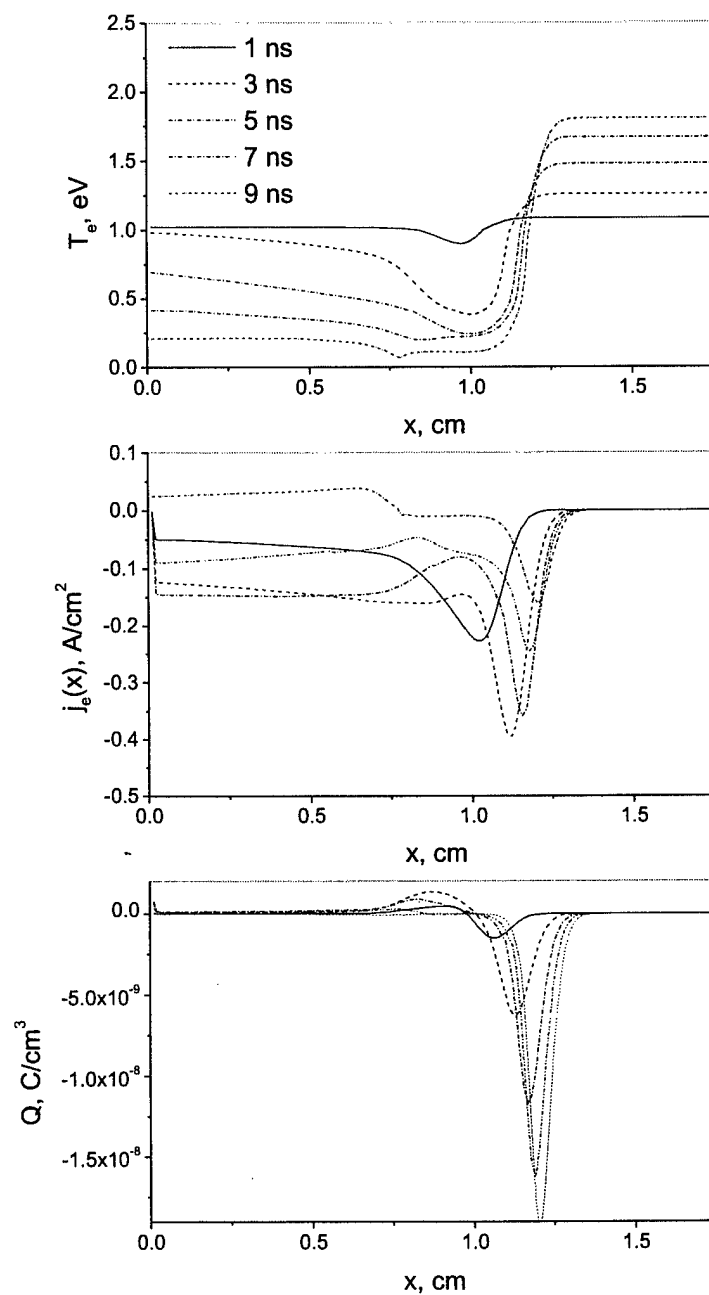
Fig.14. Time evolution of profiles of electron temperature, T_e, current density of plasma electrons, $j_e(x)$, and space charge density, Q, in the "thunderstorm" regime in air initially at STP. Electron beam current density is 50 mA/cm^2, and the energy of beam electrons is $\varepsilon_b = 15$ keV.

22. DEVELOPMENT OF NEW ELECTRON BEAM WINDOW AND ARRAY TECHNOLOGIES

J. Fox, J. Kline, R. Murray, S. Macheret, and R. Miles

Earlier, we have demonstrated that high-energy electron beams represent the most efficient source of nonequilibrium ionization. We have developed sophisticated models that allowed us to run simulations of electron beam generated plasmas. These plasmas are fully controllable, stable, and scalable to high volumes, while operating at power budgets of about 50-70 W/cm^3 for electron density of 10^{13} cm^{-3} in 1 atm, 2000 K air.

Electron beams are generated in vacuum, and then injected into the air. The transmission windows have to be thin enough to minimize beam energy losses and scattering. On the other hand, these windows must possess an adequate mechanical and thermal strength. Window technology is critical for implementation of electron beam sustained plasmas.

Princeton University, in collaboration with RSI, Inc., is developing a novel technology of thin large-area silicon nitride windows. A 100 element, 2.4 cm × 6.4 cm array of thin SiN windows etched on a silicon wafer, supported by a steel grid, was made and successfully tested. Each window is 500 nm thick and has 1 mm × 5 mm size.

Fig. 1 is a photograph of the SiN window array. The advantage of these thin non-metallic windows is that electron beam energy loss is minimal, about 2 keV, so that atmospheric plasmas can be formed with 30 keV electron beams. This relatively low beam energy minimizes X-ray generation, thus substantially increasing safety. Fig. 2 shows helium plasma at 250 Torr generated by 25 keV electron beam passing through the SiN window array. Fig. 3 shows a preliminary test in air at 1 atm. To minimize scattering, magnetic coils will be wrapped around electron guns.

Beam-generated plasmas will then be experimentally studied, and results compared with our theoretical predictions. It is planned that the new windows will be used in the definitive OSU/Princeton experiments. Additionally, in collaboration with Sandia National Laboratories, a controllable multi-element electron beam array is being developed. Its essential feature is a multi-element BaCaO cathode with separate bias control. This permits beams with controlled temporal and spatial variation. The beams will be magnetically guided, which will provide focusing and control of power deposition location.

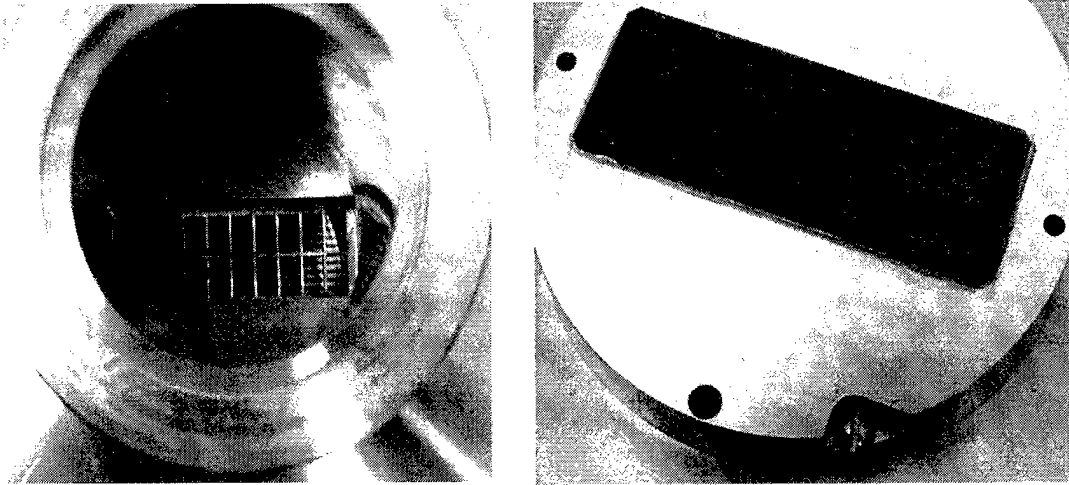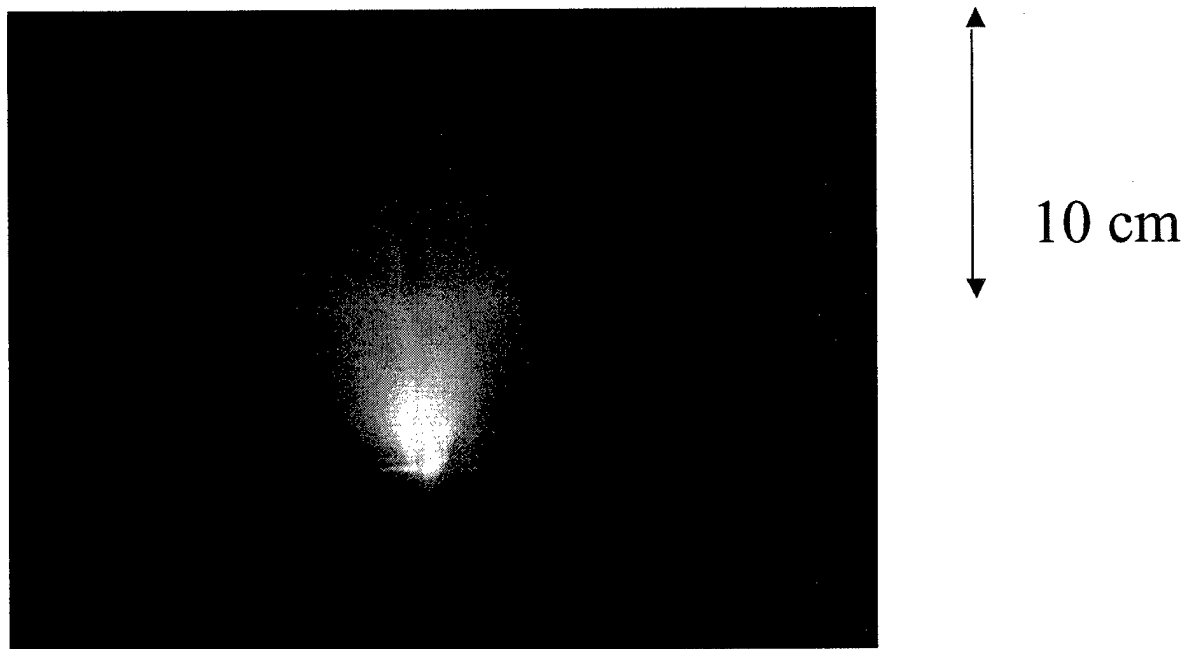**Fig. 1**. SiN window array.

Fig. 2. Helium plasma at 250 Torr generated by 25 keV electron beam passing through the SiN window array.
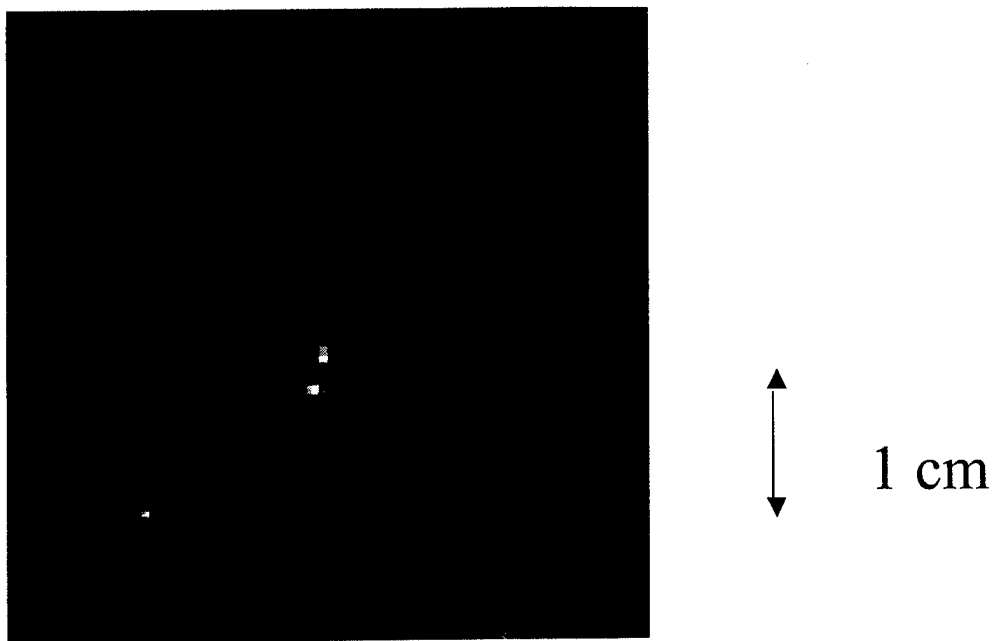
Fig. 3. Air plasma at 1 atm generated by 25 keV electron beam passing through the SiN window array.

APPENDIX

Publications:

Books and book chapters with full or partial MURI support

OSU:

1. V. V. Subramaniam, and S. M. Aithal, Chapter 9, "Laser-Assisted and Optical Pumping Techniques for Diamond Synthesis," pp. 325-423, in Diamond Films Handbook, edited by J. Asmussen, and D. Reinhard, ISBN 0-8247-9577-6, Marcel Dekker, Inc., New York, 2002.

Princeton:

2. G. G. Chernyi, S. A. Losev, S. O. Macheret, and B. V. Potapkin, *Physical and Chemical Processes in Gas Dynamics: Cross Sections and Rate Constants*, Progress in Astronautics and Aeronautics, Volume 196, AIAA Publishers, 2002.

Journal papers with full or partial MURI support

OSU:

3. W. Lee and W. R. Lempert, "Spectrally Filtered Raman/Thomson Scattering Using a Rubidium Vapor Filter", Accepted for Publication in **AIAA Journal**.

4. E. Plönjes, P. Palm, J.W. Rich, and I.V. Adamovich, "Electron-Mediated Vibration-Electronic (V-E) Energy Transfer in Optically Pumped Plasmas", **Chemical Physics,** Vol. 279, pp. 43-54, 2002

5. E. Plönjes, P. Palm, G.B. Viswanathan, V.V. Subramaniam, I.V. Adamovich, W.R. Lempert, H.L. Fraser, J.W. Rich, "Synthesis of single-walled carbon nanotubes in vibrationally nonequilibrium carbon monoxide", **Chemical Physics Letters**, vol. 352, No. 5-6, pp. 342-347, 2002

6. P. Palm, E. Plönjes, M. Buoni, V.V. Subramaniam, and I.V. Adamovich, "Electron Density and Recombination Rate Measurements in CO-Seeded Optically Pumped Plasmas", **Journal of Applied Physics,** vol. 89, issue 11, pp. 5903-5910, 2001

7. E. Plönjes, P. Palm, W. Lee, W.R. Lempert, and I.V. Adamovich, "RF Energy Coupling to High-Pressure Optically Pumped Nonequilibrium Plasmas", **Journal of Applied Physics,** vol. 89, issue 11, pp. 5911-5918, 2001

8. J.L. Lilly and V.V. Subramaniam, "A Cold Thermionically Emitting Dusty Air Plasma Formed by Radiative Heating of Graphite Particulates", **IEEE Transactions on Plasma Science**, vol. 29, No. 6, 2001, pp. 927-934

9. W. Lee, I.V. Adamovich, and W.R. Lempert, "Optical Pumping Studies of Vibrational Energy Transfer in High-Pressure Diatomic Gases", **Journal of Chemical Physics**, vol. 114, No. 13, 2001, pp. 1178-1186

10. I.V. Adamovich, "Control of Electron Recombination Rate and Electron Density in Optically Pumped Nonequilibrium Plasmas", **Journal of Physics D**: Applied Physics, vol. 34, 2001, pp.319-325

11. E. Plönjes, P. Palm, I.V. Adamovich, and J.W. Rich, "Ionization Measurements in Optically Pumped Discharges", **Journal of Physics D: Applied Physics**, vol. 33, No. 16, pp. 2049-2056, 2000

12. Yano. R., Contini, V., Ploenjes, E., Palm, P., Merriman, S., Aihal, S., Adamovich, I., Lempert. W., Subramaniam. V., and Rich, J.W., "Supersonic Nonequilibium Plasma Wind Tunnel Measurements of Shock Modification and Flow Visualization", **AIAA Journal**, vol. 38, No. 10, 2000, pp. 1879-1888

13. S. Aithal and V.V. Subramaniam, "On the Characteristics of a Spark Generated Shock Wave", **Physics of Fluids**, vol. 12, No. 4, 2000, pp. 924-934

14. E. Plönjes, P. Palm, W. Lee, M. D. Chidley, I.V. Adamovich, W.R. Lempert, and J. William Rich, "Vibrational Energy Storage in High-Pressure Mixtures of Diatomic Molecules", **Chemical Physics**, vol. 260, pp. 353-366, 2000

Princeton:

15. S. O. Macheret and I. V. Adamovich, "Semiclassical Modeling of State-Specific Dissociation Rates in Diatomic Gases," **J. Chem. Phys.**, 2000, Vol. 113, No. 17, p. 7351.

16. S. O. Macheret, M. N. Shneider, and R. B. Miles, "Modeling of Discharges Generated by Electron Beams in Dense Gases: Fountain and Thunderstorm Regimes", **Physics of Plasmas**, 2001, Vol. 8, No. 5, pp. 1518-1528.

17. S. O. Macheret, M. N. Shneider, and R. B. Miles, "Modeling of Air Plasma Generation by Repetitive High-Voltage Nanosecond Pulses," **IEEE Transactions on Plasma Science**, June 2002.

18. J. H. Grinstead, P. F. Barker, "Coherent Rayleigh Scattering," *Phys. Rev. Lett.*, 85, 1222, 2000

19. P. F. Barker and M. N. Shneider, "Drift and Optical Landau Damping with Periodic Dipole Forces," *Phys. Rev.* A 64, 033408, 2001.

20. X. Pan, P.F. Barker, A. Meschanov, J.H. Grinstead, M.N. Shneider, and R.B. Miles, "Temperature Measurements by Coherent Rayleigh Scattering," **Opt. Lett.**, Vol. 27, No. 3, p. 161, 2002

21. S.H. Zaidi, Z. Tang, A.P. Yalin, P. Barker, and R.B. Miles, "Filtered Thomson Scattering in an Argon Plasma," *AIAA Journal*, 2002, Vol. 40, No. 6, pp. 1087-1093

22. X. Pan, M.N. Shneider, and R.B. Miles, "Coherent Rayleigh-Brillouin Scattering," accepted in **Phys. Rev. Lett.**, 2002.

Conference Papers with full or partial MURI support

OSU:

23. P. Palm, E. Plönjes, I. Adamovich, and J.W. Rich, "Mitigation of electron attachment and recombination in atmospheric pressure air plasmas", AIAA 2002-2224, 33rd AIAA Plasmadynamics and Lasers Conference, May 2002, Maui, HI

24. W. Lee and W. R. Lempert, "Rubidium Vapor Filter Spectrally Filtered Thomson Scattering," AIAA-2002-3236, 22nd AIAA Aerodynamic Measurement Technology and Ground Testing Conference, St. Louis, MS, June 24-26, 2002.

25. J.W. Rich, E. Plönjes, P. Palm, and I. Adamovich, "High-power CO lasers and some recent applications", SPIE's International Symposium on High-Power Laser Ablation 2002, April 2002, Taos, NM

26. K.Frederickson, P. Palm, E. Ploenjes, I. Adamovich, J.W. Rich, and W. Lempert, "Singlewalled carbon nanotube synthsis, by anharmonic V-V pumping," American Chemical Society Spring Meeting, Orlando, FL, March, 2002.

27. P. Palm, E. Plönjes, I.V. Adamovich, and J.W. Rich, "E-Beam Sustained Low Power Budget Air Plasmas", AIAA 2002-0637, 40th AIAA Aerospace Sciences Meeting & Exhibit, 14-17 January 2002 / Reno, NV

28. R. J. Leiweke and W. R. Lempert, "CO/Helium Glow Discharge Temperature Measurments Using CO 4th Positive Band LIF, Paper AIAA-2002-0397, 40th AIAA Aerospace Sciences Meeting, Reno, NV, January 14-17,2002.

29. W. Lee and W. R. Lempert, "Rubidium Vapor Filter Spectrally Filtered Raman/Thomson Scattering, Paper AIAA-2002-0394, 40th AIAA Aerospace Sciences Meeting, Reno, NV, January 14-17,2002.

30. P. Palm, E. Ploenjes, I.V. Adamovich, V.V. Subramaniam, J.W. Rich, "Optically Enhanced E-Beam Sustained Air Plasmas", Paper JWP.079, 54th Annual Gaseous Electronics Conference, October 2001, State College, PA

31. E. Ploenjes, P. Palm, J.W. Rich, I.V. Adamovich, "Electron-Mediated Vibration-Electronic (V-E) Energy Transfer in Optically Pumped Plasmas", Paper JWP.081, 54th Annual Gaseous Electronics Conference, October 2001, State College, PA

32. P. Palm, E. Ploenjes, W. Lee, K. Frederickson, W.R. Lempert, J.W. Rich, I.V. Adamovich, "RF Energy Coupling to Atmospheric Pressure Nonequilibrium Plasmas", 15th International Symposium on Plasma Chemistry, Orleans, 2001

33. E. Ploenjes, K. Frederickson, P. Palm, G.B. Viswanathan, I.V. Adamovich, V.V. Subramaniam, W.R. Lempert, H.L. Fraser, J.W. Rich, "Single-Walled Carbon Nanotube Synthesis in CO Laser Pumped

Carbon Monoxide Plasmas", Paper JWP.082, 54th Annual Gaseous Electronics Conference, October 2001, State College, PA

34. W. Lee and W.R. Lempert, ""Spectrally Filtered Raman/Thomson Scattering Measurements in High Pressure Plasmas," 54nd Annual Gaseous Electronics Conference, October 9-12, 2001, State College, PA.

35. E. Ploenjes, P. Palm, G.B. Viswanathan, K. Frederickson, I.V. Adamovich, V.V. Subramaniam, W.R. Lempert, H.L. Fraser, J.W. Rich, "Single-Walled Carbon Nanotube Synthesis in a Nonequilibrium Carbon Monoxide Plasma", 15th International Symposium on Plasma Chemistry, Orleans, 2001

36. P. Palm, E. Ploenjes, I.V. Adamovich, W.R. Lempert, J.W. Rich, "Electron-Beam Sustained Plasmas in Optically pumped Atmospheric Pressure Air", ICOPS 2001, Pulsed Power Plasma Science Conference, June 2001, Las Vegas, NV

37. P. Palm, E. Ploenjes, M. Buoni, V.V. Subramaniam, J.W. Rich, I.V. Adamovich, "Electron Removal Rate Modification in Optically Pumped Plasmas", ICOPS 2001, Pulsed Power Plasma Science Conference, June 2001, Las Vegas, NV

38. W.R. Lempert, R.J. Leiweke, and W. Lee, "Temperature Measurements in Nonequilibrium Plasmas, 27th International Conference on Plasma Science, Las Vegas, NV, June 18-22, 2001.

39. E. Ploenjes, P. Palm, G.B. Viswanathan, I.V. Adamovich, V.V. Subramaniam, H.L. Fraser and J.W. Rich, "Single-Walled Carbon Nanotube Formation in a High-Pressure Nonequilibrium Carbon Monoxide Plasma", ICOPS 2001, Pulsed Power Plasma Science Conference, June 2001, Las Vegas, NV

40. P. Palm, E. Plönjes, I. Adamovich, and J. W. Rich, "High Pressure Air Plasmas Sustained by Electron Beam and Enhanced by Optical Pumping", AIAA 2001-2937, 32nd AIAA Plasmadynamics and Lasers Conference, June 2001, Anaheim, CA

41. R.J. Leiweke and W.R. Lempert, "Optically-Pumped Co Lif Temperature Measurements Using the $A^1\Pi \rightarrow X^1\Sigma+$ 4th Positive Bands", Paper 2001-2936, presented at 32nd AIAA Plasmadynamics and Lasers Conference, Anaheim, CA, 11-14 June 2001.

42. E. Plönjes, P. Palm, G.B. Viswanathan, K. Frederickson, I. Adamovich, V. Subramaniam, W. R. Lempert, H.L. Fraser and J. Rich, "Single-Walled Carbon Nanotube Production in CO Laser Pumped Carbon Monoxide Plasmas", AIAA 2001-2942, 32nd AIAA Plasmadynamics and Lasers Conference, June 2001, Anaheim, CA

43. E. Plönjes, P. Palm, J. W. Rich, and I. V. Adamovich, "Electron-mediated Vibration-Electronic (V-E) Energy Transfer in Optically Pumped Plasmas", AIAA 2001-3180, 32nd AIAA Plasmadynamics and Lasers Conference, June 2001, Anaheim, CA

44. P. Palm, E. Plönjes, M. Buoni, V. V. Subramaniam, I. V. Adamovich, and J. W. Rich "Electron-beam generated high pressure air plasmas enhanced by optical pumping" AIAA Paper 2001-0346, 39th AIAA Aerospace Sciences Meeting and Exhibit, January 2001, Reno, NV

45. P. Palm, E. Plönjes, W. Lee, K. Frederickson, W. R. Lempert, and I. V. Adamovich, "RF energy coupling to high-pressure optically pumped nonequilibrium plasmas", AIAA Paper 2001-0637, 39th AIAA Aerospace Sciences Meeting and Exhibit, January 2001, Reno, NV

46. E. Plönjes, P. Palm, I.V. Adamovich, V.V. Subramaniam, J.W. Rich, G.B. Viswanathan, H.L. Fraser "Carbon Nanotube Production in CO Laser Pumped Carbon Monoxide Plasmas", AIAA Paper 2001-0651, 39th AIAA Aerospace Sciences Meeting and Exhibit, January 2001, Reno, NV

47. P. Palm, E. Ploenjes, I. Adamovich, and J. W. Rich, "High-Pressure Unconditionally Stable Nonequilibrium Molecular Plasmas", Paper LR1.003, 53rd Annual Gaseous Electronics Conference, October 2000, Houston, TX

48. W.R. Lempert, W. Lee, R. Leiweke, and I. Adamovich, "Spectroscopic Measurements of Temperature and Vibrational Distribution Function in Weakly Ionized Gases," Paper AIAA-2000-2451, 21st Aerodynamic Measurement Technology and Ground Testing Conference, Denver, CO, June 19 - 22, 2000.

49. E. Ploenjes, P. Palm, V. Subramaniam, I. Adamovich, J.W. Rich, B. Viswanathan, and H. Fraser, "Carbon Nanotube Production in CO Laser Pumped Carbon Monoxide Plasmas", Paper JWP.033, 53rd Annual Gaseous Electronics Conference, October 2000, Houston, TX

50. E. Ploenjes, P. Palm, W. Lee, I.V. Adamovich, W.R. Lempert, and J.W. Rich, "Vibrational Energy Storage in High-Pressure Mixtures of Diatomic Molecules", V International School-Seminar "Nonequilibrium Processes and Their Applications", September 2000, Minsk, Belarus

51. E. Ploenjes, P. Palm, I.V. Adamovich, and J.W. Rich, "Control of Stability and Electron Removal Rate in Optically Pumped RF Discharges", V International School-Seminar "Nonequilibrium Processes and Their Applications", September 2000, Minsk, Belarus

52. R. Leiweke, W. Lee, and W.R. Lempert, "Single Photon Planar Laser Induced Fluorescence Imaging of Vibrationally Excited Carbon Monoxide, " Paper AIAA-2000-0199, 38th AIAA Aerospace Sciences Meeting, Reno, NV. Jan 10 - 13, 2000.

53. A.R. White, K.A. Essenhigh, I. Adamovich, W. Lempert, and V.V. Subramaniam, "Effects of Thermal Gradients on the Propagation of Spark Generated Shock Waves, Paper AIAA-99-4855, 9th AIAA International Space Planes and Technologies Conference, Norfolk, VA, Nov 1 - 5, 1999.

54. E. Ploenjes, P. Palm, I.V. Adamovich, J.W. Rich, "Energy Transfer Processes between Diatomic Molecules in Optically Pumped Plasmas", XXIV International Conference on Phenomena in Ionized Gases (ICPIG), July 1999, Warsaw, Poland

55. Ploenjes, E., Palm, P., Adamovich, I.V., and Rich, J.W., "Control of Stability and Electron Removal Rate in Optically Pumped RF Discharges" Paper 99-3665, AIAA 30th Plasmadynamics and Lasers Conference, Norfolk, VA, June 1999

56. J. Eastman, K. Essenhigh, S.Merriman, I.V. Adamovich, and W.R. Lempert, "Guiding of Electric Discharges by a Continuous Wave CO Laser," Paper AIAA-99-3481, 30th AIAA Plasmadynamics and Lasers Conference, Norfolk, VA, June 28 - July 1, 1999.

57. W. Lee, M. Chidley, R. Leiweke, I. Adamovich, and W.R. Lempert, "Determination of O_2 and N_2 Vibrational State Distributions in CO Laser-Sustained Plasmas," Paper AIAA-99-3723, 30th AIAA Plasmadynamics and Lasers Conference, Norfolk, VA, June 28 - July 1, 1999.

58. A.R. White, W.C. Lee, I.V. Adamovich, V. V. Subramaniam, W. Lempert, J.W. Rich, "Shock Propagation through a Thomson Discharge", paper IWP4.34 presented at 52st Annual Gaseous Electronics Conference, October 5-8, 1999, Norfolk, VA.

59. W.R. Lempert, R. Leiweke, and I. Adamovich, "CO Planar Laser Induced Fluorescence Imaging in Laser Sustained Plasmas," 52nd Annual Gaseous Electronics Conference, October 5-8, 1999, Norfolk, VA.

60. Ploenjes, E., Palm, P, Lee, W., Chidley, M. D., Adamovich, I.V., Lempert, W.R., and Rich, J.W., "Vibrational Energy Storage in High Pressure Mixtures of Diatomic Molecules", Paper 99-3480, AIAA 30th Plasmadynamics and Lasers Conference, Norfolk, VA, June 1999

61. Adamovich, I., Chidley, M., Lee, W., Lempert, W., Palm P., Ploenjes, E., and Rich, J.W., "Large Scale Laser-Pumped Optical Discharges", Paper 99-3722, AIAA 30th Plasmadynamics and Lasers Conference, Norfolk, VA, June 1999

62. R. Yano, S. M. Aithal, V. V. Subramaniam, V. Contini, P. Palm, S. Merriman, I. Adamovich, W. Lempert, and J. W. Rich "Experimental characterization of shock dispersions in weakly ionized nonequilibrium plasmas", AIAA Paper 99-3671, AIAA 30th Plasmadynamics and Lasers Conference, Norfolk, VA, June 1999

63. E. Ploenjes, P. Palm, I.V. Adamovich, J.W. Rich, "Stability and Electron Loss Rate Control in Optically Pumped Plasmas", paper ETP1.17, 52nd Annual Gaseous Electronics Conference, October 1999, Norfolk, VA

64. I.V. Adamovich, M. Chidley, E. Ploenjes, P. Palm, J.W. Rich, "Cold Atmospheric Pressure Plasmas Created by Resonance Laser Optical Pumping", paper NR2.06, 52nd Annual Gaseous Electronics Conference, October 1999, Norfolk, VA

65. E. Ploenjes, P. Palm, I.V. Adamovich, J.W. Rich, "RF-enhanced Nonequilibrium Ionization in Optically Pumped Plasmas", XXIV International Conference on Phenomena in Ionized Gases (ICPIG), July 1999, Warsaw, Poland

66. E. Plönjes, I. Adamovich, P. Palm, and J.W. Rich, "Vibration-Vibration Energy Transfer and Associative Ionization of CO in Optically Pumped Plasmas", paper GT13, 51st Annual Gaseous Electronics Conference & 4th International Conference on Reactive Plasmas, October 1998, Maui, Hawaii

67. I.V. Adamovich, E. Plönjes, P. Palm, J.W. Rich, and A. Chernukho, "Modeling of Vibration-to-Vibration and Vibration-to-Electronic Energy Transfer Processes in Optically Pumped Plasmas", paper presented at 51st Annual Gaseous Electronics Conference & 4th International Conference on Reactive Plasmas, October 1998, Maui, Hawaii

Princeton:

69. S. O. Macheret, "Molecular Dissociation at High Temperatures", *Paper AIAA-97-2501.*

70. S. O. Macheret and I. V. Adamovich, "Nonequilibrium Dissociation at High Temperature: the Role of Vibrational and Rotational Energy," *Paper AIAA 99-0351.*

71. S. O. Macheret, M. N. Shneider, and R. B. Miles, "New Types of Electron Beam Generated Electric Discharges in Dense Gases: a "Fountain" and a "Thunderstorm"", *Paper AIAA 99-3721.*

72. S. O. Macheret, P. F. Barker, K. Waichman, R. B. Miles, E. Ploenjes, P. Palm, I. V. Adamovich, W. R. Lempert, and J. W. Rich, "Optically Pumped and Controlled Electric Discharges", *Paper AIAA 99-3636.*

73. S. O. Macheret, Y. Z. Ionikh, L. Martinelli, P. F. Barker, and R. B. Miles, "External Control of Plasmas for High-Speed Aerodynamics," *Paper AIAA 99-4853.*

74. S. O. Macheret, M. N. Shneider, and R. B. Miles, "Modeling of Air Plasma Generation by Electron Beams and High-Voltage Pulses," Paper AIAA 2000-2569, presented at 31st AIAA Plasmadynamics and Lasers Conference, June 2000, Denver, CO.

75. S. O. Macheret, M. N. Shneider, and R. B. Miles, "Energy-Efficient Generation of Nonequilibrium Plasmas and Their Applications to Hypersonic MHD Systems," Paper AIAA 2001-2880, presented at 32nd AIAA Plasmadynamics and Lasers Conference, June 2001, Anaheim, CA

76. S. O. Macheret, M. N. Shneider, and R. B. Miles, "Modeling of Plasma Generation in Repetitive Ultra-Short High-Power DC, Microwave, and Laser Pulses," Paper AIAA 2001-2940, presented at 32nd AIAA Plasmadynamics and Lasers Conference, June 2001, Anaheim, CA

77. Tang Z., Zaidi S.H., Miles R.B., "Density gradient rubidium dispersive absorption filter for low wave number Raman and Thomson scattering," Paper AIAA 2000-0644, 38th Aero. Scien. Meeting and Exhib., 10-13 January, 2000, Reno, NV.

78. S. H. Zaidi, Z. Tang, A. Yalin, P. Barker, and R. B. Miles, "Filtered Thomson Scattering in an Argon Plasma," Paper AIAA 2001-0415, presented at 39th AIAA Aerospace Sciences Meeting and Exhibit, January 2001, Reno, NV

79. X. Pan, P. F. Barker, A. V. Meschanov, R. B. Miles, and J. H. Grinstead, "Temperature Measurements in Plasmas Using Coherent Rayleigh Scattering," Paper AIAA 2001-0416, presented at 39th AIAA Aerospace Sciences Meeting and Exhibit, January 2001, Reno, NV

80. S. O. Macheret, M. N. Shneider, and R. B. Miles, "Dynamics of Plasmas Sustained by Repetitive Ultrahigh-Voltage DC, Microwave, or Laser Pulses," ICOPS 2001, Pulsed Power Plasma Science Conference, June 2001, Las Vegas, NV

81. M. N. Shneider, S. O. Macheret, and R. B. Miles, "Properties of Electron Beam Generated Steady-State Weakly Ionized Plasma in Air," ICOPS 2001, Pulsed Power Plasma Science Conference, June 2001, Las Vegas, NV

82. S. H. Zaidi, Z. Tang, A. Yalin, P. Barker, and R. B. Miles, "Rubidium Filtered Thomson Scattering Measurement in an Atmospheric Pressure Argon Arc," ICOPS 2001, Pulsed Power Plasma Science Conference, June 2001, Las Vegas, NV

83. X. Pan, L. Qian, M. N. Shneider, and R. B. Miles, "Plasma Measurements Using Ponderomotive Forces to Perturb the Translational Motion of Particles," ICOPS 2001, Pulsed Power Plasma Science Conference, June 2001, Las Vegas, NV

84. R. B. Miles, S. O. Macheret, and M. N. Shneider, "High Efficiency Nonequilibrium Plasmas Sustained by High-Energy Electrons," ICOPS 2001, Pulsed Power Plasma Science Conference, June 2001, Las Vegas, NV

85. S. O. Macheret, M. N. Shneider, and R. B. Miles, "Efficient Generation of Nonequilibrium Plasmas by High-Energy Electrons," The Third Workshop on Magneto- and Plasma Aerodynamics for Aerospace Applications, Institute of High Temperatures, Russian Academy of Sciences, Moscow, 24 - 26 April 2001